

**Photochemistry and Ultrafast Dynamics of
Mass-selected Multinuclear Coinage Metal Complexes
Studied by Electronic Photodissociation Ion Spectroscopy
in an Ion Trap**

Vom Fachbereich Chemie der Technischen Universität Kaiserslautern zur
Verleihung des akademischen Grades „Doktor der Naturwissenschaften“
genehmigte Dissertation

(D 386)



vorgelegt von

Dipl.-Chem. Sebastian Volker Kruppa

geboren in Tübingen

Betreuer: Priv.-Doz. Dr. C. Riehn

Datum der wissenschaftlichen Aussprache: 15.01.2021

Die vorliegende Arbeit wurde im Zeitraum von April 2015 bis Oktober 2020 im Fachbereich Chemie der Technischen Universität Kaiserslautern unter Betreuung von Priv.-Doz. Dr. C. Riehn angefertigt.

Datum des Antrags der Eröffnung des Promotionsverfahrens: 06.07.2020

Promotionskommission:

Vorsitzender	Prof. Dr. W. R. Thiel
1. Berichterstatter	Priv.-Doz. Dr. C. Riehn
2. Berichterstatter	Prof. Dr. Dr. G. Niedner-Schatteburg

Meinen Eltern gewidmet

*„Chemistry is a science of
analogies and coincidence“*

- Pekka Pyykkö -

List of Publications

This thesis is based on the following publications.

Publication 1:

„Ultrafast Excited-State Relaxation of a Binuclear Ag(I) Phosphine Complex in Gas Phase and Solution“

S. V. Kruppa, F. Bappler, W. Klopper, S. P. Walg, W. R. Thiel, R. Diller, C. Riehn
Physical Chemistry Chemical Physics, 2017, 19(34), 22785-22800

doi: 10.1039/C7CP04128D

Publication 2:

„Vibrational Coherence Controls Molecular Fragmentation: Ultrafast Photodynamics of the [Ag₂Cl]⁺ Scaffold“

S. V. Kruppa, F. Bappler, C. Holzer, W. Klopper, R. Diller, C. Riehn
The Journal of Physical Chemistry Letters, 2018, 9(4), 804-810

doi: 10.1021/acs.jpcllett.7b03167

Publication 3:

„Photoinitiated Charge Transfer in a Triangular Silver(I) Hydride Complex and its Oxophilicity“

S. V. Kruppa, C. Gro, X. Gui, F. Bappler, B. Kwasigroch, Y. Sun, R. Diller, W. Klopper, G. Niedner-Schatteburg, C. Riehn, W. R. Thiel

Chemistry A European Journal, 2019, 25(48), 11269-11284

doi: 10.1002/chem.201901981

Publication 4:

„Gas-Phase Photoluminescence and Photodissociation of Silver-Capped Hexagold Clusters“

J.-F. Greisch, A. Ballester-Caudet, S. V. Kruppa, Z. Lei, Q.-M. Wang, C. Riehn, F. Remacle

The Journal of Physical Chemistry A, 2018, 122(27), 5799-5810

doi: 10.1021/acs.jpca.8b01864

Publication 5:

„Fragmentation pathways of dianionic [Pt₂(μ-P₂O₅H₂)₄+X,Y]²⁻ (X,Y = H, K, Ag) species in an ion trap induced by collisions and UV photoexcitation“

S. V. Kruppa, Y. Nosenko, M.-O. Winghart, S.P. Walg, M.M. Kappes, C. Riehn

International Journal of Mass Spectrometry, 2016, 395, 7-19

doi: 10.1016/j.ijms.2015.11.007

Conference Proceedings:

1. „*Ultrafast Vibrational and Electronic Dynamics of Metal-Metal Interactions Studied by Transient Photo-Induced Dissociation (Gas Phase) and Transient Absorption (Solution)*”
S. V. Kruppa, F. Bäßler, Y. Nosenko, S. P. Walg, R. Diller, C. Riehn
Conference Proceedings, XX International Conference on Ultrafast Phenomena (UP 2016), Santa Fe, USA, OSA Technical Digest, 2016, paper UW4A.33
doi: 10.1364/UP.2016.UW4A.33
2. „*Excited state vibrational coherence in a binuclear metal adduct: wave packet phase dependant molecular fragmentation under variation of ligand size*”
S. V. Kruppa, F. Bäßler, C. Holzer, F. Dietrich, R. Diller, W. Klopper, C. Riehn
Conference Proceedings, XXI International Conference on Ultrafast Phenomena (UP 2018), Hamburg, Germany, EPJ Web Conf., 2019, 205, 09019
doi: 10.1051/epjconf/201920509019

The following publications incidentally emerged from scientific cooperations.

Joined Publications:

1. „*Time-resolved photoelectron spectroscopy of a dinuclear Pt(II) complex: Tunneling autodetachment from both singlet and triplet excited states of a molecular dianion*”
M.-O. Winghart, J.-P. Yang, M. Vonderach, A.-N. Unterreiner, D.-L. Huang, L.-S. Wang, S. Kruppa, C. Riehn, M.M. Kappes
The Journal of Chemical Physics, 2016, 144, 054305
doi: 10.1063/1.4940795
2. „*Bimetallic d¹⁰-Metal Complexes of a Bipyridine Substituted N-Heterocyclic Carbene*”
C. Kaub, S. Lebedkin, A. Li, S. V. Kruppa, P. H. Strebart, M. M. Kappes, C. Riehn, P.W. Roesky
Chemistry A European Journal, 2018, 24(23), 6094-6104
doi: 10.1002/chem.201705757

List of Abbreviations and Acronyms

AC	Alternating current
API	Atmospheric pressure ionization
BBO	β -barium borate (BaB_2O_4)
cc	Cross correlation
CEM	Channel electron multiplier
CI	Chemical ionization
CID	Collision-induced dissociation
CMC	Coinage metal complex
CPA	Chirped-pulse amplification
CRM	Charge residue mechanism
CT	Charge transfer
cw	Continuous wave
Cy	Cyclohexyl, C_6H_{11} -
DC	Direct current
DPSS	Diode-pumped solid state laser
EA	Electron affinity
EC	Electron capture ionization
EI	Electron impact ionization
ESI	Electrospray ionization
ETD	Electron transfer dissociation
ETR	Electron transfer reduction
FA	Fluoranthene, $\text{C}_{16}\text{H}_{10}$

FC	F ranck- C ondon
fs	F emto s econd (1fs = 10 ⁻¹⁵ s)
FT	F ourier t ransform
fwhm	F ull w idth at h alf m aximum
GVD	G roup velocity d ispersion
HOMO	H ighest o ccupied m olecular o rbital
IC	I nternal c onversion
ICC	I on c harge c ontrol
IE	I onization e nergy
IEM	I on e vaporation m echanism
IR(M)PD	I nfrared (m ultiple) p hoton d issociation
ISC	I ntersystem c rossing
IVR	I tramolecular v ibrational e nergy r edistribution
KIT	K arlsruhe I nstitute of T echnology
KLM	K err- l ens m odelocking
Laser	L ight a mplification by s timulated e mission of r adiation
LC	L igand- c entered
LM(M)CT	L igand-to- m etal(- m etal) c harge t ransfer
LUMO	L owest u noccupied m olecular o rbital
MC	M etal- c entered
Me	M ethyl, CH ₃ -
MLCT	M etal-to- l igand c harge t ransfer
MMCT	M etal-to- m etal c harge t ransfer

MS	Mass spectrometer / mass spectrometry
MS-1	<i>„amaZon speed“ mass spectrometer (Bruker Daltonics)</i>
MS-2	<i>„amaZon ETD“ mass spectrometer (Bruker Daltonics)</i>
<i>m/z</i>	Mass-to-charge ratio
nCI	Negative chemical ionization
Nd:YAG	Neodymium (Nd³⁺):yttrium aluminium garnet (Y₃Al₅O₁₂)
NHC	N-heterocyclic carbene
NIR	Near infrared
OC	Output coupler
OPA	Optical parametric amplifier/amplification
PD	Photodissociation
PEEK	Polyether ether ketone polymer
PES	Photoelectron spectroscopy /
(PH)OLED	(Phosphorescent) organic light-emitting diode
PL	Photoluminescence
ps	Picosecond (1ps = 10⁻¹² s)
QIT, 3D-QIT	<i>Paul</i> -type (three-dimensional) quadrupole ion trap
RC	Reaction coordinate
RE	Resonant excitation/ejection
RF	Radiofrequency
RM	Rear mirror
RRKM	Rice-Ramsperger-Kassel-Marcus theory
SOC	Spin-orbit coupling

TA	Transient absorption
Ti:Sa	Titanium (Ti³⁺):sapphire (Al₂O₃)
TM	Transition metal
τ-PD	Transient photodissociation
TUK	Technische Universität Kaiserslautern
UV	Ultraviolet
Vis	Visible
WLC	White-light continuum
YAG	Yttrium aluminium garnet (Y₃Al₅O₁₂)
YLF	Yttrium lithium fluoride (YLiF₄)

Table of Contents

Part I: Introduction, Theoretical Background and Methodology

1. Femtochemistry of Transition Metal Complexes	1
2. The Metallophilicity Phenomenon.....	7
3. Aim and Motivation.....	13
4. Outline.....	19
4.1. Publication 1 (PCCP)	20
4.2. Publication 2 (JPCLett).....	21
4.3. Publication 3 (ChemEur)	22
4.4. Publication 4 (JPCA)	23
4.5. Publication 5 (IJMS).....	24
5. Electronic Photodissociation Ion Spectroscopy	27
5.1. Static UV-PD action spectroscopy.....	27
5.2. Transient photodissociation (τ -PD) detection scheme	35
6. Experimental Setup and Methods	47
6.1. Quadrupole ion trap mass spectrometer (QIT-MS)	47
6.1.1. Electrospray ionization (ESI) ion source.....	49
6.1.2. Ion transfer optics	52
6.1.3. Negative chemical ionization (nCI) source.....	54
6.1.4. Working principle of Paul type ion trap and mass analysis	55
6.1.5. Detector unit.....	61
6.1.6. Mass isolation and tandem MS (MS^n).....	62
6.1.7. Modifications of MS-1	63
6.2. Femtosecond laser system	66
6.2.1. Principle of mode-locked laser operation.....	66
6.2.2. Ti:Sa gain medium	70

6.2.3.	Kerr-lens mode-locking (KLM)	70
6.2.4.	Optical chirp	72
6.2.5.	Ti:Sa oscillator system.....	74
6.2.6.	Chirped-pulse amplification (CPA)	76
6.2.7.	Ti:Sa regenerative CPA system (<i>Wyvern 1000</i>).....	77
6.2.8.	Wavelength converter system (<i>TOPAS-C</i>).....	80
6.2.9.	Overview of PD/ τ -PD experimental setup.....	84
7.	Danksagung	87
8.	References.....	91

Part II: Published Work

Publication 1 (PCCP)
 Publication 2 (JPCLett)
 Publication 3 (ChemEurJ)
 Publication 4 (JPCA)
 Publication 5 (IJMS)
 Conference Proceedings
 Joined Publications

Appendix

Curriculum Vitae
 Eidstattliche Erklärung

***Part I: Introduction, Theoretical Background and
Methodology***

1. Femtochemistry of Transition Metal Complexes

At the fundamental atomic level, chemical reactions, that is, the transformation from reactants into products, emanate from ultrafast dynamic primary processes that involve the breaking and formation of chemical bonds along with changes in electronic and structural configurations, proceeding on the timescale of molecular vibrations within tens to hundreds of femtoseconds ($1 \text{ fs} = 10^{-15} \text{ s}$). Consequently, one major goal in the field of chemistry is to obtain a „molecular movie“ of a chemical reaction, by following the evolution of an elementary process along its reaction pathway in real time. This should lead to a deeper insight into reaction mechanisms and intermediate states governing chemical reactivity.

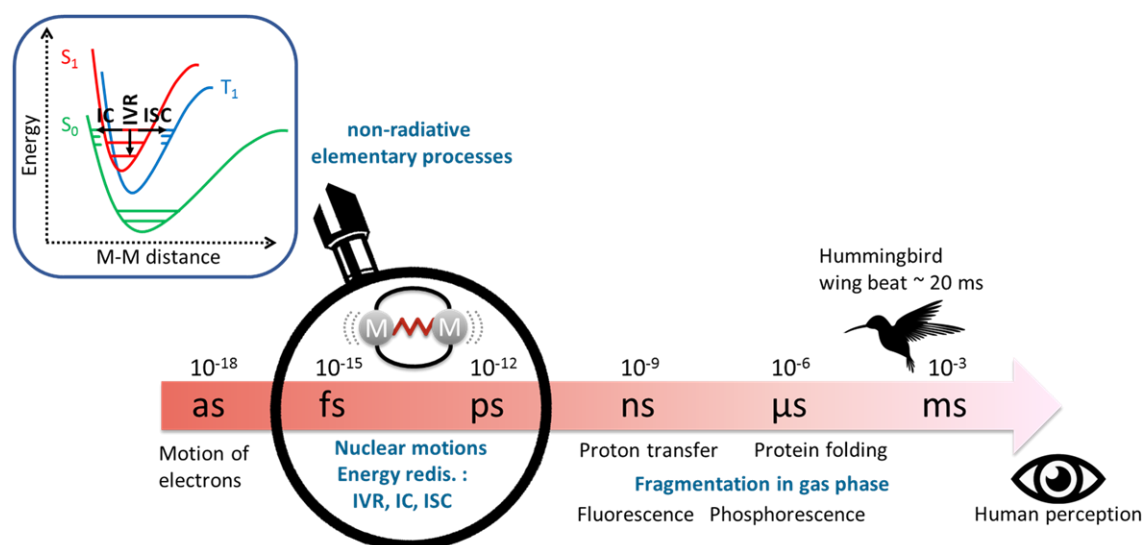


Fig. 1.1 Typical timescales of dynamical example phenomena highlighting ultrafast *nonradiative* elementary processes. Inset: illustrated singlet/triplet state potential curves for bimetallic complexes featuring metallophilic contacts (see chapter 2) as a function of metal-metal distance. Sketches taken from Refs. [1-3].

The growing field of *Femtochemistry*, which was pioneered by the 1999 Nobel laureate *Ahmed Zewail* [4-7], is concerned with the exploration of ultrafast reaction dynamics [8], especially within the transition-state region of molecular elementary reactions (short-lived transient states), following the motion of electrons and atomic nuclei with fs time resolution. The major focus of this research area lies on

the investigation and tracking of light-induced ultrafast processes (excited-state dynamics), where photons represent reagents or products of photochemical reactions [9]. The reason for using (laser) light as the „tool of choice“ originates in the advent of sophisticated optical techniques that can readily produce and amplify femtosecond laser pulses (pulse duration $t_p < 100$ fs, see chapter 6.2) in combination with the high speed of light (in vacuum, $c \approx 3 \cdot 10^8$ m/s), which in turn facilitates the measurement of ultrafast excited-state relaxation processes, by utilizing a so called „*pump-probe*“ scheme [5].

In a *pump-probe* spectroscopic experiment (see chapter 5.2) an ultrashort optical „*pump*“ pulse resonantly excites an ensemble of molecules, initiating the ensuing excited-state relaxation dynamics and photo-reactions, and serves as a temporal reference point („*time zero*“, t_0). After a specified time delay (Δt) the dynamic excited-state population is interrogated by a second „*probe*“ pulse, whose time delay with respect to the *pump* pulse is controlled via an optical delay line by changing its optical pathway. In an ideal case, the absorption of *probe* pulses is specific to particular transient states (excited-state absorption) or rapidly generated photoproducts, and induces a specific system response (signal), e.g. change in absorption, fluorescence or fragment yield, provided that the molecular target system is transparent for the *probe* irradiation in its electronic ground state. By repeated measurements with sequential increments of *pump-probe* delay (Δt), the time evolution of excited-state population transfer is sampled. The resulting transient signal $S(\Delta t)$, is then fitted by applying appropriate kinetic models from which the time constants (τ_i), reflecting the lifetime of specific transient states, can be extracted. The most commonly established ultrafast spectroscopic techniques are *transient broadband absorption spectroscopy* (TA) [10-11], *transient fluorescence up-conversion* [10-13] and *time-resolved photoelectron spectroscopy* [11, 14].

Upon photoexcitation, proceeding within ~ 1 fs [15], a so called *Franck-Condon* (FC) excited state [15] ($\hat{=}$ localized wavepacket [9]) is prepared, based on a „vertical“ excitation within the *Born-Oppenheimer approximation* [16], meaning that the system retains its nuclear geometry during electronic excitation. In this FC excited state the

system is typically in the ground state geometry, shifted from the equilibrium structure of the excited state potential surface, and all the ensuing elementary processes are launched from this starting point. Following photoexcitation, energy is redistributed within the electronic and vibrational configuration space of the system via a variety of ultrafast *nonradiative* deactivation pathways [11], typically involving structural changes (e.g. isomerization [17]) and crossings between singlet/triplet excited states, such as: *intramolecular vibrational energy redistribution* (IVR) [18-20], singlet-singlet / triplet-triplet *internal conversion* (IC) [20], singlet-triplet *intersystem crossing* (ISC) [20-23], *charge transfer* (CT) [20, 24], fast *photodissociation* (PD) in the case of small di/tri-atomic molecules [5], as well as solvent reorientation dynamics [25-28]. All these processes can occur within the range of femtoseconds to picoseconds (10^{-15} - 10^{-12} s) [11, 29] (see Fig. 1.1) and the lowest-energy excited state is typically populated as an outcome (e.g. a long lived triplet excited state).

However, the classical simplistic picture that excited-state evolution proceeds sequentially through temporally well separated elementary relaxation processes in a cascade type scheme, which may be a reasonable assumption for most purely organic molecules ($\tau_{IVR} \ll \tau_{IC} \ll \tau_{ISC}$), does not necessarily hold in the case of metal based molecular complexes, clusters or organometallic compounds. On the contrary, the early excited-state dynamics of ligand-facilitated transition metal (TM) complexes can become quite convoluted due to the fact that they exhibit a high density of electronic and vibrational states which can couple with each other. As a result the elementary relaxation processes typically proceed on similar timescales, competing with each other ($\tau_{IVR} \lesssim \tau_{IC} \lesssim \tau_{ISC}$) [11-12, 15, 29-30], which has been nicely demonstrated for the polypyridyl prototype complexes $[M(\text{bpy})_3]^{2+}$ ($M = \text{Fe, Ru}$; bpy = 2,2'-bipyridine) [11, 30-32]. Consequently, the elucidation of the excited state deactivation scheme for TM complexes and the assignment of experimentally determined time constants can become convoluted and may, in some cases, correspond to the kinetics of population transfer from one state into the other rather than being inherent to individual elementary processes [11].

In the context of light-induced dynamical phenomena and photochemistry, TM-based molecular complexes have attracted great interest over the last decades [33-35]. They feature unique photophysical and photochemical properties that make them favorable for various potential applications, encompassing (photo)catalysis [15, 36], solar energy conversion (e.g. photovoltaic devices) [37-39], light emitting devices such as (phosphorescent) organic light-emitting diodes ((PH)OLEDs) [11, 40-42], chemical sensors [43-45], and light conversion into mechanical energy by so-called artificial molecular machines [46-49]. Additionally, TM-based compounds provide versatile tuning opportunities by chemical modifications (e.g. type of metal, nuclearity and ligands with functional groups), by which their emission properties can be controlled (quantum yield, emission wavelength, lifetime of emissive states) [35]. Many of their unique photophysical properties, differing from purely organic molecules, originate from the propensity of TM-based chromophors for efficient photo-induced charge separations enabled by the existence of intramolecular charge transfer states, governing photo-redox reactivity, with either metal-to-metal- (MMCT), ligand-to-metal- (LMCT), or metal-to-ligand-(MLCT) charge-transfer character [15]. In addition, very fast ISC and spin-change dynamics are often observed on account of energetically closely-lying singlet and triplet states and large spin-orbit coupling (SOC) constants of the metals [11]. However, there is growing evidence that SOC by itself may not be the most determining parameter with respect to ultrafast ISC dynamics [29-30]. For example, for the prototypical binuclear platinum complex $[\text{Pt}_2(\text{pop})_4]^{4-}$ ($\text{pop} = (\text{P}_2\text{O}_5\text{H}_2)^{2-}$), a rather slow ISC rate has been found ($\tau_{\text{ISC}} = 10\text{-}30$ ps) [10-11] when compared to mononuclear $[\text{M}(\text{bpy})_3]^{2+}$ ($\text{M} = \text{Fe}, \text{Ru}$) complexes ($\tau_{\text{ISC}} \leq 30$ fs) [11, 30-32], despite higher nuclearity and larger atomic number.

It is therefore an open and intriguing question, how metal nuclearity influences ISC rates and electronic and structural relaxation dynamics. Systematic investigations on simple binuclear models systems, exhibiting two metal centers in direct proximity to each other (M-M) (see Fig. 1.1), are therefore promising starting points in dealing with this topic. Among them are ligand-stabilized closed shell d^{10} coinage metal complexes (CMCs, $\text{M} = \text{Cu}^+, \text{Ag}^+, \text{Au}^+$) that feature metallophilic contacts [50]

(see chapter 2), having received particular interest due to their intense room temperature luminescent properties [41, 45]. In this case, the auspicious elucidation of metal-centered excited state relaxation dynamics can potentially provide additional information from *vibrational coherences* [10, 51-55], enabled by coherent photoexcitation of FC-active metal-localized vibrational modes. These are to some extent decoupled from the ligand framework and provide information about the strength and character of M-M bonding interactions [10, 50].

Since the interpretation of time-resolved experimental data of TM-based systems is usually ambiguous, often lacking information in order to distinguish between several kinetic models and the fact that environmental effects such as solvent dynamics typically being superimposed on and/or influence the intrinsic intramolecular deactivation pathways [25, 27-28, 53, 56], reliable predictions by sophisticated computational methods are highly desirable to rationalize the physico-chemical processes involved in the early excited-state dynamics. However, the simulation of ultrafast excited-state molecular dynamics, especially for larger molecules containing transition metals (tens to hundreds of atoms), is quite a challenge for theory due to the high density of electronic states, spin-orbit and nonadiabatic coupling between states and large dimensionality of the problem [21, 29]. Therefore, the development of new experimental time-resolved tools, enabling the investigation of isolated and well defined systems in the gas phase, is crucial in order to assess the intrinsic intramolecular excited-state dynamics, to evaluate environmental effects (solvent molecules and counterions) on deactivation pathways by comparison between the isolated vs solvated system, and to provide benchmark data for theory.

To summarize, the characterization of the photo-induced dynamics (excited state lifetimes, relaxation pathways, quantum yields, reactivity) of coinage-metal based molecular complexes, governing their photophysical, (photo)chemical and (photo)catalytic properties, is of fundamental interest and of high importance for the development, rational design, and synthetic optimization of new photonic materials for enhanced optical and catalytic processes.

2. The Metallophilicity Phenomenon

Over the last few decades there has been a large number of observations which are suggestive of distinct inter- and intra-molecular attractive interactions, involving formally positively charged metal ions with a closed-shell $[d^{10}]$ and $[d^{10},s^2]$ electronic configuration (e.g. Cu^+ , Ag^+ , Au^+ and Tl^+) [57-62] as well as a pseudo-closed shell $[d^8]$ electronic configuration (e.g. Pt^{2+}) [10, 50, 63-64]. On first glance, these homo- and/or heterometallic weak noncovalent „ (M^+-M^+) “ bonding situations seem counterintuitive owing to the expectation of internuclear electrostatic repulsion. Since the concept of chemical bonding is paramount in chemistry, the question of the nature of this unconventional attraction, which appears to elude classical bonding concepts, is of fundamental interest [62-63, 65-70]. In fact, there is a rapidly growing number of publications on the subject of these *metallophilic interactions* (see Fig. 2.1).

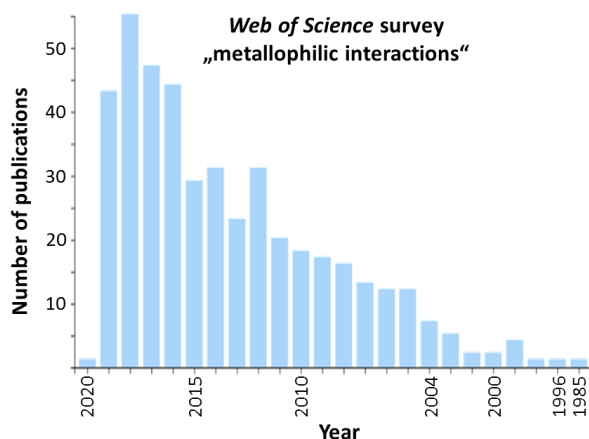


Fig. 2.1 Number of publications by year based on a Web of Science survey on the topic „metallophilic interactions“, indicating a clear rise in interest on the topic (data retrieved november 2019).

Most prominently, the metallophilic attraction between d^{10} coinage metal ions have been suggested and repeatedly reviewed and scrutinized [62-63, 65-66, 69, 71-72]. Meanwhile, the terms „*aurophilicity*“ [68, 70, 73-75], „*argentophilicity*“ [72] and, more controversially, „*cuprophilicity*“ [71, 76] have been well established. This

2. The Metallophilicity Phenomenon

nomenclature is linguistically derived from the latin words for the respective metals (Au: aurum, Ag: argentum, Cu: cuprum) and the greek word „philein“ which translates as „affinity“ [72]. According to *Schmidbauer* [68, 72], the variety of possible metallophilic bonding situations can be classified into a) intermolecular attraction (unsupported), and b) intramolecular M-M bonding, facilitated/enforced either by bridging ligands (semi-/fully-supported) or hyper-coordination by a central atom e.g. hypervalent carbon [77-79] (see Fig. 2.2).

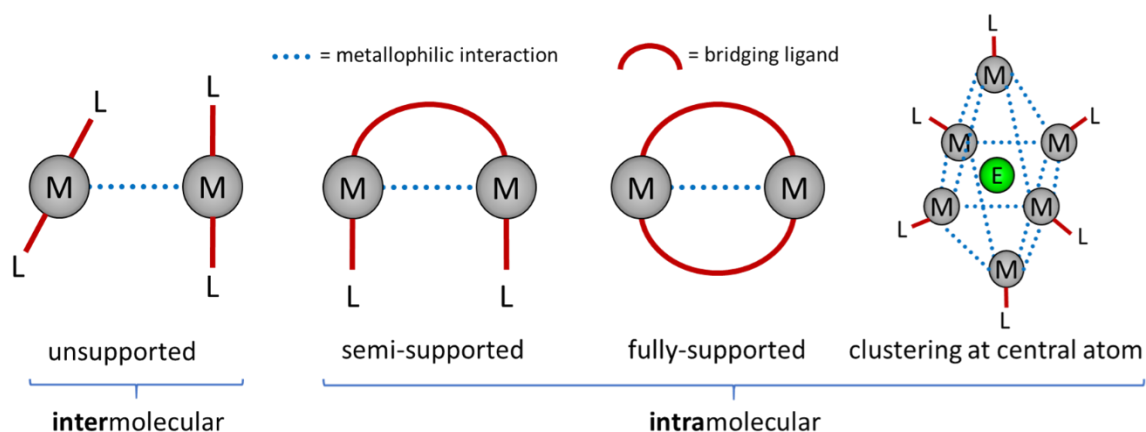


Fig. 2.2 Categories of intra/inter-molecular metallophilic interactions (indicated by dotted blue lines).

The observation of metallophilic attraction, lacking a specific directionality, is not limited to metal pairs. Compounds of the univalent coinage metal ions (Cu^+ , Ag^+ , Au^+ , $[\text{nd}^{10}(\text{n}+1)\text{s}^0]$ $\text{n}=3, 4, 5$) often display the propensity to form aggregates such as dimers, oligomers, clusters and two-/three-dimensional metallopolymers, which can display unique optical properties [35, 61, 72, 80-81]. This tendency for self-assembly is associated with a delicate interplay between various noncovalent interactions (driving forces) including among others: electrostatic attraction/repulsion, dispersion, hydrogen bonding and $\text{d}^{10}\text{-d}^{10}$ metallophilic bonding [62, 72]. It is therefore not further surprising that metallophilic bonding is highly sensitive towards environmental effects such as metal-solvent/-counterion interactions and other external stimuli (e.g. pressure, temperature, concentration) [56, 70, 82-87]. Thus, experimental studies with controlled and systematically parametrized settings are key for the elucidation of this phenomenon [57, 88]. In a recent study [82], the

unequivocal correlation between luminescence energy and Au-Au distance was evidenced, whereby metal-metal interaction could be enforced by the systematic increase of pressure in a diamond-anvil cell. Intriguingly, there seem to be an apparent correlation between luminescence properties and metal-metal distance, and therefore intermetallic interaction. Given the sheer complexity of prevailing forces in molecular systems, it is difficult to isolate the particular contribution of metallophilic bonding. Nearly isomorphous multinuclear model systems, allowing for the systematic variation of a single chemical parameter at a time (metal centers, nuclearity, ligands, counterions, charge state), are therefore a good starting point, in order to achieve a meaningful evaluation of intermetallic bonding strength and verifiable relationship between molecular structure and physicochemical properties [57, 75]. Thus, there is a clear need for a fundamental understanding of synergistic metallophilic attraction, with the objective of being able to tune photophysical properties of complexes by design [61, 81, 89]. Potential applications encompass luminescent materials, (chemo)sensors, (photo)catalysts, and (PH)OLEDs [35, 43-45, 83-84, 90-93]. Regarding the vast complexity of the topic of closed-shell metallophilic interactions, being still subject of controversial debate [62-63, 65-70, 72, 74], the following questions are integral: Which are the deciding criteria that indicate whether metallophilic attractions are operational? How can the intermetallic bonding/interaction energy be quantified? What are the origins of this seemingly unusual of chemical bonding?

The presence of d^{10} - d^{10} metallophilic contacts is most often recognized by X-ray crystallographic data, revealing short intermetallic separations significantly below the sum of *van der Waals radii* (r_{vdW} see Tab. 2.1) of the coinage metal atoms („sub-*van der Waals* contact“) [63, 68, 72, 88, 94]. In this context, the lower end in the range of metallophilic M-M distances (M= Cu, Ag, Au), is marked by the covalent bond length observed for the respective M_2 dimers in the gas phase (see Tab. 2.1). However, judging metallophilic attraction solely based on metal-metal distance and the sub-*van der Waals* contact criterion is questionable since many other factors which can also determine intermetallic distances, involving ligands and counterions, need to be taken into account (packing/steric effects, coordination mode and number,

2. The Metallophilicity Phenomenon

charge delocalization, non-covalent interactions) [72]. As for the concept of *van der Waals radii* of atoms, several definitions and differing values (r_{vdW}) have been put forward [67, 94-97]. Therefore, the oversimplified evaluation of metallophilic interactions based on pairwise sum of *van der Waals radii* (Σr_{vdW}) should be taken with reservation [67]. However, as a general rule, metallophilic attraction is expected to decrease in strength with increasing coordination number [72]. This is mostly relevant in the case of Cu^+ and Ag^+ ions since they can easily adopt coordination numbers larger than two. In contrast, Au^+ centers exhibit the distinct propensity to be in a linear two-coordinate state [70].

Tab. 2.1 Summary of parameters relevant for the discussion of M-M interactions (M = Cu, Ag, Au), $2 \cdot r_{vdW}$: pairwise sum of van der Waals radii; r_{ion} : ionic radii of M^+ ; r_e : equilibrium distance in M_2 dimer; $\tilde{\nu}_e$: harmonic frequency of M-M stretching mode; D_e : binding energy. Last column: structural and vibrational parameters of $[\text{M}_2(\text{L}^{\text{Cy}})_2](\text{anion})_2$ compounds (see Fig. 4.1 A, L^{Cy} = bis(dicyclohexylphosphino)methane, anion = PF_6^- , ClO_4^- , CF_3SO_3^-). r_{M-M} : ground state M-M distance; $\tilde{\nu}_{M-M}$ and F_{M-M} : vibrational frequency and force constant of M-M stretching mode.

M	$2 \cdot r_{vdW}$ /Å	$r_{ion}(\text{M}^+)$ /Å	M_2 dimer in gas phase ($r_e/\text{Å}$; $\tilde{\nu}_e/\text{cm}^{-1}$; D_e/kJmol^{-1})	$[\text{M}_2(\text{L}^{\text{Cy}})_2](\text{anion})_2$, ($r_{M-M}/\text{Å}$; $\tilde{\nu}_{M-M}/\text{cm}^{-1}$; $F_{M-M}/\text{mdyn Å}^{-1}$)
Cu	2.80 [94]	1.13 [98]	(2.22; 266; 201) [99-100]	(2.73; 104; 0.20) [57]
Ag	3.44 [94]	1.33 [98]	(2.53; 192; 163) [72, 99, 101]	(2.96; 80; 0.20) [57]
Au	3.32 [94]	1.25 [98]	(2.47; 191; 224) [99]	(2.92; 88; 0.45) [57]

A better diagnostic tool for the evaluation of attractive d^{10} - d^{10} interactions is the occurrence and frequency of the M-M vibrational stretching mode ($\tilde{\nu}_{M-M}$) [102]. Thus, the intermetallic bond strength in binuclear compounds can generally be correlated with vibrational force constants (F_{M-M}), which can be derived from data of Raman spectroscopic experiments and enable a better comparison between systems [50, 57, 72, 103-104]. A prototypical example for fully-supported d^{10} - d^{10} interactions is represented by the $[\text{M}_2(\text{L}^{\text{Cy}})_2]^{2+}$ system (L^{Cy} = bis(dicyclohexylphosphino)methane, M = Cu, Ag, Au, see Fig. 4.1 A) [57], featuring sub-van der Waals contacts for all homometallic congeners (r_{M-M} , cf. Tab. 2.1). In this case, low frequency stretching vibrations in the range of $\tilde{\nu}_{M-M} = 80\text{-}104 \text{ cm}^{-1}$ were reported, indicative of

significant „M⁺-M⁺“ bonding contributions in the electronic ground state [57]. Here, the largest force constant was obtained for the Au-Au system ($F_{Au-Au} = 0.45$ mdyn Å⁻¹, 1 mdyn = 10⁻⁸ N), which is approximately double the value found for the Ag-Ag congener ($F_{Ag-Ag} = 0.20$ mdyn Å⁻¹), although both intermetallic distances r_{Au-Au} (2.92 Å) and r_{Ag-Ag} (2.96 Å) were found to be similar (Tab. 2.1). Based on structural and spectroscopic data of a selected set of bimetallic compounds, an empirical linear correlation between intermetallic distance r_{M-M} and $\ln(F_{M-M})$ was found [57]. In addition, metallophilic bonds in multinuclear coinage complexes can also be correlated with distinct UV/Vis absorption and photoluminescence characteristics originating from ligand-to-metal-metal charge transfer (LMMCT) or metal-centered (MC) transitions [57, 72, 84].

Despite the large variety of available structural data on closed-shell coinage metal contacts, only a few experimental studies exist on the determination of their bond energy. Based on experimental evidence (e.g. temperature-dependent NMR and Raman spectroscopy [69]) and predictions by theory, the binding energy for aurophilic „Au⁺-Au⁺“ pairs is estimated to be in the range of approx. 20-65 kJ/mol [62-63, 68, 70-73, 75], which is comparable or slightly larger to that of hydrogen bonding [105-107]. In addition, the wide range of evidenced M-M distances (r_{Au-Au} : 2.8-3.5 Å) [70] is indicative of a flat potential energy profile, placing aurophilicity in the category of weak forces in between standard *van der Waals* attraction and hydrogen bonding [70]. A recent combined experimental and theoretical study on the fragmentation behavior of isolated ([LH)AuCl]⁺⋯[(L')AuCl]) dimers in gas phase assessed the „pure“ aurophilic interactions energy to be 25-30 kJ/mol [75]. Concerning the comparison of homometallic bond strength among Cu⁺, Ag⁺ and Au⁺ centers, aurophilic interactions are considered to be the strongest or similar in strength than argentophilic bonding, whereas cuprophilic interactions are typically much more difficult to discern. Hence, the order of „M⁺-M⁺“ bonding strength is suggested to be Au ≥ Ag > Cu [57, 62, 65, 70-72, 76]. However, it should be noted that there are also reports of argentophilic interactions exceeding those between „Au⁺-Au⁺“ centers [58, 108]. In addition, the existence of the presumable „weak“ cuprophilic interactions were the first to be demonstrated among the coinage metals, by combined X-ray and electron

2. The Metallophilicity Phenomenon

diffraction experiments on cuprous oxide (Cu_2O) [109-110]. In summary, it has to be noted that the order of metallophilic bond energies among the coinage metal triad is still controversial and subject to debate, presumably since the origin of this attraction is still not fully understood and may also be strongly dependent on the nature of the ligands and other inherent factors of the respective systems [66]. On this topic, Pyykkö fittingly commented: „When comparing the three coinage metals, only silver is normal“ [69].

A similar picture of ambiguity is drawn concerning the mechanism of metallophilic bonding. Despite the fact that several computational studies have been conducted over the years, utilizing a variety of high-level theoretical methods, no consensus on the origin of closed-shell metal-metal attraction has been reached [58, 65-67]. The most commonly accepted theory suggest that this phenomenon can be regarded as another case of an electron correlation / *London dispersion* type interaction which is enhanced by relativistic effects [62-63, 69-70, 73-74, 111-112]. The best indication for the dispersion character of metallophilic bonding is represented by theoretical studies predicting a „ $V(R) \propto -R^{-6}$ “ dependency for interatomic potential energy curves $V(R)$ (R : metal-metal distance) [69, 74]. Since metallophilic attractions are stronger than „typical“ *van der Waals* bonding interactions [69, 111], the term „*Super van der Waals interaction*“ has also been put forward [69, 73]. However, besides dispersion, electron correlation and relativistic effects, it has also been suggested that both orbital interactions and *Pauli repulsion* may also play a significant role concerning „ M^+-M^+ “ bond strength [65-66, 83]. In summary, the metallophilicity phenomenon is most likely based on a collective set of synergetic, system-specific interactions which are difficult to entangle.

3. Aim and Motivation

The chief topic of this thesis lies in the exploration of photo-enhanced d^8/d^{10} *metallophilic* interactions and the question on how they govern ultrafast dynamical as well as structural and reactive molecular properties of multinuclear coinage metal complexes.

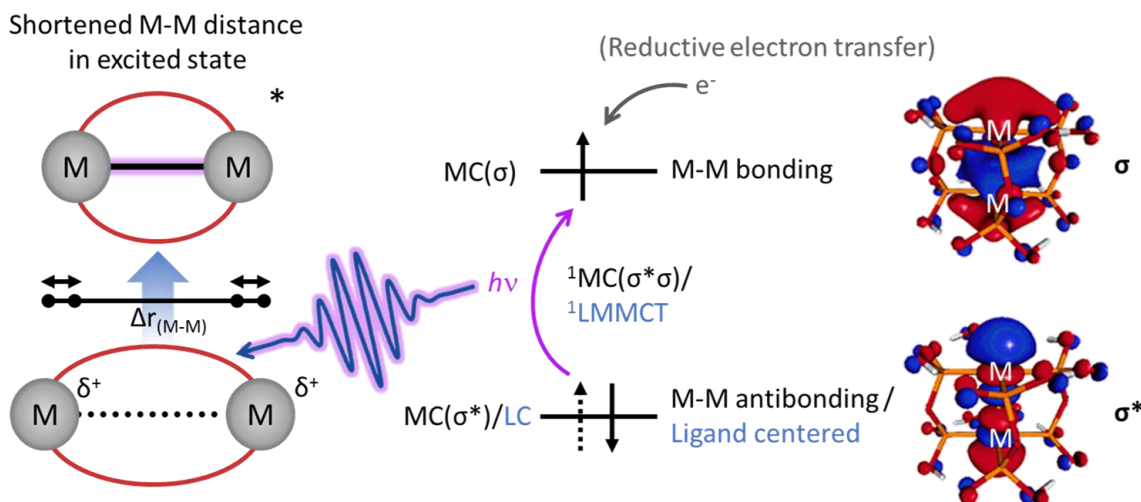


Fig. 3.1 Left: Illustration of (photo)-induced metallophilic bonding between cationic d^8/d^{10} metal centers (M) accompanied by shortening of metal-metal distance in electronic excited states. Middle: Scheme of molecular orbitals involved in metallophilic bonding as result of photoexcitation [10, 28, 50, 53-59, 64, 102, 113-119] or reductive electron transfer [64, 120-121]. Symmetries of metal-centered (MC) molecular orbitals are labeled with regard to the M-M axis as bonding (σ) or antibonding (σ^*). Right: Frontier orbitals of the binuclear $[Pt_2(pop)_4]^{4-}$ ($pop = (P_2O_5H_2)^{2-}$) complex taken from Ref [122] (see Fig. 4.1 D).

Metallophilicity [68, 72], i.e. attractive interactions between closed-shell d^8/d^{10} metal cations, can give rise to new electronic states which often lead, after photoexcitation, to enhanced intermetallic bonding (M-M) as illustrated by Fig. 3.1. The photoexcitation of these metal-metal bonding excited states typically involve the promotion of an electron from a metal-centered (MC) orbital with M-M antibonding character (or from a ligand-centered (LC) orbital) [121, 123] into a M-M bonding orbital, resulting in significant shortening of the M-M distance [10, 28, 50, 53-59, 64, 102, 113-119]. Intriguingly, the selective excitation of these chromophores can be leveraged to

facilitate and probe vibrational wavepackets (coherent nuclear motion) that oscillate with the frequency of the Franck-Condon active $\nu(\text{M-M})$ stretching normal modes, giving access to information on the type and strength of intermetallic chemical bonding [10, 28, 54-55, 113, 124]. Alternatively, metallophilic bonding can also be enhanced by reductive electron transfer (e.g. by electrochemical reduction [64, 120] or by gas phase anion-cation reactions [121]).

The methods addressed in this thesis were mainly developed within the framework of the collaborative research center „*Cooperative Effects in Homo- and Heterometallic Complexes* (abbrev. *3MET*)“, which is a collaboration of the *Technische Universität Kaiserslautern* (TUK) and the *Karlsruhe Institute of Technology* (KIT) [125]. Among others, the main objective of *3MET* is the assessment of intermetallic electronic coupling in multinuclear transition metal complexes, aiming for an understanding on a fundamental level in order to predict and potentially tailor their optical, magnetic, and catalytic properties. Of particular interest are synergetic interactions between multiple metal centers, so called *cooperative effects*, which have been categorized according to a) functional, b) enthalpic and c) entropic cooperativity, within the terminology of *3MET* [125-127]. As an example, functional intermetallic cooperative effects manifest themselves e.g. in specific optical properties, which are absent or significantly differ from those in homologous or related systems comprising only a single metal center, e.g. characteristic metal-centered electronic transitions, luminescence, energy/electron transfer processes, and vibrational coherences. Specifically, this work was conducted within the *3MET* project *C4* titled *Ultrafast Molecular Dynamics in Metal Complexes* [125] which constitutes a collaboration between Prof. Dr. R. Diller (TUK, physics department) and Priv.-Doz. Dr. C. Riehn (TUK, chemistry department), combining methods of time-resolved laser spectroscopy both in the gas phase (Riehn) and condensed/bulk phase (Diller). This combination of experimental techniques facilitates the investigating of transition-metal-based complexes as molecular ions in isolation, as well as in an environment of solvent molecules and counterions, aiming to distinguish intrinsic intramolecular photophysical properties from those brought about from the chemical environment.

For these investigations, firstly, suitable molecular target systems had to be identified that fulfill the following requirements: a) exhibit potential metallophilic contacts, b) show distinct absorption features, providing selective optical access to metal-metal bonding excited states, in absence of superimposing ligand-centered chromophors (spectroscopically „silent“ ligands), c) bear a net electric charge (cations or anions) and d) be stable enough to be transferred into the gas phase by electrospray ionization (ESI). Additionally, the target systems should ideally support a modular approach that allow for small chemical modifications without major structural changes, enabling the direct comparison of photophysical properties of congeners by isomorphic exchange of type and number of metal ions (homo/hetero-metallic, nuclearity), ligand moieties (homo/hetero-lyptic) and counterions. An overview of selected systems that partially or fully satisfy these parameters is provided in the next section (Fig. 4.1).

In essence, this thesis focuses on gas phase studies on mass-selected multinuclear d^8/d^{10} coinage metal complexes ($M = Pt^{2+} / Cu^+, Ag^+, Au^+$), combining electrospray ionization mass spectrometry (ESI-MS) and laser ion spectroscopy in order to explore their static and dynamical photo-physical properties and the role of functional cooperative metallophilic interactions therein. For this purpose, intact molecular precursor ions ($P^{n\pm}, n = 1-3$) were „gently“ transferred into the gas phase by electrospraying respective analyte sample solutions. The ESI ion source is connected to a commercial three-dimensional quadrupole ion trap mass spectrometer (3D-QIT-MS) enabling the isolation of mass-selected ions, their storage, and subsequent mass analysis. In addition, the 3D-QIT is modified to accept UV/Vis/NIR radiation from a fs laser system used to photoexcite the trapped precursor ions. The versatile capabilities of the „Paul-type“ ion trap in combination with laser irradiation represents a „gas-phase photochemical ion laboratory“ [128-129]. It provides a powerful platform to study the gas phase reactivity and dissociation pathways of stoichiometrically well-defined target systems when subjected to multiple activation/dissociation methods such as a) „heating“ by multiple collisions with neutral helium atoms (CID), b) exoergic reductive electron transfer or dissociation by anion-cation recombinations (ET(D/R)) and c) ultraviolet laser

3. Aim and Motivation

radiation ((UV)-PD). In the context of this work, an „arsenal“ of complementary ion-trap based mass spectrometric and laser spectroscopic techniques was employed (see Fig. 3.2). Only by this multi-method approach, the intricate task of evaluating the intrinsic optical and structural properties and cooperative effects of multinuclear transition metal complexes could be approached.

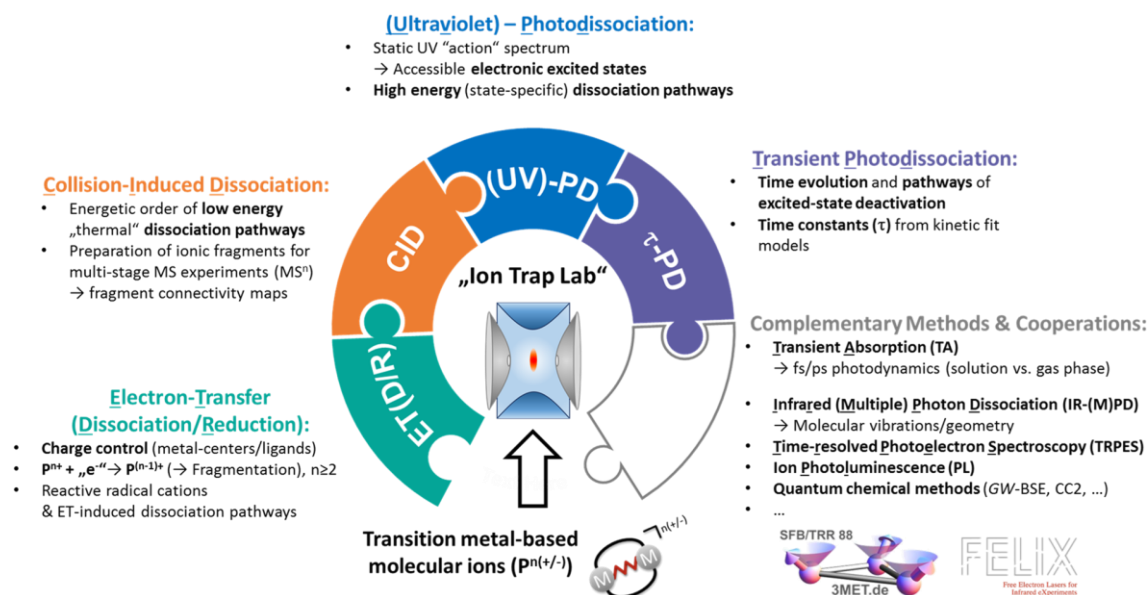


Fig. 3.2 Mass spectrometric and laser spectroscopic methods employed within the context of this thesis for the investigation of gaseous transition metal complexes in an ion trap (ET(D/R) [121, 130-132], CID [133-141], (UV)-PD [129, 142-151], τ -PD [152-161]). Complementary experimental and theoretical methods that were utilized by cooperation partners within the collaborative research center (3MET) [125] and the FELIX laboratory [162] (combined ET(D/R)/IRMPD [163]) are highlighted.

In particular, static photodissociation (UV-PD) and time-resolved pump-probe (τ -PD) action spectroscopic techniques were employed on trapped ions (close to room temperature) to ascertain electronic transition energies and to fathom ultrafast excited-state deactivation kinetics following resonant photoexcitation. For this type of *action spectroscopy* [129, 147], instead of measuring the direct absorption of photons, the photo-induced fragmentation of stored precursor ions is monitored in percentage of detectable ionic fragments after hundreds of milliseconds of storage time (chapter 5.1). In the case of τ -PD experiments, transient changes in the

fragmentation pattern (relative increase/decrease of fragment-specific signal Intensities) are monitored as a function of *pump-probe* time delay (chapter 5.2).

Previous to this work, methods combining ESI ion sources with time-of-flight (TOF) or quadrupole ion-trap (QIT) mass spectrometers and femtosecond laser sources, developed for time-resolved photodissociation ion spectroscopy, had already been pioneered to protonated amino acids [154-155, 159], dipeptides [153, 157] and other aromatic organic molecules [156, 158]. One major objective of this thesis is to ascertain whether the τ -PD method can be effectively deployed on cationic/anionic multinuclear TM complexes (with their high density of electronic states, and fast ISC dynamics) and to optimize the appropriate experimental conditions (e.g. pulse energy, wavelength, number of pulses, polarization, temporal and spatial overlap). It was therefore an important question whether triplet excited-state populations of metal complexes can be probed within this detection scheme and also whether information of electronic, vibrational or rotational coherences could be mapped onto transient fragment yields.

Furthermore, the suitability of primary and secondary ionic fragments as valid reporters of excited-state dynamics had to be clarified, given the large potential of information scrambling by: interplay and combinations between various fragmentation pathways, the large separation of timescales between signal-generating processes (fs-ps excited-state dynamics, (fs)- μ s dissociation depending on the fragmentation mechanism, ion detection after milliseconds), and effects of multiphoton absorption, photoexcitation of fragments (multiple-pulse experiment) and secondary fragmentation (dissociation of fragments).

4. Outline

This thesis is mainly based on five peer-reviewed publications (Publication 1-5) [121, 123, 164-166] covering the mass spectrometric and laser spectroscopic characterization of ionic multinuclear coinage metal complexes. A brief overview of the investigated molecular systems pertaining to each individual research study is provided below (Fig. 4.1).

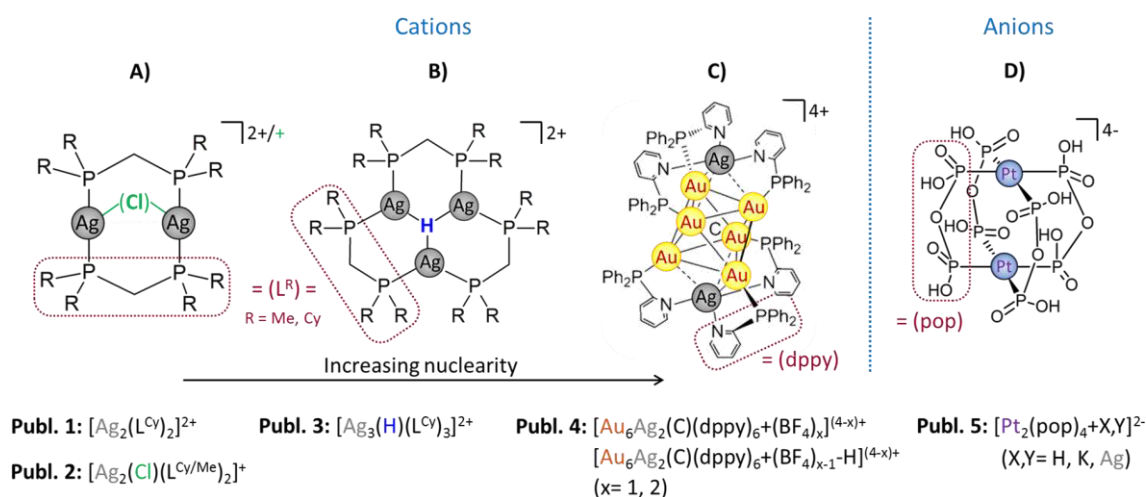


Fig. 4.1 Overview of studied multinuclear target systems featuring metallophilic contacts [121, 123, 164-168]. The molecular ions under investigation encompass: **A)** bisphosphine-bridged di-silver complexes $[\text{Ag}_2(\text{L}^{\text{Cy}/\text{Me}})_2]^{2+}$ ($\text{L}^{\text{Cy}} = \text{dcpm} = \text{bis}(\text{dicyclohexylphosphino})\text{methane}$, $\text{L}^{\text{Me}} = \text{dmpm} = \text{bis}(\text{dimethylphosphino})\text{methane}$) and the chlorido adducts $[\text{Ag}_2(\text{Cl})(\text{L}^{\text{Cy}/\text{Me}})_2]^+$, **B)** a triangular tri-silver hydride complex $[\text{Ag}_3(\text{H})(\text{L}^{\text{Cy}})_3]^{2+}$, **C)** $(\text{BF}_4)^-$ adducts of an octaedral hexagold cluster containing a hypercoordinated carbon center and two Ag^+ ions at its apexes $[\text{Au}_6\text{Ag}_2(\text{C})(\text{dppy})_6+(\text{BF}_4)_{x/(x-1)}(-\text{H})_{0/1}]^{(4-x)+}$ ($x = 1, 2$; $\text{dppy} = 2\text{-pyridyl-diphenylphosphine}$, schematic structure modified from Ref. [169]), **D)** dianionic H^+ , K^+ , Ag^+ adduct species of the pyrophosphite-stabilized, square-planar diplatinum complex $[\text{Pt}_2(\text{pop})_4+\text{X,Y}]^{2-}$ ($\text{X,Y} = \text{H, K, Ag}$, $\text{pop} = (\text{P}_2\text{O}_5\text{H}_2)^{2-}$).

4.1. Publication 1 (PCCP)

Ultrafast Excited-State Relaxation of a Binuclear Ag(I) Phosphine Complex in Gas Phase and Solution, S. V. Kruppa, F. Bappler, W. Klopper, S. P. Walg, W. R. Thiel, R. Diller, C. Riehn, *Physical Chemistry Chemical Physics* 2017, 19(34), 22785-22800 (2017 PCCP HOTArticles). ^[164]

Publ. 1 reports on the excited state dynamics of the bisphosphine-bridged binuclear silver complex $[\text{Ag}_2(\text{L}^{\text{Cy}})_2]^{2+}$ (see Fig. 4.1 A), exhibiting short argentophilic contacts ($d_{\text{Ag-Ag}} = 2.94 \text{ \AA}$ ^[170]). Motivated by previous resonance Raman investigations of $[\text{M}_2(\text{L}^{\text{Cy}})_2]^{2+}$ ($\text{M} = \text{Cu}, \text{Ag}, \text{Au}$) ^[57] congeners and a fs time-resolved study on $[\text{Au}_2(\text{L}^{\text{Cy}})_2]^{2+}$ in solution and solid state ^[56], the $[\text{Ag}_2(\text{L}^{\text{Cy}})_2]^{2+}$ system has been selected for comparison of gas phase and solution dynamics. Moreover, it features UV optically transparent aliphatic phosphine ligands (L^{Cy}) which allow specific addressing of the „ $[\text{Ag}_2]$ “-chromophore by UV-irradiation. It has been established before that excitation of the dipole-allowed $^1\text{MC}(\text{d}\sigma^*-\text{p}\sigma)$ transition is accompanied by contraction of the Ag-Ag distance as a result of enhanced intermetallic bonding in the electronically excited state ^[57]. Here, the consequences of photo-enhanced metallophilic bonding in the $[\text{Ag}_2(\text{L}^{\text{Cy}})_2]^{2+}$ model system are explored with respect to absorption/luminescence properties, ultrafast excited-state relaxation pathways and gas-phase reactivity. The relevant electronic states were characterized by recording the gas-phase UV photodissociation spectra and absorption/luminescence spectra in acetonitrile, and assigned on the basis of quantum chemical calculations of the size-reduced $[\text{Ag}_2(\text{L}^{\text{Me}})_2]^{2+}$ model (cyclohexyl groups substituted for methyl groups) on the coupled-cluster singles-doubles (CC2) level of theory. The results of transient photodissociation (τ -PD) ion spectroscopy and femtosecond transient absorption (TA), gas phase and solution phase experiments, respectively, are presented and compared in order to disentangle and evaluate the intramolecular (intrinsic) and intermolecular (solvent and counterion related) processes. In addition, the suitability of primary and secondary ionic fragments as valid markers for PD/ τ -PD ion spectroscopy, in the wavelength as well as in the time domain, was explored with respect to potential scrambling of information (e.g. multi-photon/-

pulse absorption and „dark“ fragmentation channels). Collisional- and photo-induced dissociation pathways were elucidated by means of multi-stage MS² and MS³ CID/PD experiments.

4.2. Publication 2 (JPCLet)

Vibrational Coherence Controls Molecular Fragmentation: Ultrafast Photodynamics of the [Ag₂Cl]⁺ Scaffold, S. V. Kruppa, F. Bäßler, C. Holzer, W. Klopper, R. Diller, C. Riehn, *The Journal of Physical Chemistry Letters*, 2018, 9(4), 804-810. ^[123]

Publ. 2 focuses on the photophysical properties of the „[Ag₂Cl]⁺“ scaffold under isolated conditions. Having the d¹⁰-d¹⁰ complexes [Ag₂(L^R)₂]²⁺ (R = Cy, Me) already identified as versatile model systems, enabling the study of intrinsic molecular properties ^[164], the leading questions of this investigation were how the addition of anions (e.g. halides) to the „[Ag₂]²⁺“ core affects metal-metal interaction, excited-state dynamics, including generation of coherent vibrational wavepackets, and gas phase reactivity. To this end, both [Ag₂(Cl)(L^{Cy})₂]²⁺ and [Ag₂(Cl)(L^{Me})₂]²⁺ molecular ions, were generated via ESI from appropriate sample solutions and mass spectrometrically characterized in an ion trap. Their gas phase UV spectra, obtained via UV-PD ion spectroscopy, are presented and compared. In addition, quantum chemical computations on the size-reduced [Ag₂(Cl)(L^{Me})₂]²⁺ system report on the assignment of electronically excited states, their character, and ground state geometric structure. Finally, the femtosecond excited state dynamics of mass-selected [Ag₂(Cl)(L^{Cy})₂]²⁺ precursor ions were studied in an ion trap at room temperature, utilizing the previously introduced pump-probe transient photodissociation (τ-PD) method, detailing unexpected correlations between the phase of vibrational wavepackets and reported fragment types and yields.

4.3. Publication 3 (ChemEurJ)

Photoinitiated Charge Transfer in a Triangular Silver(I) Hydride Complex and its Oxophilicity, S. V. Kruppa, C. Groß, X. Gui, F. Bäßler, B. Kwasigroch, Y. Sun, R. Diller, W. Klopper, G. Niedner-Schatteburg, C. Riehn, W. R. Thiel, *Chemistry A European Journal*, 2019, 25(48), 11269-11284 (VIP Paper, Cover Picture). [121]

Publ. 3 represents a multidisciplinary and comprehensive photophysical and chemical characterization of the novel triangular silver(I) hydride complex $[\text{Ag}_3(\text{H})(\text{L}^{\text{Cy}})_3]^{2+}$ ($\cong [\mathbf{P}]^{2+}$, Fig. 4.1 B) in the gas and bulk phases (crystal, solution), reporting on its chemical synthesis, molecular structure, electronic states, optical absorption/luminescence properties and gas phase reactivity. Building on previous work on binuclear phosphine-stabilized silver complexes (Publ. 1 and 2) [123, 164], the objective here was to increase the nuclearity of metal centers while utilizing the spectroscopically „inert“ L^{Cy} bis-phosphine ligands. The design of this equilateral triangular „ $[\text{Ag}_3\text{H}]$ “ core was inspired by previous reports on the related $[\text{Ag}_3(\text{H})(\text{L}^{\text{Ph}})_3]^{2+}$ (R = Ph, phenyl) [171] and $[\text{Cu}_3(\text{H})(\text{L}^{\text{Cy}})_3]^{2+}$ [172] complexes. Complementary analytic methods were used including NMR, X-ray diffraction, CID/ETD mass spectrometric techniques, UV/Vis absorption and luminescence, and UV-PD laser spectroscopy along with high-level quantum chemical computations. In particular, the gas phase reactivity of $[\mathbf{P}]^{2+}$, i.e. fragmentation pathways and ion/ion or ion/neutral reactions, was explored in an ion trap as a function of collision-induced („thermal“), photo-induced, and electron transfer (reduction) ion activation methods. The latter leads to the formation of radical monocations which exhibit an unprecedented activation of dioxygen (O_2) in the ion trap. Focusing on the „ $[\text{Ag}_3\text{H}]$ “-centered chromophore, the electronic structure and nature of electronic transitions were elucidated via UV-PD ion and UV/Vis absorption/luminescence spectroscopy in concert with (GW-BSE) quantum chemical calculations.

4.4. Publication 4 (JPCA)

Gas-Phase Photoluminescence and Photodissociation of Silver-Capped Hexagold Clusters, J.-F. Greisch, A. Ballester-Caudet, S. V. Kruppa, Z. Lei, Q.-M. Wang, C. Riehn, F. Remacle, *The Journal of Physical Chemistry A*, 2018, 122(27), 5799-5810. ^[165]

Publ. 4 scrutinizes the combined radiative and non-radiative deactivation/fragmentation pathways of gaseous phosphine-stabilized, silver-capped hexaauriomethane clusters of type $[\text{Au}_6\text{Ag}_2(\text{C})(\text{dppy})_6+(\text{BF}_4)_x]^{(4-x)+}$ and $[\text{Au}_6\text{Ag}_2(\text{C})(\text{dppy})_6+(\text{BF}_4)_{(x-1)}(-\text{H})]^{(4-x)+}$ ($x = 1, 2$; dppy = 2-pyridyl-diphenylphosphine, see Fig. 4.1 C). These complexes feature a hypercoordinated carbon center and Au-Au and Ag-Au interactions within the bicapped octahedral „Au₆Ag₂“ motif. Polynuclear Au(I) complexes have attracted considerable interest due to their bright, long-lived luminescence in the visible spectral region ^[77, 173-174], making them promising candidates for application in (PH)OLEDs or luminescence sensing ^[91]. The Au(I)-Ag(I) target compound $[\text{Au}_6\text{Ag}_2(\text{C})(\text{dppy})_6](\text{BF}_4)_4$ is a functionalized derivative of the „Schmidbaur-type“ cluster $[\text{Au}_6(\text{C})(\text{PPh}_3)_6](\text{BF}_4)_2$ ^[79], with PPh₃ phosphine ligands replaced by dppy, providing coordination sites for additional silver(I) ions. The doping of Ag/Au clusters with respective heterometals, is generally targeted towards the optimization of their luminescence properties (intensity and quantum yield) ^[77, 173, 175-176]. Here, for the investigated $[\text{Au}_6\text{Ag}_2(\text{C})(\text{dppy})_6](\text{BF}_4)_4$ system, the addition of two Ag(I) ions results in a strong enhancement of luminescence intensity in solution, presumable due to steric shielding of the cluster core and the generation of new emissive states ^[77, 173]. The fact that the chemical environment, such as solvent molecules and counterions, has been found to drastically impact the excited-state dynamics and luminescence properties of $[\text{Au}_6\text{Ag}_2(\text{C})(\text{dppy})_6](\text{BF}_4)_4$ ^[174] was the chief motivation for the here presented gas phase study, combining Photoluminescence (PL) and Photodissociation (PD) laser spectroscopy. Here, PD and PL spectra of mass-selected precursor cations, generated via ESI, were recored in order to elucidate the influence of BF₄⁻ counterions, the cluster charge state, and losses of „HBF₄“ on the optical properties of the cluster. Dual emission observed by PL was traced back to

emission of fragment ions presumably formed by loss of the capping Ag(I) ions. In addition, TD-DFT calculations supported the assignment of the electronic transitions and emissive triplet states.

4.5. Publication 5 (IJMS)

Fragmentation pathways of dianionic $[\text{Pt}_2(\mu\text{-P}_2\text{O}_5\text{H}_2)_4 + \text{X,Y}]^{2-}$ ($\text{X,Y} = \text{H, K, Ag}$) species in an ion trap induced by collisions and UV photoexcitation, S. V. Kruppa, Y. Nosenko, M.-O. Winghart, S.P. Walg, M.M. Kappes, C. Riehn, International Journal of Mass Spectrometry, 2016, 395, 7-19. ^[166]

Publ. 5 explores the collisional and photo-induced dissociation pathways of H^+ , K^+ , Ag^+ counteranion adducts of the prototypical $d^8\text{-}d^8$ diplatinum complex $[\text{Pt}_2(\text{pop})_4]^{4-}$ (see Fig. 4.1 D), representing the first gas phase study of this well-known and extensively in solution investigated anionic complex ^[10, 15, 50, 115]. $[\text{Pt}_2(\text{pop})_4]^{4-}$ is known for its unique photochemical properties featuring a platinum-centered $^1\text{MC}(d\sigma^*\text{-}p\sigma)$ transition, which is associated with an enhancement of Pt-Pt bonding interaction in electronic excited states and concomitant shortening of the Pt-Pt distance upon photoexcitation ^[10, 115]. Additionally, $[\text{Pt}_2(\text{pop})_4]^{4-}$ in its long-lived triplet excited state is prone to form exciplexes with Ag^+/Tl^+ in aqueous solution. In the case of „ $\text{Ag}/[\text{Pt}_2(\text{pop})_4]$ “ exciplexes, a linear axial coordination motif „ Ag-Pt-Pt-(Ag) “ was proposed on the basis of time-resolved X-ray studies in solution and supported by DFT calculations ^[176]. However, the molecular structures of Ag(I) adducts of $[\text{Pt}_2(\text{pop})_4]^{4-}$, in the electronic ground state had been unknown. In order to close this knowledge-gap, mass-selected $[\text{Pt}_2(\text{pop})_4 + \text{X,Y}]^{2-}$ ($\text{X,Y} = \text{H, K, Ag}$) molecular dianions were probed by laser irradiation in an ion trap. The observed fragment channels, i.e. electron detachment, ionic and neutral fragmentation, are strongly influenced by counterion coordination. A side-on cation binding motif was inferred from these results and compared to DFT calculated molecular structures. Finally, the UV-PD ion spectra of $[\text{Pt}_2(\text{pop})_4 + \text{X,Y}]^{2-}$ are presented and shown to match nicely (for $\text{X,Y} = \text{H, K}$) the UV absorption spectrum of $\text{K}_4[\text{Pt}_2(\text{pop})_4]$ in aqueous solution.

In addition to Publications 1-5, two conference proceedings ^[167-168] and two joined publications ^[14, 177] are enclosed. For the two conference proceedings ^[167-168]: the first one reports preliminary results on the $[\text{Ag}_2(\text{L}^{\text{Cy}})_2]^{2+}$ and $[\text{Ag}_2(\text{Cl})(\text{L}^{\text{Cy}})_2]^+$ species (see Fig. 4.1 A) which are elaborated in greater detail in Publ. 1 (PCCP) and Publ. 2 (JPCLett); the second builds upon the findings of Publ. 2 (JPCLett) and additionally covers preliminary data on the size-reduced $[\text{Ag}_2(\text{Cl})(\text{L}^{\text{Me}})_2]^+$ system in comparison to $[\text{Ag}_2(\text{Cl})(\text{L}^{\text{Cy}})_2]^+$. For the two joined publications ^[14, 177]: the first one accounts for static and time-resolved photoelectron spectroscopy of gaseous $[\text{Pt}_2(\text{pop})_{4+\text{H},\text{H}}]^{2-}$ ions (see Fig. 4.1 D) that has been conducted by Dr. Marc-Oliver Winghart in the group of Prof. Dr. Kappes (KIT, Karlsruhe), in parallel to the research presented in Publ. 5 (IJMS); the second relates to the doctoral thesis of Dr. Christoph Kaub ^[178] from the group of Prof. Dr. Roesky (KIT, Karlsruhe), and contains the mass spectrometric characterization of NHC (N-heterocyclic carbene) complexes of d^{10} metal cations ($\text{M} = \text{Cu}^+, \text{Ag}^+, \text{Au}^+, \text{Zn}^{2+}, \text{Cd}^{2+}, \text{Hg}^{2+}$).

5. Electronic Photodissociation Ion Spectroscopy

5.1. Static UV-PD action spectroscopy

In contrast to conventional absorption spectroscopy, which is based upon the measurement of light absorption of a sample according to the *Lambert-Beer law* [20], the low density of ions that are typically attainable in the gas phase makes it challenging to detect the according subtle differences in light intensities. Although direct optical absorption spectra of gaseous ions have been successfully recorded [179-182], methods based on so called „*action spectroscopy*“ [20, 129, 142-151] which depend on an observable action as a related consequence of light absorption (photoresponse), are more widespread due to the fact that they are usually technically less demanding [183] and generally provide a better signal-to-noise ratio. Among them, *photodissociation* (PD) action spectroscopy relies on monitoring the extent of fragmentation of targeted (multiple) charged precursor ions ($P^{n\pm}$, $n \geq 1$, see Fig. 5.2) in a mass spectrometer as surrogate signal for photon absorption as a function of wavelength. Selected reviews that give an overview on photodissociation techniques for the field of ion spectroscopy are provided by Refs. [129, 180, 184-188].

Besides other photon-based ion activation/dissociation methods in X-ray [189-190] and infrared [191-192] spectral ranges, this thesis is primarily focused on electronic PD spectroscopy utilizing UV/(Vis) photons (abbrev. UV-PD). The experimental setup, combining a „*Paul*“-type quadrupole ion-trap mass spectrometer (3D-QIT) with two wavelength-tunable femtosecond laser systems, is described in detail in the experimental section (chapter 6). Conceptionally, the 3D-QIT facilitates the isolation of a gaseous ensemble of spatially confined, mass-selected target ions („ion cloud“) that can be stored for a controlled timeframe within tens to hundreds of milliseconds (t_{frag} , chapter 6.1.6), during which the precursor species can interact with a laser beam (multiple-shot experiment, pulse repetition rate ~ 1 kHz). Subsequently, mass analysis is performed yielding a mass spectrum of remaining precursor and photofragment ion signal intensities as a function of mass-to-charge

ratio (m/z). Hence, the main observables in a UV-PD spectroscopic experiment are: intensity of ion signals, m/z , and photon energy E_{hv} or wavelength λ , see Fig. 5.1).

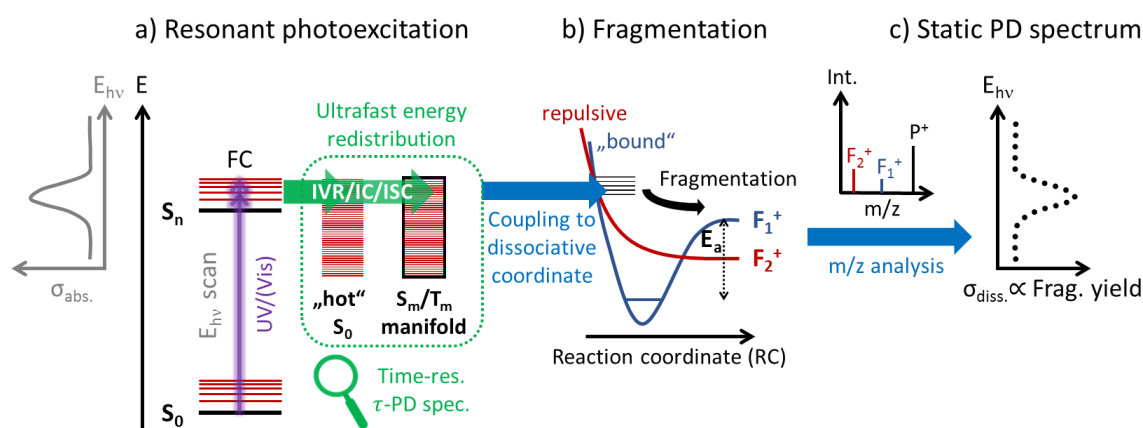


Fig. 5.1 Schematic representation of the correlation between resonant single-photon absorption (*gas phase absorption spectrum*, grey line) and photodissociation action (*PD action spectrum*, black dots) as a function of photon energy (E_{hv}). a) Schematic energy diagram corresponding to UV/(Vis) photoexcitation of gaseous precursor ions from their electronic singlet ground state (S_0) into S_n ($n \geq 1$) excited states, and ensuing dynamical processes within the excited-state manifold (FC: *Franck-Condon state*, S_m/T_m : excited singlet/triplet states, $n \geq m$). b) Exemplified potential curves along a dissociative reaction coordinate (RC), distinguishing between a „repulsive“ or „bound“ character of respective *fragmenting states* (vibrationally excited S_n , S_0 , S_m/T_m states). c) Illustrated PD action spectrum (E_{hv} versus dissociation cross section $\sigma_{diss.}$).

Figuratively speaking, the ion trap represents an ideal „test tube“ [191] for the study of gas-phase reactions and intrinsic optical properties of analyte ions under isolated conditions, i.e. the absence of solvent molecules, counter ions or other environmental effects. In principle, PD action spectra should be directly comparable to calculated electronic spectra, thereby providing a benchmark for the accuracy of computational methods. By comparing gas phase absorption with absorption in condensed phase, information on molecule-solvent or molecule-counterion interactions may be obtained e.g. from solvatochromic shifts [145, 193-195]. An additional advantage is the low sample requirement paired with the sensitive ion detection, rendering PD spectroscopy a powerful investigative tool for the

characterization of reaction intermediates or other transient species which are difficult to detect by conventional solution-phase methods [129].

In the following, the principle of UV-PD spectroscopy will be simply elucidated with the aid of Fig. 5.1. Energetically, electronic transitions are generally linked with vibrational excitation of the FC modes of the respective chromophor (initial energy deposition). Here, the „strength“ of the electronic (vibronic) transition, reflected by the cross section for photon absorption $\sigma_{abs.}(\lambda)$, is approximately governed by the electronic transition moment as well as the respective FC factors [20], and hence is dependent on photon energy (wavelength) [196]. The main premise in order to be able to reconstruct the linear gas phase absorption spectrum ($\sigma_{abs.}$ vs. photon energy, grey inset of Fig. 5.1) from photofragment mass spectra, is the assumption of a linear relationship (proportionality) between $\sigma_{abs.}(\lambda)$ and the experimentally determined dissociation cross section $\sigma_{diss.}(\lambda)$. This begs the questions of which conditions have to be satisfied for this ($\sigma_{diss.} \propto \sigma_{abs.}$) to be true and which parameters play a decisive role in this context.

First, following photon absorption, the energy that is imparted on the system must be sufficiently large to induce dissociation on the timescale of the experiment (tens/hundreds of milliseconds, see chapter 6.1.6), thereby generating fragment ion signals. Therefore, the photon energy (E_{hv}) must be at least larger than the activation energy (E_a) of the lowest energy fragmentation pathway [197-198]. One of the hallmarks of using UV(Vis) irradiation is, that a single, instantaneously absorbed UV photon provides access to fragmentation pathways with activation energies within the range of ~ 3 -6 eV (~ 300 -600 kJ/mol), in contrast to the step-wise energy transfer occurring during IRMPD [129, 186-187] or CID [133, 137-138, 141] activation methods. In addition, it has to be noted that the internal energy of gaseous photo-activated ions is conserved for a longer time period (milliseconds) inside the 3D-QIT, since thermalization of the ion cloud mainly proceeds by collisional cooling [199] with helium buffer gas ($T_{ions} \sim 300$ K, $p_{He} \approx 10^{-3}$ mbar, ~ 30 collisions/ms [166]), in contrast to the condensed phase of liquids or solid matrices where molecules are energetically coupled to a surrounding „heat bath“.

Second, the respective electronic states in which dissociation proceeds („*fragmenting states*“) play a significant role on type of activated fragmentation pathways and dissociation mechanisms, and are directly linked with the dynamic ultrafast energy conversion and redistribution processes (IVR/IC/ISC, see Fig. 5.1 a). It has been shown that differences in fragmentation mechanisms, depending on the initially excited states accessed at different photon energies, can lead to a large variability within fragment-specific action spectra and fragment branching ratios [200]. Hence, for the interpretation of action spectra, the fragment-specific behaviour has to be monitored carefully. Although it is experimentally very challenging to ascertain the underlying fragmentation mechanisms [201-204] as well as the fragmenting states, one may define two distinct processes, namely: *direct* and *indirect* dissociation, respectively [153, 158, 184-185, 196, 200, 205].

In the case of a *direct* mechanism, photoexcitation leads to immediate dissociation (sub tens of fs) without significant energy redistribution or coupling to other internal degrees of freedom. This is typically observed in the case of a „repulsive“ (nearly barrierless) character of the excited state potential energy surface (Fig. 5.1 b). Alternatively, fragmentation can directly follow from a „bound“ excited state potential energy surface, exhibiting a small dissociation barrier („predissociative“ state [184]), if the „initial“ vibrational energy along the reaction coordinate is larger than E_a (Fig. 5.1 b). Examples of direct dissociation pathways are e.g. electron detachment [14, 200], hydrogen atom loss [153, 158] or cleavage of other smaller fragments [5, 184, 196], partially bearing state-specific character.

In the case of an *indirect* mechanism, dissociation is hindered by a potential barrier or some other dynamical constraint, and is therefore preceded by dynamical processes such as internal vibrational energy redistribution (IVR) and the conversion of electronic energy into vibrational energy (IC, ISC). This „delayed“ fragmentation can take place in the vibrationally hot ground state (S_0) or hot electronically excited states (S_m/T_m) after sufficient internal energy is accumulated within the reaction coordinate (Fig. 5.1 b) to overcome the dissociation barrier (E_a), or via coupling to a repulsive excited state potential. As a result, the rate of

fragmentation strongly depends on coupling between states and energy redistribution pathways and therefore largely differs from system to system within the temporal range of hundreds of fs up to several ms [5, 196, 205-206]. Within this context, the size of the target system as well as the large state density of multinuclear transition metal complexes may be limiting factors [185], since internal energy may be statistically (ergodically) redistributed among the many size-dependent internal degrees of freedom, resulting in a sort of „energy dilution“ and therefore the suppression of fragmentation.

Furthermore, the underlying fragmentation mechanisms depend on the charge state of precursor ions and may therefore be categorized into a) neutral loss, b) ionic fragmentation and c) electron detachment as summarized in Fig. 5.2.

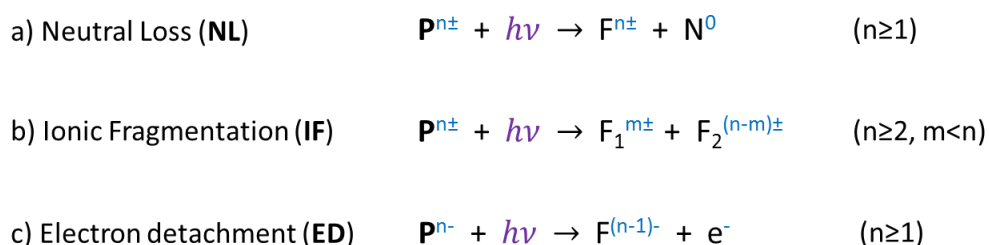


Fig. 5.2 Types of unimolecular dissociation reactions of photon-activated cationic or anionic precursor species $\mathbf{P}^{n\pm}$ including a) dissociation of a neutral moiety \mathbf{N}^0 , leaving a charged fragment $\mathbf{F}^{n\pm}$, b) fragmentation of a multiple charged ion under separation of charge [207-208] yielding the complementary fragments $\mathbf{F}_1^{m\pm}$ and $\mathbf{F}_2^{(n-m)\pm}$ ($n \geq 2$, $m < n$), c) electron detachment in the case of anionic precursor species [14, 149, 208]. UV/(Vis) photons ($h\nu$) and charge states (n , m) are indicated in violet and blue, respectively.

Third, a procedure for estimating the absorption cross section from mass spectrometrical data is presented in the following. In a simplified model, assuming single-photon absorption and detection of all ionic fragments (absence of „dark channels“), further neglecting the m/z -dependent detection efficiency of the mass spectrometer, σ_{abs} can be approximated according to Eq. (5.1):

$$\sigma_{abs.}(\lambda) \propto \frac{Y_{tot.}(\lambda, Q_{dis.})}{\underbrace{N_{\lambda}}_{\sigma'_{diss.}(\lambda)}} \cdot \frac{1}{Q_{dis.}(\lambda)} \quad (5.1)$$

where $Y_{tot.}$: total fragment yield (Eq. (5.3)), N_{λ} : number of photons per laser pulse at wavelength λ (Eq. (5.2)), and $Q_{dis.}$: photodissociation quantum yield ($\hat{=}$ ratio of the number of fragmenting precursor ions to the number of photoexcited ions).

$$N_{\lambda} = \frac{E_{pulse} \cdot \lambda}{hc} \quad (5.2)$$

E_{pulse} : laser pulse energy, h : Planck constant ($h = 6.62608 \cdot 10^{-34}$ Js [209]), c : speed of light in vacuum ($c = 2.99792458 \cdot 10^8$ m/s [209]).

The wavelength-dependent total fragment yield $Y_{tot.}(\lambda)$, representing the extent of photo-induced dissociation, can be calculated according to Eq. (5.3) for the example of monocationic precursor/fragment ions:

$$Y_{tot.}(\lambda) = \frac{\sum_i F_i^+}{\mathbf{P}^+ + \sum_i F_i^+} \quad (5.3)$$

where, F_i^+ and \mathbf{P}^+ : signal intensity of ionic fragment species i and precursor ions, respectively (integrated over their respective isotope patterns).

If the number of laser pulses N_{pulse} are kept constant (multi-shot experiment, $Y_{tot.}$ and $Q_{dis.}$ both dependent on N_{pulse}), the gas-phase absorption spectrum can be reconstructed from mass-spectrometric data as „fragment yield spectra“ by normalizing $Y_{tot.}(\lambda)$ to the number of photons per laser pulse (N_{λ}) at each wavelength position, a term that is denoted as $\sigma'_{diss.}(\lambda)$ in Eq. (5.1). It should be noted that $\sigma'_{diss.}(\lambda)$ is a unitless quantity, as it is difficult to measure $\sigma_{abs.}$ in absolute units. According to Eq. (5.1) it is clear that the premise of a linear relationship between dissociation and absorption cross-sections ($\sigma_{diss.} \approx \sigma'_{diss.} \propto \sigma_{abs.}$) is only met, provided that the photodissociation quantum yield ($Q_{dis.}$), which is difficult to

access experimentally and generally not known, is approximately constant over the spectral range that is investigated (ideally $Q_{dis.} = 1$). However, in practise $Q_{dis.}$ may be dependent on wavelength and the involved fragmenting electronic states, or be strongly influenced by competing non-fragmenting pathways such as radiative and collisional cooling (Fig. 5.4). In addition, the photodissociation cross section may also be determined from the *Lambert-Beer law* giving a „ $-\ln(Y_{tot.}(\lambda))$ “ type expression for $\sigma_{abs.}$ [149].

Alternatively, the gas phase absorption spectrum can be derived from the depletion of the precursor ion signal by calculating the ratio of depleted (laser on) to undepleted (laser off) ion intensity as a function of photon energy [147]. This has the advantage that there is no loss of signal intensity, or potential loss of information, in the case of non-detectable fragments („dark“ fragmentation channels). Consequently, the *PD depletion spectrum* may be a better representative for the absorption spectrum. However, depletion measurements are generally more noisy and are only feasible in case of a significant decrease in precursor ion signal e.g. by using single pulses of high-power ns lasers (in the mJ range). However, signal fluctuations originating from the ion source, laser pulse instabilities and possible multi-photon excitations have to be considered. In the context of this work the focus was put on recording *fragment yield spectra*, since in most cases depletion of precursor ions was only as high as a few percent.

In summary, PD spectroscopy is a prevalent tool for measuring gas-phase ion absorption spectra where the net energy deposition via photoexcitation can, to some extent, be experimentally controlled by photon energy (wavelength), pulse intensity, number of pulses and pulse repetition rate. However, there are several caveats and effects which may lead to scrambling of information and therefore complicate the interpretation of PD action spectra: In particular, a) multiple photon absorption, having been shown to strongly influence the shape of PD spectra [147], b) the existence of various isomers of the target species (same m/z ratio) [150], c) secondary fragmentation processes originating from photon absorption of trapped photofragments (multiple-shot experiment), d) non-detectable „dark“ fragments or

species with overlapping isotope patterns, e) the quantum yield for dissociation $Q_{dis.}(\lambda)$ (Eq. (5.1)) being strongly dependent on λ or influenced by non-fragmenting deactivation pathways such as luminescence and collisional cooling, f) imperfect overlap between ion cloud and laser beam or change in ion illumination by variable beam profile influencing photon density [210], and generally g) the dependence of fragmentation rates on, size of the target system (number of internal degrees of freedom), photon energy, fragmentation mechanisms (e.g. electron photodetachment [148, 166]), fragmentation kinetics [211], and fragmenting electronic states.

These effects could lead to a „mismatch“ between the acquired action and absorption spectrum [185]. In addition, fragmentation pathways may be strongly dependent on the nature of charges (single/multiple charged, anionic/cationic, see Fig. 5.2). For instance, multiply-charged anionic systems usually display *electron detachment* as the prevalent channel for dissociation which may appear on different time scales and according efficiencies (fast „direct“ detachment, excited-state tunnel detachment, and thermionic emission) [14, 149], therefore representing varyingly efficacious marker for photon absorption [185]. However, since only a proportionality between fragment yield and absorption cross section suffices in order to obtain spectroscopic information, electronic PD yield spectroscopy is meanwhile widespread for different classes of molecular systems [147-151, 183, 195, 212-214].

5.2. Transient photodissociation (τ -PD) detection scheme

The transient photodissociation (τ -PD) technique utilizes a „pump-probe“ detection scheme ^[152] with the objective of monitoring the time evolution of electronic excited target states for a mass-selected ensemble of trapped precursor ions by means of a characteristic mass spectrometric signal. As is the nature of action ion spectroscopy, this is achieved in an „indirect“ way by recording the relative variations in intensities of ionic photofragments as a function of time delay Δt between fs *pump* and *probe* pulses ^[164]. In order to qualitatively describe the operating principle of time-resolved PD spectroscopy, the following questions will be elucidated further on: How can the pump-probe delay (Δt) be controlled within the fs-to-ps temporal range? What irradiation parameters for *pump* and *probe* beams are desirable (pulse energy, wavelength)? How can a transient change in the fragmentation pattern that specifically comprises intricate information of excited-state deactivation kinetics be rationalized? What types of signals are conceivable? How can the state-specific time constants (τ_i) be derived from τ -PD data?

The relative pump-probe delay is controlled by a motorized optical delay line that changes the optical path length (Δx) of the probe beam with respect to the pump beam according to $\Delta t = \Delta x/c = 2\Delta x'/c$ (see chapter 6.2.9, $\Delta x'$: moved distance along the translation stage relative to a referenced starting position, c : $2.99792458 \cdot 10^8$ m/s ^[209], $\Delta x'$: $3 \mu\text{m} \approx \Delta t$: 20 fs). Here, the continuous time evolution of the system (t) is repeatedly sampled for defined increments of Δt . It may be noted in passing that t and Δt are two different independent parameters, the latter constituting an indirect measurement of time by the optical delay stage (observable: $\Delta x'$), and congruency is only obtained with respect to a common temporal reference point „time zero“ (t_0). Time zero can be approximately described as the time at which the ions are irradiated by the pump pulse, and is technically defined as the time delay Δt for which both pump and probe pulse arrive simultaneously at the ion cloud. The temporal reference point (t_0) can be derived from kinetic fits of experimental data, or by a separate measurement e.g. from the pump-probe cross-correlation signal obtained by multiphoton ionization of gaseous furan molecules in

the ion trap ^[164] (see chapter 6.1.7). For the experiments discussed within this thesis, the translation stage was continuously moved at a reasonable low speed during the continuous acquisition of averaged mass spectra (chapter 6.1). As a result, every data point was obtained from an averaged mass spectrum correlated to an averaged small interval of Δt ($\Delta\Delta t$) depending on the the duty cycle of the mass spectrometer.

Whereas pump photons are utilized for resonant excitation of the electronic target state (e.g. $S_0 \rightarrow S_1$), it is advantageous to select a probe wavelength (λ_{pr}) that is off-resonance with any transitions from the electronic ground state ($S_0 \rightarrow S_n$) in order to prevent „probe-only“ and „probe-pump“ induced signal artifacts. Ideally, λ_{pr} should be resonant with excited-state absorption of the singlet/triplet states that are under investigation (e.g. $S_1 \rightarrow S_n$, $T_1 \rightarrow T_m$). However, in practice it is more expedient to utilize a fixed wavelength in the near-infrared spectral range for a multitude of target systems (NIR, λ_{pr} : 1150-1200 nm), since excited-state absorption properties of molecular ions are rarely known and laborious to measure in the gas phase. In addition, all the states involved in the photodeactivation of the system are usually not known to begin with (e.g. spectroscopically „dark“ states are not deducible from static PD spectra). The choice of a fixed probe wavelength in the NIR can be justified by the fact that TM-based molecular complexes exhibit a high density of states, making it more probable that some non-resonant multiphoton-probe absorption processes may proceed from electronically excited states. As a consequence of the multiphotonic character of probe absorption, with inherent small cross sections (σ_{pr} , σ'_{pr} , see Fig. 5.3), the pulse energy of the probe beam should be significantly larger than for the pump beam ($E_{pulse,pr} \sim 100\text{-}200 \mu\text{J}$, $E_{pulse,pu} \sim 0.1\text{-}2 \mu\text{J}$) ^[123, 152, 160, 164, 215]. The drawback of this procedure is that the excited states accessed by multiphoton-probe absorption are rather elusive. For the choice of $E_{pulse,pu}$ a trade-off between operating in the single-photon absorption regime and preparing a large enough initial excited-state population of precursor ions, to obtain a good signal/noise ratio, has to be considered.

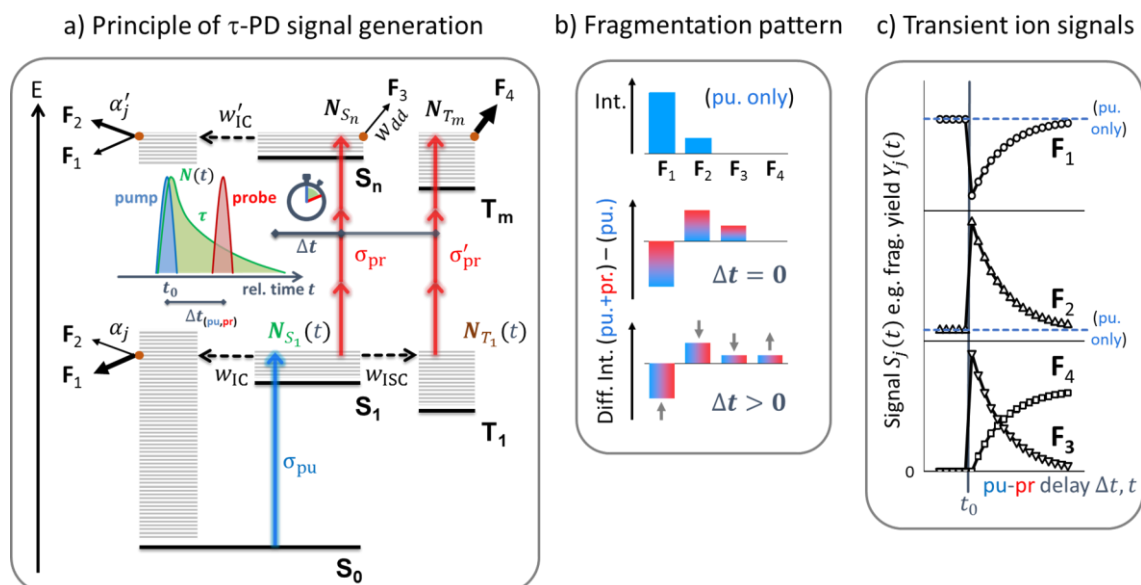


Fig. 5.3 a) Hypothetic τ -PD detection scheme and Jablonski diagram exemplified for closed-shell CMCs in the gas phase. An ensemble of precursor ions is resonantly excited from electronic ground state ($S_0 \rightarrow S_1$) via pump single-photon absorption with cross section σ_{pu} , generating the transient excited-state population $N_{S_1}(t)$. Branching probabilities for *nonradiative* deactivation processes are denoted by w_x ($x = IC, ISC, dd$: direct dissociation). Energetically higher singlet/triplet excited states ($S_n, T_m; n, m > 1$) are accessed via excited-state probe (multi)photon absorption ($\sigma_{pr}, \sigma'_{pr}$), resulting in an increase in the internal energy of the ions. This is accompanied with a change in fragmentation efficiency of photofragments F_{1-4} through alterations in the population of fragmenting states (orange dots) as well as dissociation rate constants (k_j) and therefore branching ratios ($\alpha_{j=1,2} = k_j / \sum_j k_j, \alpha_3 = w_{dd} = k_3 / (k_3 + k'_{IC}), \alpha_4 = 1$) as indicated by thickness of solid black arrows. Inset: pump-probe scheme highlighting the time dependence of excited state population $N(t)$ (t_0 : time zero, $\Delta t_{(pu,pr)}$: time delay between pump and probe pulses, sketch of stop clock modified from Ref. [216]). b) Top: Schematic fragmentation pattern (intensity distribution of fragment ion signals) obtained following „pump-only“ excitation. Bottom: difference plots indicating the respective change in fragment intensity following „pump+probe“ absorption at $\Delta t \geq 0$. c) Schematic time evolution of fragment-specific signals (e.g. fragment yield Y_j) as a function of Δt .

In order to rationalize the detection scheme of the τ -PD method, it may be expedient to contemplate conceivable mechanisms that lead to transient signal generation for a specific model case. To this end, a hypothetical example was constructed (see Fig. 5.3) by adapting the model scheme initially suggested for biomolecules by Jovet [158-

^{159]} and Weinkauff ^[157], to be representative for (multinuclear) transition metal complexes.

On that basis (Fig. 5.3), an initial excited-state population $N_{S_1}(t_0)$ shall be generated at t_0 by an optical *pump* pulse whose fixed photon energy is resonant with the lowest energy electronic transition ($S_0 \rightarrow S_1$). From this point on, the excited state reaction dynamics is initiated and evolves with relative time (t). For the sake of simplicity, the following assumptions and simplifications are applied:

a) The initial population $N_{S_1}(t_0)$ is prepared by single-photon absorption and the depopulation of S_1 obeys first-order unimolecular kinetics according to $N_{S_1}(t) \propto \sigma_{pu} \cdot e^{(-t/\tau)}$ (τ : time constant, time in which $N_{S_1}(t)$ decays to $1/e$ of its initial value at t_0), assuming that $N_{S_1}(t_0) \propto \sigma_{pu}$.

b) S_1 is exclusively deactivated by two competing parallel pathways with branching probabilities $w_{IC} = k_{IC}/(k_{IC} + k_{ISC})$ and $w_{ISC} = k_{ISC}/(k_{IC} + k_{ISC})$, respectively (k_x : rate constant for $x=IC, ISC$ process), determining $\tau = 1/(k_{IC} + k_{ISC})$.

c) All photoexcited precursor ions that undergo IC dissociate in the vibrational excited „hot“ S_0 state with branching ratios $\alpha_j = k_j/\sum_j k_j$ for the two competing dissociation pathways ($j = 1, 2$).

d) A triplet excited-state population $N_{T_1}(t)$ is generated by a percentage of photoexcited ions undergoing ISC. Since triplet excited states are usually long lived ($\sim \mu s$) compared to the observation time window in a typical pump-probe experiment utilizing an optical delay line (~ 1 ns), the time evolution of $N_{T_1}(t)$ should mainly depend on fast population transfer from S_1 , neglecting potential deactivation pathways of T_1 . Furthermore, for the sake of simplicity it is assumed that no additional fragments may directly originate from T_1 . For example, the excess internal energy distributed among the vibrational degrees of freedom may be smaller than the lowest-energy dissociation barrier and deactivation of T_1 proceeds slowly via collisional cooling.

In summary, based on the assumptions made above, only a single fragmenting state („hot“ S_0 , see Fig. 5.3 a) is populated as consequence of single-photon pump absorption, giving exclusive access to the ionic fragments F_1 and F_2 in absence of the probe beam. As a result, the „pump only“ fragmentation pattern (Fig. 5.3 b), i.e. the intensity distribution for detected F_1 and F_2 fragments, would be obtained by mass analysis after a controlled ion storage time of ~ 100 ms ($t_{frag.}$, see chapter 6.1.6).

In the case of excitation by consecutive *pump* and *probe* pulses, excited-state probe absorption can occur at a given time delay ($\Delta t \geq 0$) with cross sections σ_{pr} ($S_1 \rightarrow S_n$) and σ'_{pr} ($T_1 \rightarrow T_m$), respectively (typically $\sigma_{pr} > \sigma'_{pr}$). Here probe-absorption for ions in electronic ground state shall be excluded. Consequently, at a given Δt a portion of excited-state populations $N_{S_1}(t)$ and $N_{T_1}(t)$ is removed and transferred into energetically higher states, generating populations N_{S_n} and N_{T_m} , respectively. During these immediate processes, the total number of electronically excited ions remains constant, according to $N_{S_1} = N'_{S_1} + N_{S_n}$ and $N_{T_1} = N'_{T_1} + N_{T_m}$ (N_{S_1}, N_{T_1} : populations at $t = \Delta t$ immediately prior to probe absorption and N'_{S_1}, N'_{T_1} : remaining populations at $t = \Delta t$ immediately after probe absorption). It should be noted, that the time evolution of states generated by probe absorption is intangible in a two-pulse excitation scheme and not further relevant in this context. Here, the crucial point is that the quantities of N_{S_n} and N_{T_m} are directly correlated with the transient populations $N_{S_1}(t)$ and $N_{T_1}(t)$ as well as σ_{pr} and σ'_{pr} at a given point in time, and ideally correlated with a change in fragmentation pattern. The latter may be achieved if S_n, T_m states are differently coupled to the *fragmenting states* compared to the situation without probe excitation, or lead to the population of additional *fragmenting states*. A transient ion signal may then be observed in the event that the „fragmentation efficiency“ (see Eq. (5.4)) for any fragmentation pathway j is considerably modified (F_1, F_2) or new state-specific fragments are accessed (F_3, F_4 , see Fig. 5.3 a). Hence, for successive delays Δt , information of the time evolution of the initially excited S_1 state can be indirectly imparted on both N_{S_n} and N_{T_m} populations.

In the hypothetical model that is contemplated here, the specific fragments F_3 and F_4 ($\alpha_4 = 1$) shall be generated in S_n and T_m states, respectively e.g. by fast direct dissociation (see chapter (5.1)). Additionally, S_n is deactivated by two competing pathways, direct dissociation ($w_{dd} = k_3/(k_3 + k'_{IC}) = \alpha_3$) and internal conversion (w'_{IC}), respectively. Accordingly, the „hot“ S_0 electronic ground state (fragmenting state pertaining to F_1 and F_2) can be accessed via IC either from S_1 or S_n , determining the available amount of its internal vibrational energy ($E(S_n) > E(S_1)$). According to *RRKM* theory ^[217], unimolecular dissociation rate constants depend on internal vibrational energy of the excited precursor ion and dissociation barriers along the reaction coordinates. It can therefore be rationalized that the branching ratios of fragment channels $j = 1, 2$ following either pump+probe absorption ($\alpha'_j = k'_j/\sum_j k'_j$) or pump-only absorption ($\alpha_j = k_j/\sum_j k_j$) may drastically differ due to different amounts of available internal vibrational energy as illustrated in Fig. 5.3 a (thickness of arrows).

The channel-specific (j) transient ion signals $S_j(t)$ may thus be qualitatively described by Eqs. (5.4)-(5.6):

$$S_{j=1,2}(t) \propto \underbrace{\sigma_{pr} \cdot \frac{\sigma_{pu} e^{(-t/\tau)}}{\propto N_{S_1}(t)}}_{\propto N_{S_n}} \cdot \underbrace{(\alpha'_j w'_{IC} - \alpha_j w_{IC})}_{\substack{\text{change in "frag. eff."} \\ \text{in "hot" } S_0 \text{ frag. state}}} \quad (5.4)$$

$$S_3(t) \propto \sigma_{pr} \cdot \sigma_{pu} e^{(-t/\tau)} \cdot w_{dd} \quad (5.5)$$

$$S_4(t) \propto \sigma'_{pr} \cdot \underbrace{w_{ISC} \sigma_{pu} (1 - e^{(-t/\tau)})}_{\substack{\propto N_{T_1}(t) \\ \propto N_{T_m}}} \quad (5.6)$$

where t : relative time with respect to t_0 ; $\tau = 1/(k_{IC} + k_{ISC})$: lifetime of S_1 state; k_{IC} , k_{ISC} : IC, ISC rate constants; σ_{pu} : pump-absorption cross section; σ_{pr} and σ'_{pr} probe-absorption cross section for S_1 and T_1 state, resp.; N_x : number of precursor ions in $x = S_{1,n}, T_{1,m}$ excited states ($n, m > 1$); $\alpha'_j = k'_j/\sum_j k'_j$, $\alpha_j = k_j/\sum_j k_j$: fragmentation branching ratios with respective dissociation rate constants k_j following

pump+probe and pump-only excitation, resp.; w_y : branching probability of processes $y = IC, ISC, dd$ ($dd = \text{direct dissociation}$).

It is clear from Eqs. (5.4)-(5.6) that, for a particular fragment channel j , a transient ion signal can only be generated ($S_j(t) \neq 0$), if the fragmentation efficiency is modified ($\alpha'_j w'_{IC} - \alpha_j w_{IC} \neq 0$) either due to significant change in fragmentation branching ratios ($\alpha'_j \neq \alpha_j$) or a change in population of respective fragmenting states (e.g. $w'_{IC} \neq w_{IC}$). The relative changes in the fragmentation pattern as a result of probe photon absorption ($\sigma_{pr}, \sigma'_{pr} \neq 0$) can be highlighted by difference intensity plots (Fig. 5.3 b, bottom), obtained by subtracting the fragment ion signals observed by pump-only excitation from the fragment intensities generated by pump+probe excitation at a specific Δt . Here, a decrease in intensity of fragment F₁ and concomitant increase in F₂ and F₃ ion signal would be obtained for $\Delta t=0$, since $\alpha'_1 < \alpha_1, \alpha'_2 > \alpha_2, w'_{IC} \approx w_{IC}, \alpha_3 = w_{dd} > 0$ (Fig. 5.3 b,c; Eqs. (5.4)-(5.6)). Note, that the ensuing transient increases/decreases in F₁₋₃ ion signals ($\Delta t > 0$) all correspond to the depopulation of the S_1 state, since the respective sign of $S_j(t)$ (positive or negative) is determined by the terms ($\alpha'_j w'_{IC} - \alpha_j w_{IC}$) and (α_3), respectively. As time evolves ($\Delta t \gg 0$), the exponentially decaying transients (F₁₋₃) approach the pump-only fragmentation level (Fig. 5.3 c, indicated by dotted lines) due to $N_{S_n} \rightarrow 0$. Since the fragment F₄ originates from T_1 excited state, its transient signal increases according to $(1 - e^{(-t/\tau)})$, converging to a constant intensity for $\Delta t \gg 0$ (here, $N_{T_m}(t)$ is approx. constant for $\Delta t \gg 0$).

In order to extract information on lifetime of excited states from a τ -PD experiment (time constants τ_i), the transients have to be fitted according to suitable kinetic models. In practise, a multi-exponential decay behavior of transient ion signals is often observed [123, 152-153, 157, 159-160, 164, 215, 218]. However, it is basically impossible to determine the underlying deactivation scheme from τ -PD data alone, owing to the fact that information on type and number of populated (fragmenting) excited-states may not be directly related to or deducible from the relative changes in the fragmentation pattern as well as ambiguities in the τ -PD signal generation process

(information scrambling, non state-specific fragments, fixed λ_{pr} resulting in small σ_{pr} for some excited states). For that reason, the approach of modelling τ -PD data as a sum of n exponential (decay) functions that are numerically convoluted with a Gaussian function according to Eqs. (5.7)-(5.8) [10, 219], has been well established. The Gaussian („instrument response function“) [219] represents a mathematical weight of the signal, taking the change in overlap between the temporal profiles of pump and probe pulses into account.

$$F_j(t) = \sum_{i=1}^n A_i \cdot e^{(-t/\tau_i)} \otimes g(t, t_0, fwhm) \quad (5.7)$$

$F_j(t)$: kinetic fit of transient signal for channel j , n : number of time constants, τ_i : time constant of the i th one-exponential decay, A_i : decay associated amplitudes, t_0 : time zero, $fwhm$: full width at half maximum of Gaussian $g()$ [220], \otimes : convolution operator [220].

$$F_j(t) = F_{0,j} + \sum_{i=1}^n \left[A_i \cdot 0.5 \cdot \exp \left(0.5 \cdot \left(\frac{w}{\tau_i} \right)^2 - \frac{(t - t_0)}{\tau_i} \right) \cdot \left(1 + \operatorname{erf} \left(\frac{1}{\sqrt{2}} \cdot \left(\frac{(t - t_0)}{w} - \frac{w}{\tau_i} \right) \right) \right) \right] \quad (5.8)$$

$F_{0,j}$: ordinate offset, $w = fwhm/2\sqrt{2\ln(2)}$: width of Gaussian, $\operatorname{erf}()$: error function [220] (result from convoluting a exponential function with a Gaussian function [219]).

In addition, the time-profiles of ion signals may contain oscillatory components originating from quantum coherence phenomena such as *vibrational* [10, 123] and *electronic coherence* [221-222]. Accordingly, additional oscillatory terms $F_{osc}(t)$ (see Eq. (5.9)) can be added to Eq. (5.8). In the case of vibrational coherence an oscillating pump-probe signal may be rationalized by time-dependent probe-absorption cross sections $\sigma_{pr}(t)$, originating in time-dependent *Franck-Condon factors* determined by the evolution of the nuclear wave packet.

$$F_{osc}(t) = A_{osc} \cdot \sin\left(\frac{2\pi \cdot t}{t_{osc}} + \varphi\right) \cdot 0.5 \cdot \exp\left(0.5 \cdot \left(\frac{w}{\tau_d}\right)^2 - \frac{(t - t_0)}{\tau_d}\right) \cdot \left(1 + \operatorname{erf}\left(\frac{1}{\sqrt{2}} \cdot \left(\frac{(t - t_0)}{w} - \frac{w}{\tau_d}\right)\right)\right) \quad (5.9)$$

A_{osc} : oscillation associated amplitude, t_{osc} : oscillation period, φ : oscillation phase, τ_d : decoherence time.

In summary, the principle of τ -PD ion spectroscopy is based upon a transient change in the fragmentation pattern as a result of excited-state probe absorption. Here, the time-dependent ion signals correlate with a probe-induced transfer of excited-state population that ultimately results in variation of fragmentation efficiency or specific dissociation products within the fragmenting states of the photoexcited system.

In reality, the excited-state dynamics of molecular ions are usually rather complicated, making τ -PD signals difficult to interpret due to a multitude of unknown parameters. On that account, some additional aspects and caveats are discussed in the following:

First, since the total number of electronically excited ions at t_0 does not change directly during the probe-(multi)photon absorption process, the total number of fragments should also remain constant, assuming that every excited ion dissociates prior to mass analysis. Consequently, an overall increase in ion signal intensity for every single fragment should not be possible to observe at t_0 . As if contrary to this, however, an increase in total fragment yield (Eq. (5.3)) has been experimentally observed [123, 160, 164, 223] and is indicative of collisional and radiative cooling processes (non-fragmenting pathways) effectively competing with dissociation. In order to remedy this seeming contradiction, an effective cooling rate constant $k_{c,eff}$ could be considered for dissociation branching ratios: $\alpha_j = k_j / (\sum_j k_j + k_{c,eff})$. On these grounds, if no dependence of the precursor ion signal on pump-probe delay is observed [224], meaning that intensity is merely redistributed among all fragment ion

signals, this may be an indication that photodissociation occurs very fast with respect to radiative and collisional cooling.

Second, contributions of all fragmenting states leading to a specific fragment j need to be considered. Hence, the possibility that several different fragmenting states may lead to the production of the same product ion has to be taken into account. In addition, the primary ionic fragments (see Fig. 5.4) may further sequentially dissociate depending on their imparted internal vibrational energy, resulting in the generation of a multitude of secondary dissociation products (secondary fragments). All this would lead to „scrambling“ of information and potential „weakening“ of transient signals by compensating contributions (e.g. different signs, Eq. (5.4)).

Third, excited-state deactivation of photoexcited molecular ions could be considered as a complex cascading network of coupled, inter-dependent unimolecular elementary steps ^[138]. These sequential and/or parallel (competing) processes can occur on different or overlapping timescales (fs-ms), potentially involving a multitude of excited states as schematically illustrated by Fig. 5.4. Therefore, in order to account for more sophisticated kinetic deactivation schemes of excited-state populations $N_{state}(t)$, the qualitative descriptions for transient signals $S_j(t)$ (Eqs. (5.4)-(5.6)) may be modified depending on available information and complexity of the target system. For example, given the case that an initially excited state S_1 almost exclusively decays via ISC ($k_{ISC} \gg k_{IC} \rightarrow w_{IC} \approx 0$, Fig. 5.3) and the populated T_1 state subsequently decays via ISC (k'_{ISC}) into S_0 ground state ($S_1 \xrightarrow{k_{ISC}} T_1 \xrightarrow{k'_{ISC}} S_0$), the time-dependant populations $N_{S_1}(t)$ and $N_{T_1}(t)$ could be approximated by the following expressions:

$$N_{S_1}(t) \propto \sigma_{pu} e^{-k_{ISC} \cdot t} \quad (5.10)$$

$$N_{T_1}(t) \propto \sigma_{pu} \cdot k_{ISC} / (k'_{ISC} - k_{ISC}) \cdot [e^{-k_{ISC} \cdot t} - e^{-k'_{ISC} \cdot t}] \quad (5.11)$$

According to the example model presented above (Fig. 5.3, Eqs. (5.10),(5.11)) the transient for fragment F_4 ($S_4(t)$, see Eq. (5.6)) would, in this case, contain contributions from two exponential decay functions (k_{ISC} , k'_{ISC}), whereas the transients $S_{j=1-3}(t)$ would only contain information on S_1 lifetime ($\tau_{S_1} = 1/(k_{ISC})$).

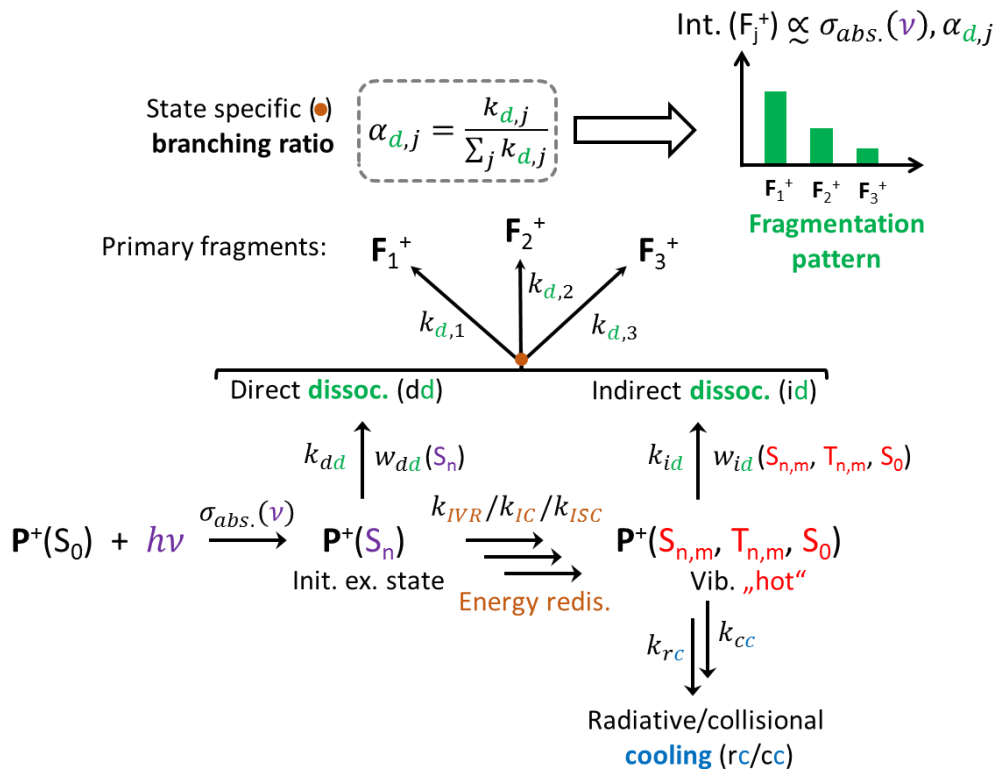


Fig. 5.4 Exemplified kinetic scheme highlighting a cascading network of coupled sequential/parallel elementary processes following UV/(Vis) photon absorption of a monocationic precursor species (P^+) in the gas phase. Rate constants (k) and branching probabilities (w) pertaining to dissociation and energy redistribution processes determine the internal energy and population of fragmenting states (illustrated as orange dot), which in turn govern state-specific branching ratios (α_j) of dissociations channels (j). Typical timescales (system specific): $k_{dd} > k_{IVR}, k_{IC}, k_{ISC} > k_{rc} \geq k_{id} > (\geq) k_{cc}(p_{He}), p_{He}$: helium pressure in the ion trap.

Last, the probe-absorption cross section may typically decrease for energetically lower-lying electronic states that are populated within the deactivation cascade (e.g. $\sigma_{pr} > \sigma'_{pr}$, Fig. 5.3), accompanied with a decrease in pump-probe signal intensity over time. This may be attributed to an „energy dilution“ within the (vibronic) excited-state manifold, the non-resonant multi-photon character of probe absorption making transition from lower-states statistically less likely, or a change in *Franck-Condon factors* due to structural rearrangement of nuclei in excited-states [225].

6. Experimental Setup and Methods

6.1. Quadrupole ion trap mass spectrometer (QIT-MS)

The mass spectrometric experiments discussed within this thesis were performed utilizing two separate quadrupole ion trap mass spectrometers (QIT-MS), *amaZon speed* (abbrev. MS-1) and *amaZon ETD* (abbrev. MS-2), respectively both from *Bruker Daltonics* and both equipped with an „*Apollo II*“ electrospray ionization (ESI) ion source. MS-1 is modified for laser access to the QIT ^[163] and for an additional feed of neutral gas (mainly furan vapour, C₆H₆O) into the trap via the helium trapping gas line (chapter 6.1.7). MS-2 provides no laser access and is used only for MS experiments. It contains a negative chemical ionization (nCI) source, facilitating the option for electron-transfer dissociation/reduction (ETD/ETR) experiments (chapter 6.1.3). The nitrogen nebulizing/drying gas was supplied from nitrogen bottles (*Air Liquide*, N₂-purity: 99.999%) for MS-1, whereas MS-2 was connected to a nitrogen generator (N₂-purity: 99%). Both QITs were purged by helium buffer gas from gas bottles (*Air Liquide*, He-purity: 99.999%). Accordingly, MS-1 was mainly used for static and time-resolved laser photodissociation (PD/ τ -PD) spectroscopy and MS-2 was exclusively used for collisional-induced dissociation (CID) and ETD/ETR experiments. Since both mass spectrometers are almost identical in any other instrumental aspects, a summarizing general schematic is depicted in Fig. 6.1, highlighting the four main unit components of the MS: a) ESI source, b) ion funnels and ion-transfer optics, c) nCI source (only MS-2) and d) ion trap module (QIT), which will be discussed in the following sections. Both QIT-MS instruments were controlled by the *trapControl* software (*Bruker Daltonics*, version 7.1 / 7.2 for MS-1 / MS-2 resp.) and could be operated in different scan modes, influencing mass range, scan speed, high vacuum pressures and resolution. These parameters are summarized in Tab. 6.1 for the most commonly used scan modes: „Ultra scan“ (us), „enhanced resolution“ (er), and „maximum resolution“ (mr) – excluding „XtremeScan“ and „Extended mass range“.

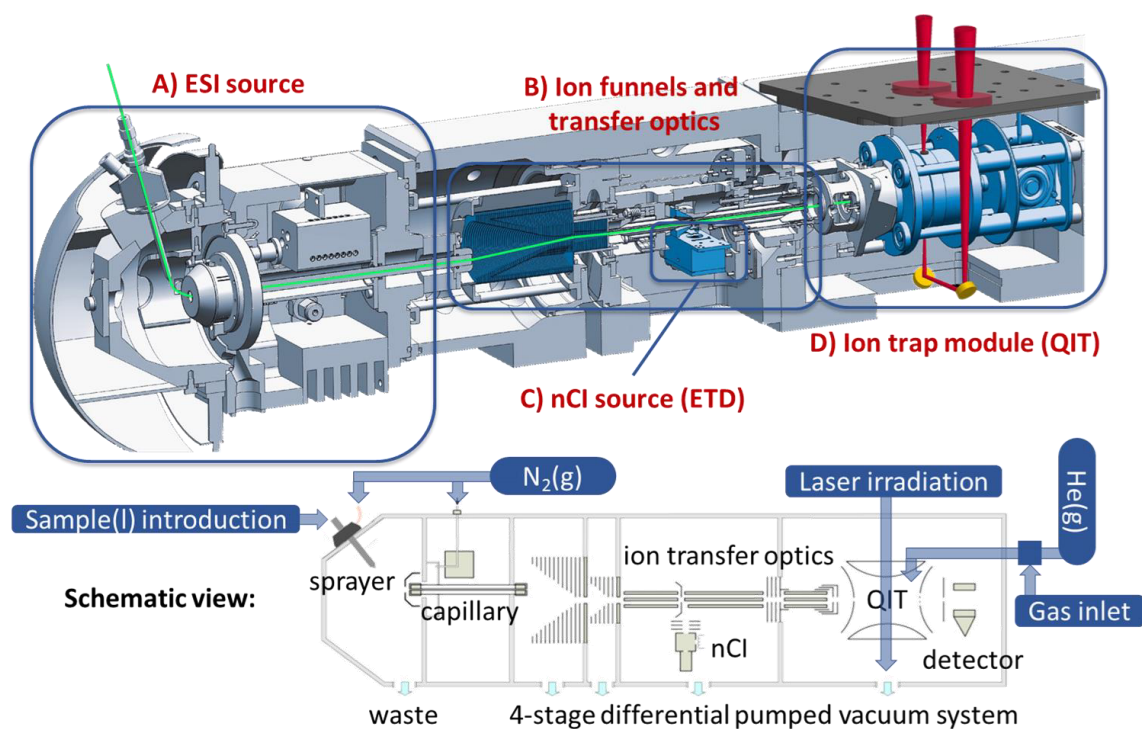


Fig. 6.1 Top: 3D schematics and main components of the *amazon Speed* (MS-1) and *amazon ETD* (MS-2) quadrupole ion trap mass spectrometers (*Bruker Daltonics*) with modification for optical access to the trapped ions (MS-1). Adapted from Ref. ^[163]. The green line describes the path of the ions throughout the MS. Bottom: Schematic view highlighting liquid sample introduction, supply of nebulizing and desolvation nitrogen gas, optical access for external UV/Vis/NIR laser irradiation and helium trapping gas line modified for inlet of an additional gas (MS-1, chapter 6.1.7). Adapted from Ref. ^[124].

Tab. 6.1 Overview of *amazon speed/ETD* scan modes and associated experimental parameters. Adapted from Ref. ^[124]

Scan mode	Mass range ^{a)} (m/z)	Scan Speed / μs^{-1}	Resolution FWHM / u	Typical pressure ^{c)} / mbar
Ultra scan (us)	70 - 3000	~ 32500	~ 0.4	$\sim 6 \cdot 10^{-6}$
Enhanced resolution (er)	50 - 3000	~ 8100	~ 0.3	$\sim 6 \cdot 10^{-6}$
Maximum resolution (mr)	50 - 3000	~ 5200	~ 0.1 ^{b)}	$\sim 5 \cdot 10^{-6}$

a) The experimental m/z window is further limited by the „lower mass cutoff“ which is dependent on isolation and MS/MS parameters.

b) For multiple charged ions ($z > 2$).

c) Pressure in the high vacuum chamber surrounding the QIT.

6.1.1. Electrospray ionization (ESI) ion source

Electrospray ionization (ESI) is an important ionization technique, allowing for the soft transfer of analytes from solution into the gas phase as intact molecular ions with little or no fragmentation. This facilitates the investigation of molecules ranging in size from small inorganic ions and complexes up to larger (bio)macromolecules, typically observed as multiple charged species ($z > 1$)^[226]. ESI belongs to atmospheric pressure ionization (API) methods^[227] and allows for the investigation of solution-phase chemical processes by gas-phase mass spectrometric detection. The development of ESI is attributed to the early works of *Dole* and co-workers^[228] and the pioneering improvements by *Fenn* et al.^[229-232], for which *J. B. Fenn* was awarded the nobel prize in chemistry in 2002^[233]. It is noted, that rather than a true ionization method that actively creates ions, ESI is in essence a solution-to-gas-phase transfer method that requires ions or charge „tags“ to begin with. Although ESI is regarded as a relatively soft technique, electrochemical processes, that change the oxidation state of analyte molecules, can occur at the spray electrode (e.g. the reduction of metal ions: $\text{Ag}^+ + \text{e}^- \rightarrow \text{Ag}^0$).

The experimental setup of the *Apollo II* ESI source and its basic operating principle are briefly described in the following (see Fig. 6.2). The ESI sprayer assembly consists of a concentric, double-walled stainless steel capillary with a narrow inner tube (spraying needle) through which a dilute sample solution (e.g. MeCN/MeOH/H₂O, $c \approx 10^{-5}$ - 10^{-7} M) is continuously supplied by means of a syringe pump (Fig. 6.2 ①, typical flow rates: 120-180 $\mu\text{l h}^{-1}$). The spraying needle is situated inside a ferrule and connected to a zero dead volume union, which is joined with the syringe (Hamilton, sample volume = 250, 500 μl) by two plastic fittings and a approx. 30 cm long PEEK tubing (PEEK = polyether ether ketone polymer, inner diameter $\varnothing = 0.005$ “). In order to pneumatically assist nebulization and droplet dispersion, a coaxial flow of nitrogen sheath gas is applied through the outer tube of the sprayer assembly (5-7 psi, 345-483 mbar). The spray shield (Fig. 6.2 ③) is held at a high voltage of ~ 3 -5 kV relative to the electrically grounded spraying needle.

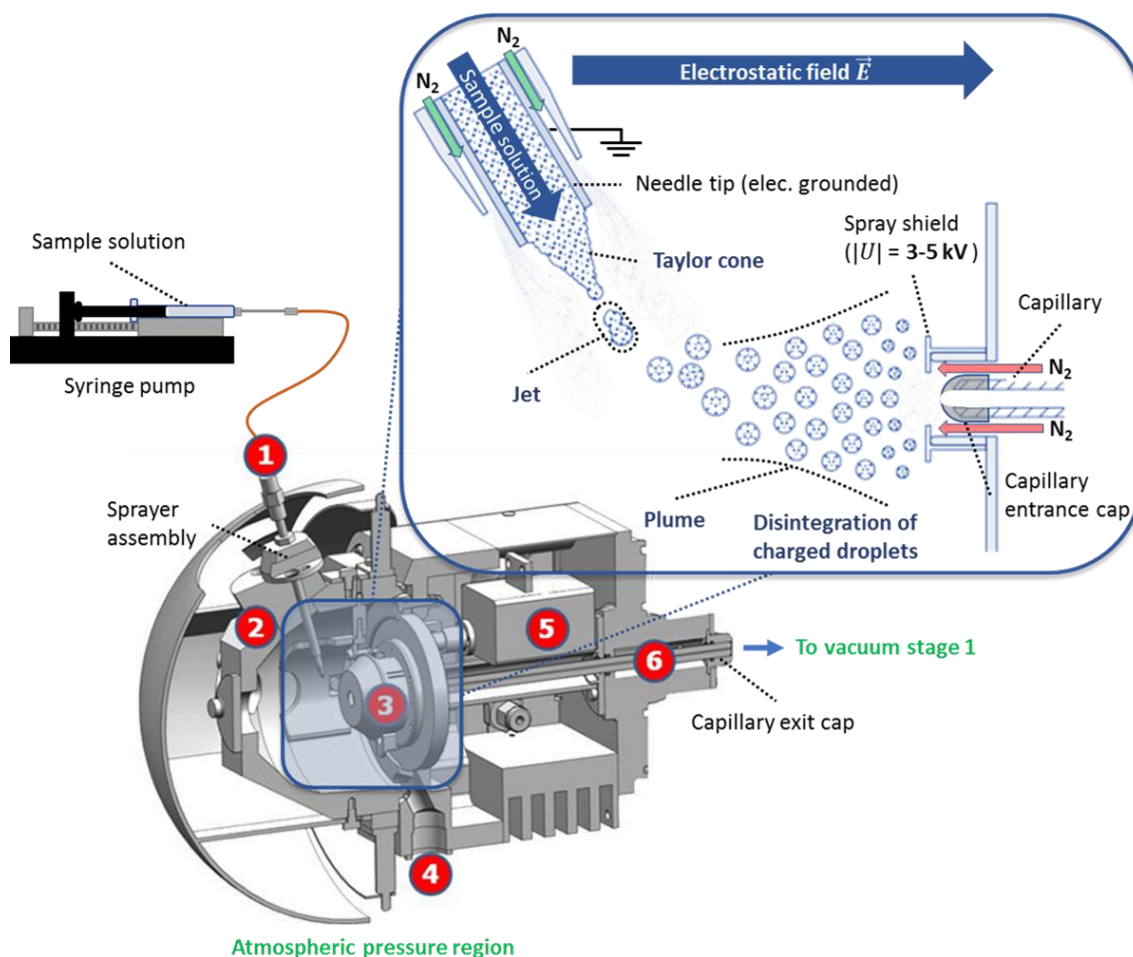


Fig. 6.2 Schematic overview of the *Apollo II* ESI source adapted from Refs. [234-235]. ① ESI sprayer assembly, ② spray chamber, ③ spray shield and capillary entrance cap, ④ waste line for solvents and neutral molecules, ⑤ temperature controlled dry gas heater, ⑥ metal-coated glass capillary for desolvation. Inset: Illustration of the ESI process and disintegration of charged droplets adapted from Refs. [234-235].

In order to assist the desolvation process and disintegration of charged droplets a counter-propagating stream of heated nitrogen gas (flow: 3-4 l min⁻¹, T = 180-220 °C), relative to the ion flow, is supplied by a temperature controlled dry gas heater. The evaporated solvent- and residual neutral molecules are removed via the waste line by a small negative pressure (Fig. 6.2 ④). A thin inlet glass capillary assists the desolvation process and separates the atmospheric pressure region from the first vacuum stage of the mass spectrometer, restricting gas flow by a narrow orifice (Fig. 6.2 ⑥, inner diameter $\varnothing \approx 0.6$ mm [235]). This desolvation capillary is metal coated at both ends and attached with two entrance/exit caps by two canted coil springs

(gold), which physically achieve the electric contact. A potential difference between the entrance cap and the spray shield of ≈ 500 V focuses the analyte ions directly onto the the capillary entrance, which are consequently driven through the desolvation capillary by an additional electrostatic gradient (potential difference of ≈ 500 V between entrance and exit of the capillary) and the pressure gradient between spray chamber and first vacuum stage. The exiting ions are further electrostatically (80-280 V) and fluid-dynamically drawn towards the entrance of the dual ion funnel system (Fig. 6.3) [234].

In the following, the process of transferring ions from liquid phase to the gas phase via ESI is described. However, the intricate details such as production mechanisms and physical properties of isolated ions still remain imperfectly understood [227, 233, 236-237]. The working principle of ESI is similar to an electrolytic cell, whereby the charge transport between the electrodes (spray needle and spray shield) occurs in the gas phase at atmospheric pressure [227]. In short, the process can conveniently be divided into three stages [227]: a) initial charged droplet formation, b) droplet disintegration by repeated solvent-evaporation / Coulombic-explosion cycles and ultimately, c) the gaseous ion formation/liberation.

a) The applied high voltage electric field induces an electrophoretic separation of positive and negative charges whereby an excess of either positive or negative charges accumulates at the surface of the emerging liquid, depending on the applied polarity (positive / negative ion mode) [137]. When a critical field strength is reached, the meniscus of the eluent is deformed into the so called *Taylor cone* [238] (see Fig. 6.2) from which a fine jet of highly charged droplets is continuously ejected due to the surface tension being exceeded by the electrostatic forces [239]. After a small distance, the jet breaks apart into a rapidly expanding plume of microdroplets because of electrostatic repulsion [233].

b) The initially emitted droplets undergo rapid solvent evaporation by collisions with neutral gas molecules resulting in an increase in charge density until the *Rayleigh limit* [240] is reached, where the Coulombic repulsion between the charges

overcome the surface tension [137, 236]. Multiple fission events create smaller and highly charged offspring droplets which further disintegrate in sequential evaporation / Coulomb fission events, creating a fine aerosol of nanodroplets which expand towards the entrance of the spray shield.

c) Two mechanisms are put forward to explain the formation of desolvated ions from charged droplets, although others have been suggested [236]: The *Ion evaporation mechanism* (IEM) [236, 241-242] describing the direct emission of ions from the droplet surface when the electric field strength is sufficiently high. And the *charge residue mechanism* (CRM) [228, 236, 243] assuming that after creation of a droplet with a single ion, solvent evaporation proceeds until the ion is completely isolated. A summarizing review of these ion release mechanisms is provided by Ref. [236].

Another aspect of ESI is the energetics of the ions which determine their extent of fragmentation and reactivity [137]. The generated ions cross the high pressure desolvation region and take up in internal energy. It has been demonstrated that their internal energy distribution is close to a thermal *Boltzmann* distribution [137, 244] with a „characteristic temperature“ of $T_{char.} \approx 700$ K (for nitrogen nebulizer gas) [245] correlating with the heat capacity of the employed sheath gas. The hot ions are thermalized by collisional cooling with helium buffer gas inside the quadrupole ion trap (Fig. 6.4).

6.1.2. Ion transfer optics

The ions exiting the desolvation capillary are expanded with the nitrogen carrier gas into the first vacuum stage housing the first ion funnel [246-248] (Fig. 6.3). As a result of the drop in pressure the ions are accelerated and tend to diverge, wherefore a two-stage off-axis ion funnel system [234] is used for ion-beam focusing and efficient transfer into the multipole transfer stage. It consists of a first ion funnel with wide entry aperture and a smaller second funnel, which is located in the second vacuum stage (Fig. 6.3). Both ion funnels comprise a stack of closely spaced, concentric ring electrodes with central apertures of subsequently decreasing inner diameters.

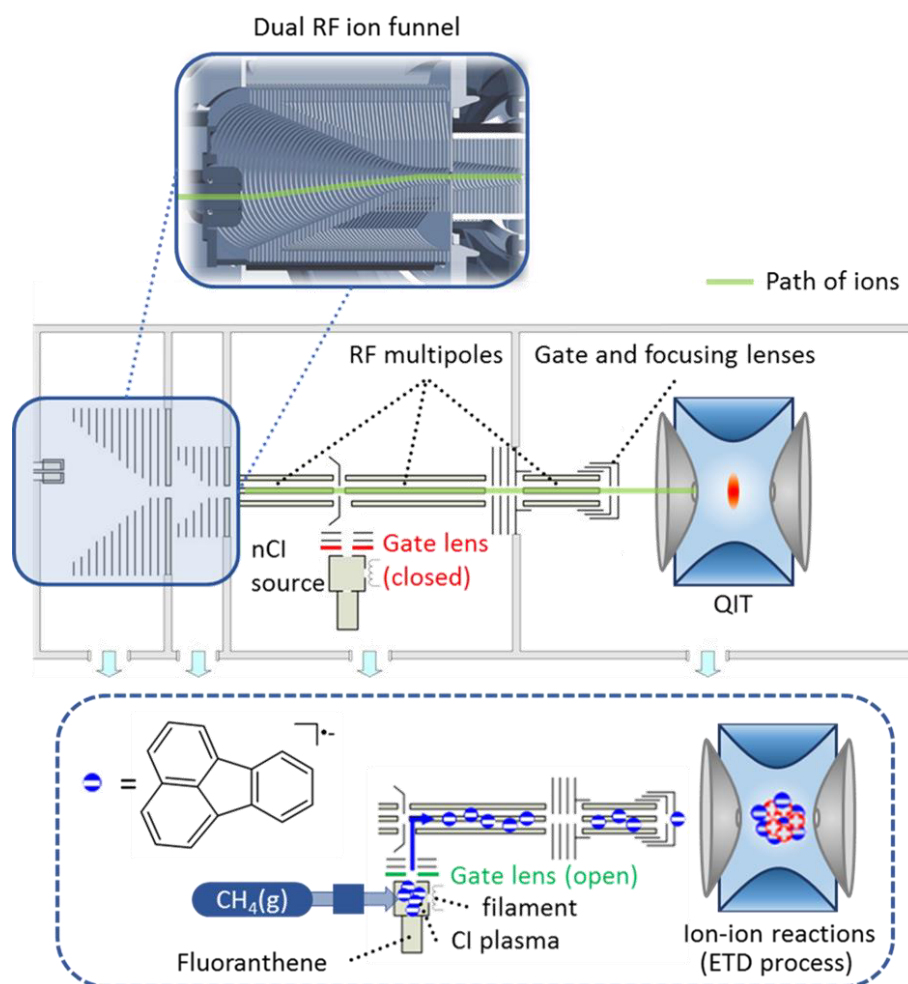


Fig. 6.3 Ion transfer optics of *amaZon* mass spectrometers MS-1 and MS-2, including the dual RF ion funnel stage and the RF multipole ion guide system. The path of ions through the system is indicated in green. Bottom: Schematic depiction of generation of fluoranthrene radical anions (FA^{•-}) within the nCl source (MS-2) and their extraction for ETD experiments. Adapted from Refs [124, 234, 249].

A radiofrequency (RF) voltage is supplied with opposite phases for adjacent ring electrodes, creating an inhomogeneous oscillating electric field that radially confines the ions, which are in turn thermalized by ion-neutral collisions. An additional axial potential gradient (DC voltage gradient between the first and last ring electrode) efficiently transports the ions through the funnel cone towards the small funnel exit orifices. The concentric funnel axis is offset relative to the capillary axis in order to avoid contaminations since only charged particles are transported by the electric field, whereas neutrals (sample and solvent molecules) hit the outer

funnel plates and are evacuated from the system. After exiting the small second funnel aperture, the focused ion stream is transported via a RF multipole ion transfer optic (hexa- and octopoles) ending with a gate and focusing lens assembly. The gate lens, located before the QIT, only allows ions to pass through into the trap during the accumulation phase of the scan sequence (see Fig. 6.6) in order to avoid contaminations during mass-selective operations (e.g. mass isolation, MS^n , mass scan).

6.1.3. Negative chemical ionization (nCI) source

Chemical ionization (CI) [250-251] is defined as a process by which ionized species are formed via ion-molecule reactions between gaseous neutral analyte molecules (here: fluoranthene (FA), $C_{16}H_{10}$) and ions generated from a reagent gas (here: methane), involving the transfer of an electron, proton or other charged moieties [237, 252]. If the outcome is the production of negatively charged analyte ions it is referred to as negative chemical ionization (nCI) [252]. However, this definition is misleading since in this case, the ionization of neutral FA molecules proceeds by electron-neutral molecule reactions via electron capture (EC) [253] of low kinetic energy electrons (EC-nCI). The nCI source is located directly underneath and perpendicular to the RF multipole transfer optics (see Fig. 6.3) and is utilized for the generation of fluoranthene radical anions ($FA^{\bullet-}$; m/z 202) [254]. These are transferred into the QIT and used for electron-transfer dissociation/reduction (ETD/ETR) [130-131] experiments. The ETD technique plays a significant role in the field of proteomics [130, 255-257] and has recently been applied to metal complexes [121, 131-132]. The operating principle of the nCI source (Fig. 6.3) is as follows:

A heated wolfram filament is used for thermionic emission of „primary“ electrons that are accelerated to typically ≈ 70 eV in the ionization chamber, where methane as reactant gas is continuously infused ($p_{CH_4} \approx 0.1$ mbar [258]). The energetic electrons collide with neutral CH_4 molecules (ionization energy, IE = 12.61(1) eV [259]), producing a series of cations via electron-impact ionization (EI)[260] including: $CH_4^{\bullet+}$, CH_3^+ , $CH_2^{\bullet+}$, CH^+ , $C^{\bullet+}$ [251, 261]. These cations undergo a cascade of ion/molecule reactions (eg. with CH_4 , H_2O , O_2), forming additional „secondary“ and „tertiary“ ions

[251]. For each EI event, less energetic secondary electrons are generated which, in turn, can produce additional low-energy electrons via EI, further lowering their energy. In addition, electrons are thermalized by inelastic collisions with methane background gas [253]. As a result, a methane/CI plasma is formed, whereby methane serves as „mediator/buffer“ gas being a source of low energy electrons (< 1 eV) that can be resonantly captured by gaseous FA molecules [253].

The gaseous fluoranthene molecules are supplied by sublimation of the solid inside a heated crucible ($T_{sub} \approx 60$ °C). The formation of the stable fluoranthene radical anions ($FA^{\bullet-}$) proceeds via electron capture (EC) of low-energy electrons by the neutral FA molecules, since FA exhibits the highest cross section for EC at ≈ 0.2 eV [262] and a positive electron affinity (EA) of 0.63 eV ($FA + e^- \rightarrow FA^{\bullet-}$) [263]. The high methane background pressure, relative to the concentration of gaseous FA molecules, suppresses electron-impact ionization of fluoranthene (IE = 7.9(1) eV [264]), which would lead to significant fragmentation. Analyte ions (multiple charged precursor cations) and reagent anions ($FA^{\bullet-}$) are transferred consecutively into the QIT by the same multipole ion guide, controlled by repulsive voltages applied either at the desolvation capillary exit (ESI) or by a gate lens (nCI, Fig. 6.3). The load of FA anions into the trap is controlled via a set „ion charge control“ (ICC) value (typically $ICC \approx 5 \cdot 10^5$). After the dual injection of anions and cations, electron transfer reactions are facilitated by lowering the „low-mass cutoff“ parameter of the ion trap (see Fig. 6.5), resulting in the contraction of the ion cloud during a set ion-ion reaction time window (typically ≈ 100 ms) [249].

6.1.4. Working principle of Paul type ion trap and mass analysis

The three-dimensional quadrupole ion trap (3D-QIT) operates with an oscillating radiofrequency (RF) quadrupolar electric field that can be used in order to trap positively and negatively charged ions alike. As a result, they experience dynamic (as a function of time) „restoring“ forces that drive them toward the center of the trap, confining them in 3D-space over a period of time. The development and design of this device was pioneered by *Paul* and *Steinwedel* [265]. *Wolfgang Paul* was awarded with the Nobel prize in physics 1989 [266]. Hence, it is often referred to as

Paul-type ion trap. This QIT is not only a ion storage device, but can also be utilized for mass selection and mass analysis, making it a powerful analytic tool which can be combined with multiple mass-spectrometric (CID, ETD, MS^n) and ion spectroscopic (PD/ τ -PD) techniques (see chapter 5).

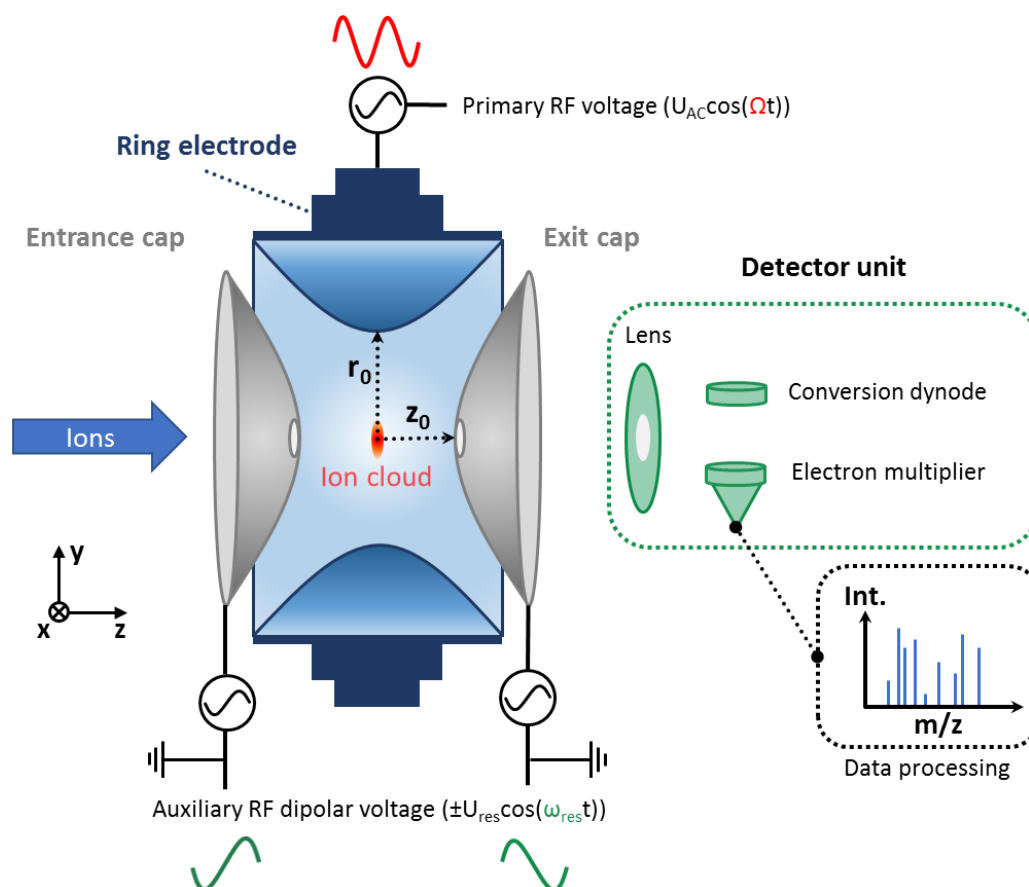


Fig. 6.4 Schematic cross section of the QIT assembly comprising the two end cap electrodes, the ring electrode and a scheme of the subsequent conversion dynode detector unit ^[124].

The basic design of the QIT module, as integrated in the *amaZon* mass spectrometers, consists of an assembly of three electrodes and a subsequent ion detector unit (Fig. 6.4). The ring electrode, possessing a hyperbolically shaped inner surface with an inner radius r_0 , is located in between two hyperbolic end caps (entrance and exit caps) at a distance z_0 between its center and the tip of each cap electrode. The near hyperbolic profiles of the electrodes are necessary to generate a three-dimensional quadrupole trapping field (Fig. 6.5). Accordingly, the electrode assembly possesses near cylindric symmetry (cf. Fig. 6.4), so that the motion of ions

can be described by the cylinder coordinates (r, z) with the center of the QIT as reference point ^[134]. Both end caps have small central apertures through which ions are gated periodically into the QIT by a gate lens, or pass through to the detector unit, respectively. The use of the QIT as mass spectrometer is facilitated by the possibility to extract ions of a specified m/z (mass-to-charge) ratio along the z axis through the cap electrodes. The means by which this can be achieved and the principle of ion trapping/storing is elaborated in the following.

In general, the dynamic quadrupole potential $\phi(r, z, t)$ applied to the electrodes can be mathematically described by Eqs. (6.1),(6.2) ^[134, 267]. In simplified terms this functions consists of a static „saddle“-shaped potential function $\phi(r, z) = (r^2 - 2z^2)$ (depicted in Fig. 6.5), dependent on the radial (r) and axial (z) cylinder coordinates, which is modulated by a time-dependent term $\phi_0(t)$ (Eq. (6.2)). The latter consists of an DC amplitude U_{DC} and the primary radiofrequency voltage term $U_{AC} \cos(\Omega t)$ with a driving angular frequency Ω and an RF amplitude U_{AC} . The constants r_0 and z_0 , depend on the construction of the QIT electrode arrangement (cf. Fig. 6.4).

$$\phi(r, z, t) = \phi_0(t) \cdot \underbrace{(r^2 - 2z^2)}_{\phi(r,z)} \cdot \frac{1}{(r_0^2 + 2z_0^2)} + \frac{2\phi_0(t)z_0^2}{(r_0^2 + 2z_0^2)} \quad (6.1)$$

$$\phi_0(t) = U_{DC} + U_{AC} \cos(\Omega t) \quad (6.2)$$

In practice, both end caps are electrically grounded during ion storage operation of the *amaZon* MS whereby a primary RF voltage at a constant radiofrequency ($U_{AC} \approx 400\text{-}800$ V_{p-p}, $\Omega/2\pi = 781$ kHz) is applied exclusively to the ring electrode, generating the oscillating trapping potential without an additional DC voltage ($U_{DC} = 0$, „RF-only mode“). In consequence, the ions experience a parabolic „*Dehmelt*“ pseudopotential well ^[268] in each z and r direction, which drives the ions towards the QIT centre. The time-dependent modulations of the electric field is driven by the RF voltage ($\phi_0(t)$) and can in simple terms be envisioned as a rotation of the saddle shaped potential surface (see Fig. 6.5). Hence, for illustration purposes, one could

6. Experimental Setup and Methods

think of a mechanical analog device consisting of a rotating saddle („electric potential“) on top of which different weighted spheres („ions“) are placed. Depending on their masses and the saddle-rotation frequency they can exhibit stable „rolling“ oscillating trajectories when certain criterias are met [266].

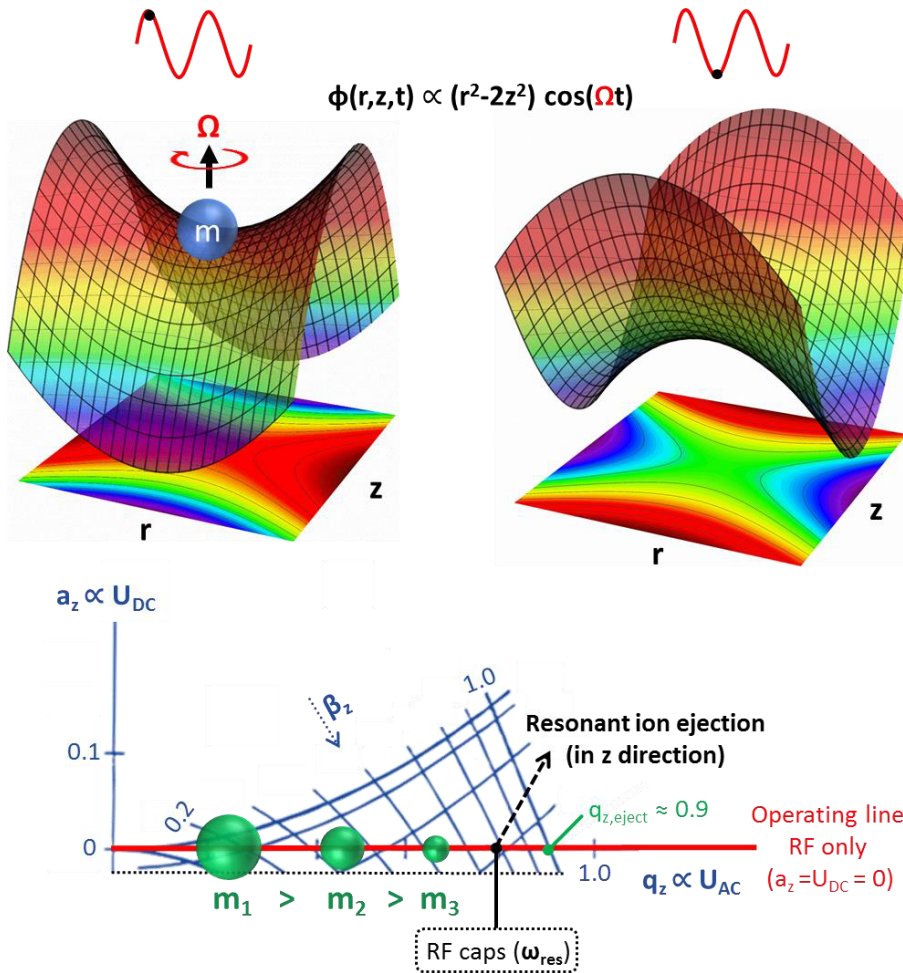


Fig. 6.5 Top: Potential surface plots of oscillating quadrupolar trapping field as a function of radial and axial cylinder coordinates (r, z), driven by the primary RF voltage at fixed angular frequency Ω . Note that the third coordinate axis is scaled differently for the left and right surface plot, respectively. Bottom: Section of the *Mathieu* stability diagram in the region of simultaneous axial and radial stability in (a_z, q_z) space adapted from Ref. [134]. Iso- β_z lines are drawn diagonally. The operating line for ion storage (red), the low-mass cutoff ejection point $q_{z,eject}$, and the working point for resonant axial ion ejection by an auxiliary dipole field applied to the end caps, resonating at the angular frequency ω_{res} , are indicated.

The time-dependent ion trajectories are described by a set of differential equations, which were first solved by the French mathematician *Mathieu* [269] and are hence referred to as *Mathieu* equations [134]. The solutions of the *Mathieu* equations, especially those describing stable ion trajectories in both axial (z) and radial (r) directions, which is a prerequisite for ion trapping, can be expressed in a pictorial manner in terms of a stability diagram as a function of the *Mathieu* parameters a_u (Eq. (6.3)), q_u (Eq. (6.4)), and β_u ($u = r, z$) [134] (see Fig. 6.5). The β_u parameter ($0 \leq \beta_u \leq 1$) is a complicated function of a_u , and q_u and is correlated with the secular frequencies ω_u , which describe the two fundamental frequency components (ω_r , ω_z) of three-dimensional ion motion inside the ion trap [134] (*Lissajous* orbits in shape of a figure-of-eight [266-267]).

$$a_z = -2a_r = \frac{-16zeU_{DC}}{m(r_0^2 + 2z_0^2)\Omega^2} \propto U_{DC} \cdot \left(\frac{m}{z}\right)^{-1} \cdot const. \quad (6.3)$$

$$q_z = -2q_r = \frac{8zeU_{AC}}{m(r_0^2 + 2z_0^2)\Omega^2} \propto U_{AC} \cdot \left(\frac{m}{z}\right)^{-1} \cdot const. \quad (6.4)$$

Since $U_{DC} = 0$ ($\rightarrow a_u = 0$) and $\Omega = \text{const}$, the most important *Mathieu* parameter to consider is q_z , which is proportional to the AC amplitude U_{AC} and reciprocally proportional to mass-to-charge ratio (m/z) of the ions. Consequently, ions with larger masses exhibit lower q_z values than those with smaller ones, at a fixed U_{AC} amplitude and identical charge states ($q_z(m_1) < q_z(m_2)$ given $m_1 > m_2$). The boundary conditions for stability fall within an operating line in the *Mathieu* stability diagram (Fig. 6.5). Depending on the applied RF amplitude applied to the ring electrode, ions at certain m/z values that fall within the boundaries of the stability diagram ($0 < \beta_u < 1$) along the operating line and are trapped. Accordingly, if an ion reaches q_z values above $q_{z,eject} \approx 0.9$, representing the low-mass cutoff, it becomes unstable (area of axial instability) and is ejected out of the trap in z direction.

In order to enhance the trapping efficiency, helium is introduced into the QIT as buffer gas. It removes „excess“ kinetic/internal energy by ion-neutral collisions,

thermalizing the trapped ion ensemble (background pressure inside QIT, $p_{He} \approx 10^{-3}$ mbar, hard-sphere collisional rate $\approx 30 \text{ (ms)}^{-1}$ assuming $T=300\text{K}$ and a cross section of 100 \AA^2 [166]). Additionally, collisional cooling in helium „bath“ gas induces a spatial focusing of the ion cloud towards the center of the trap, which is beneficial for overlapping with laser beam irradiation and also significantly improves sensitivity and mass resolution during mass analysis, presumably originating from the better defined starting point for ion ejection [270-271]. Laser-induced fluorescence imaging experiments of trapped ion ensembles inside a similarly constructed QIT yielded Gaussian-shaped ion cloud profiles with $\text{fwhm} \approx 600 \text{ }\mu\text{m}$ in radial and $\text{fwhm} \approx 200 \text{ }\mu\text{m}$ in axial dimension, respectively [272]. Interestingly, this study demonstrated that increasing the number of trapped ions (space-charge density) resulted in an expansion of the imaged ion cloud mainly in radial direction, whereas changes in axial direction were small in comparison [272]. Additionally, an onion-like stratification was observed, whereby ions with lower m/z (higher q_z) are located around the center surrounded by layers of ions with larger m/z (lower q_z) values.

As described previously, the range of masses (m/z) that can simultaneously be trapped is restricted by the low-mass cutoff point at $q_{z,eject} \approx 0.9$. Additionally, increasing U_{AC} results in larger q_z values for given mass-to-charge ratios (cf. Eq. (6.4)) and corresponds to a „right shift“ along the operating line in the *Mathieu* stability diagram (Fig. 6.5). Consequently, the trapped ions can so to speak be moved along the „scan line“ by linear ramping the RF amplitude over time in order to consecutively achieve axial instability at the working point $q_{z,eject}$ in the order of ascending m/z ratio. Thus, at maximum half of the successively scanned out ions can reach the detector unit. When the RF ramping rate and correlation between U_{AC} and the m/z ratio is precisely known (Eq. (6.4)), e.g. by calibrating the mass spectrometer with a series of ions of defined masses, the thus created ion intensity versus time profile can be converted into a mass spectrum. This technique is called *mass-selective axial ejection* [267], but is no longer in use due to its inefficiency and inflexibility.

All modern commercial QIT-MS employ the *resonant excitation/ejection* (RE) technique [134, 234], also named *axial modulation*, by which mass analysis is also achieved through mass-selective instability, however in a slightly different manner utilizing an auxiliary dipole field. In this mode an auxiliary dipolar RF voltage ($\mp U_{res} \cos(\omega_{res}t)$) is applied to the cap electrodes (Fig. 6.4). As result of the dynamic quadrupole field, ions undergo oscillating trajectories described by a set of independent axial and radial characteristic secular frequencies, which are lower than half of the driving RF angular frequency Ω due to their moments of inertia. The fundamental secular frequency for axial movement in between the two end-cap electrodes, $\omega_z = 0.5 \cdot \beta_z \cdot \Omega$ [268], is dependent on q_z (β_z increases as q_z increases, cf. Fig. 6.5) and therefore inversely proportional to m/z . In the case of the applied auxiliary RF being in resonance with the characteristic ion oscillation frequency ($\omega_{res} \hat{=} \omega_z$), energy will be transferred resulting in an increase of the amplitude of axial motion, a displacement from the centre of the QIT, and ultimately mass-selective ion ejection. The *amaZon* mass spectrometers perform mass analysis by ramping up the amplitudes of the primary and auxiliary RF voltages in parallel (see (6.6)), whereby the auxiliary angular frequency is constantly held at $\omega_{res} = \Omega/3$. Hence, ion ejection is achieved at a lower q_z value ($q_z < q_{z,eject}$) compared to the classical *mass-selective axial ejection* technique, as illustrated Fig. 6.5.

6.1.5. Detector unit

Ions enter the detector unit through a gate lens which allows only for scanned out ions to be detected and prevents unnecessary aging of the detector during isolation or fragmentation steps (discussed below). The detector comprises a Daly-type conversion dynode [124, 234, 273] in combination with a continuous dynode electron multiplier / channel electron multiplier (CEM) [124, 274-275]. Ion packages of adjacent m/z values are accelerated towards the metal surface (aluminium) of the conversion dynode held at a high potential (few kV), of polarity that is suitable to attract either positively or negatively charged ions alike. In consequence, the impinging ions create secondary electrons (ion-to-electron conversion) which are accelerated towards the CEM. The secondary electrons that strike the input face of

the electron multiplier produces additional multiple electrons that are accelerated down the channel by positive bias and thus creates an electron avalanche. The thus created electric current is converted into a voltage by a load resistor and then further converted into a digital intensity signal by an analog to digital converter (ADC) [237].

6.1.6. Mass isolation and tandem MS (MS^n)

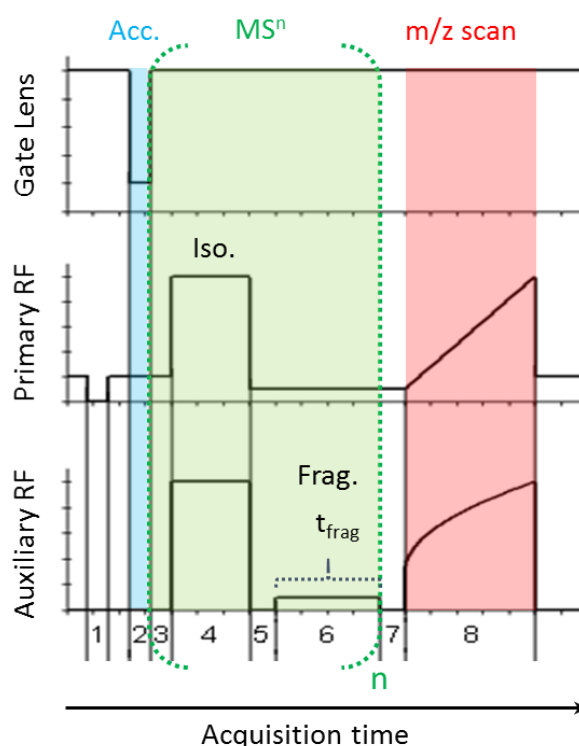


Fig. 6.6 Schematic time segments for ion accumulation (blue), m/z scan (red) and multi-stage MS^n (green, n = number of mass-selective operations) experiments, highlighting the timing of the gate lens located before the QIT and the amplitudes of primary and auxiliary RF voltages as a function of acquisition time. Segments: **1**: Clear trap (5 ms), **2**: Ion accumulation time (typically 0.01 - 50 ms), **3**: Isolation delay (5 ms), **4**: Precursor ion isolation, **5**: fragmentation delay, **6**: Fragmentation (applied aux. RF) or ion storage (no aux. RF) during a typical time period of $40 \text{ ms} \leq t_{frag} \leq 120 \text{ ms}$, **7**: Scan delay (5 ms), **8**: Mass-selective resonant ejection – mass scan. Adapted from Ref. [234].

The above discussed resonant excitation technique, applying a dipolar RF field at the end caps, can also be used in order to isolate a single ionic species within a

narrow specified m/z range or even a single isotopologue. During mass isolation a wideband composite of auxiliary RF frequencies are used to simultaneously excite and eject all ions that fall outside the specified m/z range [234]. Subsequently, the isolated precursor ions can be resonantly excited at their axial secular frequency in order to increase their kinetic energy, promoting collision-induced dissociation (CID) by ion-helium collisions (variable fragmentation amplitude U_{res} typically in the 0-3 V_{p-p} range, Fig. 6.4), or be subjected to other types of ion activation (e.g. PD, ETD) within a set time window (t_{frag} , see Fig. 6.6). These *Tandem* mass spectrometric experiments, abbreviated MS/MS or MSⁿ, generally involve the use of at least two consecutive mass-selective operations ($n \geq 2$) in conjunction with dissociation processes or ion-ion/neutral chemical reactions that induce a change in mass or charge state of isolated precursor ions. This flexibility of the QIT-MS is particularly useful for the exploration of secondary fragmentation pathways by multi-stage MSⁿ_{≥3} experiments that allow the isolation and subsequent investigation of fragments (or fragments of fragments). In practice, the number of MSⁿ operations is limited to $n \leq 4-5$ since a significant loss of ions by at least one order of magnitude occurs at each mass-selective stage. A typical schematic sequence of ion accumulation, multi-stage MSⁿ steps and mass analysis is provided by Fig. 6.6.

6.1.7. Modifications of MS-1

The *amaZon speed* mass spectrometer (MS-1) was modified for laser spectroscopy by creating optical access to the ion cloud inside the QIT (see Fig. 6.7). The modifications of the instrument were implemented in cooperation with *Bruker Daltonics* with the support of Dr. *C. R. Gebhardt*. In doing so, the top of the high vacuum chamber cover ($p \approx 10^{-6}$ mbar inside the chamber), housing the QIT module, was equipped with two openings for the beam path and a breadboard for mounting optical elements. The first opening, through which the laser beam enters the system, is connected to a tube (height = 14 cm) by a viton O-ring. On top of this tube and the second opening, two fused silica optical windows (thickness = 3 mm, W1 and W2 Fig. 6.7) are mounted and also sealed by means of two viton O-rings. The tube is

needed in order to achieve a larger beam diameter of the focused laser beam at the position of the optical window (W1) to prevent damage.

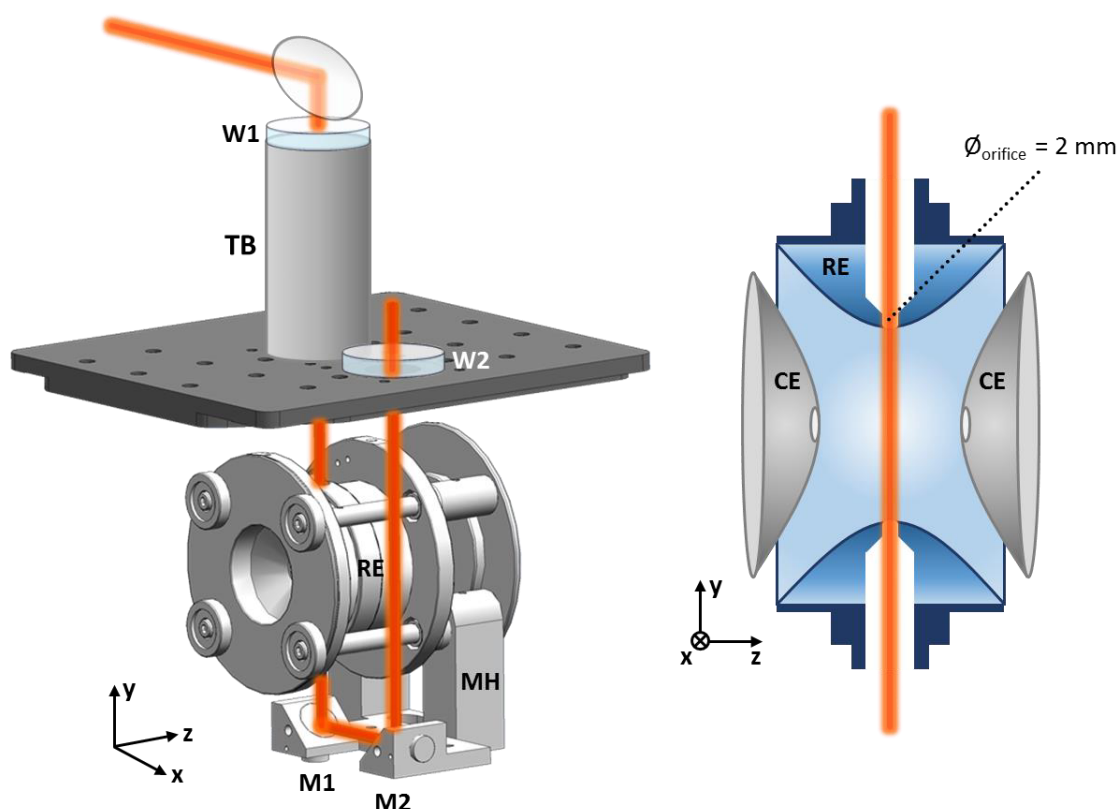


Fig. 6.7 Left: Schematics of the quadrupole ion trap that was modified for optical access. W1, W2: fused silica optical windows, TB: tube, RE: ring electrode, M1, M2: mirrors inside the vacuum chamber, MH: mirror holder, CE: cap electrodes. Laser beam path is indicated in red. Adapted from Ref. [163]. Right: cross section of the modified ring electrode with two concentric drilled holes. x-axis points towards the observer.

In addition, two diametrically opposite holes were drilled perpendicular to the surface of the ring electrode (RE) of the Paul trap (Fig. 6.7), providing an optical path through the center of the ion cloud. The openings begin with a diameter of 6 mm which, at the last 3 mm of the pathway, gradually taper to smaller orifices of 2 mm diameter at the inner surface of the RE (see Fig. 6.7 right). The latter smaller holes serve as apertures for beam alignment and also reduce the loss of helium background gas that is continuously infused into the trap, thereby ensuring proper performance of the mass spectrometer. After the incoming laser beam traverses

through W1, TB and the QIT, it is subsequently reflected out of the vacuum chamber by two mirrors (M1, M2) that are mounted at a 45° angle below the trap. The mirror mount is attached to the support rods of the QIT.

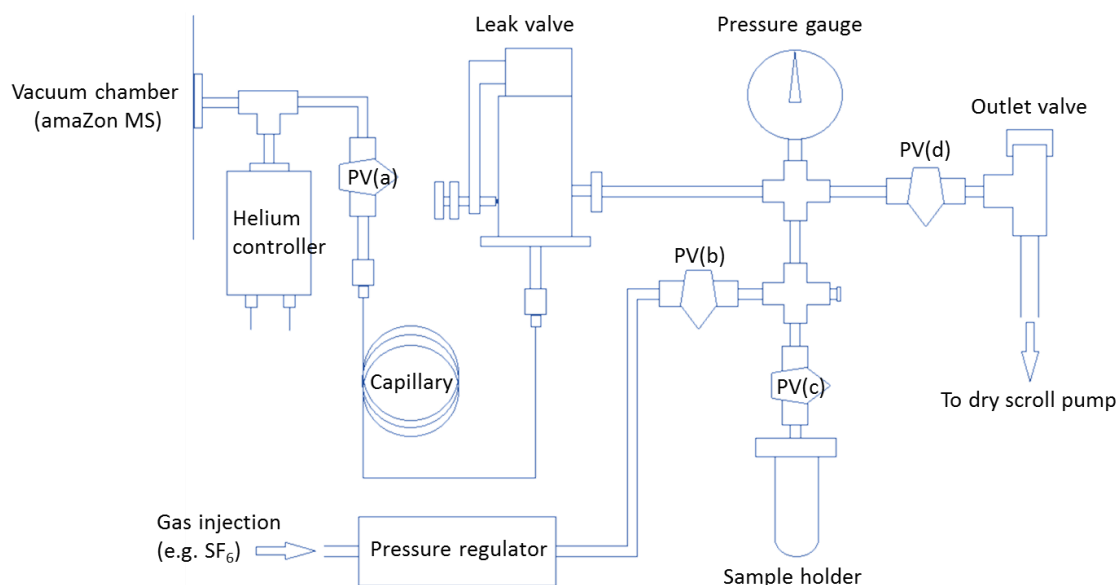


Fig. 6.8 Schematic of the gas inlet line added to the helium controller of the *amaZon* MS (MS-1). PV: plug valve. Adapted from Ref. [225].

Furthermore, a gas inlet line (Fig. 6.8) was added to the helium gas line of the mass spectrometer (MS-1) in order to introduce additional gaseous neutral compounds into the ion trap. It is connected to the helium controller that regulates helium buffer gas flow, achieving a constant helium pressure inside the QIT ($p_{He} \approx 10^{-3}$ mbar). The additional gas flow is controlled by a leak valve (sapphire poppet) followed by a narrow capillary (PEEK, inner diameter $\varnothing \approx 180$ μm , length = 1m). The gas line allows for the injection of either a) gas from a pressured cylinder (e.g. SF₆) or b) vaporization of a volatile substance (e.g. furan, C₄H₄O) that is placed into a sample holder. The infusion of furan vapor into the QIT serves for the measurement of the multiphoton ionization cross-correlation (cc) signal, that allows for the estimation of temporal resolution and time zero during time-resolved photodissociation experiments (τ -PD). A detailed description of the operating procedure for the introduction of furan is provided by Refs [224-225].

6.2. Femtosecond laser system

6.2.1. Principle of mode-locked laser operation

In the following, the basic concept of the mode-locking technique, which provides access to femtosecond laser pulses, is described in an intuitive manner. A more detailed and mathematical description is given in Refs. [276-278]. Given a laser resonator of cavity-length L , only longitudinal modes with frequencies that satisfy the standing wave condition $\nu = n \cdot c/2L$ (n : integer, c : speed of light in vacuum) can oscillate, provided that their losses are smaller than the gain by the laser medium as illustrated in Fig. 6.9. The result is a optical frequency „comb“ with equidistant spacing by $\nu_r = c/2L$ which may, for the sake of simplicity, be centered around a central frequency ν_0 . The spectral width $\Delta\nu_L = N \cdot \nu_r$ (N : number of oscillating modes) depends on the spectral gain profile of the laser medium ($\Delta\nu_L \propto$ emission band width of gain material, see Fig. 6.9 a). The time-dependent part of the electric field $E_q(t)$ of the longitudinal modes q (q : integer) can be approximated by plane waves according by Eq. (6.5):

$$E_q(t) = \text{Re}[E_q \cdot e^{i(\omega_q t + \varphi_{0q})}] \quad (6.5)$$

where E_q : field constant, $\omega_q = 2\pi \cdot \nu_q$: angular frequency, φ_{0q} : phase constant. Note that in the following only the real part of the complex wave equations is referred to, and the $\text{Re}[\dots]$ notation is omitted for the sake of conciseness. *Modelocking* is achieved in the case that all longitudinal modes q are forced to oscillate with a fixed, linear phase relationship between each other, which is e.g. satisfied by $\varphi_{0q} = \varphi_0$ ($\varphi_0 = \text{const.}$). As a result, the electric fields of all modes interfere constructively at precise, repetitive time intervals $T_r = 1/\nu_r$, adding up to a maximum in total field strength as illustrated by Fig. 6.9. In contrast, if the phases φ_{0q} are random, the superimposed total field is „noisy“ due to random constructive and destructive interference.

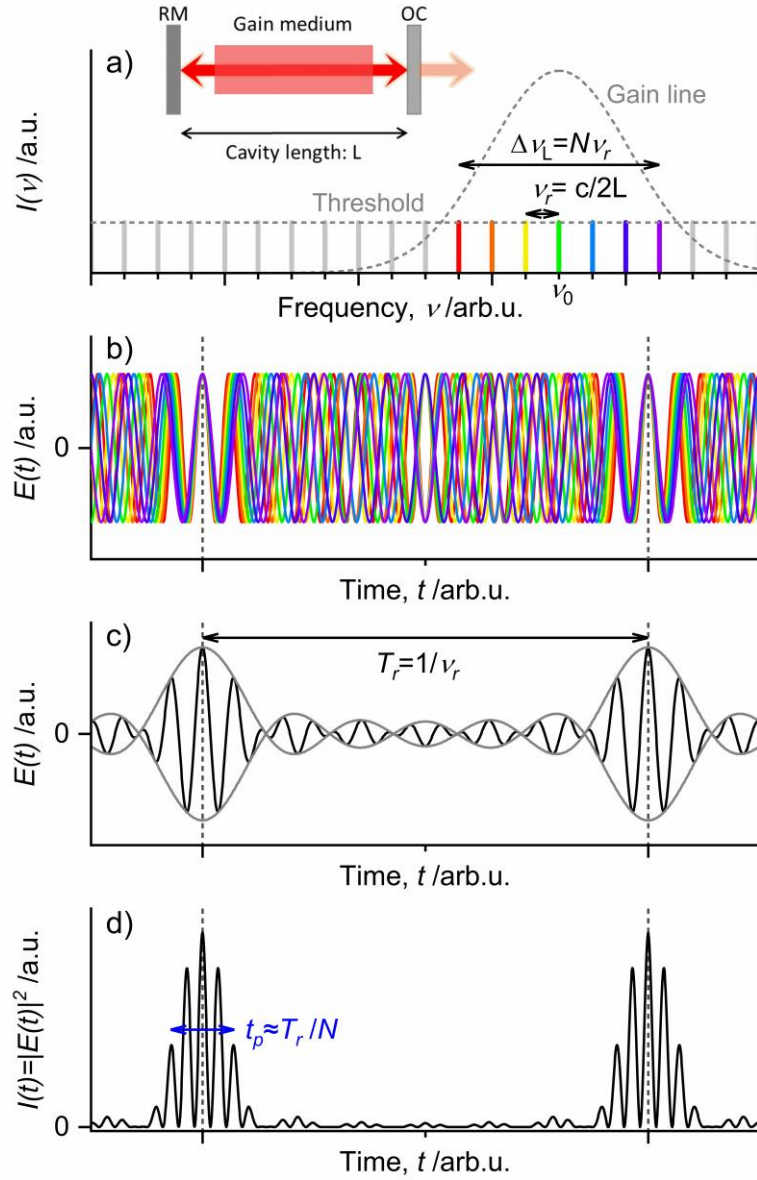


Fig. 6.9 a) Schematic depiction of an optical frequency comb of equidistant ($\nu_r = c/2L$) oscillating longitudinal modes q centered around frequency ν_0 , with an spectral width of $\Delta\nu_L = N \cdot \nu_r$ ($N =$ number of modes, $\nu_r =$ frequency difference between adjacent modes). Inset: schematic illustration of a laser resonator with an optical cavity length of L . RM: rear mirror (highly reflective), OC: output coupler. b) Time-evolution of the electric field $E(t)$ for individual longitudinal modes q at frequencies $\nu_q = \nu_0 \pm n \cdot \nu_r$ (q, n : integer, color code corresponds to panel a) in the mode-locked regime (see Eqs. (6.5),(6.6); $\varphi_{0q} = \varphi_0 = 0$, $E_q = E_0$). c) Electric field of superposition of the harmonic waves shown in panel b, representing a periodic pulse train with period $T_r = 1/\nu_r$ and with an envelope function $\pm\xi(t)$ in time domain (Eq. (6.8), indicated in gray). d) Intensity $I(t) = |E(t)|^2$ of the mode-locked pulse train with estimated single pulse duration of $t_p \approx T_r/N$, inspired by Refs. [276-277].

Given the simplified case that $\varphi_{0q} = \varphi_0$ and $E_q = E_0$, the superposition of N longitudinal modes in the mode-locked regime can be described by Eq. (6.6) [277], with $\omega_r = 2\pi \cdot \nu_r$ and $N = (2n + 1)$: number of modes, n, q : integer.

$$E(t) = N \cdot E_0 \sum_{q=-n}^n e^{i([\omega_0 + q \cdot \omega_r]t + \varphi_0)} \quad (6.6)$$

In general, the time-dependent function of an electromagnetic wavepacket can be described by Eq. (6.7) representing a carrier wave $e^{i\omega_0 t}$, whose amplitude is modulated by the time-dependent „envelope“ function $\xi(t)$, where $\varphi(t)$: time-dependent phase, ω_0 : central frequency.

$$E(t) = \xi(t) \cdot e^{i(\omega_0 t + \varphi(t))} \quad (6.7)$$

In our simple example (Fig. 6.9, $\varphi(t) = 0$, assumptions made above), $\xi(t)$ represents a periodic „envelope“ function expressed by Eq. (6.8) (derivation in Ref. [277], see gray lines in Fig. 6.9).

$$\xi(t) = E_0 \frac{\sin [N(\omega_r t + \varphi_0)/2]}{\sin [(\omega_r t + \varphi_0)/2]} \quad (6.8)$$

Since the electric field of a pulse can not be directly measured, it is convenient to refer to the pulse intensity $I(t) \propto |E(t)|^2$, which is proportional to the square of the total electric field amplitude (Fig. 6.9 d). The pulse duration t_p can be approximated by $t_p \approx T_r/N$ [277]. This is an important relationship, highlighting that the pulse duration is inversely proportional to the total number of oscillating longitudinal modes N , and therefore also inversely proportional to the spectral width $\Delta\nu_L$ (Eq. (6.9)).

$$t_p \propto \frac{1}{N} \propto \frac{1}{\Delta\nu_L} \quad (6.9)$$

Hence, a broad bandwidth of frequencies is needed in order to obtain ultrashort laser pulses. For the sake of simplicity, it is more straightforward to only regard a single ultrashort optical pulse, since the output of a mode-locked resonator constitutes a repetitive „pulse train“. A single pulse (wavepacket) can be described by Eq. (6.7), where the pulse envelope $\xi(t)$ is given by a non-periodic function such as e.g. a *Gaussian*(t) or *sech*(t) (hyperbolic secant) function, representing typical pulse shapes. Within this approximation, the pulse envelope $\xi(t)$ (time domain) and the corresponding spectral envelope $\xi(\omega)$ (frequency domain) are mathematically linked via the *Fourier*- and inverse *Fourier transform* (FT), respectively. The so called „time-bandwidth product“ (Eq. (6.10)) is a direct consequence of the Fourier transform, providing a relationship between the pulse duration Δt_{fwhm} and the spectral bandwidth $\Delta \nu_{fwhm}$, which can be seen in analogy to the „*Heisenberg uncertainty principle*“ [279].

$$\Delta t_{fwhm} \cdot \Delta \nu_{fwhm} = K \quad (6.10)$$

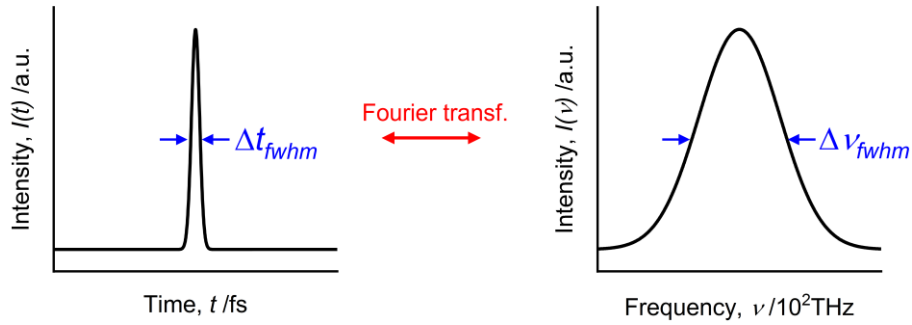


Fig. 6.10 Schematic illustration of the inverse proportionality between pulse duration and spectral width as a result of the *Fourier transform*. Typical central wavelength of Ti:Sa at ≈ 800 nm ≈ 375 THz.

Note, that both Δt_{fwhm} and $\Delta \nu_{fwhm}$ of Eq. (6.10) refer to the intensities $I(t)$ and $I(\nu)$, resp. (see Fig. 6.10) and is K a pulse-shape dependent constant. For example $K = 0.441$ for a Gaussian ($I(t) = \exp(-4 \ln 2) t^2 / 2 \Delta t_{fwhm}^2$) and $K = 0.315$ for a hyperbolic secant function ($I(t) = \text{sech}^2(1.76 t / \Delta t_{fwhm})$), resp [277]. If the time-bandwidth relation of Eq. (6.10) is satisfied, the pulse is regarded as „*Fourier-limited*“ (in absence of a „chirp“, as discussed later on) or „bandwidth-limited“. The

Fourier limit corresponds to the shortest achievable pulse duration at a given spectral bandwidth.

6.2.2. Ti:Sa gain medium

As mentioned before, the generation of ultrashort (fs) laser pulses requires a broad spectral emission width, which is typically fulfilled by a solid-state or dye laser medium. Nowadays, the self-modelocked titanium:sapphire (Ti:Sa) laser, which was developed in the 1990s [280-283], is the „working horse“ in many laboratories with the most widespread use. The Ti:Sa medium [284] consists of monocrystalline sapphire (Al_2O_3) which is doped with titanium Ti^{3+} ions and provides several desirable physical/optical properties, making it ideal for the application in ultrashort oscillator and amplifier systems. The favorable characteristics of Ti:Sa crystals encompass e.g.: a) a broad gain-bandwidth ($\Delta\lambda_{fwhm} \approx 235$ nm centered around ≈ 800 nm [284-285], $\Delta\nu_{fwhm} \approx 100$ THz); b) a broad absorption band centered at ≈ 500 nm [284], ideal for pumping with frequency-doubled (2ω) Nd:YAG or Nd:YLF lasers ($\lambda_{em} \approx 532$ nm and 527 nm, resp.) [277]; c) high damage threshold; d) thermal conductivity (reducing thermal lensing effects [286]) and d) Kerr nonlinearity, which is exploited for Kerr-lens self-modelocking (KLM) [287] as described below.

6.2.3. Kerr-lens mode-locking (KLM)

As already discussed, a broad emission spectrum is a prerequisite for an ultrashort laser pulse, but additionally its generation requires a fixed phase relationship between its frequency components (Fig. 6.9). Mode-locking can be achieved by several active and passive mechanism [276-277]. In general, mode-locking requires an effect which ensures that within the laser cavity, the ultrashort pulse regime experiences a higher gain than the continuous wave (cw) regime. This is achieved by decreasing the losses for the former and increasing losses of the latter regime in the cavity, suppressing modes with random phase relations. Here, only one specific type will be described, the so called „*Kerr-lens modelocking*“ (KLM) technique, which is based on self-locking by utilizing the optical *Kerr effect* [287]. The *Kerr effect* is a nonlinear ($\chi^{(3)}$) process [276-277, 288], where the refractive index n of the material is dependent on the light intensity I (Eq. (6.11)):

$$n(I) = n_0 + n_2 \cdot I \quad (6.11)$$

where n_0 and n_2 are the linear and nonlinear refractive index, resp. (for sapphire: $n_0 \approx 1.76$ @ 800-900nm [289], $n_2 \approx 3 \cdot 10^{-16}$ cm²/W @ 800-900 nm [290]). If the propagating laser beam exhibits e.g. a radial Gaussian intensity profile $I(r) = \text{Gaussian}(r)$, the refractive index also follows a radial gaussian profile $n(r)$. As a result the Kerr medium behaves as a lens, which focuses the propagating beam until linear diffraction balances this self-focusing effect [276]. It follows, that high peak intensities of $I \approx 10^{11}$ W/cm² [285] are necessary (see Eq. (6.11)) to significantly change the refractive index in order to induce the nonlinear self-focusing.

This is only achieved by mode-locked fs pulses. Fig. 6.11 schematically illustrates the resulting beam-waist narrowing of the pulsed mode during the propagation through the Ti:Sa crystal as a result of the Kerr lens. By placing an aperture inside the cavity, the losses for the cw regime can be increased („hard aperture“ KLM [287]). However, the used *Griffin-W* (KMLabs) Ti:Sa oscillator setup is based on „soft aperture“ KLM [287], where the spatial gain profile, induced by the tightly focused pump beam (532 nm), constitutes a natural aperture. Thus high intensity phase-locked modes are stronger focused and exhibit a larger overlap with the collinear narrow pump beam, resulting in higher amplification compared to „off-phase“/cw modes (Fig. 6.11).

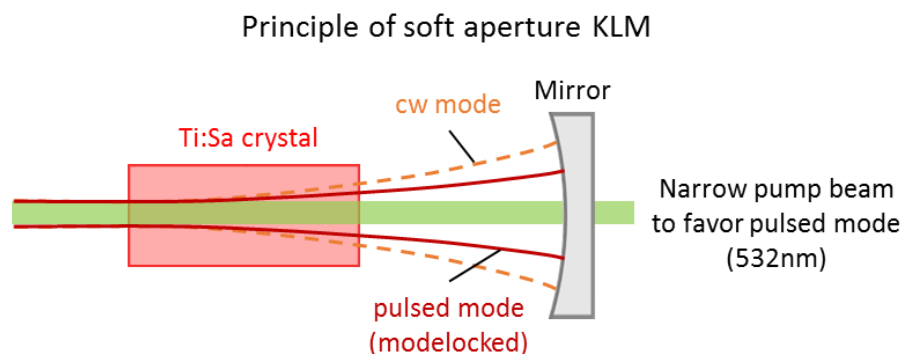


Fig. 6.11 Illustration of soft aperture Kerr-lens modelocking (KLM) based on the self focusing effect on cw and pulsed mode of a Ti:Sa oscillator.

6.2.4. Optical chirp

Ultrashort pulses are subjected to dispersion when propagating through dispersive media e.g. optics or the Ti:Sa crystal itself. This induces a temporal broadening (increase in pulse duration) and a change of the instantaneous frequency („chirp“). For a Fourier-limited pulse the instantaneous frequency $\omega(t)$ is constant ($\frac{d}{dt}\varphi(t) = \text{const.}$, see Eqs. (6.7),(6.12)). However for pulses which exhibit an optical chirp, the carrier frequency $\omega(t)$ changes in time $\frac{d}{dt}\varphi(t) = f(t)$.

$$\omega(t) = \omega_0 + \frac{d}{dt}\varphi(t) \quad (6.12)$$

For the simple case that $\varphi(t)$ follows a quadratic law in time (neglecting higher order terms) a chirped pulse can be described by Eq. (6.13), where $\xi^*(t)$ is the broadened pulse envelope compared to its Fourier-limit (e.g. Gaussian) and b is a constant.

$$E(t) = \xi^*(t) \cdot e^{i(\omega_0 t + bt^2)} \quad (6.13)$$

As illustrated by (6.12), depending on the sign of b , the instantaneous frequency is either more blue (positive chirp) or red (negative chirp) in the leading edge of the pulse. Owing to dispersion, each frequency component of the optical pulse travels at different velocities (phase and group velocities) through the material, which is the physical origin of the chirp. The spectral phase of each frequency (frequency domain) can be approximated in a Taylor series around the central frequency ω_0 (Eq. (6.14)) [277, 285].

$$\Phi(\omega) = \sum_0^{\infty} \frac{1}{n!} \left. \frac{d^n \Phi(\omega)}{d\omega^n} \right|_{\omega_0} (\omega - \omega_0)^n \quad (6.14)$$

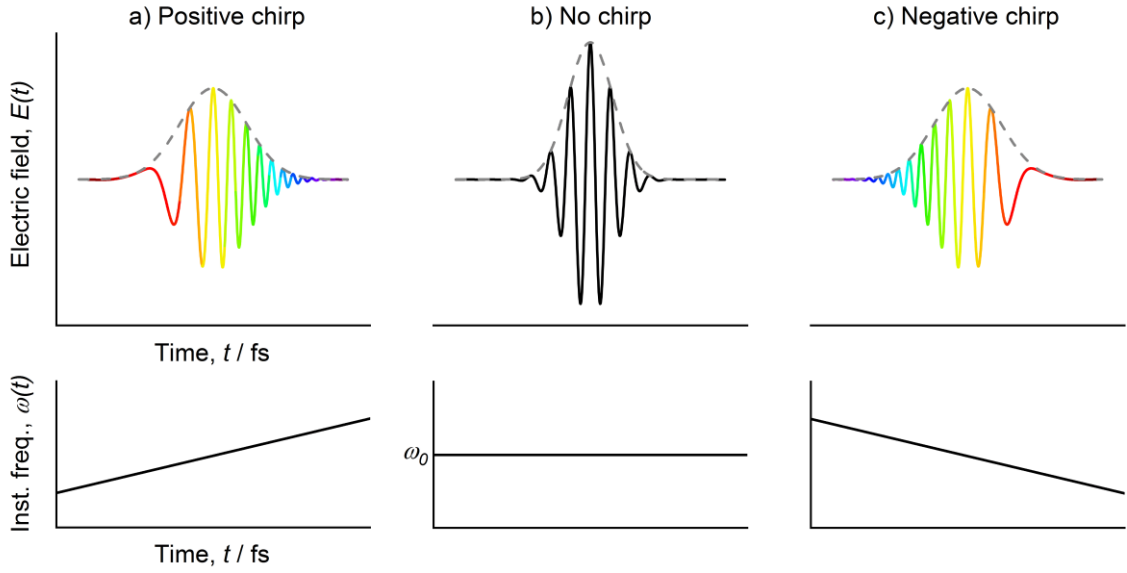


Fig. 6.12 Schematic illustration of Gaussian pulses according to Eqs. (6.12),(6.13), that exhibit a) a positive chirp ($b > 0$), b) no chirp (Fourier-limited) and c) a negative chirp ($b > 0$). The respective pulse envelope functions are indicated (dotted gray lines). The areas beneath the Gaussian envelopes are equal for a)-c) due to energy conservation.

The first two terms ($n = 0, 1$) have no influence on pulse duration, whereas the third term $\frac{1}{2} \frac{d^2\Phi(\omega)}{d\omega^2} (\omega - \omega_0)^2$ increases the pulse duration (calculated by reverse Fourier transform [276-277]). The term $\frac{d^2\Phi}{d\omega^2}$ (Eq. (6.15)) is called second-order dispersion or group velocity dispersion (GVD) and dependent on the material (L_m : path length through material, $n(\lambda)$: refractive index, c : speed of light in vacuum, $\text{GVD}(\text{air}) = 0.02 \text{ fs}^2/\text{cm}$ and $\text{GVD}(\text{sapphire}) = 581.18 \text{ fs}^2/\text{cm}$, at $\lambda = 800 \text{ nm}$ [285]).

$$\frac{d^2\Phi(\omega)}{d\omega^2} = \frac{\lambda^3 L_m}{2\pi c^2} \frac{d^2 n(\lambda)}{d\lambda^2} \quad (6.15)$$

Since the Ti:Sa medium induces a positive chirp ($\text{GVD} > 0$), this needs to be compensated by dispersive optical elements that, in turn, induce an equal negative GVD in order to achieve near Fourier-limited pulses. To this end, an arrangement of a prism pair and a mirror is commonly used in fs oscillator systems as illustrated by Fig. 6.13 [291].

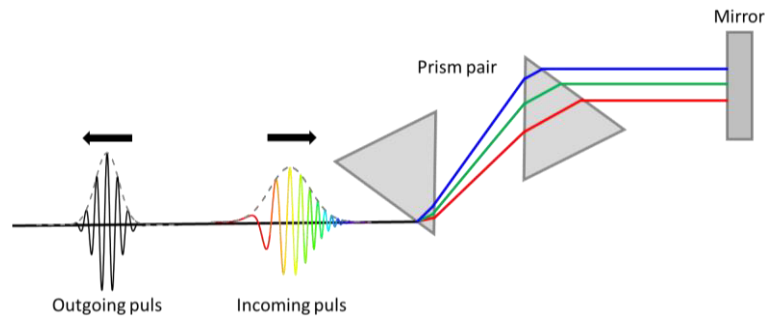


Fig. 6.13 Illustration how the positive GVD of a chirped pulse can be compensated by a prism pair and mirror arrangement (prism compressor). Each prism (typically fused silica) induces a positive GVD, however the red components have a longer pathway through the second prism, whereas the blue components have a larger travel distance through air. By choosing a delicate arrangement, the prism pair can induce an overall negative GVD.

6.2.5. Ti:Sa oscillator system

Fig. 6.14 shows the optical setup and beam path of the *Griffin-W (KMLabs)* KLM Ti:Sa oscillator system as integrated into the *Wyvern 1000 (KMLabs)* system. The laser cavity consists of a highly reflective rear mirror (RM) and an output coupler mirror (OC, $\approx 10\%$ transmittance) in a compact folded resonator design, utilizing three dielectric „folding“ mirrors (DM1-3). A frequency doubled Nd:YAG cw laser (*Opus 532, Laser Quantum* [292]) is used for pumping (532 nm, 2.25 W), focused into a Ti:Sa crystal (dimensions: 3x5x5 mm) through a lens (FL, focal length: 10 cm) and dumped after passing the two curved dichroic mirrors (CM1-2, radius of curvature: 10cm) of the resonator cavity. Two prisms both mounted on single-axis translation stages, controlled by stepper motors, are used for compensating for GVD. The cavity is aligned so that both cw and mode-locked modes are stable. Kerr-lens self mode-locking is usually achieved by a back and forth translation of prism 1 (P1). A low rotational speed dust filter (DF) was installed to minimized contamination of the optics. The resonator output (in modelocked mode: $\lambda_{center} \approx 785$ nm, fwhm = 55-65 nm, 78 MHz, 130-140 mW, $t_{pulse} \approx 20$ fs) passes through a „pickoff“ window before entering the stretcher of the CPA system. Reflection of the „pickoff“ window are guided into a photo diode (PD) and a spectrometer fiber probe (SFP), resp. in order to monitor the generated pulse train (Fig. 6.15 a) and the emission spectrum (Fig. 6.15 b) in parallel.

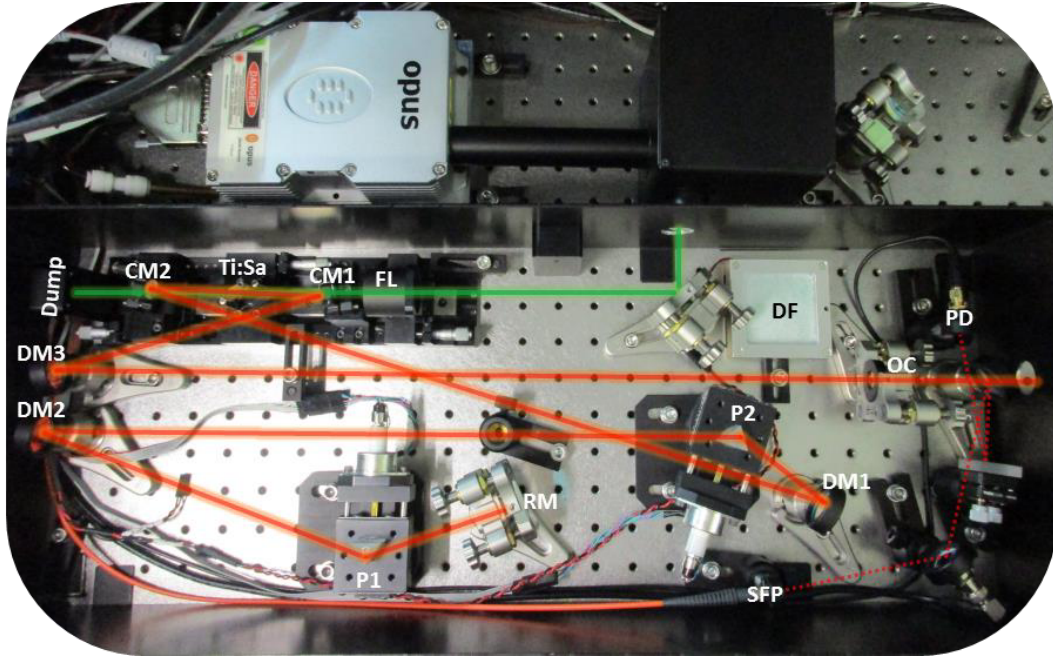


Fig. 6.14 Schematic beam path and layout of the *Griffin-W* (KMLabs) Ti:Sa oscillator as integrated into the *Wyvern 1000* (KMLabs) system. FL: focusing lens, CM1-2: curved mirrors, DM1-3: dielectric mirrors, P1-2: prisms, RM: rear mirror, OC: output coupler, DF: dust filter, PD: photodiode, SFP: spectrometer fiber probe.

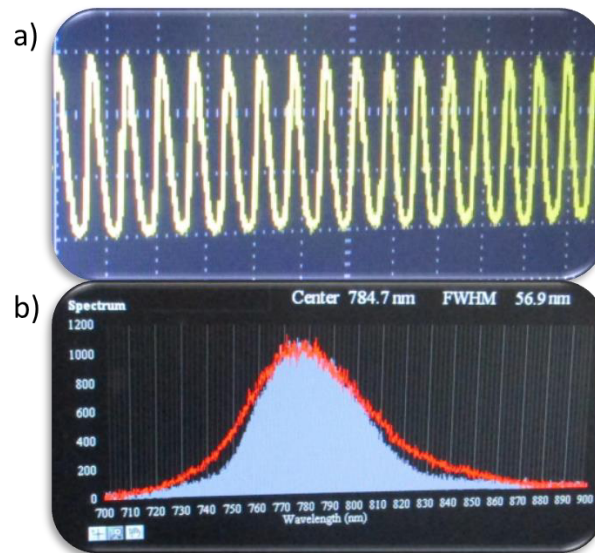


Fig. 6.15 a) Oscilloscope trace of the photodiode (*Rigol DS1302CA*, 2 channel, 300 MHz, 2Gsa/s, scale division: vertical = 50 mV, horizontal = 20 ns) displaying a typical pulse train of the *Griffin-W* oscillator in the mode-locked regime. b) Corresponding spectrum picked up by the spectrometer fiber probe ($\lambda_{center} \approx 785$ nm, fwhm = 57 nm).

6.2.6. Chirped-pulse amplification (CPA)

The chirped-pulse amplification (CPA) technique facilitates the generation of femtosecond pulses with high peak power in the terawatts range ($1 \text{ TW} = 10^{12} \text{ W}$) and is typically used in combination with the broad-bandwidth Ti:Sa laser medium [285]. The CPA technique was developed by *Gérard Mourou* and *Donna Strickland* [293] and awarded with the Nobel Prize in physics in 2018 [294]. The challenge for the amplification process of ultrafast optical pulse is, that the high pulse intensities easily exceed the damage threshold of the amplifier medium or other optical elements in the amplifier. In the CPA scheme (Fig. 6.16) this is circumvented by first lengthening the pulse duration („stretching“ in time) by the means of dispersive optics, e.g. a diffraction-grating arrangement, whereby the peak power is significantly reduced by \sim three orders of magnitude ($\text{fs} \rightarrow \text{ps}$). The chirped pulse is then amplified in multiple passes through the laser medium inside the amplifier and subsequently compressed back near the input pulse duration by a second grating pair by reversing the GVD imparted by the stretcher and amplifier.

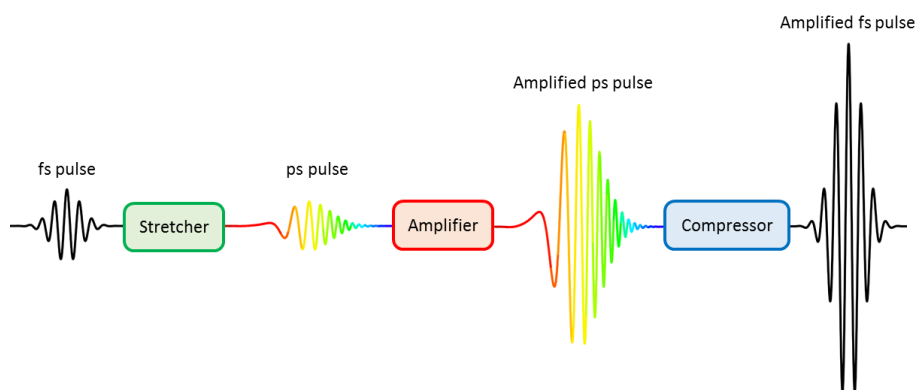


Fig. 6.16 Scheme of chirped-pulse amplification.

The utilized CPA laser system, described in the next section, is based on the so called regenerative amplifier scheme. The regenerative amplifier operates by selecting a single stretched „seed“ pulse from a pulse train by a polarization-selective optical element [295]. The selected pulse is trapped within a cavity and amplified in multiple round-trip passes (20-40) through a pumped gain medium and ultimately switched-

out through a thin-film polarizer after rotating its polarization plane by a Pockels cell after the amplification process has reached its maximum (saturation).

6.2.7. Ti:Sa regenerative CPA system (*Wyvern 1000*)

In the following, a brief introduction of the optical layout and mode of operation of the *Wyvern 1000* (*KMLabs*) CPA fs laser system is described [296-297] and illustrated by Fig. 6.17.

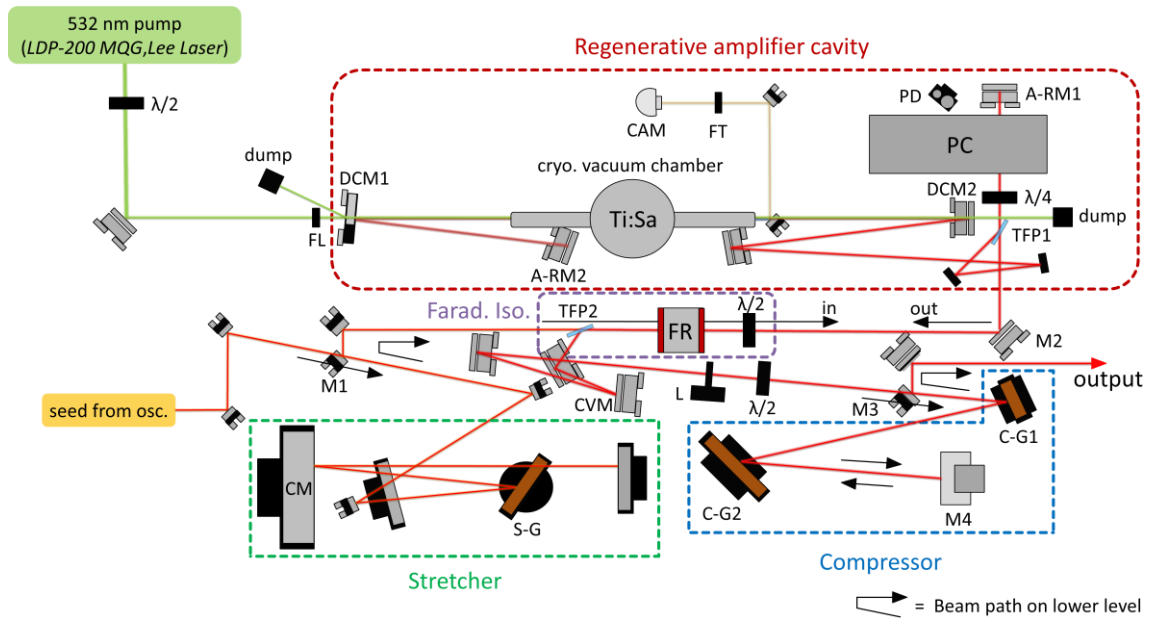


Fig. 6.17 Schematic setup of the *Wyvern 1000* (*KMLabs*) cryogenically cooled, Ti:Sa regenerative chirped-pulse amplifier (CPA) system. Abbreviations: $\lambda/2$: half-wave plate; $\lambda/4$: quarter-wave plate; FL: focusing lens; DCM1-2: dichroic mirrors; A-RM1-2: highly reflective rear mirrors of the regenerative amplifier cavity; FT: optical filter; CAM: charge-coupled device (CCD) camera; PD: photodiode; PC: Pockels cell; TFP1-2: thin film polarizers; FR: Faraday rotator; M1-4: mirrors; CVM: convex mirror; L: converging lens (CVM+L constitute a telescope for beam expansion); CM: curved mirror; S-G: stretcher grating, C-G1-2: compressor gratings. Modified from Ref. [225]

The seed beam, originating from the *Griffin-W* oscillator (130-140 mW, ≈ 20 fs, horizontally polarized), passes over mirror M1 into the stretcher. There, it is temporally chirped (≈ 20 fs $\rightarrow \approx 100$ ps, positive chirp) by being reflected four times by the dispersive stretcher grating (S-G) following a complicated beam path on three

individual height levels parallel to the laser breadboard [296]. Additionally, the beam is collimated at the entry and exit by a curved mirror (CM). The imposed GVD („stretching factor“) is determined by the distance of the stretcher-grating (S-G) to the curved mirror (CM), which is the advantage of this single grating layout. Therefore, a knob („GVG-screw“) by which S-G can be translated parallel to the CM for GVD control, is situated externally of the Wyvern housing. The temporally stretched ps pulses exit the stretcher at a lowered height, are picked off by mirror M1 and guided into the Faraday isolator consisting of a thin film polarizer (TFP2), a Faraday rotator (FR) and a half-wave plate ($\lambda/2$) (see Fig. 6.17).

The working principle of the Faraday isolator is as follows: At the entrance the beam is horizontally (p, from German „parallel“) polarized and is hence transmitted through TFP2. Subsequently, the polarization plane of „forward“ propagating pulses (into amplifier) are rotated by 90° to vertical (s, from German „senkrecht“) by the Faraday rotator and rotated back again to horizontal by a subsequent $\lambda/2$ plate. On the other hand, pulses leaving the amplifier are p-polarized and therefore turned into s-polarized by the $\lambda/2$ plate before the FR. Since the polarization of counter-propagating light (from amplifier) is not affected by the Faraday rotator, the vertical polarized amplified pulses are reflected by the thinfilm polarizer TFP2 and directed into the compressor. By this setup the amplified pulses are effectively prevented from returning back into the stretcher, in order to avoid damaging of the delicate optics. Before entering the compressor, the beam is expanded by a telescope (by a factor of ≈ 10), consisting of a convex mirror (CVM) and a converging lens (L), to reduce heating of the compressor optics, and the polarization is rotated to horizontal by another $\lambda/2$ plate.

The temporally stretched (100 ps), p-polarized pulses enter the regenerative amplifier cavity by transmission through the thin-film polarizer TFP1. A $\lambda/4$ plate, located directly after TFP1, effectively rotates the plane of polarization by 90° after each trip between the highly reflective cavity mirrors A-RM2 and A-RM1. In the case that the high speed pockels cell (PC) [295] (see Fig. 6.17) is switched off, the pulses undergo only one round trip in the amplifier cavity as follows:

Starting from TFP1, the beam traverses the $\lambda/4$ plate twice, after being reflected by A-RM1, resulting in rotation of the polarization plane by 90° (to vertical). The s-polarized beam is then reflected by TFP1 and steered into the vacuum chamber which is equipped with Brewster-angle windows and houses the amplifier medium. The Ti:Sa crystal is cryogenically cooled down to $T \approx 50$ K (PT90 Cryostat, CP950 He-compressor, Cryomech) in order to avoid thermal lensing [298] and increase gain [297, 299]. After passing the vacuum chamber, the beam is returned back by A-RM2, reflected by TFP1 towards A-RM1, p-polarized by passing the $\lambda/4$ plate twice, and ultimately transmitted through TFP1 out of the amplifier cavity. The operation principle of the regenerative amplifier is based on the fact that a single stretched pulse can be selected and trapped inside the amplifier cavity as long as a high voltage is applied to the Pockels cell, typically for a few ns [295]. The PC in the „switched on“ state acts as a quarter-wave plate and „counteracts“ the change in polarization plane that is induced by the $\lambda/4$ plate. As a result, the trapped beam remains s-polarized and is reflected by TFP1 each passing, whereas new incoming pulses can not enter the cavity since they effectively remain p-polarized and are transmitted by TFP1.

The amplification process takes place in multiple round trips, whereby the amplification „build-up“ of the last three passes can be detected by a photodiode (PD) and monitored by an oscilloscope. The frequency-doubled *LPD-200 MQG* pump laser of the amplifier (*Lee Laser*, 532 nm, 17-18 W, pulse duration ≈ 100 ns) is synchronized with the PC timing to optimize amplification and avoid pre/post pulses. Additionally, the spatial overlap between the seed and pump beam at the Ti:Sa crystal is imaged by a CCD camera. After amplification, the positive chirp imparted by the stretcher and additional optics is compensated by means of two parallel gratings (C-G1 and C-G2) within the compressor. The amplified beam enters the compressor by passing over the top of mirror M3. After being diffracted by the two gratings, the beam is retro-reflected at a lower height by the dielectric „roof“ mirror M4 and is ultimately leaving the compressor by the „pickoff“ mirror M3. The amplified pulse power is typically 3.8-4.0 W at a repetition rate of ≈ 1 kHz and pulse duration of 40-50 fs. An abstracted CPA scheme of the *Wyvern 1000* system and a typical spectrum is provided by Fig. 6.18.

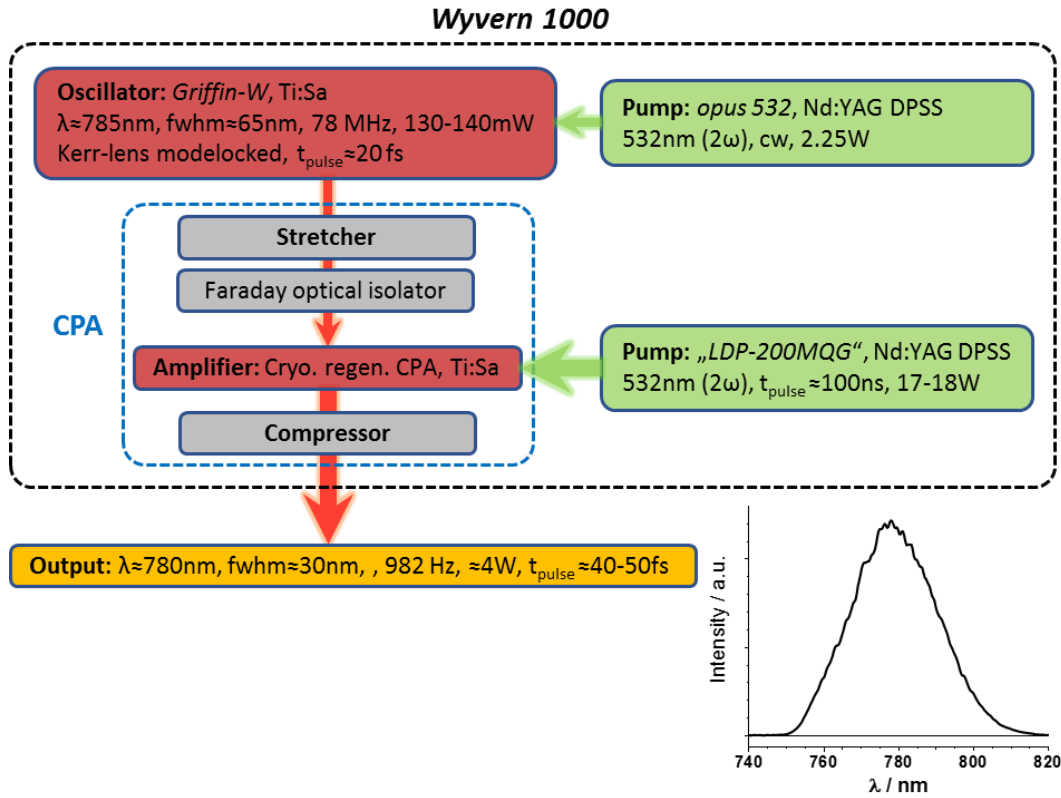


Fig. 6.18 Schematic overview of the *Wyvern 1000* (KMLabs) fs Ti:Sa oscillator/cryogenic, regenerative CPA laser system, including the two frequency doubled (2ω) *Opus 532* (*Laser Quantum*) and *LDP-200MQG* (*Lee Laser*) diode-pumped-solid-state (DPSS) Nd:YAG pump lasers, respectively. Central wavelength and fwhm of emission band, pulse repetition rate, output power and pulse duration are indicated. A typical laser emission spectrum of the *Wyvern 1000* system is shown in the bottom right.

The amplification factor is calculated according to $\frac{E_{\text{amp. pulse}}}{E_{\text{input pulse}}} = 2.3 \cdot 10^6$, where

$$E_{\text{amp. pulse}} = \frac{4\text{ W}}{1\text{ kHz}} = 4\text{ mJ}; E_{\text{input pulse}} = \frac{0.14\text{ W}}{80\text{ MHz}} = 1.75\text{ nJ}.$$

6.2.8. Wavelength converter system (TOPAS-C)

For the generation of wavelength-tunable *pump* and *probe* pulses (see chapter 5.2), two collinear optical parametric amplifier systems ^[300] (*TOPAS-C, Light Conversion, TOPAS: „Travelling-Wave Optical Parametric Amplifier of White-Light Continuum System“*) were utilized. The *TOPAS-C* system is an automated two-stage optical parametric amplifier (OPA) of white-light continuum (WLC) that comprises: a

white-light continuum generator, a pre-amplifier stage, and a power-amplifier stage. Its optical layout is shown in Fig. 6.19 [301].

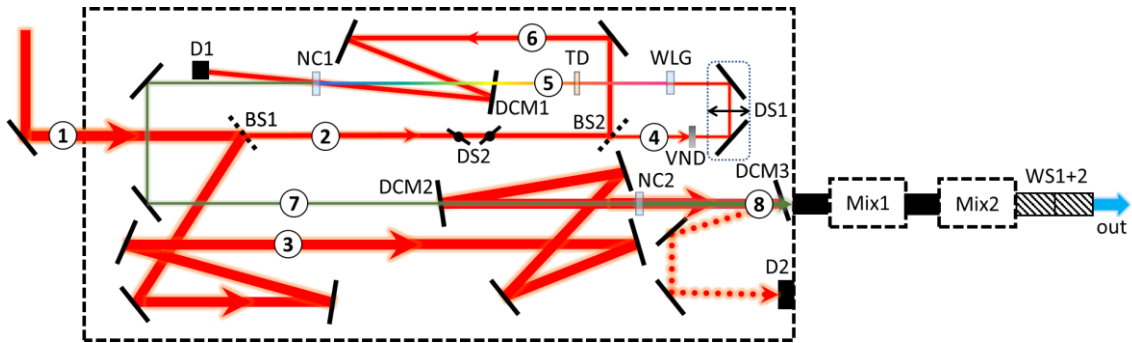


Fig. 6.19 Schematic optical layout of the *TOPAS-C (Light Conversion)* system. Some optics for beam expansion and collimation were omitted for clarity [301]. Adapted and modified from Refs [225, 301]. ① pump beam from *Wyvern-1000* system (780 nm, 1.2/1.5 mJ, ≈ 50 fs); ② pump for pre-amplification stage; ③ pump for amplification stage; ④ seed for white-light continuum generation; ⑤ white-light continuum (WLC); ⑥ pump for parametric pre-amplification of WLC; ⑦ pre-amplified signal; ⑧ amplified signal+idler and residual pump (780 nm). D1-2: beam dumps; NC1-2: non linear crystals (BBO), BS1-2: beam splitters (≈ 80 -98% reflectivity); DS1-2: delay stages (computer controlled rotation/translation); VND: variable neutral-density filter; TD: dispersive plate; WLG: white-light continuum generation in sapphire plate; DCM1-3: dichroic mirrors; Mix1-2: mixing stages housing BBO crystals; WS1+2: pair of wavelength separators.

After entering the system, the pump (Ti:Sa CPA, 780 nm, 1.2/1.5 mJ, ≈ 50 fs) is split into two paths by a beam splitter (BS1, ≈ 80 -98% reflectivity). The reflected high energy beam ③ is used as pump in the power-amplification stage, whereas the transmitted low energy fraction ② is used in the pre-amplifier. The latter passes through two *Brewster* angled plates mounted on computer controlled rotation stages (DS2) that change the length of the beam path and thereby control the temporal delay between pump and seed pulses in the power-amplifier stage. A second beam splitter (BS2) reflects ≈ 80 % for usage as pump in the pre-amplifier ⑥. The beam that is transmitted by BS2 passes through a variable neutral density filter and is retro reflected (DS1) and focused onto a sapphire plate for the generation white-light continuum (WLC). A dispersive plate (TD) stretches the WLC in time. Pump and WLC beams are combined by DCM1 and non-linearly overlapped

inside the pre-amplifier BBO crystal (NC1) where the parametric amplification process takes place.

Wavelength tuning in the pre-amplification stage is achieved by changing the temporal delay between the stretched WLC pulse and the pump pulse by means of a motorized translation stage (DS1) and tilt of the crystal angle for optimal phase-matching. The generated *idler* and pump beam are dumped (D1), whereas the *signal* beam is used as seed for the second amplification stage. In the power-amplifier the pre-amplified signal is collinearly overlapped with the high-energy pump beam ③ inside a second nonlinear crystal (NC2). As a result, amplified *signal* and *idler* beams, encompassing a spectral range of 1140-1620 nm and 1520-2500 nm, resp. can be generated. In summary, the wavelength tuning is controlled by the delay stages DS1 and DS2 and the crystal angles (NC1 and NC2). Two external frequency mixer stages are located after the *TOPAS-C* system and are used to extend the tuning range to 240-2500 nm through various nonlinear optical schemes as summarized in Tab. 6.2. The residual pump radiation can be dumped by a dichroic mirror DCM3, in case it is not needed for further non-linear optical processes. A pair of dielectric wavelength separators are mounted after the two mixer stages in order to filter undesirable residual radiation (see Fig. 6.19 and Fig. 6.20).

Tab. 6.2 Summary of non-linear optical processes (NLP) and tuning ranges for mixer 1 and 2 stages of the *TOPAS-C* systems. **I**: idler; **S**: signal, **SHI/S** second harmonic of idler/signal, **SFI/S** sum frequency generation mixing idler/signal with residual pump (780 nm), **FHI/S** fourth harmonic of idler/signal, **SHSFI/S** second harmonic of **SFI/S**. For details see Ref. [301].

NLP (wave)	wavelength range / nm
I	1520-2500
S	1140-1620
SHI	795-1160
SHS	570-810
SFI	525-580
SFS	472-527
FHI	400-485
FHS	285-400
SHSFI	262.5-287.5
SHSFS	236-263.5

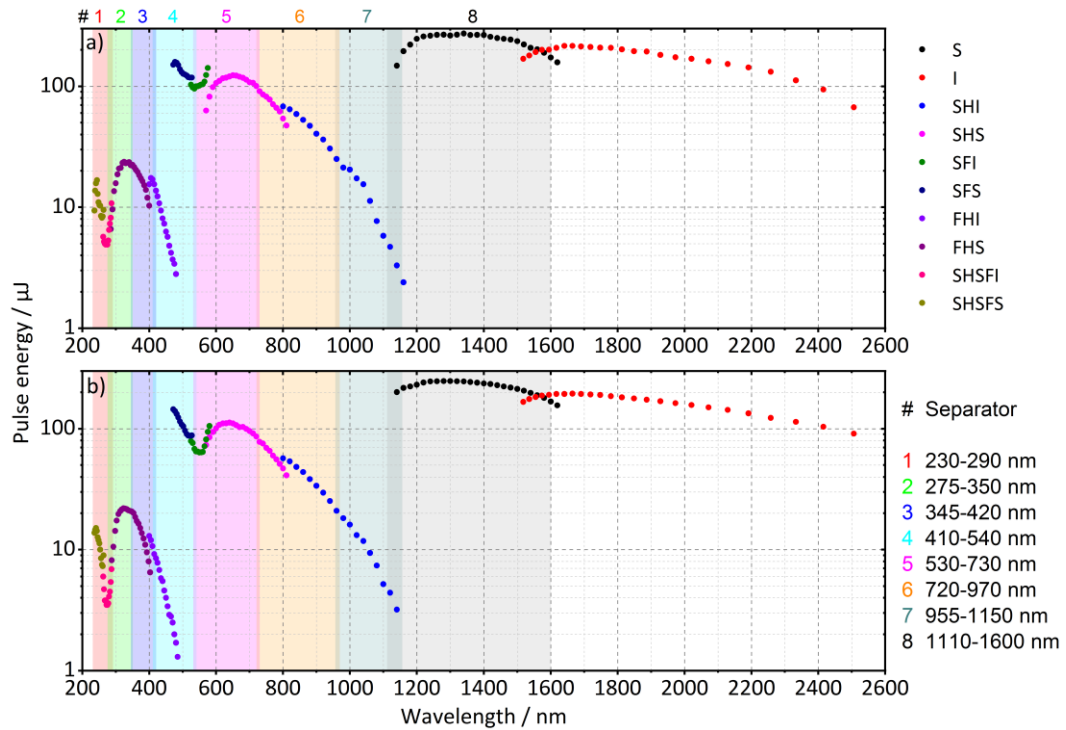


Fig. 6.20 Tuning curves of the two *TOPAS-C* systems labeled as a) „T7“ (pump: 1.2 mJ) and b) „T6“ (pump: 1.5 mJ) in Fig. 6.21, respectively. The nonlinear output schemes are labeled according to Tab. 6.2. Colored areas indicate the wavelength ranges of separators that were used after the two mixer stages. Taken from Ref. [225].

6.2.9. Overview of PD/ τ -PD experimental setup

The complete experimental setup for static and time-resolved photodissociation ion spectroscopy is depicted in Fig. 6.21. The output of the fs Ti:Sa KLM oscillator / CPA amplifier system (4mJ, 780 nm, 50 fs, 1 kHz) was split into three beam branches by the beam splitters BS1 and BS2. One branch (1.3 mJ) was used for WLG in a transient absorption/reflectivity setup (solution phase experiments) in cooperation with the group of Prof. Dr. Diller (TUK, physics department). The other two beams were used as pump of two identical optical parametric generator/amplifier systems, which were utilized for independent wavelength tuning in order to generate UV *pump* pulses (T7, spectral width ~ 3 nm @ 260 nm) and NIR *probe* pulses (T6, typical at ≈ 1150 nm). Before entering the *TOPAS-C* systems the beam diameter was reduced ($1/e^2$ width < 8 mm) by telescope 1 and 2, respectively (requirement of the systems [301]). Two sets of wavelength separators were used to filter radiation of „parasitic“ waves and pulse energies were controlled by two variable neutral density filters. The optical path of the probe pulses was varied utilizing a motorized single axis delay stage (*Physik Instrumente*) with a mounted retroreflector (RF, protected silver coating) for controlling the temporal delay with respect to pump pulses. Both beams were quasi collinearly combined ($\approx 0.8^\circ$) and focused ($f = 40/50$ cm) through a fused silica window (3 mm thickness) onto the center of the ion cloud (≈ 1 mm diameter). The relative angle of *pump* and *probe* polarization planes was set to $\approx 54.7^\circ$ by a variable half-wave plate (*Berek compensator*). The pulse repetition rate could be reduced by means of an optical chopper. A beam shutter was synchronized with the QIT-MS in order to allow radiation of the ion cloud only during the fragmentation time window (t_{frag}).

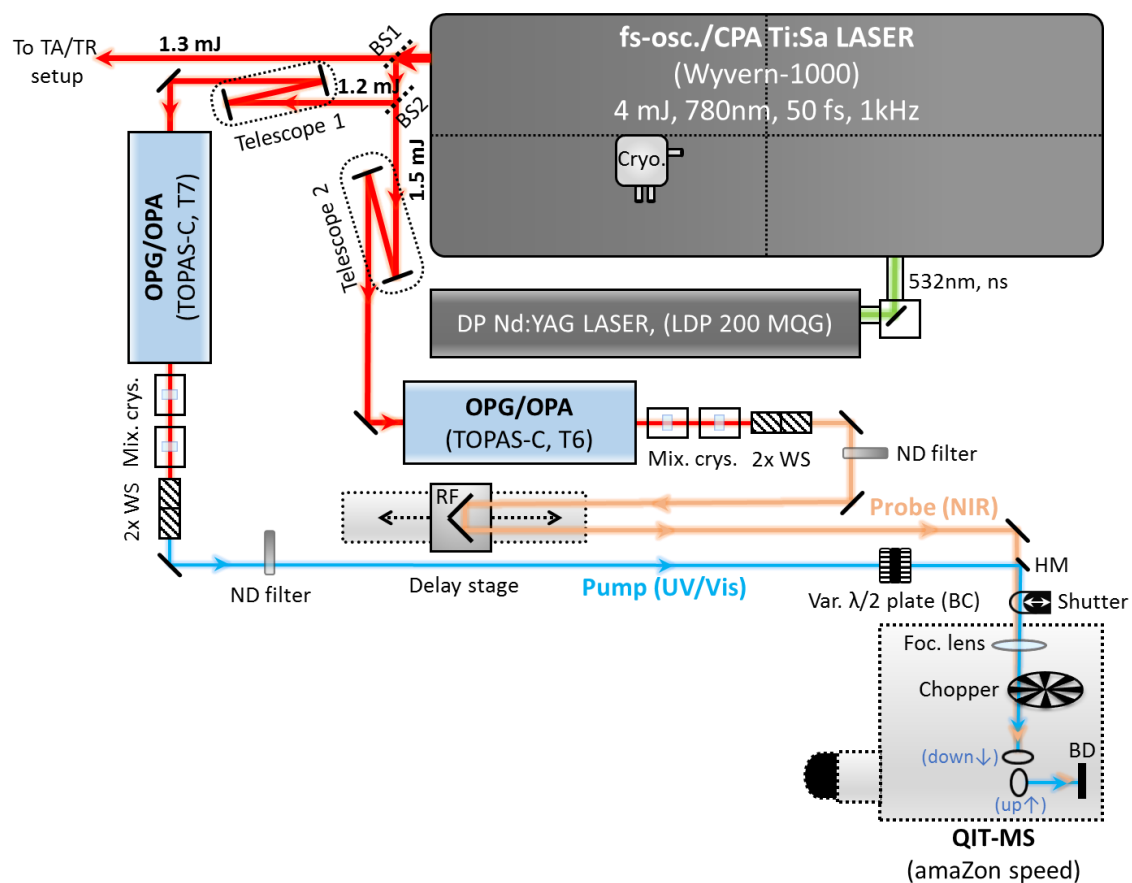


Fig. 6.21 Schematic setup for PD/ τ -PD experiments combining a tunable femtosecond *pump/probe* laser setup with a modified Paul-type ion trap mass spectrometer (QIT-MS, *amaZon speed*). Abbrev.: TA/TR: transient absorption/reflectivity, BS: beam splitter, fs-osc: femtosecond oscillator, CPA: chirped pulse amplification, Cryo.: cryostate, OPG/OPA: optic parametric generator/amplifier, DP: diode pumped, Mix. Crys.: mixing crystals, WS: wavelength separators, ND: neutral density, RF: retro reflector, BC: Berek compensator, HM: half mirror, BD: beam dump.

7. Danksagung

An dieser Stelle möchte ich mich herzlich bei allen Personen bedanken, welche mich im Rahmen meiner Promotionszeit wissenschaftlich, administrativ und freundschaftlich unterstützt haben – Professoren, Kollegen, Studenten, Familie und Freunde.

Priv.-Doz. Dr. Christoph Riehn danke ich für die gute Betreuung meiner Promotion und für die Einführung in die interessante Welt der „Ultrakurzzeit-Phänomene“, sowie für die zahlreichen Denkanstöße und seine stetige Bereitschaft für Diskussionen und Hilfestellungen. Danke dass Du die letzten Jahre immer eine offene Tür hattest.

Besonderer Dank gilt meinem „Lehrmeister“ Dr. Yevgeniy Nosenko für seine unersetzliche Hilfe und unerschütterliche Geduld in allen physikalischen und technischen Belangen - und darüber hinaus. Deine ruhige und analytische Denkweise ist bewundernswert.

Björn Kwasigroch und Mike Lembach danke ich für die heitere Arbeitsatmosphäre und für den kollegialen Zusammenhalt. Eure stetige moralische und tatkräftige Unterstützung hat mich bereichert.

Allen Forschungspraktikanten, Diplomanden und Bacheloranden*innen, welche mich auf meinem Weg begleitet haben, bin ich zu großem Dank verpflichtet: Marcel Schmitt, Isabel Manes, Michael Borchers, Björn Kwasigroch, Maximilian Luczak, Yannik Mees und Patrick Strebert – Danke für Eure Unterstützung – Es war mir eine Ehre.

Meinen neuen und ehemaligen „Femto“-Kollegen Roumany Israil und Dr. Dimitri Imanbaew danke ich für die gute Zusammenarbeit.

7. Danksagung

Mein aufrichtiger Dank gilt allen gegenwärtigen und ehemaligen Mitgliedern der physikalischen und theoretischen Chemie (AKs GNS, Gerhards und van Wüllen) - Danke für die nette und kollegiale Atmosphäre und die geselligen Stunden im Kaffeezimmer.

Prof. Dr. Dr. Gereon Niedner-Schatteburg möchte ich für die freundliche Aufnahme in den AK GNS, die fachlichen Diskussionen und die Übernahme des Zweitgutachtens danken.

Sybille Heieck und Birgit Harrison-Weber danke ich für das unerschütterliche Abarbeiten der Papierberge (Papierkrieg) und für die unterhaltsamen und aufmunternden Gespräche.

Weiterhin danke ich allen Kooperationspartnern im Sonderforschungsbereich „3MET“ für die erfolgreiche Zusammenarbeit und das inspirierende wissenschaftliche Umfeld.

Florian Bäßler, Fabian Rupp, Merten Gruppe, Philip Wolf, Lars Schüssler und Prof. Dr. Rolf Diller (TUK) danke ich für die tolle und anregende Zusammenarbeit im Projekt „C4“. Ich erinnere mich mit Freude an die zahlreichen wissenschaftlichen Diskussionen in familiärer Atmosphäre.

Bei Dr. Simon Walg, Jens Neu, und Dr. Cedric Groß möchte ich mich für die Synthese zahlreicher Proben, den regen wissenschaftlichen Austausch, und für die gute Zusammenarbeit bedanken. Prof. Dr. Werner Thiel (TUK) danke ich für die Bereitstellung seines Labors und für die Übernahme des Prüfungsvorsitzes.

Für die theoretische Unterstützung, welche eine genauere Interpretation der experimentellen Ergebnisse erst möglich machten, gilt mein besonderer Dank Xin Gui, Dr. Christof Holzer und Prof. Dr. Wim Klopper (KIT).

Dr. Marc-Oliver Winghart, Prof. Dr. Manfred Kappes (KIT) und Dr. Jean-Francois Greisch danke ich für die konstruktive Zusammenarbeit und die inspirierenden Gesprächsrunden.

8. References

- [1] Image: „magnifying glass“, <https://pixabay.com/vectors/lupe-magnifier-loupe-glass-160478/>, access date 23.01.2020
- [2] Image: „eye“, <https://pixabay.com/illustrations/eye-computer-icon-vector-2387853/>, access date 23.01.2020
- [3] Image: „hummingbird“, <https://pixabay.com/vectors/animal-bird-flying-hummingbird-2099057/>, access date 23.01.2020
- [4] A. H. Zewail, Femtochemistry: Atomic-Scale Dynamics of the Chemical Bond, *The Journal of Physical Chemistry A* **2000**, *104*, 5660-5694. doi: 10.1021/jp001460h
- [5] A. H. Zewail, Laser Femtochemistry, *Science* **1988**, *242*, 1645. doi: 10.1126/science.242.4886.1645
- [6] J. S. Baskin, A. H. Zewail, Freezing Atoms in Motion: Principles of Femtochemistry and Demonstration by Laser Stroboscopy, *Journal of Chemical Education* **2001**, *78*, 737. doi: 10.1021/ed078p737
- [7] A. H. Zewail, Femtochemistry: Recent Progress in Studies of Dynamics and Control of Reactions and Their Transition States, *The Journal of Physical Chemistry* **1996**, *100*, 12701-12724. doi: 10.1021/jp960658s
- [8] H. Eyring, M. Polanyi, Simple Gas Reactions, *Zeitschrift für Physikalische Chemie* **2013**, *227*. doi: 10.1524/zpch.2013.9023
- [9] E. J. Heller, The semiclassical way to molecular spectroscopy, *Accounts of Chemical Research* **1981**, *14*, 368-375. doi: 10.1021/ar00072a002
- [10] R. M. van der Veen, A. Cannizzo, F. van Mourik, A. Vlček, M. Chergui, Vibrational Relaxation and Intersystem Crossing of Binuclear Metal Complexes in Solution, *Journal of the American Chemical Society* **2011**, *133*, 305-315. doi: 10.1021/ja106769w
- [11] M. Chergui, On the interplay between charge, spin and structural dynamics in transition metal complexes, *Dalton Transactions* **2012**, *41*, 13022-13029. doi: 10.1039/C2DT30764B
- [12] M. Du, G. R. Fleming, Femtosecond time-resolved fluorescence spectroscopy of bacteriorhodopsin: Direct observation of excited state dynamics in the primary step of the proton pump cycle, *Biophysical Chemistry* **1993**, *48*, 101-111. doi: 10.1016/0301-4622(93)85002-Y
- [13] A. Cannizzo, F. van Mourik, W. Gawelda, G. Zgrablic, C. Bressler, M. Chergui, Broadband Femtosecond Fluorescence Spectroscopy of $[\text{Ru}(\text{bpy})_3]^{2+}$,

- Angewandte Chemie International Edition* **2006**, *45*, 3174-3176. doi: 10.1002/anie.200600125
- [14] M.-O. Winghart, J.-P. Yang, M. Vonderach, A.-N. Unterreiner, D.-L. Huang, L.-S. Wang, S. Kruppa, C. Riehn, M. M. Kappes, Time-resolved photoelectron spectroscopy of a dinuclear Pt(II) complex: Tunneling autodetachment from both singlet and triplet excited states of a molecular dianion, *The Journal of Chemical Physics* **2016**, *144*, 054305. doi: 10.1063/1.4940795
- [15] A. n. Vlček, The life and times of excited states of organometallic and coordination compounds, *Coordination Chemistry Reviews* **2000**, *200-202*, 933-978. doi: 10.1016/S0010-8545(00)00308-8
- [16] M. Born, R. Oppenheimer, Zur Quantentheorie der Molekeln, *Annalen der Physik* **1927**, *389*, 457-484. doi: 10.1002/andp.19273892002
- [17] R. W. Schoenlein, L. A. Peteanu, R. A. Mathies, C. V. Shank, The first step in vision: femtosecond isomerization of rhodopsin, *Science* **1991**, *254*, 412. doi: 10.1126/science.1925597
- [18] S. Karmakar, S. Keshavamurthy, Intramolecular vibrational energy redistribution and the quantum ergodicity transition: a phase space perspective, *Physical Chemistry Chemical Physics* **2020**, *22*, 11139-11173. doi: 10.1039/D0CP01413C
- [19] A. H. Zewail, IVR: Its Coherent and Incoherent Dynamics, *Berichte der Bunsengesellschaft für physikalische Chemie* **1985**, *89*, 264-270. doi: 10.1002/bbpc.19850890315
- [20] S. E. Braslavsky, Glossary of terms used in photochemistry, 3rd edition (IUPAC Recommendations 2006), *Pure and Applied Chemistry* **2007**, *79*, 293. doi: 10.1351/pac200779030293
- [21] T. J. Penfold, E. Gindensperger, C. Daniel, C. M. Marian, Spin-Vibronic Mechanism for Intersystem Crossing, *Chemical Reviews* **2018**, *118*, 6975-7025. doi: 10.1021/acs.chemrev.7b00617
- [22] E. Yu-Tzu Li, T.-Y. Jiang, Y. Chi, P.-T. Chou, Semi-quantitative assessment of the intersystem crossing rate: an extension of the El-Sayed rule to the emissive transition metal complexes, *Physical Chemistry Chemical Physics* **2014**, *16*, 26184-26192. doi: 10.1039/C4CP03540B
- [23] L. S. Forster, Intersystem crossing in transition metal complexes, *Coordination Chemistry Reviews* **2006**, *250*, 2023-2033. doi: 10.1016/j.ccr.2006.01.023
- [24] J. K. McCusker, Femtosecond Absorption Spectroscopy of Transition Metal Charge-Transfer Complexes, *Accounts of Chemical Research* **2003**, *36*, 876-887. doi: 10.1021/ar030111d

- [25] A. Pigliucci, G. Duvanel, L. M. L. Daku, E. Vauthey, Investigation of the Influence of Solute–Solvent Interactions on the Vibrational Energy Relaxation Dynamics of Large Molecules in Liquids, *The Journal of Physical Chemistry A* **2007**, *111*, 6135-6145. doi: 10.1021/jp069010y
- [26] M. Cho, S. J. Rosenthal, N. F. Scherer, L. D. Ziegler, G. R. Fleming, Ultrafast solvent dynamics: Connection between time resolved fluorescence and optical Kerr measurements, *The Journal of Chemical Physics* **1992**, *96*, 5033-5038. doi: 10.1063/1.462746
- [27] T. B. van Driel, K. S. Kjær, R. W. Hartsock, A. O. Dohn, T. Harlang, M. Chollet, M. Christensen, W. Gawelda, N. E. Henriksen, J. G. Kim, K. Haldrup, K. H. Kim, H. Ihee, J. Kim, H. Lemke, Z. Sun, V. Sundström, W. Zhang, D. Zhu, K. B. Møller, M. M. Nielsen, K. J. Gaffney, Atomistic characterization of the active-site solvation dynamics of a model photocatalyst, *Nature Communications* **2016**, *7*, 13678. doi: 10.1038/ncomms13678
- [28] A. O. Dohn, E. Ö. Jónsson, K. S. Kjær, T. B. van Driel, M. M. Nielsen, K. W. Jacobsen, N. E. Henriksen, K. B. Møller, Direct Dynamics Studies of a Binuclear Metal Complex in Solution: The Interplay Between Vibrational Relaxation, Coherence, and Solvent Effects, *The Journal of Physical Chemistry Letters* **2014**, *5*, 2414-2418. doi: 10.1021/jz500850s
- [29] J. Eng, C. Gourlaouen, E. Gindensperger, C. Daniel, Spin-Vibronic Quantum Dynamics for Ultrafast Excited-State Processes, *Accounts of Chemical Research* **2015**, *48*, 809-817. doi: 10.1021/ar500369r
- [30] M. Chergui, Ultrafast Photophysics of Transition Metal Complexes, *Accounts of Chemical Research* **2015**, *48*, 801-808. doi: 10.1021/ar500358q
- [31] O. Bräm, F. Messina, A. M. El-Zohry, A. Cannizzo, M. Chergui, Polychromatic femtosecond fluorescence studies of metal–polypyridine complexes in solution, *Chemical Physics* **2012**, *393*, 51-57. doi: 10.1016/j.chemphys.2011.11.022
- [32] A. M. Brown, C. E. McCusker, M. C. Carey, A. M. Blanco-Rodríguez, M. Towrie, I. P. Clark, A. Vlček, J. K. McCusker, Vibrational Relaxation and Redistribution Dynamics in Ruthenium(II) Polypyridyl-Based Charge-Transfer Excited States: A Combined Ultrafast Electronic and Infrared Absorption Study, *The Journal of Physical Chemistry A* **2018**, *122*, 7941-7953. doi: 10.1021/acs.jpca.8b06197
- [33] E. Collet, M. Cammarata, Disentangling Ultrafast Electronic and Structural Dynamics with X-Ray Lasers, *Chemistry – A European Journal* **2018**, *24*, 15696-15705. doi: 10.1002/chem.201802105
- [34] M. Oppermann, B. Bauer, T. Rossi, F. Zinna, J. Helbing, J. Lacour, M. Chergui, Ultrafast broadband circular dichroism in the deep ultraviolet, *Optica* **2019**, *6*, 56-60. doi: 10.1364/OPTICA.6.000056

8. References

- [35] V. W.-W. Yam, V. K.-M. Au, S. Y.-L. Leung, Light-Emitting Self-Assembled Materials Based on d⁸ and d¹⁰ Transition Metal Complexes, *Chemical Reviews* **2015**, *115*, 7589-7728. doi: 10.1021/acs.chemrev.5b00074
- [36] J. K. McCusker, Fuel from Photons, *Science* **2001**, *293*, 1599. doi: 10.1126/science.1064112
- [37] A. T. Yeh, C. V. Shank, J. K. McCusker, Ultrafast Electron Localization Dynamics Following Photo-Induced Charge Transfer, *Science* **2000**, *289*, 935. doi: 10.1126/science.289.5481.935
- [38] J. K. McCusker, Electronic structure in the transition metal block and its implications for light harvesting, *Science* **2019**, *363*, 484. doi: 10.1126/science.aav9104
- [39] K. Sharma, V. Sharma, S. S. Sharma, Dye-Sensitized Solar Cells: Fundamentals and Current Status, *Nanoscale Research Letters* **2018**, *13*, 381. doi: 10.1186/s11671-018-2760-6
- [40] M. Wallesch, D. Volz, D. M. Zink, U. Schepers, M. Nieger, T. Baumann, S. Bräse, Bright Coppertunities: Multinuclear Cu^I Complexes with N-P Ligands and Their Applications, *Chemistry – A European Journal* **2014**, *20*, 6578-6590. doi: 10.1002/chem.201402060
- [41] R. C. Evans, P. Douglas, C. J. Winscom, Coordination complexes exhibiting room-temperature phosphorescence: Evaluation of their suitability as triplet emitters in organic light emitting diodes, *Coordination Chemistry Reviews* **2006**, *250*, 2093-2126. doi: 10.1016/j.ccr.2006.02.007
- [42] J. M. Busch, D. M. Zink, P. Di Martino-Fumo, F. R. Rehak, P. Boden, S. Steiger, O. Fuhr, M. Nieger, W. Klopfer, M. Gerhards, S. Bräse, Highly soluble fluorine containing Cu(I) AlkylPyrPhos TADF complexes, *Dalton Transactions* **2019**, *48*, 15687-15698. doi: 10.1039/C9DT02447F
- [43] M. C.-L. Yeung, V. W.-W. Yam, Luminescent cation sensors: from host-guest chemistry, supramolecular chemistry to reaction-based mechanisms, *Chemical Society Reviews* **2015**, *44*, 4192-4202. doi: 10.1039/C4CS00391H
- [44] X. He, E. C.-C. Cheng, N. Zhu, V. W.-W. Yam, Selective ion probe for Mg²⁺ based on Au(I)···Au(I) interactions in a tripodal alkynylgold(I) complex with oligoether pendants, *Chemical Communications* **2009**, 4016-4018. doi: 10.1039/B902690H
- [45] V. Wing-Wah Yam, K. Kam-Wing Lo, Luminescent polynuclear d¹⁰ metal complexes, *Chemical Society Reviews* **1999**, *28*, 323-334. doi: 10.1039/A804249G

- [46] S. Durot, V. Heitz, A. Sour, J.-P. Sauvage, in *Molecular Machines and Motors: Recent Advances and Perspectives* (Eds.: A. Credi, S. Silvi, M. Venturi), Springer International Publishing, Cham, **2014**, pp. 35-70.
- [47] J. F. Stoddart, Molecular Machines, *Accounts of Chemical Research* **2001**, *34*, 410-411. doi: 10.1021/ar010084w
- [48] B. L. Feringa, In Control of Motion: From Molecular Switches to Molecular Motors, *Accounts of Chemical Research* **2001**, *34*, 504-513. doi: 10.1021/ar0001721
- [49] V. Balzani, A. Credi, F. M. Raymo, J. F. Stoddart, Artificial Molecular Machines, *Angewandte Chemie International Edition* **2000**, *39*, 3348-3391. doi: 10.1002/1521-3773(20001002)39:19<3348::AID-ANIE3348>3.0.CO;2-X
- [50] K. H. Leung, D. L. Phillips, C.-M. Che, V. M. Miskowski, Resonance Raman intensity analysis investigation of metal-metal bonded transitions: an examination of the ${}^1A_{2u} \leftarrow {}^1A_{1g}$ ($5d\sigma^* \rightarrow 6p\sigma$) transition of $Pt_2(P_2O_5H_2)_4^{4+}$, *Journal of Raman Spectroscopy* **1999**, *30*, 987-993. doi: 10.1002/(sici)1097-4555(199911)30:11<987::Aid-jrs471>3.0.Co;2-3
- [51] R. Monni, G. Capano, G. Auböck, H. B. Gray, A. Vlček, I. Tavernelli, M. Chergui, Vibrational coherence transfer in the ultrafast intersystem crossing of a diplatinum complex in solution, *Proceedings of the National Academy of Sciences* **2018**, *115*, E6396. doi: 10.1073/pnas.1719899115
- [52] P. Kim, M. S. Kelley, A. Chakraborty, N. L. Wong, R. P. Van Duyne, G. C. Schatz, F. N. Castellano, L. X. Chen, Coherent Vibrational Wavepacket Dynamics in Platinum(II) Dimers and Their Implications, *The Journal of Physical Chemistry C* **2018**, *122*, 14195-14204. doi: 10.1021/acs.jpcc.8b01636
- [53] M. Pižl, B. M. Hunter, G. M. Greetham, M. Towrie, S. Záliš, H. B. Gray, A. Vlček, Ultrafast Wiggling and Jiggling: $Ir_2(1,8\text{-diisocyanomenthane})_4^{2+}$, *The Journal of Physical Chemistry A* **2017**, *121*, 9275-9283. doi: 10.1021/acs.jpca.7b10215
- [54] M. Iwamura, R. Wakabayashi, J. Maeba, K. Nozaki, S. Takeuchi, T. Tahara, Coherent vibration and ultrafast dynamics upon bond formation in excited dimers of an Au(I) complex, *Physical Chemistry Chemical Physics* **2016**, *18*, 5103-5107. doi: 10.1039/C5CP06651D
- [55] M. Iwamura, K. Nozaki, S. Takeuchi, T. Tahara, Real-Time Observation of Tight Au-Au Bond Formation and Relevant Coherent Motion upon Photoexcitation of $[Au(CN)_2^-]$ Oligomers, *Journal of the American Chemical Society* **2013**, *135*, 538-541. doi: 10.1021/ja310004z
- [56] C. Ma, C. T.-L. Chan, W.-P. To, W.-M. Kwok, C.-M. Che, Deciphering Photoluminescence Dynamics and Reactivity of the Luminescent Metal-Metal-Bonded Excited State of a Binuclear Gold(I) Phosphine Complex

- Containing Open Coordination Sites, *Chemistry – A European Journal* **2015**, *21*, 13888-13893. doi: 10.1002/chem.201503045
- [57] D. L. Phillips, C.-M. Che, K. H. Leung, Z. Mao, M.-C. Tse, A comparative study on metal–metal interaction in binuclear two- and three-coordinated d^{10} -metal complexes: Spectroscopic investigation of M(I)–M(I) interaction in the $^1[\text{d}\sigma^*\text{p}\sigma]$ excited state of $[\text{M}_2(\text{dcpm})_2]^{2+}$ (dcpm=bis(dicyclohexylphosphino)methane) (M=Au, Ag, Cu) and $[\text{M}_2(\text{dmpm})_3]^{2+}$ (dmpm=bis(dimethylphosphino)methane) (M=Au, Ag, Cu) complexes, *Coordination Chemistry Reviews* **2005**, *249*, 1476-1490. doi: 10.1016/j.ccr.2004.09.015
- [58] S. T. Liddle, *Molecular Metal-Metal Bonds, chapter "Group 11 Metal–Metal Bonds"*, Wiley-VCH Verlag GmbH & Co. KGaA, **2015**.
- [59] Q.-J. Pan, H.-X. Zhang, H.-G. Fu, H.-T. Yu, Theoretical Studies on Metal–Metal Interaction and Intrinsic $^1,3[\sigma^*(\text{d})\sigma(\text{s/p})]$ Excited States of Dinuclear d^{10} Complexes with Bridging Phosphane Ligands, *European Journal of Inorganic Chemistry* **2006**, *2006*, 1050-1059. doi: 10.1002/ejic.200500729
- [60] S. A. Clodfelter, T. M. Doede, B. A. Brennan, J. K. Nagle, D. P. Bender, W. A. Turner, P. M. LaPunzina, Luminescent metal-metal-bonded exciplexes involving tetrakis(μ -diphosphito)diplatinate(II) and thallium(I), *Journal of the American Chemical Society* **1994**, *116*, 11379-11386. doi: 10.1021/ja00104a018
- [61] T. P. Seifert, N. D. Knoefel, T. J. Feuerstein, K. Reiter, S. Lebedkin, M. T. Gamer, A. C. Boukis, F. Weigend, M. M. Kappes, P. W. Roesky, Size Matters: From Two-Dimensional $\text{Au}^{\text{I}}\text{-Tl}^{\text{I}}$ Metallopolymers to Molecular Complexes by Simple Variation of the Steric Demand, *Chemistry – A European Journal* **2019**, *25*, 3799-3808. doi: 10.1002/chem.201805984
- [62] L. Barrientos, S. Miranda-Rojas, F. Mendizabal, Noncovalent interactions in inorganic supramolecular chemistry based in heavy metals. Quantum chemistry point of view, *International Journal of Quantum Chemistry* **2019**, *119*, e25675. doi: 10.1002/qua.25675
- [63] S. Sculfort, P. Braunstein, Intramolecular $d^{10}\text{-}d^{10}$ interactions in heterometallic clusters of the transition metals, *Chemical Society Reviews* **2011**, *40*, 2741-2760. doi: 10.1039/C0CS00102C
- [64] H. B. Gray, S. Záliš, A. Vlček, Electronic structures and photophysics of $d^8\text{-}d^8$ complexes, *Coordination Chemistry Reviews* **2017**, *345*, 297-317. doi: 10.1016/j.ccr.2017.01.008
- [65] L. Magnko, M. Schweizer, G. Rauhut, M. Schütz, H. Stoll, H.-J. Werner, A comparison of metallophilic attraction in $(\text{X-M-PH}_3)_2$ (M = Cu, Ag, Au; X = H, Cl), *Physical Chemistry Chemical Physics* **2002**, *4*, 1006-1013. doi: 10.1039/B110624D

- [66] M. B. Brands, J. Nitsch, C. F. Guerra, Relevance of Orbital Interactions and Pauli Repulsion in the Metal–Metal Bond of Coinage Metals, *Inorganic Chemistry* **2018**, *57*, 2603-2608. doi: 10.1021/acs.inorgchem.7b02994
- [67] Q. Zheng, S. Borsley, G. S. Nichol, F. Duarte, S. L. Cockroft, The Energetic Significance of Metallophilic Interactions, *Angewandte Chemie International Edition* **2019**, *58*, 12617-12623. doi: 10.1002/anie.201904207
- [68] H. Schmidbaur, A. Schier, Auophilic interactions as a subject of current research: an up-date, *Chemical Society Reviews* **2012**, *41*, 370-412. doi: 10.1039/C1CS15182G
- [69] P. Pyykkö, Strong Closed-Shell Interactions in Inorganic Chemistry, *Chemical Reviews* **1997**, *97*, 597-636. doi: 10.1021/cr940396v
- [70] H. Schmidbaur, A. Schier, A briefing on auophilicity, *Chemical Society Reviews* **2008**, *37*, 1931-1951. doi: 10.1039/B708845K
- [71] N. V. S. Harisomayajula, S. Makovetskyi, Y.-C. Tsai, Cuprophilic Interactions in and between Molecular Entities, *Chemistry – A European Journal* **2019**, *25*, 8936-8954. doi: 10.1002/chem.201900332
- [72] H. Schmidbaur, A. Schier, Argentophilic Interactions, *Angewandte Chemie International Edition* **2015**, *54*, 746-784. doi: 10.1002/anie.201405936
- [73] H. Schmidbaur, The auophilicity phenomenon: A decade of experimental findings, theoretical concepts and emerging applications, *Gold Bulletin* **2000**, *33*, 3-10. doi: 10.1007/bf03215477
- [74] P. Pyykkö, Theoretical chemistry of gold. III, *Chemical Society Reviews* **2008**, *37*, 1967-1997. doi: 10.1039/B708613J
- [75] E. Andris, P. C. Andrikopoulos, J. Schulz, J. Turek, A. Růžička, J. Roithová, L. Rulíšek, Auophilic Interactions in [(L)AuCl]...[(L')AuCl] Dimers: Calibration by Experiment and Theory, *Journal of the American Chemical Society* **2018**, *140*, 2316-2325. doi: 10.1021/jacs.7b12509
- [76] N. V. S. Harisomayajula, B.-H. Wu, D.-Y. Lu, T.-S. Kuo, I.-C. Chen, Y.-C. Tsai, Ligand-Unsupported Cuprophilicity in the Preparation of Dodecacopper(I) Complexes and Raman Studies, *Angewandte Chemie International Edition* **2018**, *57*, 9925-9929. doi: 10.1002/anie.201801955
- [77] J.-H. Jia, Q.-M. Wang, Intensely Luminescent Gold(I)–Silver(I) Cluster with Hypercoordinated Carbon, *Journal of the American Chemical Society* **2009**, *131*, 16634-16635. doi: 10.1021/ja906695h
- [78] Z. Lei, Q.-M. Wang, Homo and heterometallic gold(I) clusters with hypercoordinated carbon, *Coordination Chemistry Reviews* **2019**, *378*, 382-394. doi: 10.1016/j.ccr.2017.11.001

8. References

- [79] F. Scherbaum, A. Grohmann, B. Huber, C. Krüger, H. Schmidbaur, "Aurophilicity" as a Consequence of Relativistic Effects: The Hexakis(triphenylphosphaneaurio)methane Dication $[(\text{Ph}_3\text{PAu})_6\text{C}]^{2+}$, *Angewandte Chemie International Edition in English* **1988**, 27, 1544-1546. doi: 10.1002/anie.198815441
- [80] O. Hietsoi, A. S. Filatov, C. Dubceac, M. A. Petrukhina, Structural diversity and photoluminescence of copper(I) carboxylates: From discrete complexes to infinite metal-based wires and helices, *Coordination Chemistry Reviews* **2015**, 295, 125-138. doi: 10.1016/j.ccr.2015.03.009
- [81] M. T. Dau, J. R. Shakirova, A. J. Karttunen, E. V. Grachova, S. P. Tunik, A. S. Melnikov, T. A. Pakkanen, I. O. Koshevoy, Coinage Metal Complexes Supported by the Tri- and Tetrakisphosphine Ligands, *Inorganic Chemistry* **2014**, 53, 4705-4715. doi: 10.1021/ic500402m
- [82] A. J. Blake, R. Donamaría, V. Lippolis, J. M. López-de-Luzuriaga, M. Monge, M. E. Olmos, A. Seal, J. A. Weinstein, Unequivocal Experimental Evidence of the Relationship between Emission Energies and Aurophilic Interactions, *Inorganic Chemistry* **2019**, 58, 4954-4961. doi: 10.1021/acs.inorgchem.8b03621
- [83] Z.-F. Li, X.-P. Yang, H.-X. Li, G.-F. Zuo, Phosphorescent Modulation of Metallophilic Clusters and Recognition of Solvents through a Flexible Host-Guest Assembly: A Theoretical Investigation, *Nanomaterials* **2018**, 8, 685. doi: 10.3390/nano8090685
- [84] G. S. M. Tong, S. C. F. Kui, H.-Y. Chao, N. Zhu, C.-M. Che, The $^3[\text{nd}\sigma^*(\text{n}+1)\text{p}\sigma]$ Emissions of Linear Silver(I) and Gold(I) Chains with Bridging Phosphine Ligands, *Chemistry – A European Journal* **2009**, 15, 10777-10789. doi: 10.1002/chem.200901757
- [85] R. Donamaría, V. Lippolis, J. M. López-de-Luzuriaga, M. Monge, M. Nieddu, M. E. Olmos, Influence of the Number of Metallophilic Interactions and Structures on the Optical Properties of Heterometallic Au/Ag Complexes with Mixed-Donor Macrocyclic Ligands, *Inorganic Chemistry* **2018**, 57, 11099-11112. doi: 10.1021/acs.inorgchem.8b01687
- [86] W.-F. Fu, K.-C. Chan, K.-K. Cheung, C.-M. Che, Substrate-Binding Reactions of the $^3[\text{d}\sigma^*\text{p}\sigma]$ Excited State of Binuclear Gold(I) Complexes with Bridging Bis(dicyclohexylphosphino)methane Ligands: Emission and Time-Resolved Absorption Spectroscopic Studies, *Chemistry – A European Journal* **2001**, 7, 4656-4664. doi: 10.1002/1521-3765(20011105)7:21<4656::AID-CHEM4656>3.0.CO;2-D
- [87] C.-M. Che, S.-W. Lai, Structural and spectroscopic evidence for weak metal-metal interactions and metal-substrate exciplex formations in d^{10} metal

- complexes, *Coordination Chemistry Reviews* **2005**, *249*, 1296-1309. doi: 10.1016/j.ccr.2004.11.026
- [88] M. Jansen, Homoatomic d^{10} - d^{10} Interactions: Their Effects on Structure and Chemical and Physical Properties, *Angewandte Chemie International Edition in English* **1987**, *26*, 1098-1110. doi: 10.1002/anie.198710981
- [89] C. Kiefer, S. Bestgen, M. T. Gamer, M. Kühn, S. Lebedkin, F. Weigend, M. M. Kappes, P. W. Roesky, Coinage Metal Complexes of Bis-Alkynyl-Functionalized N-Heterocyclic Carbenes: Reactivity, Photophysical Properties, and Quantum Chemical Investigations, *Chemistry – A European Journal* **2017**, *23*, 1591-1603. doi: 10.1002/chem.201604292
- [90] V. W.-W. Yam, K. M.-C. Wong, Luminescent metal complexes of d^6 , d^8 and d^{10} transition metal centres, *Chemical Communications* **2011**, *47*, 11579-11592. doi: 10.1039/C1CC13767K
- [91] X.-F. Jiang, F. K.-W. Hau, Q.-F. Sun, S.-Y. Yu, V. W.-W. Yam, From $\{Au^I \cdots Au^I\}$ -Coupled Cages to the Cage-Built 2-D $\{Au^I \cdots Au^I\}$ Arrays: $Au^I \cdots Au^I$ Bonding Interaction Driven Self-Assembly and Their Ag^I Sensing and Photo-Switchable Behavior, *Journal of the American Chemical Society* **2014**, *136*, 10921-10929. doi: 10.1021/ja502295c
- [92] X.-W. Lei, F.-X. Zhou, M.-F. Wang, H.-P. Zhang, C.-Y. Yue, M.-C. Hong, Synthesis, crystal structure and characterization of new tetranuclear $Ag(I)$ complex with 5-aminoisophthalate, *Inorganic Chemistry Communications* **2013**, *27*, 171-174. doi: 10.1016/j.inoche.2012.11.001
- [93] C. Bizzarri, E. Spuling, D. M. Knoll, D. Volz, S. Bräse, Sustainable metal complexes for organic light-emitting diodes (OLEDs), *Coordination Chemistry Reviews* **2018**, *373*, 49-82. doi: 10.1016/j.ccr.2017.09.011
- [94] A. Bondi, van der Waals Volumes and Radii, *The Journal of Physical Chemistry* **1964**, *68*, 441-451. doi: 10.1021/j100785a001
- [95] S. S. Batsanov, Van der Waals Radii of Elements, *Inorganic Materials* **2001**, *37*, 871-885. doi: 10.1023/a:1011625728803
- [96] S. Alvarez, A cartography of the van der Waals territories, *Dalton Transactions* **2013**, *42*, 8617-8636. doi: 10.1039/C3DT50599E
- [97] S. S. Batsanov, Thermodynamic determination of van der Waals radii of metals, *Journal of Molecular Structure* **2011**, *990*, 63-66. doi: 10.1016/j.molstruc.2010.12.055
- [98] A. Bayler, A. Schier, G. A. Bowmaker, H. Schmidbaur, Gold Is Smaller than Silver. Crystal Structures of $[Bis(trimesitylphosphine)gold(I)]$ and $[Bis(trimesitylphosphine)silver(I)]$ Tetrafluoroborate, *Journal of the American Chemical Society* **1996**, *118*, 7006-7007. doi: 10.1021/ja961363v

8. References

- [99] Z. Tu, A. Chen, C. Xia, Z. Li, M. Yang, C. Wang, W. Wang, Theoretical investigation of the spectroscopic constants for the ground-state diatomic species Cu₂, Ag₂, and Au₂, *Computational and Theoretical Chemistry* **2017**, *1112*, 88-93. doi: 10.1016/j.comptc.2017.04.016
- [100] E. A. Rohlfing, J. J. Valentini, UV laser excited fluorescence spectroscopy of the jet-cooled copper dimer, *The Journal of Chemical Physics* **1986**, *84*, 6560-6566. doi: 10.1063/1.450708
- [101] B. Simard, P. A. Hackett, A. M. James, P. R. R. Langridge-Smith, The bond length of silver dimer, *Chemical Physics Letters* **1991**, *186*, 415-422. doi: 10.1016/0009-2614(91)90201-J
- [102] C. Latouche, Y.-R. Lin, Y. Tobon, E. Furet, J.-Y. Saillard, C.-W. Liu, A. Boucekkine, Au–Au chemical bonding induced by UV irradiation of dinuclear gold(I) complexes: a computational study with experimental evidence, *Physical Chemistry Chemical Physics* **2014**, *16*, 25840-25845. doi: 10.1039/C4CP03990D
- [103] P. D. Harvey, Reparameterized Herschbach-Laurie empirical relationships between metal-metal distances and force constants applied to homonuclear bi- and polynuclear complexes (M = Cr, Mo, Rh, Pd, Ag, W, Re, Ir, Pt, Au, Hg), *Coordination Chemistry Reviews* **1996**, *153*, 175-198. doi: 10.1016/0010-8545(95)01225-7
- [104] M. A. Omary, T. R. Webb, Z. Assefa, G. E. Shankle, H. H. Patterson, Crystal Structure, Electronic Structure, and Temperature-Dependent Raman Spectra of Tl[Ag(CN)₂]: Evidence for Ligand-Unsupported Argentophilic Interactions, *Inorganic Chemistry* **1998**, *37*, 1380-1386. doi: 10.1021/ic970694l
- [105] S. J. Grabowski, What Is the Covalency of Hydrogen Bonding?, *Chemical Reviews* **2011**, *111*, 2597-2625. doi: 10.1021/cr800346f
- [106] J.-C. Jiang, Y.-S. Wang, H.-C. Chang, S. H. Lin, Y. T. Lee, G. Niedner-Schatteburg, H.-C. Chang, Infrared Spectra of H⁺(H₂O)₅₋₈ Clusters: Evidence for Symmetric Proton Hydration, *Journal of the American Chemical Society* **2000**, *122*, 1398-1410. doi: 10.1021/ja990033i
- [107] G. Niedner-Schatteburg, V. E. Bondybey, FT-ICR Studies of Solvation Effects in Ionic Water Cluster Reactions, *Chemical Reviews* **2000**, *100*, 4059-4086. doi: 10.1021/cr990065o
- [108] M. A. Omary, M. A. Rawashdeh-Omary, M. W. A. Gonser, O. Elbjeirami, T. Grimes, T. R. Cundari, H. V. K. Diyabalanage, C. S. P. Gamage, H. V. R. Dias, Metal Effect on the Supramolecular Structure, Photophysics, and Acid–Base Character of Trinuclear Pyrazolato Coinage Metal Complexes, *Inorganic Chemistry* **2005**, *44*, 8200-8210. doi: 10.1021/ic0508730

- [109] C. J. Humphreys, Electrons seen in orbit, *Nature* **1999**, *401*, 21-22. doi: 10.1038/43323
- [110] J. M. Zuo, M. Kim, M. O'Keeffe, J. C. H. Spence, Direct observation of d-orbital holes and Cu–Cu bonding in Cu₂O, *Nature* **1999**, *401*, 49-52. doi: 10.1038/43403
- [111] J. P. Wagner, P. R. Schreiner, London Dispersion in Molecular Chemistry—Reconsidering Steric Effects, *Angewandte Chemie International Edition* **2015**, *54*, 12274-12296. doi: 10.1002/anie.201503476
- [112] P. Pyykkö, Relativity, Gold, Closed-Shell Interactions, and CsAu·NH₃, *Angewandte Chemie International Edition* **2002**, *41*, 3573-3578. doi: 10.1002/1521-3773(20021004)41:19<3573::Aid-anie3573>3.0.Co;2-r
- [113] G. Cui, X.-Y. Cao, W.-H. Fang, M. Dolg, W. Thiel, Photoinduced Gold(I)–Gold(I) Chemical Bonding in Dicyanoaurate Oligomers, *Angewandte Chemie International Edition* **2013**, *52*, 10281-10285. doi: 10.1002/anie.201305487
- [114] A. C. Durrell, G. E. Keller, Y.-C. Lam, J. Sýkora, A. Vlček, H. B. Gray, Structural Control of ¹A_{2u}-to-³A_{2u} Intersystem Crossing in Diplatinum(II,II) Complexes, *Journal of the American Chemical Society* **2012**, *134*, 14201-14207. doi: 10.1021/ja305666b
- [115] M. Christensen, K. Haldrup, K. Bechgaard, R. Feidenhans'l, Q. Kong, M. Cammarata, M. L. Russo, M. Wulff, N. Harrit, M. M. Nielsen, Time-Resolved X-ray Scattering of an Electronically Excited State in Solution. Structure of the ³A_{2u} State of Tetrakis-μ-pyrophosphitodiplatinate(II), *Journal of the American Chemical Society* **2009**, *131*, 502-508. doi: 10.1021/ja804485d
- [116] T. Hofbeck, Y. C. Lam, M. Kalbáč, S. Záliš, A. Vlček, H. Yersin, Thermally Tunable Dual Emission of the d⁸-d⁸ Dimer [Pt₂(μ-P₂O₅(BF₂)₂)₄]⁴⁻, *Inorganic Chemistry* **2016**, *55*, 2441-2449. doi: 10.1021/acs.inorgchem.5b02839
- [117] P. Coppens, O. Gerlits, I. I. Vorontsov, A. Y. Kovalevsky, Y.-S. Chen, T. Graber, M. Gembicky, I. V. Novozhilova, A very large Rh–Rh bond shortening on excitation of the [Rh₂(1,8-diisocyno-p-menthane)₄]²⁺ ion by time-resolved synchrotron X-ray diffraction, *Chemical Communications* **2004**, 2144-2145. doi: 10.1039/B409463H
- [118] K. Haldrup, T. Harlang, M. Christensen, A. Dohn, T. B. van Driel, K. S. Kjær, N. Harrit, J. Vibenholt, L. Guerin, M. Wulff, M. M. Nielsen, Bond Shortening (1.4 Å) in the Singlet and Triplet Excited States of [Ir₂(dimen)₄]²⁺ in Solution Determined by Time-Resolved X-ray Scattering, *Inorganic Chemistry* **2011**, *50*, 9329-9336. doi: 10.1021/ic2006875
- [119] B. M. Hunter, R. M. Villahermosa, C. L. Exstrom, M. G. Hill, K. R. Mann, H. B. Gray, M–M Bond-Stretching Energy Landscapes for M₂(dimen)₄²⁺ (M = Rh, Ir;

8. References

- dimen = 1,8-Diisocyanomenthane) Complexes, *Inorganic Chemistry* **2012**, *51*, 6898-6905. doi: 10.1021/ic300716q
- [120] T. V. Darnton, B. M. Hunter, M. G. Hill, S. Záliš, A. Vlček, H. B. Gray, Reduced and Superreduced Diplatinum Complexes, *Journal of the American Chemical Society* **2016**, *138*, 5699-5705. doi: 10.1021/jacs.6b02559
- [121] S. V. Kruppa, C. Groß, X. Gui, F. Bäppler, B. Kwasigroch, Y. Sun, R. Diller, W. Klopper, G. Niedner-Schatteburg, C. Riehn, W. R. Thiel, Photoinitiated Charge Transfer in a Triangular Silver(I) Hydride Complex and Its Oxophilicity, *Chemistry – A European Journal* **2019**, *25*, 11269-11284. doi: 10.1002/chem.201901981
- [122] I. V. Novozhilova, A. V. Volkov, P. Coppens, Theoretical Analysis of the Triplet Excited State of the $[\text{Pt}_2(\text{H}_2\text{P}_2\text{O}_5)_4]^{4-}$ Ion and Comparison with Time-Resolved X-ray and Spectroscopic Results, *Journal of the American Chemical Society* **2003**, *125*, 1079-1087. doi: 10.1021/ja027857b
- [123] S. V. Kruppa, F. Bäppler, C. Holzer, W. Klopper, R. Diller, C. Riehn, Vibrational Coherence Controls Molecular Fragmentation: Ultrafast Photodynamics of the $[\text{Ag}_2\text{Cl}]^+$ Scaffold, *The Journal of Physical Chemistry Letters* **2018**, *9*, 804-810. doi: 10.1021/acs.jpcllett.7b03167
- [124] Bruker training document „amaZon series_compass1.7_intro to ion trap MS“
- [125] Cooperative Effects in Homo- and Heterometallic Complexes (SFB/TRR 88, "3MET"), <https://www.uni-kl.de/3met>, access date 14.02.2020
- [126] J. Chmela, M. E. Harding, D. Matioszek, C. E. Anson, F. Breher, W. Klopper, Differential Many-Body Cooperativity in Electronic Spectra of Oligonuclear Transition-Metal Complexes, *ChemPhysChem* **2016**, *17*, 37-45. doi: 10.1002/cphc.201500626
- [127] G. Niedner-Schatteburg, in *Clusters – Contemporary Insight in Structure and Bonding* (Ed.: S. Dehnen), Springer International Publishing, Cham, **2017**, pp. 1-40.
- [128] R. A. J. O’Hair, N. J. Rijs, Gas Phase Studies of the Pesci Decarboxylation Reaction: Synthesis, Structure, and Unimolecular and Bimolecular Reactivity of Organometallic Ions, *Accounts of Chemical Research* **2015**, *48*, 329-340. doi: 10.1021/ar500377u
- [129] J. Roithová, Characterization of reaction intermediates by ion spectroscopy, *Chemical Society Reviews* **2012**, *41*, 547-559. doi: 10.1039/C1CS15133A
- [130] N. M. Riley, J. J. Coon, The Role of Electron Transfer Dissociation in Modern Proteomics, *Analytical Chemistry* **2018**, *90*, 40-64. doi: 10.1021/acs.analchem.7b04810

- [131] M. U. Munshi, S. M. Craig, G. Berden, J. Martens, A. F. DeBlase, D. J. Foreman, S. A. McLuckey, J. Oomens, M. A. Johnson, Preparation of Labile Ni⁺(cyclam) Cations in the Gas Phase Using Electron-Transfer Reduction through Ion–Ion Recombination in an Ion Trap and Structural Characterization with Vibrational Spectroscopy, *The Journal of Physical Chemistry Letters* **2017**, *8*, 5047-5052. doi: 10.1021/acs.jpcllett.7b02223
- [132] M. U. Munshi, J. Martens, G. Berden, J. Oomens, Gas-Phase Infrared Ion Spectroscopy Characterization of Cu(II/I)Cyclam and Cu(II/I)2,2'-Bipyridine Redox Pairs, *The Journal of Physical Chemistry A* **2019**, *123*, 4149-4157. doi: 10.1021/acs.jpca.9b00793
- [133] K. Brendle, M. Kordel, E. Schneider, D. Wagner, S. Bräse, P. Weis, M. M. Kappes, Collision Induced Dissociation of Benzylpyridinium-Substituted Porphyrins: Towards a Thermometer Scale for Multiply Charged Ions?, *Journal of the American Society for Mass Spectrometry* **2018**, *29*, 382-392. doi: 10.1021/jasms.8b05752
- [134] R. E. March, An Introduction to Quadrupole Ion Trap Mass Spectrometry, *Journal of Mass Spectrometry* **1997**, *32*, 351-369. doi: 10.1002/(sici)1096-9888(199704)32:4<351::Aid-jms512>3.0.Co;2-y
- [135] S. A. McLuckey, D. E. Goeringer, SPECIAL FEATURE: TUTORIAL Slow Heating Methods in Tandem Mass Spectrometry, *Journal of Mass Spectrometry* **1997**, *32*, 461-474. doi: 10.1002/(sici)1096-9888(199705)32:5<461::Aid-jms515>3.0.Co;2-h
- [136] A. Colorado, J. Brodbelt, An empirical approach to estimation of critical energies by using a quadrupole ion trap, *Journal of the American Society for Mass Spectrometry* **1996**, *7*, 1116-1125. doi: 10.1016/S1044-0305(96)00077-3
- [137] V. Gabelica, E. D. Pauw, Internal energy and fragmentation of ions produced in electrospray sources, *Mass Spectrometry Reviews* **2005**, *24*, 566-587. doi: 10.1002/mas.20027
- [138] L. Drahos, K. Vékey, MassKinetics: a theoretical model of mass spectra incorporating physical processes, reaction kinetics and mathematical descriptions, *Journal of Mass Spectrometry* **2001**, *36*, 237-263. doi: 10.1002/jms.142
- [139] A. R. Johnson, E. E. Carlson, Collision-Induced Dissociation Mass Spectrometry: A Powerful Tool for Natural Product Structure Elucidation, *Analytical Chemistry* **2015**, *87*, 10668-10678. doi: 10.1021/acs.analchem.5b01543
- [140] J. Mitchell Wells, S. A. McLuckey, in *Methods in Enzymology*, Vol. 402, Academic Press, **2005**, pp. 148-185.

8. References

- [141] L. Sleno, D. A. Volmer, Ion activation methods for tandem mass spectrometry, *Journal of Mass Spectrometry* **2004**, *39*, 1091-1112. doi: 10.1002/jms.703
- [142] F. O. Talbot, T. Tabarin, R. Antoine, M. Broyer, P. Dugourd, Photodissociation spectroscopy of trapped protonated tryptophan, *The Journal of Chemical Physics* **2005**, *122*, 074310. doi: 10.1063/1.1850459
- [143] S. Becher, B. Spengler, S. Heiles, Effects of wavelength, fluence, and dose on fragmentation pathways and photoproduct ion yield in 213 nm and 266 nm ultraviolet photodissociation experiments, *European Journal of Mass Spectrometry* **2018**, *24*, 54-65. doi: 10.1177/1469066717741747
- [144] G. Féraud, C. Dedonder-Lardeux, S. Soorkia, C. Jouvét, Photo-fragmentation spectroscopy of benzylum and 1-phenylethyl cations, *The Journal of Chemical Physics* **2014**, *140*, 024302. doi: 10.1063/1.4858409
- [145] S. Xu, J. E. T. Smith, J. M. Weber, UV Spectra of Tris(2,2'-bipyridine)-M(II) Complex Ions in Vacuo (M = Mn, Fe, Co, Ni, Cu, Zn), *Inorganic Chemistry* **2016**, *55*, 11937-11943. doi: 10.1021/acs.inorgchem.6b02054
- [146] R. Antoine, T. Tabarin, M. Broyer, P. Dugourd, R. Mitrić, V. Bonačić-Koutecký, Optical Properties of Gas-Phase Tryptophan-Silver Cations: Charge Transfer from the Indole Ring to the Silver Atom, *ChemPhysChem* **2006**, *7*, 524-528. doi: 10.1002/cphc.200500495
- [147] S. M. J. Wellman, R. A. Jockusch, Moving in on the Action: An Experimental Comparison of Fluorescence Excitation and Photodissociation Action Spectroscopy, *The Journal of Physical Chemistry A* **2015**, *119*, 6333-6338. doi: 10.1021/acs.jpca.5b04835
- [148] M. W. Forbes, A. M. Nagy, R. A. Jockusch, Photofragmentation of and electron photodetachment from a GFP model chromophore in a quadrupole ion trap, *International Journal of Mass Spectrometry* **2011**, *308*, 155-166. doi: 10.1016/j.ijms.2011.08.016
- [149] P. Jäger, K. Brendle, E. Schneider, S. Kohaut, M. K. Armbruster, K. Fink, P. Weis, M. M. Kappes, Photodissociation of Free Metalloporphyrin Dimer Multianions, *The Journal of Physical Chemistry A* **2018**, *122*, 2974-2982. doi: 10.1021/acs.jpca.8b00641
- [150] E. Matthews, C. E. H. Dessent, Locating the Proton in Nicotinamide Protomers via Low-Resolution UV Action Spectroscopy of Electrosprayed Solutions, *The Journal of Physical Chemistry A* **2016**, *120*, 9209-9216. doi: 10.1021/acs.jpca.6b10433
- [151] C. S. Hansen, B. B. Kirk, S. J. Blanksby, R. A. J. O'Hair, A. J. Trevitt, UV Photodissociation Action Spectroscopy of Haloanilinium Ions in a Linear Quadrupole Ion Trap Mass Spectrometer, *Journal of the American Society for Mass Spectrometry* **2013**, *24*, 932-940. doi: 10.1021/jasms.8b04544

- [152] D. Imanbaew, J. Lang, M. F. Gelin, S. Kaufhold, M. G. Pfeffer, S. Rau, C. Riehn, Pump-Probe Fragmentation Action Spectroscopy: A Powerful Tool to Unravel Light-Induced Processes in Molecular Photocatalysts, *Angewandte Chemie International Edition* **2017**, *56*, 5471-5474. doi: 10.1002/anie.201612302
- [153] G. Grégoire, H. Kang, C. Dedonder-Lardeux, C. Juvet, C. Desfrancois, D. Onidas, V. Lepere, J. A. Fayeton, Statistical vs. non-statistical deactivation pathways in the UV photo-fragmentation of protonated tryptophan-leucine dipeptide, *Physical Chemistry Chemical Physics* **2006**, *8*, 122-128. doi: 10.1039/B510406H
- [154] H. Kang, C. Juvet, C. Dedonder-Lardeux, S. Martrenchard, G. Grégoire, C. Desfrancois, J. P. Schermann, M. Barat, J. A. Fayeton, Ultrafast deactivation mechanisms of protonated aromatic amino acids following UV excitation, *Physical Chemistry Chemical Physics* **2005**, *7*, 394-398. doi: 10.1039/B414986F
- [155] H. Kang, C. Dedonder-Lardeux, C. Juvet, G. Grégoire, C. Desfrancois, J. P. Schermann, M. Barat, A. Fayeton, Control of Bond-Cleaving Reactions of Free Protonated Tryptophan Ion by Femtosecond Laser Pulses, *The Journal of Physical Chemistry A* **2005**, *109*, 2417-2420. doi: 10.1021/jp0407167
- [156] D. Nolting, R. Weinkauff, I. V. Hertel, T. Schultz, Excited-State Relaxation of Protonated Adenine, *ChemPhysChem* **2007**, *8*, 751-755. doi: 10.1002/cphc.200600727
- [157] D. Nolting, T. Schultz, I. V. Hertel, R. Weinkauff, Excited state dynamics and fragmentation channels of the protonated dipeptide H₂N-Leu-Trp-COOH, *Physical Chemistry Chemical Physics* **2006**, *8*, 5247-5254. doi: 10.1039/B609726J
- [158] H. Kang, C. Juvet, C. Dedonder-Lardeux, S. Martrenchard, C. Charrière, G. Grégoire, C. Desfrancois, J. P. Schermann, M. Barat, J. A. Fayeton, Photoinduced processes in protonated tryptamine, *The Journal of Chemical Physics* **2005**, *122*, 084307. doi: 10.1063/1.1851503
- [159] G. Grégoire, B. Lucas, M. Barat, J. A. Fayeton, C. Dedonder-Lardeux, C. Juvet, UV photoinduced dynamics in protonated aromatic amino acid, *The European Physical Journal D* **2009**, *51*, 109-116. doi: 10.1140/epjd/e2008-00085-3
- [160] D. Imanbaew, Y. Nosenko, C. Kerner, K. Chevalier, F. Rupp, C. Riehn, W. R. Thiel, R. Diller, Excited-state dynamics of a ruthenium(II) catalyst studied by transient photofragmentation in gas phase and transient absorption in solution, *Chemical Physics* **2014**, *442*, 53-61. doi: 10.1016/j.chemphys.2014.03.005

8. References

- [161] A. Svendsen, H. V. Kiefer, H. B. Pedersen, A. V. Bochenkova, L. H. Andersen, Origin of the Intrinsic Fluorescence of the Green Fluorescent Protein, *Journal of the American Chemical Society* **2017**, *139*, 8766-8771. doi: 10.1021/jacs.7b04987
- [162] Free Electron Lasers for Infrared eXperiments (FELIX) - Laboratory, <https://www.ru.nl/felix/>, access date 14.02.2020
- [163] J. Martens, G. Berden, C. R. Gebhardt, J. Oomens, Infrared ion spectroscopy in a modified quadrupole ion trap mass spectrometer at the FELIX free electron laser laboratory, *Review of Scientific Instruments* **2016**, *87*, 103108. doi: 10.1063/1.4964703
- [164] S. V. Kruppa, F. Bappler, W. Klopper, S. P. Walg, W. R. Thiel, R. Diller, C. Riehn, Ultrafast excited-state relaxation of a binuclear Ag(I) phosphine complex in gas phase and solution, *Physical Chemistry Chemical Physics* **2017**, *19*, 22785-22800. doi: 10.1039/C7CP04128D
- [165] J.-F. Greisch, A. Ballester-Caudet, S. V. Kruppa, Z. Lei, Q.-M. Wang, C. Riehn, F. Remacle, Gas-Phase Photoluminescence and Photodissociation of Silver-Capped Hexagold Clusters, *The Journal of Physical Chemistry A* **2018**, *122*, 5799-5810. doi: 10.1021/acs.jpca.8b01864
- [166] S. V. Kruppa, Y. Nosenko, M.-O. Winghart, S. P. Walg, M. M. Kappes, C. Riehn, Fragmentation pathways of dianionic $[\text{Pt}_2(\mu\text{-P}_2\text{O}_5\text{H}_2)_4+\text{X,Y}]^{2-}$ (X,Y=H, K, Ag) species in an ion trap induced by collisions and UV photoexcitation, *International Journal of Mass Spectrometry* **2016**, *395*, 7-19. doi: 10.1016/j.ijms.2015.11.007
- [167] S. V. Kruppa, F. Bappler, Y. Nosenko, S. P. Walg, R. Diller, C. Riehn, in *International Conference on Ultrafast Phenomena*, Optical Society of America, Santa Fe, New Mexico, **2016**, p. UW4A.33.
- [168] S. V. Kruppa, F. Bappler, C. Holzer, F. Dietrich, R. Diller, W. Klopper, C. Riehn, Excited state vibrational coherence in a binuclear metal adduct: wave packet phase dependant molecular fragmentation under variation of ligand size, *EPJ Web Conf.* **2019**, *205*, 09019. doi: 10.1051/epjconf/201920509019
- [169] M. Chen, Z. Lei, W. Feng, C. Li, Q.-M. Wang, F. Li, A phosphorescent silver(I)-gold (I) cluster complex that specifically lights up the nucleolus of living cells with FLIM imaging, *Biomaterials* **2013**, *34*, 4284-4295. doi: 10.1016/j.biomaterials.2013.02.032
- [170] C.-M. Che, M.-C. Tse, M. C. W. Chan, K.-K. Cheung, D. L. Phillips, K.-H. Leung, Spectroscopic Evidence for Argentophilicity in Structurally Characterized Luminescent Binuclear Silver(I) Complexes, *Journal of the American Chemical Society* **2000**, *122*, 2464-2468. doi: 10.1021/ja9904890

- [171] A. Zavras, G. N. Khairallah, T. U. Connell, J. M. White, A. J. Edwards, R. J. Mulder, P. S. Donnelly, R. A. J. O'Hair, Synthesis, Structural Characterization, and Gas-Phase Unimolecular Reactivity of the Silver Hydride Nanocluster $[\text{Ag}_3((\text{PPh}_2)_2\text{CH}_2)_3(\mu_3\text{-H})](\text{BF}_4)_2$, *Inorganic Chemistry* **2014**, *53*, 7429-7437. doi: 10.1021/ic5007499
- [172] Z. Mao, J.-S. Huang, C.-M. Che, N. Zhu, S. K.-Y. Leung, Z.-Y. Zhou, Unexpected Reactivities of $\text{Cu}_2(\text{diphosphine})_2$ Complexes in Alcohol: Isolation, X-ray Crystal Structure, and Photoluminescent Properties of a Remarkably Stable $[\text{Cu}_3(\text{diphosphine})_3(\mu_3\text{-H})]^{2+}$ Hydride Complex, *Journal of the American Chemical Society* **2005**, *127*, 4562-4563. doi: 10.1021/ja042335c
- [173] Z. Lei, X.-L. Pei, Z.-J. Guan, Q.-M. Wang, Full Protection of Intensely Luminescent Gold(I)–Silver(I) Cluster by Phosphine Ligands and Inorganic Anions, *Angewandte Chemie International Edition* **2017**, *56*, 7117-7120. doi: 10.1002/anie.201702522
- [174] M. Zhou, Z. Lei, Q. Guo, Q.-M. Wang, A. Xia, Solvent Dependent Excited State Behaviors of Luminescent Gold(I)–Silver(I) Cluster with Hypercoordinated Carbon, *The Journal of Physical Chemistry C* **2015**, *119*, 14980-14988. doi: 10.1021/acs.jpcc.5b03985
- [175] M. van der Linden, A. J. van Bunningen, L. Amidani, M. Bransen, H. Elnaggar, P. Glatzel, A. Meijerink, F. M. F. de Groot, Single Au Atom Doping of Silver Nanoclusters, *ACS Nano* **2018**, *12*, 12751-12760. doi: 10.1021/acsnano.8b07807
- [176] M. Christensen, K. Haldrup, K. S. Kjær, M. Cammarata, M. Wulff, K. Bechgaard, H. Weihe, N. H. Harrit, M. M. Nielsen, Structure of a short-lived excited state trinuclear Ag–Pt–Pt complex in aqueous solution by time resolved X-ray scattering, *Physical Chemistry Chemical Physics* **2010**, *12*, 6921-6923. doi: 10.1039/C002070B
- [177] C. Kaub, S. Lebedkin, A. Li, S. V. Kruppa, P. H. Strebart, M. M. Kappes, C. Riehn, P. W. Roesky, Bimetallic d^{10} -Metal Complexes of a Bipyridine Substituted N-Heterocyclic Carbene, *Chemistry – A European Journal* **2018**, *24*, 6094-6104. doi: 10.1002/chem.201705757
- [178] C. C. Kaub, doctoral thesis, Karlsruher Institut für Technologie (KIT) **2016**.
- [179] K. Egashira, A. Terasaki, Optical absorption spectrum of the chromium dimer cation: Measurements by photon-trap and photodissociation spectroscopy, *Chemical Physics Letters* **2015**, *635*, 13-15. doi: 10.1016/j.cplett.2015.06.038
- [180] T. Baer, R. C. Dunbar, Ion spectroscopy: Where did it come from; where is it now; and where is it going?, *Journal of the American Society for Mass Spectrometry* **2010**, *21*, 681-693. doi: 10.1016/j.jasms.2010.01.028

8. References

- [181] S. K. Stephenson, R. J. Saykally, Velocity Modulation Spectroscopy of Ions, *Chemical Reviews* **2005**, *105*, 3220-3234. doi: 10.1021/cr040100d
- [182] G. Berden, R. Engeln, *Cavity Ring-Down Spectroscopy: Techniques and Applications*, **2010**.
- [183] A. Dang, J. A. Korn, J. Gladden, B. Mozzone, F. Tureček, UV-Vis Photodissociation Action Spectroscopy on Thermo LTQ-XL ETD and Bruker amaZon Ion Trap Mass Spectrometers: a Practical Guide, *Journal of the American Society for Mass Spectrometry* **2019**, *30*, 1558-1564. doi: 10.1021/jasms.8b06078
- [184] R. Schinke, *Photodissociation Dynamics Spectroscopy and Fragmentation of Small Polyatomic Molecules*, **1995**.
- [185] R. Antoine, P. Dugourd, Visible and ultraviolet spectroscopy of gas phase protein ions, *Physical Chemistry Chemical Physics* **2011**, *13*, 16494-16509. doi: 10.1039/C1CP21531K
- [186] N. C. Polfer, Infrared multiple photon dissociation spectroscopy of trapped ions, *Chemical Society Reviews* **2011**, *40*, 2211-2221. doi: 10.1039/C0CS00171F
- [187] J. Oomens, B. G. Sartakov, G. Meijer, G. von Helden, Gas-phase infrared multiple photon dissociation spectroscopy of mass-selected molecular ions, *International Journal of Mass Spectrometry* **2006**, *254*, 1-19. doi: 10.1016/j.ijms.2006.05.009
- [188] H. Sato, Photodissociation of Simple Molecules in the Gas Phase, *Chemical Reviews* **2001**, *101*, 2687-2726. doi: 10.1021/cr990403l
- [189] D. Dieleman, M. Tombers, L. Peters, J. Meyer, S. Peredkov, J. Jalink, M. Neeb, W. Eberhardt, T. Rasing, G. Niedner-Schatteburg, A. Kirilyuk, Orbit and spin resolved magnetic properties of size selected $[\text{Co}_n\text{Rh}]^+$ and $[\text{Co}_n\text{Au}]^+$ nanoalloy clusters, *Physical Chemistry Chemical Physics* **2015**, *17*, 28372-28378. doi: 10.1039/C5CP01923K
- [190] V. Zamudio-Bayer, K. Hirsch, A. Langenberg, A. Ławicki, A. Terasaki, B. von Issendorff, J. T. Lau, Large orbital magnetic moments of small, free cobalt cluster ions Co_n^+ with $n \leq 9$, *Journal of Physics: Condensed Matter* **2018**, *30*, 464002. doi: 10.1088/1361-648x/aae54a
- [191] N. C. Polfer, J. Oomens, Reaction products in mass spectrometry elucidated with infrared spectroscopy, *Physical Chemistry Chemical Physics* **2007**, *9*, 3804-3817. doi: 10.1039/B702993B
- [192] S. Dillinger, J. Mohrbach, J. Hewer, M. Gaffga, G. Niedner-Schatteburg, Infrared spectroscopy of N_2 adsorption on size selected cobalt cluster cations in

- isolation, *Physical Chemistry Chemical Physics* **2015**, *17*, 10358-10362. doi: 10.1039/C5CP00047E
- [193] S. D. Fried, S. G. Boxer, Measuring Electric Fields and Noncovalent Interactions Using the Vibrational Stark Effect, *Accounts of Chemical Research* **2015**, *48*, 998-1006. doi: 10.1021/ar500464j
- [194] S. Xu, J. E. T. Smith, J. M. Weber, Hydration of a Binding Site with Restricted Solvent Access: Solvatochromic Shift of the Electronic Spectrum of a Ruthenium Polypyridine Complex, One Molecule at a Time, *The Journal of Physical Chemistry A* **2016**, *120*, 7650-7658. doi: 10.1021/acs.jpca.6b07668
- [195] L. Giacomozzi, C. Kjær, J. L. Knudsen, L. H. Andersen, S. B. Nielsen, M. H. Stockett, Absorption and luminescence spectroscopy of mass-selected flavin adenine dinucleotide mono-anions, *The Journal of Chemical Physics* **2018**, *148*, 214309. doi: 10.1063/1.5024028
- [196] I. V. Hertel, W. Radloff, Ultrafast dynamics in isolated molecules and molecular clusters, *Reports on Progress in Physics* **2006**, *69*, 1897-2003. doi: 10.1088/0034-4885/69/6/r06
- [197] S. J. Blanksby, G. B. Ellison, Bond Dissociation Energies of Organic Molecules, *Accounts of Chemical Research* **2003**, *36*, 255-263. doi: 10.1021/ar020230d
- [198] J. S. Brodbelt, Photodissociation mass spectrometry: new tools for characterization of biological molecules, *Chemical Society Reviews* **2014**, *43*, 2757-2783. doi: 10.1039/C3CS60444F
- [199] N. Snider, Effect of multiple encounters on vibrational to translational energy transfer, *Canadian Journal of Chemistry* **1994**, *72*, 484-491. doi: 10.1139/v94-070
- [200] J. C. Marcum, J. M. Weber, Electronic photodissociation spectra and decay pathways of gas-phase IrBr_6^{2-} , *The Journal of Chemical Physics* **2009**, *131*, 194309. doi: 10.1063/1.3265956
- [201] R. B. Metz, Photofragment spectroscopy of covalently bound transition metal complexes: a window into C-H and C-C bond activation by transition metal ions, *International Reviews in Physical Chemistry* **2004**, *23*, 79-108. doi: 10.1080/01442350310001654065
- [202] J. C. Lorquet, Landmarks in the theory of mass spectra, *International Journal of Mass Spectrometry* **2000**, *200*, 43-56. doi: 10.1016/S1387-3806(00)00303-1
- [203] J. Bowman, A. Suits, Roaming reactions: The third way, *Physics Today* **2011**, *64*, 33. doi: 10.1063/PT.3.1330

8. References

- [204] N. Herath, A. G. Suits, Roaming Radical Reactions, *The Journal of Physical Chemistry Letters* **2011**, *2*, 642-647. doi: 10.1021/jz101731q
- [205] E. W. G. Diau, J. L. Herek, Z. H. Kim, A. H. Zewail, Femtosecond Activation of Reactions and the Concept of Nonergodic Molecules, *Science* **1998**, *279*, 847. doi: 10.1126/science.279.5352.847
- [206] R. C. Dunbar, Photodissociation of trapped ions, *International Journal of Mass Spectrometry* **2000**, *200*, 571-589. doi: 10.1016/S1387-3806(00)00368-7
- [207] L. Radom, P. M. W. Gill, M. W. Wong, Simple models for describing the fragmentation behavior of multiply charged cations, *International Journal of Quantum Chemistry* **1988**, *34*, 567-573. doi: 10.1002/qua.560340861
- [208] W. E. Boxford, C. E. H. Dessent, Probing the intrinsic features and environmental stabilization of multiply charged anions, *Physical Chemistry Chemical Physics* **2006**, *8*, 5151-5165. doi: 10.1039/B609123G
- [209] E. R. Cohen, B. N. Taylor, The 1986 CODATA Recommended Values of the Fundamental Physical Constants, *Journal of Physical and Chemical Reference Data* **1988**, *17*, 1795-1803. doi: 10.1063/1.555817
- [210] A. Schweizer, J. M. Weber, S. Gilb, H. Schneider, D. Schooss, M. M. Kappes, Electronic photodissociation spectroscopy of $\text{Au}_4^+ \cdot \text{Ar}_n$, $n=0-4$: Experiment and theory, *The Journal of Chemical Physics* **2003**, *119*, 3699-3710. doi: 10.1063/1.1590752
- [211] C. Lifshitz, Kinetic Shifts, *European Journal of Mass Spectrometry* **2002**, *8*, 85-98. doi: 10.1255/ejms.476
- [212] S. M. J. Wellman, R. A. Jockusch, Tuning the Intrinsic Photophysical Properties of Chlorophyll a, *Chemistry – A European Journal* **2017**, *23*, 7728-7736. doi: 10.1002/chem.201605167
- [213] C. S. Byskov, J. M. Weber, S. B. Nielsen, Gas-phase spectroscopy of singly reduced tris(bipyridine)ruthenium ions, $\text{Ru}(\text{bipy})^{3+}$, *Physical Chemistry Chemical Physics* **2015**, *17*, 5561-5564. doi: 10.1039/C4CP05477F
- [214] M. W. Forbes, R. A. Jockusch, Gas-Phase Fluorescence Excitation and Emission Spectroscopy of Three Xanthene Dyes (Rhodamine 575, Rhodamine 590 and Rhodamine 6G) in a Quadrupole Ion Trap Mass Spectrometer, *Journal of the American Society for Mass Spectrometry* **2011**, *22*, 93-109. doi: 10.1021/jasms.8b03880
- [215] Y. Nosenko, C. Riehn, W. Klopper, UV fragmentation and ultrafast dynamics of trinuclear silver/1-methylthymine and silver/1-methyluracil metal-base pairs in an ion trap, *Chemical Physics Letters* **2016**, *659*, 55-60. doi: 10.1016/j.cplett.2016.07.002

- [216] Image: „stop clock“, <https://www.free-powerpoint-templates-design.com/stopwatch-pie-charts-powerpoint-diagram>, access date 25.06.2020
- [217] T. Baer, P. M. Mayer, Statistical Rice-Ramsperger-Kassel-Marcus quasiequilibrium theory calculations in mass spectrometry, *Journal of the American Society for Mass Spectrometry* **1997**, *8*, 103-115. doi: 10.1016/S1044-0305(96)00212-7
- [218] F. Liedy, F. Bäßler, E. Waldt, Y. Nosenko, D. Imanbaew, A. Bhunia, M. Yadav, R. Diller, M. M. Kappes, P. W. Roesky, D. Schooss, C. Riehn, Photodynamics and Luminescence of Mono- and Tri-Nuclear Lanthanide Complexes in the Gas Phase and in Solution, *ChemPhysChem* **2018**, *19*, 3050-3060. doi: 10.1002/cphc.201800599
- [219] I. H. M. van Stokkum, D. S. Larsen, R. van Grondelle, Global and target analysis of time-resolved spectra, *Biochimica et Biophysica Acta (BBA) - Bioenergetics* **2004**, *1657*, 82-104. doi: 10.1016/j.bbabi.2004.04.011
- [220] A. Jeffrey, in *Handbook of Mathematical Formulas and Integrals (Third Edition)* (Ed.: A. Jeffrey), Academic Press, Burlington, **2004**, pp. 239-244.
- [221] J. J. Radler, D. B. Lingerfelt, F. N. Castellano, L. X. Chen, X. Li, Role of Vibrational Dynamics on Excited-State Electronic Coherence in a Binuclear Platinum Complex, *The Journal of Physical Chemistry A* **2018**, *122*, 5071-5077. doi: 10.1021/acs.jpca.8b01352
- [222] M. Simmermacher, N. E. Henriksen, K. B. Møller, A. Moreno Carrascosa, A. Kirrander, Electronic Coherence in Ultrafast X-Ray Scattering from Molecular Wave Packets, *Physical Review Letters* **2019**, *122*, 073003. doi: 10.1103/PhysRevLett.122.073003
- [223] D. Imanbaew, M. F. Gelin, C. Riehn, Rotational and vibrational dynamics in the excited electronic state of deprotonated and protonated fluorescein studied by time-resolved photofragmentation in an ion trap, *Structural Dynamics* **2016**, *3*, 043211. doi: 10.1063/1.4953367
- [224] S. V. Kruppa, diploma thesis, TU Kaiserslautern **2014**.
- [225] D. Imanbaew, doctoral thesis, TU Kaiserslautern **2017**.
- [226] D. M. Good, J. J. Coon, Advancing proteomics with ion/ion chemistry, *BioTechniques* **2006**, *40*, 783-789. doi: 10.2144/000112194
- [227] S. J. Gaskell, Electrospray: Principles and Practice, *Journal of Mass Spectrometry* **1997**, *32*, 677-688. doi: 10.1002/(sici)1096-9888(199707)32:7<677::Aid-jms536>3.0.Co;2-g

8. References

- [228] M. Dole, L. L. Mack, R. L. Hines, R. C. Mobley, L. D. Ferguson, M. B. Alice, Molecular Beams of Macroions, *The Journal of Chemical Physics* **1968**, *49*, 2240-2249. doi: 10.1063/1.1670391
- [229] M. Yamashita, J. B. Fenn, Electrospray ion source. Another variation on the free-jet theme, *The Journal of Physical Chemistry* **1984**, *88*, 4451-4459. doi: 10.1021/j150664a002
- [230] M. Yamashita, J. B. Fenn, Negative ion production with the electrospray ion source, *The Journal of Physical Chemistry* **1984**, *88*, 4671-4675. doi: 10.1021/j150664a046
- [231] C. M. Whitehouse, R. N. Dreyer, M. Yamashita, J. B. Fenn, Electrospray interface for liquid chromatographs and mass spectrometers, *Analytical Chemistry* **1985**, *57*, 675-679. doi: 10.1021/ac00280a023
- [232] J. Fenn, M. Mann, C. Meng, S. Wong, C. Whitehouse, Electrospray ionization for mass spectrometry of large biomolecules, *Science* **1989**, *246*, 64-71. doi: 10.1126/science.2675315
- [233] J. B. Fenn, Electrospray Wings for Molecular Elephants (Nobel Lecture), *Angewandte Chemie International Edition* **2003**, *42*, 3871-3894. doi: 10.1002/anie.200300605
- [234] amaZon series user manual (2009, rev.1) , Bruker Daltonics
- [235] Bruker training document "intro to electrospray ionization"
- [236] L. Konermann, E. Ahadi, A. D. Rodriguez, S. Vahidi, Unraveling the Mechanism of Electrospray Ionization, *Analytical Chemistry* **2013**, *85*, 2-9. doi: 10.1021/ac302789c
- [237] J. H. Gross, *Mass Spectrometry*, Springer International Publishing, **2017**.
- [238] G. I. Taylor, Disintegration of water drops in an electric field, *Proceedings of the Royal Society of London. Series A. Mathematical and Physical Sciences* **1964**, *280*, 383-397. doi: 10.1098/rspa.1964.0151
- [239] M. G. Ikonomidou, A. T. Blades, P. Kebarle, Electrospray-ion spray: a comparison of mechanisms and performance, *Analytical Chemistry* **1991**, *63*, 1989-1998. doi: 10.1021/ac00018a017
- [240] L. Rayleigh, XX. On the equilibrium of liquid conducting masses charged with electricity, *The London, Edinburgh, and Dublin Philosophical Magazine and Journal of Science* **1882**, *14*, 184-186. doi: 10.1080/14786448208628425
- [241] B. A. Thomson, J. V. Iribarne, Field induced ion evaporation from liquid surfaces at atmospheric pressure, *The Journal of Chemical Physics* **1979**, *71*, 4451-4463. doi: 10.1063/1.438198

- [242] J. V. Iribarne, B. A. Thomson, On the evaporation of small ions from charged droplets, *The Journal of Chemical Physics* **1976**, *64*, 2287-2294. doi: 10.1063/1.432536
- [243] A. T. Iavarone, E. R. Williams, Mechanism of Charging and Supercharging Molecules in Electrospray Ionization, *Journal of the American Chemical Society* **2003**, *125*, 2319-2327. doi: 10.1021/ja021202t
- [244] L. Drahos, R. M. A. Heeren, C. Collette, E. De Pauw, K. Vékey, Thermal energy distribution observed in electrospray ionization, *Journal of Mass Spectrometry* **1999**, *34*, 1373-1379. doi: 10.1002/(sici)1096-9888(199912)34:12<1373::Aid-jms907>3.0.Co;2-#
- [245] Z. Takáts, L. Drahos, G. Schlosser, K. Vékey, Feasibility of Formation of Hot Ions in Electrospray, *Analytical Chemistry* **2002**, *74*, 6427-6429. doi: 10.1021/ac020547r
- [246] T. Kim, A. V. Tolmachev, R. Harkewicz, D. C. Prior, G. Anderson, H. R. Udseth, R. D. Smith, T. H. Bailey, S. Rakov, J. H. Futrell, Design and Implementation of a New Electrodynamic Ion Funnel, *Analytical Chemistry* **2000**, *72*, 2247-2255. doi: 10.1021/ac991412x
- [247] S. A. Shaffer, D. C. Prior, G. A. Anderson, H. R. Udseth, R. D. Smith, An Ion Funnel Interface for Improved Ion Focusing and Sensitivity Using Electrospray Ionization Mass Spectrometry, *Analytical Chemistry* **1998**, *70*, 4111-4119. doi: 10.1021/ac9802170
- [248] S. A. Shaffer, K. Tang, G. A. Anderson, D. C. Prior, H. R. Udseth, R. D. Smith, A novel ion funnel for focusing ions at elevated pressure using electrospray ionization mass spectrometry, *Rapid Communications in Mass Spectrometry* **1997**, *11*, 1813-1817. doi: 10.1002/(sici)1097-0231(19971030)11:16<1813::Aid-rcm87>3.0.Co;2-d
- [249] Bruker application Tutorial, ETD and PTR with the amaZon ETD, (2009, rev. 1)
- [250] B. Munson, Development of chemical ionization mass spectrometry, *International Journal of Mass Spectrometry* **2000**, *200*, 243-251. doi: 10.1016/S1387-3806(00)00301-8
- [251] W. J. Richter, H. Schwarz, Chemical Ionization—A Mass-Spectrometric Analytical Procedure of Rapidly Increasing Importance, *Angewandte Chemie International Edition in English* **1978**, *17*, 424-439. doi: 10.1002/anie.197804241
- [252] J. F. J. Todd, Recommendations for nomenclature and symbolism for mass spectroscopy, *International Journal of Mass Spectrometry and Ion Processes* **1995**, *142*, 209-240. doi: 10.1016/0168-1176(95)93811-F

8. References

- [253] V. S. Ong, R. A. Hites, Electron capture mass spectrometry of organic environmental contaminants, *Mass Spectrometry Reviews* **1994**, *13*, 259-283. doi: 10.1002/mas.1280130305
- [254] J. Martens, G. Berden, J. Oomens, Structures of Fluoranthene Reagent Anions Used in Electron Transfer Dissociation and Proton Transfer Reaction Tandem Mass Spectrometry, *Analytical Chemistry* **2016**, *88*, 6126-6129. doi: 10.1021/acs.analchem.6b01483
- [255] M.-S. Kim, A. Pandey, Electron transfer dissociation mass spectrometry in proteomics, *PROTEOMICS* **2012**, *12*, 530-542. doi: 10.1002/pmic.201100517
- [256] K. O. Zhurov, L. Fornelli, M. D. Wodrich, Ü. A. Laskay, Y. O. Tsybin, Principles of electron capture and transfer dissociation mass spectrometry applied to peptide and protein structure analysis, *Chemical Society Reviews* **2013**, *42*, 5014-5030. doi: 10.1039/C3CS35477F
- [257] B. Paizs, M. Van Stipdonk, Focus issue on peptide fragmentation, *Journal of the American Society for Mass Spectrometry* **2008**, *19*, 1717-1718. doi: 10.1016/j.jasms.2008.10.009
- [258] R. Hartmer, D. A. Kaplan, C. R. Gebhardt, T. Ledertheil, A. Brekenfeld, Multiple ion/ion reactions in the 3D ion trap: Selective reagent anion production for ETD and PTR from a single compound, *International Journal of Mass Spectrometry* **2008**, *276*, 82-90. doi: 10.1016/j.ijms.2008.05.002
- [259] J. Berkowitz, J. P. Greene, H. Cho, B. Ruscić, The ionization potentials of CH₄ and CD₄, *The Journal of Chemical Physics* **1987**, *86*, 674-676. doi: 10.1063/1.452268
- [260] T. D. Mark, Fundamental aspects of electron impact ionization, *International Journal of Mass Spectrometry and Ion Physics* **1982**, *45*, 125-145. doi: 10.1016/0020-7381(82)80103-4
- [261] EI mass spectrum of methane, <https://webbook.nist.gov/cgi/cbook.cgi?ID=C74828&Mask=200#Mass-Spec>, access date 09.13.2019
- [262] W. F. Frey, R. N. Compton, W. T. Naff, H. C. Schweinler, Electron impact studies of some cyclic hydrocarbons, *International Journal of Mass Spectrometry and Ion Physics* **1973**, *12*, 19-32. doi: 10.1016/0020-7381(73)80083-X
- [263] J. Michl, Electronic structure of non-alternant hydrocarbons: Their analogues and derivatives: XVIII. The electronic spectrum and electron affinity of fluoranthene, *Journal of Molecular Spectroscopy* **1969**, *30*, 66-76. doi: 10.1016/0022-2852(69)90236-7
- [264] R. Dabestani, I. N. Ivanov, A Compilation of Physical, Spectroscopic and Photophysical Properties of Polycyclic Aromatic Hydrocarbons,

- Photochemistry and Photobiology* **1999**, *70*, 10-34. doi: 10.1111/j.1751-1097.1999.tb01945.x
- [265] P. Wolfgang, S. Helmut, **1960**, US Patent 2939952
- [266] W. Paul, Electromagnetic Traps for Charged and Neutral Particles (Nobel Lecture), *Angewandte Chemie International Edition in English* **1990**, *29*, 739-748. doi: 10.1002/anie.199007391
- [267] R. E. March, Quadrupole ion traps, *Mass Spectrometry Reviews* **2009**, *28*, 961-989. doi: 10.1002/mas.20250
- [268] V. S. Edmond de Hoffmann, *Mass Spectrometry: Principles and Applications*, 3rd ed., Wiley, **2007**.
- [269] E. Mathieu, Le mouvement vibratoire d'une membrane de forme elliptique, *J. Math. Pure Appl. (J. Liouville)* **1868**, *13*, 137. doi:
- [270] G. Stafford, Ion trap mass spectrometry: a personal perspective, *Journal of the American Society for Mass Spectrometry* **2002**, *13*, 589-596. doi: 10.1016/S1044-0305(02)00385-9
- [271] G. C. Stafford, P. E. Kelley, J. E. P. Syka, W. E. Reynolds, J. F. J. Todd, Recent improvements in and analytical applications of advanced ion trap technology, *International Journal of Mass Spectrometry and Ion Processes* **1984**, *60*, 85-98. doi: 10.1016/0168-1176(84)80077-4
- [272] F. O. Talbot, S. V. Sciuto, R. A. Jockusch, Fluorescence Imaging for Visualization of the Ion Cloud in a Quadrupole Ion Trap Mass Spectrometer, *Journal of The American Society for Mass Spectrometry* **2013**, *24*, 1823-1832. doi: 10.1007/s13361-013-0742-6
- [273] N. R. Daly, Scintillation Type Mass Spectrometer Ion Detector, *Review of Scientific Instruments* **1960**, *31*, 264-267. doi: 10.1063/1.1716953
- [274] Channeltron electron multiplier handbook for mass spectrometry applications, <https://www.triumf.ca/sites/default/files/ChannelBookBurle.pdf>, access date 09.10.2019
- [275] Photonis 5902 magnum electron multiplier™ for K&M optics from Agilent, Bruker, Hitachi, <https://www.sisweb.com/ms/burle/5902.htm#1>, access date 09.10.2019
- [276] C. Rulliere, *Femtosecond Laser Pulses, Principles and Experiments*, 2nd ed., Springer-Verlag New York, **2005**.
- [277] H. Abramczyk, *Introduction to Laser Spectroscopy*, Elsevier Science, Amsterdam, **2005**.

8. References

- [278] R. Trebino, K. W. DeLong, D. N. Fittinghoff, J. N. Sweetser, M. A. Krumbügel, B. A. Richman, D. J. Kane, Measuring ultrashort laser pulses in the time-frequency domain using frequency-resolved optical gating, *Review of Scientific Instruments* **1997**, *68*, 3277-3295. doi: 10.1063/1.1148286
- [279] W. Heisenberg, Über den anschaulichen Inhalt der quantentheoretischen Kinematik und Mechanik, *Zeitschrift für Physik* **1927**, *43*, 172-198. doi: 10.1007/BF01397280
- [280] D. E. Spence, P. N. Kean, W. Sibbett, 60-fsec pulse generation from a self-mode-locked Ti:sapphire laser, *Opt. Lett.* **1991**, *16*, 42-44. doi: 10.1364/OL.16.000042
- [281] N. Sarukura, Y. Ishida, H. Nakano, Generation of 50-fsec pulses from a pulse-compressed, cw, passively mode-locked Ti:sapphire laser, *Opt. Lett.* **1991**, *16*, 153-155. doi: 10.1364/OL.16.000153
- [282] C.-P. Huang, M. T. Asaki, S. Backus, M. M. Murnane, H. C. Kapteyn, H. Nathel, 17-fs pulses from a self-mode-locked Ti:sapphire laser, *Opt. Lett.* **1992**, *17*, 1289-1291. doi: 10.1364/OL.17.001289
- [283] M. T. Asaki, C.-P. Huang, D. Garvey, J. Zhou, H. C. Kapteyn, M. M. Murnane, Generation of 11-fs pulses from a self-mode-locked Ti:sapphire laser, *Opt. Lett.* **1993**, *18*, 977-979. doi: 10.1364/OL.18.000977
- [284] P. F. Moulton, Spectroscopic and laser characteristics of Ti:Al₂O₃, *J. Opt. Soc. Am. B* **1986**, *3*, 125-133. doi: 10.1364/JOSAB.3.000125
- [285] S. Backus, C. G. D. III, M. M. Murnane, H. C. Kapteyn, High power ultrafast lasers, *Review of Scientific Instruments* **1998**, *69*, 1207-1223. doi: 10.1063/1.1148795
- [286] S. Cho, J. Jeong, S. Hwang, T. J. Yu, Thermal lens effect model of Ti:sapphire for use in high-power laser amplifiers, *Applied Physics Express* **2018**, *11*, 092701. doi: 10.7567/apex.11.092701
- [287] S. Yefet, Pe, #039, A. er, A Review of Cavity Design for Kerr Lens Mode-Locked Solid-State Lasers, *Applied Sciences* **2013**, *3*, 694-724. doi: 10.3390/app3040694
- [288] R. H. Stolen, A. Ashkin, Optical Kerr effect in glass waveguide, *Applied Physics Letters* **1973**, *22*, 294-296. doi: 10.1063/1.1654644
- [289] Optical constants of crystals, <https://refractiveindex.info/?shelf=3d&book=crystals&page=sapphire>, access date 23.10.2019

- [290] A. Major, F. Yoshino, I. Nikolakakos, J. S. Aitchison, P. W. E. Smith, Dispersion of the nonlinear refractive index in sapphire, *Opt. Lett.* **2004**, *29*, 602-604. doi: 10.1364/OL.29.000602
- [291] Dispersion-Compensating Prism Pairs for Ultrafast Lasers, https://www.thorlabs.com/newgrouppage9.cfm?objectgroup_id=3242#31685395-FA1C-4AE1-9DFB-D2B3426831E3-3242, access date 28.10.19
- [292] opus 532 laser system, <https://www.laserquantum.com/products/detail.cfm?id=34>, access date 29.10.2019
- [293] D. Strickland, G. Mourou, Compression of amplified chirped optical pulses, *Optics Communications* **1985**, *56*, 219-221. doi: 10.1016/0030-4018(85)90120-8
- [294] Press release, The nobel prize in physics 2018, "Tools made of light", <https://www.nobelprize.org/uploads/2018/10/press-physics2018.pdf>, access date 31.10.2019
- [295] A. V. V. Nampoothiri, T. Kundu, B. P. Singh, Single pulse selection from a cw mode-locked laser, *Review of Scientific Instruments* **1998**, *69*, 1240-1242. doi: 10.1063/1.1148757
- [296] Operators manual, Wyvern 500/1000 cryogenic ultrafast laser amplifier system, 08/2009, v2
- [297] S. Backus, C. G. Durfee, G. Mourou, H. C. Kapteyn, M. M. Murnane, 0.2-TW laser system at 1 kHz, *Opt. Lett.* **1997**, *22*, 1256-1258. doi: 10.1364/OL.22.001256
- [298] S. Backus, R. Bartels, S. Thompson, R. Dollinger, H. C. Kapteyn, M. M. Murnane, High-efficiency, single-stage 7-kHz high-average-power ultrafast laser system, *Opt. Lett.* **2001**, *26*, 465-467. doi: 10.1364/OL.26.000465
- [299] H. Burton, C. Debardelaben, W. Amir, T. A. Planchon, Temperature dependence of Ti:Sapphire fluorescence spectra for the design of cryogenic cooled Ti:Sapphire CPA laser, *Opt. Express* **2017**, *25*, 6954-6962. doi: 10.1364/OE.25.006954
- [300] P. Tzankov, I. Buchvarov, T. Fiebig, Broadband optical parametric amplification in the near UV-VIS, *Optics Communications* **2002**, *203*, 107-113. doi: 10.1016/S0030-4018(02)01107-0
- [301] TOPAS-C user's manual (Light Conversion)

Part II: Published Work

Publication 1 (PCCP)

Ultrafast Excited-State Relaxation of a Binuclear Ag(I) Phosphine Complex in Gas Phase and Solution

Preamble

The following chapter has been published in the journal „*Physical Chemistry Chemical Physics*“. For the supporting information the reader is referred to the electronic version of the article. All measurements and data processing related to gas-phase ion spectroscopy and mass spectrometry (UV PD, τ -PD, CID, MS²/MS³) were conducted by myself. The sample compound was synthesized by Dr. Simon P. Walg with my assistance. Static and time-resolved spectroscopic experiments in solution phase were performed by Dr. Florian B  ppler and ab initio calculations were implemented by Prof. Dr. Wim Klopper. The initial manuscript was written by myself, supported by Dr. Florian B  ppler, and was revised with the help of Prof. Dr. Rolf Diller and Priv.-Doz. Dr. Christoph Riehn.

S. V. Kruppa, F. B  ppler, W. Klopper, S. P. Walg, W. R. Thiel, R. Diller, C. Riehn, *Phys. Chem. Chem. Phys.*, **2017**, 19(34), 22785-22800,
<https://doi.org/10.1039/C7CP04128D>

Copyright   2017 the Owner Societies

Reproduced by permission of the PCCP Owner Societies.

Reprint Licence

Physical chemistry chemical physics

Article Ultrafast excited-state relaxation of a binuclear Ag(I) phosphine complex in gas phase and solution.

GENERAL INFORMATION

Request ID	600022451	Request Date	27 Aug 2020
Request Status	Accepted	Price	0,00 EUR ? Special Terms

ALL DETAILS

ISSN:	1463-9084	Publisher:	ROYAL SOCIETY OF CHEMISTRY
Type of Use:	Republish in a thesis/dissertation	Portion:	Chapter/article

LICENSED CONTENT

Publication Title	Physical chemistry chemical physics	Rights holder	Royal Society of Chemistry
Article Title	Ultrafast excited-state relaxation of a bi...	Publication Type	e-Journal
Author/Editor	Royal Society of Chemistry (Great Britain)	URL	http://firstsearch.odc.org/journal=1463-...
Date	01/01/1999	Start Page	22785
Language	English	Issue	34
Country	United Kingdom of Great Britain and N...	Volume	19

REQUEST DETAILS

Portion Type	Chapter/article	Rights Requested	Main product
Page range(s)	22785-22800	Distribution	Worldwide
Total number of pages	16	Translation	Original language of publication
Format (select all that apply)	Print, Electronic	Copies for the disabled?	Yes
Who will republish the content?	Academic institution	Minor editing privileges?	No
Duration of Use	Life of current edition	Incidental promotional use?	Yes
Lifetime Unit Quantity	More than 2,000,000	Currency	EUR

NEW WORK DETAILS

Title	Photochemistry and Ultrafast Dynamics ...	Institution name	TU Kaiserslautern
Instructor name	Dr. Christoph Riehn	Expected presentation date	2020-10-31

ADDITIONAL DETAILS

The requesting person / organization to appear on the license	Sebastian Kruppa
---	------------------

REUSE CONTENT DETAILS

Title, description or numeric reference of the portion(s)	Photochemistry and Ultrafast Dynamics ...	Title of the article/chapter the portion is from	Ultrafast excited-state relaxation of a bi...
Editor of portion(s)	Kruppa, S. V.; Bappler, F.; Kloppe, W.; ...	Author of portion(s)	Kruppa, S. V.; Bappler, F.; Kloppe, W.; ...
Volume of serial or monograph	19	Issue, if republishing an article from a serial	34
Page or page range of portion	22785-22800	Publication date of portion	2017-09-14



Cite this: *Phys. Chem. Chem. Phys.*,
2017, 19, 22785

Ultrafast excited-state relaxation of a binuclear Ag(I) phosphine complex in gas phase and solution†

S. V. Kruppa,^{†a} F. Bäßler,^{‡b} W. Klopffer,^c S. P. Walg,^d W. R. Thiel,^{†a}
R. Diller^{†b} and C. Riehn^{†*ae}

The binuclear complex $[\text{Ag}_2(\text{dcpm})_2](\text{PF}_6)_2$ (dcpm = bis(dicyclohexylphosphino)methane) exhibits a structure with a close silver–silver contact mediated by the bridging ligand and thus a weak argentophilic interaction. Upon electronic excitation this cooperative effect is strongly increased and determines the optical and luminescence properties of the compound. We have studied here the ultrafast electronic dynamics in parallel in gas phase by transient photodissociation and in solution by transient absorption. In particular, we report the diverse photofragmentation pathways of isolated $[\text{Ag}_2(\text{dcpm})_2]^{2+}$ in an ion trap and its gas phase UV photodissociation spectrum. By pump–probe fragmentation action spectroscopy ($\lambda_{\text{ex}} = 260$ nm) in the gas phase, we have obtained fragment-specific transients which exhibit a common ultrafast multiexponential decay. This is fitted to four time constants (0.6/5.8/100/>1000 ps), highlighting complex intrinsic photophysical processes. Remarkably, multiexponential dynamics (0.9/8.5/73/604 ps) are as well found for the relaxation dynamics in acetonitrile solution. *Ab initio* calculations at the level of approximate coupled-cluster singles-doubles (CC2) theory of ground and electronically excited states of the reduced model system $[\text{Ag}_2(\text{dmpm})_2]^{2+}$ (dmpm = bis(dimethylphosphino)methane) indicate a shortening of the Ag–Ag distance upon excitation by 0.3–0.4 Å. In C_2 geometry two close-lying singlet states S_1 ($^1\text{MC}(\text{d}\sigma^*-\text{p}\pi)$, ^1B , 4.13 eV) and S_2 ($^1\text{MC}(\text{d}\sigma^*-\text{p}\sigma)$, ^1A , 4.45 eV) are found. The nearly dark S_1 state has not been reported so far. The excitation of the S_2 state carries a large oscillator strength for the calculated vertical transition (266 nm). Two related triplets are calculated at T_1 (3.87 eV) and T_2 (3.90 eV). From these findings we suggest possible relaxation pathways with the two short time constants ascribed to ISC/IVR and propose from the obtained similar values in gas phase that the fast solution dynamics is dominated by intramolecular processes. A further relaxation by IC/IVR in the triplet manifold is likely to account for the observed intermediate time constants. For the acetonitrile relaxation dynamics additional modifications are invoked based on solvent-induced shifts of the energy levels and the possible formation of solvent and counterion exciplexes on a longer timescale.

Received 19th June 2017,
Accepted 10th August 2017

DOI: 10.1039/c7cp04128d

rscl/pccp

1. Introduction

Metal–metal (M–M) interaction in molecular transition metal compounds is a chief topic in the field of inorganic cluster chemistry and homogeneous catalysis,^{1–7} e.g. in the transmetallation

step of metal-catalyzed decarboxylative coupling reactions.⁸ The fundamental understanding of the binding situation between metal centers, in particular for closed-shell d^{10} – d^{10} coinage metal cations and also d^8 – d^8 complexes with unique optical and luminescence properties, is an ongoing subject to theoretical and experimental investigations.^{5,9–13} The discovery of the archetypical binuclear d^8 – d^8 $[\text{Pt}_2(\text{pop})_4]^{4-}$ ($[\text{Pt}_2(\mu\text{-P}_2\text{O}_5\text{H}_2)_4]^{4-}$) complex¹⁴ and the continuous elucidation of its remarkable photophysical properties^{15,16} particularly kindled an interest in the spectroscopy and dynamics of similar luminescent binuclear d^{10} – d^{10} metal complexes.^{5,17} Among them, the phosphine-ligand supported $[\text{M}_2(\mu\text{-dcpm})_2]$ (M = Cu, Ag, Au; dcpm = bis(dicyclohexylphosphino)methane, see Fig. 1) metal complexes^{18–20} are known for exhibiting $^1\text{MC}(\text{d}\sigma^*-\text{p}\sigma)$ electronic transitions, which give rise to UV bands in the 250–380 nm region and broad, strongly redshifted luminescence recognized in the visible region as exciplex formation in solution.^{21,22}

^a Department of Chemistry, TU Kaiserslautern, Erwin-Schrödinger-Str. 52, D-67663 Kaiserslautern, Germany. E-mail: riehn@chemie.uni-kl.de

^b Department of Physics, TU Kaiserslautern, Erwin-Schrödinger-Str. 46, D-67663 Kaiserslautern, Germany. E-mail: diller@physik.uni-kl.de

^c Karlsruhe Institute of Technology (KIT), Institute of Physical Chemistry, Fritz-Haber-Weg 2, D-76131 Karlsruhe, Germany

^d Institute of Chemistry, Inorganic Chemistry, University of Graz, Schubert-Str. 1, 8010 Graz, Austria

^e Forschungszentrum OPTIMAS, Erwin-Schrödinger-Str. 46, D-67663 Kaiserslautern, Germany

† Electronic supplementary information (ESI) available. See DOI: 10.1039/c7cp04128d
‡ S. V. Kruppa and F. Bäßler contributed equally to this work.

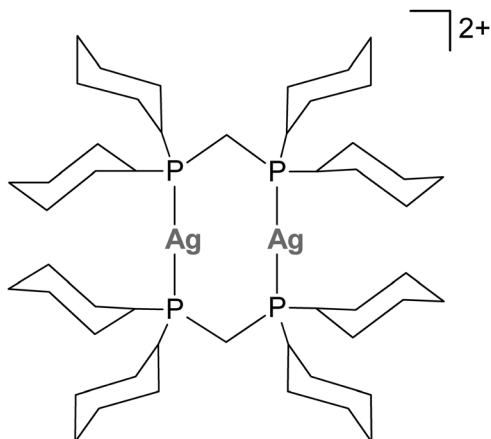


Fig. 1 Schematic structure of $[\text{Ag}_2(\text{dcpm})_2]^{2+}$, dcpm = bis(dicyclohexylphosphino)methane.

The aliphatic phosphine ligand (dcpm) is optically transparent in this wavelength region, which facilitates the spectroscopic assignment. The electronic excitation is accompanied by enhancement of the (M–M) binding and contraction of the (M–M) distance²¹ as explored by UV-Vis and resonance Raman spectroscopic investigations.^{18–20} Intriguingly, already their electronic ground state molecular structure commonly displays M–M distances shorter than the sum of their van der Waals radii indicating metallophilic interactions.²³

Since the extent of metallophilic interaction depends on the nature of the metal centers, the ligand coordination environment, and the nuclearity, it should be possible to specifically tailor (by chemical synthesis) the photochemical and luminescence properties of such M–M systems. Potential applications encompass *e.g.* engineered light-emitting (self-assembled) functional materials,^{9,24} sensory/(bio)diagnostic applications^{10,25,26} and the photocatalytic cleavage of DNA.²⁷ Hence, it is of crucial importance to understand the fundamental and intrinsic nature of metallophilic interactions and moreover their dynamic response to photoexcitation at least for the simple bimetallic case.

The ultrafast dynamics of d^{10} – d^{10} systems, although decisive for their photochemical properties, are still rather unexplored and studies are scarce.^{20,28} In this article we focus on the exploration of the spectroscopic and ultrafast dynamic properties of $[\text{Ag}_2(\text{dcpm})_2]^{2+}$ (Fig. 1), to investigate the consequences of argentophilicity²³ with respect to photoexcitation dynamics. In order to distinguish and separate intrinsic dynamics from environmentally affected ones, we conduct these studies, both at room temperature, in solution and in the gas phase. In detail, we studied the excited state dynamics of the Ag_2 -centered $^1\text{MC}(d\sigma^* - p\sigma)$ excited state by means of transient absorption spectroscopy (TA) in acetonitrile and by transient photodissociation^{29,30} (τ -PD), *i.e.* pump–probe fragmentation action spectroscopy, in a mass spectrometric ion trap.^{31–33} These experiments are supported by *ab initio* quantum chemical calculations at the level of approximate coupled-cluster singles-doubles (CC2) theory, which provides a treatment of electron correlation that is deemed imperative for the

description of metallophilic interaction.³⁴ The energies, structures and multiplicities of ground and electronically excited states are obtained for a size-reduced model system $[\text{Ag}_2(\text{dmpm})_2]^{2+}$ (dmpm = bis(dimethylphosphino)methane). These theoretical results by way of their geometries and energetics set constraints that govern the possible scenarios of the electronic relaxation pathway for the photoexcited $[\text{Ag}_2(\text{dcpm})_2]^{2+}$ complex.

2. Experimental methods, materials and computational details

Materials

$[\text{Ag}_2(\text{dcpm})_2](\text{PF}_6)_2$ was synthesized according to established procedures¹⁸ and characterized *via* UV-absorption spectroscopy using a Lambda 950 UV/Vis/NIR spectrometer (PerkinElmer, $c = 60 \mu\text{M}$ in acetonitrile, LC-MS grade) and ^{31}P NMR spectroscopy (168.1 MHz, MeCN-d_3 , see Fig. S3, ESI[†]), δ 32.9 ppm (dm, $J = 516.1$ Hz), -144.7 (qi., $J = 732.9$ Hz); Lit.:¹⁸ ^{31}P NMR (202 MHz, CD_3Cl_3), δ 36.3 (dm, $J = 690$ Hz).

Ion trap mass spectrometry

ESI-MS was performed using a 3D quadrupole ion trap mass spectrometer (amaZon speed, Bruker Daltonics) modified for laser irradiation experiments^{35,36} by electrospraying sample solutions of $[\text{Ag}_2(\text{dcpm})_2](\text{PF}_6)_2$ ($c = 10^{-6}$ M, acetonitrile, LC-MS grade) at a continuous infusion rate of $120 \mu\text{l h}^{-1}$ assisted by nitrogen sheath gas (5–7 psi, 345–483 mbar). Nitrogen as drying gas was set to a flow rate of 4 l min^{-1} at 180°C and the spraying needle was held at 4.5 kV. The mass-isolation window was typically $\Delta m/z = 4$ selecting the full isotope pattern of molecular precursor species m/z 515 (low mass cutoff at *ca.* m/z 140). Helium pressure inside the trap was estimated to $\sim 10^{-3}$ mbar. For collision-induced dissociation (CID) experiments a resonance excitation voltage was applied to the endcaps of the trap accelerating the isolated precursor ions which then undergo multiple collisions with the He buffer and eventually generate fragments. The instrument was controlled and data analysis was performed with software provided by Bruker.

Femtosecond laser system

Femtosecond laser pulses were generated using a titanium:sapphire (Ti:Sa) chirped pulse cryogenic regenerative amplifier system (Wyvern 1000[™], KMLabs). The oscillator and amplifier stages were pumped by a diode-pumped solid state laser (Opus 532) and a frequency doubled Nd^{3+} :YAG laser (LDP-200MQG, Lee Laser), respectively. The output pulse train (~ 780 nm, fwhm ~ 30 nm, ~ 4 W, 982 Hz, $\Delta\tau \sim 50$ fs) was split into three beams to pump two identical nonlinear frequency converters (TOPAS-C, Light Conversion, tuning range: 240–2600 nm, abbrev. TC₁ and TC₂). The third beam was used for broad-band continuum white-light generation (330–760 nm, WL) by means of self-phase modulation in a constantly moving CaF_2 -window. The relative linear polarization between the pump and probe pulses for the TC₁/TC₂ (transient photodissociation, τ -PD) and the TC₁/WL (transient absorption, TA) experiment was set to $\sim 54.7^\circ$ by a

half-wave plate (Berek compensator). Temporal delay between the pump and probe pulses was controlled using a single axis delay stage (Physik Instrumente, PI) varying the optical path length of TC₂ respective to TC₁ or TC₁ respective to WL. Pulse energies were controlled by variable neutral density filters.

Gas phase photodissociation (PD, τ -PD)

The experimental setup for PD (static) and τ -PD (time-resolved) experiments was depicted³⁶ and described elsewhere in detail.^{29,30,37} Briefly, quasi collinearly combined ($\sim 0.8^\circ$) UV-pump (λ_{pump} : 275–245 nm, 1 μJ , TC₁) and NIR-probe (λ_{probe} : 1150 nm, 150–160 μJ , TC₂) beams were focused ($f = 50$ cm) through a fused silica window (3 mm thickness) onto the ion trap center (~ 1 mm diameter). For PD experiments only the pump beam (TC₁) is used and stepwise wavelength scanned in the range of 240–350 nm at constant pulse energy (~ 2 μJ , spectral width $\Delta\lambda \sim 2$ –4 nm, see Fig. S6, ESI[†]). Each isolated precursor ion packet was irradiated with ~ 118 UV pulses (PD) or ~ 98 pump/probe pulse pairs (τ -PD), respectively, followed by fragment mass analysis.

From the resulting mass spectrum the individual (Y_i) and total fragment yields (TFY) are calculated as $Y_i = F_i/(\Sigma F_i + P)$ and $\text{TFY} = \Sigma F_i/(\Sigma F_i + P)$, respectively. F_i and P are the integrated mass peak intensities of product species i and precursor ions, respectively and ΣF_i is the sum of all fragment ion signals. For PD spectra the fragment yields were normalized to the number of photons $N = E_{\text{pulse}} \lambda / (h \cdot c)$. Furthermore, a scaling factor of 1.43 is applied in the range of 237–263 nm compared to the longer wavelength range (262–287 nm). This accounts for a change in the nonlinear optical output scheme of the TOPAS system, which in turn requires a reoptimization of the overlap of the laser beam with the ion cloud. The scaling factor has been obtained from measurements in the wavelength overlap region of both tuning ranges.

We noticed upon irradiation of the mass spectrometer entrance window by the (for PD) necessary UV laser intensities (*ca.* 0.3 GW) the quick (\sim minutes) development of a red luminescence in the fused silica. This prompted us to record the transmittance of the window in the 240–290 nm range at equivalent photon density to the PD experiments (see Fig. S7, ESI[†]), which gave a *ca.* 20% reduced transmittance at ~ 240 nm compared with ~ 290 nm. However, a correction of the PD spectrum based on these values was not performed, since the fragment yield exhibits a non-linear, fragment-specific power dependence (see discussion in section 3.3, Fig. S8, ESI[†]). Moreover, from cross-correlation measurements (see below) we confirmed that the laser pulse duration and thus τ -PD experiments were not affected by this fused silica luminescence.

For τ -PD experiments individual 4 ps (9 cycles), 40 ps (6 cycles), 400 ps (4 cycles) and 1600 ps (4 cycles) scans were averaged, processed by introducing an ordinate offset correction (4 ps scan as reference) due to fluctuating fragmentation yields at negative time delay and concatenated (32–72 averaged mass spectra/data point).

The time zero position and cross correlation was estimated by measuring the multiphoton ionization of neutral furan

(C₄H₄O) molecules which were introduced at small concentration into the ion trap with the trapping gas (He) (see Fig. S21, ESI[†]). The transient data was fitted by convoluting a Gaussian system response function with a multiexponential decay function according to $S(t) = \Sigma_i A_i (\exp(-t/\tau_i) \times g(t, t_0, t_p))$ using the Origin 2015G software (τ_i : decay time constants, t_0 : time zero, t_p : fwhm of Gaussian, A_i : amplitude of τ_i component, see eqn (S1) and (S2), ESI[†] for fit formula).

Absorption and luminescence spectroscopy (solution)

Static absorption spectra were recorded with a Jasco V-670 spectrophotometer and PerkinElmer Lambda 950 spectrometer. Fluorescence spectroscopy was performed with a Perkin-Elmer LS 55 Fluorescence Spectrometer. Acetonitrile (Uvasol grade) was used.

Transient UV/Vis absorption spectroscopy (solution)

[Ag₂(dcpm)₂](PF₆)₂ was dissolved in MeCN (Uvasol grade) with the concentration set to *ca.* 1.4 OD units in the absorption maximum at 261 nm in a CaF₂ sample cell (25 mm diam., 1 mm pathlength). The cuvette was moved constantly to exchange the irradiated sample volume on a shot-to-shot basis. Steady state absorption spectra were recorded before and after each transient absorption measurement, in order to evaluate and ensure sample integrity. Only minor degradation was observed. The focal width of the exciting laser beam ($\lambda = 262$ nm, $E \sim 400$ nJ) was 75 μm (fwhm) at the sample position. The spectrally dispersed probe pulses were detected with an integrated 512 pixel PDA camera device (Stresing). Chopping the probe-pulses at half the repetition rate of the pump-pulses the pump induced absorbance change $\Delta A(\lambda, t)$ was detected on a shot-to-shot basis. Pump-probe cross-correlation of 150 fs (fwhm) was determined by the rise of the pump-induced signal $\Delta A(\lambda, t)$. The dataset was fitted by convoluting a Gaussian system response function with a multiexponential decay function according to $\Delta A(\lambda, t) = [A_0(\lambda) + \Sigma_i A_i(\lambda) \cdot \exp(-t/\tau_i)] \times g(t, t_0, t_p)$ using the Glotaran 1.5.1 software (τ_i : decay time constants, t_0 : time zero, t_p : fwhm of Gaussian, $A_i(\lambda)$: decay associated spectra, DAS). In addition, singular value decomposition analysis (SVD) was applied to determine the number of spectral species. The results from the TA experiments, *i.e.* the fitted time constants and DAS were reproduced within given errors by evaluation of various sample batches, as well as measurements with reduced excitation energy (200, 400, 600 nJ per pulse), to exclude artifacts from two-photon absorption processes and degradation. The experiments were performed at room temperature.

Computational details

We have chosen to perform quantum chemical calculations at the coupled cluster (CC) level of theory since an advanced treatment of electron correlation is considered to be important for the description of metallophilic systems.³⁴ These high-level computations of electronic and molecular structure for exploration of the [Ag₂(dcpm)₂]²⁺ target ion were undertaken for a reduced molecular model system replacing the cyclohexyl groups by methyl groups on the phosphine ligands (*i.e.* [Ag₂(dmpm)₂]²⁺,

dmpm = bis(dimethylphosphino)methane). This was necessary in order to keep the CPU time and costs manageable. We believe that, despite the reduced ligand size, the relative energies of the different electronic states of the model complex should closely match those of $[\text{Ag}_2(\text{dcpm})_2]^{2+}$ since they are mainly determined by the Ag_2 chromophoric unit. Thus, valuable and realistic insights into the electronic structure of $[\text{Ag}_2(\text{dcpm})_2]^{2+}$, e.g. given by the vertical and adiabatic excitation and emission energies for singlets and triplets, should emerge from these calculations. A similar strategy was applied by other groups on different computational levels.^{21,38,39}

The *ab initio* computations were performed at the coupled-cluster singles-and-doubles level in the CC2 approximation^{40,41} with the TURBOMOLE program package.^{42,43} We used the def2-TZVPP basis set⁴⁴ with an effective core potential for Ag substituting 14 core orbitals.⁴⁵ The 1s orbitals of C and 1s, 2s and 2p orbitals of P were not included in the correlation treatment.

3. Results and discussion

3.1 Mass spectrometry and photodissociation pathways

Electrospray ionization MS of acetonitrile solution of $[\text{Ag}_2(\text{dcpm})_2](\text{PF}_6)_2$ in the cationic mode gives an overview mass spectrum (Fig. S5, ESI[†]), which is dominated by the corresponding molecular peak besides smaller contributions of counter ion adducts. The elemental composition and charge state of the $[\text{Ag}_2(\text{dcpm})_2]^{2+}$ ion (m/z 515, nominal mass) were unequivocally assigned by the excellent agreement of the experimental and simulated isotopic patterns (*cf.* inset Fig. 2(a)). The precursor ion $[\text{Ag}_2(\text{dcpm})_2]^{2+}$ is isolated in the ion trap for all subsequent laser spectroscopic and dynamic investigations.

Upon photoexcitation at $\lambda_{\text{ex}} = 260$ nm of isolated $[\text{Ag}_2(\text{dcpm})_2]^{2+}$ thirteen different fragmentation products could be observed (Fig. 2(b)) in the range of m/z 211 to m/z 819. These fragments originate from two major pathways: (i) ionic fragmentation by fission into singly charged products (charge separation) and (ii) neutral loss fragmentation by cleavage of neutral moieties (charge retention). Furthermore, these photofragmentation pathways are categorized into four groups associated with primary/secondary ionic fragmentation (IF_p/IF_s) and single/multiple neutral loss(es) (NL_p/NL_s) as listed in Table 1. This diverse dissociation pattern motivated us to investigate the connectivity and pathways in detail by multiple MS^2 and MS^3 experiments (Fig. S15–S19, ESI[†]) to determine whether the detected fragment ions (Fig. 2(b)) originate from primary dissociation channels or are formed *via* secondary ones. The resulting overview photofragmentation scheme (Fig. 3) is elucidated in the following.

Primary and secondary ionic fragmentation (IF_p)/(IF_s). The schematic ionic fragmentation pathways of $[\text{Ag}_2(\text{dcpm})_2]^{2+}$ are depicted in Fig. 3 (left). Three different photo-induced IF_p pathways are observed:

(A) intra-ligand fission into $\text{CH}_2\text{P}(\text{Cy})_2^+$ (m/z 211, F_{13}) and the corresponding m/z 819 (F_1) fragment (Table 1) retaining the Ag_2 core.

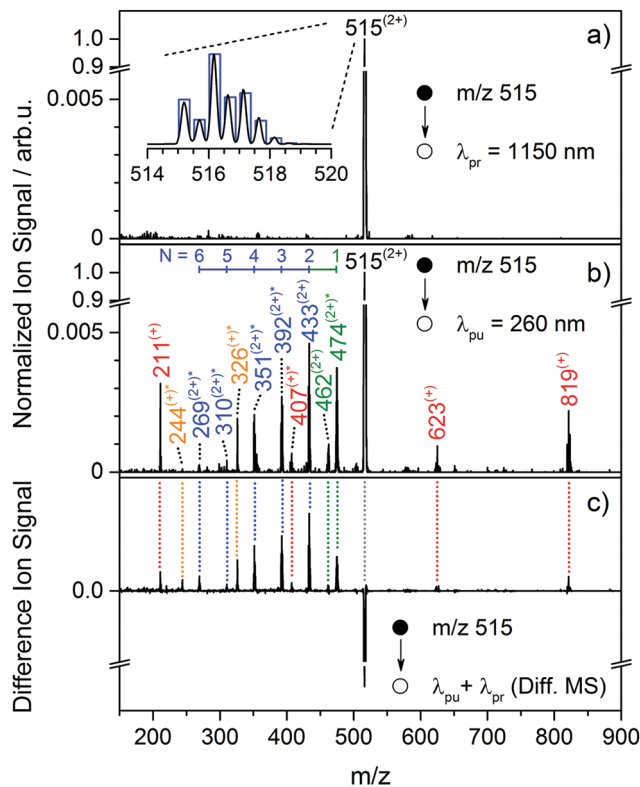


Fig. 2 Photodissociation mass spectra of $[\text{Ag}_2(\text{dcpm})_2]^{2+}$ (m/z 515) at (a) $\lambda_{\text{probe}} = 1150$ nm (160 μJ , ~ 98 pulses) and (b) $\lambda_{\text{pump}} = 260$ nm (1 μJ , ~ 98 pulses), respectively. Integer nominal masses are indicated with charge states in parentheses, asterisks denote contributions of multiple species to the isotope pattern differing by the number of hydrogens (see Table 1 and Tables S2–S4, ESI[†]). Color coding for masses indicates the respective fragmentation processes in analogy to Fig. 3. Insets: (a) Experimental (black line) and simulated (blue bars) isotope pattern of isolated precursor ions without irradiation. (b) N indicates the number of $\text{Cy}/(\text{Cy}-\text{H})$ losses. (c) Difference mass spectrum (Diff. MS) for pump + probe experiment obtained by subtracting the mass spectrum at negative pump–probe time delay (~ -1 ps) from the mass spectrum at positive delay (~ 3 ps). Positive and negative Diff. MS signals correspond to an enhancement and depletion, respectively when the UV-excited $[\text{Ag}_2(\text{dcpm})_2]^{2+}$ ions absorb probe pulses at 1150 nm.

(B) Loss of a complete dcpm ligand and concomitant formal “ H^- ” transfer from this phosphine ligand to the Ag_2 core yielding the $(\text{dcpm} - \text{H})^+$ product (m/z 407, F_6) and presumably a $[\text{Ag}_2(\text{H})\text{dcpm}]^+$ hydride species (m/z 623, F_2), similar to the previously reported $[\text{Ag}_2(\text{H})\text{dppm}]^+$ ion⁴⁶ (see Table 1, schematic structure depicted in Fig. S20, ESI[†]). Notably, the ion signal of $(\text{dcpm} - \text{H})^+$ is also superimposed by the protonated ligand species ($(\text{dcpm} + \text{H})^+$, m/z 409) which is produced *via* secondary fragmentation processes (see Tables S2 and S3, ESI[†]).

(C) Symmetric fission into two equal $[\text{Ag}(\text{dcpm})]^+$ units (m/z 515, F_{dark}). Although this channel cannot be directly observed (“dark channel”), since its ion signal is superimposed with the intense $[\text{Ag}_2(\text{dcpm})_2]^{2+}$ precursor signal at equal m/z ratio, its existence is inferred from the presence of mono-cationic species at m/z 326 (F_9) and m/z 244 (F_{12} , Table 1). Those are assigned as secondary fragmentation products of $[\text{Ag}(\text{dcpm})]^+$

Table 1 Photofragment assignments of $[\text{Ag}_2(\text{dcpm})_2]^{2+}$ (see Fig. 2b), (Cy = C_6H_5). Integer nominal masses (m/z) and charge states (z/e) are indicated. For the sake of simplicity the photofragments are categorized into four groups associated with primary and secondary ionic fragmentation (IF_p , IF_s), single neutral loss (NL_s) and multiple neutral losses (NL_p). Photofragment yield percentages relative to the total yield (Y_i/Y_{TFY}) are given (258 nm, 2 μJ , 118 pulses)

Label	m/z	z/e	Assigned formula	Fragments lost	Category	$Y_i/Y_{\text{TFY}}/\%$ (258 nm, 2 μJ)
F ₁	819	1	$[\text{Ag}_2\text{P}_3(\text{CH}_2)(\text{Cy})_6]^+$	$[\text{P}(\text{CH}_2)(\text{Cy})_2]^+$	IF_p	8
F ₂	623	1	$[\text{Ag}_2\text{P}_2(\text{CH}_2)(\text{Cy})_4\text{H}]^+$	$[\text{P}_2(\text{CH}_2)(\text{Cy})_3(\text{Cy-H})]^+$	IF_p	2
P	515	2	$[\text{Ag}_2\text{P}_4(\text{CH}_2)_2(\text{Cy})_8]^{2+}$		Precursor	—
F _{dark} ^b	515	1	$[\text{AgP}_2(\text{CH}_2)(\text{Cy})_4]^+$	$[\text{AgP}_2(\text{CH}_2)(\text{Cy})_4]^+$	IF_p/IF_s	—
F ₃ ^a	474	2	$[\text{Ag}_2\text{P}_4(\text{CH}_2)_2(\text{Cy})_7\text{H}]^{2+}$	(Cy-H)	NL_p	20
			$[\text{Ag}_2\text{P}_4(\text{CH}_2)_2(\text{Cy})_7]^{2+}$	(Cy)		
F ₄	462	2	$[\text{AgP}_4(\text{CH}_2)_2(\text{Cy})_8]^{2+}$	Ag^0	NL_p	3
F ₅	433	2	$[\text{Ag}_2\text{P}_4(\text{CH}_2)_2(\text{Cy})_6\text{H}]^{2+}$	(Cy), (Cy-H)	NL_s	21
F ₆ ^a	407	1	$[\text{P}_2(\text{CH}_2)(\text{Cy})_3(\text{Cy-H})]^+$	$[\text{Ag}_2\text{P}_2(\text{CH}_2)(\text{Cy})_4\text{H}]^+$	IF_p	3
	(409)		$[\text{P}_2(\text{CH}_2)(\text{Cy})_4\text{H}]^+$	" $[\text{Ag}_2\text{P}_2(\text{CH}_2)(\text{Cy})_3(\text{Cy-H})]^+$ "	IF_s	
F ₇ ^a	392	2	$[\text{Ag}_2\text{P}_4(\text{CH}_2)_2(\text{Cy})_5\text{H}_2]^{2+}$	(Cy), 2(Cy-H)	NL_s	17
	(391)		$[\text{Ag}_2\text{P}_4(\text{CH}_2)_2(\text{Cy})_5\text{H}]^{2+}$	2(Cy), (Cy-H)		
F ₈ ^a	351	2	$[\text{Ag}_2\text{P}_4(\text{CH}_2)_2(\text{Cy})_4\text{H}_3]^{2+}$	(Cy), 3(Cy-H)	NL_s	14
	(350)		$[\text{Ag}_2\text{P}_4(\text{CH}_2)_2(\text{Cy})_4\text{H}_2]^{2+}$	2(Cy), 2(Cy-H)		
F ₉ ^a	326	1	$[\text{P}_2(\text{CH}_2)(\text{Cy})_3\text{H}]^+$	" $[\text{AgP}_2(\text{CH}_2)(\text{Cy})_4]^+$, Ag^0 , (Cy-H)"	IF_s	5
	(325)		$[\text{P}_2(\text{CH}_2)(\text{Cy})_3]^+$	" $[\text{AgP}_2(\text{CH}_2)(\text{Cy})_4]^+$, Ag^0 , (Cy)"		
F ₁₀	310	2	$[\text{Ag}_2\text{P}_4(\text{CH}_2)_2(\text{Cy})_3\text{H}_4]^{2+}$	(Cy), 4(Cy-H)	NL_s	1
F ₁₁ ^a	269	2	$[\text{Ag}_2\text{P}_4(\text{CH}_2)_2(\text{Cy})_2\text{H}_6]^{2+}$	6(Cy-H)	NL_s	2
	269		$[\text{Ag}_2\text{P}_4(\text{CH}_2)_2(\text{Cy})_2\text{H}_5]^{2+}$	(Cy), 5(Cy-H)		
	(268)		$[\text{Ag}_2\text{P}_4(\text{CH}_2)_2(\text{Cy})_2\text{H}_4]^{2+}$	2(Cy), 4(Cy-H)		
F ₁₂ ^a	244	1	$[\text{P}_2(\text{CH}_2)(\text{Cy})_2\text{H}_2]^+$	" $[\text{AgP}_2(\text{CH}_2)(\text{Cy})_4]^+$, Ag^0 , 2(Cy-H)"	IF_s	1
	(243)		$[\text{P}_2(\text{CH}_2)(\text{Cy})_2\text{H}]^+$	" $[\text{AgP}_2(\text{CH}_2)(\text{Cy})_4]^+$, Ag^0 , (Cy-H), (Cy)"		
F ₁₃	211	1	$[\text{P}(\text{CH}_2)(\text{Cy})_2]^+$	$[\text{Ag}_2\text{P}_3(\text{CH}_2)(\text{Cy})_6]^+$	IF_p/IF_s	4

^a Contributions of multiple species to the isotope pattern relatively differing in number of hydrogens (*cf.* Tables S2–S4, ESI species with minor contributions to the isotope pattern are given in parentheses). ^b Ion signal is superimposed with the strong precursor ion signal (m/z 515, see Fig. S15, ESI).

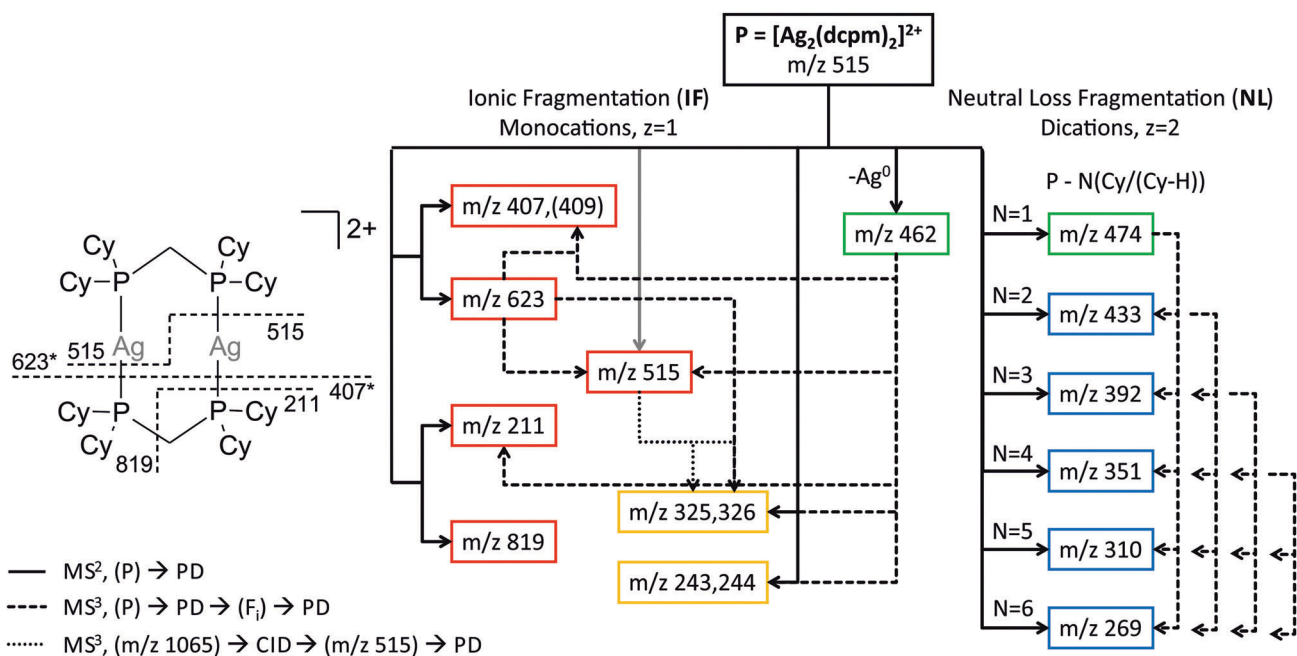


Fig. 3 (left) Simplified ionic fragmentation scheme (cleavage into two monocationic moieties, *cf.* Table 1) upon UV excitation. Asterisks indicate additional hydrogen transfer yielding a hydride-bridged species (m/z 623, see Table 1 and Fig. S20, ESI[†]) similar to the previously reported $[\text{Ag}_2(\text{H})\text{dppm}]^+$ ion.⁴⁶ (right) Fragmentation scheme of $[\text{Ag}_2(\text{dcpm})_2]^{2+}$ precursor ions (m/z 515, P) based on MS^2 (black solid arrows) and MS^3 (dashed and dotted arrows) collision- and photo-induced dissociation experiments (CID, PD, *cf.* Fig. S15–S19, ESI[†]). Main fragmentation products (integer nominal masses) are categorized into four groups based on primary, secondary ionic fragmentation processes (IF_p : red, IF_s : yellow) and single, multiple neutral losses (NL_p : green, NL_s : blue), respectively. N indicates number of Cy + (Cy-H) losses. The $[\text{Ag}(\text{dcpm})]^+$ species (m/z 515) cannot be directly observed from fragmentation of $[\text{Ag}_2(\text{dcpm})_2]^+$ (m/z 515) since the ion signals overlap (indicated by gray solid arrow). Therefore it was generated *via* CID of the halide adduct $[\text{Ag}_2(\text{Cl})(\text{dcpm})_2]^+$ (m/z 1065) and subsequently photodissociated in a MS^3 step (dotted arrows, see Fig. S16, ESI[†]).

by subsequent neutral losses, since their corresponding mono-cationic counterparts could not be observed.

This could be also verified in a MS³ PD experiment of isolated [Ag(dcpm)]⁺ precursors generated *via* CID of [Ag₂(Cl)(dcpm)₂]⁺ (see Fig. S15, ESI[†]), yielding the *m/z* 326/325 (F₉) photoproducts at λ_{ex} = 260 nm. Furthermore, [Ag(dcpm)]⁺ can be generated as a product ion from *m/z* 623 (F₂) and *m/z* 462 (F₄) ions (see Fig. S18 and S19, ESI[†]).

Single neutral loss (NL_p). The intense PD product ion signal at *m/z* 474 (F₃) is assigned to a superposition of two species corresponding to loss of either a cyclohexyl radical (Cy)[•] or a cyclohexene (Cy-H), respectively (Table 1 and Table S2, ESI[†]). For the latter it is reasonable to assume that a β-hydrogen of the leaving Cy moiety is transferred to a phosphorus atom, since the (Cy-H) carbene is certainly thermodynamically less favored. The thermodynamics of Cy/Cy-H loss fragmentation pathways are given in the ESI.[†] The loss of (Cy)[•] leads to a radical dication (P^{•2+}) that probably stabilizes by further (Cy)[•] loss, also manifested in the relatively large signal intensity of the fragment ions that underwent a loss of an even number of Cy units *vs.* the odd-numbered Cy losses. Thus the ion signal at *m/z* 433 (loss of two Cy units) is also considered as stemming from a single pump-probe photoexcitation.

The weak photofragment signal at *m/z* 462 (F₄) might result from an electron transfer to a silver center leading to the observed loss of neutral Ag⁰. This could be an indication for an excited state with ligand-to-metal charge transfer (^{1,3}LMCT) character. Notably, this channel could not be accessed by CID (see Fig. S15, ESI[†]) and is therefore specific to fragmentation *via* the photoexcited state. However, our theoretical analysis (see below) does not support the existence of CT states in the energy range of the first excited state, so that it could be tentatively ascribed to result from two-photon excitation.

Multiple neutral losses (NL_s). Upon photoexcitation fragments are observed which could be assigned to *N*·((Cy)/(Cy-H)) losses, *i.e.* up to *N* = 6. Since the calculated average carbon-phosphorus dissociation energy (BDE) > 300 kJ mol⁻¹,⁴⁷ the photon energy at 258 nm equals ~464 kJ mol⁻¹ and the precursor ion cloud is irradiated with multiple UV pulses (see Experimental section), it is possible that those products are formed in secondary fragmentation processes stemming from multiple irradiation events. MS³ experiments of isolated *N*·(Cy)/(Cy-H) loss fragments as precursor ions for subsequent, secondary PD (λ_{ex} = 260 nm, 2 μJ, 118 pulses) confirm this possibility, but also reveal that irradiation of a fragment intermediate directly leads (again) to multiple *N*·(Cy)/(Cy-H) losses (see Fig. S17, ESI[†]). Furthermore, threshold experiments at very low laser intensity or with a small number of laser pulses (10 pulses, see Fig. S10–S12, ESI[†]) disclosed that already under these conditions the fragment ions due to multiple neutral losses appear. Also, at the relatively low total yield of ~2.5% at 100 irradiation laser pulses (conditions of Fig. 2(b)) we believe that the probability of generating fragment ions by successive multiple irradiation is very small so that these contributions can be neglected.

Finally, we conclude from this general analysis of fragmentation pathways that we have identified the primary ionic and

neutral fragmentation steps and related fragment ions and their connections for the UV-PD of [Ag₂(dcpm)₂]²⁺. The fragmentation pattern is however not arrested at this primary level but modified by secondary processes mainly driven by excess energy from the photoexcitation. We exclude a significant contribution to the fragment yield by multiple irradiation events, *i.e.* further irradiation of fragment ions. Thus, we emphasize, that primary and secondary fragments are valid markers for the photodissociation action spectroscopy in the wavelength and time domain for [Ag₂(dcpm)₂]²⁺ that we present in the following.

Comparison of PD and CID results. In order to elucidate the fragmentation pathways further, we like to point out that the photo- and collision-induced dissociation channels of [Ag₂(dcpm)₂]²⁺ differ drastically (Fig. S15 and Table S1, ESI[†]). No asymmetric IF_p products (*m/z* 819, 211, 623, 407) under retention of the Ag₂ core are observed by CID. Instead, the main dissociation channel seems to be the symmetric ionic fission (*m/z* 515) as indicated by observation of multiple secondary IF_s products of [Ag(dcpm)]⁺.

We therefore assume, that the photodissociation of [Ag₂(dcpm)₂]²⁺ mainly proceeds *via* long lived electronically excited (probably triplet) states rather than from vibrationally hot ground state levels (populated by IC). The quantification of the electronically excited states lifetimes will be given in the following chapters of this work.

Furthermore, we interpret this difference in fragmentation patterns (PD *vs.* CID) as an indication for the strengthening of the Ag–Ag argentophilic interaction in the electronically excited states of [Ag₂(dcpm)₂]²⁺ since the barrier for symmetric IF upon photoexcitation appears to be increased compared to the electronic ground state. This also opens competing asymmetric IF and NL fragmentation pathways from the photoexcited states.

3.2 Computational results

Using coupled-cluster theory in the CC2 approximation, we began our study by investigating the model compound [Ag₂(dmpm)₂]²⁺, dmpm = bis(dimethylphosphino)methane in two conformations of different symmetry (see Fig. S27–S29, ESI[†]). One conformer exhibits C_{2v} symmetry, the other C_{2h} symmetry, differing in the relative orientation of the bridging CH₂ group of the dmpm ligands. Both conformers exhibit similar Ag–Ag distances (*cf.* Table S6, ESI[†]) and are nearly isoenergetic (*E*(C_{2v}) – *E*(C_{2h}) = 0.1 kJ mol⁻¹). However, we then found that both conformers exhibit an imaginary harmonic vibrational frequency (12.5i cm⁻¹ for the C_{2v} and 10.6i cm⁻¹ for the C_{2h} structure), and a subsequent geometry optimization of the C_{2h} structure along the corresponding normal mode finally led to a structure of C₂ symmetry (Fig. 4). This structure was found 1.3 kJ mol⁻¹ below the C_{2h} structure and is a true minimum on the potential energy hypersurface. In the C₂ structure, the Ag–Ag distance amounts to 2.91 Å, which is about 0.03 Å shorter than in the C_{2v} and C_{2h} structures, and the P–Ag–Ag–P dihedral angle is 160°.

Electronically excited states of singlet and triplet character were studied in all three symmetries. The low-lying states are characterized as HOMO → LUMO and HOMO → LUMO+1 excitations.

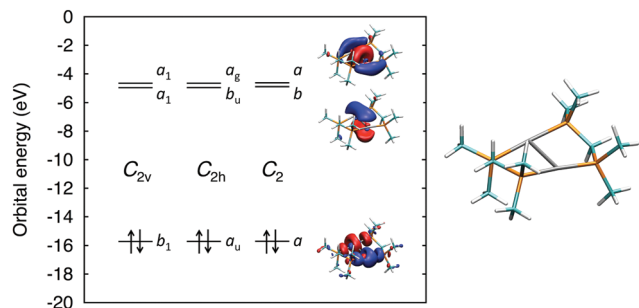


Fig. 4 (left) MO diagram showing the HOMO, LUMO and LUMO+1 levels for structures of the model compound $[\text{Ag}_2(\text{dmpm})_2]^{2+}$ exhibiting C_{2v} , C_{2h} (see Fig. S27–S29, ESI†) and C_2 symmetry, respectively. Iso-surface plots at $\pm 0.04 (a_0)^{-3/2}$ for C_2 symmetry are depicted. (right) Molecular structure of $[\text{Ag}_2(\text{dmpm})_2]^{2+}$ (C_2 symmetry); color code (capped sticks): Ag (silver), P (yellow), C (cyan), H (white).

Fig. 4 shows the molecular orbital diagrams including the HOMO, LUMO and LUMO+1 orbitals for the C_2 structure (the orbitals are indistinguishable for the three structures). With respect to the symmetry labels, note that in the C_{2v} structure, the x -axis goes through the two Ag nuclei (as usual, the axis of rotation is chosen as z -axis). In the C_{2h} and C_2 structures, the z -axis goes through the two Ag nuclei.

The electronic excitations to the LUMO and LUMO+1 orbitals give rise to two closely lying electronic states S_1 and S_2 , respectively. In the C_{2v} structure, both states display B_1 symmetry while in the C_{2h} and C_2 structures, the two states display

B_g/A_u and B/A symmetry, respectively (see Table 2 and Table S6, ESI†). The two singlet states can also be characterized as $^1\text{MC}(\text{d}\sigma^*-\text{p}\pi)$ and $^1\text{MC}(\text{d}\sigma^*-\text{p}\sigma)$, respectively. The S_1 state with nearly zero oscillator strength has not been reported so far for this system. A similar dark S_1 ($^1\text{MC}(\sigma^*-\pi)$) state was theoretically predicted for the $\text{d}^{10}-\text{d}^{10}$ $[\text{Au}(\text{CN})_2]^-$ dimer.⁴⁸ The excitation of the S_2 state carries large oscillator strength and agrees in wavelength and character with results from former calculations at similar model systems and other levels of theory.^{21,38}

The energies of the corresponding singlet and triplet states are given in Table 2 and Table S6 (ESI†). Clearly, the differences between the three structures are insignificant. This becomes immediately clear by comparing their simulated UV/Vis spectra (Fig. 5b). The absorption bands at ca. 266 nm of the three structures are almost indistinguishable. Hence, all three conformers seem to be equally well-suited models for the system of interest (with cyclohexyl-phosphino ligands). The CC2 single-excitations vector of the 1B excited state attaches a weight of 89% to the HOMO \rightarrow LUMO excitation, the CC2 single-excitations vector of the 1A excited state attaches a weight of 87% to the HOMO \rightarrow LUMO+1 excitation. A further discussion of the calculated electronic transitions will be given in comparison to the experimental data in the next chapter. A more detailed summary of all excitation energies, oscillator strengths and geometry parameters for the C_{2v} , C_{2h} and C_2 symmetries is provided in the ESI† (Table S6). We have also optimized the equilibrium structures of the singlet (S_1 and S_2) and triplet (T_1 and T_2) excited states. The results of these geometry

Table 2 Calculated (CC2/TZVPP) electronic adiabatic transitions, absorptions (vertical), emissions (vertical) and optimized Ag–Ag distances for the C_2 conformer of the $[\text{Ag}_2(\text{dmpm})_2]^{2+}$ (dmpm = bis(dimethylphosphino)methane) model complex, compared to experimental absorption/emission of $[\text{Ag}_2(\text{dcpm})_2]^{2+}$ in different chemical environments. Data on related model systems taken from ref. 18, 21, 38 and 50 are listed for comparison (dpm = bis(diphosphanyl)methane)

Species (level of theory)	Point group	State (sym.)	Adiab. trans./eV	Vert. trans./eV, $\lambda_{\text{abs}}/\text{nm}$ (oscillator strength)	Vert. em./eV, $\lambda_{\text{em}}/\text{nm}$ (oscillator strength)	$d(\text{Ag}-\text{Ag})/\text{\AA}$
Theory						
$[\text{Ag}_2(\text{dmpm})_2]^{2+}$ (CC2/TZVPP)	C_2	S_0 (1A)				2.91
		S_1 (1B)	4.13	4.48, 277 (0.004)	3.82, 324 (0.008)	2.56
		S_2 (1A)	4.45	4.67, 266 (0.41)	4.25, 292 (0.38)	2.66
		T_1 (3A)	3.90	4.10, 302	3.74, 331	2.66
		T_2 (3B)	3.87	4.16, 298	3.60, 345	2.58
$[\text{Ag}_2(\text{dpm})_2]^{2+}$ (TD-DFT) ³⁸	C_{2h}	S_0				2.93
		T_1			332	2.66
		S_1		262		
$[\text{Ag}_2(\text{dpm})_2]^{2+}$ (MP2/TD-DFT/CIS) ²¹	C_i	S_0 (1A_g)				3.16
		S_1 (1A_u)			302 (0.09)	2.98
		T_1 (3A_u)			356	3.06
$[\text{Ag}_2(\text{dpm})_2(\text{MeCN})_2]^{2+}$ (MP2/TD-DFT/CIS) ²¹		S_0 (1A_g)				3.07
		S_1 (1A_u)		256 (0.13)	366 (0.09)	2.99
		T_1 (3A_u)			424	3.05
Experiment						
$[\text{Ag}_2(\text{dmpm})_2](\text{PF}_6)_2$				254 (EtOH) ⁵⁰		3.04 (crystal) ⁵⁰
$[\text{Ag}_2(\text{dcpm})_2]^{2+}$				258 (in vacuum)		
$[\text{Ag}_2(\text{dcpm})_2](\text{PF}_6)_2$				261 (MeCN)	381, ~600 (MeCN)	2.94 (crystal) ¹⁸
				260 (MeOH)	349, ~441, ~615 (MeOH)	

optimizations are given in Table 2 and in the ESI.† Moreover, it is important to note that the energetic order of the triplet T_1 and T_2 states is reversed upon optimization of the equilibrium geometries of these states. In C_2 symmetry, for example, $T_1 = {}^3A$ and $T_2 = {}^3B$, whereas after optimization $T_1 = {}^3B$ and $T_2 = {}^3A$.

3.3 UV absorption, photodissociation and computational spectrum

The UV absorption spectrum of $[\text{Ag}_2(\text{dcpm})_2](\text{PF}_6)_2$ in MeCN (Fig. 5(a)) displays a distinct band centered at 261 nm ($\lambda_{\text{max}} = 261 \text{ nm}^{18}$) which is assigned to a silver centered ${}^1\text{MC}(4d\sigma^* \rightarrow 5p\sigma)$ transition originating from argentophilic interaction. This assignment for the solution spectrum is supported by results from the literature on TD-DFT calculations ($\lambda_{\text{calc}} = 256 \text{ nm}^{21}$)

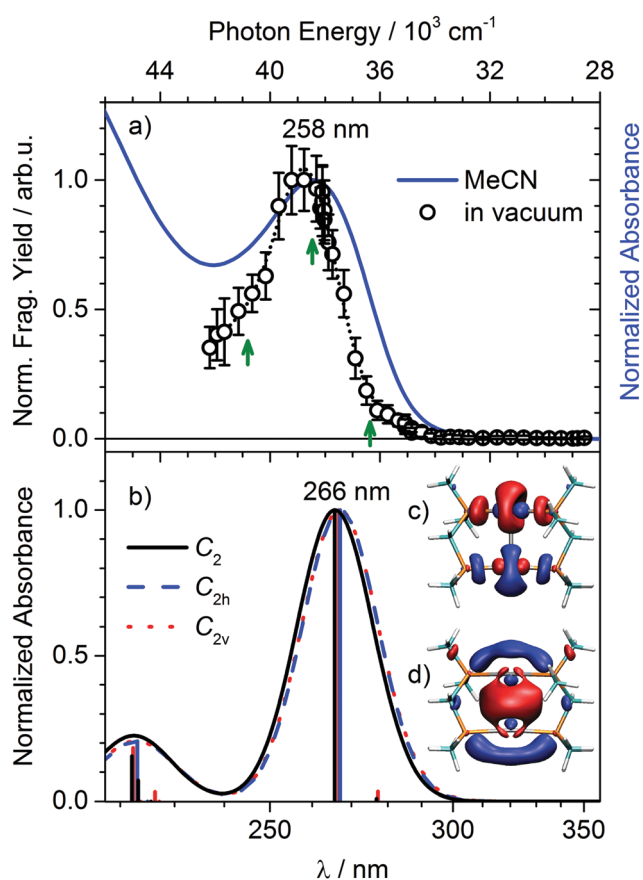


Fig. 5 (a) UV-PD total yield spectrum of gaseous $[\text{Ag}_2(\text{dcpm})_2]^{2+}$ ions (open circles, $2 \mu\text{J}$, 118 pulses) compared to the UV absorption in MeCN at room temperature (solid line, $c = 60 \mu\text{M}$, PF_6 salt). Spectra are normalized to unity, PD total yield at maximum (258 nm) corresponds to $\sim 4\%$. Error bars represent one standard deviation ($\pm 1\sigma$, at least 170 mass spectra). The line profile (dotted line, fit by sum of 2 Gaussians) is shown to guide the eye. Green arrows indicate pump wavelengths for τ -PD experiments. (b) Calculated electronic absorption spectra (Gaussian broadening, $\text{fwhm} = 0.4 \text{ eV}$) of the $[\text{Ag}_2(\text{dmpm})_2]^{2+}$ model complex for its nearly isoenergetic C_2 (black solid line), C_{2h} (blue dashed line) and C_{2v} (red dotted line), isomers. Stick spectra indicate symmetry allowed transitions. Insets (c) and (d) show the most important occupied and virtual natural transitional orbitals (iso-surfaces at $0.04 (a_0)^{-3/2}$), respectively, of the ${}^1\text{MC}(d\sigma^* - p\sigma)$ transition at 266 nm for the C_2 isomer.

and resonance Raman experiments.¹⁸ Furthermore, ligand centered contributions can be excluded since the dcpm ligand is optically transparent in the investigated spectral region substantiating the assumption of a purely Ag_2 -centered chromophore.

The UV PD spectrum of gaseous $[\text{Ag}_2(\text{dcpm})_2]^{2+}$ ions (Fig. 5(a)) closely resembles the absorption spectrum in MeCN solution, peaking at $\lambda_{\text{max}} \sim 258 \text{ nm}$, with a small blueshift (-450 cm^{-1}) and a slightly narrowed band. The former is in accordance with the small solvatochromism observed in solution phase (Table 2). The solvent induced-shift in MeCN might originate from a weak $\text{Ag} \cdots \text{NCCH}_3$ interaction in the ground and a to some extent stronger interaction in the electronically excited state.^{18,21} In analogy to the solution, we ascribe the characteristic band at 258 nm in gas phase to the Ag_2 -centered ${}^1\text{MC}(4d\sigma^* \rightarrow 5p\sigma)$ transition. Interestingly, the spectral shape of the channel specific PD spectra (Fig. S14, ESI†) is similar for all fragment ions. The energy dependence of the total fragment yield of $[\text{Ag}_2(\text{dcpm})_2]^{2+}$ reveals a one-photon absorption process indicated by a slope $n \sim 1$ on a double logarithmic plot (see Fig. S8, ESI†). Therefore the comparison to solution absorption spectra is justified.^{37,49} The energy dependence of the channel-specific yields, however, reveals slopes in the range of $n = 0.4\text{--}2.2$ which points to some contributions by multi-photon excitation.

The spectral assignment for $[\text{Ag}_2(\text{dcpm})_2]^{2+}$ is in good agreement with the results of our $\text{CC2}/\text{def2-TZVPP}$ calculations for the $[\text{Ag}_2(\text{dmpm})_2]^{2+}$ model system. It predicts the main dipole-allowed transition at $\lambda_{\text{calc}} = 266 \text{ nm}$ ($\text{HOMO-LUMO}+1$, ${}^1\text{MC}(d\sigma^* - p\sigma)$, see Fig. 5(b) and Table 2) for the C_2 type structure. In our ion trap experiment at room temperature it is not possible to distinguish between energetically so close isomers and probably a mixture of the species (C_{2h} , C_{2v} , C_2) is present and subject to our study (Fig. S27, ESI†). However, from the calculations additionally a weakly dipole-allowed transition at $\lambda_{\text{calc}} = 277 \text{ nm}$ was found (see Table 2) whose contribution to the experimental spectrum cannot be excluded. Ligand-centered electronic transitions do not have to be considered since the key feature of the dcpm ligand is its optical transparency in the mid-UV spectral region, which allows for the selective excitation of the Ag_2 chromophore.¹⁸ The choice of the $[\text{Ag}_2(\text{dmpm})_2]^{2+}$ model and the level of calculations is strongly supported by the obtained ground state Ag-Ag distance (2.91 \AA) which is in good agreement with the data from the X-ray analysis (*cf.* Table 2). This structural parameter sensitively controls the type and intensity of the dominating electronic transitions.

Fig. 5(c) and (d) display the most important occupied and virtual natural transitional orbitals (NTOs), respectively, illustrating the photoinduced Ag-Ag bonding interaction in the ${}^1\text{MC}(d\sigma^* - p\sigma)$ excited state which results in a shortening of the Ag-Ag distance by $\Delta d_{\text{calc}} \sim -0.25 \text{ \AA}$ (*cf.* Table 2) for the C_2 structure. This structural feature of the excited state was similarly obtained before by TD-DFT calculations on comparable model systems^{21,38} (see Table 2) and also extracted from analysis of resonance Raman investigations.^{18,19} In particular, from the latter experimental study a shortening of the Ag-Ag distance by -0.2 \AA was estimated in response to the photoexcitation at 262 nm.

We like to emphasize here an important finding of our quantum chemical analysis: the optically dark S_1 states (1B_g , 1B_1 and 1B in C_{2h} , C_{2v} and C_2 symmetry, respectively) have been obtained for the first time. These states are positioned *ca.* 0.3 eV lower in energy than the optically accessible S_2 (1A_u , 1B_1 , 1A) states. The S_1 states NTOs display an electronic transition of metal-centered π -type character with only very low oscillator strength. They also exhibit a shortening in the Ag–Ag distance with respect to the ground state, comparable to the values of the S_2 and triplet states. Although the S_1 states are not directly populated by photoexcitation, they may be crucial stepping levels for the relaxation of the primary excited S_2 states.

3.4 Transient photodissociation (τ -PD) in the ion trap

In order to investigate the ultrafast excited-state dynamics of the initially excited $^1MC(d\sigma^* - p\sigma)$ state of gaseous $[Ag_2(dcpm)_2]^{2+}$ ions, we use transient photodissociation (τ -PD),^{29,30} a pump–probe fragmentation action spectroscopy. Hereby, the fragment yield was monitored as a function of relative time delay between UV pump (245, 260, 275 nm, respectively as indicated in Fig. 5) and NIR probe pulses (1150 nm). Note, that the UV pump excitation (pump-only) induces a delay time independent fragmentation signal and the NIR irradiation (probe-only) yields a vanishingly

small signal (*cf.* Fig. 2). Hence, the S/N ratio of the τ -PD signal is governed by the increase in the fragmentation yield and/or change in the fragmentation pattern induced by the NIR probe excited state absorption, compared to the sum of pump-only and probe-only yields. This phenomenological requirement for τ -PD is fulfilled, when the fragment yield/pattern depends on the internal energy of the excited ions and/or the probe absorption cross section or fragmentation pathways specific for the excited states are accessed during the electronic deactivation process.^{29,31–33}

For $[Ag_2(dcpm)_2]^{2+}$ we observe a small total fragment yield ($\sim 2.6\%$, 260 nm, 1 μ J) upon UV pump excitation (see ordinate offset in Fig. 6 and 7(b)). The precursor ions are transparent for the 1150 nm NIR wavelength in the electronic ground state (*cf.* Fig. 2(a)). Thus, upon temporal overlap of pump/probe pulses an enhancement in intensity of all individual fragment signals and corresponding depletion for the precursor ion signal is observed as shown in the difference mass spectrum (Diff. MS, Fig. 2(c)). The latter was obtained by subtracting the mass spectrum at negative pump–probe time delay (~ -1 ps) from the one at positive delay (~ 3 ps). The change in intensity of the ion signals reflects the change in fragmentation yield between the initially excited state and higher excited states reached by (multi-photon) NIR excited-state absorption. This enhancement

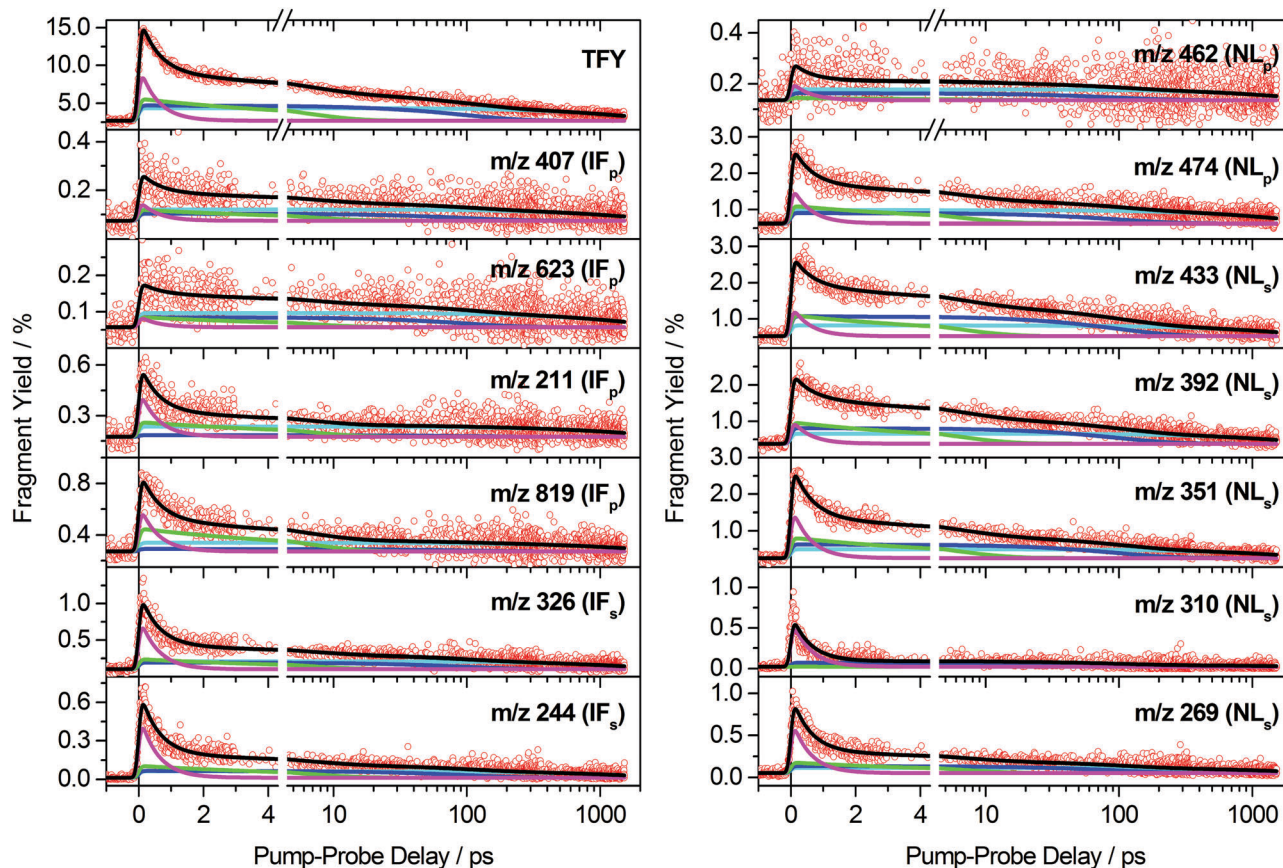


Fig. 6 Comparison between the τ -PD total fragmentation yield signal (TFY) and its individual channel-specific transients of $[Ag_2(dcpm)_2]^{2+}$ ($\lambda_{\text{pump}} = 260$ nm, $\lambda_{\text{probe}} = 1150$ nm). Fragment specific yield signals were globally fitted (black lines) using the parameters obtained from tetra-exponential fit of the TFY signal (see Fig. S23 and S24, ESI,† Table 3), only releasing ordinate offsets and decay associated amplitudes. Individual relaxation contributions are shown as colored lines (τ_1 : magenta, τ_2 : green, τ_3 : blue, τ_4 : cyan), time delay after 4.5 ps is plotted on a logarithmic scale.

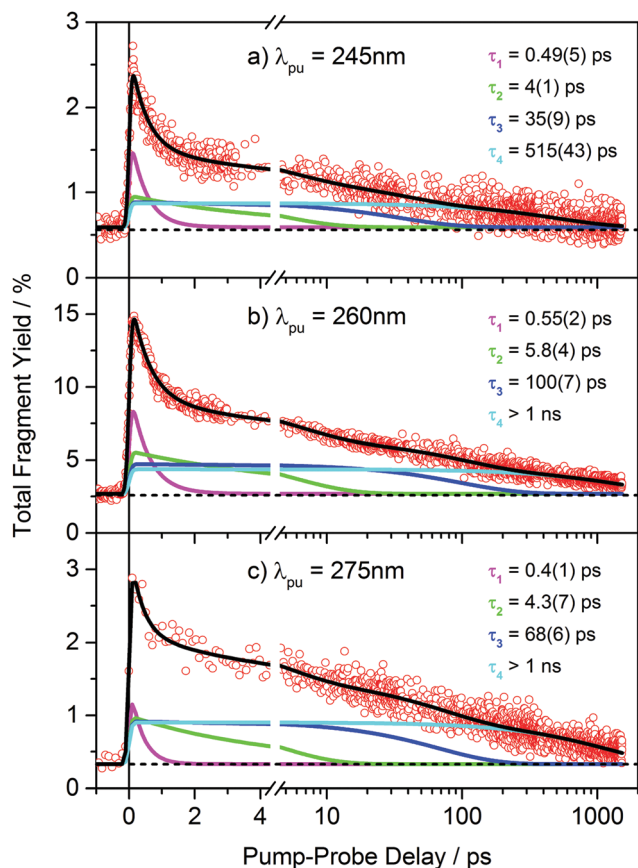


Fig. 7 Transient PD total yield signals (open circles) of $[\text{Ag}_2(\text{dcpm})_2]^{2+}$ as a function of time delay between UV-pump ($\lambda_{\text{pump}} =$ (a) 245 nm, (b) 260 nm, (c) 275 nm; 1 μJ ; ~ 98 pulses) and NIR-probe pulses ($\lambda_{\text{probe}} = 1150$ nm; (a) 150 μJ , (b) 160 μJ , (c) 150 μJ ; ~ 98 pulses). Time delay after 4.5 ps is plotted on a logarithmic scale. Best kinetic fits (black solid lines) were obtained using a parallel relaxation model by convolution of a Gaussian and tetra-exponential decay function (Fig. S24 and S25, ESI †). Time constants, standard errors (in parentheses) and their individual relaxation contributions (colored solid lines, τ_1 : magenta, τ_2 : green, τ_3 : blue, τ_4 : cyan) are shown. The pump-only fragmentation yield is indicated as dashed line (negligible probe-only PD yield).

can reach, under the here applied conditions, up to a factor of 6–7, nearly independent of fragment channel. Since no new dissociation channels were accessed and the excited-state absorption induced dissociation displays similar fragment intensity ratios compared to the pump-only fragmentation pattern, the probe-enhanced fragmentation signal seems to be mainly governed by the increase in internal energy of the ions. This is observed for primary (NLP, IFp) as well as secondary (NLS, IFs) fragment ions which indicates that the signal intensity of the latter fragments also reflects the dynamics of the primary processes and further supports our comprehensive analysis based on the total fragment yield which will be discussed in the following.

Fig. 6 depicts the channel specific τ -PD transients as well as the corresponding trace for the total fragment yield (TFY), *i.e.* sum of all fragment channel signals, upon resonant excitation at 260 nm. From a detailed fitting analysis of all of these traces we conclude that the transients of the different channels can be

reduced to a general time evolution scheme based on four decay constants (τ_1 – τ_4) that are very similar for all traces but differ in their respective weighting amplitudes (A_1 – A_4 , see Fig. S23, S26 and Table S5, ESI †). Also, the TFY transient could be mathematically best reproduced by a tetra-exponential decay fit (*cf.* Experimental methods) revealing four, each by an order of magnitude separated, time constants on ultrafast, intermediate, slow and ns timescales, respectively (τ_1 – τ_4 : 0.55(2), 5.8(4), 100(7), > 1000 ps, Table 3). A direct comparison between tri- and tetra-exponential decay fits as well as residuals is shown in the ESI † (*cf.* Fig. S24). Technically, the fragment-specific transients were now globally fitted using the fixed lifetimes obtained from the TFY-fit while releasing ordinate offsets and amplitudes. Fits to these traces illustrating the individual contributions of the time constants (τ_1 – τ_4) are additionally plotted (Fig. 6). Hereby, a good agreement between tetra-exponential fits and channel specific transient signals were observed for nearly all primary and also for secondary fragmentation channels (with the largest deviation being noticed for the fragment m/z 310). A rationalization for this apparent variation in the amplitudes over the different fragment channels could be only given by detailed consideration of the signal-generating process for pump-probe fragmentation action spectroscopy (τ -PD). The amplitudes related to the time constants and thus electronically excited state lifetimes do not exclusively reflect populations, but give additionally differences in excited state cross sections or differences in the number and type of higher lying excited states reachable for the probe laser interrogation. This could lead to an individual fragmentation pattern for a specific electronically excited state (see Fig. S23, ESI †). For example, the high ratio of amplitudes of τ_1/τ_4 in m/z 211 and m/z 819 means that the first/short-lived state is fragmenting stronger into this channel than the long-lived state (τ_4). On the other hand, for m/z 407 and m/z 623 the τ_1 and τ_4 amplitudes are very similar. In this way, the “fragment pattern/spectrum” reflects to some extent an excited state spectrum, as known from TA and thus global fitting should be suitable. However, the cross sections and also the higher electronic states are generally not known and the probe absorption is not necessarily resonant, but of multi-photon character. The current status of our research renders a more detailed modelling of the signal-generating process not possible. Nonetheless, the comprehensive and consistent fitting result comprising all

Table 3 Comparison of relaxation time constants as a function of excitation wavelength (λ_{pump}) and environment (gas phase/solution) for kinetic fits shown in Fig. 8 and 9. Errors given in parentheses correspond to standard errors. Normalized amplitudes are defined as $nA_i = A_i/(\sum A_i) \times 100$. The respective widths (fwhm) of fitted instrument response functions (IRF, Gaussian) are indicated

$\lambda_{\text{pump}}/\text{nm}$	In vacuum			In MeCN
	245	260	275	262
τ_1/ps , ($nA_1/\%$)	0.49(5), (55)	0.55(2), (53)	0.4(1), (39)	0.9(1)
τ_2/ps , ($nA_2/\%$)	4(1), (18)	5.8(4), (21)	4.3(7), (22)	8.5(1)
τ_3/ps , ($nA_3/\%$)	35(9), (14)	100(7), (14)	68(6), (20)	73(2)
τ_4/ps , ($nA_4/\%$)	515(43), (13)	1564(94), (12)	1162(56), (19)	604(18)
IRF: fwhm/fs	158(10)	185(5)	162(29)	150(25)

major transient fragment signals gives us confidence that the recorded change in total fragment yields by τ -PD reflects the intrinsic relaxation dynamics of the initially excited state $^1\text{MC}(\text{d}\sigma^*-\text{p}\sigma)$ of $[\text{Ag}_2(\text{dcpm})_2]^{2+}$ under ion trap conditions. The remarkable result is, that we observe an intrinsically multi-exponential electronic relaxation after photoexcitation of isolated $[\text{Ag}_2(\text{dcpm})_2]^{2+}$ with time constants from the sub-ps to the ns regime (see Table 3) which points to the involvement of several excited states and a complex pathway already for this “naked” silver-centered chromophore.

In order to learn more on the nature of the underlying excited state processes we have performed τ -PD studies at different pump wavelengths within the UV absorption band of the complex. The τ -PD traces at $\lambda_{\text{pump}} = 245$ and 275 nm, respectively, obtained by exciting at the edges of the absorption band reveal similar tetra-exponential decay dynamics (Fig. 7(a) and (c)). The relevant fit parameters are summarized in Table 3. Hereby, the short and intermediate time constant (averaged: $\tau_1 \sim 0.5$ ps, $\tau_2 \sim 5$ ps) are nearly not affected by excitation wavelength, whereas τ_3 and τ_4 significantly decrease at higher, but also at lower excitation energy. Notably, an increase of the TFY by a factor of ~ 6 ($\text{TFY}_{(\text{pu}+\text{pr})}/\text{TFY}_{\text{pu}}$) is observed at time zero, independent of the pump wavelength ($\lambda_{\text{pu}} = 245, 260, 275$ nm, respectively), while the best S/N ratio is observed for excitation at the absorption maximum at 260 nm. This behavior suggests that the same excited state is populated by pump excitation of different absorption cross sections depending on the excitation wavelength.

3.5 Transient absorption (TA) spectroscopy in acetonitrile

Transient absorption measurements on $[\text{Ag}_2(\text{dcpm})_2]^{2+}$ in acetonitrile with excitation at 262 nm were performed between 330 and 600 nm with pump-probe delay times up to 1.2 ns. Absorbance difference spectra (ADS) at various delay times and corresponding absorbance transients at selected probe wavelengths are shown in Fig. 8 (top) and Fig. 9, respectively. The ADS data show an instantaneous rise of excited state absorption (ESA) between *ca.* 440 and 600 nm which decays multiexponentially in the covered time range. The early evolution is different around 350 nm where an initial signal increase (caused by decay of stimulated emission (SE) or rise of ESA) within tens of picoseconds and a concomitant spectral red-shift of absorbance strength is observed with a subsequent slow signal decay. At 1 ns time delay a strong residual product spectrum with a life-time much longer than 1 ns is observed. The absorbance transients at 355, 420 and 600 nm (Fig. 9) illustrate the complex and progressive dynamics of photoexcited $[\text{Ag}_2(\text{dcpm})_2]^{2+}/\text{MeCN}$ with spectrally varying ESA/SE contributions.

Global analysis (*cf.* Experimental methods) reveals decay associated spectra A_1 – A_4 and A_0 (Fig. 8 (bottom)). Best fit results were obtained with a sum of four exponentials, *i.e.* $\tau_1 = 0.9 \pm 0.1$ ps, $\tau_2 = 8.5 \pm 0.1$ ps, $\tau_3 = 73 \pm 2$ ps and $\tau_4 = 604 \pm 18$ ps, whereas three exponentials led to significant fit residua. This is supported by SVD analysis. A_1 and A_2 are of small amplitude and of similar spectral shape with a distinct negative band around 360 nm and positive absorbance strength above *ca.* 440 nm. They reflect the early signal

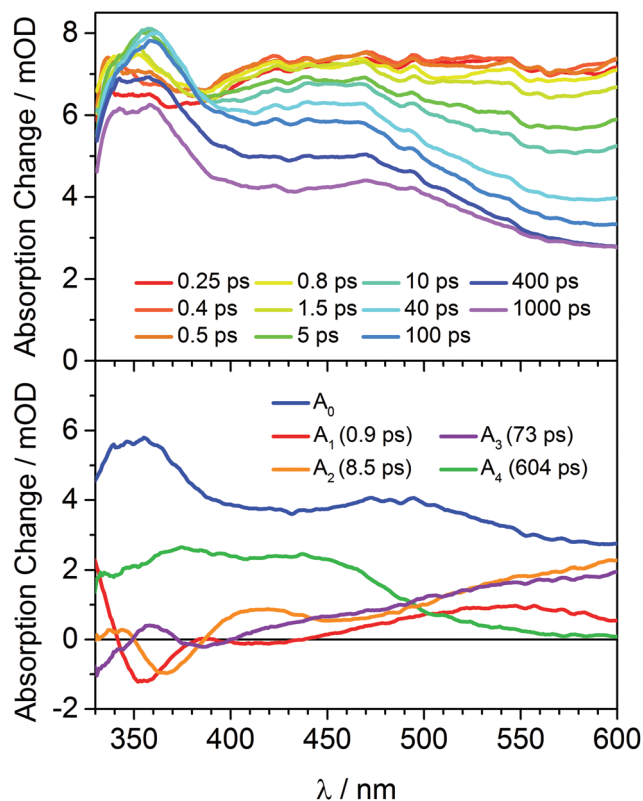


Fig. 8 (top) TA difference spectra of $[\text{Ag}_2(\text{dcpm})_2](\text{PF}_6)_2$ (MeCN, $\lambda_{\text{ex}} = 262$ nm) at various pump-probe time delays (colored solid lines). (bottom) Decay associated spectra (DAS) obtained from global analysis (tetra-exponential model, *cf.* Experimental methods). Related time constants τ_1 – τ_4 (*cf.* Table 3) are indicated in parentheses.

evolution with τ_1 and τ_2 in the respective spectral regions of the difference spectra in Fig. 8 (top) as described above. Considering this timescale and the spectral characteristics, these dynamics are assigned to decay of SE or rise of ESA below, and decay of ESA above *ca.* 440 nm. Assuming ESA changes as dominating processes, the observed spectro-temporal evolution is consistent with blue-shifting absorption strength in the course of interconverting consecutive excited electronic states or by intramolecular vibrational relaxation and vibrational cooling. A_3 and A_4 comprise spectrally complementary absorbance strength (ESA) in the low- and high energy region. A_0 , the strongest and long living component ($\gg 1$ ns) extends over the entire spectral range with increasing ESA strength in the high energy region.

4. Discussion of dynamics in gas phase and solution

Gas phase (ion trap)

Based on the results of the τ -PD experiments in gas phase and the quantum chemical calculations we like to propose different scenarios for ultrafast relaxation pathways that are conceivable in isolated photoexcited $[\text{Ag}_2(\text{dcpm})_2]^{2+}$ ions after UV photoexcitation (Fig. 10, left). We leave out the largest time constant because its determination contains a significant error due to

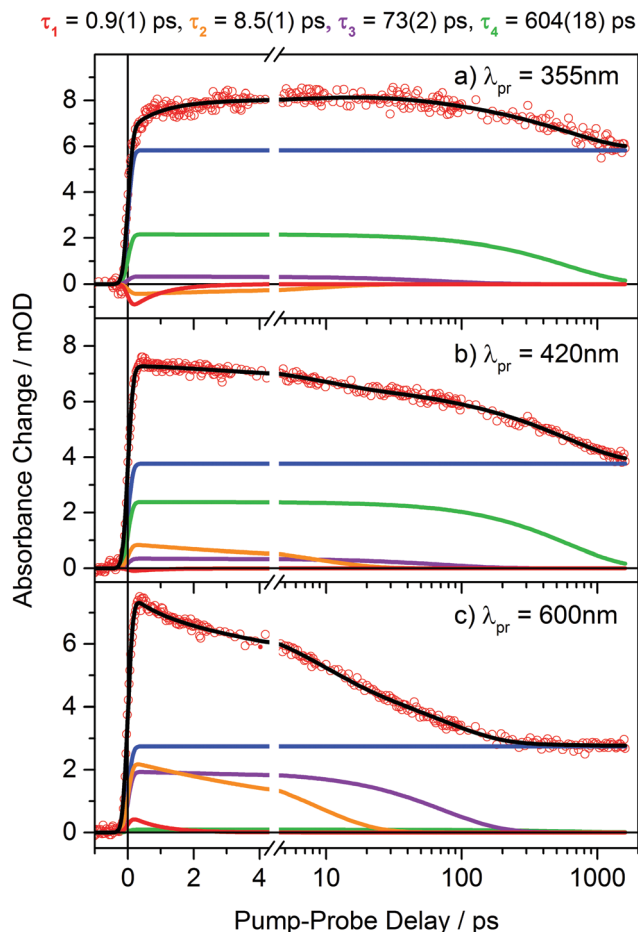


Fig. 9 Absorption transients of $[\text{Ag}_2(\text{dcpm})_2](\text{PF}_6)_2$ (MeCN, $\lambda_{\text{ex}} = 262$ nm) for selected wavelengths (a) 355 nm, (b) 420 nm and (c) 600 nm (see Fig. 8). Tetraexponential global fit (black lines, cf. Table 3) and individual decay contributions ($\tau_1 = 0.9$ ps, red; $\tau_2 = 8.5$ ps, orange; $\tau_3 = 73$ ps, purple; $\tau_4 = 604$ ps, green; constant offset, blue) are plotted. Errors given in parentheses correspond to standard errors.

the limited experimental delay time and its small amplitude, so that its correct physical value is rather vague.

Firstly, photoexcitation into the S_2 state ($^1\text{MC}(\text{d}\sigma^*-\text{p}\sigma)$, experimental $\lambda_{\text{abs.}} \sim 260$ nm) generates ions with approximately 0.22 eV of excess energy (1774 cm^{-1} , vertical transition – adiabatic transition as estimated from CC2 calculations, cf. Table 2) with presumably vibrational excitation in the Ag–Ag mode (ca. 10–12 quanta, $\nu_{(\text{Ag}-\text{Ag})} = 150\text{--}180 \text{ cm}^{-1}$).¹⁹

From this starting point we can invoke different possible ways for the molecular system to relax into the lowest triplet manifold. These pathways are sketched in the state diagram in Fig. 10 (left), but have to be regarded as mere combinations constructed from the experimental time constants (three processes, each with order of magnitude difference in kinetics) and the theoretically derived energy levels (two singlet states, two triplet states) within the accessible energy region. For these gas phase dynamics data additional information, e.g. from gas phase luminescence,^{49,51} could be of help in the future for assignment of the obtained time constants to elementary processes. The strategy of this work is to combine quantum chemical calculations and TA dynamics from solution with our gas phase results. However, the general lack of ultrafast data for such systems (i.e., multinuclear coinage metal phosphine complexes) with the exception of ref. 20, 28 and 52–54, in particular, the lack of relevant gas phase data renders this evaluation quite challenging. One considerable aspect is that the gas phase investigations are performed on microcanonical systems (constant energy, at least for the timescale of the electronic dynamics), whereas in solution energy transfer to the solvent is significant, often efficient and can start immediately after excitation. However, we believe that the eight cyclohexyl substituents on the phosphine ligands may act like an enormous dissipative heat bath so that the dynamics in both phases become comparable. This justifies the non-horizontally arrows drawn for the different processes in Fig. 10 (left) taking place under gas

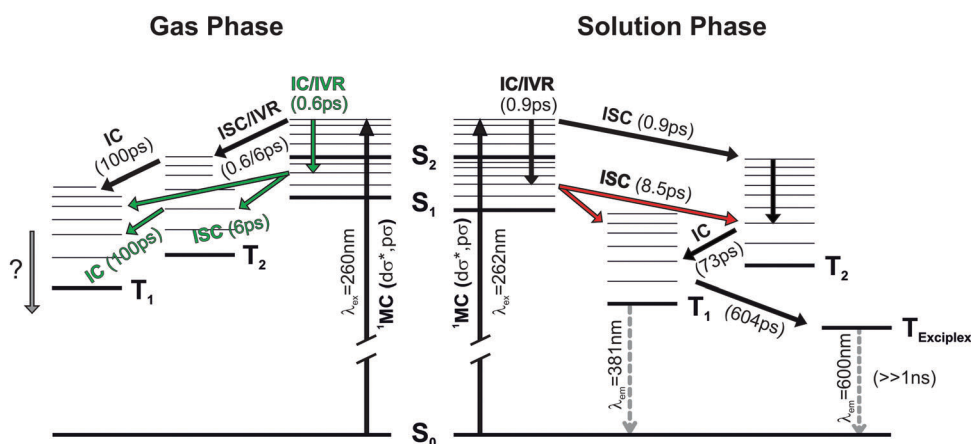


Fig. 10 Proposed simplified excited state deactivation pathways and timescales for the $^1\text{MC}(\text{d}\sigma^*-\text{p}\sigma)$ excited state of $[\text{Ag}_2(\text{dcpm})_2]^{2+}$ in gas phase (left) and in MeCN at room temperature (right). Gas phase: different alternative sequential pathways are indicated by black and green arrows, respectively. Deactivation via either routes proceeding in parallel cannot be excluded. Gray arrow indicates deactivation processes on timescales beyond our experimentally accessible timeframe. Note that the total internal energy of excited gaseous ions remains constant within our ps timeframe of observation. Hence, vertical and diagonal arrows are mainly drawn for stylistic reasons. Solution phase: red arrows indicate alternative paths for processes correlated with τ_2 (8.5 ps). Dashed gray lines indicate luminescence (cf. Fig. S1, ESI†).

phase conditions. At the current status of our research we have to leave the interpretation on this basic descriptive level.

Thus, the short time constant τ_1 could be ascribed to an efficient ISC, not unusual for metal containing complexes and recently assigned to the Au_2 congener in solution,²⁰ or IVR within the S_2 state or IC to the dark, lower energy S_1 state. We cannot give a clear preference for any of these first steps. The ISC time constant for the related d^8-d^8 $[\text{Pt}_2(\text{pop})_4]^{4-}$ complex in gas phase has been estimated to be 0.7 ps.⁵⁵ A similar rate was recently reported for MeCN solution, whereas a strong solvent influence, slowing down ISC by more than a factor of 10, was found for other solvents.^{15,16,56} In other recent accounts, a two-channel reaction model for ISC in $[\text{Pt}_2(\text{pop})_4]^{4-}$ was suggested. It contained a direct, temperature independent ISC path and a parallel temperature dependent way *via* a deactivating, yet unknown, state.^{16,57}

In summary, for $[\text{Ag}_2(\text{dcpm})_2]^{2+}$ we propose that both of the first two time constants (τ_1 , τ_2) are probably related to the ISC process and preceding or following IVR/IC. An activation barrier could not be observed. From our calculations we would estimate upon triplet formation the total excess energy to be $\sim 6200 \text{ cm}^{-1}$ (4.67–3.90 eV, Table 2). Furthermore, the third time constant τ_3 is certainly related to IVR/IC redistribution within the triplet manifold. We have found, albeit with less accuracy, additionally a ns time component (τ_4) which could be ascribed tentatively to the return (*via* ISC) to the electronic ground state. This first working model within the experimental and theoretical constraints gives possible intrinsic electronic relaxation pathways for $[\text{Ag}_2(\text{dcpm})_2]^{2+}$ in gas phase but has to be refined by further experiments and calculations. However, it should be emphasized that its dynamics is (already) intrinsically of multiexponential nature.

Solution (acetonitrile)

Solute–solvent interaction is anticipated to alter structure and electronic state energies of the isolated $[\text{Ag}_2(\text{dcpm})_2]^{2+}$ complex, thereby modulating its static properties as well as the relaxation dynamics after photoexcitation, and invoking additional deactivation pathways.

As described above (Fig. 5), the solvatochromic shift of electronic ground state absorption in MeCN compared to the isolated species is only small (*ca.* -450 cm^{-1}), whereas luminescence is observed at 381 nm and, weaker, at 600 nm (Fig. S1, ESI[†]). Both luminescence bands originate from the same excited state as shown by the accordance between their excitation spectra and the ground state absorption spectrum (in MeCN), peaking at 261 nm (Fig. S2, ESI[†]). Since the absorption spectra of isolated $[\text{Ag}_2(\text{dcpm})_2]^{2+}$ and the complex in solution are basically identical (Fig. 5), the observed dual luminescence is not due to an inhomogeneous ground state distribution in solution but rather due to the formation of two different luminescent molecular species after excitation of $[\text{Ag}_2(\text{dcpm})_2]^{2+}$.

Dual luminescence with emission wavelengths similarly red-shifted with respect to ground state absorption has been observed earlier for a number of related phosphine–ligand supported metal complexes $[\text{M}_2(\text{dcpm})_2]$ ($\text{M} = \text{Cu}, \text{Ag}, \text{Au}$) in

solution.^{20–22,58,59} The common photophysical feature of these systems is the $^1\text{MC}(d\sigma^*-p\sigma)$ electronic transition, leading to a shortening of the M–M bond,^{19,21} giving grounds to expect similar mechanisms for intra- and intermolecular molecular relaxation pathways. The strongly red-shifted luminescence bands have been attributed to exciplex formation between the excited complex and solvent molecules on a fast, picoseconds time-scale or dissolved anions/counterions on slower time-scales.^{58,59}

For example, Ma *et al.*²⁰ suggested sub-ps ISC for photo-excited ($\lambda_{\text{exc}} = 280 \text{ nm}$) $[\text{Au}_2(\text{dcpm})_2]^{2+}$ in MeCN and formation ($\sim 4 \text{ ps}$) of a long living solute–solvent exciplex exhibiting a very broad luminescence around 480 nm. These findings were supported by quantum chemical calculations on the photo-excited $[\text{Au}_2(\text{dpm})_2]^{2+}$ model system (dpm = bis(diphosphino)-methane) interacting with MeCN molecules, revealing luminescence strongly red-shifted with respect to that in the absence of MeCN.⁶⁰

For a different d^8-d^8 complex ($[\text{Ir}_2(\text{dimen})_4]^{2+}$, dimen = *para*-diisocyanomethane) recently a microscopic scenario for the solvation relaxation was presented based on ultrafast diffuse X-ray scattering.¹³ QM/MM calculations on this (excited) complex in MeCN showed the fast (a few ps) reorientation of an Ir-coordinating solvent molecule, rapidly adapting to the altered electron density distribution, the contraction of the Ir–Ir bond and the accompanying pronounced ligand deformation. We note that the dimen ligands, in contrast to the dcpm ligands used in this study, are very flexible with small moments of inertia and therefore easily distorted and are, due to the polar isocyanide groups, themselves interacting with the solvent.¹³

In turn for the $[\text{Ag}_2(\text{dcpm})_2]^{2+}$ complex under study, our calculations for the unsolvated species reveal (vertical) emission from the $T_2(^3\text{B})$ at 345 nm with (vertical) ground state absorption at 266 nm (experiment: 261 nm, Table 2). The additional red-shift to the observed emission at 381 nm is likely linked to interaction with the solvent. Thus, our observation of dual luminescence and multiexponential kinetics on time-scales up to the nanosecond regime is consistent with firstly fast substrate (MeCN) binding of the excited complex and secondly slower formation of a long living ($> 1 \text{ ns}$) anion (counterion) exciplex with even more red-shifted luminescence.

Besides its impact on “static” absorption and emission, solvent-induced alteration of electronic coupling brings along changes of transition rates between electronic states and corresponding kinetic branching ratios. This concerns in particular IC and ISC as exemplified for the related $d^{10}-d^{10}$ Au_2 complex²⁰ and the d^8-d^8 Pt_2 complex (*cf.* above). In addition, collision-assisted intra- and intermolecular energy redistribution and relaxation (including vibrational cooling) in molecules of this size, affects, and in general accelerates, the relaxation dynamics on time-scales up to 20 ps or more.^{61–65} Thus, given the number of the most probably participating excited electronic states (S_2, S_1, T_2, T_1), at present the proposed kinetic scheme given in Fig. 10 (right) can only be of preliminary character. Based on the features in A_1 and A_2 we suggest two intersystem crossing pathways, followed by internal

conversion within the triplet manifold. We propose the formation of long living exciplexes of the excited $[\text{Ag}_2(\text{dcpm})_2]^{2+}$ complex and a solvent molecule, as suggested for the Au_2 congener in MeCN ,²⁰ or an available counterion. Note, that this simplified kinetic scheme incorporates, without contradiction, essential features of the gas-phase working model shown in Fig. 10 (left).

In addition, we note that no vibrational wavepacket dynamics has been observed for $[\text{Ag}_2(\text{dcpm})_2]^{2+}$ by us, neither in solution nor in gas phase. This is remarkable, since the complex displays a pronounced metal–metal geometry change which is held responsible for the observation of coherent wavepackets in the related $[\text{Ir}_2(\text{dimen})_4]^{2+}$ and $[\text{Pt}_2(\text{pop})_4]^{4-}$ binuclear complexes.^{15,66} Coherent nuclear vibrations have also been observed for excited-state complexes of $[\text{Au}(\text{CN})_2^-]_2$ and $[\text{Au}(\text{CN})_2^-]_3$ induced by strong Au–Au interaction.^{28,52–54}

We tentatively ascribe the distinct behavior of $[\text{Ag}_2(\text{dcpm})_2]^{2+}$ to the efficient “heat sink” of the ligand moiety which is strongly coupled to damp the Ag stretch by ligand backbone bending and dissipation into low frequency cyclohexyl modes. Further intricacies for observation of vibrational wavepackets in such systems have been treated by QM/MM simulations in a recent contribution.⁶⁷ It should be noted, however, that we recently reported in a preliminary study the observation of wavepackets upon counterion modification of the binuclear metal scaffold.³⁶

In summary, the remarkable similarity of the specific number and the values of the time constants observed for the isolated and the solvated (MeCN) $[\text{Ag}_2(\text{dcpm})_2]^{2+}$ complex by τ -PD and TA, respectively, suggests that its photoinduced relaxation dynamics is dominated by intramolecular processes, presumably involving transitions between the electronic states S_2 , S_1 , T_2 and T_1 as well as intramolecular energy redistribution. In solution, the initiated intramolecular dynamics are probably modulated by intermolecular interactions, such as exciplex formation, solvation and vibrational cooling.

5. Conclusion

Our results for a binuclear d^{10} – d^{10} complex provide interesting and complex primary photophysics and -chemistry. This is caused by metal–metal interaction, which gives rise to specific and strong metal-centered $^1\text{MC}(d\sigma^*-\text{p}\sigma)$ electronic transitions, a pronounced geometry change and coupling to other singlet and triplet states as well as, in solution, a multitude of subsequent or parallel intermolecular processes. For a better understanding of the dynamics we present here an approach combining high level quantum-chemical calculations for characterization of relevant electronic states with both gas phase and solution fs time-resolved pump–probe spectroscopy, exemplified on the $[\text{Ag}_2(\text{dcpm})_2]^{2+}$ complex. It had been chosen for its spectroscopically “silent” ligand sphere and with the goal to unravel experimentally intra- and intermolecular dynamics with a strong support from theory for evaluation of the intrinsic molecular properties.

The results from the quantum chemical CC2 method applied to the structurally simplified model system $[\text{Ag}_2(\text{dmpm})_2]^{2+}$

provided accurate excited state energies and geometries and reproduced nicely the experimental UV absorption spectrum for $[\text{Ag}_2(\text{dcpm})_2]^{2+}$. The computational results are also in qualitative agreement with former results on simpler model systems. However, we report on an additional, energetically lower, dark singlet state (S_1) with $^1\text{MC}(d\sigma^*-\text{p}\pi)$ character, that could be accessed *via* electronic relaxation and might be involved in the deactivation dynamics. The obtained two, nearly degenerate, triplet states account for the reported luminescence and subsequent internal conversion dynamics.

The gas phase results by CID and τ -PD have been carefully analyzed with respect to all fragment channels. We scrutinized the fragmentation pathways and found strong support for their usage as reporters of transient dynamics, also benchmarking the τ -PD method. As result of the multiexponential fitting of the total fragment yield decay curve, we report time constants 0.6/5.8/100/>1000 ps for $\lambda_{\text{ex}} = 260$ nm.

The acetonitrile solution results by TA show broad excited state absorptions that give by global fitting comparable dynamics with time constants 0.9/8.5/73/604 ps. The solvent is involved by stabilization of levels (see triplet emission) and by cooling, *i.e.* transfer of excess energy. On the longer time-scales probably exciplex formation sets in.

As we demonstrate here, at least for this specific binuclear complex, already the isolated system exhibits intricate, multi-step dynamics after photoexcitation, emphasizing its intrinsic, intramolecular deactivation pathways and mechanisms. Thus, our approach to combine quantum chemical, gas phase and solution studies for one particular complex is an important step forward to disentangle intramolecular (metal chromophore and ligand related) and intermolecular (solvent and counterion related) processes in the important class of luminescing metal–metal complexes. We put here for the first time $[\text{Ag}_2(\text{dcpm})_2]^{2+}$ into the spotlight of ultrafast spectroscopy and provide the application of a new methodology for the exploration of the photodynamics of multi-metallic chromophores. Work will be expanded by employing related binuclear complexes under systematic variation of the metal ions, ligands, counter ions and solvent.

Conflicts of interest

There are no conflicts to declare.

Acknowledgements

We like to thank for financial support by the DFG-funded transregional collaborative research center SFB/TRR 88 “Cooperative Effects in Homo- and Heterometallic Complexes (3MET)” (projects C1, C4 and B2). We are also thankful to the Stiftung Rheinland-Pfalz für Innovation (Project 965) for funding. Dr Yevgeniy Nosenko is acknowledged for technical support and fruitful collaboration. We thank Cedric Groß for measurement of NMR spectra and Björn Kwasigroch for supporting DFT calculations.

References

- 1 K. Duanmu and D. G. Truhlar, *J. Phys. Chem. C*, 2015, **119**, 9617–9626.
- 2 A. Zavras, A. Ariafard, G. N. Khairallah, J. M. White, R. J. Mulder, A. J. Canty and R. A. J. O'Hair, *Nanoscale*, 2015, **7**, 18129–18137.
- 3 S. Daly, M. Krstić, A. Giuliani, R. Antoine, L. Nahon, A. Zavras, G. N. Khairallah, V. Bonacic-Koutecky, P. Dugourd and R. A. J. O'Hair, *Phys. Chem. Chem. Phys.*, 2015, **17**, 25772–25777.
- 4 L.-J. Xu, J.-Y. Wang, L.-Y. Zhang, L.-X. Shi and Z.-N. Chen, *Organometallics*, 2013, **32**, 5402–5408.
- 5 S. Sculfort and P. Braunstein, *Chem. Soc. Rev.*, 2011, **40**, 2741–2760.
- 6 J.-H. Jia and Q.-M. Wang, *J. Am. Chem. Soc.*, 2009, **131**, 16634–16635.
- 7 C. Kiefer, S. Bestgen, M. T. Gamer, M. Kühn, S. Lebedkin, F. Weigend, M. M. Kappes and P. W. Roesky, *Chem. – Eur. J.*, 2017, **23**, 1591–1603.
- 8 H. Al Sharif, K. L. Vikse, G. N. Khairallah and R. A. J. O'Hair, *Organometallics*, 2013, **32**, 5416–5427.
- 9 V. W.-W. Yam, V. K.-M. Au and S. Y.-L. Leung, *Chem. Rev.*, 2015, **115**, 7589–7728.
- 10 V. Wing-Wah Yam and K. Kam-Wing Lo, *Chem. Soc. Rev.*, 1999, **28**, 323–334.
- 11 P. Pyykkö, *Angew. Chem., Int. Ed.*, 2004, **43**, 4412–4456.
- 12 P. Pyykkö and Y. Zhao, *Angew. Chem., Int. Ed. Engl.*, 1991, **30**, 604–605.
- 13 T. B. van Driel, K. S. Kjær, R. W. Hartsock, A. O. Dohn, T. Harlang, M. Chollet, M. Christensen, W. Gawelda, N. E. Henriksen, J. G. Kim, K. Haldrup, K. H. Kim, H. Ihee, J. Kim, H. Lemke, Z. Sun, V. Sundström, W. Zhang, D. Zhu, K. B. Møller, M. M. Nielsen and K. J. Gaffney, *Nat. Commun.*, 2016, **7**, 13678.
- 14 M. A. F. D. R. Pinto, P. J. Sadler, S. Neidle, M. R. Sanderson, A. Subbiah and R. Kuroda, *J. Chem. Soc., Chem. Commun.*, 1980, 13–15.
- 15 R. M. van der Veen, A. Cannizzo, F. van Mourik, A. Vlček and M. Chergui, *J. Am. Chem. Soc.*, 2011, **133**, 305–315.
- 16 H. B. Gray, S. Zálíš and A. Vlček, *Coord. Chem. Rev.*, 2017, **345**, 297–317.
- 17 P. D. Harvey and H. B. Gray, *J. Am. Chem. Soc.*, 1988, **110**, 2145–2147.
- 18 C.-M. Che, M.-C. Tse, M. C. W. Chan, K.-K. Cheung, D. L. Phillips and K.-H. Leung, *J. Am. Chem. Soc.*, 2000, **122**, 2464–2468.
- 19 D. L. Phillips, C.-M. Che, K. H. Leung, Z. Mao and M.-C. Tse, *Coord. Chem. Rev.*, 2005, **249**, 1476–1490.
- 20 C. Ma, C. T.-L. Chan, W.-P. To, W.-M. Kwok and C.-M. Che, *Chem. – Eur. J.*, 2015, **21**, 13888–13893.
- 21 Q.-J. Pan, H.-X. Zhang, H.-G. Fu and H.-T. Yu, *Eur. J. Inorg. Chem.*, 2006, 1050–1059.
- 22 W.-F. Fu, K.-C. Chan, V. M. Miskowski and C.-M. Che, *Angew. Chem., Int. Ed.*, 1999, **38**, 2783–2785.
- 23 H. Schmidbaur and A. Schier, *Angew. Chem., Int. Ed.*, 2015, **54**, 746–784.
- 24 C. Yue, C. Yan, R. Feng, M. Wu, L. Chen, F. Jiang and M. Hong, *Inorg. Chem.*, 2009, **48**, 2873–2879.
- 25 V. W.-W. Yam and K. K.-W. Lo, *Coord. Chem. Rev.*, 1999, **184**, 157–240.
- 26 K. K.-W. Lo, A. W.-T. Choi and W. H.-T. Law, *Dalton Trans.*, 2012, **41**, 6021–6047.
- 27 V. W.-W. Yam, S. W.-K. Choi, K. K.-W. Lo, W.-F. Dung and R. Y.-C. Kong, *J. Chem. Soc., Chem. Commun.*, 1994, 2379–2380.
- 28 M. Iwamura, R. Wakabayashi, J. Maeba, K. Nozaki, S. Takeuchi and T. Tahara, *Phys. Chem. Chem. Phys.*, 2016, **18**, 5103–5107.
- 29 Y. Nosenko, C. Riehn and W. Klopper, *Chem. Phys. Lett.*, 2016, **659**, 55–60.
- 30 D. Imanbaew, J. Lang, M. F. Gelin, S. Kaufhold, M. G. Pfeffer, S. Rau and C. Riehn, *Angew. Chem., Int. Ed.*, 2017, **56**, 5471–5474.
- 31 D. Nolting, R. Weinkauff, I. V. Hertel and T. Schultz, *ChemPhysChem*, 2007, **8**, 751–755.
- 32 D. Nolting, T. Schultz, I. V. Hertel and R. Weinkauff, *Phys. Chem. Chem. Phys.*, 2006, **8**, 5247–5254.
- 33 H. Kang, C. Juvet, C. Dedonder-Lardeux, S. Martrenchard, C. Charrière, G. Grégoire, C. Desfrancois, J. P. Schermann, M. Barat and J. A. Fayeton, *J. Chem. Phys.*, 2005, **122**, 084307.
- 34 C. Daniel and C. Gourlaouen, *Coord. Chem. Rev.*, 2017, **344**, 131–149.
- 35 Y. Nosenko, F. Menges, C. Riehn and G. Niedner-Schatteburg, *Phys. Chem. Chem. Phys.*, 2013, **15**, 8171–8178.
- 36 S. V. Kruppa, F. Böppler, Y. Nosenko, S. P. Walg, R. Diller and C. Riehn, *International Conference on Ultrafast Phenomena*, 2016, UW4A.33.
- 37 S. V. Kruppa, Y. Nosenko, M.-O. Winghart, S. P. Walg, M. M. Kappes and C. Riehn, *Int. J. Mass Spectrom.*, 2016, **395**, 7–19.
- 38 G. S. M. Tong, S. C. F. Kui, H.-Y. Chao, N. Zhu and C.-M. Che, *Chem. – Eur. J.*, 2009, **15**, 10777–10789.
- 39 Q.-J. Pan and H.-X. Zhang, *J. Phys. Chem. A*, 2004, **108**, 3650–3661.
- 40 O. Christiansen, H. Koch and P. Jørgensen, *Chem. Phys. Lett.*, 1995, **243**, 409–418.
- 41 C. Hättig and F. Weigend, *J. Chem. Phys.*, 2000, **113**, 5154–5161.
- 42 F. Furche, R. Ahlrichs, C. Hättig, W. Klopper, M. Sierka and F. Weigend, *Wiley Interdiscip. Rev.: Comput. Mol. Sci.*, 2014, **4**, 91–100.
- 43 TURBOMOLE v6.5 2013, a development of University Karlsruhe and Forschungszentrum Karlsruhe GmbH 1989–2007, TURBOMOLE GmbH, since 2007, available from www.turbomole.com.
- 44 F. Weigend and R. Ahlrichs, *Phys. Chem. Chem. Phys.*, 2005, **7**, 3297–3305.
- 45 D. Andrae, U. Häussermann, M. Dolg, H. Stoll and H. Preuß, *Theor. Chim. Acta*, 1990, **77**, 123–141.
- 46 A. Zavras, G. N. Khairallah, M. Krstić, M. Girod, S. Daly, R. Antoine, P. Maitre, R. J. Mulder, S.-A. Alexander, V. Bonačić-Koutecký, P. Dugourd and R. A. J. O'Hair, *Nat. Commun.*, 2016, **7**, 11746.
- 47 K. Hemelsoet, F. Van Durme, V. Van Speybroeck, M.-F. Reyniers and M. Waroquier, *J. Phys. Chem. A*, 2010, **114**, 2864–2873.

- 48 G. Cui, X.-Y. Cao, W.-H. Fang, M. Dolg and W. Thiel, *Angew. Chem., Int. Ed.*, 2013, **52**, 10281–10285.
- 49 S. M. J. Wellman and R. A. Jockusch, *J. Phys. Chem. A*, 2015, **119**, 6333–6338.
- 50 D. Piché and P. D. Harvey, *Can. J. Chem.*, 1994, **72**, 705–713.
- 51 J.-F. Greisch, J. Chmela, M. E. Harding, W. Kloppe, M. M. Kappes and D. Schooss, *Inorg. Chem.*, 2016, **55**, 3316–3323.
- 52 M. Iwamura, K. Nozaki, S. Takeuchi and T. Tahara, *J. Am. Chem. Soc.*, 2013, **135**, 538–541.
- 53 K. H. Kim, J. G. Kim, K. Y. Oang, T. W. Kim, H. Ki, J. Jo, J. Kim, T. Sato, S. Nozawa, S.-i. Adachi and H. Ihee, *Struct. Dyn.*, 2016, **3**, 043209.
- 54 K. H. Kim, J. G. Kim, S. Nozawa, T. Sato, K. Y. Oang, T. W. Kim, H. Ki, J. Jo, S. Park, C. Song, T. Sato, K. Ogawa, T. Togashi, K. Tono, M. Yabashi, T. Ishikawa, J. Kim, R. Ryoo, J. Kim, H. Ihee and S.-i. Adachi, *Nature*, 2015, **518**, 385–389.
- 55 M.-O. Winghart, J.-P. Yang, M. Vonderach, A.-N. Unterreiner, D.-L. Huang, L.-S. Wang, S. Kruppa, C. Riehn and M. M. Kappes, *J. Chem. Phys.*, 2016, **144**, 054305.
- 56 R. Monni, G. Auböck, D. Kinschel, K. M. Aziz-Lange, H. B. Gray, A. Vlček and M. Chergui, *Chem. Phys. Lett.*, 2017, **683**, 112–120.
- 57 Y. C. Lam, H. B. Gray and J. R. Winkler, *J. Phys. Chem. A*, 2016, **120**, 7671–7676.
- 58 W.-F. Fu, K.-C. Chan, K.-K. Cheung and C.-M. Che, *Chem. – Eur. J.*, 2001, **7**, 4656–4664.
- 59 C.-M. Che and S.-W. Lai, *Coord. Chem. Rev.*, 2005, **249**, 1296–1309.
- 60 H.-X. Zhang and C.-M. Che, *Chem. – Eur. J.*, 2001, **7**, 4887–4893.
- 61 A. Pigliucci, G. Duvanel, L. M. L. Daku and E. Vauthey, *J. Phys. Chem. A*, 2007, **111**, 6135–6145.
- 62 S. A. Kovalenko, R. Schanz, H. Hennig and N. P. Ernsting, *J. Chem. Phys.*, 2001, **115**, 3256–3273.
- 63 M. M. N. Wolf, R. Groß, C. Schumann, J. A. Wolny, V. Schünemann, A. Døssing, H. Paulsen, J. J. McGarvey and R. Diller, *Phys. Chem. Chem. Phys.*, 2008, **10**, 4264–4273.
- 64 M. Zimmer, F. Rupp, P. Singer, F. Walz, F. Breher, W. Kloppe, R. Diller and M. Gerhards, *Phys. Chem. Chem. Phys.*, 2015, **17**, 14138–14144.
- 65 D. Imanbaev, Y. Nosenko, C. Kerner, K. Chevalier, F. Rupp, C. Riehn, W. R. Thiel and R. Diller, *Chem. Phys.*, 2014, **442**, 53–61.
- 66 R. W. Hartsock, W. Zhang, M. G. Hill, B. Sabat and K. J. Gaffney, *J. Phys. Chem. A*, 2011, **115**, 2920–2926.
- 67 A. O. Dohn, E. Ö. Jónsson, K. S. Kjær, T. B. van Driel, M. M. Nielsen, K. W. Jacobsen, N. E. Henriksen and K. B. Møller, *J. Phys. Lett.*, 2014, **5**, 2414–2418.

Publication 2 (JPCLett)

Vibrational Coherence Controls Molecular Fragmentation: Ultrafast Photodynamics of the [Ag₂Cl]⁺ Scaffold

Preamble

The following chapter has been published in the journal „The Journal of Physical Chemistry Letters“. For the supporting information the reader is referred to the electronic version of the article. The experimental work, data processing and evaluation were performed by myself. Dr. Christof Holzer and Prof. Dr. Wim Klopper provided quantum chemical calculations. Static absorption and emission spectra in solution phase were measured by Dr. Florian Bappler. The initial draft of the manuscript was written by myself and revised by Priv.-Doz. Dr. Christoph Riehn.

S.V. Kruppa, F. Bappler, C. Holzer, W. Klopper, R. Diller, C. Riehn, *J. Phys. Chem. Lett.*, **2018**, 9(4), 804-810,
<https://doi.org/10.1021/acs.jpcllett.7b03167>

Copyright ©2018 American Chemical Society

Reprint Licence



RightsLink®

Vibrational Coherence Controls Molecular Fragmentation: Ultrafast Photodynamics of the [Ag₂Cl] Scaffold

Author: Sebastian V. Kruppa, Florian Böppler, Christof Holzer, et al

Publication: Journal of Physical Chemistry Letters

Publisher: American Chemical Society

Date: Feb 1, 2018

Copyright © 2018, American Chemical Society



PERMISSION/LICENSE IS GRANTED FOR YOUR ORDER AT NO CHARGE

This type of permission/license, instead of the standard Terms & Conditions, is sent to you because no fee is being charged for your order. Please note the following:

- Permission is granted for your request in both print and electronic formats, and translations.
- If figures and/or tables were requested, they may be adapted or used in part.
- Please print this page for your records and send a copy of it to your publisher/graduate school.
- Appropriate credit for the requested material should be given as follows: "Reprinted (adapted) with permission from (COMPLETE REFERENCE CITATION). Copyright (YEAR) American Chemical Society." Insert appropriate information in place of the capitalized words.
- One-time permission is granted only for the use specified in your request. No additional uses are granted (such as derivative works or other editions). For any other uses, please submit a new request.

BACK

CLOSE WINDOW

Vibrational Coherence Controls Molecular Fragmentation: Ultrafast Photodynamics of the $[\text{Ag}_2\text{Cl}]^+$ Scaffold

Sebastian V. Kruppa,^{*,†,‡} Florian Bäßler,[‡] Christof Holzer,[§] Wim Klopper,[§] Rolf Diller,^{‡,||} and Christoph Riehn^{*,†,||}

[†]Department of Chemistry, TU Kaiserslautern, Erwin-Schrödinger-Straße 52-54, 67663 Kaiserslautern, Germany

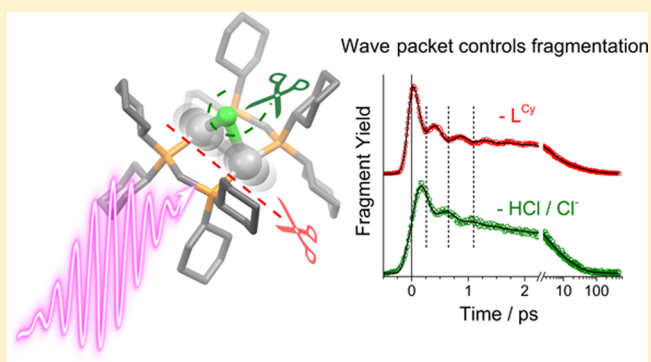
[‡]Department of Physics, TU Kaiserslautern, Erwin-Schrödinger-Straße 46, 67663 Kaiserslautern, Germany

[§]Institute of Physical Chemistry, Karlsruhe Institute of Technology, Fritz-Haber Weg 2, 76131 Karlsruhe, Germany

^{||}Landesforschungszentrum OPTIMAS, Erwin-Schrödinger-Straße 46, 67663 Kaiserslautern, Germany

Supporting Information

ABSTRACT: The recently introduced pump–probe fragmentation action spectroscopy reveals a unique observation of excited state vibrational coherence (430–460 fs) in the isolated metal complex $[\text{Ag}_2(\text{Cl})(\text{dcpm})_2]^+$ (dcpm = bis-(dicyclohexylphosphino)methane) containing the $[\text{Ag}_2\text{Cl}]^+$ scaffold. After photoexcitation by an $^1\text{XMCT}$ transition (260 nm) in an ion trap, an unexpected correlation between specific fragment ions (loss of HCl/Cl^- vs loss of dcpm) and the phase of the wave packet is probed (1150 nm). Based on *ab initio* calculations, we assign the primary electronically excited state and ascribe the observed coherences ($72\text{--}78\text{ cm}^{-1}$) to contain predominantly Ag–Ag stretch character. We propose specific probe absorption and vibronic coupling at the classical turning points to switch remarkably early on between the different fragmentation pathways. The overall excited state dynamics are fitted to a multiexponential decay with time constants: 0.2–0.4/3–4/19–26/104–161 ps. These findings open new perspectives for further dynamics investigations and possible applications in photocatalysis.



Ligand-stabilized multimetallic complexes are currently attracting a lot of attention in spectroscopic and dynamics investigations due to their broad application potential, e.g., in organic light emitting diodes (OLEDs), sensors, and photocatalysts.¹ The improvement of functionality and efficiency of these compounds by rational design is crucially based on the understanding of subtle aspects of metal–metal interaction showing in electronic states ultrafast dynamics.^{2,3} Thus, gaining insights into intrinsic femtosecond dynamics of the metal core moiety is of utmost interest, particularly if gas phase investigations in the absence of surrounding solvent molecules could be performed.⁴ To this end we feature here results utilizing a newly implemented mass- and charge-selective gas phase approach for ultrafast dynamics of large multimetallic complexes at room temperature.⁵ It allows us to analyze quantum effects (damped vibrational wave packets) in the electronically excited state revealing a delicate correlation between a mass spectrometric observable and the wave packet's phase. We expect that these results give perspectives for further mechanistic theoretical and experimental investigations and stimulate fundamental studies for control of photocatalyst activation processes.

Metal–metal interaction in multinuclear, ligand-bridged coinage metal ($d^{10}\text{--}d^{10}$) complexes affords electronic states

that give rise to strong broadband luminescence, sensitive response to external stimuli, and specific photocatalysis.¹ Among others, typical examples of such systems are given by bis-phosphino-bridged dimeric Cu^I , Ag^I , or Au^I complexes.² These have been intensively studied in solution and solid state by luminescence and resonance Raman spectroscopy since they feature a significant shortening in the metal–metal distance ($r_{\text{M-M}}$) upon electronic excitation of $^1\text{MC}(d\sigma^* - p\sigma)$ states. For the complex $[\text{Ag}_2(\text{dcpm})_2]^{2+}$ (dcpm = bis-(dicyclohexylphosphino)methane, L^{Cy}) $\Delta r_{\text{M-M}} \approx -0.2\text{ \AA}$ is observed, indicating strong metallophilic interaction in the excited state.³

These dicationic systems are easily complexed by anionic, in particular halide, counterions which give rise to new electronic states of $^1\text{XMCT}$ character.^{6–8} Related halogen-bridged copper dimers play a key role for the development of new efficient and tunable OLED materials based on coinage complexes.⁹ For photocatalysis, a very recent study on the related $[\text{Ag}_2\text{H}]^+$ scaffold, introduced a new concept for releasing H_2 from formic

Received: November 29, 2017

Accepted: January 25, 2018

Published: January 25, 2018

acid, backed up by mass spectrometric analysis with computational modeling of the reaction path.¹⁰

Surprisingly, ultrafast time-resolved studies on these systems are still very rare, although the course for the possible excited-state deactivation pathways is likely decided on very rapidly after photoexcitation. Recently, Ma et al.¹¹ applied femtosecond transient absorption (TA) spectroscopy to $[\text{Au}_2(\text{L}^{\text{Cy}})_2]^{2+}$ in acetonitrile (MeCN). We studied comprehensively the related Ag congener $[\text{Ag}_2(\text{L}^{\text{Cy}})_2]^{2+}$ isolated in an ion trap and in MeCN solution.⁴ Related complexes are found in ligand bridged d^8-d^8 systems, e.g., $[\text{M}_2(\text{dimen})_4]^{2+}$ (M = Rh, Ir; dimen = 1,8-diisocyanomenthane) and $[\text{Pt}_2(\text{pop})_4]^{4-}$ (pop = pyrophosphite, $\text{H}_2\text{P}_2\text{O}_5^{2-}$) as the most prominent ones.^{12–14} These complexes have been thoroughly investigated in solution by ultrafast time-resolved spectroscopy¹⁵ and front edge X-ray methods.¹⁶

Here, we report on the gas-phase femtosecond dynamics, in particular excited state coherent vibrational motion, of the chlorido adduct of a binuclear silver phosphine complex: $[\text{Ag}_2(\text{Cl})(\text{L}^{\text{Cy}})_2]^+$, abbreviated $[\text{Ag}_2\text{Cl}]^+$ (Figure 1). This

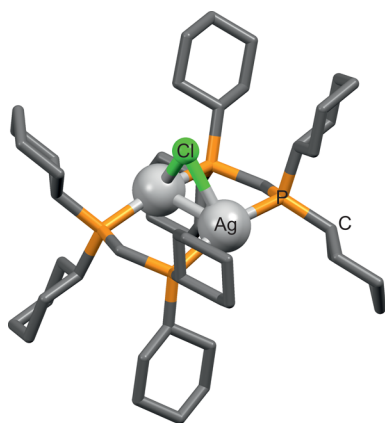


Figure 1. Schematic structure of $[\text{Ag}_2\text{Cl}]^+$. H atoms omitted.

molecular monocation was isolated in an ion trap and analyzed by photodissociation (PD) and transient photodissociation action spectroscopy (τ -PD).^{4,5,17} In the latter method, after a pump pulse (one-photon resonant electronic excitation), a variably time-delayed probe pulse (multiphoton NIR excitation) interrogates the sample and “projects” the photoinduced ultrafast dynamics of the involved excited states by their state specific cross sections onto the transient fragment ion yield. Furthermore, we study by quantum chemical methods the relevant electronic states and structures of $[\text{Ag}_2\text{Cl}]^+$, which as a 149-atom system poses a challenge to theory. Thus, we report plausible interpretations furnished by *ab initio* calculations for a size-reduced molecular model system, i.e., $[\text{Ag}_2(\text{Cl})(\text{dmpm})_2]^+$ (dmpm = bis(dimethylphosphino)methane, L^{Me}).

The presentation of our data is organized as follows: first we describe the mass spectrometric characterization of $[\text{Ag}_2\text{Cl}]^+$ followed then by reporting its UV spectrum and computational results on structure and electronic transitions. Finally, we provide femtosecond transient data and close with a simplified model focusing on the early picosecond dynamics.

Gaseous $[\text{Ag}_2\text{Cl}]^+$ ions are generated by electrospaying an acetonitrile solution of $[\text{Ag}_2(\text{L}^{\text{Cy}})_2](\text{PF}_6)_2$ and $[\text{NBu}_4]\text{Cl}$ (1:1) yielding the chlorido adduct $[\text{Ag}_2(\text{Cl})(\text{L}^{\text{Cy}})_2]^+$ (m/z 1065), unambiguously identified by its isotope pattern (Figure S3). Upon collision-induced dissociation (CID) the major fragmen-

tation channel was found to be the loss of a L^{Cy} ligand (m/z 657). At a smaller percentage loss of $\text{AgCl}(\text{L}^{\text{Cy}})$, and loss of HCl or AgCl was observed. By contrast, upon photoexcitation at 236 nm a broader fragmentation pattern is obtained (Figure S7, Table S2). Using pump–probe excitation (260 nm/1150 nm) we observe an increase in total fragment yield and the appearance of new fragment ions. Noteworthy here is the loss of Cl^- by the back dissociation of the halide adduct (Figures S3 and S4).

Based on this analysis and additional results on the excited state dynamics (presented later) we divide the fragment channels into three groups (Tables 1 and S1): a group of

Table 1. Main Photofragments of $[\text{Ag}_2\text{Cl}]^{+a}$

group	m/z	assigned formula	loss	rel. phase	%
precursor	1065	$[\text{Ag}_2(\text{Cl})(\text{L}^{\text{Cy}})_2]^+$			
gF ₁	923	$[\text{Ag}(\text{L}^{\text{Cy}})_2]^+$	AgCl	($\sim\pi$)	35
	819	$[\text{Ag}_2(\text{L}^{\text{Cy}})(\text{P}(\text{Cy})_2)]^+$	Cl, P(CH ₂) ₂ (Cy) ₂		28
gF ₂	1029	$[\text{Ag}_2(\text{L}^{\text{Cy}})_2-\text{H}]^+$	HCl	$\sim\pi$	51
	515	$[\text{Ag}_2(\text{L}^{\text{Cy}})_2]^{2+}$	Cl^-		49
gF ₃	657	$[\text{Ag}_2(\text{Cl})(\text{L}^{\text{Cy}})]^+$	L^{Cy}	0	69
	326	$(\text{P}_2(\text{CH}_2)(\text{Cy})_3\text{H})^+$	$\text{Ag}_2(\text{Cl})(\text{L}^{\text{Cy}}),$ (Cy-H)		21

^aDetails provided in Table S1. Percentages of gF_{1,3} signals are indicated. $\text{L}^{\text{Cy}} = \text{P}_2(\text{CH}_2)(\text{Cy})_4$, Cy = (C₆H₁₁).

fragments gF₁ appears mostly by the loss of AgCl or Cl + PCH₂(Cy)₂, gF₂ exhibits the loss of HCl or Cl^- , while the gF₃ fragments show mostly loss of one ligand (L^{Cy}).

In order to characterize the structure of $[\text{Ag}_2\text{Cl}]^+$ and its change upon photoexcitation, we have performed quantum chemical computations on the size-reduced model system $[\text{Ag}_2(\text{Cl})(\text{L}^{\text{Me}})_2]^+$, where the cyclohexyl groups of the phosphine ligand have been replaced by the smaller methyl groups. We have employed this approach recently successfully for the study of the nonchlorido $[\text{Ag}_2(\text{L}^{\text{Cy}})_2]^{2+}$ complex.⁴ In order to obtain more information on the electronically excited states, the equilibrium geometries were optimized at the CC2/def2-TZVPP and PBE0-D3(BJ) levels in C_{2v} symmetry. At the PBE0-D3(BJ) geometries, quasi-particle energies were determined at the eigenvalue-only self-consistent GW level (evGW), and singlet excitation energies were determined from the Bethe-Salpeter equation (BSE).¹⁸

The ground state minimum structure as calculated at the CC2/def2-TZVPP level in C_{2v} (1A_1) symmetry displays a bridging, symmetrically positioned chloride ion and an Ag–Ag distance of 2.87 Å, only slightly shorter than calculated before for the $[\text{Ag}_2(\text{L}^{\text{Me}})_2]^{2+}$ complex (Tab. S5).⁴ The distance of Cl with respect to the Ag–Ag axis $d_{\text{Cl}-(\text{AgAg})}$ amounts to 2.18 Å and the Ag_2P_4 frame is nonplanar. The ligands are slightly bent from the Ag–Ag axis, given by the angle $\angle(\text{P}-\text{Ag}-\text{P}) = 165^\circ$. Additionally, we have located four electronically excited singlet states related to $^1\text{XMCT}$ (1A_1 , 1B_1 , 1B_2) and ^1MC (1A_2) transitions and corresponding triplets (see Figure 2 and Tables S7–S9 for energies, oscillator strengths, and natural transition orbitals).

The UV-PD spectrum of isolated $[\text{Ag}_2\text{Cl}]^+$ (Figure 2a) exhibits a plateau-like absorption at 250–280 nm and a stronger band rising up at 240 nm. Both features resemble

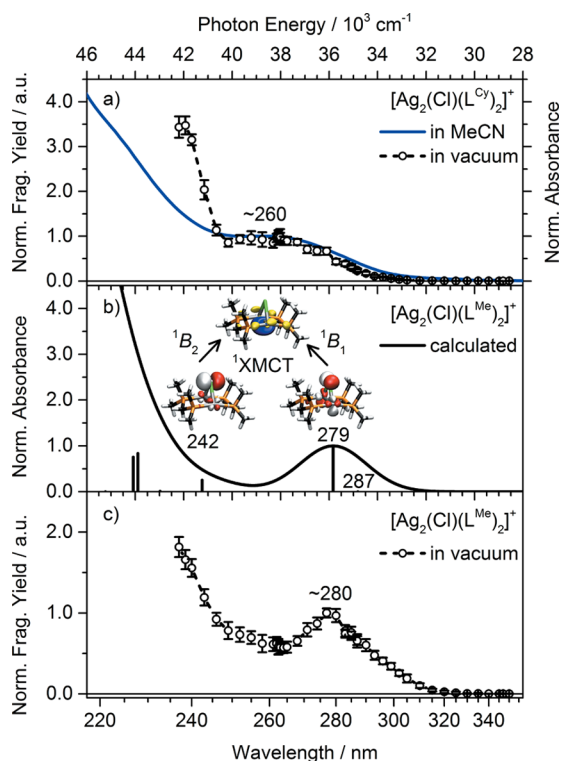


Figure 2. (a) Normalized UV-PD spectrum of $[\text{Ag}_2\text{Cl}]^+$ (black circles) compared to absorbance of $[\text{Ag}_2(\text{L}^{\text{Cy}})_2](\text{PF}_6)_2/[\text{NBu}_4]\text{Cl}$ (1:2.6) in MeCN ($c = 5.7$ mM). (b) Calculated electronic absorption (fwhm = 0.4 eV) and stick spectra (PBE0-D3(BJ)/evGW-BSE/def2-SVPD) for the $[\text{Ag}_2(\text{Cl})(\text{L}^{\text{Me}})_2]^+$ model system (C_{2v}). Inset: most important occupied (red-white) and virtual (yellow-blue) natural transition orbitals for the 1B_1 and 1B_2 transitions at 279 and 242 nm, respectively (isosurfaces at $0.05 (a_0)^{-3/2}$). (c) Experimental normalized UV-PD spectrum of $[\text{Ag}_2(\text{Cl})(\text{L}^{\text{Me}})_2]^+$.

closely the absorption spectrum of $[\text{Ag}_2\text{Cl}]^+$ in MeCN solution ($[\text{Ag}_2(\text{L}^{\text{Cy}})_2]^{2+}$ with an excess of $[\text{NBu}_4]\text{Cl}$), which is consistent with the calculated small change of dipole moment upon excitation (-0.93 D, CC2/def2-TZVPP). It further agrees with its luminescence excitation spectrum (Figures S13 and S14).

Our evGW-BSE calculation on the model complex $[\text{Ag}_2(\text{Cl})(\text{L}^{\text{Me}})_2]^+$ resulted in an electronic spectrum with similar but shifted features (Figure 2b). It predicts the main dipole allowed transition at $\lambda_{\text{calc}} = 279$ nm (HOMO-1 \rightarrow LUMO, ${}^1\text{XMCT}({}^1B_1)$, see Figure 2b and Table S8). A weakly dipole-allowed transition was found at $\lambda_{\text{calc}} = 242$ nm (HOMO-2 \rightarrow LUMO, ${}^1\text{XMCT}({}^1B_2)$) probably also contributing to the experimental spectrum.

Since we cannot completely rule out an influence of the phosphorus substituents on the spectra, e.g., by ligand backbone bending, we have performed a reference UV-PD experiment employing the L^{Me} ligand, which gave a spectrum that agrees well with the calculated one and supports our quantum theoretical assignment (Figure 2c). Note that the L^{Me} ligand is pyrophoric, which renders its mass spectrometric handling difficult, preventing a complete study for $[\text{Ag}_2(\text{Cl})(\text{L}^{\text{Me}})_2]^+$ here (Figure S6).

In the following, we will present and discuss the femtosecond time-resolved data obtained by ion trap pump-probe (260 nm/1150 nm) fragmentation.⁵ The fragment-specific transients (gF_{1-3} , Figure 3) are analyzed by fitting each of these to a sum of exponentials (Table S3).

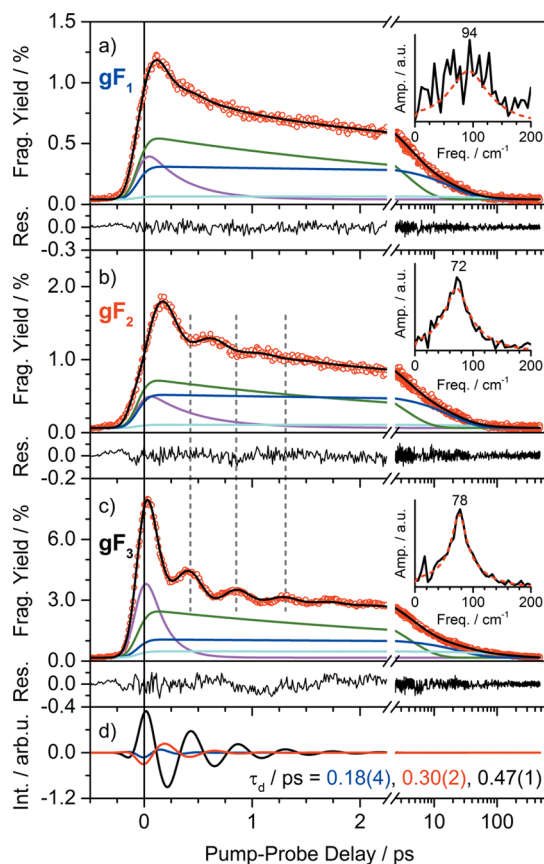


Figure 3. (a–c) Grouped τ -PD signals (gF_{1-3} , open circles) for $\lambda_{\text{pu}}/\lambda_{\text{pr}}$ 260 nm/1150 nm at magic angle. Note that data for pump-probe delay >2.4 ps is plotted on a logarithmic scale. Best kinetic fits (black lines), individual contributions (colored lines, τ_1 : magenta, τ_2 : green, τ_3 : blue, τ_4 : cyan) and residuals are shown (Table S3). Insets: Fourier transforms of residuals obtained by subtracting tetra-exponential decay contribution (black solid lines) and of fitted oscillating components shown in panel d (red dotted lines), respectively. (d) Oscillating parts of transients fits (gF_1 : blue, gF_2 : red, gF_3 : black; pump-only fragmentation yields were subtracted) and dephasing time constants (τ_d).

Similar to the nonchlorido adduct $[\text{Ag}_2(\text{L}^{\text{Cy}})_2]^{2+}$,⁴ a multi-exponential decay with four time constants 0.2–0.4/3–4/19–26/104–161 ps is observed with the total lifetime being clearly shorter compared to $[\text{Ag}_2(\text{L}^{\text{Cy}})_2]^{2+}$. Moreover and remarkably we observe pronounced oscillatory features (period ~ 430 – 460 fs) for the transients of gF_2 and gF_3 , that can be fitted to a strongly damped sine function (dephasing time constant = 0.18–0.47 ps) and assigned to vibrational wave packets. The Fourier transformation of these features provided frequencies of 72 and 78 cm^{-1} , respectively (Figure 3). We exclude the assignment to an electronic coherence,¹⁴ since no closely lying electronic state is known and no polarization dependence was observed (cf. Figure S10). Note, that accompanying experiments in MeCN solution gave no hints on coherent wave packet activity (Figure S15). It is further noted that the occurrence and observation of vibrational wave packets in such metal complexes seems to depend sensitively on the internal vibrational mode structure and interaction of the specific system with its environment and is not easily predictable.¹⁹

Evidently, the dephasing time constant (τ_d) falls into the range of the first time constant (τ_1), which could be assigned to either (a) intramolecular vibrational redistribution (IVR), (b)

internal conversion (IC) into the energetically lower lying 1A_1 excited state, or (c) fast intersystem crossing (ISC) into the triplet manifold. All three processes are expected to change the cross-section for (multiphoton) probe absorption and should therefore be detectable with our experimental method. Based on the experimental gas phase data alone, a definite assignment is not possible. Consequently, we suggest, as in ref 4, that the two fast time constants are related to a combination or sequence of IVR/IC/ISC processes, whereas the two slower ones should be related to relaxation processes within the triplet manifold.

However, here, we like to highlight the unexpected observation that the wave packet's oscillation exhibits a phase shift of $\sim \pi$ between the signals of the different grouped fragments (Figure 3d). We found that the transient for gF_2 (loss of HCl/Cl $^-$) displays a phase shift of $\sim \pi$ compared to the one for gF_3 (loss of L Cy). For the transient of gF_1 (loss of AgCl) we note a delay, in accordance with an $\sim \pi$ phase shift, accompanied by a strongly damped oscillation (Table 1, Table S3). We would like to emphasize that the formation of fragment ions, which is key to the detection scheme for pump probe action spectroscopy, is usually considered to be a slow process (μ s regime) and based on statistical decay. Therefore, it is intriguing to see in these examples of dissimilar fragmentation channels that a switch between the corresponding fragmentation pathways is operative already at very early time delay (~ 400 fs).

The questions now arising are: To which excited-state vibrational mode of [Ag $_2$ Cl] $^+$ can we assign the observed coherent wave packet? And how can we rationalize the phase shift between the transients of different fragment channels?

The initiation of vibrational wave packets by photoexcitation is a frequent observation in ultrafast spectroscopy and occurs when an electronically excited state is structurally shifted in a certain coordinate from the ground state.^{16,20–22} Since no experimental results on the low-frequency vibrations of [Ag $_2$ Cl] $^+$ are available, we extracted the modes for the ground state from our quantum chemical calculation, with the excited states frequencies being computationally too costly.

Six low-frequency normal modes between 60 and 100 cm $^{-1}$ (Figure S17) were obtained including Cl bending $\delta(\text{Ag}_2\text{-Cl}) \sim 72$ cm $^{-1}$, and two modes with Ag–Ag stretching character at $\nu(\text{Ag-Ag}) \sim 76$ cm $^{-1}$ and ~ 95 cm $^{-1}$, respectively. We neglect low-frequency modes from the cyclohexyl units of L Cy upon choosing the L Me ligand for the computations. However, we believe that Franck–Condon activation of cyclohexyl modes can be disregarded due to presumed small structural changes in the cyclohexyl groups upon photoexcitation.

Thus, for assignment of the coherences we have to rely on qualitative reasoning. Upon inspection of the calculated excited state structure (1B_1 , Table S5), we find the strongest relative change in the distance $d_{\text{Ag-Ag}}$ (-3.6%) and the angle $\angle(\text{P-Ag-P})$ ($+3.3\%$) so that both coordinates would qualify for the formation of wave packets. However, we would assume modes with strong ligand bending character to shift to lower values for the experimentally investigated L Cy ligand compared to L Me (computational model) due to its larger reduced mass. Therefore, we propose to assign the wave packet motion to the $\nu_{\text{Ag-Ag}}$ stretching vibration in the 1B_1 state, concluding that enforcement of intermetallic interaction leads to the vibrational wave packet in [Ag $_2$ Cl] $^+$.

The phase shift between the transient's modulation of the HCl/Cl $^-$ loss (gF_3) and ligand loss (gF_2) channels could now

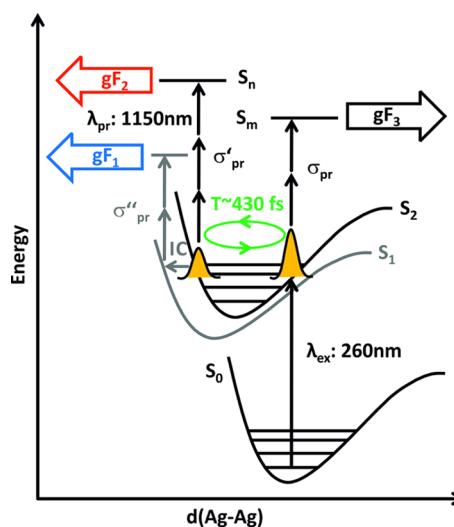


Figure 4. Simplified potential energy level diagram highlighting probe absorption cross sections (σ_{pr}) modulated by the wavepacket. Triplet states not shown.

only be understood assuming a different probe transition and absorption cross section for the wave packet state at the inner respectively outer turning point of the potential (Figure 4). Thus, the Ag–Ag distance serves as a sensitive coordinate to steer the probe excitation into higher-lying electronic states. This eventually leads to either loss of a phosphine ligand possibly via another XMCT (or LMCT) state weakening the Ag–P bonds at long Ag–Ag distance or a loss of HCl/Cl $^-$, possibly via an ion pair state [(Ag $_2$) $^{2+}$ Cl $^-$] at short Ag–Ag distance with an associated large dissociation energy. The latter was estimated to be 798 kJmol $^{-1}$ (CC2/def2-TZVPP) and 744 kJmol $^{-1}$ (PBE0-D3(BJ)/def2-SVPD), respectively. Hence, this ionic fragmentation pathway ([Ag $_2$ (Cl)(L Cy) $_2$] $^+$ \rightarrow [Ag $_2$ (L Cy) $_2$] $^{2+}$ + Cl $^-$) would be accessible by a UV (260 nm) + 3 NIR (1150 nm) multiphoton absorption process.

The characteristics of the gF_1 channel (loss of AgCl) could be assigned to an electronic coupling (IC) at shorter Ag–Ag distance to the computed, lower lying dark state (1A_1), accompanied by quick dephasing of the wave packet (Figure 4).

It is noted that this picture of photoexcitation and fragmentation pathways of [Ag $_2$ Cl] $^+$ is a qualitative one at the current status of our research, in particular since knowledge on the higher-lying electronic states and on the fragmentation mechanisms of this system is incomplete. For the future, simulations of the nonadiabatic dynamics and resulting fragmentations would be very desirable.²³ Also, we cannot completely rule out contributions of secondary processes that influence the final types of fragments, but the detected phase relation between the primary losses of L Cy (gF_2) and HCl/Cl $^-$ (gF_3) is clear-cut and undisputable. Thus, the experimental results and their possible rationalization puts the spotlight on new and unexpected photochemical aspects of these binuclear metal complexes that might possibly be used in the future to actively control their behavior after photoexcitation. Note that, e.g., the elimination of HCl is a known key step for base-free activation of Ru(II) transfer hydrogenation catalysts.²⁴

We conclude that [Ag $_2$ Cl] $^+$ represents a versatile model system for the class of d 10 –d 10 transition metal complexes, enabling the exploration of subtle intrinsic properties such as excited state metal–metal interaction as well as quantum coherence effects. Here we report an unprecedented correlation

between the phase of coherent wave packet dynamics, tentatively assigned to vibrational coherence of predominantly Ag–Ag stretching mode character, and the generation of specific fragment ions. This observation is based on ion-trap pump–probe fragmentation action spectroscopy of isolated gaseous target ions and *uniquely demonstrates the utilization of coherence for switching of chemical reactivity via specific fragmentation pathways, as challenged in a recent contribution.*²¹

Given the absence of environmental influences this study provides benchmark data for further theoretical and experimental investigations and should stimulate the development of theoretical methods. Extended studies on $[\text{Ag}_2\text{Cl}]^+$ and related systems in terms of varying ligands, metals, and bridging groups are underway and will yield further insights into ultrafast excited-state processes for ligand-stabilized multinuclear metal complexes. Further applications of our findings in fundamental studies for control of photocatalytical processes present stimulating perspectives for the future.

MATERIALS AND METHODS

Sample Preparation. Synthesis and characterization of the compound $[\text{Ag}_2(\text{dcpm})_2](\text{PF}_6)_2$ (dcpm = bis-(dicyclohexylphosphino)methane, L^{Cy}) were reported elsewhere.^{3,4} The $[\text{Ag}_2(\text{Cl})(\text{L}^{\text{Cy}})_2]^+$ precursor ions ($[\text{Ag}_2\text{Cl}]^+$, chloride adduct of $[\text{Ag}_2(\text{L}^{\text{Cy}})_2]^{2+}$) were generated via electrospray ionization (ESI) from sample solutions of $[\text{Ag}_2(\text{L}^{\text{Cy}})_2]^{2+}(\text{PF}_6)_2$ and $[\text{NBu}_4]\text{Cl}$ (tetrabutylammonium chloride, 97%, Sigma-Aldrich) in acetonitrile (HPLC grade, $c = 10^{-7}$ M, stoichiometric ratio 1:1). $[\text{Ag}_2(\text{Cl})(\text{L}^{\text{Me}})_2]^+$ ($\text{L}^{\text{Me}} = \text{bis}(\text{dimethylphosphino})\text{methane}$) ions were produced by electrospraying solutions of L^{Me} (97%, Sigma-Aldrich), AgPF_6 (98%, Sigma-Aldrich), and $[\text{NBu}_4]\text{Cl}$ (97%, Sigma-Aldrich) in acetonitrile (1:1:1 stoichiometric ratio, $c = 10^{-6}$ M). Due to the fact that L^{Me} is pyrophoric, a stock solution of L^{Me} in degassed MeCN ($c = 10^{-3}$ M) was prepared in a nitrogen atmosphere and subsequently further diluted.

Quadrupole Ion Trap Mass Spectrometry and Collision-Induced Dissociation (CID). Electrospray ionization mass spectrometry (ESI-MS) was performed utilizing a 3D quadrupole ion trap mass spectrometer (amaZon speed, Bruker Daltonics) modified for laser irradiation experiments.^{25,26} The ion source was operated in positive ESI mode and sample solutions were electrosprayed by continuous infusion into the ESI chamber ($120\text{--}180 \mu\text{L h}^{-1}$) assisted by nitrogen sheath gas (7 psi, 483 mbar). The electrospray needle was held at 4.5 kV and nitrogen dry gas was used to assist desolvation (4 L min^{-1} , 180°C). The mass isolation window was typically $\Delta m/z = 8$ selecting the full isotope pattern of $[\text{Ag}_2\text{Cl}]^+$. The scan range was $m/z = 50\text{--}1200$ with a scan speed of $32.500 m/z \text{ s}^{-1}$ (UltraScan mode, $m/z \sim 0.3$ fwhm, full width at half-maximum) and $8.100 m/z \text{ s}^{-1}$ (Enhanced Resolution mode, $m/z \sim 0.25$ fwhm) for τ -PD and UV-PD experiments, respectively. To initiate collision-induced dissociation a resonance excitation voltage was applied to the end-caps of the Paul-type ion trap in order to accelerate the isolated precursor ions, which then undergo multiple collisions with the Helium buffer gas with subsequent fragmentation and mass analysis. The instrument control and data analysis was performed using standard Bruker Daltonics software.

Static and Time-Resolved Photodissociation (PD/ τ -PD) Experiments (Gas Phase). The experimental setup is described in detail elsewhere.^{4,5,26} Briefly, femtosecond pulses are generated in a (Ti:Sa) chirped pulse cryogenic regenerative amplifier system (Wyvern 1000, KMLabs) generating an output pulse train

(~ 780 nm, fwhm ~ 30 nm, $\sim 4\text{W}$, 982 Hz, $\Delta\tau \sim 50$ fs), which is used to pump two identical nonlinear frequency converters “T₁” and “T₂” (TOPAS-C, Light Conversion, tuning range 240–2600 nm). Their relative linear polarization was set to $\sim 54.7^\circ$ by a variable half-wave plate (Berek compensator) and pulse energies were controlled by variable neutral density filters. NIR-probe pulses (1150 nm) were temporally delayed with respect to UV-pump pulses (260 nm) by varying the optical path length utilizing a single axis delay stage (Physik Instrumente, PI) with a mounted retroreflector. Both beams where quasi collinearly combined ($\sim 0.8^\circ$) and focused ($f = 50$ cm) through a fused silica window (3 mm thickness, transmittance in the spectral range of 240–285 nm is reported in the Supporting Information (SI) of ref 4) into the ion trap center of the mass spectrometer (~ 1 mm diameter). The ion cloud was illuminated during a fragmentation time window of 120 and 100 ms for PD and τ -PD experiments, respectively.

Static PD spectra were recorded stepwise at each wavelength position in the range of 237–350 nm at constant pulse energy of $2 \mu\text{J}$ (spectral width $\Delta\lambda \sim 2\text{--}4$ nm, see SI of ref 4). From the resulting PD mass spectra the fragment specific (Y_i) and total fragment yields (TFY) are calculated as $Y_i = F_i/(\Sigma F_i + P)$ and $\text{TFY} = \Sigma F_i/(\Sigma F_i + P)$, respectively. F_i and P are the integrated mass peak intensities of photo products i and precursor ions, respectively and ΣF_i is the sum of all fragment ion signals. Additionally, Y_i and TFY were normalized to the number of photons $N = E_{\text{pulse}} \cdot \lambda / (h \cdot c)$. Different nonlinear optical output schemes of “T₁” and/or wavelength filters are employed in the ranges of 237–263 nm, 263–287 nm, and 287–350 nm, respectively, requiring a reoptimization of the laser beam overlap with the ion cloud. Therefore, PD spectra were concatenated by scaling factors obtained from overlapping data points of the respective tuning ranges.

For time-resolved τ -PD experiments ($\lambda_{\text{pu}} = 260$ nm, $E_{\text{pulse}} = 1 \mu\text{J}$; $\lambda_{\text{pr}} = 1150$ nm, $E_{\text{pulse}} = 150 \mu\text{J}$; ~ 98 pulses) individual short (6 ps, 10 cycles), intermediate (40 ps, 6 cycles) and long scans (600 ps, 4 cycles) were averaged (40–80 mass spectra/data point) and concatenated by introducing an ordinate offset correction (6 ps scan as reference) to account for fluctuating fragment yields at negative pump–probe delays. The time zero position and cross correlation (typical fwhm ~ 200 fs, cf. SI of ref 4) was estimated by measuring the multiphoton ionization of neutral furan ($\text{C}_4\text{H}_4\text{O}$), which was introduced at small concentration into the ion trap with the trapping gas (He). Fragment-specific transients exhibiting similar temporal profiles were summed up and categorized into three grouped signals $g_{F_1}\text{--}g_{F_3}$ (see Table S1, Figures 3, S3, and S9). Data analysis was performed by fitting a convolution of a Gaussian (system response) with exponential decay functions and damped sine function (eq S1).

Computational Methods. We have chosen Green’s function (evGW-BSE) and coupled-cluster (CC2 approximation) approaches for calculations of electronic excitations since an advanced treatment of electron correlation and charge transfer (XMCT transitions, halogen-to-metal charge transfer) is necessary. In order to describe the electronic and molecular structures of the target ion $[\text{Ag}_2(\text{Cl})(\text{L}^{\text{Cy}})_2]^+$ and also of the nonchlorido adduct $[\text{Ag}_2(\text{L}^{\text{Cy}})_2]^{2+}$, the computations were performed for the size-reduced model systems $[\text{Ag}_2(\text{Cl})(\text{L}^{\text{Me}})_2]^+$ and $[\text{Ag}_2(\text{L}^{\text{Me}})_2]^{2+}$, respectively, by substituting the cyclohexyl groups by methyl groups on the phosphine ligand in order to reduce CPU time (see Figures S1 and S2). We recently showed for the $[\text{Ag}_2(\text{L}^{\text{Cy}})_2]^{2+}$ system that this

approach gives realistic predictions for electronic transitions since the relative energies of electronic excited states are predominantly determined by the Ag_2 and Ag_2Cl chromophoric moieties, respectively.⁴ A similar strategy was applied by other groups.^{27–29}

CC2 Approach. The coupled-cluster computations were performed at exactly the same level as in ref 4 in the CC2 approximation^{30,31} with the TURBOMOLE program package.^{32,33} We used the def2-TZVPP basis set³⁴ with an effective core potential for Ag substituting 14 core orbitals.³⁵ The 1s orbitals of C and the 1s, 2s, and 2p orbitals of P and Cl were not included in the correlation treatment.

evGW-BSE Approach. Using the TURBOMOLE program package,^{32,33} the ground-state equilibrium geometries were optimized at the PBE0-D3(BJ) level^{36–39} in C_{2v} symmetry (for both $[\text{Ag}_2(\text{Cl})(\text{L}^{\text{Me}})_2]^+$ and $[\text{Ag}_2(\text{L}^{\text{Me}})_2]^{2+}$). At these geometries, quasi-particle energies were determined at the eigenvalue-only self-consistent GW level (evGW)^{40,41} and singlet excitation energies were determined from the Bethe–Salpeter equation (BSE).¹⁸ Recently,⁴² it was shown that the evGW-BSE approach is equally efficient for singlet valence, Rydberg, and charge-transfer excitations, providing an accuracy comparable to the accuracy achievable with wave function methods such as CASPT2 and EOM-CCSD. The computations were performed in the def2-SVPD basis set (but only def2-SV(P) for hydrogen).^{34,43} For $[\text{Ag}_2(\text{L}^{\text{Me}})_2]^{2+}$, this basis set of atomic orbitals comprises 420 basis functions, while the corresponding auxiliary basis set “cbas”⁴⁴ used for the resolution-of-the-identity (RI) approximation comprises 1626 auxiliary basis functions. For $[\text{Ag}_2(\text{Cl})(\text{L}^{\text{Me}})_2]^+$, the numbers are 447 and 1704. The evGW damping parameter was set to $\eta = 0.02 E_h$. The def2-SVPD basis set for Ag includes an energy-adjusted *ab initio* pseudopotential³⁵ that replaces the $[\text{Ar}]3d^{10}$ core.

■ ASSOCIATED CONTENT

Supporting Information

The Supporting Information is available free of charge on the ACS Publications website at DOI: 10.1021/acs.jpcllett.7b03167.

Additional experimental and computational methods, supporting data, graphs and calculated molecular geometries. (PDF)

■ AUTHOR INFORMATION

Corresponding Authors

*E-mail: kruppa@chemie.uni-kl.de.

*E-mail: riehn@chemie.uni-kl.de.

ORCID

Sebastian V. Kruppa: 0000-0003-0756-2703

Rolf Diller: 0000-0002-3629-8334

Notes

The authors declare no competing financial interest.

■ ACKNOWLEDGMENTS

We thank the DFG-funded transregional collaborative research center SFB/TRR 88 “Cooperative Effects in Homo- and Heterometallic Complexes (3MET)” (Projects C1 and C4) for financial support. The assistance of Maximilian Luczak and Michael Borchers in the experiments is gratefully acknowledged.

■ REFERENCES

- (1) Yam, V. W.-W.; Au, V. K.-M.; Leung, S. Y.-L. Light-Emitting Self-Assembled Materials Based on d^8 and d^{10} Transition Metal Complexes. *Chem. Rev.* **2015**, *115*, 7589–7728.
- (2) Phillips, D. L.; Che, C.-M.; Leung, K. H.; Mao, Z.; Tse, M.-C. A Comparative Study on Metal–metal Interaction in Binuclear Two- and Three-coordinated d^{10} -metal Complexes: Spectroscopic Investigation of M(I)–M(I) Interaction in the $^1[d\sigma^*p\sigma]$ Excited State of $[\text{M}_2(\text{dcpm})_2]^{2+}$ (dcpm = bis(dicyclohexylphosphino)methane) (M = Au, Ag, Cu) and $[\text{M}_2(\text{dmpm})_3]^{2+}$ (dmpm = bis(dimethylphosphino)-methane) (M = Au, Ag, Cu) Complexes. *Coord. Chem. Rev.* **2005**, *249*, 1476–1490.
- (3) Che, C.-M.; Tse, M.-C.; Chan, M. C. W.; Cheung, K.-K.; Phillips, D. L.; Leung, K.-H. Spectroscopic Evidence for Argentophilicity in Structurally Characterized Luminescent Binuclear Silver(I) Complexes. *J. Am. Chem. Soc.* **2000**, *122*, 2464–2468.
- (4) Kruppa, S. V.; Bappler, F.; Klopfer, W.; Walg, S. P.; Thiel, W. R.; Diller, R.; Riehn, C. Ultrafast Excited-state Relaxation of a Binuclear Ag^{I} Phosphine Complex in Gas Phase and Solution. *Phys. Chem. Chem. Phys.* **2017**, *19*, 22785–22800.
- (5) Imanbaev, D.; Lang, J.; Gelin, M. F.; Kaufhold, S.; Pfeffer, M. G.; Rau, S.; Riehn, C. Pump-probe Fragmentation Action Spectroscopy: A Powerful Tool to Unravel Light-induced Processes in Molecular Photocatalysts. *Angew. Chem., Int. Ed.* **2017**, *56*, S471–S474.
- (6) Jaw, H. R. C.; Savas, M. M.; Rogers, R. D.; Mason, W. R. Crystal Structures and Solution Electronic Absorption and MCD Spectra for Perchlorate and Halide Salts of Binuclear Gold(I) Complexes Containing Bridging $\text{Me}_2\text{PCH}_2\text{PMe}_2$ (dmpm) or $\text{Me}_2\text{PCH}_2\text{CH}_2\text{PMe}_2$ (dmpe) ligands. *Inorg. Chem.* **1989**, *28*, 1028–1037.
- (7) Piche, D.; Harvey, P. D. The Lowest Energy Excited States of the Binuclear Silver(I) Halide Complexes, $\text{Ag}_2(\text{dmb})_2\text{X}_2$. Metal-centered or Charge Transfer States? *Can. J. Chem.* **1994**, *72*, 705–713.
- (8) Fu, W.-F.; Chan, K.-C.; Cheung, K.-K.; Che, C.-M. Substrate-Binding Reactions of the $^3[d\sigma^*p\sigma]$ Excited State of Binuclear Gold(I) Complexes with Bridging Bis(dicyclohexylphosphino)methane Ligands: Emission and Time-Resolved Absorption Spectroscopic Studies. *Chem. - Eur. J.* **2001**, *7*, 4656–4664.
- (9) Zink, D. M.; Bachle, M.; Baumann, T.; Nieger, M.; Kuhn, M.; Wang, C.; Klopfer, W.; Monkowius, U.; Hofbeck, T.; Yersin, H.; Brase, S. Synthesis, Structure, and Characterization of Dinuclear Copper(I) Halide Complexes with P^N Ligands Featuring Exciting Photoluminescence Properties. *Inorg. Chem.* **2013**, *52*, 2292–2305.
- (10) Zavras, A.; Khairallah, G. N.; Krstic, M.; Girod, M.; Daly, S.; Antoine, R.; Maitre, P.; Mulder, R. J.; Alexander, S.-A.; Bonaci-Koutecky, V.; Dugourd, P.; O’Hair, R. A. J. Ligand-induced Substrate Steering and Reshaping of $[\text{Ag}_2(\text{H})]^+$ Scaffold for Selective CO_2 Extrusion from Formic Acid. *Nat. Commun.* **2016**, *7*, 11746.
- (11) Ma, C.; Chan, C. T.-L.; To, W.-P.; Kwok, W.-M.; Che, C.-M. Deciphering Photoluminescence Dynamics and Reactivity of the Luminescent Metal–Metal-Bonded Excited State of a Binuclear Gold(I) Phosphine Complex Containing Open Coordination Sites. *Chem. - Eur. J.* **2015**, *21*, 13888–13893.
- (12) Gray, H. B.; Zali, S.; Vlek, A. Electronic Structures and Photophysics of d^8 - d^8 Complexes. *Coord. Chem. Rev.* **2017**, *345*, 297–317.
- (13) Hartssock, R. W.; Zhang, W.; Hill, M. G.; Sabat, B.; Gaffney, K. J. Characterizing the Deformational Isomers of Bimetallic $\text{Ir}_2(\text{dimen})_4^{2+}$ (dimen = 1,8-diisocyno-p-menthane) with Vibrational Wavepacket Dynamics. *J. Phys. Chem. A* **2011**, *115*, 2920–2926.
- (14) Cho, S.; Mara, M. W.; Wang, X.; Lockard, J. V.; Rachford, A. A.; Castellano, F. N.; Chen, L. X. Coherence in Metal–Metal-to-Ligand-Charge-Transfer Excited States of a Dimetallic Complex Investigated by Ultrafast Transient Absorption Anisotropy. *J. Phys. Chem. A* **2011**, *115*, 3990–3996.
- (15) van der Veen, R. M.; Cannizzo, A.; van Mourik, F.; Vlek, A.; Chergui, M. Vibrational Relaxation and Intersystem Crossing of Binuclear Metal Complexes in Solution. *J. Am. Chem. Soc.* **2011**, *133*, 305–315.

- (16) van Driel, T. B.; Kjær, K. S.; Hartsock, R. W.; Dohn, A. O.; Harlang, T.; Chollet, M.; Christensen, M.; Gawelda, W.; Henriksen, N. E.; Kim, J. G.; Haldrup, K.; Kim, K. H.; Ihee, H.; Kim, J.; Lemke, H.; Sun, Z.; Sundström, V.; Zhang, W.; Zhu, D.; Möller, K. B.; Nielsen, M. M.; Gaffney, K. J. Atomistic Characterization of the Active-site Solvation Dynamics of a Model Photocatalyst. *Nat. Commun.* **2016**, *7*, 13678.
- (17) Svendsen, A.; Kiefer, H. V.; Pedersen, H. B.; Bochenkova, A. V.; Andersen, L. H. Origin of the Intrinsic Fluorescence of the Green Fluorescent Protein. *J. Am. Chem. Soc.* **2017**, *139*, 8766–8771.
- (18) Krause, K.; Klopper, W. Implementation of the Bethe–Salpeter Equation in the TURBOMOLE Program. *J. Comput. Chem.* **2017**, *38*, 383–388.
- (19) Dohn, A. O.; Jónsson, E. Ö.; Kjær, K. S.; van Driel, T. B.; Nielsen, M. M.; Jacobsen, K. W.; Henriksen, N. E.; Möller, K. B. Direct Dynamics Studies of a Binuclear Metal Complex in Solution: The Interplay Between Vibrational Relaxation, Coherence, and Solvent Effects. *J. Phys. Chem. Lett.* **2014**, *5*, 2414–2418.
- (20) Gruebele, M.; Zewail, A. H. Femtosecond Wave Packet Spectroscopy: Coherences, the Potential, and Structural Determination. *J. Chem. Phys.* **1993**, *98*, 883–902.
- (21) Scholes, G. D.; Fleming, G. R.; Chen, L. X.; Aspuru-Guzik, A.; Buchleitner, A.; Coker, D. F.; Engel, G. S.; van Grondelle, R.; Ishizaki, A.; Jonas, D. M.; Lundeen, J. S.; McCusker, J. K.; Mukamel, S.; Ogilvie, J. P.; Olaya-Castro, A.; Ratner, M. A.; Spano, F. C.; Whaley, K. B.; Zhu, X. Using Coherence to Enhance Function in Chemical and Biophysical Systems. *Nature* **2017**, *543*, 647.
- (22) Consani, C.; Prémont-Schwarz, M.; ElNahhas, A.; Bressler, C.; van Mourik, F.; Cannizzo, A.; Chergui, M. Vibrational Coherences and Relaxation in the High-Spin State of Aqueous $[\text{Fe}^{\text{II}}(\text{bpy})_3]^{2+}$. *Angew. Chem., Int. Ed.* **2009**, *48*, 7184–7187.
- (23) Lisinetskaya, P. G.; Braun, C.; Proch, S.; Kim, Y. D.; Ganteför, G.; Mitrić, R. Excited State Nonadiabatic Dynamics of Bare and Hydrated Anionic Gold Clusters $\text{Au}^3[\text{H}_2\text{O}]_n$ ($n = 0-2$). *Phys. Chem. Chem. Phys.* **2016**, *18*, 6411–6419.
- (24) Taghizadeh Ghoochany, L.; Kerner, C.; Farsadpour, S.; Menges, F.; Sun, Y.; Niedner-Schatteburg, G.; Thiel, W. R. C–H Activation at a Ruthenium(II) Complex – The Key Step for a Base-Free Catalytic Transfer Hydrogenation? *Eur. J. Inorg. Chem.* **2013**, *2013*, 4305–4317.
- (25) Nosenko, Y.; Menges, F.; Riehn, C.; Niedner-Schatteburg, G. Investigation by Two-color IR Dissociation Spectroscopy of Hoogsteen-type Binding in a Metalated Nucleobase Pair Mimic. *Phys. Chem. Chem. Phys.* **2013**, *15*, 8171–8178.
- (26) Kruppa, S. V.; Bäßler, F.; Nosenko, Y.; Walg, S. P.; Diller, R.; Riehn, C. Ultrafast Vibrational and Electronic Dynamics of Metal–Metal Interactions Studied by Transient Photofragmentation (Gas Phase) and Transient Absorption (Solution). In *International Conference on Ultrafast Phenomena*; OSA Technical Digest (online): Washington, DC, 2016; paper UW4A.33.
- (27) Pan, Q.-J.; Zhang, H.-X.; Fu, H.-G.; Yu, H.-T. Theoretical Studies on Metal–Metal Interaction and Intrinsic $^1,3[\sigma^*(d)\sigma(s/p)]$ Excited States of Dinuclear d^{10} Complexes with Bridging Phosphane Ligands. *Eur. J. Inorg. Chem.* **2006**, *2006*, 1050–1059.
- (28) Tong, G. S. M.; Kui, S. C. F.; Chao, H.-Y.; Zhu, N.; Che, C.-M. The $^3[\text{nd}\sigma^*(n+1)p\sigma]$ Emissions of Linear Silver(I) and Gold(I) Chains with Bridging Phosphine Ligands. *Chem. - Eur. J.* **2009**, *15*, 10777–10789.
- (29) Pan, Q.-J.; Zhang, H.-X. Ab Initio Studies on Metal–metal Interaction and $^3[\sigma^*(d)\sigma(s)]$ Excited State of the Binuclear Au(I) Complexes Formed by Phosphine And/Or Thioether Ligands. *J. Phys. Chem. A* **2004**, *108*, 3650–3661.
- (30) Christiansen, O.; Koch, H.; Jørgensen, P. The 2nd-order Approximate Coupled-cluster Singles and Doubles Model CC2. *Chem. Phys. Lett.* **1995**, *243*, 409–418.
- (31) Hättig, C.; Weigend, F. CC2 Excitation Energy Calculations on Large Molecules Using the Resolution of the Identity Approximation. *J. Chem. Phys.* **2000**, *113*, 5154–5161.
- (32) Furche, F.; Ahlrichs, R.; Hättig, C.; Klopper, W.; Sierka, M.; Weigend, F. *Turbomole. WIREs Comput. Mol. Sci.* **2014**, *4*, 91–100.
- (33) TURBOMOLE V7.1, 2016, a development of University of Karlsruhe and Forschungszentrum Karlsruhe GmbH, 1989–2007, TURBOMOLE GmbH, since 2007; available from <http://www.turbomole.com> (accessed 9 Jan 2018).
- (34) Weigend, F.; Ahlrichs, R. Balanced Basis Sets of Split Valence, Triple Zeta Valence and Quadruple Zeta Valence Quality for H to Rn: Design and Assessment of Accuracy. *Phys. Chem. Chem. Phys.* **2005**, *7*, 3297–3305.
- (35) Andrae, D.; Häussermann, U.; Dolg, M.; Stoll, H.; Preuß, H. Energy-adjusted Abinitio Pseudopotentials for the 2nd and 3rd Row Transition-elements. *Theoret. Chim. Acta* **1990**, *77*, 123–141.
- (36) Perdew, J. P.; Burke, K.; Ernzerhof, M. Generalized Gradient Approximation Made Simple. *Phys. Rev. Lett.* **1996**, *77*, 3865–3868; **1997**, *78*, 1396.
- (37) Perdew, J. P.; Ernzerhof, M.; Burke, K. Rationale for Mixing Exact Exchange with Density Functional Approximations. *J. Chem. Phys.* **1996**, *105*, 9982–9985.
- (38) Grimme, S.; Antony, J.; Ehrlich, S.; Krieg, H. A Consistent and Accurate Ab Initio Parametrization of Density Functional Dispersion Correction (DFT-D) for the 94 Elements H–Pu. *J. Chem. Phys.* **2010**, *132*, 154104.
- (39) Grimme, S.; Ehrlich, S.; Goerigk, L. Effect of the Damping Function in Dispersion Corrected Density Functional Theory. *J. Comput. Chem.* **2011**, *32*, 1456–1465.
- (40) Blase, X.; Attaccalite, C.; Olevano, V. First-principles GW Calculations for Fullerenes, Porphyrins, Phtalocyanine, and Other Molecules of Interest for Organic Photovoltaic Applications. *Phys. Rev. B: Condens. Matter Mater. Phys.* **2011**, *83*, 115103.
- (41) Kaplan, F.; Harding, M. E.; Seiler, C.; Weigend, F.; Evers, F.; van Setten, M. J. Quasi-Particle Self-Consistent GW for Molecules. *J. Chem. Theory Comput.* **2016**, *12*, 2528–2541.
- (42) Jacquemin, D.; Duchemin, I.; Blase, X. Is the Bethe–Salpeter Formalism Accurate for Excitation Energies? Comparisons with TD-DFT, CASPT2, and EOM-CCSD. *J. Phys. Chem. Lett.* **2017**, *8*, 1524–1529.
- (43) Rappoport, D.; Furche, F. Property-optimized Gaussian Basis Sets for Molecular Response Calculations. *J. Chem. Phys.* **2010**, *133*, 134105.
- (44) Hellweg, A.; Rappoport, D. Development of New Auxiliary Basis Functions of the Karlsruhe Segmented Contracted Basis Sets Including Diffuse Basis Functions(def2-SVPD, def2-TZVPPD, and def2-QVPPD) for RI-MP2 and RI-CC Calculations. *Phys. Chem. Chem. Phys.* **2015**, *17*, 1010–1017.

Publication 3 (ChemEurJ)

Photoinitiated Charge Transfer in a Triangular Silver(I) Hydride Complex and its Oxophilicity

Preamble

The following chapter has been published in the journal „Chemistry A European Journal“. For the supporting information the reader is referred to the electronic version of the article. Experimental work and data analysis concerning ion spectroscopic and mass spectrometric experiments (CID, ETD/ETR, UV-PD) were performed by myself, with experimental support from Björn Kwasigroch and Isabel Manes (ETD/ETR). Dr. Cedric Groß conducted the synthesis of the sample compound and its structural examination (NMR, X-Ray) with support from Dr. Yu Sun (X-Ray) and Dr. Harald Kelm (NMR). Quantum chemical calculations were provided by Xin Gui (DFT, *GW*-BSE) and UV absorption/luminescence spectra were measured by Dr. Florian Bäßler. The initial draft of the manuscript was composed by myself with assistance from Prof. Dr. Werner Thiel, Dr. Cedric Groß, Xin Gui and Dr. Florian Bäßler, and revised with the help of Priv.-Doz. Dr. Christoph Riehn. The cover picture and cover profile was assembled by myself.

S. V. Kruppa, C. Groß, X. Gui, F. Bäßler, B. Kwasigroch, Y. Sun, R. Diller, W. Klopfer, G. Niedner-Schatteburg, C. Riehn, W. R. Thiel, *Chem. Eur. J.*, **2019**, 25(48), 11269-11284,

<https://doi.org/10.1002/chem.201901981>

Copyright ©2019 Wiley-VCH Verlag GmbH & Co. KGaA, Weinheim

Reprint Licence (manuscript)

Link (access date 31.08.2020):

<https://s100.copyright.com/CustomerAdmin/PLF.jsp?ref=390d045d-5a6d-4a0f-86ee-585c899697ae>

JOHN WILEY AND SONS LICENSE TERMS AND CONDITIONS

Aug 27, 2020

This Agreement between Mr. Sebastian Kruppa ("You") and John Wiley and Sons ("John Wiley and Sons") consists of your license details and the terms and conditions provided by John Wiley and Sons and Copyright Clearance Center.

License Number	4897120238289
License date	Aug 27, 2020
Licensed Content Publisher	John Wiley and Sons
Licensed Content Publication	Chemistry - A European Journal
Licensed Content Title	Photoinitiated Charge Transfer in a Triangular Silver(I) Hydride Complex and Its Oxophilicity
Licensed Content Author	Werner R. Thiel, Christoph Riehn, Gereon Niedner-Schatteburg, et al
Licensed Content Date	Aug 5, 2019
Licensed Content Volume	25
Licensed Content Issue	48
Licensed Content Pages	16
Type of Use	Dissertation/Thesis
Requestor type	Author of this Wiley article
Format	Print and electronic
Portion	Full article
Will you be translating?	No
Title	Photochemistry and Ultrafast Dynamics of Mass-selected Multinuclear Coinage Metal Complexes Studied by Electronic Photodissociation Ion Spectroscopy in an Ion Trap
Institution name	Technische Universität Kaiserslautern (TUK)
Expected presentation date	Oct 2020
Requestor Location	Mr. Sebastian Kruppa Erwin-Schrödinger-Straße 52-54 Kaiserslautern, 67663 Germany Attn: Mr. Sebastian Kruppa EU826007151
Publisher Tax ID	
Total	0.00 EUR
Terms and Conditions	

Reprint Licence (cover profile)

Link (access date 31.08.2020):

<https://s100.copyright.com/CustomerAdmin/PLF.jsp?ref=390d045d-5a6d-4a0f-86ee-585c899697ae>

JOHN WILEY AND SONS LICENSE TERMS AND CONDITIONS

Aug 31, 2020

This Agreement between Mr. Sebastian Kruppa ("You") and John Wiley and Sons ("John Wiley and Sons") consists of your license details and the terms and conditions provided by John Wiley and Sons and Copyright Clearance Center.

License Number	4899360835434
License date	Aug 31, 2020
Licensed Content Publisher	John Wiley and Sons
Licensed Content Publication	Chemistry - A European Journal
Licensed Content Title	Photoinitiated Charge Transfer in a Triangular Silver(I) Hydride Complex and Its Oxophilicity
Licensed Content Author	Werner R. Thiel, Christoph Riehn, Gereon Niedner-Schatteburg, et al
Licensed Content Date	Aug 5, 2019
Licensed Content Volume	25
Licensed Content Issue	48
Licensed Content Pages	1
Type of Use	Dissertation/Thesis
Requestor type	Author of this Wiley article
Format	Print and electronic
Portion	Full article
Will you be translating?	No
Title	Photochemistry and Ultrafast Dynamics of Mass-selected Multinuclear Coinage Metal Complexes Studied by Electronic Photodissociation Ion Spectroscopy in an Ion Trap
Institution name	Technische Universität Kaiserslautern (TUK)
Expected presentation date	Oct 2020
Requestor Location	Mr. Sebastian Kruppa Erwin-Schrödinger-Straße 52-54 Kaiserslautern, 67663 Germany Attn: Mr. Sebastian Kruppa EU826007151
Publisher Tax ID	
Total	0.00 EUR
Terms and Conditions	

Photoinitiated Charge Transfer in a Triangular Silver(I) Hydride Complex and Its Oxophilicity



Sebastian Kruppa



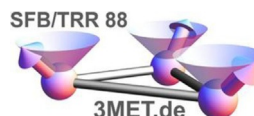
Cedric Groß



Xin Gui



Florian Böppler



Invited for the cover of this issue are the research groups of Rolf Diller, Gereon Niedner-Schatteburg, Christoph Riehn and Werner R. Thiel from the TU Kaiserslautern (TUK) and the group of Wim Klopper of the Karlsruhe Institute of Technology (KIT) collaborating within the research center "3MET" (SFB/TRR 88). The image depicts the photoinitiated charge transfer within a phosphine-stabilized triangular silver hydride complex. Read the full text of the article at [10.1002/chem.201901981](https://doi.org/10.1002/chem.201901981).

What prompted you to investigate this system?

In our collaborative research center "3MET" we are fascinated by metal-metal interactions, which determine the photo-physical/chemical properties of molecular transition metal complexes and are hitherto not fully understood. Inspired by previous studies on multinuclear silver hydrides and our work on bimetallic phosphine-stabilized compounds, we extended the nuclearity by designing a trimetallic system that allows for direct optical excitation of a metal-centered chromophore.

What was the inspiration for this cover design?

In order to emphasize the UV-induced electron transfer within the $[\text{Ag}_3\text{H}]$ scaffold, we chose a comic style illustration which highlights the resulting enforcement of argentophilic interaction within the metal core. Having in mind the explorative spirit of the scientific field of metal complexes and its search for new frontiers, we imagined the vast expanses of the universe. Finally, in an homage to the 1980s film "Tron", we attempted to illustrate the abstract inner workings of a CPU running complex quantum chemical algorithms.

Does the research open other avenues that you would like to investigate?

One aspect of the study which surprised us is the seemingly high reactivity of odd-electron silver hydride molecular ions towards dioxygen. Consequently, we are very curious about their molecular/electronic structure, envisioning their gas phase spectroscopic and theoretical characterization. We plan to probe how different ligands and other metal centers control optical properties and photoreactivity of metal hydrides also gearing towards their luminescence and ultrafast electronic dynamics in both gas phase and solution.



Front Cover:
C. Riehn, W. R. Thiel et al.
Photoinitiated Charge Transfer in a Triangular Silver(I) Hydride Complex
and Its Oxophilicity

CHEMISTRY

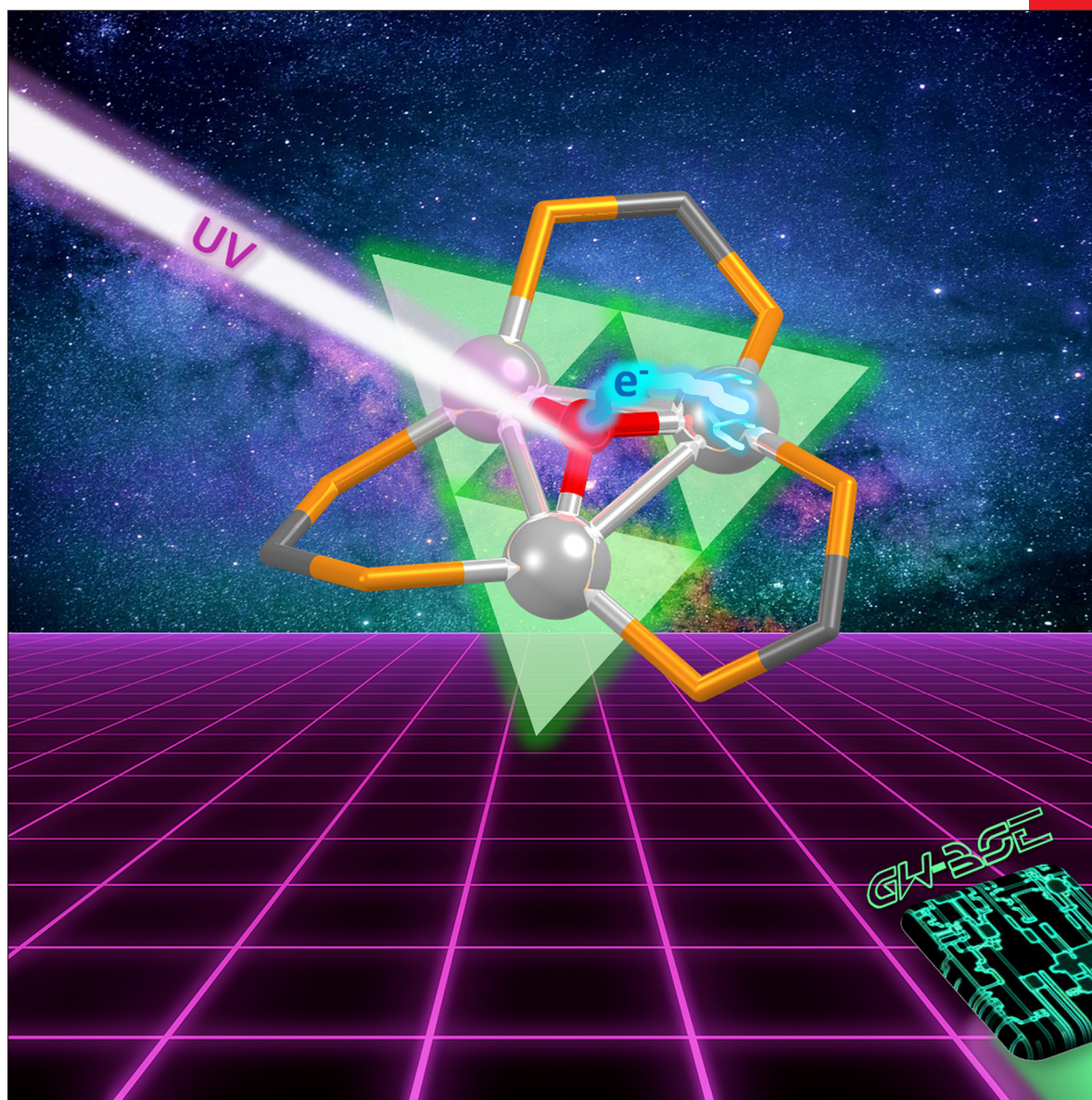
A **European** Journal

www.chemeurj.org

A Journal of



2019-25/48



Front Cover:

C. Riehn, W. R. Thiel et al.

Photoinitiated Charge Transfer in a Triangular Silver(I) Hydride Complex and Its Oxophilicity

Supported by

ACES Asian Chemical
Editorial Society

WILEY-VCH

Photochemistry | Very Important Paper |

VIP Photoinitiated Charge Transfer in a Triangular Silver(I) Hydride Complex and Its Oxophilicity

Sebastian V. Kruppa,^{+, [a]} Cedric Groß,^{+, [a]} Xin Gui,^[b] Florian Böppler,^[c] Björn Kwasigroch,^[a] Yu Sun,^[a] Rolf Diller,^[c] Wim Klopper,^[b] Gereon Niedner-Schatteburg,^[a, d] Christoph Riehn,^{*, [a, d]} and Werner R. Thiel^{*, [a]}

Abstract: The photoexcitation of a triangular silver(I) hydride complex, $[\text{Ag}_3(\mu_3\text{-H})(\mu_2\text{-dcpm})_3](\text{PF}_6)_2$ ($[\text{P}](\text{PF}_6)_2$, dcpm = bis(dicyclohexylphosphino)methane), designed with “UV-silent” bis-phosphine ligands, provokes hydride-to- Ag_3 single and double electron transfer. The nature of the electronic transitions has been authenticated by absorption and photodissociation spectroscopy in parallel with high-level quantum-chemical computations utilizing the *GW* method and Bethe-Salpeter equation (*GW*-BSE). Specific photofragments of

mass-selected $[\text{P}]^{2+}$ ions testify to charge transfer and competing pathways resulting from the unique $[\text{Ag}_3(\mu_3\text{-H})]^{2+}$ scaffold. This structural motif of $[\text{P}](\text{PF}_6)_2$ has been unequivocally verified by ^1H NMR spectroscopy in concert with DFT and X-ray diffraction structural analysis, which revealed short equilateral Ag–Ag distances ($d_{\text{AgAg}} = 3.08 \text{ \AA}$) within the range of argentophilic interactions. The reduced radical cation $[\text{P}]^{+\cdot}$ exhibits strong oxophilicity, forming $[\text{P}+\text{O}_2]^{+\cdot}$, which is a model intermediate for silver oxidation catalysis.

Introduction

Multinuclear coinage metal hydrides (CMHs) are fascinating synthetic targets that show promising applications in energy storage, as model systems for the exploration of metalphilic interactions,^[1] and also recently in photocatalysis.^[2] Binuclear systems often feature a bridging hydride ($\mu_2\text{-H}$) structural motif,^[3] a situation best described as three-center, two-electron bonding,^[4] but hydride-“capping” ($\mu_3\text{-H}$) and even $\mu_{(4-6)}\text{-H}$ coordination modes have been reported for higher nuclearities.^[5]

Beginning with Wurtz’s synthesis of polymeric CuH in the 19th century,^[6] copper hydrides are the longest-known and best-studied CMHs. Recently, the first monoligated dimeric copper hydrides were isolated by using N-heterocyclic carbene (NHC) ligands.^[7] The key chemical transformations that are

mediated by CMHs encompass reduction reactions, for example, the hydrogenation of carbonyl compounds or CO_2 ,^[8] as well as hydrosilylations (ketones)^[8a] and other hydrogenations (alkenes and alkynes).^[2a] In catalytic studies the application of copper hydrides dominates today,^[2a, 9] but interesting perspectives on silver^[2a, 10] and gold or heterometallic species have been reported^[11] and have gained in importance on account of their distinctive (photo)reactivity.^[2a, 12] With regard to the photochemistry of CMHs and also transition-metal hydrides, their chemical dynamics are largely unexplored but they provide an interesting variety of photoproducts, as reviewed recently.^[2b] For instance, monohydride complexes show homolytic M–H bond splitting, reductive elimination of RH (R = alkyl, O-alkyl, etc.), photoisomerization, or proton and hydride transfer, depending on the composition of the complex and the environment.^[2b, 13] Thus, there is a clear motivation for additional studies to correlate the physico-optical properties of CMHs (UV spectra, cross-sections, types of transitions), their molecular structures (hydride coordinating motif), and the primary photo-products.

Specifically, silver-based hydrides such as $[\text{Ag}_n\text{H}]^+$ ($n = 2, 4, 6$) “bare” cluster cations have lately been put in the spotlight through comprehensive gas-phase studies of their preparation and reactivity, utilizing ion-trap multistage mass spectrometric techniques (MS^n).^[14] Also, Ag_2H^+ , the simplest binuclear prototype system, has been scrutinized by laser-induced fragmentation spectroscopy together with high-level quantum-chemical calculations.^[3a]

In this work, we focused on silver metal hydrides stabilized by bis-phosphine ligands L^{R} [$\text{L}^{\text{R}} = \text{R}_2\text{P-CH}_2\text{-PR}_2$, with R = CH_3 (Me), C_6H_5 (Ph), C_6H_{11} (Cy)]. Pioneering gas-phase studies of the molecular ion $[\text{Ag}_2(\text{H})(\text{L}^{\text{Ph}})]^+$ highlighted the key importance of

[a] S. V. Kruppa,⁺ C. Groß,⁺ B. Kwasigroch, Dr. Y. Sun, Prof. Dr. G. Niedner-Schatteburg, Dr. C. Riehn, Prof. Dr. W. R. Thiel
Department of Chemistry, Technische Universität Kaiserslautern (TUK)
Erwin-Schrödinger, Str. 52, 67663 Kaiserslautern (Germany)
E-mail: riehn@chemie.uni-kl.de
thiel@chemie.uni-kl.de

[b] X. Gui, Prof. Dr. W. Klopper
Institute of Physical Chemistry, Karlsruhe Institute of Technology (KIT)
Fritz-Haber-Weg 2, 76131 Karlsruhe (Germany)

[c] F. Böppler, Prof. Dr. R. Diller
Department of Physics, Technische Universität Kaiserslautern (TUK)
Erwin-Schrödinger, Str. 46, 67663 Kaiserslautern (Germany)

[d] Prof. Dr. G. Niedner-Schatteburg, Dr. C. Riehn
Research Center OPTIMAS, Erwin-Schrödinger Str. 46
67663 Kaiserslautern (Germany)

[*] These authors contributed equally to this work.

Supporting information and the ORCID identification number(s) for the author(s) of this article can be found under:
<https://doi.org/10.1002/chem.201901981>.

CMHs for catalysis, revealing its reactivity with formic acid to yield $[\text{Ag}_2(\text{O}_2\text{CH})(\text{L}^{\text{Ph}})]^+$ accompanied by the loss of H_2 and followed by collisional-activated CO_2 extrusion to regenerate the hydride-bridged dinuclear silver catalyst ion, which closes the circle.^[3b,11b] By replacing the phenyl by cyclohexyl moieties ($[\text{Ag}_2(\text{H})(\text{L}^{\text{Cy}})]^+$), it was demonstrated that the silver-mediated protodecarboxylation cycle was not disrupted and an enhanced reactivity of the bimetallic hydride towards formic acid was observed ($\text{R: Cy} > \text{Ph}$).^[3b] In another study on the trinuclear dihydride $[\text{Ag}_3(\mu_2\text{-H})_2(\text{L}^{\text{Ph}})]^+$ fragment ion, photoexcitation under vacuum led to the release of H_2 , whereas collisional-induced dissociation (CID) mainly led to the loss of AgH , thereby demonstrating electronic-state-specific reactivity.^[15] However, the assignment of silver-hydride-centered electronic transitions for L^{Ph} -stabilized complexes was not clear cut and indeed is complicated owing to the significant involvement of ligand-centered $\pi\text{-}\pi^*$ transitions.^[3b,15]

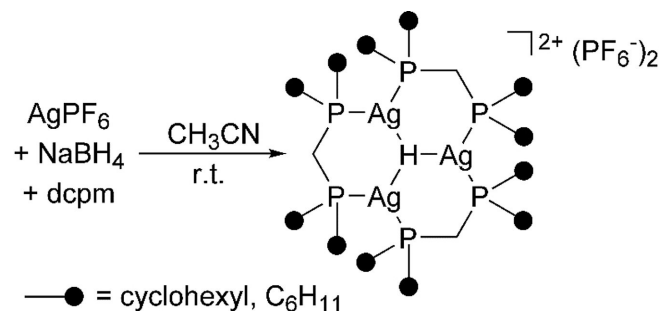
Because our research interest is focused on the static and dynamic exploration of cooperative metallophilic interactions^[16] within d^8/d^{10} electron configurations,^[17] we prefer to investigate molecular targets that provide absorption features for direct optical metal-centered excitation. To this end, we herein report on the synthesis of the triangular silver hydride complex $[\text{Ag}_3(\mu_3\text{-H})(\mu_2\text{-L}^{\text{Cy}})_3]^{2+}$ ($[\text{P}]^{2+}$, $\text{L}^{\text{Cy}} = \text{bis}(\text{dicyclohexylphosphino})\text{methane}$) featuring the UV/Vis spectroscopically innocent, alkylated bis-phosphine ligands L^{Cy} . This was motivated by preliminary studies on related triangular Ag/Cu CMHs^[5e,f] and also binuclear $[\text{M}_2(\text{L}^{\text{Cy}})_2]^{2+}$ ($\text{M} = \text{Ag}, \text{Au}$) complexes.^[17b,c,18] In addition, the relative binding energy of L^{Cy} is advantageously higher than that of L^{Ph} , as revealed by an ion-trap CID investigation of $[\text{Au}_n(\text{PR}_3)_m]^{+/2+}$ ($n = 1\text{--}11$, $m = 1\text{--}8$, $\text{R} = \text{Me}, \text{Ph}, \text{Cy}$).^[19] Thus, the expected stability of $[\text{P}]^{2+}$ facilitates parallel studies in the gas phase and in solution. Finally, we note in passing that recently there has been growing interest in the preparation of (atomically precise) ligand-protected silver subnano- and nanoclusters by the reduction of silver(I) salts with NaBH_4 , with the emphasis on $[\text{P}]^{2+}$ being a potential intermediate in cluster growth or a building block of larger entities.^[5h,8a,20]

We present herein the synthesis and also the X-ray diffraction and NMR structural analyses of the triangular silver hydride complex $[\text{P}](\text{PF}_6)_2$ supported by DFT calculations. The gas-phase reactivity of $[\text{P}]^{2+}$ was explored by mass spectrometric techniques, in particular, comparing the CID, photoinduced dissociation (PD), and electron-transfer dissociation (ETD) activation methods. Furthermore, the core-centered optical properties (absorption and luminescence) of $[\text{P}]^{2+}$ in solution and in the gas phase were investigated in parallel by utilizing photodissociation (PD) laser spectroscopy. High-level quantum-chemical calculations based on the Bethe–Salpeter formalism facilitated the assignment of electronic transitions by transition density plots. Finally, we describe an unexpected gas-phase reactivity towards molecular oxygen, a newly observed reaction type for silver radical cations, as a result of single-electron reduction by ETD in an ion trap.

Results and Discussion

Synthesis and structural examination

The trinuclear silver(I) complex $[\text{Ag}_3(\mu_3\text{-H})(\mu_2\text{-L}^{\text{Cy}})_3](\text{PF}_6)_2$ ($[\text{P}](\text{PF}_6)_2$, $\text{L}^{\text{Cy}} = \text{dcpm} = (\text{C}_6\text{H}_{11})_2\text{PCH}_2\text{P}(\text{C}_6\text{H}_{11})_2$) was prepared according to a modified literature procedure by the addition of sodium borohydride to a well-stirred suspension of dcpm and silver(I) hexafluorophosphate in acetonitrile at room temperature (Scheme 1).^[5e,f] The deuterido congener was analogously synthesized by using sodium borodeuteride.



Scheme 1. Synthesis of $[\text{Ag}_3(\mu_3\text{-H})(\mu_2\text{-L}^{\text{Cy}})_3](\text{PF}_6)_2$ ($\text{L}^{\text{Cy}} = \text{dcpm} = (\text{C}_6\text{H}_{11})_2\text{PCH}_2\text{P}(\text{C}_6\text{H}_{11})_2$, r.t. = room temperature).

Single crystals of $[\text{P}](\text{PF}_6)_2$ suitable for X-ray diffraction structural analysis were obtained by the slow diffusion of diethyl ether into a solution of the silver complex in acetonitrile under protection from light. $[\text{P}](\text{PF}_6)_2$ crystallizes in the orthorhombic space group $Fdd2$ with eight molecules in the unit cell. The solid-state structure of $[\text{P}](\text{PF}_6)_2$ reveals three silver(I) centers that are μ_3 -bridged by a central hydrido ligand and μ_2 -bridged by the three L^{Cy} bis-phosphine ligands, resulting in a distorted trigonal-planar coordination environment for each silver(I) site (Figure 1a and Figure S1 in the Supporting Information). The most obvious structural feature of $[\text{P}](\text{PF}_6)_2$ is its nearly equilateral triangular $(\mu_3\text{-H})\text{Ag}_3$ core. Within this structure, the average $\text{Ag}\text{--}\text{Ag}$ distance is 3.082 Å, which is in the range of argentophilic $d^{10}\text{--}d^{10}$ interactions (see Table 1, Σ van der Waals radii = 3.44 Å).^[1a,21] A C_2 axis running through the atoms $\text{Ag}1$ and $\text{H}1$ determines the symmetry of the $(\text{P})_3\text{Ag}_3(\text{H})$ core (Figure 1a, inset). A similar structure with comparable symmetry was obtained by quantum-chemical structure optimization at the DFT/PBE-D3(BJ)/def2-SV(P)/(def2-TZVP for hydride) level for the isolated $[\text{P}]^{2+}$ cation (Figure 1b, inset, and Table 1). The computed $\text{Ag}\text{--}\text{P}$ bond lengths and $\text{P}\text{--}\text{Ag}\text{--}\text{Ag}\text{--}\text{P}$ dihedral angles are similar to the experimental values, whereas the $\text{Ag}\text{--}\text{Ag}$ distance was calculated to be slightly shorter (see Table 1). The main difference between the experimental and computed structures lies in the position of the central hydrogen atom and the accompanying $\text{Ag}\text{--}\text{H}1$ distances. The calculation gave a clear preference for a position that is located out of the Ag_3 plane by around 0.6 Å, whereas the experimental results point more to an in-plane hydride localization, as proposed for the Cu_3H congener.^[5f] However, a small displacement of the hydrido ligand cannot be completely ruled out. Moreover, it is ex-

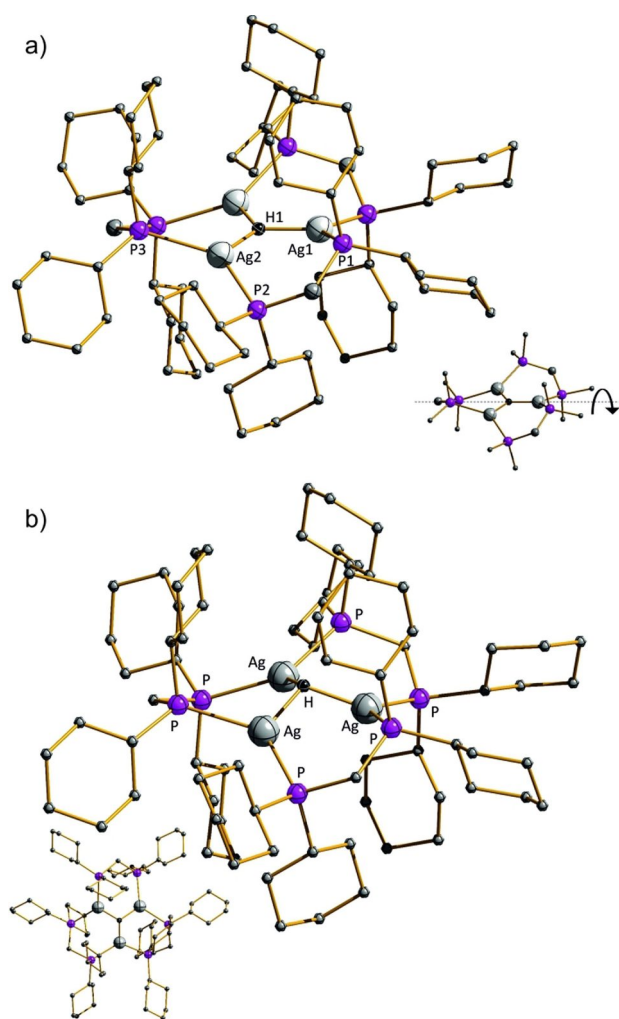


Figure 1. a) Molecular structure of $[\text{Ag}_3(\mu_3\text{-H})(\mu_2\text{-L}^{\text{Cy}})_3](\text{PF}_6)_2$ in the solid state. Hydrogen atoms and hexafluorophosphate anions have been omitted for clarity. Inset: illustration of the pseudo- C_2 axis passing through the Ag1 and H1 atoms. Characteristic bond lengths [Å] and angles [°], with standard deviations indicated in parentheses: Ag1–Ag2: 3.078(1), Ag1–P1: 2.462(3), Ag2–P2: 2.452(3), Ag2–P3: 2.450(4), Ag1–H1: 1.781(14), Ag2–H1: 1.778(7), Ag1–H1–Ag1_a: 120.539(2), Ag1–H1–Ag2: 119.730(2), P1–Ag1–P1_a: 128.42(13), P2–Ag2–P3: 130.05(12), P1_a–Ag1–H1: 115.79(8), P1–Ag1–H1: 115.79(8), P3–Ag2–H1: 114.7(4), P2–Ag2–H1: 115.2(4). b) Calculated structure of $[\text{P}]^{2+}$ optimized at the DFT/PBE-D3(BJ)/def2-SV(P) level of theory. Hydrogen atoms have been omitted for clarity. Inset: top view.

pected that hydride tunneling equilibrates possible structural asymmetries.^[3a]

Several structurally characterized hydrido silver(I) compounds are documented in the literature, ranging from mononuclear systems to small clusters with less than 10 silver nuclei. Bertrand and co-workers reported the first isolated structure of a mononuclear silver(I) hydride complex, $[(\text{NHC})\text{AgH}]$, in 2017, which is stabilized by a very bulky N-heterocyclic carbene ligand.^[22] However, due to the disordering of silver(I) ions, the position of the hydrido ligand could not be unambiguously located. By trapping this compound with $\text{B}(\text{C}_6\text{F}_5)_3$, a stable adduct with a nearly linear $\text{C}_{\text{NHC}}\text{-Ag-H-B}$ arrangement was isolated ($d_{\text{AgH}} = 1.81 \text{ \AA}$). The analogous copper(I) hydride species crystallizes as the dimer $[(\text{NHC})\text{Cu}(\mu_2\text{-H})_2]$, which exhibits two

bridging hydrido ligands ($d_{\text{CuH}} = 1.50, 1.64 \text{ \AA}$).^[22] A few years earlier, a binuclear NHC-stabilized complex, $[(\text{NHC})_2\text{Ag}_2(\mu_2\text{-H})]^+$, was reported by Sadighi and co-workers.^[8e,23] In this complex, the Ag–H distance is 1.69 \AA ,^[8e] which is distinctly shorter than those in the $[(\text{NHC})\text{AgH}][\text{B}(\text{C}_6\text{F}_5)_3]$ adduct^[22] and the herein reported trinuclear $[\text{P}](\text{PF}_6)_2$ complex. In addition, the average Ag–Ag distance in $[\text{P}](\text{PF}_6)_2$ ($d_{\text{AgAg}} = 3.08 \text{ \AA}$) is significantly longer than that in $[(\text{NHC})_2\text{Ag}_2(\mu_2\text{-H})]^+$ ($d_{\text{AgAg}} = 2.81 \text{ \AA}$),^[8e] which can be rationalized by the enhanced charge repulsion in the trinuclear, dicationic complex.

Furthermore, larger nanosized Ag_nH ($n = 7\text{--}11$) clusters with a single interstitial hydride, stabilized with chelating sulfur- and selenium-based ligands, have been structurally characterized.^[5g,24] In this regard, a tri-/tetra-capped tetrahedral Ag_4H core was found as the central structural motif of smaller nanoclusters ($n = 7\text{--}8$), whereas a hexa-capped trigonal-bipyramidal geometry was found for undecanuclear Ag_{11}H clusters.^[24e] For the latter case, X-ray diffraction analysis suggested that the hydride is located in one of the tetrahedrons of the central trigonal Ag_5 bipyramid, whereas DFT predicts an energy minimum for its position within the central trigonal plane.^[24e]

For an overview, the structural parameters of a series of related bis-phosphine-stabilized, trinuclear silver(I) and copper(I) monohydride complexes are summarized in Table 1 and will be discussed in the following. The first bis-phosphine-stabilized, trinuclear hydrido silver(I) complex, $[\text{Ag}_3(\mu_3\text{-H})(\mu_3\text{-Cl})(\mu_2\text{-L}^{\text{Ph}})_3](\text{BF}_4)$, was reported in 2013 by O’Hair and co-workers, featuring an additional “capping” ($\mu_3\text{-Cl}$) chlorido ligand, which deflects the hydrido ligand out of the Ag_3 plane by around 0.95 \AA due to charge repulsion.^[5d] As expected, the Ag–Ag distance of this monocationic complex is shorter (by ca. 0.2 \AA) than that in the $[\text{P}]^{2+}$ dicationic species. Interestingly, the calculated structure of the singly reduced $[\text{P}]^+$ complex, which we have observed by electron-transfer reduction in an ion trap, exhibits similar bond distances, which also supports here a partial reduction of the Ag_3 core (Table 1 and Tables S2 and S3 in the Supporting Information). Subsequently, in 2014, the chloride-free $[\text{Ag}_3(\mu_3\text{-H})(\mu_2\text{-L}^{\text{Ph}})_3](\text{BF}_4)_2$ complex was discovered by O’Hair and co-workers.^[5e] This complex differs from $[\text{P}]^{2+}$ of this work only in the bridging bis-phosphine ligands (L^{Ph} instead of L^{Cy}), displaying similar but slightly longer Ag–Ag distances (by ca. 0.04 \AA). This trend may be correlated with the larger electron density at the σ -donating phosphorus of the L^{Cy} ligands compared with L^{Ph} .^[19] In the same study, the analogous deuterido complex $[\text{Ag}_3(\mu_3\text{-D})(\mu_2\text{-L}^{\text{Ph}})_3](\text{BF}_4)_2$ was successfully crystallized and the position of the deuterido ligand was found to be slightly shifted out of the Ag_3 plane by around 0.3 \AA , as elucidated by neutron diffraction experiments.^[19] The analogous copper(I) congener of $[\text{P}](\text{PF}_6)_2$, $[\text{Cu}_3(\mu_3\text{-H})(\mu_2\text{-L}^{\text{Cy}})_3](\text{PF}_6)_2$, was successfully isolated in 2005 by Mao et al.^[5f] It exhibits systematically shorter M–M (ca. 2.89 \AA) and M–P (ca. 2.29 \AA) distances compared with $[\text{P}](\text{PF}_6)_2$, with similar P–M–M–P dihedral angles found for both congeners (Table 1).

Additionally, we utilized NMR spectroscopic techniques to characterize the $[\text{Ag}_3(\mu_3\text{-H})(\mu_2\text{-L}^{\text{Cy}})_3](\text{PF}_6)_2$ ($[\text{P}](\text{PF}_6)_2$) system in solution. According to the NMR data, $[\text{P}]^{2+}$ shows D_{3h} and not C_2 symmetry in deuterated acetonitrile (see Figure 2 and Figures

Table 1. Comparison of selected structural parameters for related trinuclear coinage metal hydride complexes [averaged atomic distances \bar{r} , hydride distances to the $[M_3]$ -plane, and P-M-M-P dihedral angles ($M = \text{Ag}, \text{Cu}$) obtained by XRD, DFT (PBE-D3(BJ)/def2-SV(P)/def2-TZVP for central hydrogen), and neutron diffraction methods (see Tables S1–S3 in the Supporting Information for details).

Compound	$\bar{r}(\text{M}-\text{M})$ [Å]	$\bar{r}(\text{M}-\text{H}1)$ [Å]	$\bar{r}(\text{M}-\text{P})$ [Å]	$r(\text{H}1 < \text{C}-[\text{M}_3]\text{-plane})$ [Å]	$ \angle(\text{P}-\text{M}-\text{M}-\text{P}) $ [°]	Ref.	Method
$[\text{Ag}_3(\text{H})(\text{L}^{\text{Cy}})_3](\text{PF}_6)_2$	3.08	1.78 ^[a]	2.45	0 ^[a]	33.9	this work	XRD
$[\text{Ag}_3(\text{H})(\text{L}^{\text{Cy}})_3]^{2+}$	3.02	1.85	2.46	0.62	34.4		DFT
$[\text{Ag}_3(\text{H})(\text{L}^{\text{Cy}})_3]^{+ \cdot [b]}$	2.84	1.92	2.45	1.00	32.5		DFT
$[\text{Ag}_3(\text{L}^{\text{Cy}})_3]^{2+ [c]}$	2.89		2.47		35.5		DFT
$[\text{Ag}_3(\text{H}/\text{D})(\text{L}^{\text{Ph}})_3](\text{BF}_4)_2$	3.12	1.83	2.46	0.31	12.1	[5e]	XRD/neut. diff.
$[\text{Cu}_3(\text{H})(\text{L}^{\text{Cy}})_3](\text{PF}_6)_2$	2.89	1.67 ^[a]	2.29	0 ^[a]	36.4	[5f]	XRD
$[\text{Ag}_3(\text{H})(\text{BH}_4)(\text{L}^{\text{Ph}})_3](\text{BF}_4)$	2.91	1.94 ^[a]	2.45	0.96 ^[a]	21.2	[5c]	XRD
$[\text{Ag}_3(\text{H})(\text{Cl})(\text{L}^{\text{Ph}})_3](\text{BF}_4)$	2.90	1.92	2.44	0.95	20.2	[5d]	XRD/neut. diff.

[a] The hydride position was located in the difference Fourier map. [b] Observed by electron-transfer reduction in an ion trap. [c] Main photofragment of $[\text{P}]^{2+}$ in the ion trap.

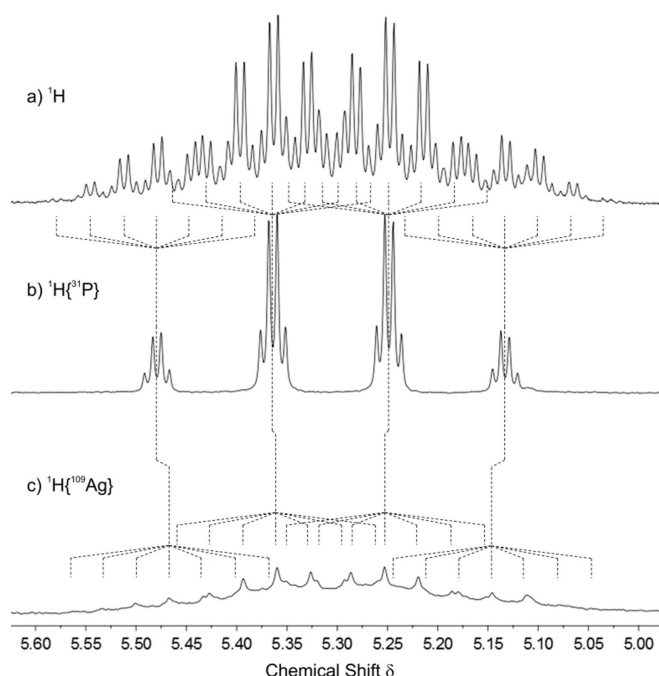


Figure 2. a) ^1H , b) $^1\text{H}\{^{31}\text{P}\}$, and c) $^1\text{H}\{^{109}\text{Ag}\}$ μ_3 -hydride NMR resonance of $[\text{P}](\text{PF}_6)_2$ ($[\text{D}_3]\text{MeCN}$, 600.1 MHz, ambient temperature).

S2–S10 in the Supporting Information), which can be explained by a rapid equilibration of the three bent six-membered (P-Ag-H1-Ag-P-CH₂-) rings (Figure 1 a).

The ambient-temperature ^1H NMR spectrum of $[\text{P}](\text{PF}_6)_2$ features an intricate multiplet centered at $\delta \approx 5.31$ ppm, which integrates for one hydrogen atom and is assigned to the μ_3 -hydride resonance (Figure 2a and Figures S2 and S6 in the Supporting Information). Its appearance at a positive ppm value is related to the strong magnetic deshielding of the central hydrogen by the three surrounding silver(I) ions and it lies within the range of reported chemical shifts of polynuclear Ag_nH complexes ($n = 2\text{--}11$; $\delta = -1.13$ to 7.5 ppm),^[5e] which strongly depends on the ligands, nuclearity, and the overall charge of the complexes. In comparison, the copper congener of

$[\text{P}](\text{PF}_6)_2$ displays an upfield-shifted μ_3 -hydride resonance at $\delta \approx 2.2$ ppm.^[5f]

The complex μ_3 - ^1H multiplet of $[\text{P}](\text{PF}_6)_2$ collapses into four quartets in the $\{^{31}\text{P}\}$ -decoupled ^1H NMR spectrum (Figure 2b), thereby substantiating the hydride coupling ($^1J_{\text{HAg}}$) to three magnetically equivalent silver nuclei for each of the four $[\text{Ag}, \text{Ag}, \text{Ag}]$ ($n = 107, 109$) isotopologues, which are present in an approximate 1:3:3:1 ratio (see Table 2). In addition the $\{^{109}\text{Ag}\}$ -decoupled ^1H NMR spectrum distinctly reveals four interlacing septets over a broad range between $\delta \approx 5.57$ and 5.07 ppm (Figure 2c, dashed lines), despite having a broadened baseline (note: both ^{109}Ag and ^{107}Ag nuclei are nearly decoupled). Based on the combined information extracted from both the $^1\text{H}\{^{31}\text{P}\}$ and $^1\text{H}\{^{109}\text{Ag}\}$ NMR spectra (Figure 2b,c) and the fact that the $^1J_{\text{HAg}}$ coupling constants are almost identical for ^{107}Ag and ^{109}Ag (both $I = 1/2$, natural abundance = 52 and 48%, respectively), the difference in the chemical shifts originating from the individual isotopologues (isotopologue shift $\Delta\delta$) and the $^1J_{\text{HAg}}$ coupling constants can be determined. Consequently, the $^1\text{H}\{^{31}\text{P}\}$ resonance shown in Figure 2b can be unambiguously assigned to four isolated quartets, for each of the four isotopologues, which are separated by a chemical shift of $\Delta\delta \approx 0.12$ ppm, as opposed to being interlacing quartets. As a result, the intricate ^1H multiplet at $\delta \approx 5.31$ ppm is assigned to four interlaced quartets of septets ($^1J_{\text{HAg}} \approx 5.0$ Hz, $^2J_{\text{HP}} = 20.1$ Hz) at chemical shifts of $\delta = 5.48, 5.36, 5.25,$ and 5.13 ppm (see Table 2). For comparison, O'Hair and co-workers reported a slightly upfield-shifted hydride multiplet for the $[\text{Ag}_3(\text{H})(\text{L}^{\text{Ph}})_3](\text{BF}_4)_2$ congener, centered at $\delta = 4.75$ ppm, and a similar H–P coupling ($^2J_{\text{HP}} = 21$ Hz).^[5e] However, a much larger value for the H–Ag coupling ($^1J_{\text{H}^{109}\text{Ag}} = 86$ Hz, $^1J_{\text{H}^{107}\text{Ag}} = 75$ Hz) and a small isotopologue shift ($\Delta\delta \approx 0.02$ ppm) was assigned,^[5e] in contrast to our findings for $[\text{P}](\text{PF}_6)_2$ (see Table 2).

The $^{31}\text{P}\{^1\text{H}\}$ NMR spectrum of $[\text{P}](\text{PF}_6)_2$ comprises a doublet of multiplets at $\delta = 25.84$ ppm, which only allowed the assignment of $^1J_{\text{AgP}} \approx 378$ Hz, which is in the typical range for silver(I) phosphine complexes.^[25] This is also consistent with reported Ag–P coupling constants for phosphine-stabilized silver(I) complexes ($^1J_{\text{AgP}} \approx 500\text{--}640$ Hz) as reported by Van Koten and co-workers.^[26] In addition, the ^{31}P signal of the PF_6^- anions is

Table 2. Calculated and experimental natural abundance ratios and chemical shifts (μ_3 - ^1H) for all silver isotopologues of $[\text{P}](\text{PF}_6)_2$ as well as coupling constants ($^1J_{\text{HAg}}$, $^2J_{\text{HP}}$) determined from the ^1H , $^1\text{H}\{^{31}\text{P}\}$, and $^1\text{H}\{^{109}\text{Ag}\}$ NMR spectra shown in Figure 2. Literature NMR parameters for related compounds are given for comparison.

Isotopologue of $[\text{Ag}_3(\mu_3\text{-H})(\mu_2\text{-L}^{\text{CY}})_3](\text{PF}_6)_2$	Calcd ratio ^[a]	Exp. ratio ^[b]	$\delta(\mu_3\text{-H})$ [ppm]	$^1J(^1\text{H}\text{-}^{107/109}\text{Ag})$ [Hz]	$^2J(^1\text{H}\text{-}^{31}\text{P})$ [Hz]
$^{109}\text{Ag}, ^{109}\text{Ag}, ^{109}\text{Ag}$	0.8	1.0	5.48 ^[c]	4.9–5.0 ^[d]	20.1 ^[d]
$^{109}\text{Ag}, ^{109}\text{Ag}, ^{107}\text{Ag}$	2.6	3.0	5.36 ^[c]		
$^{109}\text{Ag}, ^{107}\text{Ag}, ^{107}\text{Ag}$	2.8	3.0	5.25 ^[c]		
$^{107}\text{Ag}, ^{107}\text{Ag}, ^{107}\text{Ag}$	1.0	1.0	5.13 ^[c]		
Compound					
$[\text{Ag}_3(\mu_3\text{-H})(\mu_2\text{-L}^{\text{Ph}})_3](\text{BF}_4)_2$ ^[5e]			4.75	75/86	21.0
$[\text{Cu}_3(\mu_3\text{-H})(\mu_2\text{-L}^{\text{CY}})_3](\text{CF}_3\text{SO}_3)_2$ ^[5f]			2.20		16.0
$[\text{Ag}_7(\mu_4\text{-H})(\text{E}_2\text{P}(\text{OR}))_2]_6$ (E = S, Se; R = <i>i</i> Pr, Et) ^[5g]			3.50–5.65	39.4–39.6	

[a] Calculated natural abundance ratios were calculated by using the Compass Isotope Pattern software (Bruker). [b] Determined by integration of both ^1H and $^1\text{H}\{^{31}\text{P}\}$ NMR signals (600.1 MHz, Figure 2a,b). [c] It was not possible to determine whether the $^{109}\text{Ag}_3$ or $^{107}\text{Ag}_3$ isotopologue was shifted to a lower or higher field, respectively [d] Determined from the ^1H NMR spectra (600.1 MHz).

found at $\delta \approx -144.61$ ppm (septet, $^1J_{\text{PF}} = 706.1$ Hz), which confirms that no chemical modification of the counter ions occurred during synthesis.

Quantum chemical calculations

To characterize the electronic ground and excited states of $[\text{P}]^{2+}$, quantum-chemical calculations were performed with the TURBOMOLE program package.^[27] Because the commonly applied time-dependent DFT (TD-DFT) method suffers from large deficiencies in the description of charge-transfer (CT) states, the Bethe–Salpeter equation (BSE) approach applied within the *GW* approximation was employed to calculate the electronic excitations.^[28] The def2-SV(P) basis set^[29] was used with an effective core potential for silver.^[30] For the central hydrogen, the def2-TZVP basis set was used for geometry optimizations and the def2-TZVPP basis set for calculating the electronic excitation energies.

The ground-state equilibrium geometry of $[\text{P}]^{2+}$ was first optimized in C_2 symmetry at the PBE-D3(BJ) level of theory^[31] starting from the obtained X-ray diffraction structure (Figure 1a). Because the calculated harmonic vibrational frequencies comprised one imaginary frequency of 257.171 cm^{-1} , the geometry was re-optimized in C_1 symmetry yielding a true minimum with only real harmonic vibrational frequencies (see Figure S26 and Tables S2 and S3 in the Supporting Information). This optimized ground-state structure is in good agreement with the experimental X-ray diffraction and NMR results, as discussed above, and was further validated by comparison of the calculated electronic transitions with the experimental electronic absorption spectrum of the mass-selected $[\text{P}]^{2+}$ in an ion trap.

For the optimized geometry of $[\text{P}]^{2+}$ (C_1), quasi-particle energies were determined at the eigenvalue-only self-consistent *GW* (ev*GW*)^[32] level with the PBE0 functional. The total tensor space was 423151, for which the standard *GW* using the full spectral function was not applicable. Therefore, the calculations were performed with RI-*GW* (resolution-of-the-identity *GW*) employing analytic continuation for HOMO and LUMO only.^[33] The resulting orbitals about the Fermi level are present-

ed in Figure 3. We observe that the HOMO–LUMO gap, which is much too small at the PBE0 level, is increased substantially at the ev*GW* level, which aims to correct deficiencies in the PBE0 orbital energies. All the other orbital levels are shifted with the same shifts as computed for the HOMO and LUMO levels, yielding larger excitation energies. The orbital plots identify the electronic interactions between the hydride and Ag_3 moieties, which allows the experimental absorption spectrum to be unraveled (see Figure 5). Based on the quasi-particle energies obtained from the ev*GW* calculation, the singlet and triplet excitation energies were computed by using the Bethe–Salpeter equation (BSE) formalism (see Tables S11 and S12 in the Supporting Information for energies, oscillator strengths, and natural transition orbitals).

In addition, the ground-state geometries of the formally reduced odd-electron species $[\text{P}]^{+}$ and $[\text{P}\text{-H}]^{2+}$ determined by mass spectrometric techniques were optimized in the same manner and are compared in Table 1 (see Tables S2 and S3 in the Supporting Information for details). Both structures feature similar, but shortened Ag–Ag distances compared with $[\text{P}]^{2+}$

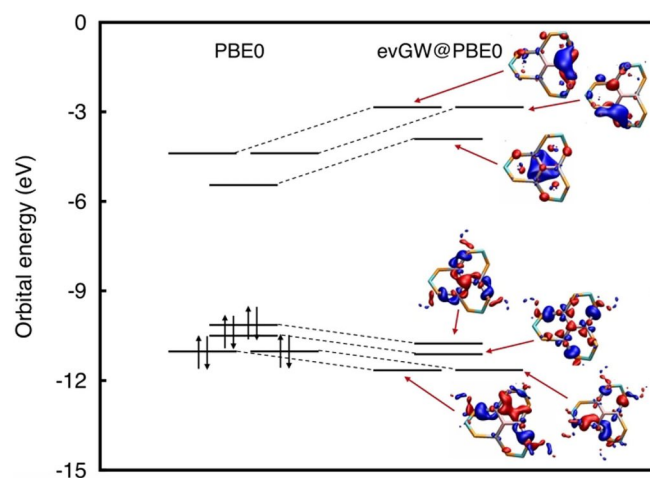


Figure 3. Energy levels of the orbitals HOMO–3 to LUMO+2 of $[\text{P}]^{2+}$ obtained at the PBE0/def2-SV(P) and ev*GW*@PBE0/def2-SV(P) levels of theory. Orbitals are shown with an isovalue of $\pm 0.04a_0^{-3/2}$ (cyclohexyls and methylene hydrogen atoms have been omitted for clarity).

($d_{\text{AgAg}} = 2.84$ and 2.89 Å, respectively), which is indicative of enhanced argentophilic interactions and also similar oxidation states of their Ag_3 cores. This is in accordance with the small partial charges of the silver centers calculated for $[\text{P}]^{2+}$ and $[\text{P}-\text{H}]^{2+}$, that is, $0.19e$ and $0.22e$, respectively (Table 3). Another interesting aspect is the fact that the central hydrogen of $[\text{P}]^{2+}$ is computed to be significantly shifted away from the Ag_3 plane, by roughly an additional 0.4 Å, compared with $[\text{P}]^{2+}$. A natural population analysis revealed that it exhibits an almost neutral charge of $0.02e$. Consequently it is predicted that the $\mu_3\text{-H}$ atom loses its hydridic character upon single electron transfer ($[\text{P}]^{2+} + e^- \rightarrow [\text{P}]^{+}$).

Table 3. Calculated averaged partial charges of Ag, $\mu_3\text{-H}$, and P atoms and L^{Cy} moieties for the $[\text{P}]^{2+}$, $[\text{P}]^{+}$, and $[\text{P}-\text{H}]^{2+}$ species based on a natural population analysis (NPA).

Species	Average partial charge [e]			
	Ag	$\mu_3\text{-H}$	P	L^{Cy}
$[\text{Ag}_3(\text{H})(\text{L}^{\text{Cy}})_3]^{2+}$	+0.56	-0.59	+0.74	+0.30
$[\text{Ag}_3(\text{H})(\text{L}^{\text{Cy}})_3]^{+}$	+0.19	+0.02	+0.01	+0.13
$[\text{Ag}_3(\text{L}^{\text{Cy}})_3]^{2+}$	+0.22		+0.03	+0.44

Mass spectrometry and gas-phase (photo)reactivity

Electrospraying a solution of $[\text{Ag}_3(\text{H/D})(\text{L}^{\text{Cy}})_3](\text{PF}_6)_2$ in acetonitrile gave rise to major mass signals at m/z 775.31 and 775.81 (most abundant masses), assigned to the molecular dication $[\text{P}]^{2+}$, which is confirmed by the excellent agreement between the experimental and simulated isotope patterns (calcd: m/z 775.32 and 775.83, respectively, see insets to Figures 4b and Figure S11). The lack of further dissociation products demonstrates the stability of this hydrido/deuterido silver(I) complex under electrospray ionization (ESI) conditions, in accordance with other observations on the $[\text{M}_3(\mu_3\text{-H})]$ ($\text{M} = \text{Cu}, \text{Ag}$) structural motif.^[5a,c-f,8a,d,20b,34]

To explore the gas-phase reactivity of $[\text{P}]^{2+}$, we applied the established mass spectrometric fragmentation techniques of 1) collisional-induced dissociation (CID),^[17d,35] 2) laser photodissociation (PD),^[17b-d,g] and 3) electron-transfer dissociation (ETD)/electron-transfer reduction (ETR),^[36] because interesting details of Ag-hydride/Ag-Ag interactions are revealed by these activations. The resulting CID, PD, and ETD mass spectra are compared in Figure 4a–c, and the major dissociation pathways are presented in Tables 4 and 5 (further details are given in the Supporting Information).

In general, the gas-phase processes that take place in collision- or photoactivated $[\text{P}]^{2+}$ can be assigned to three different reaction types (see Table 4). First, ionic fragmentation (IF) yielding two complementary monocations by charge separation, often accompanied by the fission of the $\text{Ag}_3(\mu_3\text{-H})$ cluster core, secondly, the loss of a neutral moiety (or multiple losses) retaining the overall charge and oxidation state of the metal core, and lastly, reductive elimination (mainly of the hydride) with neutral or ionic losses resulting in a formal reduction of the Ag_3 center, for example, the formation of $[\text{Ag}_3(\text{L}^{\text{Cy}})_2]^{+}$ +

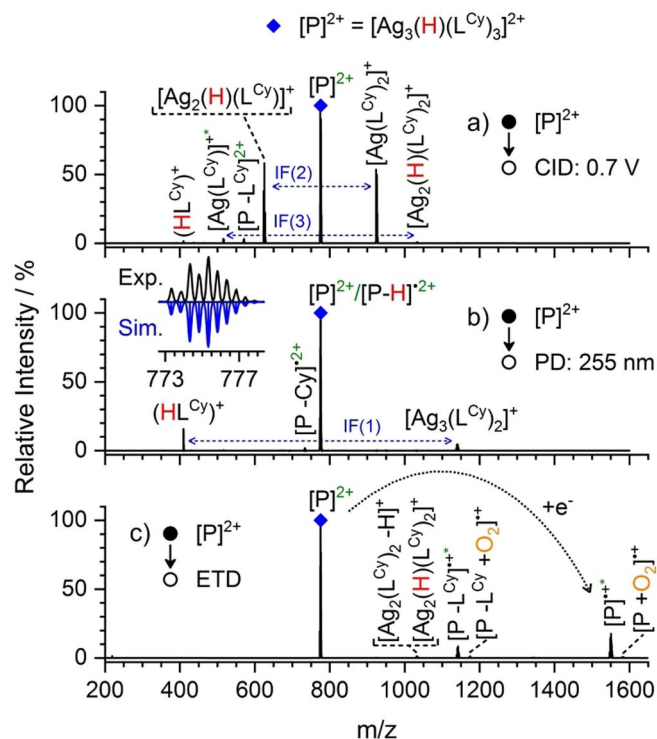


Figure 4. Comparison of the fragment mass spectra (MS^2) of isolated $[\text{P}]^{2+}$ precursor ions (m/z 773, blue diamonds) obtained by: a) collision-induced dissociation (CID, excitation amplitude = 0.7 V, 100 ms frag. time), b) photodissociation (PD, 255 nm, 2 μJ , ca. 118 pulses), c) electron-transfer dissociation (ETD, 100 ms ion-ion interaction time). Inset: Experimental (black) and simulated (blue, Gaussian profile, $\text{fwhm} = 0.2$) isotope pattern of $[\text{P}]^{2+}$ ions after isolation. Hydrogen atoms that are highlighted in red originate from the $\mu_3\text{-H}$ hydride, as verified by deuteration experiments (see Tables S5, S6, and S8 in the Supporting Information). Asterisks indicate overlapping ion signals (see Table S4). Blue dotted arrows mark the complementary ionic fragmentation products according to Equations (1)–(3) (Table 4).

$\text{H}(\text{L}^{\text{Cy}})^+$ [Eq. (1) in Table 4] or $[\text{Ag}_3(\text{L}^{\text{Cy}})_3]^{2+} + \text{H}^+$ [Eq. (6) in Table 4].

The latter reaction type is particularly interesting because it generates intermediates that could be important links between trinuclear silver hydride complexes and higher molecular clusters with respect to the reduction and nucleation processes taking place during the synthesis of silver nanoclusters in solution.^[37] In the following we will point out the specific reactivity and primary fragment channels observed for the corresponding activation methods. However, we have also explored the manifold of fragmentation pathways in multistage experiments (MS^n , $n = 2, 3$) with combinations of activation methods and tabulate the results in the form of a precursor/fragment connectivity matrix in the Supporting Information (Table S10 and Figures S22–S25).

Collision-induced dissociation (CID)

The CID mass spectrum of $[\text{P}]^{2+}$ (Figure 4a) displays the main complementary fragment ion pair $[\text{Ag}(\text{L}^{\text{Cy}})_2]^{+}$ (m/z 923) and $[\text{Ag}_2(\text{H})(\text{L}^{\text{Cy}})]^{+}$ (m/z 623) (IF(2)) with branching ratios of $Y_{\%} = 47$

Table 4. Fragment assignments of the precursor ions $[P]^{2+}$ (m/z 773) in the PD and CID experiments according to the separate reaction types. a) Ionic fragmentation (IF) and b) neutral loss (NL). $L^{Cy} = (Cy)_2PCH_2P(Cy)_2$, $Cy = C_6H_{11}$. The origin of the hydrogen atoms was determined by deuteration experiments (see Tables S4, S5 and S6 in the Supporting Information). Integer nominal masses of the product ions are indicated in parentheses.

Fragments (m/z)	Eq.	PD/CID	Fragmentation schemes
a) ionic fragmentation (IF)			
$[Ag_3(L^{Cy})_2]^+ + H(L^{Cy})^+$ (1137) + (409)	(1)	✓/✓	
$[Ag_2(H)(L^{Cy})]^+ + [Ag(L^{Cy})_2]^+$ (623) + (923)	(2)	✓/✓	
$[Ag_2(H)(L^{Cy})_2]^+ + [Ag(L^{Cy})]^+$ (1031) + (515) ^[a]	(3)	-/✓	
$[Ag_2(L^{Cy})(L^{Cy}-H)]^+ + [Ag(L^{Cy})]^+ + HH$ (1029) + (515) ^[a]	(4)	✓/-	
$[Ag_2(L^{Cy})_2-Cy]^+ + [Ag(L^{Cy})]^+ + "H" + Cy"$ (947) + (515) ^[a]	(5)	✓/-	
b) neutral loss (NL)			
$[Ag_3(L^{Cy})_3]^{2+} + H^+$ (773) ^[a]	(6)	✓/?	
$[Ag_3(H)(L^{Cy})_3-Cy]^{2+} + Cy^+$ (732)	(7)	✓/-	
$[Ag_3(H)(L^{Cy})_2]^{2+} + L^{Cy}$ (569)	(8)	-/✓	
$[Ag_2(L^{Cy})_2]^{2+} + "[Ag(H)(L^{Cy})]"^{[b]}$ (515) ^[a]	(9)	✓/✓	

[a] Superimposed ion signal due to overlapping isotope patterns of multiple ionic species. Deconvolution of the ion signal for $[Ag(L^{Cy})]^+$ and $[Ag_2(L^{Cy})_2]^{2+}$ (both m/z 515) was not attempted because of sub-optimal signal-to-noise ratio and the fact that their fragmentation behavior has recently been investigated in detail.^[17b] [b] Note: AgH loss has been substantiated by MD simulations for a related system.^[15]

Table 5. Fragment assignments of the precursor ions $[P]^{2+}$ (m/z 773) for electron-transfer dissociation/reduction (ETD/ETR) experiments ($L^{Cy} = (Cy)_2PCH_2P(Cy)_2$, $Cy = C_6H_{11}$). The origin of the hydrogen atoms was determined by deuteration experiments (see Table S8 in the Supporting Information). Integer nominal masses of the product ions are indicated in parentheses.

Fragments (m/z)	Eq.	Fragmentation schemes
$[Ag_3(H)(L^{Cy})_3]^+$ (1546)	(10)	
$[Ag_3(H)(L^{Cy})_2(L^{Cy}-H)]^+ + H^+$ (1545)	(11)	
$[Ag_3(H)(L^{Cy})_2]^+ + L^{Cy}$ (1138)	(12)	
$[Ag_3(H)(L^{Cy})(L^{Cy}-H)]^+ + "L^{Cy} + H"$ (1137)	(13)	
$[Ag_2(H)(L^{Cy})_2]^+ + [Ag(L^{Cy})]^+$ (1031)	(14)	
$[Ag_2(L^{Cy})_2-H]^+ + [Ag(L^{Cy})]^+ + HH$ (1029)	(15)	

and 48%, respectively ($Y_{\%}$ = percentage of total fragment yield, see Table S4 in the Supporting Information). Further product ions are $[Ag_2(H)(L^{Cy})_2]^+$ (m/z 1031) and $[Ag(L^{Cy})]^+$ (m/z 515), observed at only $Y_{\%} \leq 2\%$ (IF(3)), and the neutral loss products $[Ag_3(H)(L^{Cy})_3]^{2+}$ (m/z 569, $Y_{\%} = 3\%$) and $[Ag_2(L^{Cy})_2]^{2+}$ (m/z 515, overlapping isotope pattern with $[Ag(L^{Cy})]^+$).

Overall, the CID behavior of $[P]^{2+}$ is similar to that of its phenyl-substituted congener, $[Ag_3(H)(L^{Ph})_3]^{2+}$ (L^R ligands differing in $R = Ph$ instead of $R = Cy$).^[5e] However, there are some slight differences: The phenyl congener dissociates exclusively by charge separation/ionic fragmentation,^[5e] which contrasts the above-mentioned dicationic fragments (m/z 569 and 515) found for $[P]^{2+}$ and highlights the fact that "subtle" changes in

the substituents of bis-phosphine ligands impacts the gas-phase fragmentation pathways and the stability of the coinage metal clusters.^[38] Another interesting channel (although minor by CID) is the formation of the monocationic trinuclear silver species $[Ag_3(L^{Cy})_2]^+$ [m/z 1137, $Y_{\%} < 1\%$, Eq. (1)], obtained by reductive elimination of a protonated ligand $H(L^{Cy})^+$ (m/z 409, $Y_{\%} < 1\%$). This route is common to both the phenyl and cyclohexyl congeners.^[5e] The source of the hydrogen for $H(L^{Cy})^+$ was confirmed to originate from the μ_3 -hydride by deuterium labeling and multistage MS experiments (see Tables S5 and S6 in the Supporting Information).

Additionally, to qualitatively explore the energetic order of the fragmentation pathways, we recorded energy-resolved CID

appearance/breakdown curves for $[P]^{2+}$ (see Figure S13 in the Supporting Information). As a result, it is revealed that the production of the $[Ag(L^C)_2]^+ / [Ag_2(H)(L^C)_2]^+$ ion pair [m/z 923, 623, Eq. (2)] constitutes the lowest-energy channel. This is followed in parallel by the neutral loss pathways: $-L^C$ [Eq. (8)], the formation of $[Ag_2(L^C)_2]^{2+}$ [Eq. (9)], and the charge-separation product $[Ag(L^C)]^+$ (m/z 515), as indicated by a shift in the activation amplitudes for their ion yield onsets (see Figure S13). It follows further that $[Ag(L^C)]^+$ (m/z 515) is primarily formed by secondary fragmentation from both precursors at m/z 923 and 623, as confirmed by MS^3 experiments and the fact that the onset for its complementary ion $[Ag_2(H)(L^C)_2]^+$ is further shifted to a higher CID amplitude (see Table S10 and Figure S22). Lastly, requiring the highest activation energy, the ionic fragmentation pathways leading to the generation of $[Ag(L^C)]^+ / [Ag_2(H)(L^C)_2]^+$ [m/z 515, 1031, Eq. (3)] and $H(L^C)^+ / [Ag_3(L^C)_2]^+$ [m/z 409, 1137, Eq. (1)] are accessed in parallel.

Photoinduced dissociation (PD)

The photoinduced fragmentation pattern of $[P]^{2+}$ strongly contrasts that evidenced by collisional activation (Figure 4a,b). This is apparent from the strongly enhanced branching ratio for the reductive elimination of $H(L^C)^+$ ($Y_{\%255nm} = 26\%$) leading to the complementary ion $[Ag_3(L^C)_2]^+$ ($Y_{\%255nm} = 23\%$) by formal two-electron reduction of the Ag_3 center. Because both fragments have also been observed in low yield by CID (see above), it is clear that the underlying pathway of Equation (1) can be thermally or photo-activated, with the latter being more efficient. In addition, this indicates that probably hydride-to-silver charge-transfer states are involved in this excited-state pathway, typically proceeding on an ultrafast time-scale, prior to dissociation.^[17b,c] However, we cannot completely rule out that $[P]^{2+}$ dissociation also proceeds statistically from highly vibrationally excited ground-state levels.

Evidence for photoinduced single electron transfer is provided by the observation of $[Ag_2(L^C)_2-H]^+$ (m/z 1029) and $[Ag_2(L^C)_2-Cy]^+$ (m/z 947) concomitantly formed with $[Ag(L^C)]^+$ and the formal loss of “ H_2 ” [Eq. (4)] and “ Hcy ” [Eq. (5)]. These results indicate that the hydride obtains radical character upon electronic excitation, which is further substantiated by the observation of the photoinduced loss of H^{\cdot} , the origin of which is also confirmed here as the bridging μ_3 -H atom by deuterium-labeling experiments (see Table S6 in the Supporting Information). The isotope pattern of the thereby generated odd-electron ion $[P-H]^{2+}$ is superimposed on that of its precursor ion signal $[P]^{2+}$ (see Figure S17). To obtain the yield for this pathway, we deconvoluted the isotope pattern (see Figures S18 and S19) and identified $[P-H]^{2+}$ as the most abundant photo-fragment ($Y_{\%255nm} = 35\%$, with increasing yields for shorter wavelengths), formed by the probably lowest-energy photoinduced pathway.

Interestingly, a related study on the nonligated $[Ag_2H]^+$ model system revealed that loss of H^{\cdot} is only facilitated by PD, whereas collisional activation exclusively leads to the fragments Ag^+ and HAg .^[3a] Based on theory and the experimental evidence, it was deduced that the electronic excitation of

$[Ag_2H]^+$ (S_1 and S_2 states) is followed by direct state-specific fragmentation.^[3a] Another gas-phase study of the trinuclear phenyl-phosphine species $[Ag_3(H)(L^{Ph})_3]^{2+}$ demonstrated that the loss of a hydrogen atom and the reductive elimination of $H(L^{Ph})^+$ can also be achieved by both electron-capture dissociation (ECD) and electron-impact dissociation (EID).^[5e]

Through another route, photo-specific homolytic P–C bond dissociation is evidenced for the $[P]^{2+}$ target system by the loss of Cy^{\cdot} ^[39] yielding the odd-electron $[Ag_3(H)(L^C)_3-Cy]^{2+}$ dication (m/z 732, $Y_{\%255nm} = 9\%$; Table 4). This is in agreement with the already reported PD behavior of $[Ag_2(L^C)_2]^{2+}$,^[17b] revealing that single and multiple losses of neutral Cy^{\cdot} moieties are observed upon photoexcitation and rationalized by enhanced Ag–Ag bonding interactions in the photoexcited MC($d\sigma^* - p\sigma$) electronic state. Note, that similar attractive interactions may be responsible for the seemingly enhanced Ag_3 core stability observed for $[P]^{2+}$. However, contrary to the $[Ag_2(L^C)_2]^{2+}$ species, no loss of Ag^0 is detected for the $[Ag_3(H)(L^C)_3]^{2+}$ system. This may be further explained by stronger intermetallic cooperative (argentophilic) interactions in the trimeric silver system compared with the dimeric system.

Although beyond the scope of this work, we would like to add here that the photodissociation of the hydride-containing fragments of $[P]^{2+}$, as studied by multistage MS, leads to some remarkable results that underline the prevalence of photoreductive elimination. For instance, upon mass spectrometric isolation of $[Ag_2(H)(L^C)]^+$ [m/z 623, see Table 4, Eq. (2)] and irradiation at around 255 nm, we observe the gas-phase adduct $[Ag_2(L^C)(O_2)]^+$ (see Figure S23d in the Supporting Information). Similarly, we find the reaction product $[Ag_2(L^C)_2(O_2)]^+$ (see Figure S23b) from the photodissociation of the less abundant CID fragment $[Ag_2(H)(L^C)_2]^+$ [m/z 1031, Table 4, Eq. (3)]. Both dioxygen adducts seem to be formed by the reaction of the corresponding radical cations $[Ag_2(L^C)_{1/2}]^{\cdot+}$, presumably produced by the reductive photoelimination of H^{\cdot} , with traces of O_2 in the ion trap. This is a striking pathway for ligated silver radical-cation complexes that was not observed before; however, it is in accordance with the gas-phase reactivity of naked silver clusters.^[40] We will discuss this reactivity in the following.

Electron-transfer dissociation/reduction (ETD/ETR)

ETD occurs in the gas-phase ion–ion recombination between, in this case, fluoranthene radical anions ($FA^{\cdot-}$)^[36b,41] and positively charged molecular targets M^{n+} ($n > 1$). Because the resulting single-electron-transfer processes are exoergic (up to a few eV), the generated odd-electron cations subsequently undergo selective radical-driven dissociation, which points to the main application of this technique in the field of MS-based proteomics.^[36a,b]

However, in ion-trap MS, the produced radical cations can be stabilized through collisional cooling with the helium buffer gas, thereby facilitating the investigation of labile^[42] and even highly redox-reactive intermediates.^[36c] Although available for quite some time, EDT has rarely been applied to transition-metal complexes,^[36c,43] although it is viewed as an emerging

powerful tool, especially in conjunction with optical spectroscopy.^[36c,44]

In our case, $[P]^{2+}$ precursors are reduced by ETR to $[Ag_3(H)(L^{Cy})_3]^{2+}$ $[P]^{2+}$, m/z 1546, see Table 5, Eq. (1)]. Besides this odd-electron species, other ET-induced neutral-loss pathways are observed (Figure 4c and Table 5), including the formation of the second most abundant product $[P-L^{Cy}]^{2+}$ [m/z 1138, Eq. (12)] resulting from the dissociation of L^{Cy} ; ET and subsequent hydrogen loss $[P-H]^{2+}$, m/z 1545, Eq. (11), source of hydrogen: L^{Cy} , see Table S8 in the Supporting Information); the loss of $[AgL^{Cy}]^+$ yielding $[Ag_2(H)(L^{Cy})_2]^{2+}$ [m/z 1031, Eq. (14)]; and other secondary fragments. In contrast, it has been reported that the phenyl congener of $[P]^{2+}$ did not yield intact singly reduced monocations under electron-capture dissociation conditions, but exclusively secondary fragmentation products.^[5e] Interestingly, the loss of a protonated ligand, $H(L^{Cy})^+$, which would yield the neutral radical $[Ag_3(L^{Cy})_2]^\cdot$, is not observed upon ETD, although the ionic fragment $[Ag_3(L^{Cy})_2]^{2+}$ is generated by both CID and PD of $[P]^{2+}$.

Surprisingly, we observed for the reduced species $[P]^{2+}$ and $[P-L^{Cy}]^{2+}$ a hitherto undocumented reactivity of ligated silver complexes towards the formation of dioxygen adducts by ion-molecule reaction with trace amounts of O_2 present in the ion trap. Thus, the species $[P+O_2]^{2+}$ (m/z 1578) and $[P-L^{Cy}+O_2]^{2+}$ (m/z 1170) are produced (Figure 4c). Multistage MS³ experiments revealed that the signal intensity of $[P+O_2]^{2+}$ is directly proportional to the ion storage time (see Figure S16 in the Supporting Information).

It is remarkable that only the odd-electron species $[P]^{2+}$ and $[P-L^{Cy}]^{2+}$ seem to have an enhanced reactivity towards O_2 , whereas no adduct species are observed for any of the even-electron precursors. This is indicative of the reactivity towards molecular oxygen being directly correlated with the spin state of the cluster core, thereby making the mere oxidation of the phosphine ligands unlikely. In support of this hypothesis, it is well established in the literature that spin-conservation rules can mediate ion-molecule gas-phase reactivity.^[45] This is further substantiated by the observation that odd-electron bare silver clusters^[46] as well as aluminum hydride clusters^[47] exhibit an increased reactivity towards 3O_2 . Our data hence provide additional evidence that spin-conservation rules need to be considered to explain the gas-phase reactivity, not only for bare metal clusters, but also for ligated metal complexes.

Optical properties and electronic structure

UV/Vis absorption spectroscopy in the gas phase and solution

UV spectroscopic investigations of phosphine-facilitated silver hydride clusters in isolation are scarce.^[3,15] Besides the reported characterization of the bare $[Ag_2H]^+$ model system,^[3a] silver hydride clusters often comprise ligands that contain aromatic groups such as phenyl moieties (L^{Ph}), and hence spectroscopic investigations suffer from the drawback that metal-core-centered (MC) and ligand-centered ($\pi-\pi^*$) transitions are superimposed.^[3b,5c,15,20a] Here, we focused on UV-“silent” L^{Cy} ligands to elucidate the intrinsic electronic properties of the “ $(Ag_3H)^{2+}$ ” cluster core as discussed in the following.

The UV-PD action spectrum of gaseous precursor ions $[P]^{2+}$ (Figure 5a, black circles) displays several features: A low-intensity band centered at around 320 nm, a broad asymmetric band peaking at around 252 nm with a shoulder at around 270 nm, and a rising edge of the fragment yield to higher photon energies starting at around 245 nm. The total fragment yield displays a linear dependence on the laser pulse energy (0.2–2.0 μJ , see Figure S21 in the Supporting Information), which indicates a one-photon absorption process and justifies the comparison with the linear absorption spectrum in solution (see Figure S21).^[48] In fact, the overall shape of the UV-PD action spectrum closely resembles the absorption spectrum in acetonitrile solution (Figure 5a, blue line), although a pronounced blueshift of around 1400 cm^{-1} is discernible with respect to the band maximum at 261 nm observed in the condensed phase. This is in line with the reported shifts of the MLCT band of $[Ru(bpy)_3]^{2+}$ ($bpy=2,2'$ -bipyridine) from various gas-phase experiments of 1000–1500 cm^{-1} ^[49] and around 1100 cm^{-1} .^[50] Additionally, we note that the band at around 320 nm in the gas-phase spectrum is slightly broader and differently structured compared with its solution counterpart, so that the corresponding solvation shift is difficult to ascertain.

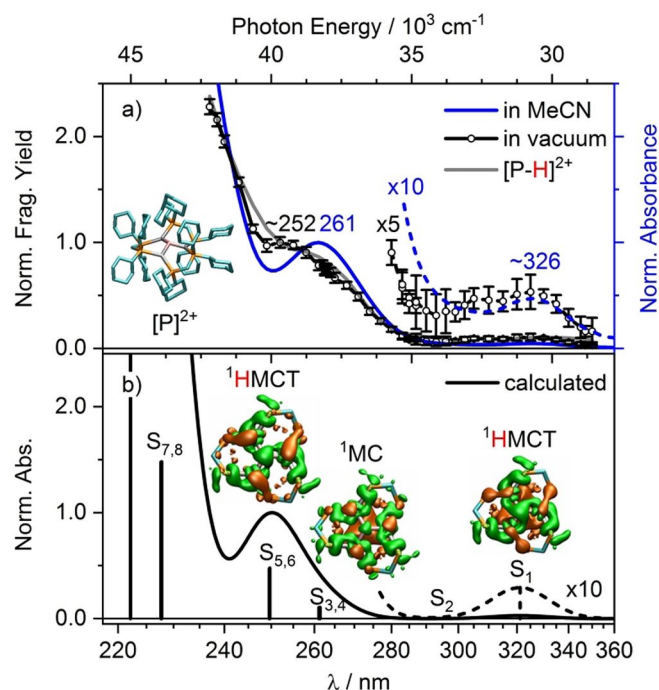


Figure 5. a) Normalized UV-PD spectrum (black circles, total fragment yield) of $[P]^{2+} = [Ag_3(H)(L^{Cy})_3]^{2+}$ (m/z 773) compared with the UV absorbance spectrum of $[P](PF_6)_2$ in MeCN (blue, $c=31 \mu M$). Error bars represent one standard deviation ($\pm 1\sigma$, at least 150 mass spectra). The yield of the H-loss channel [Table 2, Eq. (6)] obtained by isotope pattern deconvolution is shown in grey (smoothed, see Figure S19 in the Supporting Information) Inset: Calculated geometry of $[P]^{2+}$ (PBE-D3(BJ)/def2-SV(P), ligand hydrogen atoms have been omitted). b) Unscaled calculated electronic absorption (fwhm = 0.3 eV) and stick spectra [PBE0 evGW-BSE/def2-SV(P)] of $[P]^{2+}$. Inset: transition density plots for the labeled S_1 , $S_{3,4}$, and $S_{5,6}$ transitions (isovalue: $0.001 a_0^{-3}$, cyclohexyl and methylene hydrogen atoms have been omitted). Green represents a loss of electron density whereas orange represents a gain of electron density. Magnified spectra in the 277–360 nm range ($\times 5$, $\times 10$) are shown as dotted lines.

Hence, due to its low intensity and the limited spectral resolution (ca. 4 nm) of the applied femtosecond laser system, we refrain here from further discussion of its features.

The calculated absorption spectrum presented in Figure 5b is in good agreement with the optical experimental spectra recorded in the gas phase and in solution. Based on the *evGW-BSE* calculations, the weak, lowest-energy band at around 320 nm, observed both in the gas phase and in solution, is assigned to a ¹HMCT (hydride-to-metal charge transfer) transition ($\lambda_{\text{calcd}}=321$ nm, S_1), hence electron density is transferred mainly from a hydride-centered orbital to a collective Ag_3 orbital (LUMO), as illustrated by the transition density plot shown in Figure 5b (see also Table S12 in the Supporting Information). Because the LUMO facilitates cooperative binding interactions, all the electronic transitions exhibiting significant LUMO contributions are expected to enhance the stability of the Ag_3 core (Figure 3 and Table S11). Further evidence of this assignment is provided by the fact that UV-PD mainly leads to fragments with an intact cluster core in contrast to CID, which primarily displays ionic core fission. The distinct shoulder (ca. 270 nm), discernible by the apparent asymmetry of the broad PD band in the 280–245 nm spectral range, originates from two nearly degenerate S_3 and S_4 excited states ($\lambda_{\text{calcd}}=261$ nm) with mainly metal-centered character (¹MC). Furthermore, in excellent agreement with the experimental gas-phase maximum at around 252 nm, the calculated UV absorption spectrum is dominated by two almost degenerate transitions (S_5 , S_6) at $\lambda_{\text{calcd}}=250$ nm arising mainly from charge transfer from hydride to silver-centered orbitals (¹HMCT), which corresponds to the absorption maximum in MeCN at around 261 nm. The experimentally observed increase in absorption below 240 nm, both in the gas phase and in solution, is assigned to the excitation of the ¹MC states (see Tables S11 and S12). We note that the unscaled absorption spectrum calculated at the PBE0 *evGW-BSE/def2-SV(P)* level of theory is in excellent agreement with the experimental data, thereby confirming the structural and electronic characterization of $[\text{P}]^{2+}$ and providing benchmark data for other quantum-chemical approaches.

Further evidence for the predicted hydride-to-metal CT character of the S_1 and $S_{5/6}$ excited states is nicely provided by the distinct experimental fragmentation pattern observed upon photoexcitation (see above), including 1) the main photoinduced fragmentation pathway being the dissociation of the hydride ($\mu_3\text{-H}$) as the neutral H^{\cdot} atom and 2) the second most abundant pathway proceeding by ionic fragmentation as a result of a formal two-electron reduction of the cluster core to give $[\text{Ag}_3(\text{L}^{\text{C}})_2]^+ + \text{H}(\text{L}^{\text{C}})^+$.

However, the contributions of the H^{\cdot} atom channel are not included in the total yield UV-PD spectrum shown in Figure 5a (black circles). Because excitation of individual electronic excited states may lead to specific fragmentation pathways and/or branching ratios,^[3a] it is possible that the spectral information could be scrambled. Hence, it is important for ion-trap action spectroscopy to account for the individual channel-specific yields as a function of excitation wavelength.^[51] Thus, the superimposed isotope patterns for the $[\text{P}]^{2+}$ and $[\text{P-H}]^{2+}$ species were deconvoluted (see Figure S18 in the Supporting Informa-

tion) and the resulting normalized channel-specific yield spectrum for $[\text{P-H}]^{2+}$ obtained (Figures 5a and Figure S19). This spectrum closely resembles the shape of the total fragment yield spectrum, which demonstrates that the latter already comprises the relevant spectral information. We note that the loss of H^{\cdot} from the $[\text{Ag}_2\text{H}]^+$ model system was calculated to require at least 3.2 eV, and we expect a similar fragmentation energy for $[\text{Ag}_3(\text{H})(\text{L}^{\text{C}})_3]^{2+}$.^[3a]

The channel-specific PD spectra of the main products with abundant yields, of more than 5% (m/z 1137, 409, 732), all display similar spectral shapes (see Figure S20 in the Supporting Information). In contrast, fragments with yields below 5% (m/z 1029, 947, 923, 623, 515, 326, 211) display a threshold-like behavior starting at $\lambda_{\text{ex}} \approx 260$ nm with increasing yields at higher photon energies. Given that each ensemble of $[\text{P}]^{2+}$ precursor ions is irradiated by multiple laser pulses (ca. 118 pulses, 982 Hz), the photofragments generated by each pulse could absorb subsequent laser pulses and fragment further (secondary fragmentation). PD/PD multistage experiments, performed by isolating photofragments with subsequent irradiation in a MS^3 step, revealed that the low-yield photofragments of $[\text{P}]^{2+}$ (e.g., multiple losses) are indeed generated by these secondary fragmentation pathways (see Table S10). However, the wavelength-dependent yields display no discernible state-specific fragmentation signatures (see Figure S20). This is in accordance with the presumptions that first, the low-yield channels require higher excess internal energy of the precursor ions, which is proportional to the photon energy, and secondly, that ultrafast energy relaxation, presumably populating triplet states, occurs prior to fragmentation.

The electronic structure and resulting photoinduced fragmentation of the metal hydride chromophore core certainly depends on the metal nuclearity, the number and type of phosphine ligands, and the overall charge. To this end, it may be expedient to compare the obtained UV-PD spectrum of $[\text{Ag}_3(\text{H})(\text{L}^{\text{C}})_3]^{2+}$ with the reported spectra of the ligand-free $[\text{Ag}_2(\text{H})]^+$ model system,^[3a] the monoligated $[\text{Ag}_2(\text{H})(\text{L}^{\text{Ph}})]^+$ species,^[3b] and the $[\text{Ag}_3(\text{H})_2(\text{L}^{\text{Ph}})]^+$ ion.^[15] Although the spectral features of $[\text{Ag}_2(\text{H})]^+$ are very similar to those of $[\text{P}]^{2+}$ below 280 nm, it is interesting that the additional silver ion and the phosphine ligands seem to facilitate ¹HMCT and ¹MC transitions leading to a cooperative enhancement of the argentophilic bonding interactions. Furthermore, the lowest-energy ¹HMCT transition of $[\text{P}]^{2+}$ at around 320 nm seems to be specific to a ligand-supported trinuclear silver core because both $[\text{Ag}_2(\text{H})]^+$ and $[\text{Ag}_2(\text{H})(\text{L}^{\text{Ph}})]^+$ species display $S_0\text{-}S_1$ transitions at higher photon energies (< 290 nm). The $[\text{Ag}_2(\text{H})(\text{L}^{\text{Ph}})]^+$ complex exhibits a UV spectrum that is almost structureless due to the contributions of ligand-centered $\pi\text{-}\pi^*$ transitions.^[3b] The UV-PD spectrum of the $[\text{Ag}_3(\text{H})_2(\text{L}^{\text{Ph}})]^+$ monocation^[15] is similar in shape to the main absorption feature of $[\text{P}]^{2+}$ originating from the $S_3\text{-}S_6$ excited states (Figure 5). Because $[\text{Ag}_3(\text{H})_2(\text{L}^{\text{Ph}})]^+$ contains phenyl moieties, a clear assignment of purely metal-core-centered electronic transitions is difficult. However, it is interesting that its main PD fragment corresponds to the reductive elimination of H_2 generating the two-electron reduced $[\text{Ag}_3(\text{L}^{\text{Ph}})]^+$ complex. Because the UV photoexcitation of $[\text{P}]^{2+}$

also primarily results in reductive elimination yielding the reduced $[\text{Ag}_3(\text{L}^{\text{Cy}})_2]^+$ species, this provides further evidence that the photoexcitation of ligand-supported trinuclear silver hydride clusters seems to favor cluster core reduction in contrast to bimetallic silver hydride complexes.

Luminescence spectroscopy in solution

To further the general photophysical characterization of the compound $[\text{P}](\text{PF}_6)_2$, which is a candidate for applications in luminescent materials and sensing, as well as to investigate the radiative deactivation channels, we studied its luminescence in solutions of MeCN and MeOH. The corresponding 3D spectra are shown in Figure 6 together with specific luminescence and luminescence-excitation spectra. In MeCN, a single emission maximum appears at around 490 nm (in the spectral range shown). Its excitation spectrum essentially follows the absorption spectrum with a maximum at 260 nm ($\lambda_{\text{em}}=500$ nm, Figure 6b). In addition, an increase in the luminescence intensity in the UV range below 400 nm is also observed. In contrast, $[\text{P}](\text{PF}_6)_2$ in MeOH solution exhibits two luminescence features, one centered at around 480 nm (10 nm blueshifted from the maximum in MeCN) and a second, more intense peak at 347 nm. As in MeCN, excitation at 260 nm leads to a maximum of the emission intensity at 500 nm (Figure 6c). However, the excitation spectrum for $\lambda_{\text{em}}=350$ nm rises in the UV range below 260 nm.

These observations, together with the large Stokes shift in each solvent, suggest complex and solvent-dependent Frank-Condon state deactivation processes such as relaxation within the coupled singlet- and triplet-state manifold (for calculated vertical singlet- and triplet-state energies, see Table S11 in the Supporting Information) towards several emitting states, possibly in combination with the formation of exciplexes with solvent molecules or counter ions on different time scales.^[17b,18] In fact, for the dinuclear $[\text{Ag}_2(\text{L}^{\text{Cy}})_2]^{2+}$ complex, a similar dependence of the luminescence on the solvent was reported earlier.^[17b] Likewise, dual luminescence with emission wavelengths similarly redshifted with respect to the ground-state absorption has been observed previously for a number of related phosphine ligand supported metal complexes $[\text{M}_2(\text{L}^{\text{Cy}})_2]^{2+}$ ($\text{M} = \text{Cu}, \text{Ag}, \text{Au}$) in solution.^[18,52] The strongly redshifted luminescence bands have been attributed to exciplex formation between the excited complex and solvent molecules on a picosecond time scale, or dissolved anions/counter ions on slower time scales.^[17,52c,d] For example, Ma et al. suggested sub-picosecond intersystem crossing (ISC) for photoexcited $[\text{Au}_2(\text{L}^{\text{Cy}})_2]^{2+}$ in MeCN (ca. 4 ps, $\lambda_{\text{exc}}=280$ nm) and the formation of a long-lived solute-solvent exciplex exhibiting a very broad luminescence at around 480 nm.^[18] These findings were supported by quantum-chemical calculations on the interaction of the photoexcited $[\text{Au}_2(\text{L}^{\text{H}})_2]^{2+}$ model system ($\text{L}^{\text{H}} = \text{bis}(\text{diphosphino})\text{methane}$) with MeCN molecules, which revealed luminescence strongly redshifted with respect to that in the absence of MeCN.^[53]

At the current stage of our research it is not clear how the observed photoreductive electronic transitions as identified by

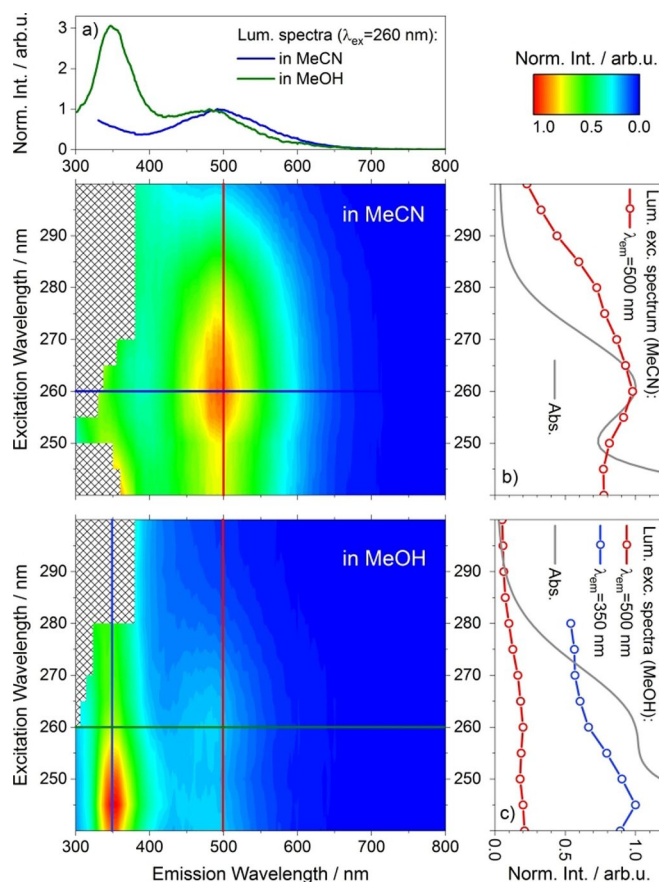


Figure 6. 3D luminescence spectra of $[\text{P}](\text{PF}_6)_2$ in MeCN and MeOH, together with cuts at specific wavelengths yielding: a) the luminescence spectra ($\lambda_{\text{exc}}=260$ nm, normalized for the band at ca. 500 nm) and the luminescence excitation spectra for b) MeCN ($\lambda_{\text{em}}=500$ nm), and c) MeOH ($\lambda_{\text{em}}=500$ and 350 nm). For comparison, the corresponding static absorption spectra are shown (b,c). The data were collected at room temperature using a concentration of $8 \mu\text{mol L}^{-1}$ in MeCN and $9 \mu\text{mol L}^{-1}$ in MeOH. Hatching: Data excluded.

the PD ion-trap experiments and the likely subsequent hydrogen-transfer processes affect the photoinduced dynamics of $[\text{P}](\text{PF}_6)_2$ in solution. However, preliminary femtosecond time-resolved experiments in MeCN ($\lambda_{\text{exc}}=260$ nm) showed that first, basically no photodegradation is discernible over the whole time (hours) of the experiment (see Figure S27 in the Supporting Information) and secondly, a complete recovery of the initial ground state after photoexcitation occurs within less than around 10 ms. It can thus be concluded that the complex is photochemically stable under solution conditions (MeCN). This provides the basis for the further investigation of ultrafast photoinduced dynamics in other solvents as well as in the gas phase.^[17b] Note, that reports on ultrafast processes in transition-metal complexes,^[54] and especially on multinuclear metal hydrides, remain rather scarce.^[55] Moreover, we will pursue the subject of silver hydride luminescence further, because it plays a major role in the design and application of atomically precise nanoclusters.^[17g,56]

Conclusions

The silver(I) hydride complex $[\text{Ag}_3(\mu_3\text{-H})(\mu_2\text{-L}^{\text{Cy}})_3]^{2+}$ ($[\text{P}]^{2+}$) possesses a nearly equilateral, triangular Ag_3 core, capped by a central μ_3 -hydrido ligand, and is stabilized by slightly twisted bis-phosphine ligands (dihedral twist ca. 34°), as inferred from combined experimental (X-ray diffraction, NMR) and theoretical (DFT) structural analyses. The $^1J_{\text{HAg}}$ nuclear spin coupling (ca. 5 Hz) within the $\text{Ag}_3(\mu_3\text{-H})$ structural motif could be unambiguously determined from collective ^1H , $^1\text{H}\{^{31}\text{P}\}$, and $^1\text{H}\{^{109}\text{Ag}\}$ NMR spectra. Furthermore, extensive ion-trap mass spectrometric studies of isolated $[\text{P}]^{2+}$ ions revealed distinct fragmentation pathways and reactivity depending on the chosen activation method, that is, collision-induced dissociation (CID), photodissociation (PD), or electron-transfer dissociation/reduction (ETD/ETR). Whereas CID primarily leads to ionic fragmentation by the fission of the $\text{Ag}_3(\mu_3\text{-H})$ core, PD mainly yields product ions with an intact cluster metal core subsequent to photoinduced charge transfer. This is rationalized by the photoinduced enforcement of $\text{Ag}^0\text{-Ag}^1/\text{Ag}^0\text{-Ag}^0$ argentophilic interactions as a result of the reductive elimination of H^\bullet or even proton transfer (of the hydride atom) onto the L^{Cy} ligand.

The gas-phase photofragment action spectrum shows hydride-to- Ag_3 charge-transfer ($^1\text{HMCT}$) and metal-core-centered (^1MC) transitions in the spectral range of 350–240 nm, in accordance with the hypsochromic shifts observed in MeCN solution. We highlight here the metal-centered optical absorption of the $[\text{P}]^{2+}$ system, addressable only by the choice of UV-transparent L^{Cy} ligands. Due to the absence of a solvent/counter-ion environment in the ion trap, the intrinsic properties of the $[\text{Ag}_3(\mu_3\text{-H})]^{2+}$ core have been explored and directly compared with the results of high-level electronic-structure quantum-chemical calculations performed by using the *GW* method and the Bethe–Salpeter equation. This theoretical approach excellently reproduced the experimental spectra and facilitated the assignment of the character of electronic transitions by means of transition density plots.

Additionally, to the best of our knowledge, an unprecedented dioxygen addition reaction was observed for ligated silver complexes at room temperature. We discovered two pathways to initiate this reaction. First, a radical monocation $[\text{P}]^{2+}$ is formed by ETD/reduction of $[\text{P}]^{2+}$. $[\text{P}]^{2+}$ then reacts promptly with trace amounts of O_2 in the ion trap. Secondly, photoreductive elimination of H^\bullet from $[\text{Ag}_2(\text{H})(\text{L}^{\text{Cy}})_{1,2}]^+$ fragments, yielding $[\text{Ag}_2(\text{L}^{\text{Cy}})_{1,2}(\text{O}_2)]^+$ under vacuum. These O_2 adducts highlight the strong oxophilicity of odd-electron multinuclear silver complexes and are currently being further characterized in our laboratory with respect to their corresponding O_2 binding motif.^[40b,57] $\text{Ag}_n\cdots\text{O}_2$ interactions play an important role in industrial processes such as silver-catalyzed selective ethylene epoxidation.^[58] Intriguingly, dioxygen adducts of silver hydride complexes were considered to be intermediates in the catalytic aerobic oxidation of aldehydes.^[10]

The further exploration of electronically excited states and the corresponding radiative deactivation pathways of $[\text{P}]^{2+}$ by static luminescence spectroscopy in MeCN and MeOH revealed distinct and bimodal luminescence with large Stokes shifts and

broad fluorescence excitation spectra, reminiscent of the reported photophysical properties of related phosphine-supported d^{10} metal complexes.^[17b,18]

Our combined experimental and theoretical results hence provide a basis for further detailed spectroscopic and ultrafast dynamics investigations, specifically for studying metal–metal interactions under electronic excitation and identification of hydride charge-transfer processes. The dynamics of the latter are largely unexplored,^[55] but present essential relaxation steps in electronically excited metal hydrides and are decisive for their photochemistry. Moreover, we believe that they could also be utilized to gain a mechanistic understanding and control of the growth of metal nanoclusters and hydrides.

In short, the new trisilver hydride complex $[\text{Ag}_3(\mu_3\text{-H})(\mu_2\text{-L}^{\text{Cy}})_3]^{2+}$ exhibits distinctive optical and photoreactive properties. In particular, photoinduced charge transfer was revealed here in the form of hydride-to- Ag_3 single and double electron transfer, as evidenced by the observed fragments and rationalized by high-level quantum-chemical theory. $[\text{P}]^{2+}$ provides a platform for studying the ultrafast dynamics of elementary photoreactions of silver hydrides.

Experimental Section

General aspects and materials

The following chemicals were commercially available and used without further purification: Acetonitrile (for ESI-MS, HPLC/LC-MS grade, VWR Chemicals), AgPF_6 (98%, Sigma-Aldrich), NaBH_4 (98%, Sigma-Aldrich), NaBD_4 (98 atom-% D, Sigma-Aldrich), bis(dicyclohexylphosphino)methane (abbr. L^{Cy} , 95%, Sigma-Aldrich). Acetonitrile (for synthesis) was dried by heating at reflux over phosphorus pentoxide under a nitrogen atmosphere. Diethyl ether was dried with a Braun MB SPS drying station and degassed by bubbling nitrogen through the solvent for 30 min. All the reactions were carried out under an inert gas atmosphere (nitrogen) using standard Schlenk techniques.

Synthesis of $[\text{Ag}_3(\mu_3\text{-H/D})(\text{L}^{\text{Cy}})_3](\text{PF}_6)_2$

Bis(dicyclohexylphosphino)methane (327 mg, 0.80 mmol) and silver(I) hexafluorophosphate (202 mg, 0.80 mmol) were suspended in dry and degassed acetonitrile (40 mL) and stirred for 5 min. Sodium borohydride (30.3 mg, 0.80 mmol) or borodeuteride was added in one portion and the mixture was stirred for 40 min resulting in a change from a colorless solution to a pale-yellow suspension. The suspension was filtered and the solvent removed from the filtrate under reduced pressure to give 338 mg of a grey solid material (69% yield). Colorless single crystals were obtained by the diffusion of diethyl ether into a concentrated acetonitrile solution of the product. ^1H NMR (400.1 MHz, CD_3CN): δ = 5.48, 5.36, 5.25, 5.13 (4 × qsept., see discussion above), 2.05–1.99 (m, 18H; PCH_2P , $\text{PCH}(\text{CH}_2)_5$), 1.90–1.17 ppm (m, 120H; $\text{PCH}(\text{CH}_2)_5$); ^{13}C NMR (100.6 MHz, CD_3CN): δ = 36.5 (24C; $\text{PCH}(\text{CH}_2)_5$), 30.2 (d, $^1J_{\text{PC}}$ = 109.6 Hz, 12C; $\text{PCH}(\text{CH}_2)_5$), 27.6 (d, $^2J_{\text{PC}}$ = 37.4 Hz, 12C), 26.6 (24C; $\text{PCH}(\text{CH}_2)_5$), 11.5 ppm (t, $^1J_{\text{PC}}$ = 12.3 Hz, 3C; PCH_2P); ^{31}P NMR (162.0 MHz, CD_3CN): δ = 25.8 (dm, 6P), –144.62 ppm (sept., $^1J_{\text{PF}}$ = 706.6 Hz, 2P; PF_6^-). MS (ESI, most abundant isotopologue): m/z : calcd for $[\text{Ag}_3\text{H}(\text{dcpm})_3]^{2+}$: 775.3; found: 775.3(1); elemental analysis calcd (%) for $\text{C}_{75}\text{H}_{139}\text{Ag}_3\text{F}_{12}\text{P}_6$: C 48.95, H 7.61; found: C 49.01, H

7.74. FTIR-ATR and FT-Raman spectra are provided in the Supporting Information (see Figure S26).

NMR spectroscopy

NMR spectra were recorded at ambient temperature with Bruker Avance AMX400 (H: 400.1 MHz, ¹³C: 100.6 MHz, ³¹P: 162.0 MHz, ¹⁹F: 376.0 MHz) and AMX600 (¹H: 600.1 MHz, ¹³C: 151.9 MHz, ³¹P: 243 MHz) Pulse-FT-NMR spectrometers. Deuterated acetonitrile ([D₃]MeCN, Eurisotop) was used as solvent without further purification.

X-ray structure analysis and refinement

Single-crystal X-ray diffraction measurements were conducted with a Gemini S Ultra diffractometer (Oxford Diffraction) and data analysis was performed by utilizing the SHELXS-97 and SHELXL-97 software packages.^[59] Crystal data and refinement parameters are provided in Table 6. The structure of [P](PF₆)₂ was solved by using the direct method of SIR92,^[60] completed by subsequent difference Fourier syntheses, and refined by full-matrix least-squares procedures.^[59] Semi-empirical absorption corrections from equivalents (Multiscan) were carried out by utilizing the CrysAlis^{Pro} software package (Rigaku Oxford Diffraction). All non-hydrogen atoms were refined with anisotropic displacement parameters. In the structure, severely disordered/partially occupied H₂O and/or Et₂O were also found. To gain a better understanding of the main structure, especially because the hydride is notoriously difficult to locate in the difference Fourier map, the SQUEEZE process integrated in PLATON was used.^[61] The hydrogen atom H1 was then observed in the following difference Fourier synthesis, and was allowed to be refined semi-freely with the help of distance restraints. All the other hydrogen atoms were placed in calculated positions and refined by using a riding model.

Table 6. Crystallographic data of [P](PF₆)₂ and details of the data collection and refinement.

empirical formula	C ₇₅ H ₁₃₉ Ag ₃ F ₁₂ P ₈
formula mass [amu]	1840.22
crystal size [mm]	0.405 × 0.260 × 0.199
T [K]	150(2)
λ [Å]	1.54184
crystal system	orthorhombic
space group	Fdd2
a [Å]	45.6021(22)
b [Å]	18.9309(8)
c [Å]	23.2622(8)
α, β, γ [°]	90
V [Å ³]	20082.0(15)
Z	8
ρ _{calcd} [g cm ⁻³]	1.217
μ [mm ⁻¹]	6.312
θ range [°]	4.267–62.773
Reflns. collected	9397
Indep. reflns	5359, R _{int} = 0.0251
Data, restraints, parameters	5359, 155, 440
Final R indices [I > 2σ(I)] ^[a]	0.0547, 0.1853
R indices (all data)	0.0586, 0.2015
Goof ^[b]	1.159
Δρ _{max,min} [e Å ⁻³]	1.417, -0.927
[a] R1 = Σ F _o - F _c / Σ F _o , ωR2 = [Σω(F _o ² - F _c ²) ² / ΣωF _o ²] ^{1/2} . [b] Goof = [Σω(F _o ² - F _c ²) ² / (n - p)] ^{1/2} .	

CCDC 1904223 contains the supplementary crystallographic data for this paper. These data are provided free of charge by The Cambridge Crystallographic Data Centre.

Ion-trap mass spectrometry (ESI-MS)

Electrospray ionization mass spectrometry (ESI-MS) was performed by utilizing two similar Paul-type quadrupole ion trap mass spectrometers (QIT-MS) amaZon speed and amaZon ETD (Bruker Daltonics) abbreviated as MS-1 and MS-2, respectively, both equipped with an Apollo II electrospray source. Solutions of [Ag₃(H/D)(L^{Cy})₃](PF₆)₂ in acetonitrile (c = 10⁻⁶ M) were electrosprayed in positive ion mode (ESI needle at 4.5 kV) at a continuous infusion rate (120–180 μL h⁻¹) assisted by a coaxial flow of nitrogen sheath gas (7–9 psi, 483–621 mbar). Dry nitrogen gas (4 L min⁻¹, 180 °C) was used to assist desolvation. MS-1/MS-2 were operated in enhanced resolution scan mode (8100 amu s⁻¹, ca. 0.25 fwhm) controlled by the trapControl 7.2 software. Data analysis was performed using by the dataanalysis 4.2 software (Bruker Daltonics).

Collisional-induced dissociation (CID)

To explore the collisional-induced dissociation (CID) pathways, the molecular [Ag₃(H/D)(L^{Cy})₃]²⁺ ([P]²⁺) target ions were isolated (Δm/z 5 mass isolation window) selecting all isotopologues, stored, and accelerated by applying a resonance excitation voltage to the end caps of the ion trap (MS-1, frag. time = 100 ms). The precursor dications undergo multiple collisions with the helium buffer gas leading to fragmentation, followed by subsequent mass analysis.

Energy-resolved CID breakdown/appearance curves were acquired (MS-2, frag. time = 40 ms) by monitoring the relative abundance of [P]²⁺ (Y_p) and total (Y_{tot}) and specific (Y) fragment yields as a function of the stepwise increased excitation amplitude (Amp_{ex}). This applied voltage corresponds to an internal energy scale of the MS and is proportional to the collisional energy. Y_{p,i} is the sum of all mass peak integral intensities of precursor (I_p) and fragment (I) species divided by the sum of all mass peak intensities [Y_{p,i} = I_{p,i} / (ΣI_i + I_p) and Y_{tot} = ΣI_i / (ΣI_i + I_p)]. Subsequently, Amp_{ex} was center-of-mass-corrected according to Amp_{com} = Amp_{ex} × m_{He} / (m_{He} + m_p), in which m_{He} and m_p are the mass of the most abundant isotopologue of helium and the precursor, respectively. Data analysis of the CID curves was performed by utilizing a home-built LabView program interfacing with the CompassXport (Bruker) software tool.

Electron-transfer dissociation/reaction (ETD/ETR)

For the electron-transfer dissociation/reduction (ETD)^[36a] experiments, fluoranthene (FA⁻)^[41] reagent ions were generated in the negative chemical ionization source (nCI) of MS-2 (reactant temp = 60.0 °C), whereby methane was used as the mediator for low-energy electron generation (ionization energy = 70 eV). The generated radical anions were accumulated for 0.8 ms (set target ion charge control, ICC = 5 × 10⁵) and subsequently injected into the ion trap, in which ion–ion electron-transfer reactions with the [P]²⁺ precursor ions proceeded within a set reaction time window of 100 ms (optimized for the signal strength of [P]²⁺). The mass spectrum of the ions generated in the nCI source is provided in Figure S15 in the Supporting Information. It reveals besides FA⁻ (C₁₆H₁₀, m/z 202), two “impurity” peaks at m/z 219 and 217, presumably assignable to the hydroxyl adduct (C₁₆H₁₀OH) and methyl adduct (C₁₆H₁₀CH₃)/fluoranthone (C₁₆H₉O), respectively.^[36b,62] The MS-2 instrument was operated in maximum resolution mode (4650 amu s⁻¹, ca. 0.15 fwhm) with a low mass cutoff of m/z 135.

Gas-phase UV-photodissociation (PD)

The experimental setup is described in detail elsewhere.^[17b,c] Briefly, a femtosecond oscillator/cryogenic regenerative amplifier laser system (Wyvern 1000, KMLabs), generating an output pulse train (ca. 780 nm, fwhm \approx 30 nm, ca. 4 W, 982 Hz, $\Delta\tau \approx$ 50 fs), was used to pump a nonlinear frequency converter (TOPAS-C, Light Conversion). The resulting output beam was tuned in the UV spectral region ($\lambda_{\text{ex}} = 237\text{--}350$ nm, $\Delta\lambda \approx 2\text{--}4$ nm) and focused ($f = 40$ cm) onto the center of the ion trap (ca. 1 mm diameter) passing through two fused silica windows (3 mm thickness) of the spectroscopically modified mass spectrometer MS-1.^[63] Photodissociation action spectra were acquired stepwise (2–5 nm steps) at a constant pulse energy ($E_{\text{pulse}} \approx 2 \mu\text{J}$) during a irradiation time window of 120 ms (ca. 118 pulses per stored ion ensemble) controlled by a synchronized shutter. From the resulting mass spectra, the individual (Y) and total fragment yields (Y_{tot}) were averaged over at least 150 mass spectra for each nm position and normalized to the number of photons N according to $N = E_{\text{pulse}}\lambda/(hc)$ (h = Planck constant, c = speed of light in vacuum). In the spectral ranges of 263–287 and 283–350 nm, scaling factors, determined by overlapping nm positions, were applied to account for the required change in the nonlinear output scheme or spectral filters, which require re-optimization of the laser beam/ion cloud spatial overlap. To disentangle contributions of the hydrogen-loss fragment $[\text{P}-\text{H}]^{2+}$ (monoisotopic m/z 772.8, notable contributions at $\lambda_{\text{ex}} < 285$ nm, see Figure S17 in the Supporting Information), which is superimposed on the isotope pattern of $[\text{P}]^{2+}$ precursor ions (monoisotopic m/z 773.3), the convoluted ion signal was fitted as the weighted sum of the theoretical normalized isotopic patterns of each species (Gaussian broadened fwhm \approx 0.23) by using the peak model fit algorithm of the LIMSA program (Lipid Mass Spectrum Analysis, “add in” for Excel 2003 software).^[64]

Absorption and luminescence spectroscopy in solution

UV/Vis absorption and luminescence spectra were recorded by utilizing a V-670 spectrophotometer (Jasco) and an LS 55 fluorescence spectrometer (PerkinElmer), respectively. Fused silica cuvettes ($d = 1$ cm, SUPRASIL) were used for measurements both in MeCN and MeOH solution (UVASOL grade).

Computational methods

All calculations were performed with the TURBOMOLE program package.^[27] The resolution-of-the-identity (RI) approximation was used for all two-electron integrals. In geometry optimizations, DFT computations were carried out in the module RIDFT. The self-consistent field convergence criterion $\text{scfconv} = 8$ and DFT grid m4 were used. For the optimized geometries, harmonic vibrational frequencies were calculated in the module AOFORCE.^[65] Subsequently, to calculate the electronic excitation energies, GW-BSE computations were carried out in the module ESCF. The evGW damping parameter was set to $\eta = 0.001$, and the convergence criterion $\text{rpaconv} = 6$ was used. All orbital and auxiliary basis sets were taken from the TURBOMOLE basis-set library. The “Coulomb-fitting” auxiliary basis sets (jbas) were used in the ground-state DFT computations, and the “MP2-fitting” auxiliary basis sets (cbas) were used in the GW-BSE computations. The calculations were performed with the def2-SV(P) basis set, except that for the hydride, def2-TZVP and def2-TZVPP were used for the geometry optimizations and excited-state computations, respectively. For $[\text{P}]^{2+}$, this basis set comprises 1512 orbital basis functions, 5777 auxiliary basis functions for “jbas”, and 6204 auxiliary basis functions for “cbas”.

Acknowledgements

We are thankful for the financial support of the DFG-funded transregional collaborative research center SFB/TRR 88 “Cooperative Effects in Homo- and Heterometallic Complexes (3MET)” (projects A5, C1, C4, and B2). C.R. thanks the SPP 2102 “Light-controlled reactivity of metal complexes” for support. We thank Dr. Harald Kelm, Isabel Manes, and Alexej Gaidoukov for their help in recording the NMR spectra (H.K.) and ETD mass spectra (I.M.) as well as evaluating the CID appearance/breakdown curves (A.G.). Michael Borchers is acknowledged for performing preliminary ESI-MS experiments within his bachelor thesis.

Conflict of interest

The authors declare no conflict of interest.

Keywords: charge transfer · hydride ligands · mass spectrometry · metal–metal interactions · photochemistry · silver

- [1] a) H. Schmidbaur, A. Schier, *Angew. Chem. Int. Ed.* **2015**, *54*, 746–784; *Angew. Chem.* **2015**, *127*, 756–797; b) L. Barrientos, S. Miranda-Rojas, F. Mendizabal, *Int. J. Quantum Chem.* **2019**, *119*, e25675.
- [2] a) A. J. Jordan, G. Lalic, J. P. Sadighi, *Chem. Rev.* **2016**, *116*, 8318–8372; b) R. N. Perutz, B. Procacci, *Chem. Rev.* **2016**, *116*, 8506–8544.
- [3] a) R. Mitrić, J. Petersen, A. Kulesza, M. I. S. Röhr, V. Bonačić-Koutecký, C. Brunet, R. Antoine, P. Dugourd, M. Broyer, R. A. J. O’Hair, *J. Phys. Chem. Lett.* **2011**, *2*, 548–552; b) A. Zavras, G. N. Khairallah, M. Krstić, M. Girod, S. Daly, R. Antoine, P. Maitre, R. J. Mulder, S.-A. Alexander, V. Bonačić-Koutecký, P. Dugourd, R. A. J. O’Hair, *Nat. Commun.* **2016**, *7*, 11746.
- [4] J. C. Green, M. L. H. Green, G. Parkin, *Chem. Commun.* **2012**, *48*, 11481–11503.
- [5] a) A. J. Clark, A. Zavras, G. N. Khairallah, R. A. J. O’Hair, *Int. J. Mass Spectrom.* **2015**, *378*, 86–94; b) H. Z. Ma, J. M. White, R. J. Mulder, G. E. Reid, A. J. Canty, R. A. J. O’Hair, *Dalton Trans.* **2018**, *47*, 14713–14725; c) A. Zavras, A. Ariafard, G. N. Khairallah, J. M. White, R. J. Mulder, A. J. Canty, R. A. J. O’Hair, *Nanoscale* **2015**, *7*, 18129–18137; d) A. Zavras, G. N. Khairallah, T. U. Connell, J. M. White, A. J. Edwards, P. S. Donnelly, R. A. J. O’Hair, *Angew. Chem. Int. Ed.* **2013**, *52*, 8391–8394; *Angew. Chem.* **2013**, *125*, 8549–8552; e) A. Zavras, G. N. Khairallah, T. U. Connell, J. M. White, A. J. Edwards, R. J. Mulder, P. S. Donnelly, R. A. J. O’Hair, *Inorg. Chem.* **2014**, *53*, 7429–7437; f) Z. Mao, J.-S. Huang, C.-M. Che, N. Zhu, S. K.-Y. Leung, Z.-Y. Zhou, *J. Am. Chem. Soc.* **2005**, *127*, 4562–4563; g) C. W. Liu, Y.-R. Lin, C.-S. Fang, C. Latouche, S. Kahlal, J.-Y. Saillard, *Inorg. Chem.* **2013**, *52*, 2070–2077; h) R. S. Dhayal, W. E. van Zyl, C. W. Liu, *Acc. Chem. Res.* **2016**, *49*, 86–95.
- [6] A. Wurtz, *C. R. Hebd. Seances Acad. Sci.* **1844**, *18*, 702–704.
- [7] N. P. Mankad, D. S. Laitar, J. P. Sadighi, *Organometallics* **2004**, *23*, 3369–3371.
- [8] a) A. W. Cook, T.-A. D. Nguyen, W. R. Buratto, G. Wu, T. W. Hayton, *Inorg. Chem.* **2016**, *55*, 12435–12440; b) C. M. Zall, J. C. Linehan, A. M. Appel, *J. Am. Chem. Soc.* **2016**, *138*, 9968–9977; c) K. M. Waldie, A. L. Ostericher, M. H. Reineke, A. F. Sasayama, C. P. Kubiak, *ACS Catal.* **2018**, *8*, 1313–1324; d) K. Nakamae, M. Tanaka, B. Kure, T. Nakajima, Y. Ura, T. Tanase, *Chem. Eur. J.* **2017**, *23*, 9457–9461; e) B. K. Tate, C. M. Wyss, J. Bacsa, K. Kluge, L. Gelbaum, J. P. Sadighi, *Chem. Sci.* **2013**, *4*, 3068–3074.
- [9] M. Krstić, Q. Jin, G. N. Khairallah, R. A. J. O’Hair, V. Bonačić-Koutecký, *ChemCatChem* **2018**, *10*, 1173–1177.
- [10] M. Liu, H. Wang, H. Zeng, C.-J. Li, *Sci. Adv.* **2015**, *1*, e1500020.
- [11] a) A. Hicken, A. J. P. White, M. R. Crimmin, *Angew. Chem. Int. Ed.* **2017**, *56*, 15127–15130; *Angew. Chem.* **2017**, *129*, 15323–15326; b) A. Zavras,

- M. Krstić, P. Dugourd, V. Bonačić-Koutecký, R. A. J. O'Hair, *ChemCatChem* **2017**, *9*, 1298–1302.
- [12] S. Takano, H. Hirai, S. Muramatsu, T. Tsukuda, *J. Am. Chem. Soc.* **2018**, *140*, 8380–8383.
- [13] T. Suenobu, D. M. Guldi, S. Ogo, S. Fukuzumi, *Angew. Chem. Int. Ed.* **2003**, *42*, 5492–5495; *Angew. Chem.* **2003**, *115*, 5650–5653.
- [14] G. N. Khairallah, R. A. J. O'Hair, *Dalton Trans.* **2005**, 2702–2712.
- [15] M. Girod, M. Krstić, R. Antoine, L. MacAleese, J. Lemoine, A. Zavras, G. N. Khairallah, V. Bonačić-Koutecký, P. Dugourd, R. A. J. O'Hair, *Chem. Eur. J.* **2014**, *20*, 16626–16633.
- [16] a) G. Niedner-Schatteburg, in *Cooperative Effects in Clusters and Oligonuclear Complexes of Transition Metals in Isolation* (Ed.: S. Dehnen), Springer, Cham, **2017**, pp. 1–40; b) G. Niedner-Schatteburg, in *Erratum to: Cooperative Effects in Clusters and Oligonuclear Complexes of Transition Metals in Isolation* (Ed.: S. Dehnen), Springer, Cham, **2017**, pp. 375–376.
- [17] a) SFB/TRR 88 "Cooperative Effects in Homo- and Heterometallic Complexes (3MET)", <https://www.uni-kl.de/3met>, Accessed 02.14.2019; b) S. V. Kruppa, F. Böppler, W. Klopfer, S. P. Walg, W. R. Thiel, R. Diller, C. Riehn, *Phys. Chem. Chem. Phys.* **2017**, *19*, 22785–22800; c) S. V. Kruppa, F. Böppler, C. Holzer, W. Klopfer, R. Diller, C. Riehn, *J. Phys. Chem. Lett.* **2018**, *9*, 804–810; d) S. V. Kruppa, Y. Nosenko, M.-O. Winghart, S. P. Walg, M. M. Kappes, C. Riehn, *Int. J. Mass Spectrom.* **2016**, *395*, 7–19; e) T. P. Seifert, N. D. Knoefel, T. J. Feuerstein, K. Reiter, S. Lebedkin, M. T. Gamer, A. C. Boukis, F. Weigend, M. M. Kappes, P. W. Roesky, *Chem. Eur. J.* **2019**, *25*, 3799–3808; f) C. Kaub, S. Lebedkin, A. Li, S. V. Kruppa, P. H. Streibert, M. M. Kappes, C. Riehn, P. W. Roesky, *Chem. Eur. J.* **2018**, *24*, 6094–6104; g) J.-F. Greisch, A. Ballester-Caudet, S. V. Kruppa, Z. Lei, Q.-M. Wang, C. Riehn, F. Remacle, *J. Phys. Chem. A* **2018**, *122*, 5799–5810.
- [18] C. Ma, C. T.-L. Chan, W.-P. To, W.-M. Kwok, C.-M. Che, *Chem. Eur. J.* **2015**, *21*, 13888–13893.
- [19] G. E. Johnson, A. Olivares, D. Hill, J. Laskin, *Phys. Chem. Chem. Phys.* **2015**, *17*, 14636–14646.
- [20] a) S. Daly, M. Krstić, A. Giuliani, R. Antoine, L. Nahon, A. Zavras, G. N. Khairallah, V. Bonačić-Koutecký, P. Dugourd, R. A. J. O'Hair, *Phys. Chem. Chem. Phys.* **2015**, *17*, 25772–25777; b) M. Krstić, A. Zavras, G. N. Khairallah, P. Dugourd, V. Bonačić-Koutecký, R. A. J. O'Hair, *Int. J. Mass Spectrom.* **2017**, *413*, 97–105.
- [21] A. Bondi, *J. Phys. Chem.* **1964**, *68*, 441–451.
- [22] E. A. Romero, P. M. Olsen, R. Jazzar, M. Soleilhavoup, M. Gembicky, G. Bertrand, *Angew. Chem. Int. Ed.* **2017**, *56*, 4024–4027; *Angew. Chem.* **2017**, *129*, 4082–4085.
- [23] B. K. Tate, J. T. Nguyen, J. Bacsá, J. P. Sadighi, *Chem. Eur. J.* **2015**, *21*, 10160–10169.
- [24] a) C. W. Liu, H.-W. Chang, C.-S. Fang, B. Sarkar, J.-C. Wang, *Chem. Commun.* **2010**, 46, 4571–4573; b) C. W. Liu, H.-W. Chang, B. Sarkar, J.-Y. Saillard, S. Kahlal, Y.-Y. Wu, *Inorg. Chem.* **2010**, *49*, 468–475; c) P.-K. Liao, K.-G. Liu, C.-S. Fang, C. W. Liu, J. P. Fackler, Y.-Y. Wu, *Inorg. Chem.* **2011**, *50*, 8410–8417; d) C. Latouche, S. Kahlal, E. Furet, P.-K. Liao, Y.-R. Lin, C.-S. Fang, J. Cuny, C. W. Liu, J.-Y. Saillard, *Inorg. Chem.* **2013**, *52*, 7752–7765; e) C. W. Liu, P.-K. Liao, C.-S. Fang, J.-Y. Saillard, S. Kahlal, J.-C. Wang, *Chem. Commun.* **2011**, 47, 5831–5833.
- [25] P. S. Pregosin, R. W. Kunz, ³¹P and ¹³C NMR of Transition Metal Phosphine Complexes, Springer, Berlin, **1979**.
- [26] A. F. M. J. Van Der Ploeg, G. Van Koten, *Inorg. Chim. Acta* **1981**, *51*, 225–239.
- [27] a) F. Furche, R. Ahlrichs, C. Hättig, W. Klopfer, M. Sierka, F. Weigend, *Wiley Interdiscip. Rev. Comput. Mol. Sci.* **2014**, *4*, 91–100; b) TURBOMOLE V7.2 2017, a development of University of Karlsruhe and Forschungszentrum Karlsruhe GmbH, 1989–2007, TURBOMOLE GmbH, since 2007, <http://www.turbomole.com>, Accessed 04.01.2019.
- [28] a) K. Krause, W. Klopfer, *J. Comput. Chem.* **2017**, *38*, 383–388; b) X. Gui, C. Holzer, W. Klopfer, *J. Chem. Theory Comput.* **2018**, *14*, 2127–2136.
- [29] F. Weigend, R. Ahlrichs, *Phys. Chem. Chem. Phys.* **2005**, *7*, 3297–3305.
- [30] D. Andrae, U. Häußermann, M. Dolg, H. Stoll, H. Preuß, *Theor. Chem. Acc.* **1990**, *77*, 123–141.
- [31] a) J. P. Perdew, K. Burke, M. Ernzerhof, *Phys. Rev. Lett.* **1996**, *77*, 3865–3868; b) J. P. Perdew, K. Burke, M. Ernzerhof, *Phys. Rev. Lett.* **1997**, *78*, 1396; c) S. Grimme, J. Antony, S. Ehrlich, H. Krieg, *J. Chem. Phys.* **2010**, *132*, 154104; d) S. Grimme, S. Ehrlich, L. Goerigk, *J. Comput. Chem.* **2011**, *32*, 1456–1465.
- [32] X. Blase, C. Attaccalite, V. Olevano, *Phys. Rev. B* **2011**, *83*, 115103.
- [33] C. Holzer, W. Klopfer, *J. Chem. Phys.* **2019**, *150*, 204116.
- [34] T. Nakajima, Y. Kamiryō, K. Hachiken, K. Nakamae, Y. Ura, T. Tanase, *Inorg. Chem.* **2018**, *57*, 11005–11018.
- [35] S. A. McLuckey, *J. Am. Soc. Mass Spectrom.* **1992**, *3*, 599–614.
- [36] a) N. M. Riley, J. J. Coon, *Anal. Chem.* **2018**, *90*, 40–64; b) R. Hartmer, D. A. Kaplan, C. R. Gebhardt, T. Ledertheil, A. Brekenfeld, *Int. J. Mass Spectrom.* **2008**, *276*, 82–90; c) M. U. Munshi, S. M. Craig, G. Berden, J. Martens, A. F. DeBlase, D. J. Foreman, S. A. McLuckey, J. Oomens, M. A. Johnson, *J. Phys. Chem. Lett.* **2017**, *8*, 5047–5052.
- [37] a) O. A. Boryak, M. V. Kosevich, V. V. Chagovets, V. S. Shelkovsky, *J. Anal. Chem.* **2017**, *72*, 1289–1294; b) Y. Xiong, I. Washio, J. Chen, M. Sadilek, Y. Xia, *Angew. Chem. Int. Ed.* **2007**, *46*, 4917–4921; *Angew. Chem.* **2007**, *119*, 5005–5009; c) Y. Xia, Y. Xiong, B. Lim, S. E. Skrabalak, *Angew. Chem. Int. Ed.* **2009**, *48*, 60–103; *Angew. Chem.* **2009**, *121*, 62–108.
- [38] G. E. Johnson, T. Priest, J. Laskin, *ChemPlusChem* **2013**, *78*, 1033–1039.
- [39] J. E. Freitas, H. J. Hwang, A. B. Ticknor, M. A. El-Sayed, *Chem. Phys. Lett.* **1991**, *183*, 165–170.
- [40] a) M. J. Manard, P. R. Kemper, M. T. Bowers, *Int. J. Mass Spectrom.* **2003**, *228*, 865–877; b) J. Zhou, Z.-H. Li, W.-N. Wang, K.-N. Fan, *Chem. Phys. Lett.* **2006**, *421*, 448–452; c) M. Schmidt, A. Masson, H.-P. Cheng, C. Bréchnignac, *ChemPhysChem* **2015**, *16*, 855–865.
- [41] J. Martens, G. Berden, J. Oomens, *Anal. Chem.* **2016**, *88*, 6126–6129.
- [42] C. S. Byskov, J. M. Weber, S. B. Nielsen, *Phys. Chem. Chem. Phys.* **2015**, *17*, 5561–5564.
- [43] M. L. Parker, S. Gronert, *Int. J. Mass Spectrom.* **2017**, *418*, 73–78.
- [44] J. Martens, J. Grzetic, G. Berden, J. Oomens, *Nat. Commun.* **2016**, *7*, 11754.
- [45] H. Schwarz, *Int. J. Mass Spectrom.* **2004**, *237*, 75–105.
- [46] a) Z. Luo, G. U. Gamboa, J. C. Smith, A. C. Reber, J. U. Reveles, S. N. Khanna, A. W. Castleman, *J. Am. Chem. Soc.* **2012**, *134*, 18973–18978; b) T. M. Bernhardt, *Int. J. Mass Spectrom.* **2005**, *243*, 1–29.
- [47] R. Burgert, H. Schnöckel, A. Grubisic, X. Li, S. T. Stokes, K. H. Bowen, G. F. Ganteför, B. Kiran, P. Jena, *Science* **2008**, *319*, 438.
- [48] S. M. J. Wellman, R. A. Jockusch, *J. Phys. Chem. A* **2015**, *119*, 6333–6338.
- [49] S. Xu, J. E. T. Smith, J. M. Weber, *J. Chem. Phys.* **2016**, *145*, 024304.
- [50] M.-B. S. Kirketerp, S. B. Nielsen, *Int. J. Mass Spectrom.* **2010**, *297*, 63–66.
- [51] M. W. Forbes, A. M. Nagy, R. A. Jockusch, *Int. J. Mass Spectrom.* **2011**, *308*, 155–166.
- [52] a) Q.-J. Pan, H.-X. Zhang, H.-G. Fu, H.-T. Yu, *Eur. J. Inorg. Chem.* **2006**, 1050–1059; b) W.-F. Fu, K.-C. Chan, V. M. Miskowski, C.-M. Che, *Angew. Chem. Int. Ed.* **1999**, *38*, 2783–2785; *Angew. Chem.* **1999**, *111*, 2953–2955; c) W.-F. Fu, K.-C. Chan, K.-K. Cheung, C.-M. Che, *Chem. Eur. J.* **2001**, *7*, 4656–4664; d) C.-M. Che, S.-W. Lai, *Coord. Chem. Rev.* **2005**, *249*, 1296–1309.
- [53] H. X. Zhang, C. M. Che, *Chem. Eur. J.* **2001**, *7*, 4887–4893.
- [54] a) R. W. Hartsock, W. Zhang, M. G. Hill, B. Sabat, K. J. Gaffney, *J. Phys. Chem. A* **2011**, *115*, 2920–2926; b) T. J. Penfold, E. Gindensperger, C. Daniel, C. M. Marian, *Chem. Rev.* **2018**, *118*, 6975–7025; c) M. Chergui, *Acc. Chem. Res.* **2015**, *48*, 801–808; d) J. K. McCusker, A. Viček, *Acc. Chem. Res.* **2015**, *48*, 1207–1208.
- [55] C. M. Taliaferro, E. O. Danilov, F. N. Castellano, *J. Phys. Chem. A* **2018**, *122*, 4430–4436.
- [56] a) M. S. Bootharaju, R. Dey, L. E. Gevers, M. N. Hedhili, J.-M. Basset, O. M. Bakr, *J. Am. Chem. Soc.* **2016**, *138*, 13770–13773; b) S. M. Aly, L. G. AbdulHalim, T. M. D. Besong, G. Soldan, O. M. Bakr, O. F. Mohammed, *Nanoscale* **2016**, *8*, 5412–5416; c) G. Soldan, M. A. Aljuhani, M. S. Bootharaju, L. G. AbdulHalim, M. R. Parida, A.-H. Emwas, O. F. Mohammed, O. M. Bakr, *Angew. Chem. Int. Ed.* **2016**, *55*, 5749–5753; *Angew. Chem.* **2016**, *128*, 5843–5847.
- [57] a) S. Klacar, A. Hellman, I. Panas, H. Grönbeck, *J. Phys. Chem. C* **2010**, *114*, 12610–12617; b) M. Pereiro, J. Botana, D. Baldomir, D. Serantes, J. E. Arias, *J. Nanosci. Nanotechnol.* **2010**, *10*, 2594–2599; c) T. Archipov, J. K. Kirkland, K. D. Vogiatzis, A. Steiner, G. Niedner-Schatteburg, P. Weis, K. Fink, O. Hampe, M. M. Kappes, *J. Phys. Chem. A* **2018**, *122*, 4357–4365.
- [58] a) J. G. Serafin, A. C. Liu, S. R. Seyedmonir, *J. Mol. Catal. A* **1998**, *131*, 157–168; b) K. C. Waugh, M. Hague, *Catal. Today* **2010**, *157*, 44–48; c) M. O. Özbek, I. Önal, R. A. van Santen, *ChemCatChem* **2011**, *3*, 150–153; d) M. O. Özbek, I. Önal, R. A. van Santen, *J. Catal.* **2011**, *284*, 230–235.
- [59] G. Sheldrick, *Acta Crystallogr. Sect. A* **2008**, *64*, 112–122.

- [60] A. Altomare, G. Cascarano, C. Giacovazzo, A. Guagliardi, M. C. Burla, G. Polidori, M. Camalli, *J. Appl. Crystallogr.* **1994**, *27*, 435.
- [61] A. Spek, *Acta Crystallogr. Sect. D* **2009**, *65*, 148–155.
- [62] J. Dang, X. Shi, Q. Zhang, J. Hu, J. Chen, W. Wang, *Sci. Total Environ.* **2014**, *490*, 639–646.
- [63] a) Y. Nosenko, F. Menges, C. Riehn, G. Niedner-Schatteburg, *Phys. Chem. Chem. Phys.* **2013**, *15*, 8171–8178; b) J. Martens, G. Berden, R. E. van Outersterp, L. A. J. Kluijtmans, U. F. Engelke, C. D. M. van Karnebeek, R. A. Wevers, J. Oomens, *Sci. Rep.* **2017**, *7*, 3363.
- [64] P. Haimi, A. Uphoff, M. Hermansson, P. Somerharju, *Anal. Chem.* **2006**, *78*, 8324–8331.
- [65] a) C. van Wüllen, *J. Comput. Chem.* **2011**, *32*, 1195–1201; b) P. Deglmann, F. Furche, R. Ahlrichs, *Chem. Phys. Lett.* **2002**, *362*, 511–518.

Manuscript received: May 2, 2019

Revised manuscript received: June 8, 2019

Accepted manuscript online: June 12, 2019

Version of record online: August 5, 2019

Publication 4 (JPCA)

Gas-Phase Photoluminescence and Photodissociation of Silver-Capped Hexagold Clusters

Preamble

The following chapter has been published in the journal „The Journal of Physical Chemistry A“. For the supporting information the reader is referred to the electronic version of the article. My contribution to this work has been the measurement of UV/Vis-PD spectra including data analysis and evaluation. I contributed text sections regarding photodissociation data and helped with revisions of the manuscript. Dr. Jean-François Greisch measured gas-phase photoluminescence spectra and composed the initial draft of the manuscript. Quantum chemical calculations were conducted by Dr. Ana Ballester-Caudet. The sample compound and high resolution mass spectra thereof were provided by Prof. Dr. Quan-Ming Wang.

J.-F. Greisch, A. Ballester-Caudet, S. V. Kruppa, Z. Lei, Q.-M. Wang, C. Riehn, F. Remacle, *The Journal of Physical Chemistry A*, **2018**, 122(27), 5799-5810, <https://doi.org/10.1021/acs.jpca.8b01864>

Copyright © 2018 American Chemical Society

Reprint Licence

Gas-Phase Photoluminescence and Photodissociation of Silver-Capped Hexagold Clusters

Author: Jean-François Greisch, Ana Ballester-Caudet, Sebastian Volker Kruppa, et al

Publication: The Journal of Physical Chemistry A

Publisher: American Chemical Society

Date: Jul 1, 2018

Copyright © 2018, American Chemical Society



PERMISSION/LICENSE IS GRANTED FOR YOUR ORDER AT NO CHARGE

This type of permission/license, instead of the standard Terms & Conditions, is sent to you because no fee is being charged for your order. Please note the following:

- Permission is granted for your request in both print and electronic formats, and translations.
- If figures and/or tables were requested, they may be adapted or used in part.
- Please print this page for your records and send a copy of it to your publisher/graduate school.
- Appropriate credit for the requested material should be given as follows: "Reprinted (adapted) with permission from (COMPLETE REFERENCE CITATION). Copyright (YEAR) American Chemical Society." Insert appropriate information in place of the capitalized words.
- One-time permission is granted only for the use specified in your request. No additional uses are granted (such as derivative works or other editions). For any other uses, please submit a new request.

BACK

CLOSE WINDOW

Gas-Phase Photoluminescence and Photodissociation of Silver-Capped Hexagold Clusters

Jean-François Greisch,^{*,†,‡} Ana Ballester-Caudet,[‡] Sebastian Volker Kruppa,[§] Zhen Lei,^{||} Quan-Ming Wang,^{||} Christoph Riehn,[§] and Françoise Remacle[‡]

[†]Institute of Nanotechnology, Karlsruhe Institute of Technology, Hermann-von-Helmholtz-Platz 1 76344 Eggenstein-Leopoldshafen, Germany

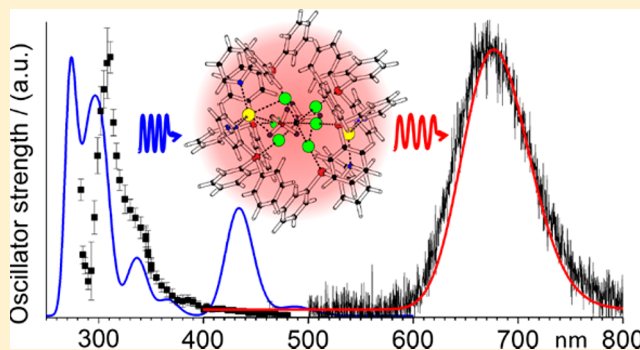
[‡]Theoretical Physical Chemistry, UR MolSys, B6c, University of Liège, B4000 Liège, Belgium

[§]Department of Chemistry and Research Center OPTIMAS, TU Kaiserslautern, Erwin-Schrödinger-Strasse 52–54, 67663 Kaiserslautern, Germany

^{||}Department of Chemistry, Tsinghua University, Beijing, 100084, P. R. China

Supporting Information

ABSTRACT: We report on the radiative and nonradiative deactivation pathways of selected charge states of the stoichiometric hexagold phosphine-stabilized ionic clusters, $[(C)(AuDppy)_6Ag_2(BF_4)_x]^{(4-x)+}$ with $x = 2$ and 3 (Dppy = diphenylphosphino-2-pyridine), combining gas-phase photoluminescence and photodissociation with quantum chemical computations. These clusters possess an identical isostructural core made of a hyper-coordinated carbon at their center octahedrally surrounded by six gold ions, and two silver ions at their apexes. Their luminescence and fragmentation behavior upon photoexcitation was investigated under mass and charge control in an ion trap. The experimental and computational results shed light on the electronic states involved in the optical transitions as well as on their core, ligand, or charge transfer character. Gas-phase results are discussed in relation with condensed phase measurements, as well as previous observations in solution and on metal–organic frameworks. The monocationic species ($x = 3$) is found to be less stable than the dicationic one ($x = 2$). In the luminescence spectrum of the monocationic species, a shoulder at short wavelength can be observed and is assigned to fragment emission. This fragment formation appears to be favored for the monocation by the existence of a low lying singlet state energetically overlapping with the triplet state manifold, which is populated quickly after photoexcitation.



INTRODUCTION

Ligated polynuclear gold clusters with an intense and long-lived room temperature luminescence in the visible spectral range as well as the ability to form nanoscale architectures are promising OLED emitters, photochemical converters, and luminescent reporters for sensing or imaging.^{1–16} The photophysical properties of such clusters have been found to be highly sensitive to the nuclearity, the size and shape of the cluster core, the nature of the coordinating ligands, as well as the Au–Au distances.^{17–21} The impact of counterions, on the other hand, has been neglected so far. Furthermore, since metal–organic frameworks (MOFs) assembled from luminescent clusters have been found to display a marked dependence of their luminescence on the solvent molecules filling their channels,⁸ a deeper understanding of the interactions between the subunits as well as a description of the nature of the emission is needed.

In gold nanocrystals slightly larger than the metal's Fermi wavelength (~ 0.5 nm for Au), energy levels are quantized with

profound consequences on optical, electronic, charging, and transport processes even under ambient conditions.^{22,23} Not only does catalytic and electrocatalytic activity emerge but also enhanced optical properties such as strong nonlinear or electro-optical effects. For the even smaller clusters investigated here (~ 0.4 nm Au core), distinctive quantum confinement effects occur. In particular, broad collective resonances completely give way to discrete electronic transitions among quantized levels resulting in a discrete electronic structure and molecule-like properties such as intrinsic magnetism and enhanced photoluminescence.^{4,23–25}

Overall, the properties of gold clusters, formally formed here of Au(I) atoms (closed-shell $5d^{10}$ electronic configuration), are governed by (1) relativistic effects involving high-speed core electrons moving close to the Au nuclei; this causes an increase

Received: February 23, 2018

Revised: May 9, 2018

Published: June 14, 2018

in the effective nuclear charge leading to a radial contraction and stabilization of the less-diffuse orbitals (such as the 6s and 6p orbitals), while more-diffuse orbitals (such as the 5d-orbitals) expand due to the enhanced shielding effect by the contracted s/p-orbitals;^{18,20} (2) configuration mixing of the 5d-orbitals with hybrid orbitals of appropriate symmetry derived from the 6s and 6p orbitals, reportedly responsible for Au(I)⋯Au(I) stabilizing interaction and Au(I)–C bonding interaction,^{17–21} and (3) electron correlation.^{17,18,26} Altogether, these three effects are often designated by the term “aurophilic” interactions. Because of a very strong spin–orbit coupling, excited singlet state populations of gold clusters also typically undergo a fast intersystem crossing²⁷ to the triplet manifold followed by long-lived luminescence. Additionally, some optical transitions are sensitive to the surrounding environment as a consequence of their charge transfer character or formation of solvent exciplexes,^{28,29} corresponding either to a ligand-to-metal charge transfer (LMCT) or a metal-to-ligand charge transfer (MLCT).³⁰

Unlike ligand-protected Au clusters with core structure and surface motif,^{4,5,31} the carbon hypercoordinated cluster studied here, [(C)(AuDppy)₆Ag₂(BF₄)₄] abbreviated [1·(BF₄)₄], contains an octahedral Au₆ core with two Ag atoms capping two opposite Au₃ triangles, and six peripheral Dppy ligands.^{32,33} The hexagold core with its interstitial carbon is characterized by short Au–Au contacts along the edges of the polyhedra.³² Its structure is similar to that of the hexaaurio-methane [(C)(AuPPh₃)₆·(CH₃OBF₃)₂] (PPh₃ = triphenylphosphine) cluster first reported by Schmidbaur and co-workers.³⁴ When considering the coordination of the silver atoms by diphenylphosphino-2-pyridine ligands, the [1](BF₄)₄ cluster can be described as the fusion of two AgAu₃ tetrahedral moieties sharing a carbon center, each moiety similar to [(E)(AuDppy)₃Ag·(BF₄)₂] with E = O, S, or Se heterometallic clusters.¹ The heterometallophilic Au–Ag interaction contributes, concurrently with the diphenylphosphino-2-pyridine ligands, to their stabilization. This affects the charge transfer dynamics as well as the photophysical and spectroscopic properties of the [1·(BF₄)₄] cluster which is characterized by (i) an energy gap small enough that absorption in the visible region occurs, (ii) ultrafast intersystem crossing (1–3 ps), (iii) solvent dependent energy transfer, and (iv) temperature dependent intensity of the phosphorescence in solution.^{28,32} The cluster room-temperature quantum yield of luminescence in solution ($\phi = 0.29$)³² is comparable to that of another set of systems stabilized by heterometallophilic Au⋯M bonding, the heterometallic copper–gold alkynyl complexes reported by Koshevoy et al. ($\phi = 0.9$).³⁵

In dichloromethane at room temperature, the [1·(BF₄)₄] cluster is characterized by an absorption onset about 475 nm, a red emission with maximum between 600 and 640 nm ($\lambda_{\text{ex}} = 350$ nm), and a single-exponential luminescence decay behavior with a luminescence lifetime of 5.7 μs .^{28,32} Analysis by Zhou et al. of femtosecond time-resolved transient absorption experiments in solution using a sequential model yields excited state dynamics by three different states (1) ¹MLCT(Au) state ($\tau = 1–3$ ps); (2) ³MLCT(Au) state ($\tau = 11–40$ ps), and (3) ³MLCT(Ag) state (long-lived) whose relative population can be modulated by the solvent's polarity and hydrogen bonding ability.²⁸ The triplet nature of the solution emission is supported by the significant redshift of the emission compared to the absorption, the long luminescence decay, as well as excited-state absorptions and dynamics

obtained from the femtosecond time-resolved transient absorption experiments. In absence of information about the counterions, the emission of the [1](BF₄)₄ cluster also appears remarkably insensitive to the nature of the solvent²⁸ while porous metal–organic frameworks formed upon silver binding of the [(C)(AuMdppz)₆](BF₄)₂ (Mdppz = 2-(3-methylpyrazinyl)diphenylphosphine) derivative display significant solvatochromism as well as a possible dual emission.⁸

In this work, mass spectrometric selection enables the separate investigation of stoichiometrically homogeneous ensembles of clusters characterized by different numbers of tetrafluoroborate counterions.³¹ The photoluminescence and photodissociation of the mass-selected [1·(BF₄)_x]^{(4–x)+} with $x = 2,3$ clusters *in vacuo* yields complementary information about their radiative and nonradiative electronic deactivation pathways. Furthermore, given that the investigated species are stored in the gas phase in an ion trap, their structure, electronic, and optical properties are unconstrained by solvent or environmental effects (packing or more generally coupling to the environment). The experimental results can thereby be directly compared to computations, providing benchmarks for computational approaches. On the application side, the present study offers a first insight into the impact of counterions and possible dynamical equilibria on the luminescence properties of gold cluster salts.

■ EXPERIMENTAL AND COMPUTATIONAL SECTION

Materials. The synthesis of [1](BF₄)₄ by Wang and co-workers was reported elsewhere.³² The purified solid sample was stored in the dark until dissolution in dichloromethane or acetonitrile for electrospray ionization. The composition of the electrosprayed species has been unambiguously established using a SYNAPT G2S-HDMS mass spectrometer (Waters, Manchester, U.K.).

Gas-Phase Photoluminescence. The gas-phase luminescence spectra were acquired using the setup previously described in ref 36 and subsequently modified to measure the gas-phase photoluminescence of lanthanoid cluster-like complexes.^{37,38} Briefly, it consists of a home-built temperature-regulated (down to 82 K) quadrupole ion trap. After being nanoelectrosprayed from a $\sim 10^{-4}$ M dichloromethane (LC-MS grade) solution using borosilicate capillaries, the ions are mass-selected and trapped before being photoexcited either using a Toptica iBEAM-SMART-405-S (405 nm) or using a Ar⁺-laser (Spectra Physics 2080–15S) (458 and 476 nm lines), while being thermalized by collisions with a helium buffer gas at a pressure of ~ 0.2 mbar in order to prevent photoinduced fragmentation. Ion photoluminescence is collected perpendicularly to the excitation beam by a Zeiss EC PlanNeofluor 5x/0.15 microscope objective imaging the ion cloud via a 3 mm diameter aperture in one of the end-caps. It is then filtered to eliminate scattered excitation light using long pass filters before being focused into a fiber and sent to a spectrograph (SpectraPro 300i, Acton Research, Roper Scientific) equipped with 150 grooves/mm gratings and an electron-multiplying charge coupled device for detection (Idus DV-401A-BV, Andor).

Time resolved measurements are performed using a diode laser (405 nm, Toptica iBEAM-SMART-405-S) operated in pulsed mode (500 ps rise and 800 ps fall times). Instead of into a fiber, the collected ion luminescence is focused directly onto the aperture of a photomultiplier (Hamamatsu H7421-40)

Table 1. Total Fragment Yields and Photoluminescence Features for $[1 \cdot (\text{BF}_4)_x]^{(4-x)+}$ and $[1 \cdot (\text{BF}_4)_{x-1} \text{H}]^{(4-x)+}$ Cluster Species (with $x = 1$ and 2)

species	m/z nominal	m/z main isotopolog.	photodissociation total frag. yield/%		photoluminescence, $\lambda_{\text{em}}/\text{nm}$ ($\lambda_{\text{ex}} = 405 \text{ nm}$)
			at 308 nm	at 408 nm	
$[1 \cdot (\text{BF}_4)_2]^{2+}$	1580	1581.06	44	2	~ 677 (phos.)
$[1 \cdot (\text{BF}_4)\text{H}]^{2+}$	1536	1537.06	72	26	<i>a</i>
$[1 \cdot (\text{BF}_4)]^{3+}$	1024	1025.04	64	8	<i>a</i>
$[1\text{H}]^{3+}$	995	995.70	27	2	not investigated
$[1 \cdot (\text{BF}_4)_3]^+$	3247	3249.13	–	–	~ 673 (phos.), ~ 586

^aNo detectable photoluminescence.

coupled to a multiple-event time digitizer (P7888, FAST ComTec).

Gas-Phase Photodissociation. UV–vis electronic action spectra of mass-selected ions were obtained employing photodissociation (PD) spectroscopy as described elsewhere.^{39–42} Briefly, a $\sim 10^{-4}$ M acetonitrile (LC-MS grade) solution of $[1](\text{BF}_4)_4$ was electrosprayed in positive mode (Apollo II electrospray source, Bruker Daltonics) at an infusion rate of 100 $\mu\text{L}/\text{h}$ assisted by nitrogen sheath gas (ca. 6 psi, 414 mbar). The ions of interest (integer nominal masses m/z 1580, 1536, 1024, 995, see Table 1) were isolated selecting their full isotope pattern, fragmented by laser irradiation, and subsequently mass analyzed in a customized 3D quadrupole ion trap mass spectrometer (amaZon speed, Bruker Daltonics). Hereby, a shutter was synchronized with the mass spectrometer in order to irradiate the ions only in a 100 ms storage time window (~ 98 laser pulses per stored ion ensemble). The abundance of species m/z 1536 and 995 was enhanced by collisional-induced dissociation (CID) of isolated m/z 1580 and 1024 precursor species and isolated for subsequent photodissociation (MS^3 step). The femtosecond laser system used is based on a Ti:sapphire chirped pulse cryogenic regenerative amplifier (Wyvern 1000, KMLabs) whose output pulse train (~ 780 nm, fwhm ~ 30 nm, ~ 4 W, 982 Hz, $\Delta\tau \sim 50$ fs) was used to pump two identical nonlinear frequency converters (TOPAS-C, Light Conversion, abbreviated TC_1 and TC_2). The resulting beams (TC_1 , 283–403 nm; TC_2 , 400–480 nm) were attenuated to 2 $\mu\text{J}/\text{pulse}$ using a neutral density filter, focused onto the ion trap center (~ 1 mm diameter), and spatially overlapped with the ion cloud. Either of the beams (TC_1 , TC_2) were used to obtain photodissociation action spectra. These were acquired stepwise (3–5 nm steps) by averaging at least 160 individual mass spectra for each wavelength position. From the resulting mass spectra the total fragment yield (TFY) was calculated as

$\text{TFY} = \frac{\sum_i F_i}{\sum_i F_i + P}$ and normalized to the number of photons

$N = E_{\text{pulse}} \cdot \frac{\lambda}{h \cdot c}$, where $\sum_i F_i$ is the sum of all fragment ion signals and P represents the integrated mass peak intensity of the precursor species. Color changes in Figure 3 indicate a change in the nonlinear output scheme or wavelength filters requiring a reoptimization of the laser beam/ion cloud overlap. The respective spectral regions were scaled by factors determined from overlapping wavelength points.

Quantum Chemical Calculation. The computed gas-phase equilibrium geometries of the $[1 \cdot (\text{BF}_4)_x]^{(4-x)+}$ ions, with $x = 1, 2, 3$, are based on the crystal structure reported by Wang et al.³² The electronic structure computations were carried out at the density functional theory level as implemented in the

Gaussian 09⁴³ quantum chemistry suite of programs. The long-range corrected functional CAM-B3LYP⁴⁴ was used. It is well suited on the one hand to account for the description of the electrostatic and noncovalent interactions between the metallic core and the tetrafluoroborates, as well as the noncovalent interactions between the ligands, and on the other hand, to describe excited states with moderate charge transfer.⁴⁵ Relativistic effects were included using relativistic energy corrected pseudopotentials and double- ζ basis set LANL2DZ^{46,47} for the gold and silver atoms. The 6-31G(d,p) Gaussian basis set was used for the other atoms. Equilibrium geometries of the ground and excited states were determined. Both singlet and triplet excited states were computed with the linear response TD-DFT methodology and the absorption and emission spectra obtained by convolution of the obtained stick spectra with Gaussian line shapes (as detailed in the captions). Partial charges on nuclei were computed using the natural population analysis (NPA) and the natural bond orbital (NBO) methodology.^{48,49}

RESULTS AND DISCUSSION

Mass Spectrometry and Ground State Computational Results. Upon nanospraying $[1](\text{BF}_4)_4$ solubilized in dichloromethane, one primarily observes the $[1 \cdot (\text{BF}_4)_3]^+$ and $[1 \cdot (\text{BF}_4)_2]^{2+}$ species (see Figure S1). Under mildly activating source conditions or when spraying from more polar solvents such as acetonitrile, the $[1 \cdot (\text{BF}_4)_3]^+$ species vanishes and the $[1 \cdot (\text{BF}_4)_2]^{2+}$ species, which retains only two tetrafluoroborates, dominates as shown in Figure 1.

Besides the $[1 \cdot (\text{BF}_4)_2]^{2+}$ dication, one also observes, as minority species in Figure 1, the doubly charged $[1 \cdot (\text{BF}_4)\text{H}]^{2+}$ cluster at m/z 1537.06 (most abundant isotopologue) formed by loss of HBF_4 from the precursor. The second most intense species under these conditions is the triply charged $[1\text{H}]^{3+}$ at m/z 995.70 likely a product of the marginally abundant $[1 \cdot (\text{BF}_4)]^{3+}$ species (m/z 1025.04) upon HBF_4 loss. Consequently, from the very low abundance of the mono-charged cluster ion sprayed from acetonitrile or from dichloromethane under mildly activating conditions and the composition of the observed species, it is suggested that a maximum of two tetrafluoroborates bind strongly enough to the cluster to be easily observed in the gas-phase.

This is further supported by the results of computations that predict the existence of two binding sites with different computed binding energies for the tetrafluoroborate (Figure 2a,b). Sites A and B are characterized by a tetrafluoroborate binding energy of -766 and -722 kJ/mol, respectively, and a distance from the boron atom to the central carbon of 4.396 and 7.519 Å, respectively. It appears therefore that the first pair of tetrafluoroborates, leading to the formation of the $[1 \cdot$

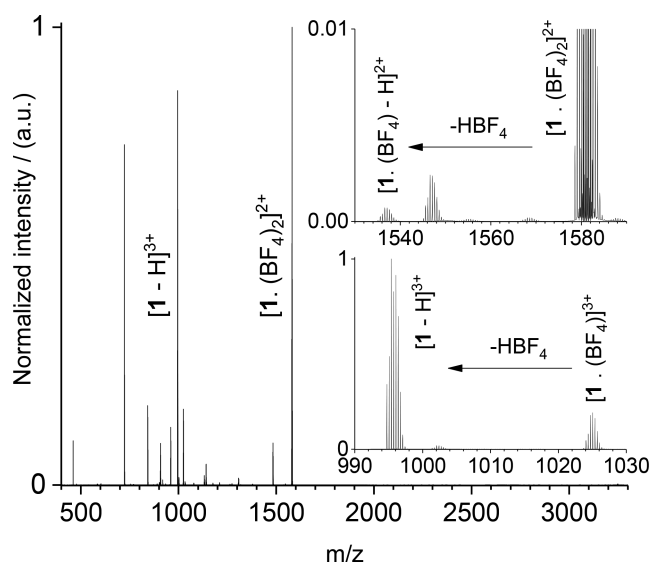


Figure 1. Electrospray mass spectrum of $[1 \cdot (\text{BF}_4)_4]$ solubilized in dichloromethane. The species formed under mildly activating in-source conditions upon HBF_4 loss are shown in the inset.

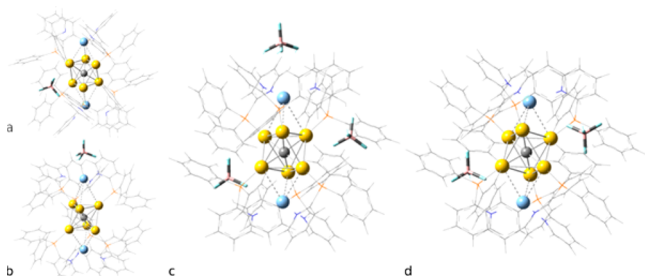


Figure 2. Equilibrium geometries of the ground state of the $[1 \cdot (\text{BF}_4)_x]^{(4-x)+}$ species with $x = 1, 2,$ and 3 . (a, b) $[1 \cdot (\text{BF}_4)_3]^+$ two binding sites for the tetrafluoroborate: site A (a) close to the gold atoms and site B (b) closer to the silver atom. (c, d) Computed equilibrium geometries of $[1 \cdot (\text{BF}_4)_3]^+$ (c) and $[1 \cdot (\text{BF}_4)_2]^{2+}$ (d) at the CAM-B3LYP level. Tetrafluoroborates are represented as capped sticks while Au atoms, Ag atoms and the central carbon atom are represented as yellow, pale blue, and gray spheres, respectively. The diphenylphosphino-2-pyridine ligand shell (Dppy) is composed of P atoms (orange), phenyl rings with C (gray), pyridine ring (N in blue), and H atoms (white) in wireframe representation.

$(\text{BF}_4)_2]^{2+}$ species, is preferentially located belt-wise (close to the gold) while the second pair, leading finally to the formation of the neutral $[1 \cdot (\text{BF}_4)_4]$ species, is in the vicinity of the silver atoms. Isomers of the $[1 \cdot (\text{BF}_4)_x]^{(4-x)+}$ ions with $x = 2, 3$ investigated at the PM7 level prior reoptimization at the CAM-B3LYP level are displayed in Figure S2.

The mass spectrometric observation (Figure 1) of the species $[1-\text{H}]^{3+}$ and $[1 \cdot (\text{BF}_4)-\text{H}]^{2+}$ —both resulting from a HBF_4 loss—and the absence of signal corresponding to the quadruply charged $[1]^{4+}$ cluster indicates that upon gas-phase dissociation, as expected, the release of the counterion as a negatively charged tetrafluoroborate is energetically unfavorable contrarily to the loss of HBF_4 which is documented in the literature for isolated coinage metal complexes containing BF_4^- counterions.⁵⁰

At the CAM-B3LYP level, the partial charge on the complex metallic core is -0.570 lel for the $[1 \cdot (\text{BF}_4)_3]^+$ complex, -0.437

lel for the $[1 \cdot (\text{BF}_4)_2]^{2+}$ complex and -0.255 lel for the $[1 \cdot (\text{BF}_4)]^{3+}$ complex.

In what follows, all species of interest are mass-selected and isolated to achieve selective characterization of pure compounds.

Gas-Phase Photodissociation. The gas-phase photodissociation spectra of the $[1 \cdot (\text{BF}_4)_x]^{(4-x)+}$ and $[1 \cdot (\text{BF}_4)_{x-1}-\text{H}]^{(4-x)+}$ clusters (with $x = 1$ and 2) are displayed in Figure 3. It was not possible to detect and analyze the $[1 \cdot (\text{BF}_4)_3]^+$ species due to the electrospray source and storage conditions of the setup employed for these investigations. We also note that the spectrum of the $[1-\text{H}]^{3+}$ species (Figure 3d) exhibits a poor signal-to-noise ratio, significantly worse than those of the other species and it is therefore only accessory to the present study.

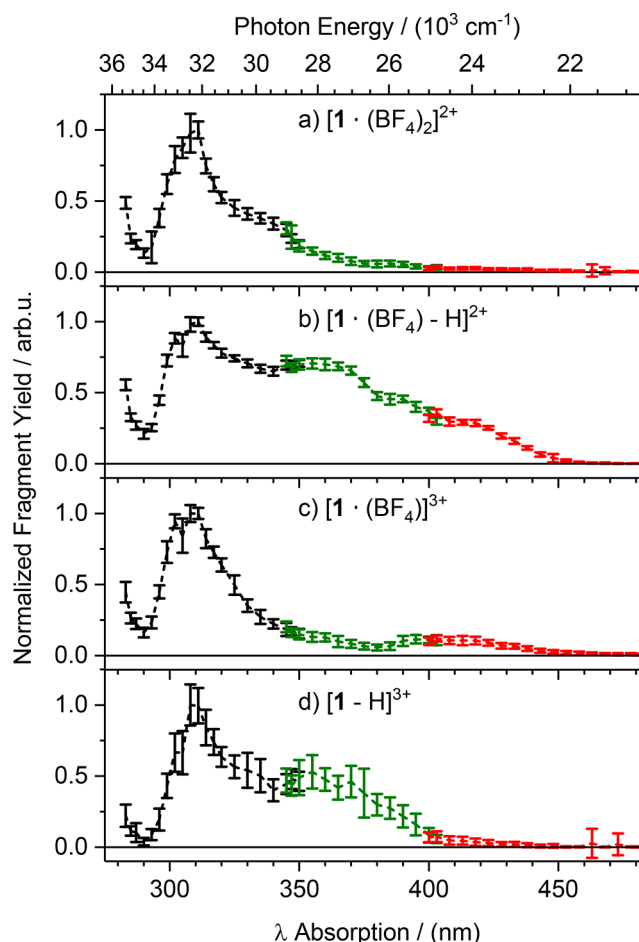


Figure 3. UV/vis-photodissociation total yield spectra of gaseous precursor species: (a) m/z 1580, (b) m/z 1536, (c) m/z 1024, and (d) m/z 995 (nominal, $2 \mu\text{J}$ per pulse, 98 pulses per ion cloud). Color changes indicate a change in the nonlinear output scheme or wavelength filters requiring a reoptimization of the laser beam/ion cloud overlap. Error bars represent one standard deviation ($\pm 1\sigma$, at least 160 mass spectra).

A detailed analysis of the various photofragments is provided in the Supporting Information (Figure S4 and Tables S1 and S2). The photofragmentation pathways of all four analyzed species range from neutral losses (charge retention) to ionic fragmentation (charge separation). Ionic fragmentation proceeds mainly via the cleavage of a $[\text{Au}(\text{Dppy})_2]^+$ moiety

while neutral loss photodissociation channels primarily encompass loss(es) of HBF_4 and/or loss(es) of Dppy ligands.

The following aspects determining the obtained photofragmentation yield are to be considered: the non-negligible heat capacity due to the respectable size of the clusters, the possible kinetic shifts pertaining to the dissociation,⁵¹ and the competing quenching by helium inside the trap. Thus, the recorded photodissociation action spectra (Figure 3) do not directly reflect linear absorption spectra.⁵² Moreover, the photofragment yield is only in the low laser fluence regime proportional to the oscillator strength and the quantum yield for dissociation. However, it was recently observed for Ru(II) complexes under ion trap conditions that gas-phase photodissociation action spectra display, albeit relatively weak electronic excitation bands at longer wavelengths comparable to solution absorption spectra.^{53,54} Laser fluence-dependent measurements at 1–4 μJ per pulse were performed for selected spectral regions (see Figures S14–S17) displaying no significant dependence of spectral profiles on intensity and therefore ensure that the PD spectra were not measured under saturated conditions. On the basis of the observed nonlinear increase of fragment yield upon doubling of the laser pulse energy (cf. Figure S15), the presumable large heat capacity of the cluster ions and the onset for HBF_4 loss at ~ 450 nm (266 kJ/mol), we assume the absorption of at least two photons prior to dissociation.

The experimental spectra obtained in this work nevertheless display a good agreement with computed data in the high energy spectral range (see next section). In particular, all investigated species (Figure 3a–d) exhibit an absorption maximum at 310 nm assigned in the next section to $^1\text{LMCT}$ transitions. This band can conveniently be used for the normalization of the photodissociation spectra as its computed intensity (see later on) does not significantly change for the different species. It should be emphasized that all spectra have been obtained under identical mass spectrometric and laser conditions (side-by-side measurements).

Interestingly, the photodissociation spectra of Figure 3 not only depend on the charge state but also on the number of associated tetrafluoroborates and the number of lost HBF_4 units. The $[\text{I} \cdot (\text{BF}_4)_2]^{2+}$ species is the only one which also displays detectable luminescence in the gas phase upon excitation in the visible (at $\lambda_{\text{ex}} = 405, 458, \text{ and } 476$ nm) as discussed in the next section. While photoexcitation and photoluminescence excitation is possible using wavelengths longer than 400 nm, no absorption bands have been observed in the photodissociation spectrum of this species at $\lambda_{\text{ex}} > 400$ nm (Figure 3a). Moreover, its total fragmentation yield (TFY) is below 3% in this wavelength range in contrast to the $[\text{I} \cdot (\text{BF}_4)\text{--H}]^{2+}$ and $[\text{I} \cdot (\text{BF}_4)]^{3+}$ species. Since the other species, with the exception of $[\text{I} \cdot (\text{BF}_4)]^{3+}$, which is not intense enough to be efficiently isolated and therefore investigated, were not found to lead to detectable photoluminescence under the conditions used, we propose that $[\text{I} \cdot (\text{BF}_4)_2]^{2+}$ photoluminescence channels efficiently compete with photodissociation. While luminescence photoexcitation spectra could help to elucidate these competing processes involving the cluster excited states manifolds,⁵² further support for this hypothesis also comes from the inspection of the photodissociation spectrum of the species $[\text{I} \cdot (\text{BF}_4)]^{3+}$ (Figure 3c). Its spectrum clearly displays a band centered about 415 nm comparable to the absorption spectra of $[\text{I}](\text{BF}_4)_4$ in CH_2Cl_2 .²⁸ Additionally, the increase of the TFY by a factor of 3–4 suggests that

fragmentation-competing processes such as photoluminescence only play a minor role for this system. This behavior is consistent with the general idea that ions with higher overall charge are more susceptible to fragmentation than the ones of lower charge.

The $[\text{I} \cdot (\text{BF}_4)\text{--H}]^{2+}$ cluster ion, whose structure we have not explored in the course of this work, shows a very high photofragment yield (Table 1) over the whole spectral range (Figure 3b). Its photodissociation spectrum gives evidence for absorption bands up to 460 nm. Its high reactivity probably originates from the activated/high energy structure of the ligand moiety formed after formal loss of a proton with the HBF_4 leaving group. This high fragment yield of $[\text{I} \cdot (\text{BF}_4)\text{--H}]^{2+}$ is in accordance with our finding (see below) that photoluminescence was not detectable for this species.

Upon comparison of the PD spectra of cluster species differing by the loss of a neutral HBF_4 moiety (Figure 3, part a vs part b and part c vs part d), pronounced spectral differences in the range of 320–450 nm are evident, whose assignments would require more detailed quantum-chemical calculations which are beyond the scope of this paper. Presumably, loss of HBF_4 should result in change of the charge density and/or charge density distribution of the $[(\text{C})\text{Au}_6\text{Ag}_2]$ metal core or radical character located at the dehydrogenated ligands, leading to new electronic states and coupling.

The channel-specific spectra are provided in the Supporting Information (see Figures S7–S10) and display a very similar shape compared to the total yield spectra suggesting that the excess energy is presumably statistically distributed in all (mostly vibrational) degrees-of-freedom (ergodic fragmentation). There is no indication of state-specific fragmentation.

Gas-Phase Photoluminescence. Gas-phase photoexcitation of the $[\text{I} \cdot (\text{BF}_4)_x]^{(4-x)+}$ clusters was found to lead to detectable emission upon excitation at $\lambda_{\text{ex}} = 405, 458, \text{ and } 476$ nm only for the mono and doubly charged species, with $x = 3$ and 2, respectively. Although $[\text{I} \cdot (\text{BF}_4)]^{3+}$ could not be unambiguously isolated on the photoluminescence setup, based on the absorption spectra of Figure 3, the absence of detectable emission for the abundant $[\text{I}\text{--H}]^{3+}$ trication suggests an increase in the efficiency of the nonradiative, probably fragmentation, channels or a reduction of the absorption cross-section as the overall charge of the cluster increases (as the number of tetrafluoroborates decreases). At threshold excitation, when no fragmentation occurs, the $[\text{I} \cdot (\text{BF}_4)_3]^+$ monocation and the $[\text{I} \cdot (\text{BF}_4)_2]^{2+}$ dication have close to identical emission profile (Figures 4 and S5). The apparent dual emission observed for the $[\text{I} \cdot (\text{BF}_4)_3]^+$ monocations ($\lambda_{\text{ex}} = 405$ nm) with the lower energy component at close to the same position as the dication (673 versus 677 nm) and a high energy component (at 586 nm) shifted to the blue by 87 nm (2200 cm^{-1}) appears to result from intersystem crossing to the triplet state and a fragmentation process induced by the excess energy deposited on the cluster.

Lifetime measurements (Figure 5) were performed in order to gain information on the nature of the transitions involved and rule out fluorescence concomitant to phosphorescence. While the onset of the photoluminescence signal is related to the population of the emitting state (including the impact of ion motion and overlap between the excitation beam and the ion cloud), the photoluminescence decays (for the spectrally integrated luminescence) are monoexponential, independent of the irradiance used, and give respective lifetime values of

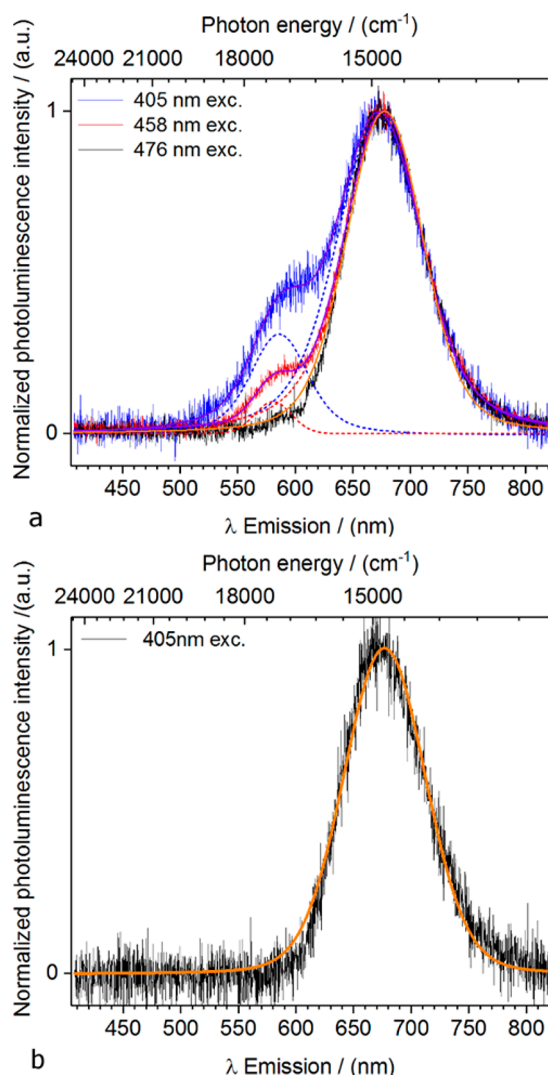


Figure 4. Emission spectra of the (a) $[1\cdot(\text{BF}_4)_3]^+$ and (b) $[1\cdot(\text{BF}_4)_2]^{2+}$ species for ions stored in a Paul trap at 83 K. The spectra taken at excitation wavelengths of 405, 458, and 476 nm being similar, only the spectrum taken at 405 nm is displayed for the dication. The spectra have been fitted using Voigt profiles (fits given as solid lines and components as dashed lines). Irradiances: 300 W/cm^2 (405 nm), 675 W/cm^2 (458 nm), and 750 W/cm^2 (476 nm).

20.4 ± 0.5 and $21.4 \pm 0.6 \mu\text{s}$ for the $[1\cdot(\text{BF}_4)_3]^+$ and $[1\cdot(\text{BF}_4)_2]^{2+}$ clusters, consistent with phosphorescence emission.

The fragment origin of the shoulder observed in Figure 4a is supported by the photoluminescence of the m/z 2700 photofragment, $[1\cdot(\text{BF}_4)\text{-Ag-Dppy-2.H}]^+$, (Figure S6). This fragment is not ejected from the trap while recording the emission of the $[1\cdot(\text{BF}_4)_3]^+$ species due to a necessary trade-off: high buffer gas pressure is needed to prevent fragmentation; cw excitation intensity cannot be reduced beyond a threshold (system dependent) due to limited emitted light collection efficiency ($\sim 0.6\%$); increasing the low mass cutoff at a fixed angular frequency (300 kHz for the trap used) implies increasing the amplitude V of the rf-potential; and going beyond the value of $V = 1090 \text{ V}$ on the setup used ($q_z = 0.46$ for the m/z 3248 species) leads to the formation of a helium plasma in the trap. Furthermore, while the coexistence of isomers is in principle possible, there is no evidence of isomers in the ion mobility measurements performed on the

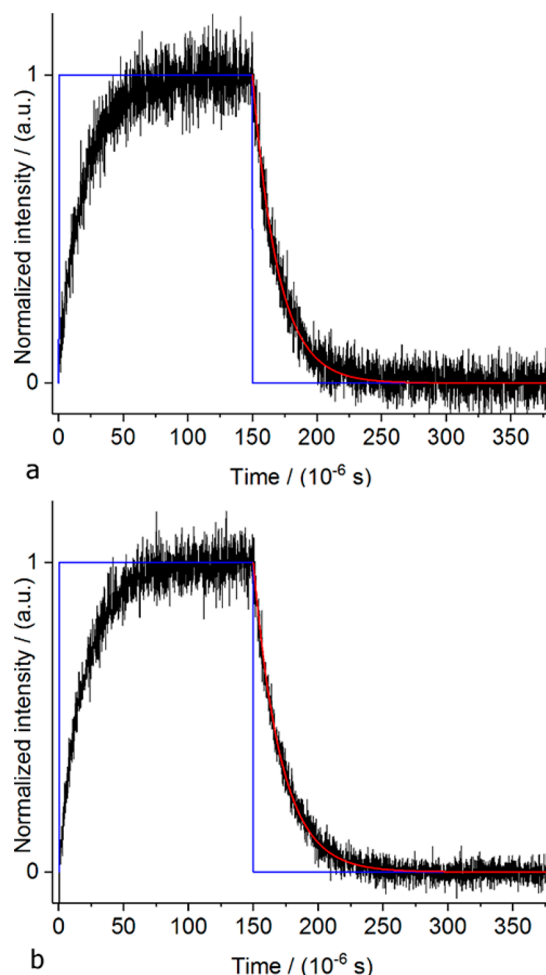


Figure 5. Lifetime measurements for (a) $[1\cdot(\text{BF}_4)_3]^+$ (405 nm, 80 W/cm^2) $\tau = 20.4 \pm 0.5 \mu\text{s}$ and (b) $[1\cdot(\text{BF}_4)_2]^{2+}$ (405 nm, 380 W/cm^2) $\tau = 21.4 \pm 0.6 \mu\text{s}$ molecular cluster cations. The blue line corresponds to the time the laser is on. Once stationarity has been achieved, the laser is turned off and photoluminescence decay measured.

ions in their ground state. Consequently, the m/z 2700 species generated upon photofragmentation and cotrapped with the monocations of interest is most likely responsible for the shoulder observed in Figure 4a.

Computations on Electronically Excited States and Comparison to Experimental Results. Insight into the structural and electronic changes undergone by the $[1\cdot(\text{BF}_4)_x]^{(4-x)+}$ gas-phase species as the overall charge of the cluster increases is provided by density functional calculations. The structures of the $[1\cdot(\text{BF}_4)_3]^+$ and $[1\cdot(\text{BF}_4)_2]^{2+}$ computed at the CAM-B3LYP level (see Figure 2c,d) and shortly described before are characterized by bond lengths between the central carbon and the Au atoms of 2.162 ± 0.046 and $2.164 \pm 0.047 \text{ \AA}$, respectively. Each Au...Ag edge is bridged by one Dppy ligand with the P atom bound to Au (2.344 ± 0.074 and $2.347 \pm 0.078 \text{ \AA}$, respectively) and the pyridyl N atom coordinated to Ag (2.457 ± 0.103 and $2.455 \pm 0.097 \text{ \AA}$, respectively) conferring together with the Au...Ag metal-philic interactions (3.078 ± 0.201 and $2.993 \pm 0.081 \text{ \AA}$, respectively) extra rigidity. Overall values inferred from the computations on charged structures and crystallographic values for the neutral species³² are found to be in good agreement. The gas-phase computed ground state equilibrium structures

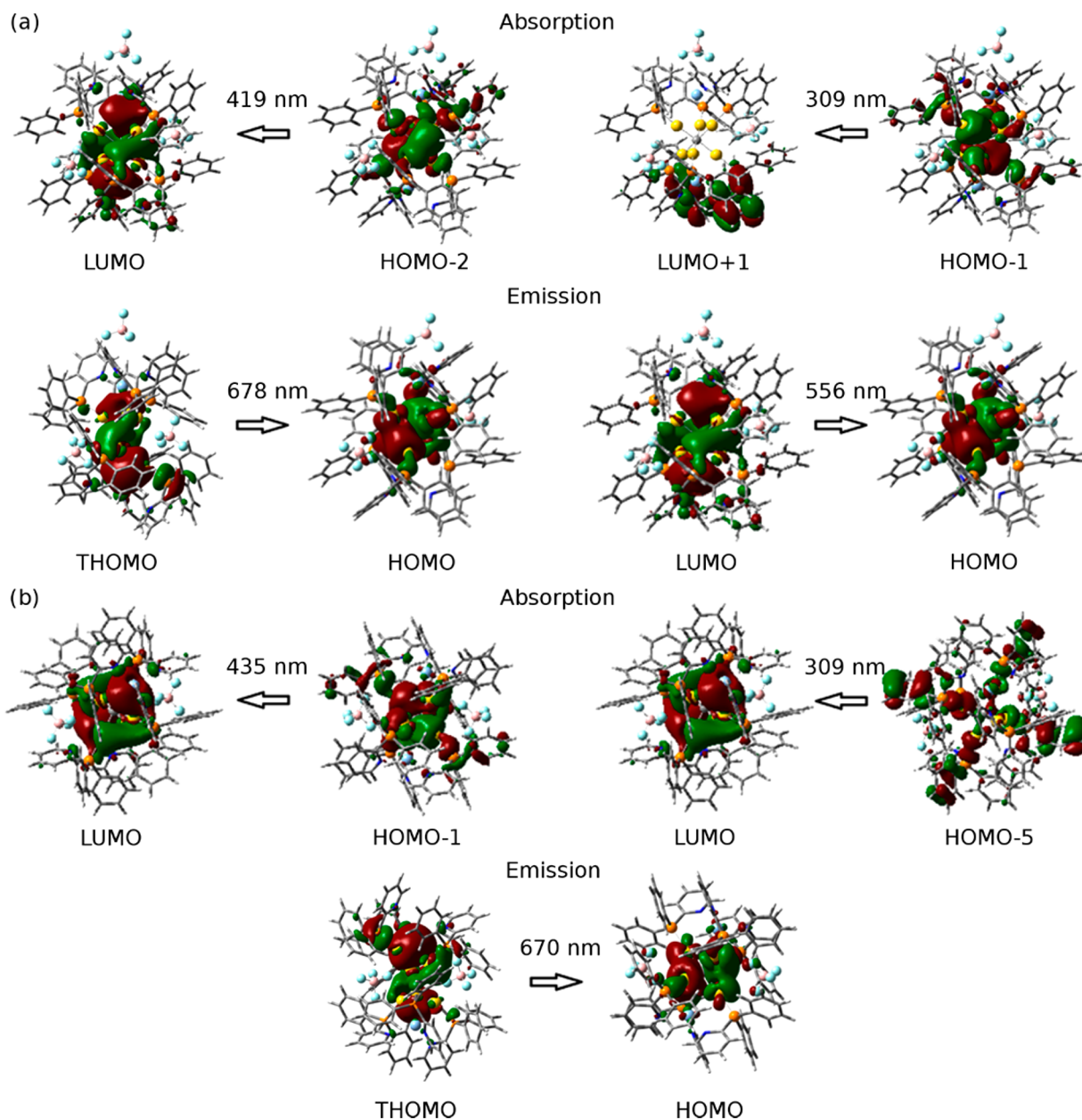


Figure 6. Representation of the main orbitals involved in the optical transitions of (a) [1·(BF₄)₃]⁺ and (b) [1·(BF₄)₂]²⁺. The MO's involved in the excitation of the electronic states leading to the absorption and emission spectra are separately represented. Emission mainly comes from the lowest triplet state with singly occupied molecular orbitals (THOMO).

retain the “capped sphere” structural motif and bond lengths are systematically longer than those of the crystallographic structure, the changes in structural parameters being on the order of 0.1 Å. The elongation of the Au···C, Au···Au, Ag···C, and Ag···N distances is expected when going from a crystallographic structure to a gas-phase equilibrium geometry for which there is no crystal “pressure”. In the lowest-lying triplet state, the “capped sphere” structural motif and cluster are perturbed but the Au···Ag and Au···P distances show no or only minor changes compared to the singlet ground state.

The cluster equilibrium geometry, two AgAu₃(Dppy)₃ units bridged by a carbon atom, favors triplet states with a high luminescence quantum yield⁵⁵ as evidenced by the emission band reported for the [1·(BF₄)₄] solubilized in CH₂Cl₂ and found to be between 600 nm³² and 640 nm.²⁸ This band has been previously assigned to phosphorescence from a low-lying

spin-forbidden excited state due to its significant red shift from the absorption onset (at 485 nm in CH₂Cl₂) and long lifetime ($\tau_0 = 4.7 \mu\text{s}$ in CH₂Cl₂).²⁸ The gas-phase luminescence lifetimes, being about 20 μs for the [1·(BF₄)₃]⁺ and [1·(BF₄)₂]²⁺ species, are similarly ascribed to phosphorescence (see below). Furthermore, the solution absorption band position displays a hypsochromic (blue) shift of approximately 10 nm when the solvent is changed from CH₂Cl₂ or CH₃CN to CH₃OH, while a larger (>35 nm) red-shift is observed in the gas phase compared to solution measurements. Because of the shielding of the gold-core from the environment by the ligands (see Figure S7 for a space filling representation), it appears likely that this gas-phase red shift compared to solution is caused by solvent interactions either stabilizing a ligand-centered ground state (in the case of a ³MLCT transition), destabilizing a ligand-centered excited state (in the case of a

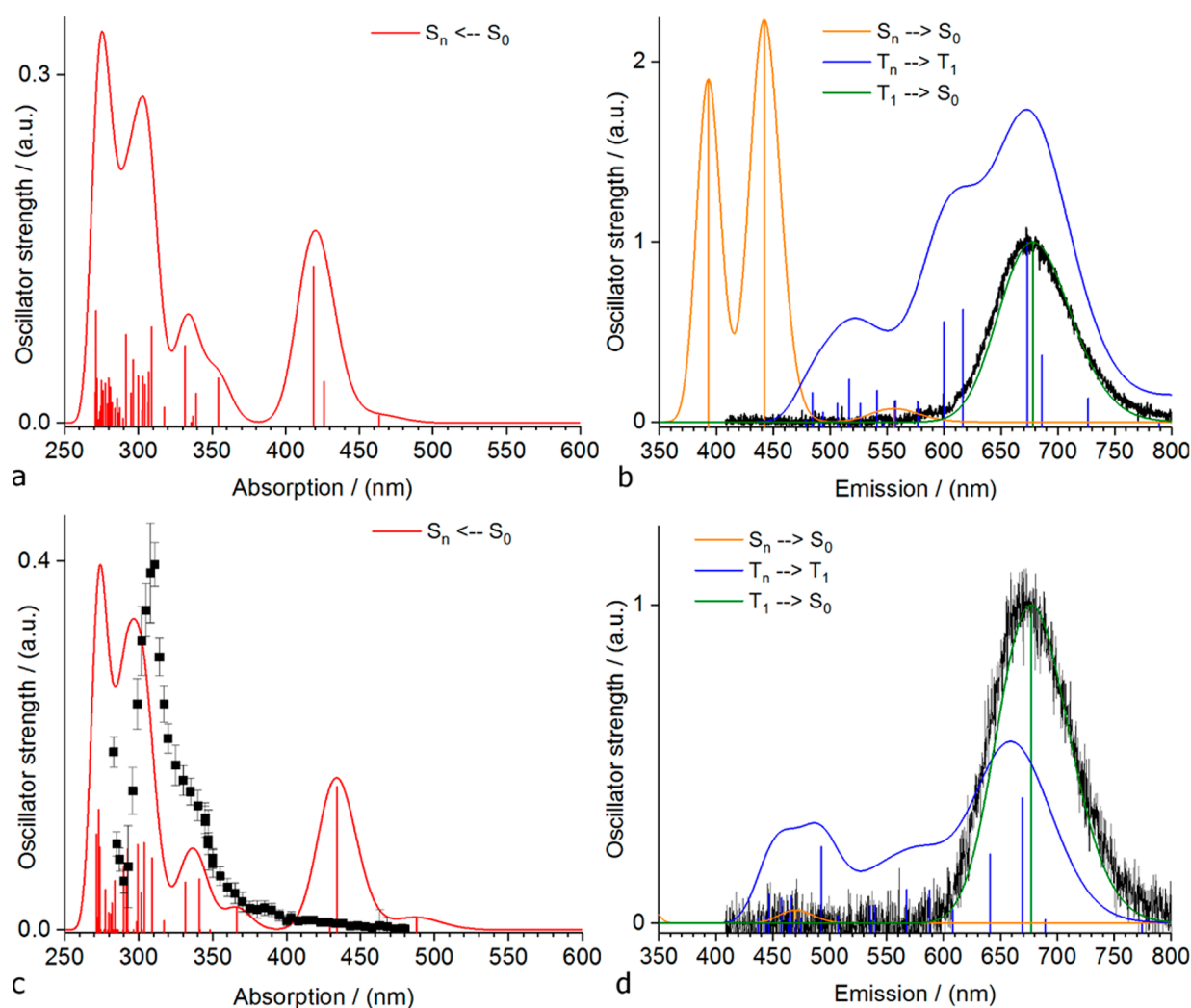


Figure 7. Computed absorption (left) and emission (right) spectra of (a, b) $[1\cdot(\text{BF}_4)_3]^+$ and (c, d) $[1\cdot(\text{BF}_4)_2]^{2+}$ at the TD-DFT CAM-B3LYP level. Absorption profiles (red) are obtained at the equilibrium geometry of the S_0 state and spectrum convolution has been done using Gaussian functions with variance $\sigma = 0.085$ eV. Emission spectra are computed at the equilibrium geometry of the S_1 and T_1 states. The computed absorption and emission profiles have been respectively red-shifted in energy by 0.682 (a) and 0.701 eV (c) and blue-shifted in energy by 0.536 (b) and 0.265 eV (d) in order to match the main features of the experimental photodissociation and photoluminescence spectra (see text). The gas-phase experimental data is displayed in black. The accuracy of computed excitation energies at the TD-DFT level is expected to be about 0.5–1 eV, depending on the character of the excited states.

$^3\text{LMCT}$), or is induced by the number of counterions bound in solution. The featureless gas-phase emission bands also display characteristics typical of metal centered (MC) transitions as discussed hereafter with the support of TD-DFT computations.

The nature of the electronic states involved in the gas-phase photoluminescence of the $[1\cdot(\text{BF}_4)_3]^+$ and $[1\cdot(\text{BF}_4)_2]^{2+}$ species has been investigated at the TD-DFT CAM-B3LYP computational level. Mainly, two types of transitions can be distinguished in the absorption and emission spectra of the species studied. On the one hand, there are excitations involving molecular orbitals “purely” localized on the metallic core (Figure 6). On the other hand, there are excitations between core localized and ligand localized MO that yield electron charge transfer from the metallic core to the ligands (MLCT) or reciprocally (LMCT).

The three HOMO, HOMO–1, HOMO–2 orbitals of the $[1\cdot(\text{BF}_4)_3]^+$ cluster are nearly degenerate and mainly consist of Au core orbitals (see Supporting Information, Figure S8).

They correspond to a set of superatomic p orbitals⁵⁶ localized on the cluster core. The LUMO resembles a superatomic d orbital delocalized on the Au core split by more than 2.3 eV from the other much higher in energy d-like superatomic orbitals. The LUMO+1 up to LUMO+6 MO’s, on the other hand, are preferably localized on the Dppy ligand shell. A representation of the main MO’s involved in the optical transitions of the $[1\cdot(\text{BF}_4)_3]^+$ cluster is displayed in Figure 6a.

The highest occupied and lowest unoccupied MO’s of the $[1\cdot(\text{BF}_4)_2]^{2+}$ cluster are very similar to those of $[1\cdot(\text{BF}_4)_3]^+$ cluster (see Supporting Information, Figure S9). The three highest occupied MO’s of the $[1\cdot(\text{BF}_4)_2]^{2+}$ cluster mainly consist of Au core orbitals with a superatomic p character⁵⁶ while the core-centered superatomic d-like LUMO is separated from similar d-like orbitals by more than 5 eV and the LUMO +1 to LUMO+6 MO’s are delocalized on the Dppy surface ligands, as displayed in Figure 6-b.

The shifted computed absorption and emission spectra of $[1\cdot(\text{BF}_4)_3]^+$ are displayed in Figure 7-a,b. The computed

absorption and emission profiles have been respectively red-shifted in energy by 0.682 (a) and 0.701 eV (c) and blue-shifted in energy by 0.536 (b) and 0.265 eV (d) in order to match the main features of the experimental photodissociation and photoluminescence spectra. For the absorption, the onset of the 310 nm band shared by all species (see Figure 3) and assumed to be similar for the $[(C)(AuDppy)_6Ag_2(BF_4)_3]^+$ monocation was taken as reference while for the emission the parameters were adjusted such as to match the observed triplet emission. The absorption spectrum of $[1\cdot(BF_4)_3]^+$ (Figure 7a) shows multiple molecule-like singlet-type bands at 420, 334, 303, and 275 nm associated with core-centered as well as metal-to-ligand charge transfer (1MLCT) transitions. The low energy tail explains photoexcitation in the visible range up to 476 nm. The computed emission spectrum of Figure 7-b displays multiple bands corresponding to (1) experimentally unobserved excited singlet fluorescence (556, 442, and 393 nm, orange line) with the weak 556 and 442 nm bands corresponding to core-centered transitions while the peak at 393 nm corresponds to a ligand-to-metal charge transfer transition, (2) mostly metal-centered lowest triplet state phosphorescence (678 nm, green line), and (3) excited triplet–triplet emission (about 672, 614, and 522 nm, blue line) associated with ligand-to-metal charge transfer (LMCT) transitions in all three cases. Only a single intense phosphorescent transition was found computationally (Figure 7b, green line), which agrees with the simple luminescent band profile measured experimentally. Accordingly, an energy diagram is provided in Figure 8.

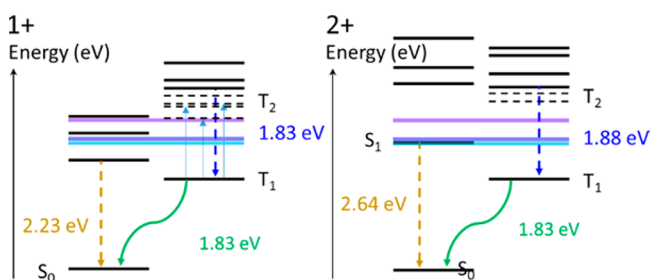


Figure 8. Semiquantitative energy diagram of the lowest-energy levels involved in the emission spectrum of the $[1\cdot(BF_4)_3]^+$ cluster (1+) and the $[1\cdot(BF_4)_2]^{2+}$ cluster (2+) adjusted to experimental data. Orange lines correspond to decay from the lowest excited singlet state while dashed blue lines describe transitions to the lowest excited triplet state. Solid green lines are associated with phosphorescence from the “ground state” triplet to the ground state singlet. The dashed levels correspond to the excited triplet states involved in the lowest energy transition lines of Figure 7b,d. The horizontal colored lines corresponds to the excitation energies (light blue 476 nm, dark blue 458 nm, and purple 405 nm).

The shifted computed absorption and emission spectra of $[1\cdot(BF_4)_2]^{2+}$ are plotted in Figure 7c,d. The absorption spectrum (Figure 7c) shows multiple molecule-like bands at 434, 337, 297, and 274 nm associated with core-centered and metal-to-ligand charge transfer (1MLCT) transitions. Once again the low energy tail explains the experimentally observed excitation up to 476 nm. The marked difference around 420 nm between the absorption spectrum computed for the $[1\cdot(BF_4)_2]^{2+}$ species and the photodissociation spectrum (Figure 7c) is, as previously mentioned, likely due to the effectively competing radiative (photoluminescence) channel, the emitted energy being unavailable for fragmentation. It should be noted

that the solution (CH_2Cl_2) absorption spectrum of $[1](BF_4)_4$ also exhibits a broad, although weak, band in the 380–470 nm region.²⁸

The computed emission spectrum of Figure 7d corresponds to (1) experimentally unobserved singlet-type fluorescence bands significantly blue-shifted compared to the $[1\cdot(BF_4)_3]^+$ cluster (orange line). Of those, only the 470 nm singlet-type fluorescence band corresponding to a core-centered transition involving fluorescence from the lowest excited singlet state is visible in the computed spectrum (the other bands being significantly higher in energy), (2) a mostly core-centered triplet phosphorescence band at 677 nm (green line) used as in the previous case as reference for the computed spectra, and (3) multiple excited triplet–triplet emission band (659, 575, 486, and 460 nm band, blue line) associated with ligand-to-metal charge transfer (LMCT) transitions. Overall, the single intense phosphorescent transition calculated for $[1\cdot(BF_4)_2]^{2+}$ (Figure 7d) agrees well with the experimental one suggesting that only the triplet phosphorescence band is experimentally observed. A summarizing energy diagram is provided in Figure 8.

In summary, the low energy peak at about 675 nm of Figure 7 shared by both the $[1\cdot(BF_4)_3]^+$ and $[1\cdot(BF_4)_2]^{2+}$ species is clearly identified as mostly core-centered phosphorescence from the lowest energy triplet state while the high energy component of $[1\cdot(BF_4)_3]^+$ emission corresponds to the emission from fragments. Unfortunately, we could not unambiguously identify the fragment ions responsible. We presume, however, that they are formed by loss of one or both capping Ag of the Au_cAg_2 cluster unit, because it was reported that $[(C)(AuDppy)_6](BF_4)_2$ exhibits blue-shifted luminescence ($\lambda_{em} \approx 440$ nm) in CH_2Cl_2 solution compared to $[1](BF_4)_4$ ($\lambda_{em} \approx 600$ nm).³² As displayed in Figure 8, the lowest energy triplet (T_1) to S_0 energy gap is about 1.83 eV and the excited triplet (T_2) to lowest energy triplet (T_1) gap is at least 1 eV. An alternative explanation to the emission spectra involving fluorescence inside the triplet manifold—it would imply the population of an excited triplet state via a (sequential) two photon excitation likely requiring much higher irradiances than the ones used here—is ruled out based on luminescence lifetimes. A study involving time-resolved (as well as irradiance dependent) measurements will be reported elsewhere. Interestingly dual luminescence in the green and orange-red regions has also been observed in assemblies of discrete molecular decanuclear gold(I) sulfido complexes.⁵⁷ The high-energy emission with a comparatively smaller intensity has been ascribed in these systems to a metal-perturbed intraligand phosphorescence while the low-energy emission was tentatively assigned either to emission from triplet states with a ligand-to-metal charge transfer (3LMCT) or metal/core-based (ds/dp) character.⁵⁷

Overall, many photophysical properties of the lowest excited states and corresponding transitions of organometallic compounds are determined by the extent of metal participation in the excited state wave functions. This metal participation not only alters their spatial extension, but also induces significant mixtures of singlet and triplet states by spin–orbit coupling.⁵⁸ Additionally the solvent significantly affects charge transfer processes characterized by a substantial change in electronic distribution between the initial and final states. The surrounding solvent molecules responding to this change can substantially influence the electron transfer rate as well as cause significant shifts in absorption or emission.⁵⁹ Accordingly, the

present work provides valuable information about both excited states and intramolecular charge transfer processes, which underlie numerous conversions of light into chemical, electrical, and/or mechanical energy, by enabling characterization in the absence of polarizable medium and proton translocation.⁵⁹ Differences are highlighted with solution data. According to ref 28, the 405 nm excitation of the solvated $[1 \cdot (\text{BF}_4)_4]$ species—the computations of ref 28 were performed on the $[1]^{4+}$ ion—selectively (though not solely) populate the surface ligand states and correspond to a $^1\text{MLCT}$ transition between Au(I) and surface ligands in solution resulting in a single emission band with $^3\text{MLCT}$ character. In the gas phase, while the process is essentially the same, the excess energy deposited on the $[1 \cdot (\text{BF}_4)_3]^+$ cluster upon 405 nm excitation (the emission is red-shifted by about 35 nm compared to solution data) as well as intersystem crossing to the triplet state, leads to fragmentation as evidenced from the observed dual emission. Since the same observation is not made for the $[1 \cdot (\text{BF}_4)_2]^{2+}$ species, it is suggested that the interpretation of the solution results may be complicated by superposition effects.

CONCLUSION

In summary, the experimental and computational results reported here suggest that the main luminescence band of the $[1 \cdot (\text{BF}_4)_x]^{(4-x)+}$ species originates from low lying mostly core-centered localized triplet states. Using gas-phase measurements on mass selected ions we have enabled direct comparison with computations and thereby considerably simplified the analysis. Gas-phase excitation at 476 nm (and 83 K) is found to involve a transition between states localized at the cluster core and the ligand shell, followed by intersystem crossing to the triplet manifold and a core-centered emission from a mostly core-centered state. Dual emission is observed for the $[1 \cdot (\text{BF}_4)_3]^+$ species upon 405 nm excitation (at 83 K). This is rationalized by the fragmentation of the observed species (supposedly forming an entity without capping Ag) when the energy deposited upon excitation is sufficient for dissociation. Interestingly, while the computed results concur with the limited photoexcitation data, the photodissociation spectra were found to highlight nonradiative, i.e., fragmenting processes or the absence thereof, complementary to the observation of photoluminescence.

Consequently, the present work provides a deeper understanding of the nature of the optical transitions, the impact of tetrafluoroborates on these transitions, as well as a better understanding of the environment dependence of ultrasmall gold clusters' photophysical properties. It may thereby contribute to the rational design of tunable ligand protected gold clusters with a fast and efficient intersystem crossing (ISC) from the excited singlet to the light emitting triplet states for application as emitters and sensors. In particular, the present work suggests a systematic study of counterions effects may help optimize properties with ion trap experiments playing a decisive role for these studies. We have demonstrated here, that the isolation and separate spectroscopic investigation of different counterion adducts is feasible by this technique so that unprecedented insights into details of microsolvation and also their ultrafast dynamics are within reach.

ASSOCIATED CONTENT

Supporting Information

The Supporting Information is available free of charge on the ACS Publications website at DOI: 10.1021/acs.jpca.8b01864.

Mass spectrum, comparison of $[1 \cdot (\text{BF}_4)_3]^+$ and $[1 \cdot (\text{BF}_4)_2]^{2+}$ isomers, unpaired electron density for $[1]^{3+}$, PD mass spectra, channel-specific PD spectra, photo-fragments assignments, comparison emission spectra of $[1 \cdot (\text{BF}_4)_3]^+$ and $[1 \cdot (\text{BF}_4)_2]^{2+}$, photoluminescence spectrum of m/z 2700 fragment, space filling representation of the $[1 \cdot (\text{BF}_4)_3]^+$ cluster, MO energy diagram of $[1 \cdot (\text{BF}_4)_3]^+$ and $[1 \cdot (\text{BF}_4)_2]^{2+}$, channel specific PD spectra, and PD total yields (PDF)

AUTHOR INFORMATION

Corresponding Author

*(J.-F.G.) E-mail: j.greisch@uu.nl.

ORCID

Jean-François Greisch: 0000-0002-0761-8191

Sebastian Volker Kruppa: 0000-0003-0756-2703

Quan-Ming Wang: 0000-0002-3764-6409

Christoph Riehn: 0000-0001-7021-1055

Françoise Remacle: 0000-0001-7434-5245

Present Address

¹Utrecht University, Hecklab, Padualaan 8, 3584CH, Utrecht, The Netherlands.

Notes

The authors declare no competing financial interest.

ACKNOWLEDGMENTS

This work has been supported by the Deutsche Forschungsgemeinschaft (DFG) through CRC/TRR 88 "Cooperative Effects in Homo- and Heterometallic Complexes (3MET)" (Projects C4 and C7). J.-F.G. acknowledges support from the Hector Fellow Academy (HFA) and would like to express his deepest thanks to Prof. Manfred M. Kappes and PD Dr. Detlef Schooss for fruitful discussions. A.B.-C. acknowledges the University of Liege and the EU in the context of the MSCA-COFUND-BelIPD project. F.R. acknowledges the Fonds de la Recherche Fondamentale Collective (FRFC 2.5020.11) for computational resources and Fonds National de la Recherche Scientifique (FRS-FNRS) for its support. The Bundesministerium für Bildung und Forschung (BMBF) through the Helmholtz Research Program POF Science and Technology of Nano-systems is also acknowledged by J.-F.G. for support and for providing the necessary infrastructure.

REFERENCES

- (1) Wang, Q.-M.; Lee, Y. A.; Crespo, O.; Deaton, J.; Tang, C.; Gysling, H. J.; Concepción Gimeno, M. C.; Larraz, C.; Villacampa, M. D.; Laguna, A.; et al. Intensely Luminescent Gold(I) - Silver(I) Cluster Complexes with Tunable Structural Features. *J. Am. Chem. Soc.* **2004**, *126*, 9488–9489.
- (2) Yam, V. W. W.; Cheng, E. C. C. Highlights on the Recent Advances in Gold Chemistry—a Photophysical Perspective. *Chem. Soc. Rev.* **2008**, *37*, 1806–1813.
- (3) Whetten, R. L.; Shafiqullin, M. N.; Khoury, J. T.; Schaaff, T. G.; Vezmar, I.; Alvarez, M. M.; Wilkinson, A. Crystal Structures of Molecular Gold Nanocrystal Arrays. *Acc. Chem. Res.* **1999**, *32*, 397–406.
- (4) Jin, R. Quantum Sized, Thiolate-Protected Gold Nanoclusters. *Nanoscale* **2010**, *2*, 343–362.

- (5) Templeton, A. C.; Wuelhing, W. P.; Murray, R. W. Monolayer Protected Cluster Molecules. *Acc. Chem. Res.* **2000**, *33*, 27–36.
- (6) Chen, Y. S.; Kamat, P. V. Glutathione-Capped Gold Nanoclusters as Photosensitizers. Visible Light-Induced Hydrogen Generation in Neutral Water. *J. Am. Chem. Soc.* **2014**, *136*, 6075–6082.
- (7) Chen, Y. S.; Choi, H.; Kamat, P. V. Metal-Cluster-Sensitized Solar Cells. A New Class of Thiolated Gold Sensitizers Delivering Efficiency Greater Than 2%. *J. Am. Chem. Soc.* **2013**, *135*, 8822–8825.
- (8) Lei, Z.; Pei, X.-L.; Jiang, Z.-G.; Wang, Q.-M. Cluster Linker Approach: Preparation of a Luminescent Porous Framework with NbO Topology by Linking Silver Ions with Gold(I) Clusters. *Angew. Chem., Int. Ed.* **2014**, *53*, 12771–12775.
- (9) Chen, M.; Lei, Z.; Feng, W.; Li, C.; Wang, Q.-M.; Li, F. A Phosphorescent Silver(I)-Gold (I) Cluster Complex that Specifically Lights up the Nucleolus of Living Cells with FLIM Imaging. *Biomaterials* **2013**, *34*, 4284–4295.
- (10) Weiss, D. N.; Brokmann, X.; Calvet, L. E.; Kastner, M. A.; Bawendi, M. G. Multi-Island Single-Electron Devices from Self-assembled Colloidal Nanocrystal Chains. *Appl. Phys. Lett.* **2006**, *88*, 143507.
- (11) Cheng, E. C. C.; Lo, W. Y.; Lee, T. K. M.; Zhu, N.; Yam, V. W. W. Synthesis, Characterization, and Luminescence Studies of Discrete Polynuclear Gold(I) Sulfido and Selenido Complexes with Intramolecular Auophilic Contacts. *Inorg. Chem.* **2014**, *53*, 3854–3863.
- (12) Yao, L. Y.; Hau, F. K. W.; Yam, V. W. W. Addition Reaction-Induced Cluster-to-Cluster Transformation: Controlled Self-Assembly of Luminescent Polynuclear Gold(I) μ -3-Sulfido Clusters. *J. Am. Chem. Soc.* **2014**, *136*, 10801–10806.
- (13) Lee, T. K. M.; Zhu, N.; Yam, V. W. W. An Unprecedented Luminescent Polynuclear Gold(I) μ -3-Sulfido Cluster With a Thiacrown-like Architecture. *J. Am. Chem. Soc.* **2010**, *132*, 17646–17648.
- (14) Cunningham, A.; Mühligh, S.; Rockstuhl, C.; Bürgi, T. Coupling of Plasmon Resonances in Tunable Layered Arrays of Gold Nanoparticles. *J. Phys. Chem. C* **2011**, *115*, 8955–8960.
- (15) Mühligh, S.; Cunningham, A.; Scheeler, S.; Pacholski, C.; Bürgi, T.; Rockstuhl, C.; Lederer, F. Self-Assembled Plasmonic Core Shell Clusters with an Isotropic Magnetic Dipole Response in the Visible Range. *ACS Nano* **2011**, *5*, 6586–6592.
- (16) Evans, R. C.; Douglas, P.; Winscom, C. J. Coordination Complexes Exhibiting Room-temperature Phosphorescence: Evaluation of their Suitability as Triplet Emitters in Organic Light Emitting Diodes. *Coord. Chem. Rev.* **2006**, *250*, 2093–2126.
- (17) Pyykkö, P. Strong Closed-Shell Interactions in Inorganic Chemistry. *Chem. Rev.* **1997**, *97*, 597–636.
- (18) Pyykkö, P. Theoretical Chemistry of Gold. *Angew. Chem., Int. Ed.* **2004**, *43*, 4412–4456.
- (19) Schmidbaur, H. Ludwig Mond Lecture. High-carat gold compounds. *Chem. Soc. Rev.* **1995**, *24*, 391–400.
- (20) Schmidbaur, H. The Fascinating Implications of New Results in Gold Chemistry. *Gold Bull.* **1990**, *23*, 11–21.
- (21) Li, Q.; Li, H.; Li, R.; Jing, B.; Liu, Z.; Li, W.; Luan, F.; Cheng, J.; Gong, B.; Sun, J. Influence of Hybridization and Cooperativity on the Properties of Au-Bonding Interaction: Comparison with Hydrogen Bonds. *J. Phys. Chem. A* **2011**, *115*, 2853–2858.
- (22) Ingram, R. S.; Hostetler, M. J.; Murray, R. W.; Schaaff, T. G.; Khoury, J. T.; Whetten, R. L.; Bigioni, T. P.; Guthrie, D. K.; First, P. N. 28 kDa Alkanethiolate-Protected Au Clusters Give Analogous Solution Electrochemistry and STM Coulomb Staircases. *J. Am. Chem. Soc.* **1997**, *119*, 9279–9280.
- (23) Chen, S.; Ingram, R. S.; Hostetler, M. J.; Pietron, J. J.; Murray, R. W.; Schaaff, T. G.; Khoury, J. T.; Alvarez, M. M.; Whetten, R. L. Gold Nanoelectrodes of Varied Size: Transition to Molecule-Like Charging. *Science* **1998**, *280*, 2098–2101.
- (24) Negishi, Y.; Nobusada, K.; Tsukuda, T. Glutathione-Protected Gold Clusters Revisited: Bridging the Gap between Gold(I)-Thiolate Complexes and Thiolate-Protected Gold Nanocrystals. *J. Am. Chem. Soc.* **2005**, *127*, 5261–5270.
- (25) Green, T. D.; Knappenberger, K. L. J. Relaxation Dynamics of Au₂₅L₁₈ Nanoclusters Studied by Femtosecond Time-resolved near Infrared Transient Absorption Spectroscopy. *Nanoscale* **2012**, *4*, 4111–4118.
- (26) Muñiz, J.; Wang, C. R.; Pyykkö, P. Auophilicity: The Effect of the Neutral Ligand L on [ClAuL]₂ Systems. *Chem. - Eur. J.* **2011**, *17*, 368–377.
- (27) Vogt, R. A.; Gray, T. G.; Crespo-Hernández, C. E. Subpicosecond Intersystem Crossing in Mono- and Di(organophosphine)-gold(I) Naphthalene Derivatives in Solution. *J. Am. Chem. Soc.* **2012**, *134*, 14808–14817.
- (28) Zhou, M.; Lei, Z.; Guo, Q. X.; Wang, Q.-M.; Xia, A. Solvent Dependent Excited State Behaviors of Luminescent Gold(I) – Silver(I) Cluster with Hypercoordinated Carbon. *J. Phys. Chem. C* **2015**, *119*, 14980–14988.
- (29) Fu, W. F.; Chan, K. C.; Miskowski, V. M.; Che, C. M. The Intrinsic 3[dσ* pσ] Emission of Binuclear Gold(I) Complexes with Two Bridging Diphosphane Ligands Lies in the Near UV; Emissions in the Visible Region Are Due to Exciplexes. *Angew. Chem., Int. Ed.* **1999**, *38*, 2783–2785.
- (30) Yam, V. W. W.; Lo, K. K. W. Luminescent Polynuclear d10 Metal Complexes. *Chem. Soc. Rev.* **1999**, *28*, 323–324.
- (31) Qian, H.; Zhu, M.; Wu, Z.; Jin, R. Quantum Sized Gold Nanoclusters with Atomic Precision. *Acc. Chem. Res.* **2012**, *45*, 1470–1479.
- (32) Jia, J. H.; Wang, Q.-M. Intensely Luminescent Gold(I) - Silver(I) Cluster with Hypercoordinated Carbon. *J. Am. Chem. Soc.* **2009**, *131*, 16634–16635.
- (33) Lei, Z.; Wang, Q.-M. Homo and Heterometallic Gold(I) Clusters with Hypercoordinated Carbon. *Coord. Chem. Rev.* **2017**, DOI: 10.1016/j.ccr.2017.11.001.
- (34) Scherbaum, F.; Grohmann, A.; Huber, B.; Krüger, C.; Schmidbaur, H. "Auophilicity" as a Consequence of Relativistic Effects: The Hexakis(triphenylphosphaneaurio)methane Dication [(Ph₃PAu)₆C]²⁺. *Angew. Chem., Int. Ed. Engl.* **1988**, *27*, 1544–1546.
- (35) Koshevoy, I. O.; Lin, Y. C.; Karttunen, A. J.; Chou, P. T.; Vainiotalo, P.; Tunik, S. P.; Haukka, M.; Pakkanen, T. Intensely Luminescent Alkynyl - Phosphine Gold(I) - Copper(I) Complexes: Synthesis, Characterization, Photophysical, and Computational Studies. *Inorg. Chem.* **2009**, *48*, 2094–2102.
- (36) Kordel, M.; Schooss, D.; Neiss, C.; Walter, L.; Kappes, M. M. Laser-Induced Fluorescence of Rhodamine 6G Cations in the Gas Phase: A Lower Bound to the Lifetime of the First Triplet State. *J. Phys. Chem. A* **2010**, *114*, 5509–5514.
- (37) Greisch, J. F.; Chmela, J.; Harding, M. E.; Klopfer, W.; Kappes, M. M.; Schooss, D. Gas-Phase Photoluminescence Characterization of Stoichiometrically Pure Nonanuclear Lanthanoid Hydroxo Complexes Comprising Europium or Gadolinium. *Inorg. Chem.* **2016**, *55*, 3316–3323.
- (38) Greisch, J. F.; Harding, M. E.; Schäfer, B.; Ruben, M.; Klopfer, W.; Kappes, M. M.; Schooss, D. Characterization of Nonanuclear Europium and Gadolinium Complexes by Gas-Phase Luminescence Spectroscopy. *J. Phys. Chem. Lett.* **2014**, *5*, 1727–1731.
- (39) Kruppa, S. V.; Nosenko, Y.; Winghart, M. O.; Walg, S. P.; Kappes, M. M.; Riehn, C. Fragmentation Pathways of Dianionic [Pt₂(μ-P₂O₅H₂)₄+X,Y]²⁻ (X,Y = H,K,Ag) Species in an Ion Trap Induced by Collisions and UV Photoexcitation. *Int. J. Mass Spectrom.* **2016**, *395*, 7–19.
- (40) Kruppa, S. V.; Bäßler, F.; Nosenko, Y.; Walg, S. P.; Diller, R.; Riehn, C. Ultrafast Vibrational and Electronic Dynamics of Metal-Metal Interactions Studied by Transient Photofragmentation (Gas Phase) and Transient Absorption (Solution). *Int. Conf. Ultrafast Phenom.* **2016**, UW4A.33.
- (41) Nosenko, Y.; Riehn, C.; Klopfer, W. UV Fragmentation and Ultrafast Dynamics of Trinuclear Silver/1-methylthymine and Silver/1-methyluracil Metal-base Pairs in an Ion Trap. *Chem. Phys. Lett.* **2016**, *659*, 55–60.
- (42) Kruppa, S. V.; Bäßler, F.; Klopfer, W.; Walg, S. P.; Thiel, W. R.; Diller, R.; Riehn, C. Ultrafast Excited-state Relaxation of a

Binuclear Ag(I) Phosphine Complex in Gas Phase and Solution. *Phys. Chem. Chem. Phys.* **2017**, *19*, 22785–22800.

(43) Frisch, M. J.; Trucks, G. W.; Schlegel, H. B.; Scuseria, G. E.; Robb, M. A.; Cheeseman, J. R.; Scalmani, G.; Barone, V.; Mennucci, B.; Petersson, G. A.; et al. *Gaussian 09, Revision D01*; Gaussian, Inc.: Wallingford, CT, 2009.

(44) Yanai, T.; Tew, D.; Handy, N. A New Hybrid Exchange-correlation Functional using the Coulomb-attenuating Method (CAM-B3LYP). *Chem. Phys. Lett.* **2004**, *393*, 51–57.

(45) Peach, M. J. G.; Benfield, P.; Helgaker, T.; Tozer, D. Excitation Energies in Density Functional Theory: An Evaluation and a Diagnostic Test. *J. Chem. Phys.* **2008**, *128*, 044118.

(46) Hay, P. J.; Wadt, W. R. Ab Initio Effective Core Potentials for Molecular Calculations. Potentials for the Transition Metal Atoms Sc to Hg. *J. Chem. Phys.* **1985**, *82*, 270–283.

(47) Hay, P. J.; Wadt, W. R. Ab Initio Effective Core Potentials for Molecular Calculations. Potentials for K to Au Including the Outermost Core Orbitals. *J. Chem. Phys.* **1985**, *82*, 299–310.

(48) Foster, J. P.; Weinhold, F. Natural Hybrid Orbitals. *J. Am. Chem. Soc.* **1980**, *102*, 7211–7218.

(49) Reed, A. E.; Curtiss, L. A.; Weinhold, F. Intermolecular Interactions from a Natural Bond Orbital, Donor-Acceptor Viewpoint. *Chem. Rev.* **1988**, *88*, 899–926.

(50) Zavras, A.; Khairallah, G. N.; Connell, T. U.; White, J. M.; Edwards, A. J.; Mulder, R. J.; Donnelly, P. S.; O'Hair, R. A. J. Synthesis, Structural Characterization, and Gas-Phase Unimolecular Reactivity of the Silver Hydride Nanocluster $[Ag_3((PPh_2)_2CH_2)_3(\mu_3-H)](BF_4)_2$. *Inorg. Chem.* **2014**, *53*, 7429–7437.

(51) Lifshitz, C. Kinetic shifts. *Eur. J. Mass Spectrom.* **2002**, *8*, 85–98.

(52) Wellman, S. M. J.; Jockusch, R. A. Moving in on the Action: An Experimental Comparison of Fluorescence Excitation and Photodissociation Action Spectroscopy. *J. Phys. Chem. A* **2015**, *119*, 6333–6338.

(53) Imanbaew, D.; Nosenko, Y.; Kerner, C.; Chevalier, K.; Rupp, F.; Riehn, C.; Thiel, W. R.; Diller, R. Excited-state Dynamics of a Ruthenium(II) Catalyst Studied by Transient Photofragmentation in Gas Phase and Transient Absorption in Solution. *Chem. Phys.* **2014**, *442*, 53–61.

(54) Imanbaew, D.; Lang, J.; Gelin, M. F.; Kaufhold, S.; Pfeffer, M. G.; Rau, S.; Riehn, C. Pump-Probe Fragmentation Action Spectroscopy: A Powerful Tool to Unravel Light-Induced Processes in Molecular Photocatalysts. *Angew. Chem.* **2017**, *129*, 5563–5566.

(55) Kasha, M.; Rawls, H. R.; El-Bayoumi, M. A. The Exciton Model in Molecular Spectroscopy. *Pure Appl. Chem.* **1965**, *11*, 371–392.

(56) Walter, M.; Akola, J.; Lopez-Acevedo, O.; Jadzinsky, P. D.; Calero, G.; Ackerson, C. J.; Whetten, R. L.; Grönbeck, H.; Häkkinen, H. A Unified View of Ligand-protected Gold Clusters as Superatom Complexes. *Proc. Natl. Acad. Sci. U. S. A.* **2008**, *105*, 9157–9162.

(57) Hau, F. K. W.; Lee, T. K. M.; Cheng, E. C. C.; Au, V. K. M.; Yam, V. W. W. Luminescence Color Switching of Supramolecular Assemblies of Discrete Molecular Decanuclear Gold(I) Sulfido Complexes. *Proc. Natl. Acad. Sci. U. S. A.* **2014**, *111*, 15900–15905.

(58) Yersin, H.; Strasser, J. Chemically Tuned Zero-field Splittings and Spin-lattice Relaxation Investigation by Time-resolved Emission. *J. Lumin.* **1997**, *72–74*, 462–463.

(59) Chen, P.; Meyer, T. J. Medium Effects on Charge Transfer in Metal Complexes. *Chem. Rev.* **1998**, *98*, 1439–1478.

Publication 5 (IJMS)

Fragmentation pathways of dianionic $[Pt_2(\mu-P_2O_5H_2)_4 + X, Y]^{2-}$ ($X, Y = H, K, Ag$) species in an ion trap induced by collisions and UV photoexcitation

Preamble

The following chapter has been published in the journal „International Journal of Mass Spectrometry“. For the supporting information the reader is referred to the electronic version of the article. Experimental work, data analysis, and DFT/TD-DFT calculations were performed by myself with support from Dr. Yevgeniy Nosenko. Dr. Simon P. Walg synthesized the sample complex with my assistance. The initial version of the manuscript is largely based on my diploma thesis and was written during my doctoral studies. The final draft was revised with the help of Dr. Marc-Oliver Winghart, Prof. Dr. Manfred M. Kappes and Priv.-Doz. Dr. Christoph Riehn.

S.V. Kruppa, Y. Nosenko, M.-O. Winghart, S.P. Walg, M.M. Kappes, C. Riehn, *Int. J. Mass Spectrom.*, 2016, 395, 7-19,
<https://doi.org/10.1016/j.ijms.2015.11.007>

Copyright © 2015 Elsevier B.V. All rights reserved.

Reprint Licence



Fragmentation pathways of dianionic [Pt₂(μ-P₂O₅H₂)₄ +X, Y]²⁻ (X, Y=H, K, Ag) species in an ion trap induced by collisions and UV photoexcitation

Author: Sebastian V. Kruppa, Yevgeniy Nosenko, Marc-Oliver Winghart, Simon P. Walz, Manfred M. Kappes, Christoph Riehn

Publication: International Journal of Mass Spectrometry

Publisher: Elsevier

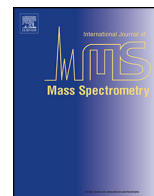
Date: 5 February 2016

Copyright © 2015 Elsevier B.V. All rights reserved.

Please note that, as the author of this Elsevier article, you retain the right to include it in a thesis or dissertation, provided it is not published commercially. Permission is not required, but please ensure that you reference the journal as the original source. For more information on this and on your other retained rights, please visit: <https://www.elsevier.com/about/our-business/policies/copyright#Author-rights>

BACK

CLOSE WINDOW



Fragmentation pathways of dianionic $[\text{Pt}_2(\mu\text{-P}_2\text{O}_5\text{H}_2)_4 + \text{X,Y}]^{2-}$ ($\text{X,Y} = \text{H, K, Ag}$) species in an ion trap induced by collisions and UV photoexcitation



Sebastian V. Kruppa^a, Yevgeniy Nosenko^a, Marc-Oliver Winghart^c, Simon P. Walg^a,
Manfred M. Kappes^c, Christoph Riehn^{a,b,*}

^a Fachbereich Chemie, Technische Universität Kaiserslautern, Erwin-Schrödinger-Str. 52-54, 67663 Kaiserslautern, Germany

^b Forschungszentrum OPTIMAS, Erwin-Schrödinger-Str. 46, 67663 Kaiserslautern, Germany

^c Institute of Physical Chemistry, Karlsruhe Institute of Technology, P.O. Box 6980, 76049 Karlsruhe, Germany

ARTICLE INFO

Article history:

Received 4 September 2015

Received in revised form

20 November 2015

Accepted 27 November 2015

Available online 7 December 2015

Keywords:

Spectroscopic properties

Diplatinum(II,II) complex

Electron-transfer

fs-UV photo-induced dissociation

Electron photodetachment

Action spectroscopy

ABSTRACT

We report on the first gas phase study of dianionic species $[\text{Pt}_2(\mu\text{-P}_2\text{O}_5\text{H}_2)_4 + \text{X,Y}]^{2-}$ ($\text{X,Y} = \text{H, K, Ag}$) derived by counterion attachment to the dimetallic $[\text{Pt}_2(\mu\text{-P}_2\text{O}_5\text{H}_2)_4]^{4-}$ complex (abbrev. Ptpop). The combined electrospray ionization mass spectrometry and laser spectroscopy investigation provides intrinsic properties and fragmentation pathways without solvent interaction in comparison to calculations by density functional theory (DFT) methods. Drastic differences between collision induced (loss of water) and UV photo-induced fragmentation (electron photodetachment or loss of Ag^0) in a quadrupole ion trap are observed. The underlying fragmentation pathways are explored in detail by MS^n . Upon UV photoexcitation $[\text{Ptpop} + \text{H,Ag}]^{2-}$ and $[\text{Ptpop} + 2\text{Ag}]^{2-}$ exhibit dissociation of Ag^0 indicating an intramolecular electron transfer, whereas mainly electron photodetachment is observed for $[\text{Ptpop} + 2\text{H}]^{2-}$ and $[\text{Ptpop} + \text{H,K}]^{2-}$. Channel specific photo-induced dissociation spectra in the range of 250–400 nm reveal the main band at ~370 nm in remarkable resemblance to aqueous absorption spectra. Additional absorption features, distinct broadening and spectroscopic shifts depending on counterions and fragment channels are also observed. For the ground state structures a side-on coordination of metal counterions to the $[\text{Pt}_2(\mu\text{-P}_2\text{O}_5\text{H}_2)_4]^{4-}$ framework is deduced based on fragmentation pathways, results of geometry optimizations and calculated absorption spectra.

© 2015 Elsevier B.V. All rights reserved.

1. Introduction

The study of molecular multiply charged anions (MCAs) in gas phase is of interest in various areas of theoretical and experimental

physical chemistry. For example, comparison of their peculiar reaction and fragmentation behavior in gas-phase with corresponding solution or microsolvation studies provides insights into charge interaction and electron correlation [1–4]. The main dissociation pathways for isolated MCAs are electron (auto)detachment, fragmentation into two (or more) anions and loss of neutral fragments [4–6]. Depending on the system, the latter occurs preferentially although charge separation would be energetically favored. The kinetic hindrance results from a repulsive Coulomb barrier (RCB). RCBs governing (auto)detachment processes originate in the interplay of long-range Coulomb repulsion between an anion and an outgoing electron and short-range attractive interaction of this electron [1–3]. The height and width of the corresponding repulsive Coulomb barrier influence the rate of spontaneous tunneling autodetachment, a phenomenon which occurs in a wide range of electronically metastable MCAs when isolated as ground state species in gas-phase [7–9]. The corresponding lifetimes can be on the order of seconds or even longer. Much faster excited state electron tunneling detachment (ESETD) – on picosecond

Abbreviations: CID, collision-induced dissociation; COM, center of mass; CT, charge transfer; DFT, density functional theory; ECP, effective core potential; ED, electron detachment; ePD, electron photodetachment; ESETD, excited state electron tunneling detachment; ESI, electrospray ionization; fs, femtosecond; IC, internal conversion; IF, ionic fragmentation; IR-MPD, infrared multiple photon dissociation; ISC, intersystem crossing; LMCT, ligand-to-metal charge transfer; LMMCT, ligand-to-metal–metal charge transfer; MCA, multiple charged anion; MC, metal centered; MMCT, metal-to-metal charge transfer; mNL, multiple neutral loss; MS, mass spectrometry; NTOs, natural transition orbitals; PID, photo-induced dissociation; ps, picosecond; Ptpop, $[\text{Pt}_2(\mu\text{-P}_2\text{O}_5\text{H}_2)_4]^{4-}$; QIT, quadrupole ion trap; RCB, repulsive Coulomb barrier; SCE, standard calomel electrode; sNL, single neutral loss; TD-DFT, time dependent density functional theory; TFY, total fragment yield.

* Corresponding author at: Fachbereich Chemie, Technische Universität Kaiserslautern, Erwin-Schrödinger-Str. 52-54, 67663 Kaiserslautern, Germany.
Tel.: +49 6312054859.

E-mail address: riehn@chemie.uni-kl.de (C. Riehn).

<http://dx.doi.org/10.1016/j.ijms.2015.11.007>

1387–3806/© 2015 Elsevier B.V. All rights reserved.

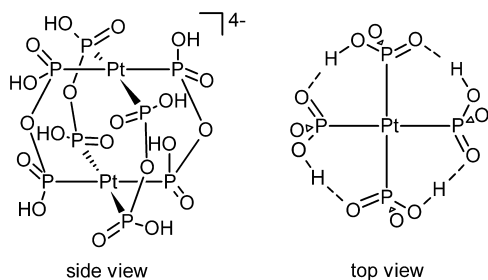


Fig. 1. Schematic structure of [Ptpop]⁴⁻ (left) and view along the Pt-Pt axis (right, eclipsed conformation [65]). P–O–P bridging oxygen atoms are connected by hollow stereo bonds.

timescales – has been shown to occur upon photoexcitation of MCA chromophores [10]. This phenomenon is itself useful toward elucidating photoinduced ultrafast relaxation dynamics within the (excited state) RCBs of MCAs utilizing photoelectron spectroscopy as a probe [10,11].

By attaching counterions to isolated MCAs one can tune their electronic states and resulting optical properties. Electron detachment rates as well as nuclear fragmentation pathways are correspondingly influenced [5,12–14]. In turn, gas-phase measurements of these processes in counterion-MCA adducts can provide valuable hints on the MCA's structure and dynamics in solution where both solvent molecules and counterions are present. Here we have studied such counterion adducts of the multiple charged anion [Pt₂(μ-P₂O₅H₂)₄]⁴⁻ (Tetrakis(μ-diphosphito)-diplatinate(II) [15,16], abbrev. [Ptpop]⁴⁻). Specifically, molecular dianions [Ptpop + X,Y]²⁻ (X,Y = H, K, Ag) were probed in gas phase in a 3D quadrupole ion trap held at room temperature. The ions are obtained by electrospray ionization of aqueous solutions of K₄[Ptpop] containing AgNO₃ for X,Y = Ag.

[Ptpop]⁴⁻ is a dimetallic complex comprised of two square planar P-coordinated d⁸-Pt(II) units facing each other and bridged by four, doubly negatively charged pyrophosphite ligands (see Fig. 1). It was synthesized in 1977 [17], structurally characterized in 1980 [18] and has meanwhile been thoroughly spectroscopically studied in solution [15,16,18–26]. [Ptpop]⁴⁻ is known for its unique photochemical properties, like the photocatalytic dehydrogenation of alcohols [27], halogen abstraction [28], its strong reducing character as manifested by electron transfer [29,30], photolytic cleavage of DNA [31,32] and its strong and persisting phosphorescence at room temperature ($\tau \sim 9.8 \mu\text{s}$ [19]).

Briefly, the UV–vis spectrum of Ptpop in aqueous solution is dominated by a strong band at 368 nm assigned to a ¹A_{2u} ← ¹A_{1g} (¹MC(dσ*–pσ)) transition of the Pt–Pt chromophore [26,33]. To first order this reflects the excitation of an electron from an anti-bonding 5dσ* (dz² derived) to a bonding 6pσ (p_z derived) orbital, which is associated with a shortening of the Pt–Pt bond by ~0.24 to 0.31 Å [20,22]. This bond shortening upon excitation is also manifested in the vibrational progression observed in low-temperature phosphorescence [19]. Subsequently to the primary photoexcitation, efficient ISC ($\tau_{\text{ISC}} \sim 10$ to 30 ps [21]) yields a long-lived triplet state ³A_{2u} giving intense green luminescence ($\lambda_{\text{max}} \approx 520$ nm). ISC can occur directly and (in parallel) also via an activated pathway [19]. The ISC rates depend strongly on spin-orbit coupling and ligand rigidity and have recently been theoretically modeled by spin-orbit TDDFT [34,35]. Photoexcitation at 267 nm into the weakly absorbing higher-lying ¹B_{2u} state, assigned to a ¹LMMCT transition, also leads to the luminescing triplet state via IC, energy relaxation and ISC [20]. Recent ultrafast laser studies have documented the strong solvent dependence of the photodynamics and revealed long-lasting vibrational wave packets [21]. The formation of the long-lived triplet state with shortened Pt–Pt bond was

also substantiated by time-resolved X-ray spectroscopy in solution [20,22,36].

[Ptpop]⁴⁻ in this triplet state is prone to form luminescent exciplexes with metal cations like Tl⁺ or Ag⁺, and also with Au(CN)₂⁻, as was reported early on and quantified via red shifts of the corresponding luminescence bands. [37–39]. An associative exciplex formation mechanism by diffusional encounter was proposed for [Ptpop]⁴⁻ (³A_{2u}) and Tl⁺ as opposed to the static formation from an electronically excited [Ptpop + Tl]³⁻ ion pair complex [38]. For the structure of the exciplex with Tl⁺, an “inner-sphere”, axial coordination at the Pt–Pt unit was considered [37] and later on supported by time-resolved X-ray studies and TDDFT calculations for Tl⁺ and Ag⁺ [40–42]. At high metal cation concentrations (M = Tl⁺, Ag⁺) red-shifted bands at 391 nm (M = Tl⁺) and 396 nm (M = Ag⁺) were observed in the absorption spectra [38,40]. However, a conclusive structural analysis of the corresponding ground state adducts is still missing. Furthermore, despite the numerous experimental and theoretical studies on [Ptpop]⁴⁻ and its derivatives in solution, there are no reports on gas phase investigations for these species.

We begin to fill this knowledge-gap here by providing results obtained with electrospray ionization (ESI) ion trap mass spectrometry in combination with UV laser photo-induced dissociation. These techniques allow for the preparation, investigation and comparison of isolated species [Ptpop + X,Y]²⁻ (X,Y = H, K, Ag) under mass and charge control. We focus here on the types of [Ptpop]⁴⁻-derived species that can be generated by electrospray ionization in gas phase, their structures and coordination patterns. We explore their fragmentation channels upon collisional or photoexcitation and relate these observations to their MCA character, also under consideration of results from an accompanying photoelectron spectroscopic investigation [43]. Furthermore, we study how the relative yields obtained for electron detachment, ionic and neutral fragmentation could be influenced by (H⁺, K⁺, Ag⁺) counterion coordination and whether the counterion binding site can be inferred from these results in comparison to DFT and to TD-DFT calculations. Finally, we present and compare fragment-specific “action” spectra of the various gas phase species and discuss the role of solvation and counterions for the spectroscopy and photodynamics of [Ptpop]⁴⁻ and its derivatives in solution.

2. Experimental and theoretical methods

2.1. Sample preparation

K₄[Pt₂(μ-P₂O₅H₂)₄] was synthesized according to established procedures [23] with the modification that all steps were carried out in an argon atmosphere. The sample was characterized via UV–vis absorption spectroscopy (Fig. S1) using a Lambda 950 UV/Vis/NIR spectrometer (Perkin–Elmer). [Ptpop + X,Y]²⁻ (X,Y = H, K, Ag) species were prepared by electrospraying acetonitrile/water (1:1, v/v, LC–MS grade) solutions of (a) K₄[Ptpop] ([Ptpop + H,K]²⁻), (b) K₄[Ptpop] and formic acid (~1 μl formic acid to 1 ml solution at c = 10⁻⁴ M, [Ptpop + 2H]²⁻) and (c) K₄[Ptpop] and AgNO₃ (99.8% purity, stoichiometric ratio 1:2 and 1:10 for [Ptpop + H,Ag]²⁻ and [Ptpop + 2Ag]²⁻, respectively) at c = 10⁻⁴ to 10⁻⁵ M.

2.2. Quadrupole ion trap mass spectrometry and laser setup

The experimental setup was previously described in detail [44]. Briefly, (precursor) ions were generated via electrospray ionization at an infusion flow rate of at least 2 μl/min assisted by a drying gas (nitrogen) flow rate of 3.5 l/min at 180–220 °C. They were then mass-selected, fragmented and analyzed in a 3D quadrupole ion trap (QIT) mass spectrometer (amaZon Speed, Bruker Daltonics) modified for UV laser spectroscopic applications (similar setup

described in [45]). The spraying needle was held at 4.5 kV and lowered to minimally 3.2 kV for Ag⁺ containing solutions optimized on precursor signal strength. The mass-isolation window was typically $\Delta(m/z)$ 8 selecting the full isotopic distribution of the precursor species. The instrument was controlled and data analysis was performed with software provided by Bruker.

The fs-laser system consists of a titanium:sapphire (Ti:Sa) oscillator/chirped pulse regenerative amplifier (Wyvern 1000TM, KMLabs, 4 mJ at 780 nm, 981 Hz, $\Delta\tau \sim 50$ fs) pumping a nonlinear frequency converter (TOPAS-C, Light Conversion) providing tunable radiation in the range of 240–2600 nm. The output beam was attenuated to 0.5 $\mu\text{J}/\text{pulse}$ for each wavelength position using a neutral density filter, chopped to 327 Hz and focused by a $f = 50$ cm fused silica lens through a fused silica window into the ion trap. A shutter triggered from the mass spectrometer controlled illumination during the fragmentation time window of 120 ms (39 UV pulses per sampled ion cloud). Photo-induced dissociation (PID) spectra were recorded stepwise per wavelength position by averaging the fragment yield over at least 170 mass spectra. Color changes of the traces in the PID spectra (Fig. 5) indicate a change in the non-linear optical output scheme or wavelength filters of the TOPAS system requiring an reoptimization of the overlap of the laser beam with the ion cloud in the trap. Spectral regions displaying systematic signal intensity shifts were scaled appropriately.

2.3. Collisional-induced dissociation (CID)

During a CID experiment a resonance excitation voltage was applied to the endcaps of the QIT accelerating the trapped precursor ions which then undergo multiple collisions with the He buffer gas, resulting in a slow heating of the sample molecules which eventually leads to fragmentation [46]. The He pressure was constant at $\sim 4.5 \times 10^{-6}$ mbar in the vacuum chamber surrounding the QIT and estimated to be $\sim 10^{-3}$ mbar inside the QIT. The latter corresponds to a hard-sphere collision rate of $\sim 32,000/\text{s}$ (~ 32 collisions per ms) employing an estimated collision cross section of $\sim 100 \text{ \AA}^2$ ([47], see supporting material). The excitation amplitude Amp_{ex} was tuned typically in the range of 0.0–1.0 arb. units which corresponds to an internal scale of the mass spectrometer and is proportional to the collision energy. However, it is difficult to extract quantitative information on the related collision and appearance energies under the applied conditions [48]. It has been suggested to calibrate the experimental appearance thresholds to the known fragmentation energies of so-called thermometer ions [49], but we believe that this procedure is only applicable to well-characterized fragmentation pathways [50]. Therefore, we did not attempt to evaluate the fragmentation energies from the recorded CID curves in this work. For comparison of different precursor masses the appearance/breakdown curves were center-of-mass transformed according to Eq. (1), where m_{He} and $m_{\text{precursor}}$ are the nominal masses of helium and the precursor species, respectively.

$$Amp_{COM} = \left(\frac{m_{\text{He}}}{m_{\text{He}} + m_{\text{precursor}}} \right) \cdot Amp_{ex} \quad (1)$$

To compare gas-phase stabilities of different species we refer to the $Amp_{COM}^{50\%}$ value which is related to the collisional energy necessary to achieve a total fragment yield (TFY) of 50%.

2.4. Fragment yield calculations

The partial fragment yield (Y_i) of a fragment species (i) upon CID or laser PID is determined from the mass spectrum obtained after a certain fragmentation storage period (for CID: 40 ms; for PID: 120 ms). It is calculated as the mass peak integral intensity of species (i) divided by the sum of all fragment and precursor

intensities (Eq. (2)). The total fragment yield (TFY) equals to the sum of all partial fragment yields (Eq. (3)).

$$Y_i = \frac{I_i}{\sum_i I_i + I_p} \quad (2)$$

$$TFY = \sum_i Y_i \quad (3)$$

For PID spectra the fragment yields were additionally normalized to N , the number of photons ($N = E_{\text{pulse}} \cdot \lambda / (h \cdot c)$; $TFY_{\text{norm}} = TFY/N$).

2.5. Computational methods

Geometry optimizations were performed without constraints in the singlet ground-state employing analytical gradient techniques and density functional theory (DFT) at the B3LYP [51,52]/cc-pVTZ [53] (H, O, P) level of theory as implemented in the Gaussian 09 program package [54]. For Pt, K and Ag atoms, the effective core potential basis set Stuttgart RSC 1997 ECP [55,56] was used. Starting geometries were taken from literature as far as available [41]. Harmonic vibrational frequency analysis was performed to confirm true minima structures. Electronic absorption spectra of $[\text{Ptpop} + 2\text{H}]^{2-}$ and $[\text{Ptpop} + \text{H,Ag}]^{2-}$ species (Fig. 6 and Table 3) were calculated for 30 singlet and triplet excited states, respectively using the TD-DFT method (B3LYP/aug-cc-pVDZ(H, O, P)/Stuttgart RSC 1997 ECP(Ag, Pt)) based on their minimum energy ground state structures optimized at the same theoretical level without symmetry constraints. A selection of the obtained geometries, vertical transition energies and corresponding occupied and virtual natural transition orbital pairs (NTOs) is given in the supporting material.

3. Results and discussion

3.1. ESI mass spectra and identification of species

Upon electrospray ionization (ESI) of the different mixed analyte solutions (see Section 2.1) we observe the following main species: $[\text{Ptpop} + 2\text{H}]^{2-}$ (m/z 484), $[\text{Ptpop} + \text{H,K}]^{2-}$ (m/z 503), $[\text{Ptpop} + \text{H,Ag}]^{2-}$ (m/z 537) and $[\text{Ptpop} + 2\text{Ag}]^{2-}$ (m/z 590) (Figs. S2 and S3). These complexes are assigned to adducts of H⁺, K⁺ and Ag⁺ to the tetra-anionic diplatinum $[\text{Ptpop}]^{4-}$ unit. Their elemental compositions and charge state were unequivocally assigned by the excellent agreement of experimental and simulated isotopic patterns (cf. Fig. 3).

Attempts to prepare bare $[\text{Ptpop}]^{4-}$ by ESI were not successful presumably due to its high charge density which leads to the uptake of counteranions or its frailty with respect to spontaneous electron detachment. However, a tri-anion of type $[\text{Ptpop}]^{3-}$, with a presumably mixed valence Pt(III)Pt(II) core, was observed (Fig. S2) but is not the subject of investigation in this work. Moreover, the doubly protonated adduct ($[\text{Ptpop} + 2\text{H}]^{2-}$, m/z 484) was electrosprayed from an acidified solution to prevent the generation of a mixture of (singly-), doubly- and non-protonated species exhibiting different Pt oxidation states and overlapping isotopic patterns (Fig. S3).

3.2. Ground state geometries of $[\text{Ptpop} + \text{X,Y}]^{2-}$ (X,Y = H, K, Ag) by DFT calculations

Since the molecular structures of the investigated complexes are important starting points for the discussion of their counterion dependent fragmentation pathways, we first provide the results of DFT calculations based on the described method (see Section 2.5). Geometry optimized minimum energy structures of $[\text{Ptpop} + \text{X,Y}]^{2-}$ (X,Y = H, K, Ag) complexes (Fig. 2) reveal strong intramolecular hydrogen-bonding interactions resulting in six

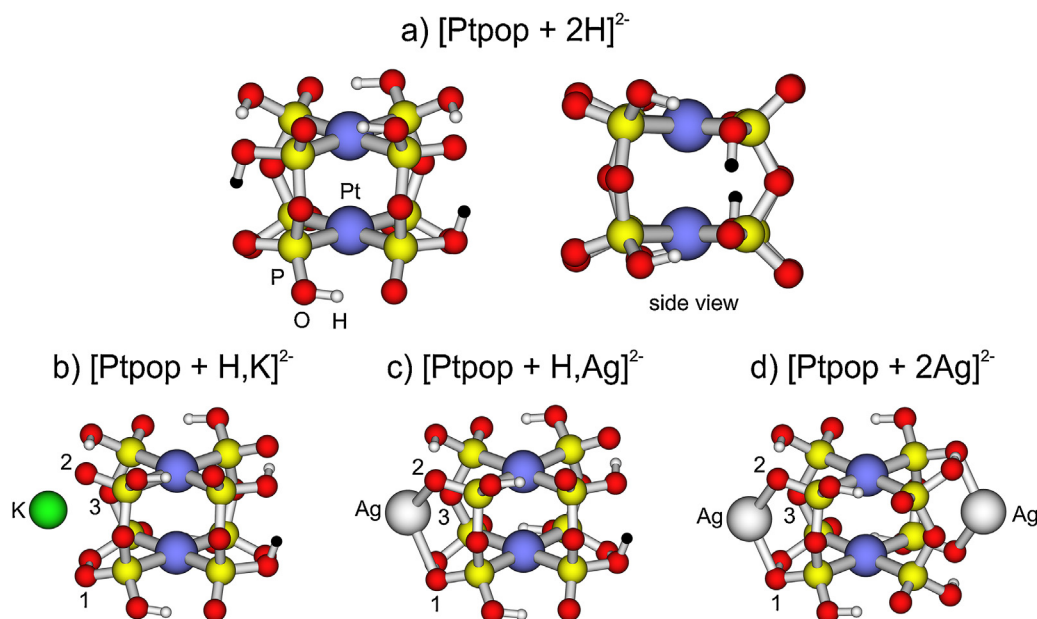


Fig. 2. Calculated minimum-energy structures of (a)–(d) $[\text{Ptpop} + \text{X,Y}]^{2-}$ ($\text{X,Y} = \text{H, K, Ag}$). B3LYP/cc-pVTZ (H, O, P), Stuttgart RSC 1997 ECP (Pt, K, Ag). Color coding: H (white), additional interplanar protons (black), O (red), P (yellow), K (green), Ag (gray), Pt (blue). Oxygen atoms adjacent to K/Ag ions are labeled 1–3.

membered ring structures in individual pyrophosphite ligands ($\text{P}_2\text{O}_5\text{H}_2$) for protonated species. In the lowest energy structures, the metal counterions K^+ and Ag^+ are side-on coordinated to the $[\text{Ptpop}]^{4-}$ unit in close proximity to three oxygen atoms. Only minor structural changes are induced upon side-on counterion binding, in particular there is nearly no influence on the Pt–Pt distance of $\sim 3.0 \text{ \AA}$ (see Table 1). Isomeric structures with an axial metal–Pt–Pt motif on the other hand are calculated to be significantly ($\Delta(\Delta G) > 30 \text{ kJ/mol}$) higher in energy (see Table S4) and the Pt–Pt distance is strongly influenced in case of the silver adducts (see supporting material). This holds also upon variation of functionals, basis sets and for the addition of empirical dispersion corrections in the case of $[\text{Ptpop} + \text{H,Ag}]^{2-}$ (cf. Table S5). Notably, the side-on silver complexes exhibit a clearly bidentate O–Ag–O binding motif with Ag–O bond lengths of 2.27–2.29 Å. This suggests stronger silver–oxygen interactions compared to potassium–oxygen interactions (K–O bond length: 2.66–2.69 Å), which presumably have more of an electrostatic nature (cf. Table 1).

3.3. Collision-induced (CID) and photo-induced dissociation (PID)

Besides the loss of neutrals [57,58], collisional or photoexcitation of gas-phase MCAs is usually associated with two major decay pathways involving charge separation: (i) electron detachment and (ii) ionic fragmentation, into two (or more) anions [4,59–62]. It has been shown that metal-cation complexation can affect these fragmentation characteristics, e.g. by inhibiting ionic fragmentation [12,13].

Here, CID of the dianionic precursors leads nearly exclusively to neutral-loss fragmentation irrespective of the counterion.

Table 1
Bond distances of calculated structures (a)–(d) (Fig. 2) and $[\text{Ptpop}]^{4-}$ (see supporting material).

Structure	Pt–Pt distance/Å	M–O(1), O(2), O(3)/Å
$[\text{Ptpop}]^{4-}$	3.05	
(a) $[\text{Ptpop} + 2\text{H}]^{2-}$	3.02	
(b) $[\text{Ptpop} + \text{H,K}]^{2-}$	3.04	2.69, 2.66, 2.75
(c) $[\text{Ptpop} + \text{H,Ag}]^{2-}$	3.03	2.29, 2.27, 2.73
(d) $[\text{Ptpop} + 2\text{Ag}]^{2-}$	3.06	2.28, 2.28, 2.78

Fragmentation by infrared multiple photon dissociation (IR-MPD) yielded the same results [63]. Neither electron detachment nor ionic fragmentation, detectable by the corresponding monoanionic species, was observed (cf. Fig. 3). However, it should be noted that fragments $< m/z 160$ could not be detected due to the low-mass cut-off of the QIT. By contrast, fs-UV excitation gave products arising from electron detachment whose yields are strongly counterion-dependent. In the following we will analyze this fragmentation behavior in detail.

Fig. 3 depicts mass spectra of the fragmentation products of isolated (a) $[\text{Ptpop} + 2\text{H}]^{2-}$, (b) $[\text{Ptpop} + \text{H,K}]^{2-}$, (c) $[\text{Ptpop} + \text{H,Ag}]^{2-}$ and (d) $[\text{Ptpop} + 2\text{Ag}]^{2-}$ species upon collision-induced and photo-induced dissociation in the QIT. Their assignments are listed in Table 2. When subjected to CID, all investigated dianions decay similarly via dehydration, exhibiting single and multiple loss of water molecules, while retaining their coordinated metal ions and charge. In the case of $[\text{Ptpop} + 2\text{H}]^{2-}$ and $[\text{Ptpop} + \text{H,Ag}]^{2-}$, we additionally observed small percentages of fragments arising from the loss of phosphorous acid (H_3PO_3) and/or a sequential loss of H_2O and HPO_2 . This fragmentation behavior suggests the presence of a comparatively high repulsive Coulomb barrier (RCB) for both ionic fragmentation (IF) and electron detachment (ED) – thus favoring neutral fragmentation on the experimental time scale of $\sim 120 \text{ ms}$. Note that in accompanying photoelectron spectroscopic measurements of $[\text{Ptpop} + 2\text{H}]^{2-}$ [43] we have found $\text{RCB}_{(\text{ED})} > 3.5 \text{ eV}$. The only exception from this behavior is shown by $[\text{Ptpop} + \text{H,K}]^{2-}$, manifested by some monoanionic products, however at very low abundances (see Fig. S5).

The observed multi-dehydration and dephosphorization products can be rationalized assuming fast proton migration upon collisional heating with the He buffer gas. This implies a strongly coupled hydrogen bonded $\text{P}=\text{O} \cdots \text{H} \cdots \text{O}=\text{P}$ network between the pyrophosphite ligands as illustrated by Figs. 1 and 2 and S18 (also supported by the broad and structureless IR-MPD spectra [63]). The view of high interligand proton mobility and accompanying structural fluctuations of the complexes discussed here is also supported by QM/MM simulations of $[\text{Ptpop}]^{4-}$ [64]. Furthermore, a cursory DFT based search for the minimum energy geometry yielded two local minima structures of $[\text{Ptpop}]^{4-}$, an “eclipsed” and a 3 kJ/mol higher in energy “staggered” structure both varying in the

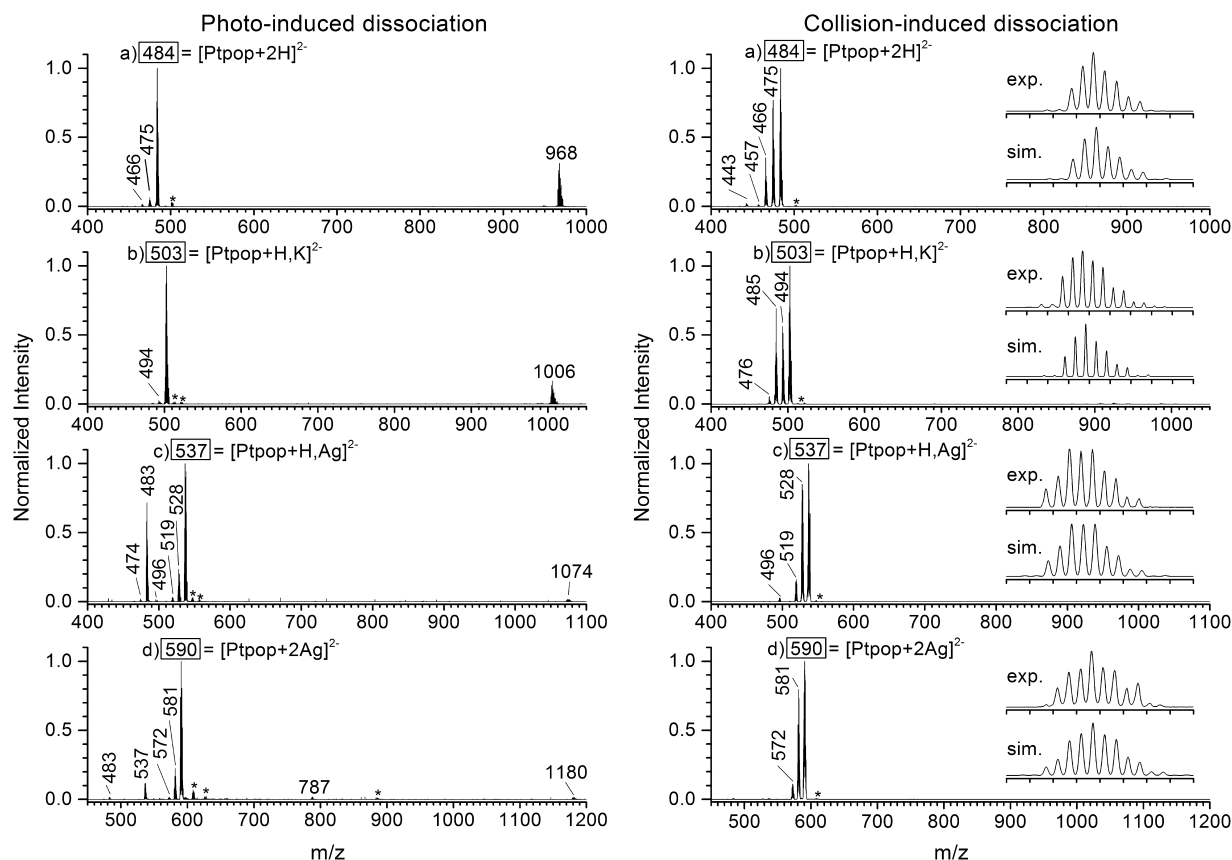


Fig. 3. Photo-induced dissociation (PID) mass spectra (left) of (a) $[\text{Ptpop} + 2\text{H}]^{2-}$, (b) $[\text{Ptpop} + \text{H}, \text{K}]^{2-}$ both irradiated at 370 nm and (c) $[\text{Ptpop} + \text{H}, \text{Ag}]^{2-}$, (d) $[\text{Ptpop} + 2\text{Ag}]^{2-}$ both irradiated at 375 nm. Collision-induced dissociation (CID) mass spectra (right) of (a)–(d) at different fragmentation amplitudes chosen so that the intensity of the major fragments and precursors are comparable. Asterisks indicate gas phase reaction products/unidentified species. *Insets:* Experimental (top) and simulated (bottom) isotope pattern of precursors isolated in a MS^2 step without laser irradiation. The ticks in insets are incremented by m/z 1.

Table 2

PID and CID product assignments and corresponding percentages of the total fragment yields (TFY). The m/z values indicate nominal masses ($(\text{pop}) = (\text{P}_2\text{O}_5\text{H}_2)^{2-}$). Only fragments with $(Y_i) \geq 1\%$ are given. Percentages are given for the respective PID maxima shown in Fig. 5 at 365 nm ($[\text{Ptpop} + 2\text{H}]^{2-}$), 370 nm ($[\text{Ptpop} + \text{H}, \text{K}]^{2-}$), 375 nm/281 nm ($[\text{Ptpop} + \text{H}, \text{Ag}]^{2-}$) and 380/281 nm ($[\text{Ptpop} + 2\text{Ag}]^{2-}$) and for CID at $\text{Amp}_{\text{COM}} \sim 50\%$ fragmentation as indicated in Fig. 4.

Precursor	m/z	Assigned formula	Loss	Percentage of TFY		
				PID ($\lambda_{\text{ex}}/\text{nm}$)	CID ($\text{Amp}_{\text{COM}}/10^{-3}$ arb. units.)	
$[\text{Ptpop} + 2\text{H}]^{2-}$	484			(370)	(1.40)	
	475	$[\text{H}_2\text{Pt}_2(\text{pop})_3(\text{P}_2\text{O}_4)]^{2-}$	H_2O	13	72	
	466	$[\text{H}_2\text{Pt}_2(\text{pop})_2(\text{P}_2\text{O}_4)_2]^{2-}$	$2\text{H}_2\text{O}$	4	25	
	457	$[\text{H}_2\text{Pt}_2(\text{pop})(\text{P}_2\text{O}_4)_3]^{2-}$	$3\text{H}_2\text{O}$		1	
	443	$[\text{H}_2\text{Pt}_2(\text{pop})_2(\text{P}_2\text{O}_4)(\text{PO}_3\text{H})]^{2-}$	$\text{H}_3\text{PO}_3/(\text{H}_2\text{O}, \text{HPO}_2)$		2	
	968	$[\text{H}_2\text{Pt}_2(\text{pop})_4]^-$	e^-	83		
$[\text{Ptpop} + \text{H}, \text{K}]^{2-}$	503			(370)	(1.39)	
	494	$[\text{HKPt}_2(\text{pop})_3(\text{P}_2\text{O}_4)]^{2-}$	H_2O	9	48	
	485	$[\text{HKPt}_2(\text{pop})_2(\text{P}_2\text{O}_4)_2]^{2-}$	$2\text{H}_2\text{O}$		48	
	476	$[\text{HKPt}_2(\text{pop})(\text{P}_2\text{O}_4)_3]^{2-}$	$3\text{H}_2\text{O}$		4	
1006	$[\text{HKPt}_2(\text{pop})_4]^-$	e^-	91			
$[\text{Ptpop} + \text{H}, \text{Ag}]^{2-}$	537			(375)	(281)	(1.19)
	528	$[\text{HAgPt}_2(\text{pop})_3(\text{P}_2\text{O}_4)]^{2-}$	H_2O	26	26	90
	519	$[\text{HAgPt}_2(\text{pop})_2(\text{P}_2\text{O}_4)_2]^{2-}$	$2\text{H}_2\text{O}$	3	29	8
	496	$[\text{HAgPt}_2(\text{pop})_2(\text{P}_2\text{O}_4)(\text{PO}_3\text{H})]^{2-}$	$\text{H}_3\text{PO}_3/(\text{H}_2\text{O}, \text{HPO}_2)$	1		2
	483	$[\text{HPt}_2(\text{pop})_4]^{2-}$	Ag	65	29	
	474	$[\text{HPt}_2(\text{pop})_3(\text{P}_2\text{O}_4)]^{2-}$	$\text{Ag}, \text{H}_2\text{O}$	2		
	1074	$[\text{HAgPt}_2(\text{pop})_4]^-$	e^-	3	17	
$[\text{Ptpop} + 2\text{Ag}]^{2-}$	590			(375)	(281)	(1.05)
	581	$[\text{Ag}_2\text{Pt}_2(\text{pop})_3(\text{P}_2\text{O}_4)]^{2-}$	H_2O	50	38	93
	572	$[\text{Ag}_2\text{Pt}_2(\text{pop})_2(\text{P}_2\text{O}_4)_2]^{2-}$	$2\text{H}_2\text{O}$	4	24	7
	537	$[\text{AgPt}_2(\text{pop})_4]^{2-}$	Ag	33		
	483	$[\text{Pt}_2(\text{pop})_4]^{2-}$	2Ag	3		18
	787	$[\text{Ag}_2\text{Pt}_2(\text{pop})_4]^{3-}$ (see Fig. S4)		5		7
	1180	$[\text{Ag}_2\text{Pt}_2(\text{pop})_4]^-$	e^-	5		14

Pt-P-O-P dihedral angle and the relative orientation of hydrogen bonds [65]. Considering the complexity of the hydrogen-bonded network in the $[\text{Ptpop} + \text{X}, \text{Y}]^{2-}$ aggregates, an additional in-depth theoretical study is necessary in order to find the global minima. Here, we use our calculations merely to provide simple sketches of three conceivable mechanisms for proton transfer (Fig. S18), single water loss (Figs. S19–21) and an estimation of the thermodynamic energy for the latter (Table S6, $\Delta H_{(\text{water loss})}^0 \sim 162 \text{ kJ/mol}$).

As opposed to CID, the photo-induced dissociation (PID) channels depend strongly on the counteraction. In addition to the single and multi-dehydration channels we also observe electron photodetachment and loss of Ag^0 (cf. Fig. 3). In general, $[\text{Ptpop} + 2\text{H}]^{2-}$ and $[\text{Ptpop} + \text{H}, \text{K}]^{2-}$ display a very similar fragmentation behavior. After photoexcitation they decay primarily by electron photodetachment (80–90%) and secondarily by dehydration (cf. Table 2). Evidently, the energy uptake of the ions by a $\sim 3.4 \text{ eV/UV}$ photon (370 nm) is above the second adiabatic electron affinity. Intriguingly, the attachment of Ag^+ ions results in a significant decrease of the relative photodetachment yield (for both $[\text{Ptpop} + \text{H}, \text{Ag}]^{2-}$ and $[\text{Ptpop} + 2\text{Ag}]^{2-}$). Instead, $[\text{Ptpop} + \text{H}, \text{Ag}]^{2-}$ and $[\text{Ptpop} + 2\text{Ag}]^{2-}$ display pronounced Ag^0 atom loss upon photoexcitation, complementary to electron emission. Also, in contrast to species without silver, there is a relatively high yield of dehydration (Table 2).

The observed photo-induced Ag^0 dissociation clearly shows that an intramolecular electron-transfer must occur from the photoexcited Pt-Pt-centered chromophore to the attached Ag^+ ion, perhaps on an ultrafast timescale, prior to Ag^0 dissociation. Similar CT-mediated photo-induced dissociation pathways for attached Ag^+ species have been reported for cationic complexes comprised of benzene derivatives [66] and biomolecular species, like tryptophan and cytosine [67,68]. In the case of $[\text{Ptpop} + \text{H}, \text{Ag}]^{2-}$ this dissociation process would lead to the formal oxidation of a Pt(II) to a Pt(III) center. Support for this mechanism is given by the documented strong reductive capability of the triplet excited state ($^3\text{A}_{2u}$) possessing an estimated standard redox potential smaller than -1.5 V versus SCE [30]. Moreover, several mixed valence Pt(II)/Pt(III) and Pt(III)/Pt(III) derivatives of Ptpop have been characterized [23,29]. In addition, the observed loss of two Ag^0 atoms (m/z 483) in the case of photoexcited $[\text{Ptpop} + 2\text{Ag}]^{2-}$ suggests a 2-electron reductive capability of $[\text{Ptpop}]^{4-}$ ($^3\text{A}_{2u}$) with respect to silver cations. A charge transfer mechanism mediated by a silver-centered electronically excited state would also be conceivable (see Section 3.5.2). However, attaching two Ag^+ ions, as opposed to a single Ag^+ and H^+ ion, does not result in an increase of the Ag^0 dissociation yield. Instead single dehydration becomes the major deactivation pathway (cf. Table 2).

In summary, we find that uptake of energy by multiple collisions (CID) or multiple IR photons (IR-MPD) promotes decay by dehydration whereas excitation by a high energetic UV photon mainly leads to electron detachment and loss of Ag^0 .

3.4. Collisional-induced dissociation (CID) appearance/breakdown curves

We have determined CID appearance/breakdown curves (Fig. 4) in order to investigate the relative gas-phase stabilities of $[\text{Ptpop} + \text{X}, \text{Y}]^{2-}$ ($\text{X}, \text{Y} = \text{H}, \text{K}, \text{Ag}$) species, their partial fragment yields and the appearance energies ($\propto \text{Amp}_{\text{COM}}$) of the different fragments. In general, the lowest energy and major fragmentation pathway was identified to be loss of a single water molecule followed in energy by the double water-loss channel (compare onsets in Fig. 4). In the case of $[\text{Ptpop} + \text{H}, \text{K}]^{2-}$ the onset difference between the single-dehydration and double-dehydration channel is very small suggesting a similar activation energy. For $[\text{Ptpop} + \text{H}, \text{K}]^{2-}$ it was also found that at higher Amp_{COM} values (1.6×10^3 arb. units) the

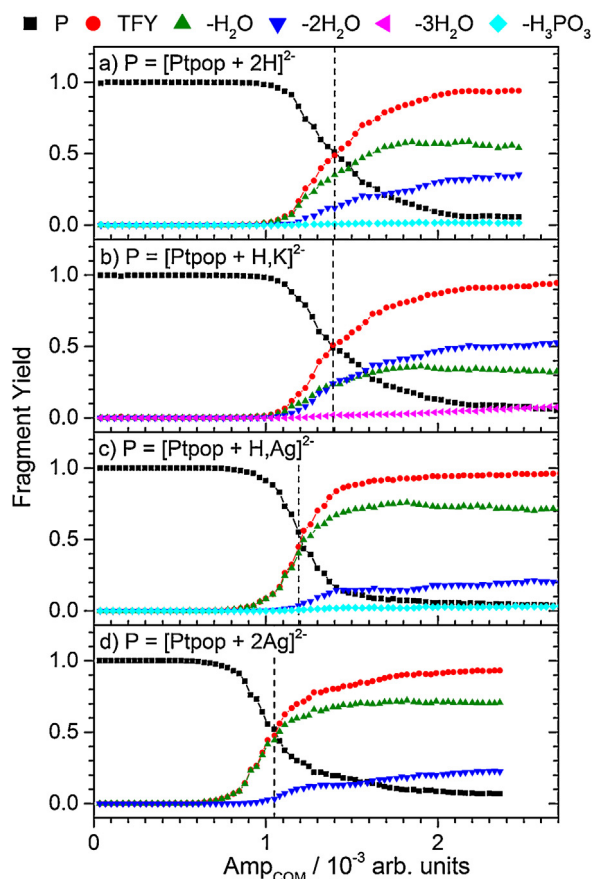


Fig. 4. Fragment specific CID-appearance/breakdown curves for the partial fragment yields (Y_i) and total fragment yields (TFY) of (a)–(d) $[\text{Ptpop} + \text{X}, \text{Y}]^{2-}$ ($\text{X}, \text{Y} = \text{H}, \text{K}, \text{Ag}$) as a function of the excitation amplitude ($\text{Amp}_{\text{COM}} \propto$ collision energy). Dashed vertical lines indicate $\sim \text{Amp}_{\text{COM}}^{50\%}$ values for the corresponding precursor species.

double-water loss channel becomes dominant. The lack of measurable H_3PO_3 loss may be related to this. Surprisingly, the precursor $[\text{Ptpop} + 2\text{H}]^{2-}$ (Fig. 4a) which has a high protonation degree and which might therefore display preformed H_2O with accordingly high dehydration propensity, displays instead: $Y_{(-\text{H}_2\text{O})} > Y_{(-2\text{H}_2\text{O})}$ for all excitation amplitudes. This may be rationalized by a stronger intramolecular hydrogen-bonding network as induced by the additional protons and therefore a higher activation energy for double water-loss compared to $[\text{Ptpop} + \text{H}, \text{K}]^{2-}$. This is illustrated by Fig. 2a which shows the calculated minimum energy geometry.

Finally, we compare the general fragmentation behavior of the different $[\text{Ptpop} + \text{X}, \text{Y}]^{2-}$ species as a function of collision energy. Fig. 4 gives the total fragment yields and CID breakdown curves for all precursor ions (m/z 484, 503, 537, 590, respectively). They are slightly distorted from a sigmoidal shape owing to the interplay of the different decay pathways. It is also apparent that even at high Amp_{COM} values it was not possible to achieve 100% fragment yield. This originates from gas phase back reactions with water molecules present in the QIT, i.e. reattachment of H_2O to dehydration products. The energies at which precursor intensities are reduced to half of their initial value ($\text{Amp}_{\text{COM}}^{50\%}$; Fig. 4, dashed vertical lines) clearly demonstrate the decreasing gas phase stability of the dianions with increasing number of attached silver ions, $\text{Amp}_{\text{COM}}^{50\%}([\text{Ptpop} + 2\text{Ag}]^{2-}) < \text{Amp}_{\text{COM}}^{50\%}([\text{Ptpop} + \text{H}, \text{Ag}]^{2-}) < \text{Amp}_{\text{COM}}^{50\%}([\text{Ptpop} + \text{H}, \text{K}]^{2-}) \approx \text{Amp}_{\text{COM}}^{50\%}([\text{Ptpop} + 2\text{H}]^{2-})$. Apparently, the strong Ag–O interactions involved with side-on coordination of Ag^+ weaken P–O bonds and facilitate dehydration at a lower internal energy (see corresponding structure in Fig. 2). In contrast, the K^+ adduct, ($[\text{Ptpop} + \text{H}, \text{K}]^{2-}$), shows no significant change in $\text{Amp}_{\text{COM}}^{50\%}$

compared to $[\text{Ptpop} + 2\text{H}]^{2-}$ indicating a weaker interaction of electrostatic type between the potassium cation and the pyrophosphite ligands.

3.5. Electronic photo-induced dissociation (PID) spectra

3.5.1. Power dependence

In order to ensure the comparability of gas-phase PID action spectra with solution-phase linear absorption spectra, the absence of multi-photon absorption processes in the former type of spectra is crucial [69]. The dependence of the total fragment yield (TFY) on the laser power for $[\text{Ptpop} + \text{X,Y}]^{2-}$ ($\text{X,Y} = \text{H, K, Ag}$) complexes (Fig. S7) reveals a one-photon absorption process at ~ 370 nm (~ 320 kJ/mol), though saturation effects are clearly discernible as indicated by a slope $n < 1$ on a double logarithmic plot. Noticeably, the power dependence of fragmentation channels originating from the loss of two neutral moieties displays a steeper slope in contrast to single neutral-loss and electron-loss decay channels. Since the ions were irradiated by multiple laser pulses (39 pulses/ion cloud) during a storage period of 120 ms, this observation emphasizes the occurrence of secondary fragmentation processes arising from a secondary excitation of primary fragments, i.e. the primary product ions absorb photons from subsequent laser pulses causing further neutral losses.

On the other hand, at ~ 280 nm (~ 430 kJ/mol) all fragmentation channels of (c) $[\text{Ptpop} + \text{H,Ag}]^{2-}$ and (d) $[\text{Ptpop} + 2\text{Ag}]^{2-}$ display a similar power dependence with $n \sim 0.75$ (Fig. S8). This suggests that sequential fragmentation can occur after a single photon excitation at this wavelength—considering also the large fraction of single neutral-loss photofragments expected to have internal energies at the high-energy tail of the Boltzmann distribution.

Overall, we do not find evidence for a significant contribution of UV multiple photon excitation processes to the PID spectra. However, the results do indicate onsets of signal saturation (sub-linear energy dependence) and secondary fragmentation contributions. The former affects the comparability of band intensities between solution and gas phase action spectra, the latter motivated us to explore the fragmentation routes in more detail by systematic MSⁿ (see Section 3.6).

3.5.2. PID yield spectra and calculated absorption spectra

The UV-PID yield spectra of (a) $[\text{Ptpop} + 2\text{H}]^{2-}$ and (b) $[\text{Ptpop} + \text{H,K}]^{2-}$ (Fig. 5) are strikingly similar to the aqueous phase absorption spectrum of $\text{K}_4[\text{Ptpop}]$ at room temperature – with a slight hypsochromic shift and additional minor broadening, respectively. This supports the picture that an aqueous solution of $[\text{Ptpop}]^{4-}$ comprises an equilibrium mixture of H^+ and K^+ counterion adducts. By contrast, the gas-phase spectra of the silver adducts (c) $[\text{Ptpop} + \text{H,Ag}]^{2-}$ and (d) $[\text{Ptpop} + 2\text{Ag}]^{2-}$ are significantly broadened compared to solution and show systematic bathochromic-shifts with absorption bands centered at ~ 375 nm and ~ 280 nm (weak). Furthermore, an additional non-resonant fragmentation contribution becomes discernible as an offset at wavelengths below ~ 350 nm. This is more pronounced for the double Ag^+ adduct and will be discussed later on.

We assign the strong absorption features peaking at ~ 365 and ~ 370 nm for $[\text{Ptpop} + 2\text{H}]^{2-}$ and $[\text{Ptpop} + \text{H,K}]^{2-}$, respectively, to the Pt-Pt-centered $^1\text{MC}(\text{d}\sigma^*-\text{p}\sigma)$ transition based on TD-DFT (B3LYP) calculations ($\lambda_{\text{calc}} = 347$ nm, see Fig. 6 and Table 3) and the fact that the gas phase spectra resemble those in aqueous solution (367 nm, $\epsilon = 34,500 \text{ M}^{-1} \text{ cm}^{-1}$ [25]) which is consistent with the reported weak solvatochromism of the Pt-Pt-centered $[\text{Ptpop}]^{4-}$ chromophore [25]. We note in passing, that the calculated transition wavelength for the main absorption band of $[\text{Ptpop}]^{4-}$ in gas

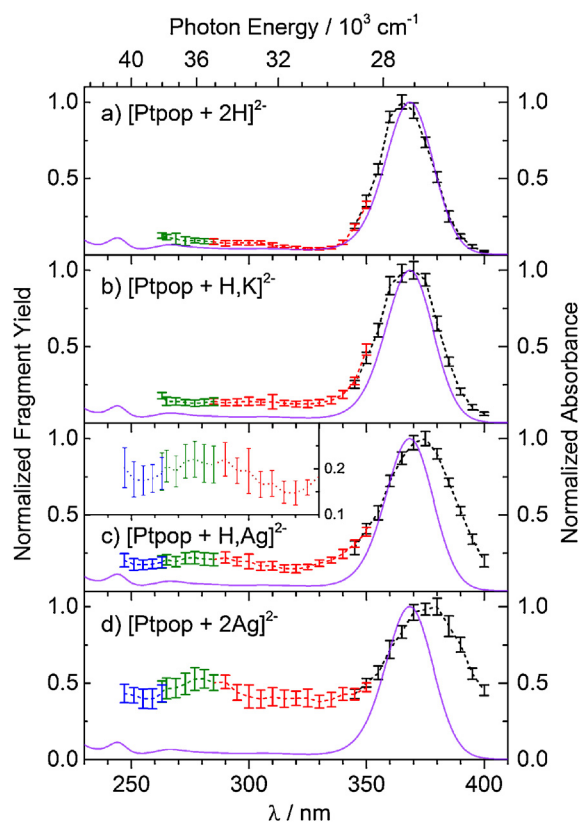


Fig. 5. UV-PID yield spectra (TFY) of (a)–(d) $[\text{Ptpop} + \text{X,Y}]^{2-}$ ($\text{X,Y} = \text{H, K, Ag}$) species compared to the UV-vis absorption spectrum of $\text{K}_4[\text{Ptpop}]$ (purple solid lines) in deoxygenated H_2O ($c = 72 \mu\text{M}$, Fig. S1). All spectra are normalized to unity. Error bars ($\pm 1\sigma$, 170 mass spectra) are connected by dashed lines to guide the eye. Color changes indicate a change in either the output wave or wavelength filters and the total fragment yields of (b) are scaled by a factor of 1.71 in the range of 263–285 nm (see Section 2.2). *Inset:* Magnified PID spectrum of (c) in the range of 230–330 nm. (For interpretation of the references to colour in this figure legend, the reader is referred to the web version of this article.)

phase ($\lambda_{\text{calc}} = 367$ nm [24]) agrees very well to our experimental data $[\text{Ptpop} + 2\text{H}]^{2-}$ (Fig. 5a).

Concerning the interactions with metal cations it is known, as mentioned in the introduction that the photoexcited triplet state, ($^3\text{A}_{2u}$), has a strong affinity for metal ions M^+ such as Ti^+ and Ag^+ yielding luminescent exciplexes with an axial M-Pt-Pt(-M) geometry [38,40–42]. However, ground state $[\text{Ptpop}]-\text{Ag}$ interactions in solution, as indicated by a Ag^+ concentration dependent decrease of the 367 nm band and concomitantly by an increase of a bathochromic-shifted feature (~ 400 nm, [40]), are not well understood. Here we observe a very small bathochromic shift ($\Delta\lambda \sim 5$ nm) for gaseous $[\text{Ptpop} + \text{H,Ag}]^{2-}$ and $[\text{Ptpop} + 2\text{Ag}]^{2-}$ with respect to silver-free species and take this as a strong indication for a side-on coordination motif (Fig. 2). We have also measured the PID spectra in the range of 410–445 nm at higher laser fluence ($3 \mu\text{J}/\text{pulse}$) revealing no additional bands for both $[\text{Ptpop} + \text{H,Ag}]^{2-}$ and $[\text{Ptpop} + 2\text{Ag}]^{2-}$ (Fig. S6). Consequently, the band observed at ~ 375 nm for the Ag^+ -attached species in gas phase should also derive from a Pt-Pt-centered $^1\text{MC}(\text{d}\sigma^*-\text{p}\sigma)$ transition. Potentially a Pt-to-Ag charge transfer state is also contributing. TD-DFT calculations (see Fig. 6 and Table 3) support this assignment revealing only a small relative shift of the $^1\text{MC}(\text{d}\sigma^*-\text{p}\sigma)$ transition between $[\text{Ptpop} + 2\text{H}]^{2-}$ and $[\text{Ptpop} + \text{H,Ag}]^{2-}$ (side-on coordination motif) and an additional ligand-to-silver CT transition ($^1\text{LMCT}$) transition close in energy rationalizing intramolecular electron transfer and dissociation of Ag^0 upon photoexcitation. In contrast, the calculated absorption spectrum for an axial $\text{Ag}-\text{Pt}-\text{Pt}$ geometry differs strongly

Table 3
Fragmentation channel specific absorption bands of [Ptpop + X,Y]²⁻ (X,Y = H, K, Ag) (Fig. 7, Fig. S13) compared to absorption of K₄[Ptpop] in aqueous solution (Fig. S1), and total fragment yields (TFY) at selected wavelengths. The spectral fwhm of the fs laser is: ~8 nm and ~4 nm at 375 nm and 281 nm, respectively. The last two columns contain calculated vertical transitions (B3LYP/aug-cc-pVDZ, *f* = oscillator strength) and their respective assignments (see Fig. 6 and supporting material).

Species	λ_{\max}/nm			λ/nm (TFY)	$\lambda_{\text{calc}}/\text{nm}$ ($f \geq 0.008$)	Character	
	ePD	Single neutral loss.	Multiple neutral loss				
(a) [Ptpop + 2H] ²⁻	370	360 300	365	370 (0.30)	347 (0.200) 303 (0.009) 279 (0.009)	¹ MC (dσ*-pσ) ¹ LMMCT ¹ LMMCT	
(b) [Ptpop + H,K] ²⁻	370	360 305	–	370 (0.21)			
(c) [Ptpop + H,Ag] ²⁻	360	375 290	375 270	375 (0.44) 281 (0.07)	353 (0.020) 341 (0.188) 308 (0.011) 269 (0.013)	¹ LMCT (L→Ag) ¹ MC (dσ*-pσ)	
(d) [Ptpop + 2Ag] ²⁻	355	375 325 280	385 280	375 (0.23) 281 (0.09)			
K ₄ [Ptpop] in H ₂ O	λ_{\max}/nm ($\epsilon/M^{-1} \text{cm}^{-1}$) [25]			TD-DFT/PCM (B3LYP) [78]			
	367 (34500)			351 (0.276)			¹ MC (dσ*-pσ)
	305 (990)			301 (0.008)			¹ LMMCT
	266 (1550), 243 (3350)			243 (0.024)			

(see Fig. S22). Additional support for our structural conclusion is based on the reported ground state interaction of [Ptpop]⁴⁻ with Pb²⁺ or Sn²⁺. In these solution experiments bathochromic shifts of ~25 nm and ~70 nm, respectively, and additional low-energy bands were observed [70]. It was proposed that the primary carriers of these absorptions are aggregates, formed by coordination at the axial Pt sites. These likely compete with other species such as aggregates at peripheral sites of the pyrophosphite ligands. Furthermore, in another study, axial coordination of SO₂ was clearly demonstrated to give rise to a significantly bathochromic-shifted band in the UV–vis absorption spectrum [71].

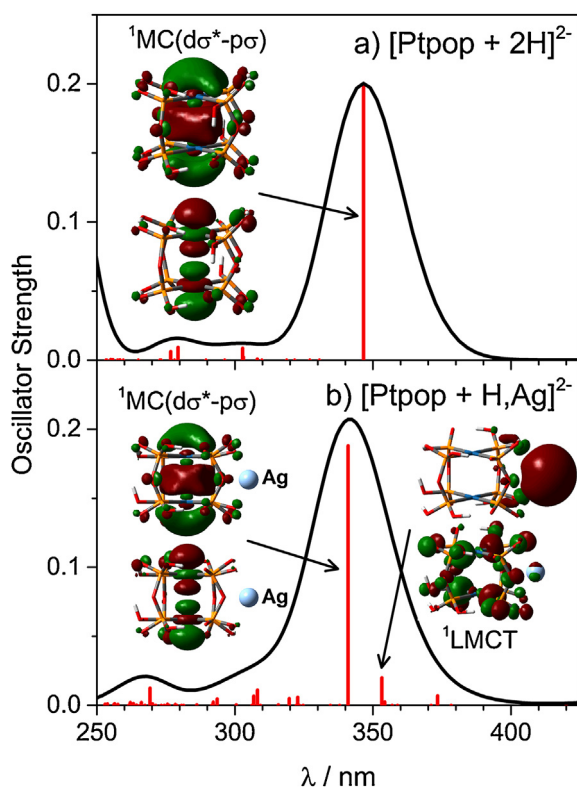


Fig. 6. Calculated absorption spectra (B3LYP/aug-cc-pVDZ) of (a) [Ptpop + 2H]²⁻ and (b) [Ptpop + H,Ag]²⁻ (Gaussian band shapes, fwhm = 0.33 eV). Insets show relevant occupied (bottom) and virtual (top) NTO pairs (isovalue = 0.03).

To conclude, Pt-to-metal (here: Ag) charge transfer (MMCT) states are expected for complexes of axial structure and should show an intrinsic strong spectral shift [48,49] with additional bands at longer wavelength. We observe only remarkably small shifts for the [Ptpop]-Ag⁺ aggregates in gas phase and therefore ascribe a side-on structure to these complexes in agreement with TD-DFT results. However, upon solvation an increase of this bathochromic spectral shift may be expected due to some charge transfer character of the corresponding Pt-Pt centered transition (see Fig. 6). We note that a more detailed theoretical survey of the [Ptpop + X,Y]²⁻ species reported here would be desirable. In particular, it would be interesting to compare the gas phase data presented here to calculated excitation energies upon inclusion of spin-orbit coupling (e.g. obtained by SO-TD-DFT [35]). Furthermore, the energies of charge-transfer transitions are notoriously underestimated by TD-DFT [72,73] and a better treatment is required. Finally, a systematic investigation of solvent effects is called for.

3.5.3. Channel specific PID spectra

In general, a variety of possible energy relaxation pathways such as internal conversion (IC), intersystem-crossing (ISC) and internal vibrational redistribution (IVR) could govern the (consecutive) fragmentation processes of the photoexcited dianions. We cannot distinguish unequivocally between them by the experimental evidence in this work, but we can invoke different scenarios. Fragmentation can occur (a) directly from a photoexcited electronic state which is coupled to a fragmentation coordinate or (b) indirectly from a vibrationally “hot” electronic ground state populated after IC. Our collisional and photoexcitation data for [Ptpop + X,Y]²⁻ suggests that all dehydration/dephosphorization photoproducts most likely originate from fragmentation of a vibrationally excited “hot” electronic ground state since they can be afforded both by CID and PID. By contrast, electron detachment and Ag⁰ dissociation are characteristic for electronic excitation and possibly reflect direct decay processes out of one or more electronically excited-states (see Fig. 6).

In the following we present and discuss the channel specific decomposition of the PID spectra. We observe strong variations in the branching ratios of the individual fragmentation channels as a function of photon energy (Figs. S9–S11). The displayed PID behavior is complex and comprised of contributions from (i) excited electronic states and (ii) a variety of fragmentation mechanisms, as already mentioned, which cause a partial scrambling

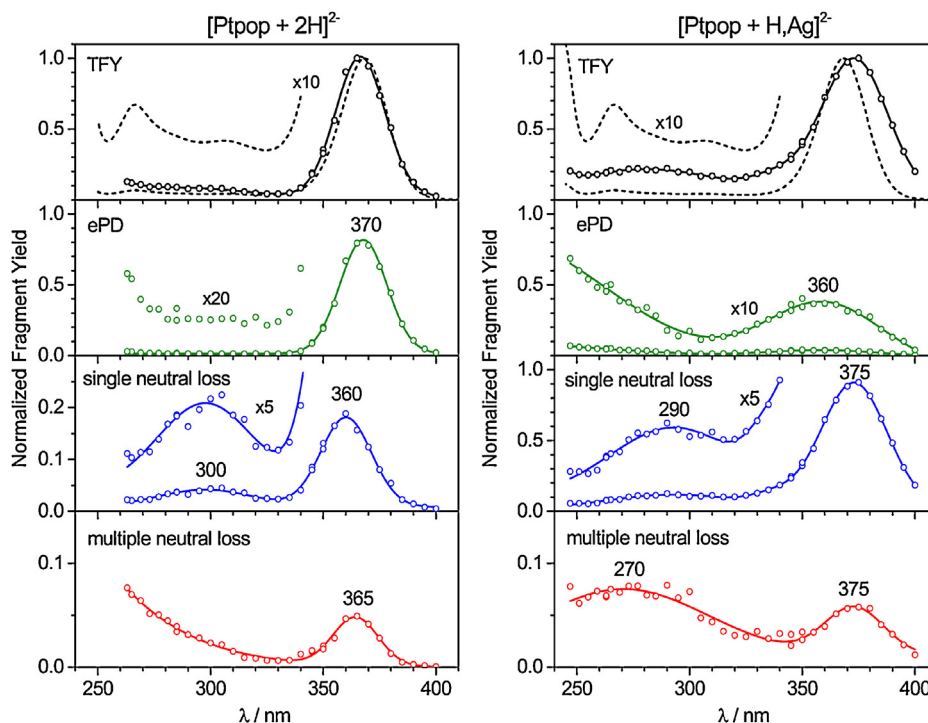


Fig. 7. Fitted band profiles and corresponding “grouped-channel” PID spectra (see Fig. S12) for (a) $[\text{Ptpop} + 2\text{H}]^{2-}$ (left) and (b) $[\text{Ptpop} + \text{H,Ag}]^{2-}$ (right) classified into: total fragment yield (TFY, black circles) and grouped decay channels: electron photodetachment (ePD, green circles), single neutral loss (sNL, blue circles) including (a) m/z 475 ($-\text{H}_2\text{O}$); (b) m/z 528 ($-\text{H}_2\text{O}$), m/z 483 ($-\text{Ag}$) and multiple neutral loss (mNL, red circles) including (a) m/z 466 ($-2 \text{H}_2\text{O}$), m/z 457 ($-3 \text{H}_2\text{O}$), m/z 443 ($-\text{H}_2\text{O, HPO}_2$) (b) m/z 519 ($-2 \text{H}_2\text{O}$), m/z 496 ($-\text{H}_2\text{O, HPO}_2$), m/z 474 ($-\text{Ag, H}_2\text{O}$). Dashed black lines in the top panels show the normalized aqueous UV absorption features of $\text{K}_4[\text{Ptpop}]$. Insets show magnifications. (For interpretation of the references to colour in this figure legend, the reader is referred to the web version of this article.)

of spectral information. Similar observations have been reported for other dianionic metal complexes [74,75], underscoring the importance of elucidating the fragmentation mechanisms for interpretation of PID spectra. Consequently, in order to disentangle the different contributions to the PID spectra (Fig. 7) we categorize the photoproducts into three groups associated with (i) electron photodetachment (ePD), (ii) single neutral loss (sNL) and (iii) multiple neutral loss (mNL).

Electron photodetachment (ePD): The cross section for ePD is governed by the absorption cross section and the height and shape of the inner repulsive Coulomb barrier $\text{RCB}_{(\text{ED})}$ of dianions. When the photon energies for the resonantly excited electronic state is lower than the inner $\text{RCB}_{(\text{ED})}$ but above the second adiabatic electron affinity, the ePD yield should relate to the probability of excited state electron tunneling detachment (ESETD) which is a known phenomenon for MCAs [76]. Higher photon energies additionally facilitate direct photodetachment which can be indicated by a threshold in the electron detachment yield [74].

Single neutral loss (sNL): Considering the fact that sNL photofragments can only originate from primary fragmentation, the corresponding PID spectrum should directly be related to electronic excitation of the $[\text{Ptpop} + \text{X, Y}]^{2-}$ chromophore. It can therefore provide information similar to an absorption spectrum under the assumption that electronic excitation at each wavelength yields sNL fragments with equal probability [77], i.e.: (i) the excess energy after photoexcitation should be higher than possible activation barriers for fragmentation, (ii) the dissociation rates should be fast on the experimental time scale (=negligible kinetic shift) and (iii) competing decay processes such as photoluminescence or excited state electron tunneling detachment should not be significant (or not dependent on excitation wavelength).

Multiple neutral loss (mNL): mNL products can originate from secondary fragmentation processes due to multiple illumination

of the ion cloud and therefore relate to a superposition of the PID spectra of several fragments. At higher photon energies, i.e. shorter wavelengths, a sequential loss mechanism may also be feasible when single neutral loss photofragments contain enough internal energy to fragment further.

It is convenient to discuss channel specific PID spectra in terms of a “grouped-channel” representation, i.e. by integrating over all channels corresponding to either electron photodetachment (ePD), single neutral loss sNL or multiple neutral loss (mNL). The corresponding “grouped-channel” PID spectra (Fig. 7, Figs. S12 and S13) display a variety of spectrally distinct contributions to the total fragment yields. For clarity, fitted envelopes to PID spectra are shown in Fig. 7 and Fig. S13 and the corresponding spectroscopic features are summarized in Table 3. No evident correlation between sNL and mNL channels is discernible from the spectra supporting our inference, that the total fragment yield (TFY) spectra comprise a superposition of primary and secondary fragmentation contributions. As already pointed out, the TFY spectra obtained for the silver adducts look quite similar qualitatively to those of $[\text{Ptpop} + \text{H, K}]^{2-}$ and $[\text{Ptpop} + 2\text{H}]^{2-}$. The differences between (a) $[\text{Ptpop} + 2\text{H}]^{2-}$ and (b) $[\text{Ptpop} + \text{H, Ag}]^{2-}$ with respect to the channel-specific spectra (Fig. 7) are more pronounced and will be discussed next.

The electron photodetachment (ePD) yield spectra (Fig. 7) display a distinct band centered at 370 nm for $[\text{Ptpop} + 2\text{H}]^{2-}$ and an analogous, somewhat broadened band at 360 nm for $[\text{Ptpop} + \text{H, Ag}]^{2-}$. On the basis of a time-resolved photoelectron spectroscopy study performed in parallel [43] we conclude that these spectral features most likely reflect resonant $^1\text{MC}(\text{d}\sigma^* - \text{p}\sigma)$ excitation of the Pt-Pt-centered chromophore at photon energies below the inner repulsive Coulomb barrier ($\text{RCB}_{(\text{ED})} > 3.5 \text{ eV}$) and therefore originate from excited state electron tunneling detachment (ESETD). In this study [43] we further show that ESETD

may occur from either singlet and/or triplet excited states of $[\text{Ptpop} + 2\text{H}]^{2-}$ with presumably different heights and shapes of their repulsive Coulomb barriers. Interestingly, in the case of $[\text{Ptpop} + 2\text{H}]^{2-}$ the ePD absorption band is bathochromically shifted by ~ 10 nm (800 cm^{-1}) relative to the major feature for single neutral loss. In contrast, the electron photodetachment feature for $[\text{Ptpop} + \text{H}, \text{Ag}]^{2-}$ exhibits a significant hypsochromic shift by ~ 15 nm (1100 cm^{-1}) relative to the major band of the sNL spectrum. In a simplified scenario, the Ag^+ ions could act as internal electron acceptors which capture the “tunneling electrons” thus explaining the occurrence of Ag^0 dissociation channel and the correspondingly lower relative electron detachment yield for silver adducts. The electron tunneling processes can obviously only take place within the lifetimes of the respective excited states. In solution phase an ultrafast ISC from the $^1\text{A}_{2u}$ ($\tau \sim 8$ ps) to the $^3\text{A}_{2u}$ ($\tau \sim 9.8$ μs) excited state has been observed [19,21].

In the range of ~ 340 nm to 240 nm the electron photodetachment spectrum of $[\text{Ptpop} + 2\text{H}]^{2-}$ shows no pronounced spectral features and comparatively little overall electron detachment, whereas the K^+/Ag^+ adduct species (Fig. 7, Fig. S13) exhibit an onset at ~ 305 nm to a nearly linearly rising electron detachment yield as photon energy is increased further. The latter may indicate additional detachment pathways besides excited state electron tunneling detachment, presumably from energetically lower lying ligand-centered orbitals or direct electron detachment governed by Franck-Condon factors connecting the dianion $^1\text{A}_{1g}$ ground state with vibronic states of the resulting monoanion.

The single neutral loss (sNL) spectra are generally more structured and display a weak feature centered at 300 nm and 290 nm for $[\text{Ptpop} + 2\text{H}]^{2-}$ and $[\text{Ptpop} + \text{H}, \text{Ag}]^{2-}$, respectively. Similar features are observed in this region for $[\text{Ptpop} + \text{H}, \text{K}]^{2-}$ and $[\text{Ptpop} + 2\text{Ag}]^{2-}$, the latter exhibiting two distinct bands peaking at ~ 325 nm and ~ 280 nm (Table 3, Fig. S13). We tentatively attribute these features to a resonant enhancement in the fragmentation cross section originating in the excitation of low-intensity bands which were also detected in the solution spectrum of $[\text{Ptpop}]^{4-}$ (cf. dashed lines in Fig. 7). These bands at 305 nm and 266 nm, observed in aqueous solution, are attributed to $^1\text{LMMCT}$ transitions and display a distinct shift in less polar solvents, e.g., acetonitrile [25,34]. Consequently, electronic transitions with $^1\text{LMMCT}$ character should be susceptible to interactions of the pyrophosphite ligands with metal cations. Hence, the observed variability of the sNL 300 nm/ 290 nm bands in relation to the attached cations for $[\text{Ptpop} + \text{X}, \text{Y}]^{2-}$ species (Table 3) support a side-on coordination motif and a $^1\text{LMMCT}$ character of the corresponding transitions.

The multiple neutral loss (mNL) yield spectra reveal broad features at wavelength below 300 nm and therefore contribute to the non-resonant offsets observed in the total PID (TFY) spectra. We do not discuss individual mNL spectral features further due to the complexity of the possible underlying processes. Nevertheless, a few possible routes to the multiple neutral loss decay products observed are discussed in the following.

3.6. Fragmentation routes and mechanisms

Multiple MS^3 experiments were conducted on isolated dehydrated $[\text{Ptpop} + \text{X}, \text{Y} - \text{H}_2\text{O}]^{2-}$ fragments generated via CID to explore their photo-induced and collision-induced fragmentation channels (Figs. S14–S16). As an example for the typical fragmentation phenomena observed, we have summarized the possible fragmentation routes of $[\text{Ptpop} + \text{H}, \text{Ag}]^{2-}$ in Fig. 8. PID of preselected $[\text{Ptpop} + \text{H}, \text{Ag} - \text{H}_2\text{O}]^{2-}$ yielded multiple dehydrated fragments ($-\text{H}_2\text{O}$, m/z 519; $-2\text{H}_2\text{O}$, m/z 510) and the elimination of HPO_2 (m/z 496). This is a strong indication for a sequential mechanism of the multi dehydration process and clearly shows that the “formation of H_3PO_3 ” can originate from a sequential loss of H_2O and

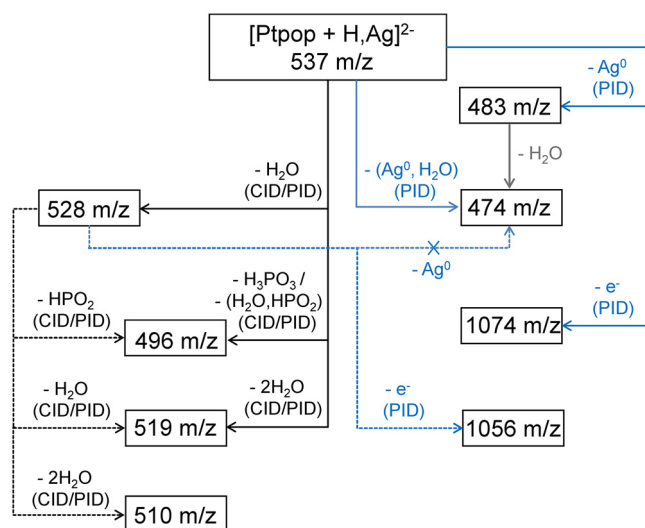


Fig. 8. Fragmentation scheme of $[\text{Ptpop} + \text{H}, \text{Ag}]^{2-}$ based on MS^2 (solid arrows) and MS^3 (dashed arrows) collision-induced and photo-induced fragmentation experiments. MS^3 experiments were conducted by first producing the single dehydration fragment (m/z 528) via CID followed by isolation and subsequent irradiation/fragmentation (Figs. S14–S16). Products which are formed via both CID and PID (black arrows) are listed on the left, and products only generated by PID are indicated on the right (blue arrows). The assumed pathway ($483\text{ m/z} \rightarrow 474\text{ m/z}$) is indicated in gray. (For interpretation of the references to colour in this figure legend, the reader is referred to the web version of this article.)

HPO_2 . Interestingly, electron photodetachment was observed for all (preselected) $[\text{Ptpop} + \text{X}, \text{Y} - \text{H}_2\text{O}]^{2-}$ species whereas Ag^0 dissociation could not be achieved – neither by CID nor PID. Therefore, the “ $-(\text{Ag}^0, \text{H}_2\text{O})$ ” photofragment (m/z 474) can only be generated in a sequential mechanism by first eliminating Ag^0 , yielding a species with m/z 483, and subsequently by loss of a H_2O molecule (Fig. 8, gray arrow). We conclude from these observations that Ag^+ is stronger bound to the dehydrated species than to its non-dehydrated precursor.

CID appearance curves determined in MS^3 experiments for $[\text{Ptpop} + \text{X}, \text{Y} - \text{H}_2\text{O}]^{2-}$ species (Fig. S17) indicate $\text{Amp}_{\text{COM}}^{50\%}([\text{Ptpop} + 2\text{Ag} - \text{H}_2\text{O}]^{2-}) \ll \text{Amp}_{\text{COM}}^{50\%}([\text{Ptpop} + \text{H}, \text{K} - \text{H}_2\text{O}]^{2-}) < \text{Amp}_{\text{COM}}^{50\%}([\text{Ptpop} + \text{H}, \text{Ag} - \text{H}_2\text{O}]^{2-}) \approx \text{Amp}_{\text{COM}}^{50\%}([\text{Ptpop} + 2\text{H} - \text{H}_2\text{O}]^{2-})$. This provides further evidence for side-on $\text{Ag}-\text{O}$ binding in the corresponding precursors (Fig. 2). The associated interactions apparently lower the activation energy for single water loss thereby opening an energetically favored dehydration pathway. An analogous dehydration step is no longer accessible in the $[\text{Ptpop} + \text{H}, \text{Ag} - \text{H}_2\text{O}]^{2-}$ product but presumably it can still occur in $[\text{Ptpop} + 2\text{Ag} - \text{H}_2\text{O}]^{2-}$ which exhibits two independent side-on Ag^+ coordination sites (cf. Fig. 2). As mentioned before, a thorough theoretical investigation of the dehydration mechanism, the involvement of silver and determination of the relevant transition states would be desirable, but is beyond the scope of this paper.

4. Conclusions

The aim of this study was to explore the collisional- and photo-induced fragmentation pathways of dianionic $[\text{Ptpop} + \text{X}, \text{Y}]^{2-}$ ($\text{X}, \text{Y} = \text{H}, \text{K}, \text{Ag}$) species in vacuo and whether the counterion binding site could be inferred from this data in comparison to theory.

CID reveals nearly exclusively neutral-loss fragmentation mainly by dehydration, whereas UV-PID yields primarily electron detachment and – in the case of Ag^+ adducts ($[\text{Ptpop} + \text{H}, \text{Ag}]^{2-}$, $[\text{Ptpop} + 2\text{Ag}]^{2-}$) – loss of Ag^0 . We attribute the latter to either excited state intramolecular electron transfer from the Pt-Pt chromophore to a side-on coordinated Ag^+ or excitation of a $^1\text{LMCT}(\text{L} \rightarrow \text{Ag})$ transition supported by TD-DFT results.

We find that the electron photodetachment yield (ePD) is strongly counter-cation dependent. Protonated and potassium species mainly are deactivated by ePD, whereas the addition of Ag^+ increases the relative amount of neutral-loss fragmentation. Additionally, we infer from a photoelectron spectroscopy study performed in parallel [43] that excited state electron tunneling detachment processes contribute strongly to the ePD decay channel observed here. In particular, the heights of the corresponding repulsive Coulomb barriers and adiabatic detachment energies inferred in the latter study are consistent with this mechanism.

PID spectra were recorded in the 250–400 nm wavelength range and display a resemblance to the aqueous absorption spectrum of $\text{K}_4[\text{Ptpop}]$. Spectroscopically, only a small bathochromic shift by ~ 5 nm ($\sim 500 \text{ cm}^{-1}$) is observed for the Ag^+ adducts compared to the silver-free species. This is a strong indication for a side-on coordination motif as supported by the displayed fragmentation behavior, ground state geometry optimizations and TD-DFT results. The $\text{Ag}^+[\text{Ptpop}]$ complex thus formed acquires some CT character and therefore displays a solvent-induced red-shift in aqueous solution for its main excitation band [40]. We do not observe experimental evidence for axial Ag-Pt interaction in this ground-state aggregate as known for the $[\text{Ag-Ptpop}]^{3-}$ exciplex in aqueous solution [40].

The wavelength dependence of the various primary decay channels reveals that several decay/fragmentation routes contribute to the total photofragment yields. We have decomposed their fragment specific contributions and have discussed underlying fragmentation mechanisms in detail due to the fact that secondary fragmentation processes were discernible, particularly at higher laser fluence.

Motivated by preliminary evidence for electron transfer and intersystem crossing on an ultrafast timescale, we are presently exploring the photodynamics of $[\text{Ptpop} + \text{H}_2\text{Ag}]^{2-}$ employing fs/ps-resolved pump-probe photo-induced dissociation and photoelectron spectroscopy—and will report on this in forthcoming publications [43].

To conclude, this study provides the first gas-phase data on the photophysical properties of mass selected $\text{H}^+/\text{K}^+/\text{Ag}^+$ adducts of $[\text{Ptpop}]^{4-}$. Inferences are directly comparable to structural theory and contribute to a better understanding of the intrinsic properties of this multiple charged anion and its ground state interactions with metal cations.

Acknowledgements

We would like to thank Werner R. Thiel (Department of Chemistry, Inorganic Chemistry, TU Kaiserslautern) for providing his facilities and expertise in preparing $\text{K}_4[\text{Ptpop}]$. Financial support by the DFG-funded transregional collaborative research center SFB/TRR 88 “3MET” (projects C4 and C7) and by the state research center OPTIMAS is gratefully acknowledged. We also thank the Stiftung Rheinland-Pfalz für Innovation (Project 965) for funding. Y. N. thanks the Carl-Zeiss-Stiftung for a postdoctoral stipend. We thank Gereon Niedner-Schatteburg for making the IR-MPD setup available for this study.

Appendix A. Supplementary data

Supplementary data associated with this article can be found, in the online version, at <http://dx.doi.org/10.1016/j.ijms.2015.11.007>.

References

- [1] M.K. Scheller, R.N. Compton, L.S. Cederbaum, Gas-phase multiply charged anions, *Science* 270 (1995) 1160–1166, <http://dx.doi.org/10.1126/science.270.5239.1160>.
- [2] A. Dreuw, L.S. Cederbaum, Multiply charged anions in the gas phase, *Chem. Rev.* 102 (2002) 181–200, <http://dx.doi.org/10.1021/cr0104227>.
- [3] X.-B. Wang, L.-S. Wang, Photoelectron spectroscopy of multiply charged anions, *Annu. Rev. Phys. Chem.* 60 (2009) 105–126, <http://dx.doi.org/10.1146/annurev.physchem.59.032607.093724>.
- [4] W.E. Boxford, C.E.H. Dessent, Probing the intrinsic features and environmental stabilization of multiply charged anions, *Phys. Chem. Chem. Phys.* 8 (2006) 5151–5165, <http://dx.doi.org/10.1039/B609123G>.
- [5] S. Ard, N. Mirsaleh-Kohan, J.D. Steill, J. Oomens, S.B. Nielsen, R.N. Compton, Dissociation of dicarboxylate and disulfonate dianions, *J. Chem. Phys.* 132 (2010) 094301, <http://dx.doi.org/10.1063/1.3292577>.
- [6] C.N. Hansen, M.-B.S. Kirketerp, M.B. Kristensen, S.B. Nielsen, K. Støchkel, J.A. Wyer, On the stability of isolated dianions in vacuo and action spectroscopy experiments, *Chem. Phys. Lett.* 502 (2011) 53–56, <http://dx.doi.org/10.1016/j.cplett.2010.12.025>.
- [7] X.-B. Wang, L.-S. Wang, Observation of negative electron-binding energy in a molecule, *Nature* 400 (1999) 245–248, <http://dx.doi.org/10.1038/22286>.
- [8] K. Arnold, T.S. Balaban, M.N. Blom, O.T. Ehrler, S. Gilb, O. Hampe, J.E. van Lier, J.M. Weber, M.M. Kappes, Electron autodetachment from isolated nickel and copper phthalocyanine-tetrasulfonate tetraanions: isomer specific rates, *J. Phys. Chem. A* 107 (2003) 794–803, <http://dx.doi.org/10.1021/jp022141o>.
- [9] P. Weis, O. Hampe, S. Gilb, M.M. Kappes, Metastability of isolated platinum and palladium tetrahalide dianions and the role of electron tunneling, *Chem. Phys. Lett.* 321 (2000) 426–432, [http://dx.doi.org/10.1016/S0009-2614\(00\)00360-2](http://dx.doi.org/10.1016/S0009-2614(00)00360-2).
- [10] O.T. Ehrler, J.-P. Yang, A.B. Sugiharto, A.N. Unterreiner, M.M. Kappes, Excited state dynamics of metastable phthalocyanine-tetrasulfonate tetra-anions probed by pump/probe photoelectron spectroscopy, *J. Chem. Phys.* 127 (2007) 184301, <http://dx.doi.org/10.1063/1.2780842>.
- [11] J.R.R. Verlet, D.A. Horke, A.S. Chatterley, Excited states of multiply-charged anions probed by photoelectron imaging: riding the repulsive Coulomb barrier, *Phys. Chem. Chem. Phys.* 16 (2014) 15043–15052, <http://dx.doi.org/10.1039/C4CP01667J>.
- [12] R.M. Burke, W.E. Boxford, C.E.H. Dessent, Counter-ion perturbation of the fragmentation pathways of multiply charged anions: evidence for exit channel complexes on the fragmentation potential energy surfaces, *J. Chem. Phys.* 125 (2006) 021105, <http://dx.doi.org/10.1063/1.2219116>.
- [13] R.M. Burke, W.E. Boxford, C.E.H. Dessent, Characterizing the intrinsic stability of gas-phase clusters of transition metal complex dianions with alkali metal counterions: counterion perturbation of multiply charged anions, *J. Chem. Phys.* 126 (2007) 064308, <http://dx.doi.org/10.1063/1.2432118>.
- [14] W.E. Boxford, R.M. Burke, C.E.H. Dessent, New insights into dianion-cation contact ion-pairs: understanding the effect of cation complexation on the electron detachment and ionic fragmentation pathways of multiply charged anions, *Phys. Scr.* 76 (2007) C56, <http://dx.doi.org/10.1088/0031-8949/76/3/N08>.
- [15] A.P. Zipp, The behavior of the tetra- μ -pyrophosphito-diplatinum(II) ion $\text{Pt}_2(\text{P}_2\text{O}_5\text{H}_2)_4^{4-}$ and related species, *Coord. Chem. Rev.* 84 (1988) 47–83, [http://dx.doi.org/10.1016/0010-8545\(88\)80031-6](http://dx.doi.org/10.1016/0010-8545(88)80031-6).
- [16] D.M. Roundhill, H.B. Gray, C.M. Che, Pyrophosphito-bridged diplatinum chemistry, *Acc. Chem. Res.* 22 (1989) 55–61, <http://dx.doi.org/10.1021/ar00158a002>.
- [17] R.P. Sperline, M.K. Dickson, D.M. Roundhill, New route to the directed synthesis of mixed metal chain oligomers. Identification of a platinum complex having an intense emission in the visible spectrum in aqueous solution, *Chem. Commun.* (1977) 62–63, <http://dx.doi.org/10.1039/C39770000062>.
- [18] M.A.F.D.R. Pinto, P.J. Sadler, S. Neidle, M.R. Sanderson, A. Subbiah, R. Kuroda, A novel di-platinum(II) octaphosphite complex showing metal-metal bonding and intense luminescence; a potential probe for basic proteins. X-ray crystal and molecular structure, *Chem. Commun.* (1980) 13–15, <http://dx.doi.org/10.1039/C39800000013>.
- [19] S.J. Milder, B.S. Brunschwig, Factors affecting nonradiative decay: temperature dependence of the picosecond fluorescence lifetime of $\text{Pt}_2(\text{pop})_4^{4-}$, *J. Phys. Chem.* 96 (1992) 2189–2196, <http://dx.doi.org/10.1021/j100184a030>.
- [20] M. Christensen, K. Haldrup, K. Bechgaard, R. Feidenhansl, Q. Kong, M. Cammarata, M.L. Russo, M. Wulff, N. Harrit, M.M. Nielsen, Time-resolved X-ray scattering of an electronically excited state in solution. Structure of the $^3A_{2u}$ state of tetrakis- μ -pyrophosphitodiplatinate(II), *J. Am. Chem. Soc.* 131 (2009) 502–508, <http://dx.doi.org/10.1021/ja804485d>.
- [21] R.M. van der Veen, A. Cannizzo, F. van Mourik, A. Vlček, M. Chergui, Vibrational relaxation and intersystem crossing of binuclear metal complexes in solution, *J. Am. Chem. Soc.* 133 (2011) 305–315, <http://dx.doi.org/10.1021/ja106769w>.
- [22] R.M. van der Veen, C.J. Milne, A. El Nahhas, F.A. Lima, V.-T. Pham, J. Best, J.A. Weinstein, C.N. Borca, R. Abela, C. Bressler, M. Chergui, Structural determination of a photochemically active diplatinum molecule by time-resolved EXAFS spectroscopy, *Angew. Chem. Int. Ed.* 48 (2009) 2711–2714, <http://dx.doi.org/10.1002/anie.200805946>.
- [23] C.M. Che, L.G. Butler, P.J. Grunthaner, H.B. Gray, Chemistry and spectroscopy of binuclear platinum diphosphite complexes, *Inorg. Chem.* 24 (1985) 4662–4665, <http://dx.doi.org/10.1021/ic00220a047>.
- [24] S.R. Stoyanov, J.M. Villegas, D.P. Rillema, Spectroscopic properties of $[\text{Pt}_2(\mu\text{-P}_2\text{O}_5\text{H}_2)_4]^{4-}$: a time-dependent density functional theory and conductor-like polarizable continuum model investigation, *J. Phys. Chem. B* 108 (2004) 12175–12180, <http://dx.doi.org/10.1021/jp048360m>.
- [25] A.E. Stieglman, S.F. Rice, H.B. Gray, V.M. Miskowski, Electronic spectroscopy of d^8-d^8 diplatinum complexes. $^1A_{2u}$ ($d\sigma^* \rightarrow p\sigma$), 3E_u ($d_{xz}, d_{yz} \rightarrow p\sigma$), and $^3B_{2u}$ ($d\sigma^* \rightarrow d_{x^2-y^2}$) excited states of $\text{Pt}_2(\text{P}_2\text{O}_5\text{H}_2)_4^{4-}$, *Inorg. Chem.* 26 (1987) 1112–1116, <http://dx.doi.org/10.1021/ic00254a029>.

- [26] C.M. Che, L.G. Butler, H.B. Gray, Spectroscopic properties and redox chemistry of the phosphorescent excited state of $\text{Pt}_2(\text{P}_2\text{O}_5)_4\text{H}_8^{4-}$, *J. Am. Chem. Soc.* 103 (1981) 7796–7797, <http://dx.doi.org/10.1021/ja00416a021>.
- [27] A. Vlček Jr., The life and times of excited states of organometallic and coordination compounds, *Coord. Chem. Rev.* 200–202 (2000) 933–978, [http://dx.doi.org/10.1016/S0010-8545\(00\)00308-8](http://dx.doi.org/10.1016/S0010-8545(00)00308-8).
- [28] D.M. Roundhill, S.J. Atherton, Bromine atom abstraction from aryl and alkyl bromides by the triplet excited state of tetrakis(μ -pyrophosphito)diplatinum(II) tetranoion, *Inorg. Chem.* 25 (1986) 4071–4072, <http://dx.doi.org/10.1021/ic00243a004>.
- [29] D.M. Roundhill, S.J. Atherton, Detection and kinetics of formation and disproportionation of the mixed-valence diplatinum(II, III) complex $\text{Pt}_2(\mu\text{-P}_2\text{O}_5\text{H}_2)_4^{3-}$ using transient difference spectroscopy, *J. Am. Chem. Soc.* 108 (1986) 6829–6831, <http://dx.doi.org/10.1021/ja00281a075>.
- [30] W.B. Heuer, M.D. Totten, G.S. Rodman, E.J. Hebert, H.J. Tracy, J.K. Nagle, Electron-transfer reactions and luminescent quantum yield of the triplet excited state of tetrakis(μ -diphosphito(2-)-P,P')diplatinate(II), *J. Am. Chem. Soc.* 106 (1984) 1163–1164, <http://dx.doi.org/10.1021/ja00316a083>.
- [31] K.M. Breiner, M.A. Daugherty, T.G. Oas, H.H. Thorp, An anionic diplatinum DNA photocleavage agent: chemical mechanism and footprinting of λ repressor, *J. Am. Chem. Soc.* 117 (1995) 11673–11679, <http://dx.doi.org/10.1021/ja00152a007>.
- [32] W.A. Kalsbeck, N. Grover, H.H. Thorp, Photolytic cleavage of DNA by $[\text{Pt}_2(\text{P}_2\text{O}_5\text{H}_2)_4]^{4-}$, *Angew. Chem. Int. Ed.* 30 (1991) 1517–1518, <http://dx.doi.org/10.1002/anie.199115171>.
- [33] Y. Shimizu, Y. Tanaka, T. Azumi, Assignment of the lower electronic states of potassium tetrakis(μ -diphosphonato)diplatinate(II), *J. Phys. Chem.* 88 (1984) 2423–2425, <http://dx.doi.org/10.1021/j150655a049>.
- [34] A.C. Durrell, G.E. Keller, Y.-C. Lam, J. Sýkora, A. Vlček, H.B. Gray, Structural control of $^1\text{A}_{2u}$ -to- $^3\text{A}_{2u}$ intersystem crossing in diplatinum(II,II) complexes, *J. Am. Chem. Soc.* 134 (2012) 14201–14207, <http://dx.doi.org/10.1021/ja305666b>.
- [35] S. Zláliš, Y.-C. Lam, H.B. Gray, A. Vlček, Spin-orbit TDDFT electronic structure of diplatinum(II,II) complexes, *Inorg. Chem.* 54 (2015) 3491–3500, <http://dx.doi.org/10.1021/acs.inorgchem.5b00063>.
- [36] R.M. van der Veen, C. Bressler, C.J. Milne, V.-T. Pham, A. El Nahhas, F.A. Lima, W. Gawelda, C.N. Borca, R. Abela, M. Chergui, Retrieving photochemically active structures by time-resolved EXAFS spectroscopy, *J. Phys.: Conf. Ser.* 190 (2009) 012054, <http://dx.doi.org/10.1088/1742-6596/190/1/012054>.
- [37] J.K. Nagle, B.A. Brennan, Luminescent exciplex formation involving tetrakis(μ -diphosphito)diplatinate(II) and -thallium(I) in aqueous solution, *J. Am. Chem. Soc.* 110 (1988) 5931–5932, <http://dx.doi.org/10.1021/ja00225a071>.
- [38] S.A. Clodfelter, T.M. Doede, B.A. Brennan, J.K. Nagle, D.P. Bender, W.A. Turner, P.M. LaPunzina, Luminescent metal-metal-bonded exciplexes involving tetrakis(μ -diphosphito)diplatinate(II) and thallium(I), *J. Am. Chem. Soc.* 117 (1994) 11379–11386, <http://dx.doi.org/10.1021/ja00104a018>.
- [39] C.N. Pettijohn, E.B. Jochowitz, B. Chuong, J.K. Nagle, A. Vogler, Luminescent excimers and exciplexes of Pt^{II} compounds, *Coord. Chem. Rev.* 171 (1998) 85–92, [http://dx.doi.org/10.1016/S0010-8545\(98\)90015-7](http://dx.doi.org/10.1016/S0010-8545(98)90015-7).
- [40] M. Christensen, K. Haldrup, K.S. Kjaer, M. Cammarata, M. Wulff, K. Bechgaard, H. Weihe, N.H. Harrit, M.M. Nielsen, Structure of a short-lived excited state trinuclear Ag-Pt-Pt complex in aqueous solution by time resolved X-ray scattering, *Phys. Chem. Chem. Phys.* 12 (2010) 6921–6923, <http://dx.doi.org/10.1039/C002070B>.
- [41] Q. Kong, K.S. Kjaer, K. Haldrup, S.P.A. Sauer, T.B. van Driel, M. Christensen, M.M. Nielsen, M. Wulff, Theoretical study of the triplet excited state of PtPOP and the exciplexes M-PtPOP (M = Tl, Ag) in solution and comparison with ultrafast X-ray scattering results, *Chem. Phys.* 393 (2012) 117–122, <http://dx.doi.org/10.1016/j.chemphys.2011.11.034>.
- [42] K. Haldrup, M. Christensen, M. Cammarata, Q. Kong, M. Wulff, S.O. Mariager, K. Bechgaard, R. Feidenhans'l, N. Harrit, M.M. Nielsen, Structural tracking of a bimolecular reaction in solution by time-resolved X-ray scattering, *Angew. Chem. Int. Ed.* 48 (2009) 4180–4184, <http://dx.doi.org/10.1002/anie.200900741>.
- [43] M.-O. Wingham, J.-P. Yang, A.N. Unterreiner, S.V. Kruppa, C. Riehn, L.-S. Wang, M.M. Kappes, unpublished results.
- [44] D. Imanbaev, Y. Nosenko, C. Kerner, K. Chevalier, F. Rupp, C. Riehn, W.R. Thiel, R. Diller, Excited-state dynamics of a ruthenium(II) catalyst studied by transient photofragmentation in gas phase and transient absorption in solution, *Chem. Phys.* 442 (2014) 53–61, <http://dx.doi.org/10.1016/j.chemphys.2014.03.005>.
- [45] Y. Nosenko, F. Menges, C. Riehn, G. Niedner-Schatteburg, Investigation by two-color IR dissociation spectroscopy of Hoogsteen-type binding in a metalated nucleobase pair mimic, *Phys. Chem. Chem. Phys.* 15 (2013) 8171–8178, <http://dx.doi.org/10.1039/C3CP44283G>.
- [46] D.E. Goeringer, S.A. McLuckey, Evolution of ion internal energy during collisional excitation in the Paul ion trap: a stochastic approach, *J. Chem. Phys.* 104 (1996) 2214–2221, <http://dx.doi.org/10.1063/1.471812>.
- [47] M.W. Forbes, A.M. Nagy, R.A. Jockusch, Photofragmentation of and electron photodetachment from a GFP model chromophore in a quadrupole ion trap, *Int. J. Mass Spectrom.* 308 (2011) 155–166, <http://dx.doi.org/10.1016/j.ijms.2011.08.016>.
- [48] P.M. Mayer, C. Poon, The mechanisms of collisional activation of ions in mass spectrometry, *Mass Spectrom. Rev.* 28 (2009) 608–639, <http://dx.doi.org/10.1002/mas.20225>, and references therein.
- [49] C. Collette, E. De Pauw, Calibration of the internal energy distribution of ions produced by electrospray, *Rapid Commun. Mass Spectrom.* 12 (1998) 165–170, [http://dx.doi.org/10.1002/\(SICI\)1097-0231\(19980227\)12:4<165::AID-RCM140>3.0.CO;2-1](http://dx.doi.org/10.1002/(SICI)1097-0231(19980227)12:4<165::AID-RCM140>3.0.CO;2-1).
- [50] K.V. Barylyuk, K. Chingin, R.M. Balabin, R. Zenobi, Fragmentation of benzylpyridinium thermometer ions and its effect on the accuracy of internal energy calibration, *J. Am. Soc. Mass Spectrom.* 21 (2010) 172–177, <http://dx.doi.org/10.1016/j.jasms.2009.09.023>.
- [51] A.D. Becke, Density-functional thermochemistry. III. The role of exact exchange, *J. Chem. Phys.* 98 (1993) 5648–5652, <http://dx.doi.org/10.1063/1.464913>.
- [52] C. Lee, W. Yang, R.G. Parr, Development of the Colle-Salvetti correlation-energy formula into a functional of the electron density, *Phys. Rev. B* 37 (1988) 785–789, <http://dx.doi.org/10.1103/PhysRevB.37.785>.
- [53] T.H. Dunning, Gaussian basis sets for use in correlated molecular calculations. I. The atoms boron through neon and hydrogen, *J. Chem. Phys.* 90 (1989) 1007–1023, <http://dx.doi.org/10.1063/1.456153>.
- [54] M.J. Frisch, G.W. Trucks, H.B. Schlegel, G.E. Scuseria, M.A. Robb, J.R. Cheeseman, G. Scalmani, V. Barone, B. Mennucci, G.A. Petersson, H. Nakatsuji, M. Caricato, X. Li, H.P. Hratchian, A.F. Izmaylov, J. Bloino, G. Zheng, J.L. Sonnenberg, M. Hada, M. Ehara, K. Toyota, R. Fukuda, J. Hasegawa, M. Ishida, T. Nakajima, Y. Honda, O. Kitao, H. Nakai, T. Vreven, J.A. Montgomery Jr., J.E. Peralta, F. Ogliaro, M.J. Bearpark, J. Heyd, E.N. Brothers, K.N. Kudin, V.N. Staroverov, R. Kobayashi, J. Normand, K. Raghavachari, A.P. Rendell, J.C. Burant, S.S. Iyengar, J. Tomasi, M. Cossi, N. Rega, N.J. Millam, M. Klene, J.E. Knox, J.B. Cross, V. Bakken, C. Adamo, J. Jaramillo, R. Gomperts, R.E. Stratmann, O. Yazyev, A.J. Austin, R. Cammi, C. Pomelli, J.W. Ochterski, R.L. Martin, K. Morokuma, V.G. Zakrzewski, G.A. Voth, P. Salvador, J.J. Dannenberg, S. Dapprich, A.D. Daniels, Ö. Farkas, J.B. Foresman, J.V. Ortiz, J. Cioslowski, D.J. Fox, *Gaussian 09, Revision C.01*, Gaussian, Inc., Wallingford, CT, USA, 2009.
- [55] A. Bergner, M. Dolg, W. Küchle, H. Stoll, H. Preuß, Ab initio energy-adjusted pseudopotentials for elements of groups 13–17, *Mol. Phys.* 80 (1993) 1431–1441, <http://dx.doi.org/10.1080/00268879300103121>.
- [56] M. Dolg, H. Stoll, H. Preuss, R.M. Pitzer, Relativistic and correlation effects for element 105 (hahnium, Ha): a comparative study of M and MO (M = Nb, Ta, Ha) using energy-adjusted ab initio pseudopotentials, *J. Phys. Chem.* 97 (1993) 5852–5859, <http://dx.doi.org/10.1021/j100124a012>.
- [57] G. Bojesen, P. Hvelplund, T.J.D. Jørgensen, S.B. Nielsen, Probing the lowest coordination number of dianionic platinum–cyanide complexes in the gas phase: dynamics of the charge dissociation process, *J. Chem. Phys.* 113 (2000) 6608–6612, <http://dx.doi.org/10.1063/1.1310610>.
- [58] S.M. Bachrach, M. Hare, S.R. Kass, Alkali metal salts of dianions: a theoretical and experimental study of $(\text{C}_6\text{H}_4)_2^{2-} \text{M}^+$ (M = Li and Na), *J. Am. Chem. Soc.* 120 (1998) 12646–12649, <http://dx.doi.org/10.1021/ja9825478>.
- [59] J. Friedrich, S. Gilb, O.T. Ehrler, A. Behrendt, M.M. Kappes, Electronic photodissociation spectroscopy of isolated IrX_6^{2-} (X = Cl, Br), *J. Chem. Phys.* 117 (2002) 2635–2644, <http://dx.doi.org/10.1063/1.1490921>.
- [60] X.-B. Wang, L.-S. Wang, Photodetachment of free hexahalogenometallate doubly charged anions in the gas phase: $[\text{ML}_6]^{2-}$ (M = Re, Os, Ir, Pt; L = Cl and Br), *J. Chem. Phys.* 111 (1999) 4497–4509, <http://dx.doi.org/10.1063/1.479213>.
- [61] X.-B. Wang, L.-S. Wang, Probing the electronic structure and metal–metal bond of $\text{Re}_2\text{Cl}_8^{2-}$ in the gas phase, *J. Am. Chem. Soc.* 122 (2000) 2096–2100, <http://dx.doi.org/10.1021/ja994200q>.
- [62] S.H. Kaufman, J.M. Weber, M. Pernpointner, Electronic structure and UV spectrum of hexachloroplatinate dianions in vacuo, *J. Chem. Phys.* 139 (2013) 194310, <http://dx.doi.org/10.1063/1.4830407>.
- [63] We have recorded the IR-MPD spectrum of $[\text{Ptppop} + 2\text{H}]^{2-}$, $[\text{Ptppop} + \text{HK}]^{2-}$ and $[\text{Ptppop} + 2\text{Ag}]^{2-}$. It revealed a broad, nearly structureless band within the range of 2900–3600 cm^{-1} presumably originating from hydrogen bonded OH-oscillators and is thus not further discussed or used for analysis here.
- [64] T.J. Penfold, B.F.E. Curchod, I. Tavernelli, R. Abela, U. Rothlisberger, M. Chergui, Simulations of X-ray absorption spectra: the effect of the solvent, *Phys. Chem. Chem. Phys.* 14 (2012) 9444–9450, <http://dx.doi.org/10.1039/C2CP24080G>.
- [65] G.I. Gellene, D.M. Roundhill, Computational studies on the isomeric structures in the pyrophosphito bridged diplatinum(II) complex, platinum pop, *J. Phys. Chem. A* 106 (2002) 7617–7620, <http://dx.doi.org/10.1021/jp0147325>.
- [66] K.F. Willey, C.S. Yeh, D.L. Robbins, M.A. Duncan, Charge-transfer in the photodissociation of metal ion–benzene complexes, *J. Phys. Chem.* 96 (1992) 9106–9111, <http://dx.doi.org/10.1021/j100202a007>.
- [67] R. Antoine, T. Tabarin, M. Broyer, P. Dugourd, R. Mitrić, V. Bonačić-Koutecký, Optical properties of gas-phase tryptophan–silver cations: charge transfer from the indole ring to the silver atom, *ChemPhysChem* 7 (2006) 524–528, <http://dx.doi.org/10.1002/cphc.200500495>.
- [68] M.I. Taccone, G. Féraud, M. Berdakin, C. Dedonder-Lardeux, C. Jouvot, G.A. Pino, Communication UV photoionization of cytosine catalyzed by Ag^+ , *J. Chem. Phys.* 143 (2015) 041103, <http://dx.doi.org/10.1063/1.4927469>.
- [69] S.M.J. Wellman, R.A. Jockusch, Moving in on the action: an experimental comparison of fluorescence excitation and photodissociation action spectroscopy, *J. Phys. Chem. A* 119 (2015) 6333–6338, <http://dx.doi.org/10.1021/acs.jpca.5b04835>.
- [70] D.P. Bender, J.K. Nagle, Metal–metal interactions of aqueous lead(II) and tin(II) ions with the ground and excited states of tetrakis(μ -diphosphito)diplatinate(II), *Inorg. Chim. Acta.* 225 (1994) 201–205, [http://dx.doi.org/10.1016/0020-1693\(94\)04048-6](http://dx.doi.org/10.1016/0020-1693(94)04048-6).
- [71] K.A. Alexander, P. Stein, D.B. Hedden, D.M. Roundhill, Emission quenching of binuclear pyrophosphito platinum(II) complexes in aqueous solution by sulphur dioxide. Spectroscopic measurements on sulphur dioxide addition and chromous ion reduction, *Polyhedron* 2 (1983) 1389–1392, [http://dx.doi.org/10.1016/S0277-5387\(00\)84403-4](http://dx.doi.org/10.1016/S0277-5387(00)84403-4).

- [72] T.A. Niehaus, T. Hofbeck, H. Yersin, Charge-transfer excited states in phosphorescent organo-transition metal compounds: a difficult case for time dependent density functional theory? *RSC Adv.* 5 (2015) 63318–63329, <http://dx.doi.org/10.1039/C5RA12962A>.
- [73] A. Vlček Jr., S. Zálaiš, Modeling of charge-transfer transitions and excited states in d^6 transition metal complexes by DFT techniques, *Coord. Chem. Rev.* 251 (2007) 258–287, <http://dx.doi.org/10.1016/j.ccr.2006.05.021>.
- [74] A. Sen, C.E.H. Dessent, Mapping the UV photophysics of platinum metal complexes bound to nucleobases: laser spectroscopy of isolated Uracil: $\text{Pt}(\text{CN})_4^{2-}$ and Uracil: $\text{Pt}(\text{CN})_6^{2-}$ complexes, *J. Phys. Chem. Lett.* 5 (2014) 3281–3285, <http://dx.doi.org/10.1021/jz501749j>.
- [75] J.C. Marcum, J.M. Weber, Electronic photodissociation spectra and decay pathways of gas-phase IrBr_6^{2-} , *J. Chem. Phys.* 131 (2009) 194309, <http://dx.doi.org/10.1063/1.3265956>.
- [76] M.-O. Winghart, J.-P. Yang, M. Kuhn, A.-N. Unterreiner, T.J.A. Wolf, P.D. Dau, H.-T. Liu, D.-L. Huang, W. Klopper, L.-S. Wang, M.M. Kappes, Electron tunneling from electronically excited states of isolated bisdisulizole-derived trianion chromophores following UV absorption, *Phys. Chem. Chem. Phys.* 15 (2013) 6726–6736, <http://dx.doi.org/10.1039/C3CP50497B>.
- [77] K. Egashira, A. Terasaki, Optical absorption spectrum of the chromium dimer cation: measurements by photon-trap and photodissociation spectroscopy, *Chem. Phys. Lett.* 635 (2015) 13–15, <http://dx.doi.org/10.1016/j.cplett.2015.06.038>.
- [78] Q.-J. Pan, H.-G. Fu, H.-T. Yu, H.-X. Zhang, Theoretical insight into electronic structures and spectroscopic properties of $[\text{Pt}_2(\text{pop})_4]^{4-}$, $[\text{Pt}_2(\text{pcp})_4]^{4-}$, and Related Derivatives ($\text{pop} = \text{P}_2\text{O}_5\text{H}_2^{2-}$ and $\text{pcp} = \text{P}_2\text{O}_4\text{CH}_4^{2-}$), *Inorg. Chem.* 45 (2006) 8729–8735, <http://dx.doi.org/10.1021/ic060336v>.

Ultrafast Vibrational and Electronic Dynamics of Metal-Metal Interactions Studied by Transient Photo-Induced Dissociation (Gas Phase) and Transient Absorption (Solution)

Preamble

The following chapter is a reprint of a conference paper from the conference proceedings “XX International Conference on Ultrafast Phenomena (UP 2016)”. Gas phase τ -PD spectra were measured and by myself and transient absorption spectra were provided by Dr. Florian Bappler. The paper draft was written by myself and revised with the help of Prof. Dr. Rolf Diller and Priv.-Doz. Dr. Christoph Riehn.

S. V. Kruppa, F. Bappler, Y. Nosenko, S. P. Walg, R. Diller, C. Riehn, *Conference Proceedings, XX International Conference on Ultrafast Phenomena (UP 2016), Santa Fe, USA, OSA Technical Digest, 2016*, paper UW4A.33, <https://doi.org/10.1364/UP.2016.UW4A.33>

Copyright © 2016 Optical Society of America

Reprint Licence

General Terms and Conditions

5. The Author(s) grant OSA permission to use his/her name, likeness and biography for the purpose of promoting the aforementioned Work, the presentation of the Work, or related OSA activities.
6. The Submitting Author warrants and represents that he/she has the authority to make this license and release, and is authorized to act as agent for all listed authors for the purpose of submitting the Work to OSA.
7. With regard to the Work and any presentation thereof, the Author(s) warrant that he/she has complied with the requirements of the Health Insurance Portability and Accountability Act of 1996 ("HIPAA") by obtaining consent for the disclosure of Protected Health Information ("PHI"), as defined in HIPAA, and/or removing PHI, as required by law.
8. You retain copyright ownership of the Work. However, you agree that OSA and any co-sponsors shall have the right to register copyright to a collective work (such as a conference technical digest) containing the Work. Such registration will not affect the copyright status of the individual articles, papers, or manuscripts contained in the collective work.

Ultrafast Vibrational and Electronic Dynamics of Metal-Metal Interactions Studied by Transient Photo-Induced Dissociation (Gas Phase) and Transient Absorption (Solution)

S. V. Kruppa¹, F. Bäßler², Y. Nosenko¹, S. P. Walg¹, R. Diller², C. Riehn^{1,3}

Department of Chemistry¹/Physics², Forschungszentrum OPTIMAS³, TU Kaiserslautern, Erwin-Schrödinger-Str.52/46, D-67663 Kaiserslautern, Germany
E-mail: riehn@chemie.uni-kl.de

Abstract: Femtosecond photo-induced dissociation (gas phase) and transient absorption (solution) revealed multi-exponential electronic dynamics in a ($\text{Ag}^{\text{I}}\text{-Ag}^{\text{I}}$) phosphine complex. This is extended to vibrational wavepacket dynamics for its chlorine adduct ($\text{Ag}^{\text{I}}\text{-Ag}^{\text{I}}\text{-Cl}$).

OCIS codes: (300.0300) Spectroscopy; (300.6250) condensed matter; (300.6520) trapped ion; (300.6530) ultrafast; (300.6540) ultraviolet

1. Introduction

Metallophilic, and more specifically argentophilic effects, based on internuclear attractive interactions of d^{10} transition metal ions, have been studied in structural chemistry for some time [1]. Moreover, many of these compounds exhibit interesting optical and luminescence properties useful for photocatalysis, OLED materials or sensing applications. This functionality can be tailored by chemical modification of the ligands and adjustment of the environment through variation of solvents or counterion adduct formation, which both influence the metal-metal interaction. The exploration of ultrafast vibrational and electronic coupling dynamics of multimetallic complexes should shed light on energy partition and relaxation pathways and therefore leads to a deeper understanding of the response of metal-metal interactions to photoexcitation. To this end, and because studies on the ultrafast dynamics on such systems are still rather scarce [2], we investigated a promising prototypical binuclear model system $[\text{Ag}_2(\text{dcpm})_2]^{2+}$, $\mathbf{1}^{2+}$, (dcpm = bis(dicyclohexylphosphino)methane), whose static optical properties like absorption cross sections, luminescence and Raman spectra as well as quantum yields have been well documented [3]. In particular, by performing both gas phase and solution experiments we have studied chemical environment effects (solvated vs. solvent-free chromophore) for $\mathbf{1}^{2+}$ and extend these investigations here by reporting on the excited state dynamics of its chloride ion adduct $[\text{Ag}_2(\text{dcpm})_2\text{Cl}]^+$, $\mathbf{2}^+$ in gas phase.

2. Experimental Setup

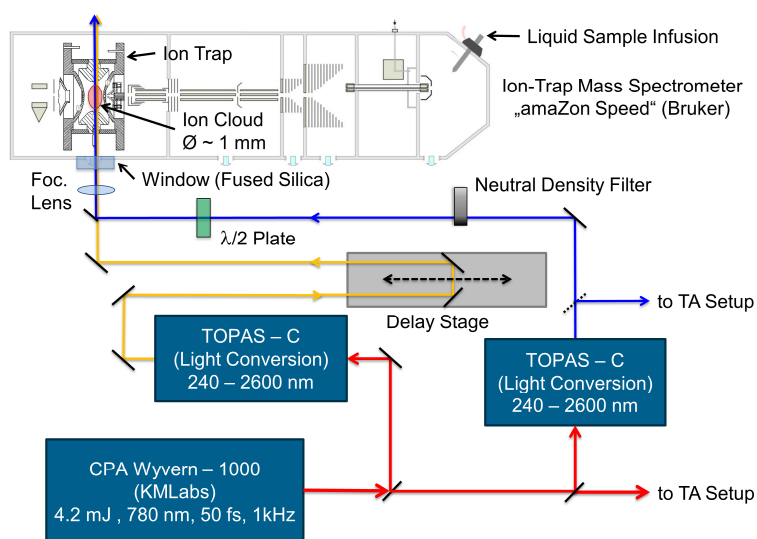


Fig. 1. Scheme of experiment: Paul-type ion trap electrospray mass-spectrometer (ESI-MS) combined with femtosecond laser setup. The fs laser is utilized for both, femtosecond transient photo-induced dissociation (τ -PID) and transient absorption (TA) experiments.

The ultrafast studies are based on femtosecond transient photo-induced dissociation (τ -PID) for gas phase [4, Fig.1] and transient absorption (TA) for solution experiments. We use a 1 kHz 50 fs-amplified Ti:Sa-laser system equipped with two optical parametrical generator/amplifier units for independent wavelength tuning (240-2600 nm) of pump (UV, spectral width \sim 4 nm FWHM) and probe pulses (NIR for τ -PID / continuum generated white light in CaF₂ for TA) in combination with a modified electrospray ionization (ESI) Paul-type ion trap mass spectrometer (MS) for ion selection, storage and fragment mass analysis (up to m/z 3000). Laser beams are introduced into the ion trap through fused silica windows (3 mm thickness) and focused to \sim 1 mm diameter at position of the ion cloud. The relative polarization of pump/probe beams was set to magic angle using a Berek compensator as $\lambda/2$ plate for both, τ -PID and TA. The experimental time resolution was estimated by measurement of the cross-correlation (λ_{pump} : 260 nm / λ_{probe} : 1150 nm) using multi-photon ionization of neutral furan background gas in the ion trap (FWHM \sim 200 fs, τ -PID) and cross-phase modulation in CaF₂ (FWHM \sim 120 fs, TA). The pump and probe pulse energies for τ -PID are set to \sim 1 μ J and \sim 160 μ J, respectively, whereas for TA a pump pulse energy of 200-600 nJ is used.

3. Results and discussion

The first complex (1^{2+} , inset Fig. 2a) displays only weak luminescence in acetonitrile, but exhibits two main bands at \sim 380 nm and 520-660 nm upon UV excitation. From resonance Raman experiments a $\nu(\text{Ag-Ag})$ stretching vibration of 80 cm^{-1} in the electronic ground state was obtained [3]. Furthermore, as response to excitation of the metal-centered $^1\text{MC}(\text{d}\sigma^*-\text{p}\sigma)$ transition at 262 nm, a shortening of the Ag-Ag distance by -0.20 \AA was estimated [3].

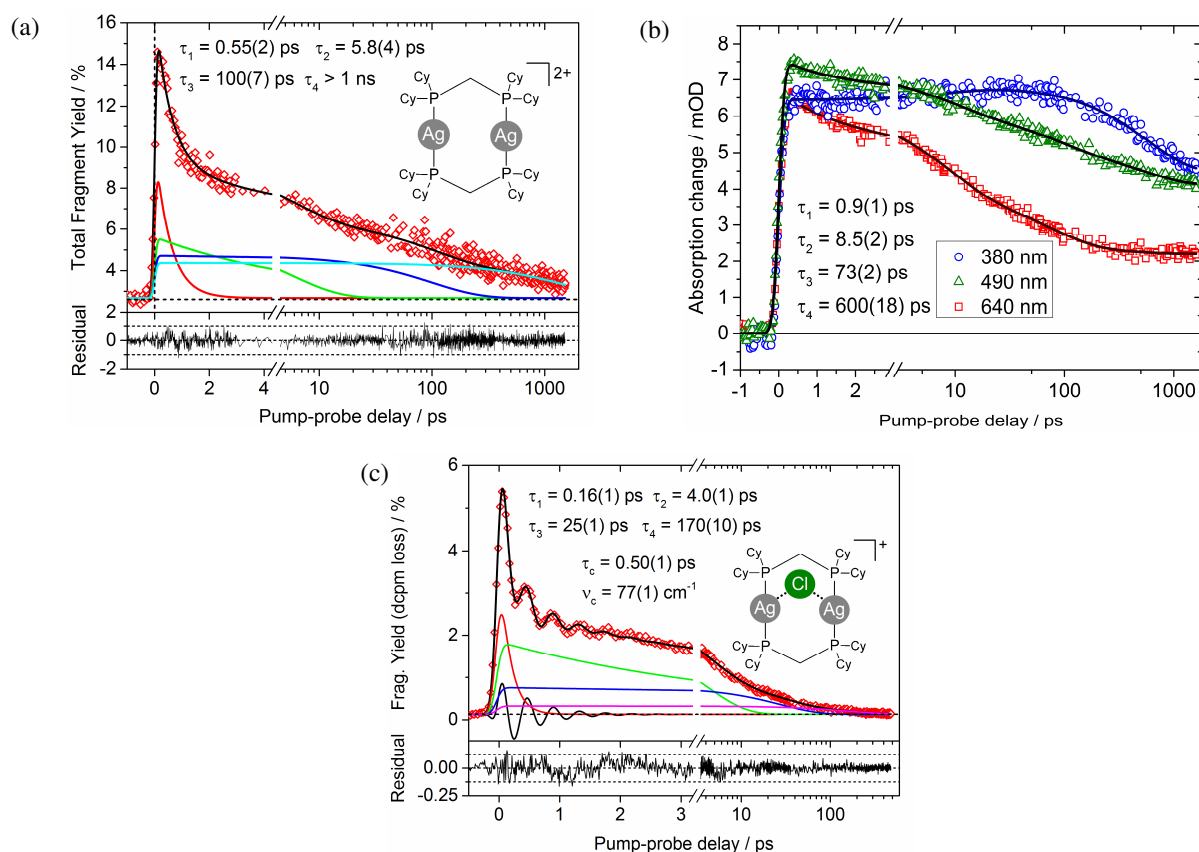


Fig. 2. (a) Decay dynamics in the ion trap given by the transient total fragment yield of 1^{2+} (λ_{pump} : 260 nm, 1 μ J / λ_{probe} : 1150 nm, 160 μ J). Inset: schematic structure of 1^{2+} (Cy= cyclohexyl). (b) Transient absorption of 1^{2+} in acetonitrile (λ_{pump} : 260 nm / λ_{probe} : 380, 490, 640 nm), (c) Decay dynamics of 2^+ in the ion trap given by dcpm-loss fragment yield (λ_{pump} : 260 nm, 1 μ J / λ_{probe} : 1150 nm, 150 μ J). Dataset was fitted by convolution of a Gaussian (FWHM = 80 fs) with sum of tetra-exponential decay function and a damped sine function. Inset: schematic structure of 2^+ . Fitted values are indicated with errors in parentheses corresponding to one standard deviation.

Recording the photofragmentation yield of mass selected ions 1^{2+} as a function of wavelength revealed a characteristic absorption band (250-280 nm) in gas phase, very similar to the absorption spectrum in solution [3]. The gas phase excited state dynamics (λ_{exc} : 260 nm) extracted from the transient total fragment yield (Fig. 2a) is fitted by a tetra-exponential decay function (time constants: 0.55(2), 5.8(4), 100(7), >1000 ps). In parallel, transient absorption spectroscopy in acetonitrile (Fig. 2b) using femtosecond UV pump and white light probe pulses (350-700 nm) revealed lifetimes of ca. 0.9(1), 8.5(2), 73(2), 600(18) ps and additionally a long-lived residual (> 1ns) for the same excitation wavelength. Due to this very similar dynamics in gas phase and solution, we interpret the tetra-exponential decay as mainly intrinsic electronic dynamics of the Ag-Ag chromophore and attribute the respective smallest time constants (0.55 gas phase / 0.9 ps in acetonitrile) to ultrafast intersystem crossing (ISC) in comparison to the (Au^I-Au^I) congener of 1^{2+} ($\tau(\text{ISC}) \sim 0.15$ ps [2]). ISC is followed by successive deactivation processes, presumably by internal conversion within the triplet manifold. Here an influence of solvent molecules is clearly discernible, in particular for the larger time constants.

Additionally, the observed long-lived excited state in solution could be related to the formation of specific complexes with the solvent molecules or long lived exciplex-type states, as was recently put forward for the related Au^I-Au^I complex [2]. To this point the nature of the complex-solvent interaction governing the excited state dynamics, e.g. direct coordination of acetonitrile molecules to silver centers or vibrational coupling facilitating energy dissipation, is speculative and awaits further studies. Moreover, theoretical investigations of the energies and structures of the excited states are mandatory for a thorough analysis.

The second molecular target (2^+ , inset Fig. 2c) is represented by the chloride ion adduct (Ag^I-Ag^I)-Cl ($[\text{Ag}_2(\text{dcpm})_2\text{Cl}]^+$), which was generated by electrospray ionization (from solution of $1(\text{PF}_6)_2$ salt and tetrabutylammonium chloride in acetonitrile), isolated and identified by mass analysis via its characteristic isotope pattern around m/z 1067 (most abundant mass). We propose a bridging coordination motif of Cl⁻ (μ -chlorido) on the basis of known structures of similar halide-adduct complexes. The photo-induced dissociation spectrum [5] reveals two gas phase spectroscopic features, a rising edge at < 245 nm and a band at 250-300 nm. Since the latter peaking at ~ 260 nm may be related to the $^1\text{MC}(\text{d}\sigma^*-\text{p}\sigma)$ transition observed for 2^+ , we used this wavelength for excitation. In the following the influence of Cl⁻ coordination on the excited-state dynamics will be discussed.

The transient photo-induced dissociation signal (Fig. 2c) of 2^+ is dominated by dcpm-loss ($-m/z$ 408, loss of one complete diphosphine ligand) displaying a tetra-exponential decay (time constants: 0.16(1), 4.0(1), 25(1), 170(10) ps) with an apparent, damped oscillatory component (time constant of damping: $\sim 0.50(1)$ ps, frequency: $\sim 77(1)$ cm⁻¹). The latter is assigned to vibrational wavepacket dynamics, presumably related to the excited-state $\nu(\text{Ag}-\text{Ag})$ stretching vibration (modified by the bridging chloride ion).

Surprisingly, this vibrational wavepacket displays a phase shift (of π) depending on the detected fragment channel (e.g. HCl loss, $-m/z$ 36), which is indicative of specific coupling at the classical turning points of the Ag-Ag(Cl) oscillation, governing very early on in the relaxation dynamics the subsequent pathways for fragmentation. Furthermore, it is clearly discernible that Cl⁻ addition leads to a faster electronic deactivation (Fig. 2c).

The question arises why vibrational coherence is observed for 2^+ at all and not for 1^{2+} , neither in gas phase nor in solution, although the overall dynamics and structural changes on the Ag^I-Ag^I chromophore are supposedly similar? For an answer we have to await theoretical *ab-initio* investigations of the relevant excited electronic states and potential energy scans, e.g., along the Ag^I-Ag^I and Ag^I-Ligand coordinates.

Acknowledgments Financial support by the DFG-funded transregional collaborative research center SFB/TRR 88 “3MET” is gratefully acknowledged (Project C4).

References

- [1] H. Schmidbaur, A. Schier, *Angew. Chem. Int. Ed.* **54**, 746-784 (2015).
- [2] C. Ma, C. T.-L. Chan, W.-P. To, W.-M. Kwok, C.-M. Che, *Chem. Eur. J.* **21**, 13888-13893 (2015).
- [3] D. L. Phillips, C.-M. Che, K. H. Leung, Z. Mao, M.-C. Tse, *Coord. Chem. Rev.* **249**, 1476-1490 (2005).
- [4] Y. Nosenko, C. Riehn, W. Klopper, *Chem. Phys. Lett.*, **659**, 55-60 (2016).
- [5] S. V. Kruppa, Y. Nosenko, M.-O. Winghart, S. P. Walg, M. M. Kappes, C. Riehn, *Int. J. Mass. Spectrom.*, **395**, 7-19 (2016).

Excited state vibrational coherence in a binuclear metal adduct: wave packet phase dependant molecular fragmentation under variation of ligand size

Preamble

The following chapter is a reprint of a conference paper from the conference proceedings “XXI International Conference on Ultrafast Phenomena (UP 2018)”. Experimental work and data analysis was performed by myself. The paper draft was written by myself and revised by Priv.-Doz. Dr. Christoph Riehn.

S. V. Kruppa, F. Bäßler, C. Holzer, F. Dietrich, R. Diller, W. Klopper, C. Riehn, *Conference Proceedings, XXI International Conference on Ultrafast Phenomena (UP 2018), Hamburg, Germany, EPJ Web Conf., 2019, 205, 09019, <https://doi.org/10.1051/epjconf/201920509019>*

Copyright © 2019 The Authors, published by EDP Sciences

Reprint Licence

Open Access

Issue	EPJ Web Conf. Volume 205, 2019 XXI International Conference on Ultrafast Phenomena 2018 (UP 2018)
Article Number	09019
Number of page(s)	3
Section	Ultrafast Photochemistry and Photosynthesis
DOI	https://doi.org/10.1051/epjconf/201920509019
Published online	16 April 2019

EPJ Web of Conferences 205, 09019 (2019)

<https://doi.org/10.1051/epjconf/201920509019>

Excited state vibrational coherence in a binuclear metal adduct: wave packet phase dependant molecular fragmentation under variation of ligand size

Sebastian Volker Kruppa^{1*}, Florian Böppler², Christof Holzer³, Fabian Dietrich¹, Rolf Diller², Wim Klopper³ and Christoph Riehn^{1,4*}

¹ TU Kaiserslautern, Chemistry Dept., Erwin-Schrödinger Str. 52-54, 67663 Kaiserslautern, Germany

² TU Kaiserslautern, Physics Dept., Erwin-Schrödinger Str. 46, 67663 Kaiserslautern, Germany

³ Karlsruhe Institute of Technology, Institute of Physical Chemistry, Fritz-Haber Weg 2, 76131 Karlsruhe, Germany

⁴ Landesforschungszentrum OPTIMAS, Erwin-Schrödinger Str. 46, 67663 Kaiserslautern, Germany

* Corresponding authors: kruppa@chemie.uni-kl.de, riehn@chemie.uni-kl.de

Published online: 16 April 2019

Abstract

Ultrafast vibrational coherence with metal-metal stretching mode character is observed for phosphine-bridged d10-d10 complexes of different size, containing the binuclear [Ag₂Cl]⁺ chromophore in an ion trap. Fragmentation pathways are governed by the wave packet's phase.

© The Authors, published by EDP Sciences, 2019



This is an Open Access article distributed under the terms of the [Creative Commons Attribution License 4.0](https://creativecommons.org/licenses/by/4.0/), which permits unrestricted use, distribution, and reproduction in any medium, provided the original work is properly cited.

Excited state vibrational coherence in a binuclear metal adduct: wave packet phase dependant molecular fragmentation under variation of ligand size

Sebastian Volker Kruppa^{1,*}, Florian Bäßler², Christof Holzer³, Fabian Dietrich¹, Rolf Diller², Wim Klopper³, and Christoph Riehn^{1,4,*}

¹TU Kaiserslautern, Chemistry Dept., Erwin-Schrödinger Str. 52-54, 67663 Kaiserslautern, Germany

²TU Kaiserslautern, Physics Dept., Erwin-Schrödinger Str. 46, 67663 Kaiserslautern, Germany

³Karlsruhe Institute of Technology, Institute of Physical Chemistry, Fritz-Haber Weg 2, 76131 Karlsruhe, Germany

⁴Landesforschungszentrum OPTIMAS, Erwin-Schrödinger Str. 46, 67663 Kaiserslautern, Germany

Abstract. Ultrafast vibrational coherence with metal-metal stretching mode character is observed for phosphine-bridged d^{10} - d^{10} complexes of different size, containing the binuclear $[\text{Ag}_2\text{Cl}]^+$ chromophore in an ion trap. Fragmentation pathways are governed by the wave packet's phase.

1 Introduction

Ultrafast photo-induced dynamics of ligand-stabilized transition metal complexes is a rapidly advancing field due to their widespread applications e.g. in organic light emitting diodes (OLEDs), sensors, light harvesting (dye-sensitized solar cells), photocatalysis and medicine. Thus, many femto/picosecond-resolved methods are currently employed such as transient optical spectroscopy, 4D electron diffraction as well as front-edge X-ray techniques. However, gas phase studies giving insight into the intrinsic dynamics in the absence of a surrounding medium are still scarce.

Our gas phase approach is based on time-resolved photodissociation (τ -PD) action spectroscopy [1-3] of mass-selected, ion-trapped molecular systems, probing their electronic dynamics by way of transient fragmentation patterns as a function of pump-probe delay. Besides information on excited state kinetics, we focus on the question of how a subtle quantum phenomenon such as vibrational coherence is influenced by structural and electronic parameters, modulating cooperative metal-metal interaction.

Therefore, we studied d^{10} - d^{10} complexes by example of the phosphine-ligand bridged $[\text{Ag}_2(\text{Cl})]^+$ scaffold (Fig. 1), providing opportunities for chemical modifications e.g. by variation of the ligand size. We compare the wave packet dynamics of complexes with the bulky L^{Cy} ligands (**2**⁺, 149 atoms, R = C₆H₁₁, cyclohexyl) to those of the smaller L^{Me} ligands (**1**⁺, 45 atoms, R = CH₃, methyl) and observe a correlation between the wave

* Corresponding authors: kruppa@chemie.uni-kl.de, riehn@chemie.uni-kl.de

packet's phase and fragment type and an (at first glance) astonishing slow-down of vibrational dynamics as discussed in the next section.

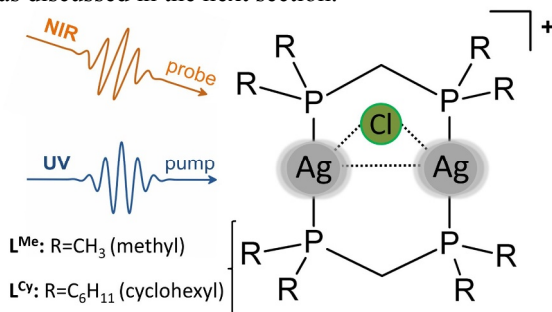


Fig. 1. Schematic structures of complexes $[\text{Ag}_2(\text{Cl})(\text{L}^{\text{Me}})_2]^+$, $\mathbf{1}^+$ and $[\text{Ag}_2(\text{Cl})(\text{L}^{\text{Cy}})_2]^+$, $\mathbf{2}^+$, respectively (L^{Me} = bis(dimethylphosphino)methane, L^{Cy} = bis(dicyclohexylphosphino)methane). For τ -PD experiment UV-pump (280 nm) and NIR-probe (1150 nm) pulses were used.

2 Results and Discussion

The experimental setup and methodology is described elsewhere [1-3]. The chloride adducts $[\text{Ag}_2(\text{Cl})(\text{L}^{\text{Me}})_2]^+$ ($\mathbf{1}^+$) and $[\text{Ag}_2(\text{Cl})(\text{L}^{\text{Cy}})_2]^+$ ($\mathbf{2}^+$) were generated by electrospray ionization from acetonitrile sample solutions, isolated and identified by mass analysis via their characteristic isotope patterns ($m/z = 521$ and 1065 , resp. nominal masses). The static photo-induced dissociation (PD) spectra show a band at $\lambda_{\text{max}} \sim 280$ nm and a plateau-like form centered at ~ 260 nm for $\mathbf{1}^+$ and $\mathbf{2}^+$, resp. Based on calculations (PBE0-D3(BJ)/evGW-BSE/def2-SVPD) [4], using $\mathbf{1}^+$ as model system, we assign these excitations to HOMO-1 \rightarrow LUMO ($^1\text{XMCT}$) transitions with chloride-to-metal-metal charge transfer character [1]. Hereby a contraction of the Ag-Ag distance by ~ 0.1 Å is predicted (CC2/def2-TZVPP), indicating a strengthening of Ag-Ag interaction in the electronically excited state.

The τ -PD signals of $\mathbf{1}^+$ at positive time delay show an increase in the channels corresponding to neutral loss of Cl, AgCl and $\text{AgCl} + \text{L}^{\text{Me}}$, resp., and a concomitant decrease in intensity for $-\text{L}^{\text{Me}}$ fragment species (Fig. 2 c). The early decay dynamics of $\mathbf{1}^+$ with time constants 0.2-0.5 / 4-6 ps (Fig. 2) is very similar compared to that of $\mathbf{2}^+$ with 0.2-0.4 / 3-4 ps [1]. Interestingly, a correlation between specific fragment ions (Cl loss vs loss of $\text{L}^{\text{Me}} + \text{AgCl}$) and the phase of the wave packet is observed, as evident by strongly damped (damping constant ~ 0.1 -0.5 ps) oscillatory components in their τ -PD signals (Fig. 2 a, b), exhibiting a relative phase difference of $\sim \pi$. A similar result was obtained for the $[\text{Ag}_2(\text{Cl})(\text{L}^{\text{Cy}})_2]^+$ molecular target displaying an analogous relation mainly for the fragmentations $-\text{HCl}/-\text{Cl}^-$ vs loss of L^{Cy} . Note that the parallel investigation of $[\text{Ag}_2(\text{Cl})(\text{L}^{\text{Cy}})_2]^+$ in condensed phase (acetonitrile) by transient absorption does not yield detectable vibrational wave packet activity.

Since the largest structural changes upon photoexcitation correspond to the decrease of metal distance ($d(\text{Ag}-\text{Ag}) = -3.6\%$) and the bending of P-Ag-P angle ($\alpha(\text{P}-\text{Ag}-\text{P}) = +3.3\%$), this observation strengthens our previous assignment for the vibrational coherence to contain mainly Ag-Ag stretching mode character [1].

Intriguingly, the oscillation frequency for $\mathbf{1}^+$ (43 - 60 cm^{-1}) is significantly smaller than that for $\mathbf{2}^+$ (72 - 78 cm^{-1}). Since a higher frequency value would be expected for $\mathbf{1}^+$ ($\text{mass}(\text{L}^{\text{Me}}) \ll \text{mass}(\text{L}^{\text{Cy}})$) this indicates a significantly weaker Ag-Ag bonding interaction for $\mathbf{1}^+$ compared to $\mathbf{2}^+$ in the excited state. Therefore, we assume that in the excited state metallophilic Ag-Ag interaction is subtly influenced by the ligand moieties (methyl vs cyclohexyl), presumably due to polarization or electron inductive effects.

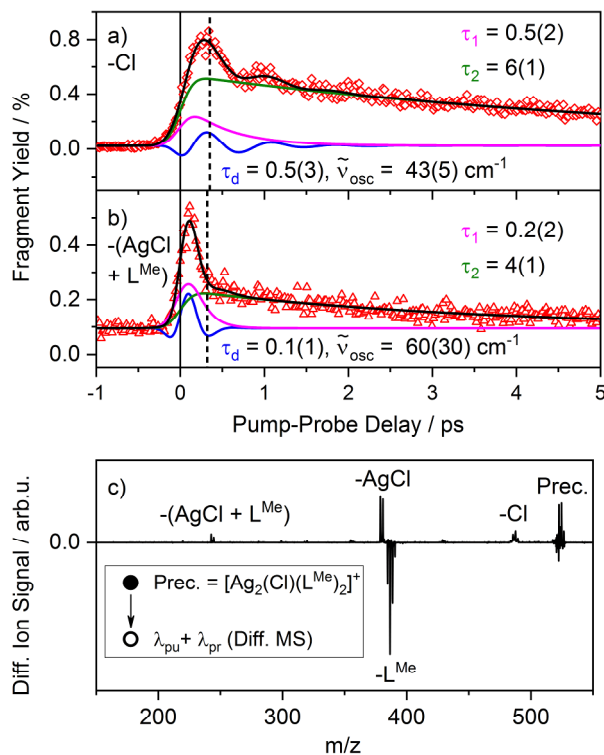


Fig. 2. Fragment-specific transients of $[\text{Ag}_2(\text{Cl})(\text{L}^{\text{Me}})_2]^+$ (λ_{pump} : 280 nm / λ_{probe} : 1150 nm) corresponding to a) loss of Cl atom and b) loss of AgCl + L^{Me}, respectively. Kinetic fits (black lines) and individual decay contributions associated with time constants τ_1 (magenta), τ_2 (green), oscillatory components with coherence decay times τ_d (blue) and oscillation frequencies ν_{osc} are displayed. The fit function corresponds to a convolution of a Gaussian (FWHM \sim 300 fs) with a sum of a biexponential decay function and a damped sine function. c) Difference mass spectrum (Diff. MS) obtained by subtracting the mass spectrum at negative pump-probe delay (\sim -1-0.3 ps) from the spectrum at positive delay (\sim 0.2-0.6 ps). Positive and negative Diff. MS signals correspond to an enhancement and depletion, respectively. Fragment mass peaks are labelled according to their neutral losses relative to the intact precursor ion (Prec.).

Further, we conclude that the cross section for probe absorption, and thus specific excitation, is modulated by the vibrational wave packet at the classical turning points of the Ag-Ag oscillation, leading to the phase-dependent branching ratios of molecular fragmentation channels. These results open new perspectives in leveraging vibrational coherence for chemical processes and should therefore stimulate further experimental and theoretical studies.

References

1. S. V. Kruppa, F. Bappler, C. Holzer, W. Klopper, R. Diller, C. Riehn, J. Phys. Chem. Lett., **9**, 804-810 (2018)
2. S. V. Kruppa, F. Bappler, W. Klopper, S. P. Walg, W. R. Thiel, R. Diller, C. Riehn, Phys. Chem. Chem. Phys., **34**, 22785-22800 (2017)
3. D. Imanbaew, J. Lang, M. F. Gelin, S. Kaufhold, M. G. Pfeffer, S. Rau, C. Riehn, Angew. Chem. Int. Ed., **56**, 5471-5474 (2017)
4. K. Krause, W. Klopper, J. Comput. Chem., **38**, 383-388 (2017)

Time-resolved photoelectron spectroscopy of a dinuclear Pt(II) complex: Tunneling autodetachment from both singlet and triplet excited states of a molecular dianion

Preamble

Since the reprint licence for the complete version of the original manuscript could not be obtained, the reader is referred to the electronic version of the article. My contribution has been support for revising the manuscript.

M.-O. Winghart, J.-P. Yang, M. Vonderach, A.-N. Unterreiner, D.-L. Huang, L.-S. Wang, S. Kruppa, C. Riehn, M.M. Kappes, *J. Chem.Phys.*, **2016**, 144, 054305, <https://doi.org/10.1063/1.4940795>

Copyright © 2016 AIP Publishing LLC

Bimetallic d^{10} -Metal Complexes of a Bipyridine Substituted N-Heterocyclic Carbene

Preamble

The following chapter has been published in the journal „Chemistry A European Journal“. For the supporting information the reader is referred to the electronic version of the article. This publication is based on the PhD thesis of Dr. Christoph Kaub. My contribution to the manuscript has been the mass spectrometric characterization of two sample complexes and the evaluation of their collisional-induced fragmentation behavior in the gas phase. I received experimental support from Patrick H. Strebert, who conducted the mass spectrometric measurements under my supervision.

C. Kaub, S. Lebedkin, A. Li, S. V. Kruppa, P. H. Strebert, M. M. Kappes, C. Riehn, P.W. Roesky, *Chem. Eur. J.*, **2018**, 24(23), 6094-6104,
<https://doi.org/10.1002/chem.201705757>

Copyright ©2018 Wiley-VCH Verlag GmbH & Co. KGaA, Weinheim

Reprint Licence

JOHN WILEY AND SONS LICENSE TERMS AND CONDITIONS

Aug 27, 2020

This Agreement between Mr. Sebastian Kruppa ("You") and John Wiley and Sons ("John Wiley and Sons") consists of your license details and the terms and conditions provided by John Wiley and Sons and Copyright Clearance Center.

License Number	4897130285101
License date	Aug 27, 2020
Licensed Content Publisher	John Wiley and Sons
Licensed Content Publication	Chemistry - A European Journal
Licensed Content Title	Bimetallic d10-Metal Complexes of a Bipyridine Substituted N-Heterocyclic Carbene
Licensed Content Author	Peter W. Roesky, Christoph Riehn, Manfred M. Kappes, et al
Licensed Content Date	Feb 28, 2018
Licensed Content Volume	24
Licensed Content Issue	23
Licensed Content Pages	11
Type of Use	Dissertation/Thesis
Requestor type	Author of this Wiley article
Format	Print and electronic
Portion	Full article
Will you be translating?	No
Title	Photochemistry and Ultrafast Dynamics of Mass-selected Multinuclear Coinage Metal Complexes Studied by Electronic Photodissociation Ion Spectroscopy in an Ion Trap
Institution name	Technische Universität Kaiserslautern (TUK)
Expected presentation date	Oct 2020
Requestor Location	Mr. Sebastian Kruppa Erwin-Schrödinger-Straße 52-54 Kaiserslautern, 67663 Germany Attn: Mr. Sebastian Kruppa
Publisher Tax ID	EU826007151
Total	0.00 EUR
Terms and Conditions	

N-Heterocyclic Carbenes

Bimetallic d¹⁰-Metal Complexes of a Bipyridine Substituted N-Heterocyclic CarbeneChristoph Kaub,^[a] Sergei Lebedkin,^[b] Alina Li,^[b, c] Sebastian V. Kruppa,^[d] Patrick H. Strebart,^[d] Manfred M. Kappes,^[b, c] Christoph Riehn,^[d, e] and Peter W. Roesky^{*[a]}

Abstract: The hybrid ligand 3-(2,2'-bipyridine-6-ylmethyl)-1-mesityl-1H-imidazolylidene (NHC^{Bipy}) featuring both carbene and N-donor sites, was selectively complexed with various d¹⁰ metal cations in order to examine its coordination behavior with regard to homo and heterometallic structures. Respective silver complexes can be obtained by the silver oxide route and are suitable transmetallation reagents for the synthesis of gold(I) compounds. Starting from the mononuclear complexes [(NHC^{Bipy})AuCl], [(NHC^{Bipy})Au(C₆F₅)] and [(NHC^{Bipy})₂Au][ClO₄], open-chain as well as cyclic heterobimetallic complexes containing Cu⁺, Ag⁺, Zn²⁺, Cd²⁺, and Hg²⁺ were synthesized. Furthermore, the homobimetallic species

[(NHC^{Bipy})₂M₂][ClO₄]₂ (M = Cu, Ag) were obtained. All bimetallic compounds were fully characterized including single-crystal X-ray analysis. Their photoluminescence (PL) properties were investigated in the solid state at temperatures between 15 and 295 K and compared with those of the mononuclear species. There is a clear difference in PL properties between the open chain and the cyclic heterobimetallic complexes. The latter species show different PL properties, depending on the metals involved. In addition, collision-induced dissociation (CID) experiments were performed on electrosprayed cations of the cyclic heterobimetallic compounds, to compare the metal binding at the carbene and N-donor sites.

Introduction

The properties of polynuclear metal complexes may be strongly modified in comparison to their mononuclear precursors, particularly, due to possible intermetallic interactions. For instance, among complexes of gold(I), many examples of com-

pounds exhibiting close arrangements of the metal ions beneath the sum of their van der Waals radii are known. This prompted Schmidbaur in the late 1980s to introduce the term "aurophilicity" for this phenomenon.^[1] Later, it became evident that such attractive forces are not limited to gold but also observed for other heavy-metal closed-shell cations and can be described by the general term "metallophilicity".^[2] Besides gold(I), metallophilic interactions have been observed for copper,^[3] silver,^[4] and mercury^[5] as well as in heterometallic d¹⁰/d¹⁰,^[6] d¹⁰/d⁸,^[7] or d¹⁰/s² systems.^[8] These compounds with short intermetallic distances often feature interesting photo-physical properties.^[9] We and many other researchers have already taken advantage of the easy "tunability" of N-heterocyclic carbenes (NHCs) to design tailor-made ligands for multinuclear complexes. Many examples of symmetric, typically phosphine functionalized NHCs are known and have been used in the coordination chemistry of coinage metals.^[10,11] Due to a similar coordination behaviour of NHCs and phosphines, this type of ligands is suitable for the synthesis of homometallic compounds, while heterometallic examples are hardly accessible.^[12] For this purpose, the use of N-donor functionalized ligands is beneficial, as they feature different coordination behaviour. The latter can be classified according to the HSAB concept as soft and hard donors in the case of the NHC and N-donor sites, respectively.^[13,14] As a result, they can be selectively loaded with different metals. Although several N-donor functionalized NHCs are already known for years, their use for the synthesis of heterometallic complexes is scarcely explored.^[15-18] Recently, we reported a ligand having N-heterocyclic carbenes (NHCs) separated by a methylene bridge in the center and two

[a] Dr. C. Kaub, Prof. Dr. P. W. Roesky
Institute of Inorganic Chemistry
Karlsruhe Institute of Technology (KIT)
Engesserstr. 15, 76131 Karlsruhe (Germany)
E-mail: roesky@kit.edu

[b] Dr. S. Lebedkin, A. Li, Prof. Dr. M. M. Kappes
Institute of Nanotechnology
Karlsruhe Institute of Technology (KIT)
Hermann-von-Helmholtz-Platz 1, 76344
Eggenstein-Leopoldshafen (Germany)

[c] A. Li, Prof. Dr. M. M. Kappes
Institute of Physical Chemistry
Karlsruhe Institute of Technology (KIT)
Fritz-Haber Weg 2, 76131 Karlsruhe (Germany)

[d] S. V. Kruppa, P. H. Strebart, Dr. C. Riehn
Department of Chemistry
TU Kaiserslautern
Erwin-Schrödinger Str. 52-54
67663 Kaiserslautern (Germany)

[e] Dr. C. Riehn
Forschungszentrum OPTIMAS
TU Kaiserslautern
Erwin-Schrödinger-Str. 46
67663 Kaiserslautern (Germany)

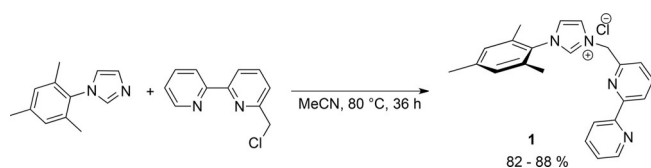
Supporting information and the ORCID identification number(s) for the author(s) of this article can be found under:
<https://doi.org/10.1002/chem.201705757>.

bipyridine moieties tethered to the NHCs. By using this we have synthesized tetranuclear heterodimetallic gold/copper and gold/silver complexes.^[19] These compounds show unprecedented V-shape or linear MAu₂M (M = Cu, Ag) geometry in the solid state. In order to further extend the field of heterometallic complexes having a combination of coinage metals with other transition metals, we decided to apply the bipyridine substituted N-heterocyclic carbene ligand 3-(2,2'-bipyridine-6-ylmethyl)-1-mesityl-1*H*-imidazolylidene (NHC^{BiPy}) and examine its coordination behaviour in homo- and heterometallic complexes of d¹⁰ cations. Here, we report on the synthesis and characterization of several homo- and heterometallic complexes of NHC^{BiPy}. Furthermore, their photophysical properties in the solid state as well as collision-induced dissociation (CID) experiments^[20] in the gas phase are presented.

Results and Discussion

Ligand synthesis

The proligand 3-(2,2'-bipyridine-6-ylmethyl)-1-mesityl-1*H*-imidazolylidene hydrochloride (NHC^{BiPy}) (1) was prepared according to a literature procedure from 6-chloromethyl-2,2'-bipyridine and mesitylimidazole (Scheme 1).^[21]

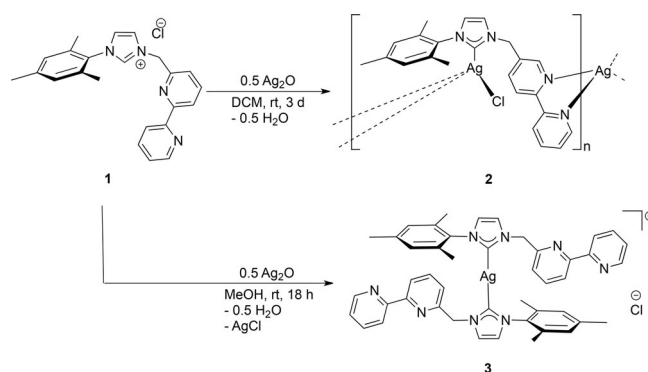


Scheme 1. Synthesis of the proligand 3-(2,2'-bipyridine-6-ylmethyl)-1-mesityl-1*H*-imidazolylidene hydrochloride (NHC^{BiPy}·HCl) (1).

Silver complexes

As a synthetic approach for the formation of metal complexes of NHC^{BiPy}·HCl (1) we chose the well-established silver oxide route.^[22] In dependence of the solvent used, different products are formed upon reaction of 1 with 0.5 equivalents of Ag₂O. Using dichloromethane leads to the neutral silver complex [(NHC^{BiPy})AgCl] (2), whereas the reaction in methanol gave the ionic species [(NHC^{BiPy})₂Ag]Cl (3) (Scheme 2). It is known that the formation of either neutral or ionic silver species depends on the solvents used and the substituents of the NHC. The equilibrium between both species is well documented.^[23,24]

For both products, the resonance of the proton at the C1 position in the ¹H NMR spectrum ($\delta = 9.78$ ppm) is absent, indicating a complete transformation of the imidazolium salt to the silver complexes. In agreement with this, in the ¹³C[¹H] NMR spectrum of 2, a doublet at $\delta = 182.1$ ppm with a coupling constant of $^1J_{Ag,C} = ca. 241$ Hz is observed. Due to the broadness of the signal, the expected set of two doublets corresponding to the nuclei ¹⁰⁷Ag and ¹⁰⁹Ag cannot be resolved as separate signals. Also, the intensity of this signal is very weak. For complex 3, as expected, two doublets at $\delta = 183.7$ ppm



Scheme 2. Synthesis of the silver complexes [(NHC^{BiPy})AgCl] (2) and [(NHC^{BiPy})₂Ag]Cl (3).

with the coupling constants $^1J(^{107}Ag,C) = 181.4$ Hz and $^1J(^{109}Ag,C) = 208.8$ Hz are observed. All described shifts and coupling constants are in the range that is typical for NHC-silver complexes.^[25] The identity of compound 3 was further confirmed by ESI-MS spectrometry. The most abundant mass at $m/z = 817.28$ and isotopic pattern is consistent with the formulation as [(NHC^{BiPy})₂Ag]⁺. The molecular structure of compound 2 was established by single-crystal X-ray analysis (Figure 1).

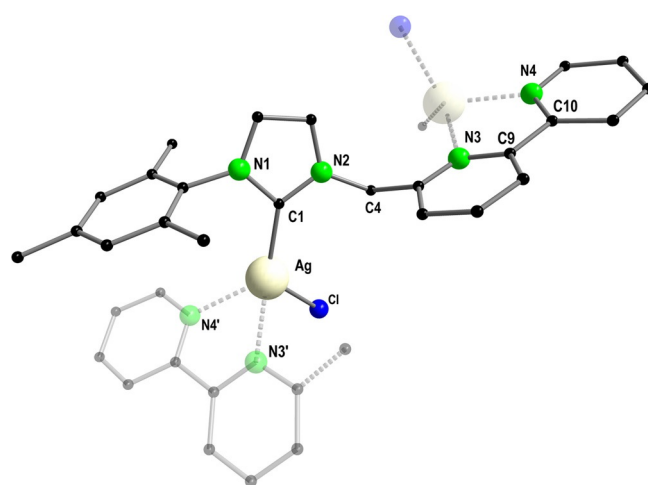


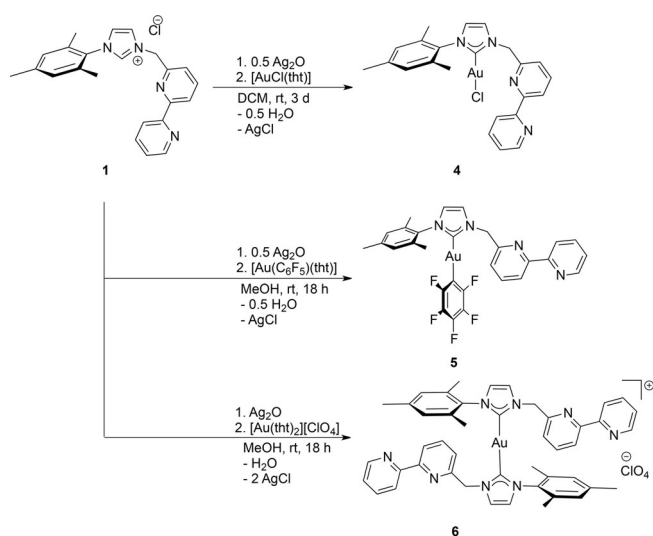
Figure 1. Molecular structure of 2 in the solid state. Hydrogen atoms are omitted for clarity. Atoms that belong to the neighbouring molecular unit are shaded. Selected bond lengths [Å] and angles [°]: Ag–C1 2.1067(4), Ag–Cl1 2.5852(6), Ag–N3' 2.4140(5), Ag–N4' 2.3698(6), N1–C1 1.3798(4), N2–C1 1.3567(3); C1–Ag–Cl1 122.6, C1–Ag–N3' 125.3, C1–Ag–N4' 126.6, N3'–Ag–N4' 69.1, Cl1–Ag–N3' 97.5, Cl1–Ag–N4' 101.7, N1–C1–N2 101.888(14), N1–C1–Ag 125.279(7), N2–C1–Ag 132.4555(9), N3–C9–C10–N4 14.02(2).

Compound 2 crystallizes in the monoclinic space group *P*2₁/*n* with one molecule in the asymmetric unit. In the solid state, a polymeric structure is formed, in which each silver atom is bound to one chlorine atom, the NHC carbon atom, and additionally to the bipyridine moiety of the neighbouring molecule in a chelating mode. This results in a distorted tetrahedral environment around the silver atom. The C1–Ag and

Ag–Cl bond lengths are 2.1067(4) and 2.5852(6) Å, which is significantly longer than in linear coordinated [(NHC)AgCl] complexes. The Ag–N bond lengths of 2.3698(6) and 2.4140(5) Å are similar to those in the simple [(Bipy)₂Ag][ClO₄] complex.^[26] To the best of our knowledge (research in CCDC database),^[27] no comparable fourfold coordinated AgCl complexes with one NHC and two nitrogen donors have been published yet.

Gold complexes

The synthesis of the gold complexes [(NHC^{Bipy})AuCl] (**4**), [(NHC^{Bipy})Au(C₆F₅)] (**5**) and [(NHC^{Bipy})₂Au][ClO₄] (**6**) was achieved by transmetalation with the corresponding gold reagents [AuCl(tht)], [AuC₆F₅(tht)], and [Au(tht)₂][ClO₄] (Scheme 3). Both silver complexes **2** and **3** were suitable for this procedure.



Scheme 3. Synthesis of the gold complexes [(NHC^{Bipy})AuCl] (**4**), [(NHC^{Bipy})Au(C₆F₅)] (**5**) and [(NHC^{Bipy})₂Au][ClO₄] (**6**).

However, when dichloromethane was used as a solvent, the yield as well as the purity after a simple workup were repeatedly slightly superior to the results obtained with methanol. Therefore, we chose dichloromethane despite much longer reaction times. Upon addition of the gold reagents, rapid precipitation of AgCl clearly indicated successful transmetalation. After workup, products **4–6** were obtained as colourless solids, which are soluble in common polar solvents like methanol, dichloromethane or acetonitrile.

Compounds **4–6** were fully characterized using standard analytical techniques and the solid-state structures of **4** and **5** were deduced by X-ray analysis (Figure 2). The ¹H NMR spectra of **4–6** are almost identical and show no significant differences compared to those of the silver complexes. The signals of the bipyridine moiety are seen in the region between 8.68–7.33 and show well structured coupling patterns. The protons of the imidazole backbone show doublets at 7.37 and 6.91 ppm. The protons of the methylene linker give a singlet at 5.67 ppm. The carbene resonances in the ¹³C{¹H} spectra are found at δ = 172.8 ppm (**4**), 190 ppm (**5**) and 185.4 ppm (**6**). These are typical values for NHC gold complexes bearing chlorido,^[28] or pentafluorophenyl^[29,10] substituents or (bis)NHC complexes.^[30] In the solid-state, compounds **4** and **5** show the common coordination number of two around the gold atoms with only small deviations from linearity (177.4(2)° (**4**) and 176.7(2)° (**5**)). For the chlorido complex bond lengths C1–Au: 1.975(5) Å and Au–Cl1: 2.274(2) Å are observed, which are typical values for this type of compound.^[31] The Au–C distance for the NHC carbon atom in **5** (2.017(5) Å) is slightly longer than in **4**, most likely due to a higher *trans* influence of the pentafluorophenyl substituent. The buried volume (%V_{bur}) of the ligand **1** was determined using *SambVca 2*.^[32] Due to the flexibility of the ligand it varies from 32.2 to 36.2% for **4** and **5** and reaches up to 40.3% in **13** (see below). The solid-state structure of **6** remains undisclosed, as several attempts to grow single crystals failed.

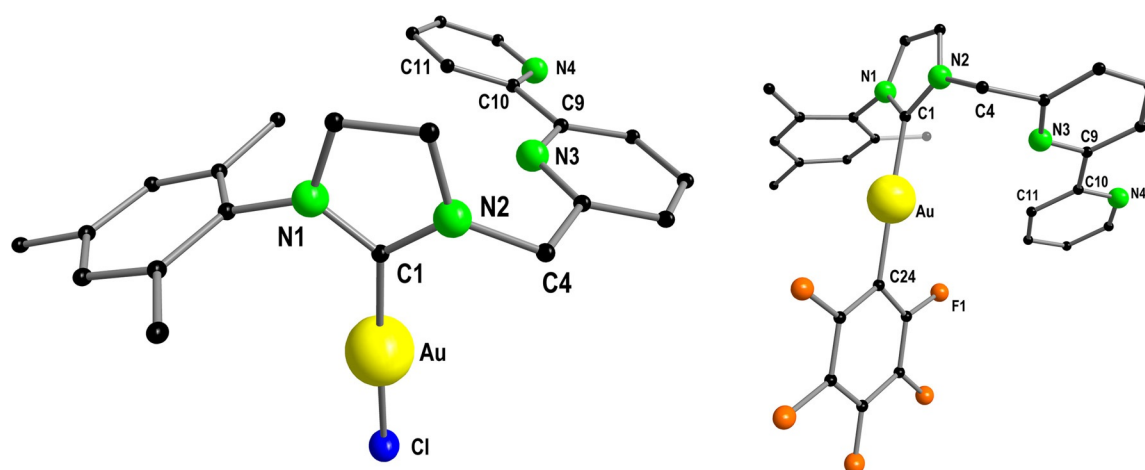
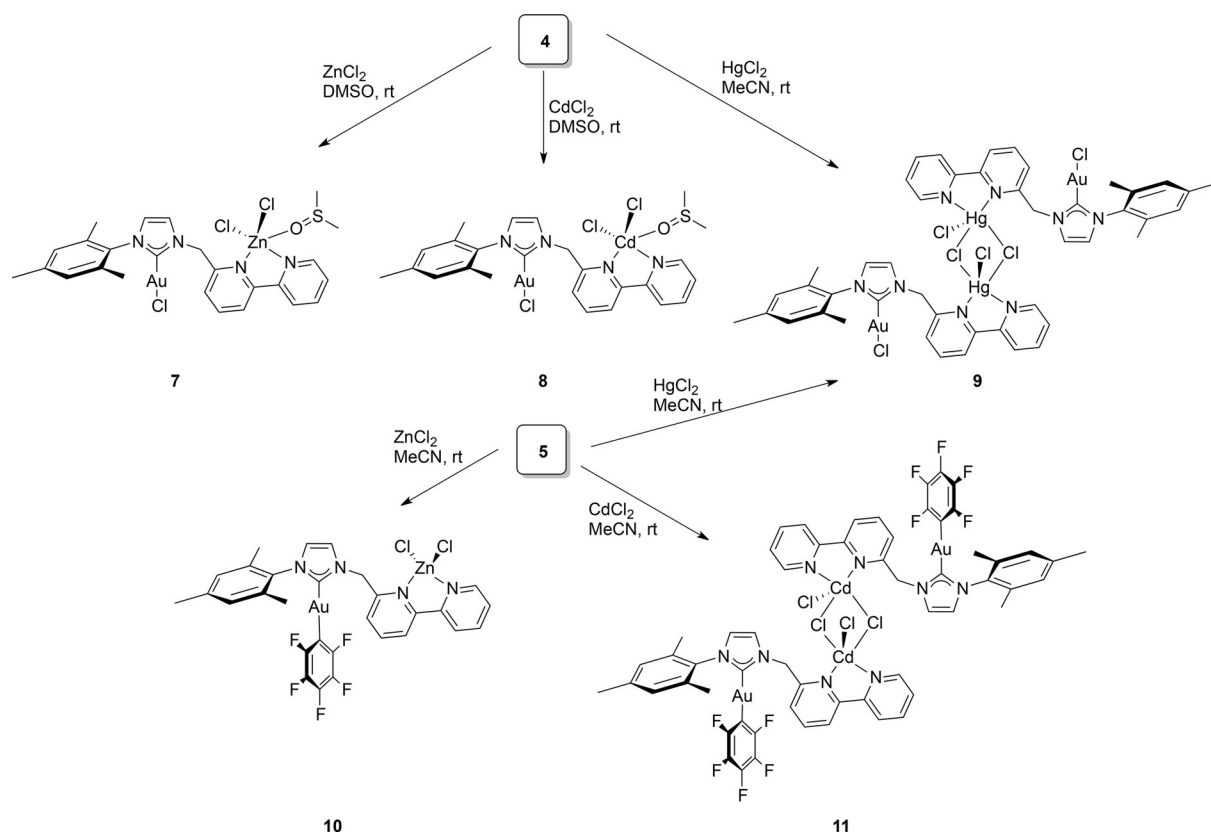


Figure 2. Molecular structure of **4** (left) and **5** (right) in the solid state. Hydrogen atoms are omitted for clarity. Selected bond lengths [Å] and angles [°] of **4**: Au–C1 1.972(4), Au–Cl 2.2752(12), N1–C1 1.365(5), N2–C1 1.342(5); C1–Au–Cl 177.53(13), N1–C1–Au 127.8(3), N2–C1–Au 127.4(3), N1–C1–N2 104.8(4), N3–C9–C10–C11 9.0(1). Selected bond lengths [Å] and angles [°] of **5**: Au–C1 2.018(5), Au–C24 2.035(5), N1–C1 1.348(6), N2–C1 1.339(6); C1–Au–C24 176.7(2), N1–C1–Au 124.7(4), N2–C1–Au 130.2(4), N1–C1–N2 105.0(4), N3–C9–C10–C11 3.2(7), N2–C1–C24–C25 73.2(6).



Scheme 4. Synthesis of the heterobimetallic complexes [(NHC^{Bipy})AuCl(ZnCl₂)(DMSO)] (7), [(NHC^{Bipy})AuCl(CdCl₂)(DMSO)] (8), [(NHC^{Bipy})AuCl(HgCl₂)₂] (9), [(NHC^{Bipy})Au(C₆F₅)(ZnCl₂)] (10) and [(NHC^{Bipy})Au(C₆F₅)(CdCl₂)₂] (11).

Open-chain heterobimetallic complexes

To investigate the coordination behaviour of ligand 1 in bimetallic complexes, the gold compounds 4 and 5 were reacted with the dichlorides of group 12 metals to add a second d¹⁰ cation in the bipyridine compartment (Scheme 4). Reaction of the gold chlorido complex 4 with the metal salts ZnCl₂, CdCl₂ and HgCl₂ gave the desired products [(NHC^{Bipy})AuCl(ZnCl₂)(DMSO)] (7), [(NHC^{Bipy})AuCl(CdCl₂)(DMSO)] (8), and [(NHC^{Bipy})AuCl(HgCl₂)₂] (9) in good yields of about 80% after crystallization. Due to their poor solubility in other solvents, compounds 7 and 8 had to be crystallized from dimethylsulfoxide (DMSO). The corresponding mercury compound 9 decomposes in DMSO within several hours and therefore was crystallized from (a large amount of) acetonitrile.

For all three new products, ¹H as well as ¹³C{¹H} spectra remain virtually unchanged compared to the starting compound 4. In the solid state, coordination of the second metal does not notably affect the coordination geometry of the gold atom. All bond lengths and angles stay the same within a deviation range of 0.01 Å or 2°, respectively. The bipyridine moiety is turned away from the carbene center, which results in large metal–metal distances of 6.8272(6)–7.080(3) Å (Figure 3).

Any closed-shell interactions that can often be observed in d¹⁰ coinage metal complexes are therefore excluded.^[2] Zinc and cadmium show a distorted trigonal bipyramidal coordination sphere with oxygen and one of the bipyridine nitrogen atoms in the axial positions, while the chlorine atoms and the

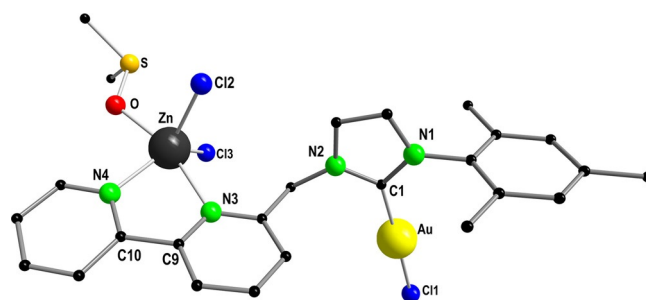


Figure 3. Molecular structure of 7 in the solid state. Hydrogen atoms are omitted for clarity. Intermetallic distance [Å]: Au–Zn 6.909(3). Selected bond lengths [Å] and angles [°]: Au–C1 1.980(5), Au–Cl1 2.273(2), Zn–N3 2.261(4), Zn–N4 2.074(4), Zn–Cl2 2.305(2), Zn–Cl3 2.281(2), Zn–O 2.101(4), N1–C1 1.348(7), N2–C1 1.347(7); C1–Au–Cl1 178.3(2), N3–Zn–N4 76.6(2), N3–Zn–Cl2 94.34(11), N3–Zn–Cl3 97.968(11), N3–Zn–O 162.53(14), N4–Zn–O 85.96(15), N4–Zn–Cl2 17.63(12), N4–Zn–Cl3 128.40(12), O–Zn–Cl2 94.94(13), O–Zn–Cl3 91.74(12), Cl2–Zn–Cl3 113.93(5), N1–C1–Au 128.0(4), N2–Au–Cl1 127.1(4), N1–C1–N2 104.8(5), N3–C9–C10–N4 12.6(5).

second nitrogen atom are in the equatorial positions. In 7 and 8 the M–N bond lengths are strongly unsymmetrical (N3–Zn: 2.261(4), N4–Zn: 2.074(4) Å; N3–Cd: 2.4345(10), N4–Cd: 2.2712(7) Å, while in the similar complexes [(bipy)MCl₂(DMSO)] (M = Zn, Cd) they are almost equidistant (N–Zn: ca. 2.15 Å; N–Cd: ca. 2.34 Å).^[33]

In the absence of DMSO, which could saturate the coordination sphere of Hg in 9, the molecules are aggregated μ -chloro-

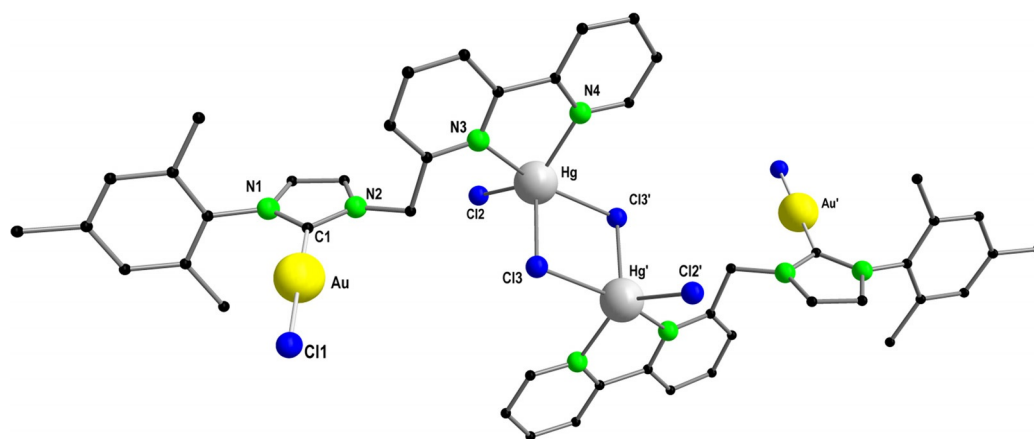


Figure 4. Molecular structure of **9** in the solid state. Hydrogen atoms are omitted for clarity. Intermetallic distance [Å]: Au–Hg 6.827(2). Selected bond lengths [Å] and angles [°]: Au–C1 1.954(10), Au–Cl1 2.285(3), Hg–N3 2.459(8), Hg–N4 2.295(7), Hg–Cl2 2.419(3), Hg–Cl3 2.638(2), N1–C1 1.370(13), N2–C1 1.398(12); C1–Au–Cl1 179.4(3), N3–Hg–N4 70.6(3), N3–Hg–Cl2 101.8(2), N3–Hg–Cl3 84.7(2), N3–Hg–Cl3' 157.8(2), N4–Hg–Cl2 137.7(2), N4–Hg–Cl3 110.5(2), N4–Hg–Cl3' 92.4(2), Cl2–Hg–Cl3 110.07(8), Cl2–Hg–Cl3' 100.32(8), Cl3–Hg–Cl3' 88.20(7), N1–C1–Au 130.3(7), N2–C1–Au 127.9(7), N1–C1–N2 101.8(8), N3–C9–C10–N4 2.2(1).

ride bridged dimers (Figure 4). With two chlorides in the bridging positions, a Hg₂Cl₂ diamond square is formed. The coordination sphere of Hg is saturated with another chloride and the bipyridine moiety, resulting in a distorted trigonal bipyramidal structure around the metal. The axial positions are occupied by one nitrogen and one chlorine atom.

When compound **5** having a pentafluorophenyl substituent at the gold atom is used as a starting material for bimetallic complexes, the results are quite similar to those obtained with its chloride analogue. Reaction of **5** with ZnCl₂, CdCl₂ and HgCl₂ resulted in [(NHC^{Bipy})Au(C₆F₅)(ZnCl₂)] (**10**), [(NHC^{Bipy})Au(C₆F₅)(CdCl₂)₂] (**11**), and, surprisingly, in the chloride species **9** (Scheme 4). Due to better solubility as compared to the gold-chlorido complex, compounds **10** and **11** could be crystallized from acetonitrile instead of DMSO. Single-crystal X-ray analysis revealed the formation of [(NHC^{Bipy})Au(C₆F₅)(ZnCl₂)] (**10**; Figure 5) and [(NHC^{Bipy})Au(C₆F₅)(CdCl₂)₂] (**11**). When **5** was reacted with HgCl₂, the only crystalline material that could be separated was compound **9**, which had formed upon abstraction of the C₆F₅-substituent. The fluorine-containing by-product was not isolated. Again, the NMR spectra remain almost unchanged compared to the starting material. Also, the bond lengths and angles around the gold atom do not notably change. Similar to **7** and **8**, the bipyridine moiety in **10** and **11** is turned away from the carbene function, resulting in long M–M distances (Au–Zn: 6.792(2) Å; Au–Cd: 6.858(2) Å).

Cyclic heterobimetallic complexes

In the next step, we envisioned the synthesis of cyclic heterobimetallic complexes, using bis(NHC)Au-complex **6** as the starting material. In a straightforward procedure, after treatment with one equivalent of [Cu(MeCN)₄][ClO₄], AgClO₄, [Zn(H₂O)₆][ClO₄]₂ or [Cd(H₂O)₆][ClO₄]₂, the products [(NHC^{Bipy})₂AuCu][ClO₄]₂ (**12**), [(NHC^{Bipy})₂AuAg][ClO₄]₂ (**13**), [(NHC^{Bipy})₂AuZn][ClO₄]₃ (**14**) and [(NHC^{Bipy})₂AuCd(MeCN)(ClO₄)][ClO₄]₂ (**15**) could be crystallized (Scheme 5). All products were fully characterized and

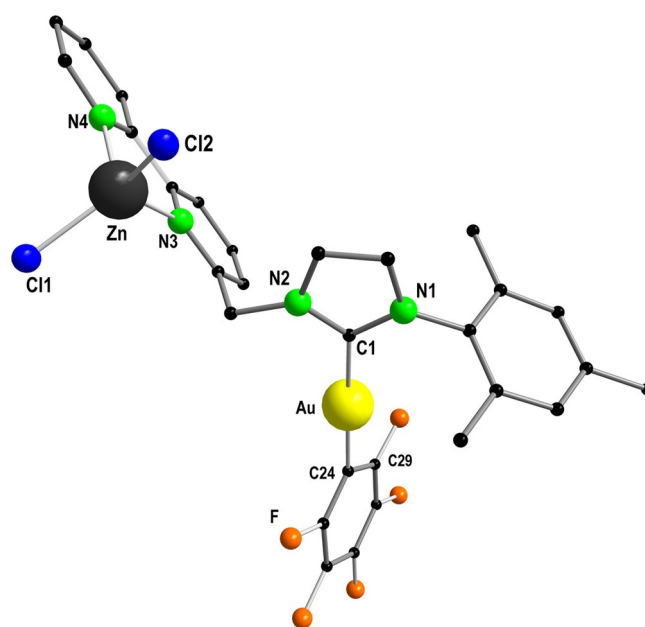
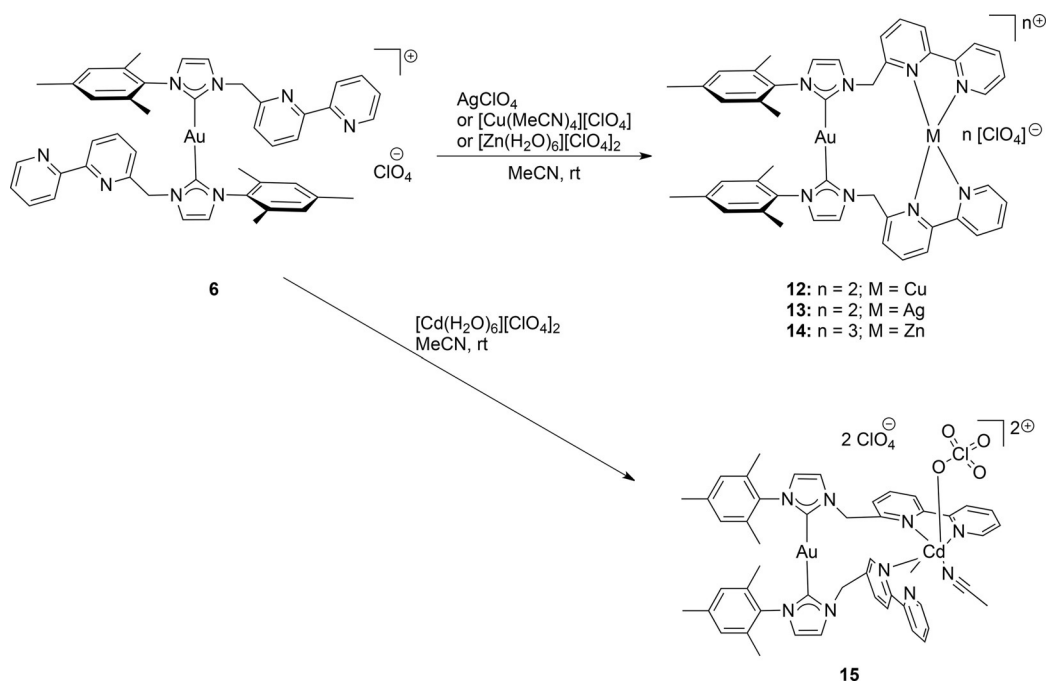


Figure 5. Molecular structure of **10** in the solid state. Hydrogen atoms are omitted for clarity. Intermetallic distance [Å]: Au–Zn 6.971(2). Selected bond lengths [Å] and angles [°]: Au–C1 2.018(5), Au–C24 2.049(5), Zn–N3 2.070(4), Zn–N4 2.022(4), Zn–Cl1 2.221(2), Zn–Cl2 2.172(2), N1–C1 1.347(7), N2–C1 1.359(6); C1–Au–C24 176.4(2), N3–Zn–N4 81.3(2), N3–Zn–Cl1 110.18(12), N3–Zn–Cl2 119.57(13), N4–Zn–Cl1 110.38(14), N4–Zn–Cl2 110.61(14), Cl1–Zn–Cl2 118.55(7), N1–C1–Au 126.1(4), N2–C1–Au 129.4(4), N1–C1–N2 104.1(4), N3–C9–C10–N4 1.4(6), N1–C1–C24–C29 64.0(6).

their solid-state structures were revealed using single-crystal X-ray analysis.

All compounds show the typical, slightly bent linear coordination of the gold atom, with C–Au–C angles between 172.7(3)^o and 178.5(3)^o. The bond lengths lie between 1.994(7) and 2.034(4) Å which are typical values for bis(NHC)Au-complexes.^[34] In each compound, the second metal is nested in the {N₄} pocket of the two bipyridine moieties. The copper ion in **12** (Figure 6, left) shows the expected tetrahedral coordination with N–Cu distances close to 2.0 Å, which is in good agree-



Scheme 5. Synthesis of the heterobimetallic complexes [(NHC^{Bipy})₂AuCu][ClO₄]₂ (**12**), [(NHC^{Bipy})₂AuAg][ClO₄]₂ (**13**), [(NHC^{Bipy})₂AuZn][ClO₄]₃ (**14**) and [(NHC^{Bipy})₂AuCd(MeCN)(ClO₄)][ClO₄]₂ (**15**).

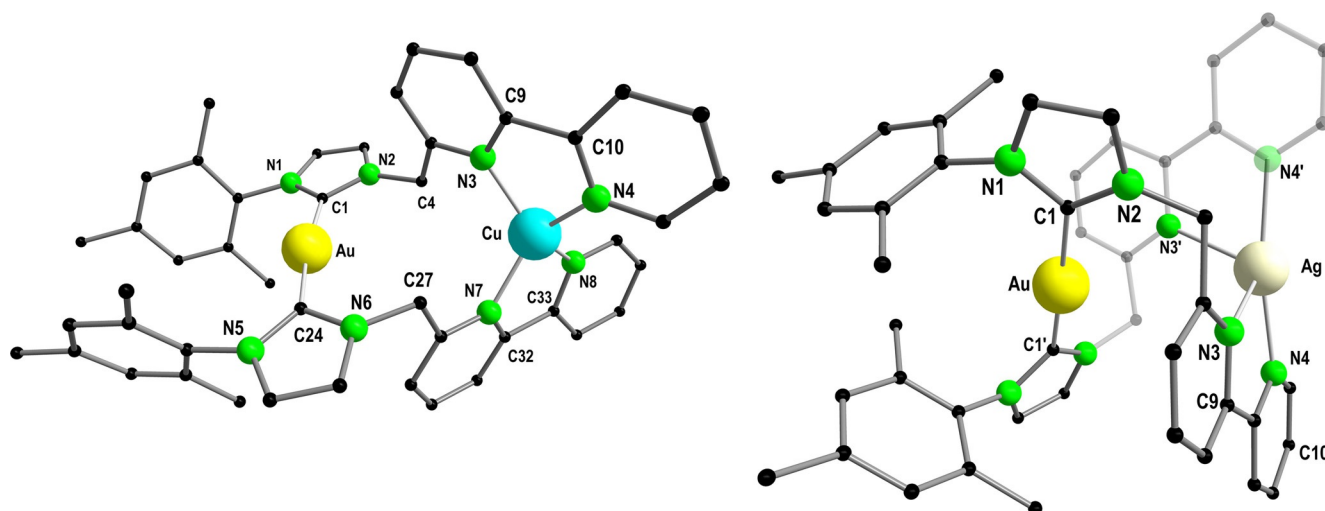


Figure 6. Molecular structure of **12** (left) and **13** (right) in the solid state. Hydrogen atoms are omitted for clarity. Intermetallic distances of **12** and **13** [Å]: Au–Cu 5.09148(11), Au–Ag 4.3205(9). Selected bond lengths [Å] and angles [°] of **12**: Au–C1 1.994(7), Au–C24 1.995(7), Cu–N3 2.042(5), Cu–N4 1.995(6), Cu–N7 2.028(5), Cu–N8 2.036(5), N1–C1 1.363(8), N2–C1 1.358(8), N5–C24 1.366(8), N6–C24 1.362(8); C1–Au–C24 172.7(3), N1–C1–Au 131.3(5), N2–C1–Au 125.7(5), N5–C24–Au 133.3(5), N6–C24–Au 123.3(5), N3–Cu–N4 82.0(2), N3–Cu–N7 117.3(2), N3–Cu–N8 135.3(2), N4–Cu–N7 131.7(2), N4–Cu–N8 116.5(2), N7–Cu–N8 81.7(2), N1–C1–N2 103.0(5), N5–C24–N6 103.1(5), N2–C1–C24–N6 5.6(7), N3–C9–C10–N4 6.4(6), N7–C32–C33–N8 10.6(8). Selected bond lengths [Å] and angles [°] of **13**: Au–C1 2.034(4), Ag–N3 2.415(4), Ag–N4 2.289(4), N1–C1 1.358(6), N2–C1 1.341(7); C1–Au–C1' 178.5(3), N1–C1–Au 125.9(3), N2–C1–Au 129.6(4), N3–Ag–N4 70.75814, N3–Ag–N3' 105.68(18), N3–Ag–N4' 116.30(14), N4–Ag–N4' 169.23(19), N1–C1–N2 104.5(4), N2–C1–C1'–N2' 127.7(4), N3–C9–C10–N4 6.2(4).

ment with the simple [(Bipy)₂Cu][ClO₄] complex.^[35] The Au–Cu distance of 5.0914(11) Å excludes any metallophilic interaction. In **13** (Figure 6, right), the intermetallic Au–Ag distance is much smaller (4.3205(9) Å) but still exceeding the sum of their van der Waals radii (3.4 Å) by far. The coordination of the silver ion is strongly distorted tetrahedral, with Ag situated closely to the centre of a plane defined by N3', N4 and N4' (sum of angles = 356.2°). The almost linear arrangement N4–Ag–N4'

(169.2(2)°) reflects the propensity of silver(I) to adopt low coordination numbers and a linear coordination. In the Au–Zn compound **14**, the zinc ion is again surrounded by the nitrogen atoms of the bipyridine substituents in a tetrahedral fashion with Zn–N bond lengths between 1.99 and 2.08 Å, which is comparable to similar complexes.^[36]

In the Au–Cd complex **15** (Figure 7), the bipyridine moieties are a part of an octahedral coordination of cadmium, which is

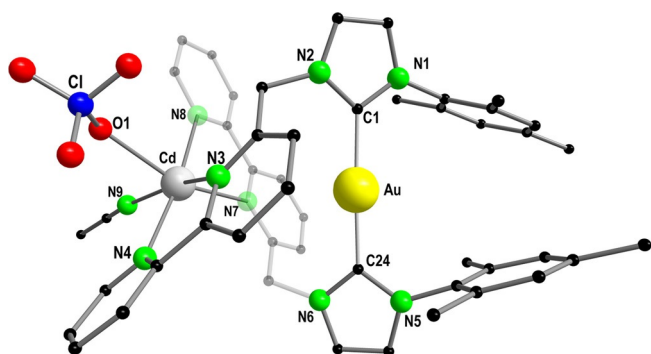


Figure 7. Molecular structure of **15** in the solid state. Hydrogen atoms are omitted for clarity. Intermetallic distance [Å]: Au–Cd 4.553(5). Selected bond lengths [Å] and angles [°]: Au–C1 2.017(4), Au–C24 2.016(4), Cd–O1 2.390(3), Cd–N3 2.370(3), Cd–N4 2.294(3), Cd–N7 2.359(3), Cd–N8 2.329(3), Cd–N9 2.336(4), N1–C1 1.345(5), N2–C1 1.350(5), N5–C24 1.339(5), N6–C24 1.354(5); C1–Au–C24 177.6(2), N1–C1–Au Au1 125.8(3), N2–C1–Au 129.8(3), N5–C24–Au 126.4(3), N6–C24–Au 128.8(3), N3–Cd–N4 71.82(11), N3–Cd–N7 102.92(11), N3–Cd–N8 111.55(11), N3–Cd–N9 160.89(12), N3–Cd–O1 88.87(11), N4–Cd–N7 114.14(11), N4–Cd–N8 172.98(12), N4–Cd–N9 90.27(12), N4–Cd–O1 90.23(11), N7–Cd–N8 71.60(11), N7–Cd–N9 90.27(12), N7–Cd–O1 155.14(12), N8–Cd–O1 83.76(11), N8–Cd–N9 85.56(13), N9–Cd–O1 84.49(12), N1–C1–N2 104.3(3), N5–C24–N6 104.6(3), N2–C1–C24–N6 41.2(2), N3–C9–C10–N4 16.6(1), N7–C32–C33–N8 0.72(8).

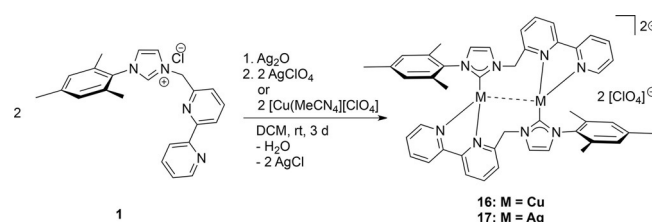
completed by one molecule of acetonitrile and one perchlorate anion. The coordination of perchlorate is somewhat unexpected, as it is considered to be a weakly coordinating anion. However, there are numerous literature reports of comparable cadmium complexes with the metal in an octahedral environment coordinated to at least one perchlorate anion.^[37] In the ¹H NMR spectrum of **15** (in [D₆]DMSO), no acetonitrile is observed, which means that it must have been removed while drying the crystalline sample under vacuum. Powder diffraction also shows that the crystal structure is not retained after drying under vacuum, confirming a change in the crystal lattice upon removal of acetonitrile ligand (Figure S47).

It should be noted that the bimetallic complexes **12–15** show helical chirality: a distinctive axis is defined by the C–Au–C bonding axis, around which the bipyridine strands can be wrapped in left turn or right turn, thus giving rise to helical enantiomers of Δ and Λ configuration. These are present as a racemic mixture in the crystal. In the ¹³C{¹H} NMR spectra, all carbene resonances are seen between 186.6 and 185.8 ppm and therefore are virtually unchanged compared to the starting material. The ¹H spectra of **12** and **13** remain nearly unaffected, whereas for **14** and **15**, all resonances of the imidazole and bipyridine protons are shifted about 0.5 ppm downfield. In the spectrum of the Au–Zn complex **14**, the signals of the methylene protons as well as the *o*-mesityl protons are split into two singlets and significantly broadened. We attribute this to a hindered interconversion of the isomers in solution at room temperature. A similar behavior has been observed before in a heterobimetallic Au–Cu complex of a pyridazine-bridged NHC/pyrazole ligand.^[38] The spectrum of **15** (in [D₃]acetonitrile) also evidences dynamic processes in solution, as the resonances of the methylene protons are massively

broadened over a range from ca. 5.7 to 4.5 ppm. No broadening is observed in [D₆]DMSO. Thus, we conclude that the broad signals in acetonitrile are associated with rearrangement processes in the coordination sphere of cadmium, involving dissociation/association of the acetonitrile ligand.

Homobimetallic complexes

To complete the series of bimetallic d¹⁰ metal compounds of NHC^{Bipy} we sought to synthesize homometallic complexes of this ligand. After reaction of the imidazoliumchloride with silver oxide, anion exchange can be achieved by adding two equivalents of AgClO₄ (Scheme 6). Crystallization through slow diffusion of diethylether into an acetonitrile solution yields the product [(NHC^{Bipy})₂Ag₂][ClO₄]₂ (**17**) as colourless crystals. In the same way, red crystals of [(NHC^{Bipy})₂Cu₂][ClO₄]₂ (**16**) can be obtained after transmetalation with [Cu(MeCN)₄][ClO₄]. Both compounds are air stable as solids but slowly decompose in wet solvents.



Scheme 6. Synthesis of the homobimetallic complexes [(NHC^{Bipy})₂Cu₂][ClO₄]₂ (**16**) and [(NHC^{Bipy})₂Ag₂][ClO₄]₂ (**17**).

In the ¹H NMR spectra of **16** and **17**, the signals of the ligand are seen between 8.11–7.41 ppm and show strongly overlapping multiplets, making a clear assignment impossible. The carbene resonance in the ¹³C{¹H} spectrum of the copper complex **16** is seen at 181.6 ppm, which is a typical value for this type of compounds.^[17,18,24] The carbene signal of the silver complex **17** could not be detected in a 1D NMR experiment, but was clearly identified in the HMBC spectrum at 183.2 ppm. In the solid-state, **16** and **17** are head-to-tail connected dimers with the metal coordinated to the carbene and the bipyridine of the neighboring ligand (Figure 8 and S46).

This results in a trigonal planar environment with a sum of angles of exactly 360°. The M–C distances in **16** are 1.890(3)/1.882(2) Å which matches the values of similar copper compounds (Figure S45),^[17] whereas in the silver complex **17** the Ag–C bond lengths (2.042(7)/2.045(7) Å) are about 3–4 pm shorter than in similar complexes reported in literature.^[16,39] Despite the larger van der Waals radius, the silver complex shows a smaller intermetallic distance (3.1034(11) Å) than the copper homologue (3.2168(9) Å). Since both are isostructural and crystallize in the same space group *P2₁/c*, a higher tendency of silver to form metallophilic contacts rather than packing effects seems to account for this observation.

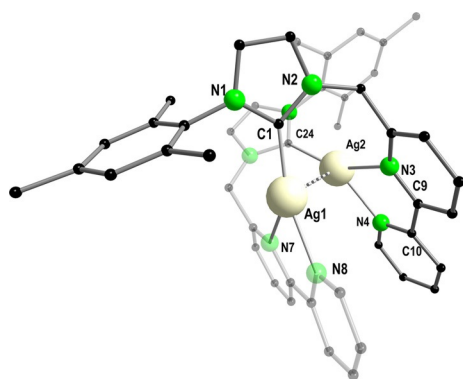


Figure 8. Molecular structure of **17** in the solid state. Hydrogen atoms are omitted for clarity. Intermetallic distance [Å]: Ag1–Ag 2 3.1034(11). Selected bond lengths [Å] and angles [°]: Ag1–C1 2.045(7), Ag1–N7 2.359(6), Ag1–N8 2.237(6), Ag2–C24 2.043(7), Ag2–N3 2.331(7), Ag2–N4 2.259(6), N1–C1 1.355(8), N2–C1 1.377(8); C1–Ag1–N7 140.3(3), C1–Ag1–N8 147.8(3), N7–Ag1–N8 71.9(2), N1–C1–Ag1 126.1(4), N2–C1–Ag1 132.1(5), C24–Ag2–N3 146.6(3), C24–Ag2–N4 142.0(3), N3–Ag2–N4 71.4(3), C1–Ag1–Ag2 91.11(17), C24–Ag2–Ag1 96.3(2), N1–C1–N2 101.8(6), N3–C9–C10–N4 12.5(6), N7–C32–C33–N8 8.3(6).

Photoluminescence properties

All complexes described above with the exception of **12** and **16** are colorless crystalline powders, that is, they possess strong absorption transitions only in the UV spectral region. This also holds for the absorption of selected complexes in solution (Figure S48). The monometallic gold (**4–6**) and open-chain bimetallic gold–zinc (**7, 10**) compounds demonstrate rather similar photoluminescence (PL) properties in the solid state, despite of the different motifs of the carbene–gold units. These include a weak UV emission at ≈ 360 nm (except for **7** in which this band is dominant) and a moderately intense at temperatures below ≈ 100 K, vibronically structured, greenish emission around 480 nm (Figure 9). The wavelengths of the vibronic peaks of these and other compounds (see below) are listed in Table S5. These features roughly conform to the PL of the solid ligand compound **1** (Figure S48, Supporting Information). The visible emission broadens and strongly decreases in intensity by increasing the temperature (practically absent for **4, 6, 7** at ambient temperature). The excitation (PLE) spectra of **4–7, 10** are similar and show the onset of absorption at about 350 nm, corresponding to the colorless appearance of the compounds. The UV emission excited by nanosecond laser pulses at 266 nm decays faster than ≈ 10 nsec as limited by the time resolution of our apparatus (see experimental details in the Supporting Information) and can be assigned to fluorescence. Decay traces of the visible emission include minor nanosecond and major (sub)microsecond components, with the latter becoming more pronounced at longer emission wavelengths (as shown exemplary for **7** and **10** in Figure S50).

Based on the decay kinetics and large Stokes shift, the visible band can be assigned to phosphorescence. Both emission bands likely arise from the bipyridine moieties in the NHC^{Bipy} complexes. The above PL signatures roughly match spectrally those observed for bipyridine in solution, sol–gel glasses and polymers.^[40] Regarding the UV fluorescence, there might also be some contribution of the NHC groups. Indeed, a low-tem-

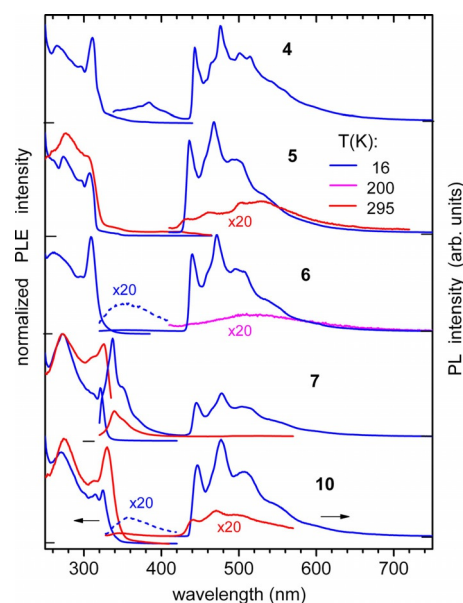


Figure 9. Photoluminescence emission (PL) and excitation (PLE) spectra of solid (crystalline) monometallic Au^I (**4, 5, 6**) and open-chain bimetallic AuZn complexes (**7, 10**), respectively, at different temperatures. The emission was excited at 300 nm. The PLE spectra were recorded at 500 nm at $T = 16$ K and at 540 nm for **5, 6**, 350 nm for **7**, and 500 nm for **10** at elevated temperatures.

perature PL at about 400 nm has been observed and attributed to these groups in the dinuclear Au^I complex with similar NHC groups and absent Au–Au interaction.^[41] Note that the coordination of bipyridine (and fixing its planar geometry) with ZnCl₂(DMSO) in **7** strongly enhances the UV fluorescence both at low and ambient temperatures (Figure 9). However, the corresponding emission in the closely related complex **10** remains for some reasons weak. In difference to the similar PL of the monometallic and open-chain compounds, the cyclic bimetallic complexes with gold, silver, zinc and copper (**12–14, 16, 17**) show more diverse PL properties (Figures 10, S50 and S51), which partly may be a result of cooperative effects.

These complexes emit no detectable UV fluorescence. The well-structured visible PL of AuZn complex **14**—with zinc coordinating both bipyridine units—resemble those of the monometallic and open-chain complexes and can also be ascribed to the bipyridine-centered phosphorescence (Figure 10). However, in contrast to the fast phosphorescence of the latter, emission of **14** is long-living with a lifetime of 1.7 msec at 16 K (Figure S50). The minor contributions of the fast bipyridine emission are seen in the low-temperature spectra of **13** and **17**. The major PL component is, however, a broad orange–red phosphorescence at about 550–600 nm. It decays within few microseconds in **13**, both at low and elevated temperatures. In **17**, the PL kinetics is complicated and unusual. Its decay traces extend over broad time scales and can only be well fit by at least three exponential components. The slow component is dominating at 16 K and has a lifetime as long as 23 msec. However, the PL decay accelerates strongly by increasing the temperature and proceeds within tens of microseconds at 295 K (Figure S50). We tentatively assign the phosphorescence of **13** and **17** to excitations in the Ag–bipyridine groups. Metal-

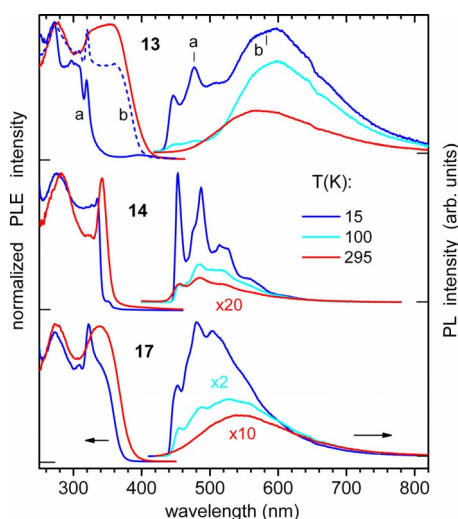


Figure 10. Photoluminescence emission (PL) and excitation (PLE) spectra of solid (polycrystalline) bimetallic complexes **13** (Au–Ag), **14** (Au–Zn), and **17** (Ag–Ag). The PL and PLE spectra were excited at 300 nm and recorded at 480 (a), 580 (b)/580 (**13**), 520/520 (**14**) and 550/550 nm (**17**) at 15/ 295 K, respectively.

lophilic Ag–Ag interactions in **17** (see above) might conceivably contribute to the unusual PL kinetics observed for this complex.

The NHC^{Bipy} complexes described above emit only moderately/ weakly at ambient temperature, with **10**, **14** and **17** being the “strongest” emitters. PL efficiency of **17** was determined by using an integrating sphere and excitation at 350 nm to be 0.4% at ambient temperature. It increases up to about 9% at $T = 15$ K, as can be estimated from Figure 10.

The cyclic bimetallic copper AuCu and CuCu complexes **12** and **16** are dark red and red solids, respectively (producing yellow solutions in DCM or MeCN with absorption at ≈ 450 nm, Figure S48), thus indicating a significant lowering of the HOMO–LUMO gap in these compounds, presumably via a HOMO contribution of the d-orbitals of copper. Compounds **12** and **16** demonstrate very efficient non-radiative electronic relaxation: no PL and only very weak broad near-infrared emission at ≈ 800 nm (Figure S51) were detected for **16** and **12**, respectively. The PLE spectrum of the NIR emission reveals the onset of absorption at ≈ 700 nm and absorption bands at about 450 and 600 nm, in accordance with the dark-red color of **12**.

Finally, we note that only very weak PL was observed for the UV-excited complexes in solution at ambient temperature. **4–6** and **13** only show an UV emission at ≈ 350 nm; **7**, **10** and **14** also display a visible emission roughly corresponding to that observed in the solid state, as illustrated for selected compounds in Figure S52. No NIR emission could be detected for **12** in MeCN.

Collision induced dissociation

Upon electrospraying MeCN solutions of $[(\text{NHC}^{\text{Bipy}})_2\text{AuM}][\text{ClO}_4]_2$ salts **12** and **13** the major species is observed at m/z 905, corresponding to a loss of M^+ (ESI-MS of complexes **12** and **13**,

see experimental details). In addition, the molecular dications $[(\text{NHC}^{\text{Bipy}})_2\text{AuM}]^{2+}$ at m/z 484 ($\text{M} = \text{Cu}$) and m/z 506 ($\text{M} = \text{Ag}$) are discernible, respectively.

In order to gain insights into the relative metal–ligand bond strengths a collision-induced dissociation (CID) study was conducted in an ion-trap mass spectrometer. We found that CID of isolated $[(\text{NHC}^{\text{Bipy}})_2\text{AuM}]^{2+}$ ($\text{M} = \text{Cu}$, Ag) precursor ions exclusively leads to ionic fragmentation (charge separation) into two monocationic $[(\text{NHC}^{\text{Bipy}})\text{Au}]^+$ and $[(\text{NHC}^{\text{Bipy}})\text{M}]^+$ moieties (Figure 11). No neutral loss fragmentation pathways are observed. Correspondingly, one Au–C and two M–N bonds are dissociated. A comparison of the CID appearance curves clearly shows that $[(\text{NHC}^{\text{Bipy}})_2\text{AuCu}]^{2+}$ is more stable than $[(\text{NHC}^{\text{Bipy}})_2\text{AuAg}]^{2+}$ reflecting the difference in collisional energy necessary to achieve fragmentation (Figure 12). This

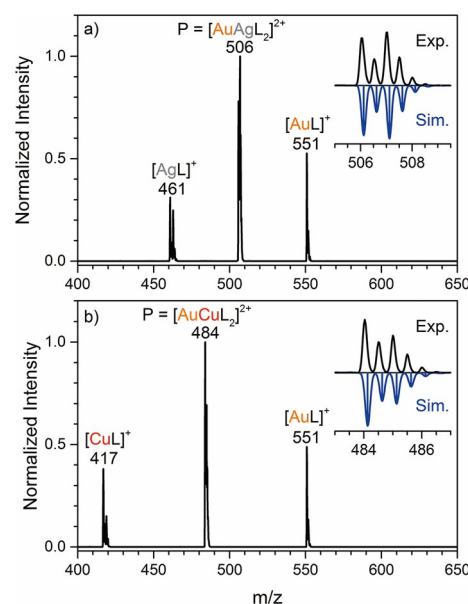


Figure 11. Collision-induced dissociation mass spectra of a) $[(\text{NHC}^{\text{Bipy}})_2\text{AuAg}]^{2+}$ ($m/z = 506$) and b) $[(\text{NHC}^{\text{Bipy}})_2\text{AuCu}]^{2+}$ ($m/z = 484$) precursor ions (P) at excitation amplitudes of ≈ 0.9 V. Nominal integer masses are indicated. The ligand NHC^{Bipy} is abbreviated as L. Insets show experimental (black) and simulated (blue, Gaussian broadened $m/z = 0.2$ fwhm, full width at half maximum) isotope patterns of isolated precursor ions at zero excitation amplitude.

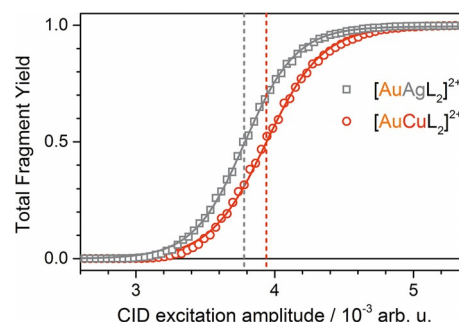


Figure 12. Collision-induced dissociation (CID) appearance curves comparing total fragment yields of $[(\text{NHC}^{\text{Bipy}})_2\text{AuAg}]^{2+}$ (gray squares) and $[(\text{NHC}^{\text{Bipy}})_2\text{AuCu}]^{2+}$ (red circles) as a function of CID excitation amplitude (Amp_{COM}). Dashed vertical lines indicate 50% fragment yield amplitude values as extracted from sigmoidal fits (solid lines).

can be correlated to the different affinity of the d^{10} metal ions (Cu^+ vs. Ag^+) to the $\{\text{N}_4\}$ bipyridine pocket of the complexes which qualitatively follows the predictions of the HSAB concept.^[13,14]

Conclusion

We investigated the coordination chemistry of NHC^{Bipy} in mono- and bimetallic d^{10} metal complexes. Silver complexes were obtained by the silver oxide route, which led to the species $[(\text{NHC}^{\text{Bipy}})\text{AgCl}]_n$ or $[(\text{NHC}^{\text{Bipy}})_2\text{Ag}]\text{Cl}$, depending on the solvent. The silver complexes proved to be suitable transmetallation reagents for the synthesis of gold(I) complexes. Open-chain bimetallic complexes were synthesized by coordination of ZnCl_2 , CdCl_2 and HgCl_2 to the bipyridine substituents of the gold chlorido- and pentafluorophenyl complexes. A second metal could also be introduced to the $\text{bis}(\text{NHC})\text{Au}$ complex, resulting in cyclic bimetallic complexes, with the second metal being chelated in the $\{\text{N}_4\}$ pocket of the two bipyridine moieties. In all cases, the binding parameters of the gold center remained unchanged. Although the NHC^{Bipy} ligands show a notable flexibility and are able to provide a linear, tetrahedral or octahedral coordination environment to a second metal center, no metallophilic interactions was observed in the heterometallic complexes. Two homobimetallic complexes of copper and silver were characterized, in which two ligands are bridged in head-to-tail fashion by two metal ions. In contrast to the copper species, the silver compound shows a short intermetallic distance of 3.1034(11) Å, reflecting a stronger tendency of silver to form metallophilic contacts. The photoluminescence (PL) of the mono- and open-chain bimetallic complexes in the solid (polycrystalline) state is quite similar and may be ascribed to the bipyridine moieties. In contrast, the cyclic bimetallic compounds feature different PL properties, depending on the metals involved. Ion trap collision-induced dissociation experiments revealed a higher affinity of the $\{\text{N}_4\}$ pocket to Cu^+ compared to Ag^+ cations based on the relative gas phase stabilities of $[(\text{NHC}^{\text{Bipy}})_2\text{AuM}]^{2+}$ ($\text{M} = \text{Cu}, \text{Ag}$) species, in accordance with the HSAB concept.

Experimental Section

Experimental details are given in the Supporting Information.

Acknowledgements

Financial support by the DFG-funded transregional collaborative research center SFB/TRR 88 "Cooperative Effects in Homo and Heterometallic Complexes (3MET)" is gratefully acknowledged (projects C3, C4 and C7). C.K. thanks the Helmholtz research school "Energy-Related Catalysis" for generous fellowships. Dr. Michael Gamer is acknowledged for designing the cover picture.

Conflict of interest

The authors declare no conflict of interest.

Keywords: coinage metals • metallophilicity • N-heterocyclic carbenes • photoluminescence • silver

- [1] a) F. Scherbaum, A. Grohmann, B. Huber, C. Krüger, H. Schmidbaur, *Angew. Chem. Int. Ed. Engl.* **1988**, *27*, 1544; *Angew. Chem.* **1988**, *100*, 1602; b) H. Schmidbaur, A. Schier, *Chem. Soc. Rev.* **2008**, *37*, 1931; c) H. Schmidbaur, A. Schier, *Chem. Soc. Rev.* **2012**, *41*, 370.
- [2] P. Pyykkö, *Chem. Rev.* **1997**, *97*, 597.
- [3] a) J.-M. Poblet, M. Benard, *Chem. Commun.* **1998**, 1179; b) M. A. Carvajal, S. Alvarez, J. J. Novoa, *Chem. Eur. J.* **2004**, *10*, 2117.
- [4] a) H. Schmidbaur, A. Schier, *Angew. Chem.* **2015**, *127*, 756; b) S. V. Kruppa, F. Bäßler, W. Klopfer, S. P. Walg, W. R. Thiel, R. Diller, C. Riehn, *Phys. Chem. Chem. Phys.* **2017**, *19*, 22785.
- [5] H. Schmidbaur, A. Schier, *Organometallics* **2015**, *34*, 2048.
- [6] a) J.-X. Chen, W.-H. Zhang, X.-Y. Tang, Z.-G. Ren, H.-X. Li, Y. Zhang, J.-P. Lang, *Inorg. Chem.* **2006**, *45*, 7671; b) R. Donamaria, M. C. Gimeno, V. Lippolis, J. M. López-de-Luzuriaga, M. Monge, M. E. Olmos, *Inorg. Chem.* **2016**, *55*, 11299; c) R. V. Bojan, R. Czerwieńnik, A. Laguna, T. Lasanta, J. M. Lopez-de-Luzuriaga, M. Monge, M. E. Olmos, H. Yersin, *Dalton Trans.* **2013**, *42*, 4267; d) E. J. Fernández, A. Laguna, J. M. Lopez-de-Luzuriaga, M. Monge, M. Montiel, M. E. Olmos, M. Rodríguez-Castillo, *Dalton Trans.* **2009**, 7509; e) C. E. Strasser, V. J. Catalano, *J. Am. Chem. Soc.* **2010**, *132*, 10009.
- [7] a) M. Baya, ú. Belío, I. Fernández, S. Fuertes, A. Martín, *Angew. Chem.* **2016**, *128*, 7092; b) J. Moussa, L. M. Chamoreau, M. P. Gullo, A. Degli Esposti, A. Barbieri, H. Amouri, *Dalton Trans.* **2016**, *45*, 2906.
- [8] E. J. Fernández, J. M. López-de-Luzuriaga, M. Monge, M. E. Olmos, J. Pérez, A. Laguna, A. A. Mohamed, J. P. Fackler, *J. Am. Chem. Soc.* **2003**, *125*, 2022.
- [9] a) V. W. Yam, K. K. Lo, *Chem. Soc. Rev.* **1999**, *28*, 323; b) V. W.-W. Yam, E. C.-C. Cheng, *Chem. Soc. Rev.* **2008**, *37*, 1806; c) Z.-N. Chen, N. Zhao, Y. Fan, J. Ni, *Coord. Chem. Rev.* **2009**, *253*, 1; d) E. R. T. Tiekink, J.-G. Kang, *Coord. Chem. Rev.* **2009**, *253*, 1627; e) V. W.-W. Yam, K. M.-C. Wong, *Chem. Commun.* **2011**, *47*, 11579; f) X. He, V. W.-W. Yam, *Coord. Chem. Rev.* **2011**, *255*, 2111; g) V. W.-W. Yam, V. K.-M. Au, S. Y.-L. Leung, *Chem. Rev.* **2015**, *115*, 7589.
- [10] S. Bestgen, M. T. Gamer, S. Lebedkin, M. M. Kappes, P. W. Roesky, *Chem. Eur. J.* **2015**, *21*, 601.
- [11] a) T. Simler, P. Braunstein, A. A. Danopoulos, *Dalton Trans.* **2016**, *45*, 5122; b) P. Ai, A. A. Danopoulos, P. Braunstein, K. Y. Monakhov, *Chem. Commun.* **2014**, *50*, 103; c) P. Ai, A. A. Danopoulos, P. Braunstein, *Inorg. Chem.* **2015**, *54*, 3722.
- [12] a) P. Ai, M. Mauro, L. De Cola, A. A. Danopoulos, P. Braunstein, *Angew. Chem.* **2016**, *128*, 3399; b) P. Ai, M. Mauro, C. Gourlaouen, S. Carrara, L. de Cola, Y. Tobon, U. Giovanella, C. Botta, A. A. Danopoulos, P. Braunstein, *Inorg. Chem.* **2016**, *55*, 8527.
- [13] R. G. Pearson, *J. Am. Chem. Soc.* **1963**, *85*, 3533.
- [14] R. G. Pearson, *Inorg. Chim. Acta* **1995**, *240*, 93.
- [15] a) J. Nitsch, F. Lacomon, A. Lorbach, A. Eichhorn, F. Cisnetti, A. Steffen, *Chem. Commun.* **2016**, *52*, 29332; b) T. Wagner, A. Pöthig, H. M. S. Augenstein, T. D. Schmidt, M. Kaposi, E. Herdtweck, W. Brütting, W. A. Herrmann, F. E. Kühn, *Organometallics* **2015**, *34*, 1522; c) L. B. Munro, V. J. Catalano, *Eur. J. Inorg. Chem.* **2014**, *2014*, 4994; d) V. J. Catalano, L. B. Munro, C. E. Strasser, A. F. Samin, *Inorg. Chem.* **2011**, *50*, 8465; e) B. Liu, W. Chen, S. Jin, *Organometallics* **2007**, *26*, 3660.
- [16] B. Liu, M. Liu, H. Wu, W. Chen, *J. Organomet. Chem.* **2014**, *772–773*, 113.
- [17] B. Liu, C. Chen, Y. Zhang, X. Liu, W. Chen, *Organometallics* **2013**, *32*, 5451.
- [18] S. Gu, J. Huang, X. Liu, H. Liu, Y. Zhou, W. Xu, *Inorg. Chem. Commun.* **2012**, *21*, 168.
- [19] C. Kaub, S. Lebedkin, S. Bestgen, R. Koppe, M. M. Kappes, P. W. Roesky, *Chem. Commun.* **2017**, *53*, 9578.
- [20] a) S. V. Kruppa, Y. Nosenko, M.-O. Winghart, S. P. Walg, M. M. Kappes, C. Riehn, *Int. J. Mass Spectrom.* **2016**, *395*, 7; b) J. Lang, M. Cayir, S. P. Walg,

- P. Di Martino-Fumo, W. R. Thiel, G. Niedner-Schatteburg, *Chem. Eur. J.* **2016**, *22*, 2345.
- [21] E. Fogler, E. Balaraman, Y. Ben-David, G. Leitus, J. W. Shimon, Linda, D. Milstein, *Organometallics* **2011**, *30*, 3826.
- [22] H. M. J. Wang, I. J. B. Lin, *Organometallics* **1998**, *17*, 972.
- [23] a) E. Caytan, S. Roland, *Organometallics* **2014**, *33*, 2115; b) H.-L. Su, L. M. Pérez, S.-J. Lee, J. H. Reibenspies, H. S. Bazzi, D. E. Bergbreiter, *Organometallics* **2012**, *31*, 4063.
- [24] J. C. Y. Lin, R. T. W. Huang, C. S. Lee, M. Bhattacharyya, W. S. Hwang, I. J. B. Lin, *Chem. Rev.* **2009**, *109*, 3561.
- [25] J. Rieb, B. Dominelli, D. Mayer, C. Jandl, J. Drechsel, W. Heydenreuter, S. A. Sieber, F. E. Kuhn, *Dalton Trans.* **2017**, *46*, 2722.
- [26] G. A. Bowmaker, Effendy, S. Marfuah, B. W. Skelton, A. H. White, *Inorg. Chim. Acta* **2005**, *358*, 4371.
- [27] C. R. Groom, I. J. Bruno, M. P. Lightfoot, S. C. Ward, *Acta Crystallogr. Sect. B* **2016**, *72*, 171.
- [28] A. Collado, A. Gomez-Suarez, A. R. Martin, A. M. Z. Slawin, S. P. Nolan, *Chem. Commun.* **2013**, *49*, 5541.
- [29] A. Johnson, M. C. Gimeno, *Chem. Commun.* **2016**, *52*, 9664.
- [30] C. Hemmert, A. Fabié, A. Fabre, F. Benoit-Vical, H. Gornitzka, *Eur. J. Med. Chem.* **2013**, *60*, 64.
- [31] P. de Frémont, N. M. Scott, E. D. Stevens, S. P. Nolan, *Organometallics* **2005**, *24*, 2411.
- [32] L. Falivene, R. Credendino, A. Poater, A. Petta, L. Serra, R. Oliva, V. Scarano, L. Cavallo, *Organometallics* **2016**, *35*, 2286.
- [33] a) L. Hashemi, M. Hosseinifard, V. Amani, A. Morsali, *J. Inorg. Organomet. Polym.* **2013**, *23*, 519; b) K. Marjani, M. Mousavi, H. R. Khavasi, M. Ansari, H. R. Qumi, *Acta Crystallogr. Sect. E* **2007**, *63*, m2645.
- [34] a) O. Santoro, F. Lazreg, D. B. Cordes, A. M. Z. Slawin, C. S. J. Cazin, *Dalton Trans.* **2016**, *45*, 4970.
- [35] M. Munakata, S. Kitagawa, A. Asahara, H. Masuda, *Bull. Chem. Soc. Jpn.* **1987**, *60*, 1927.
- [36] Q.-Q. Xu, D.-H. Wang, S.-M. Chi, X. Gan, W.-F. Fu, *Inorg. Chim. Acta* **2009**, *362*, 2529.
- [37] a) L. M. Gruia, F. D. Rochon, A. L. Beauchamp, *Inorg. Chim. Acta* **2007**, *360*, 1825; b) Z. R. Ranjbar, A. Morsali, L.-G. Zhu, *J. Coord. Chem.* **2007**, *60*, 667.
- [38] J. Wimberg, S. Meyer, S. Dechert, F. Meyer, *Organometallics* **2012**, *31*, 5025.
- [39] J. Wimberg, U. J. Scheele, S. Dechert, F. Meyer, *Eur. J. Inorg. Chem.* **2011**, *2011*, 3340.
- [40] a) G. Qian, M. Wang, *Mater. Lett.* **2002**, *56*, 71; b) A. Harriman, *J. Photochem.* **1978**, *8*, 205; c) U.-W. Grummt, E. Birkner, M. Al-Higari, D. A. M. Egbe, E. Klemm, *J. Fluoresc.* **2001**, *11*, 41.
- [41] T. P. Pell, B. D. Stringer, C. Tubaro, C. F. Hogan, D. J. D. Wilson, P. J. Barnard, *Eur. J. Inorg. Chem.* **2017**, *2017*, 3661.

Manuscript received: December 5, 2017

Accepted manuscript online: January 26, 2018

Version of record online: February 28, 2018

Curriculum Vitae

Personal Details

Name	Kruppa
Given Name	Sebastian Volker
Nationality	German

Education

04/2015 – today	PhD student at TUK (physical chemistry dept.)
04/2008 – 09/2014	Studies in chemistry at TUK Diploma degree in chemistry (Dipl.-Chem., grade 1.0), Title of thesis: „ <i>Ultrafast photodynamics of dianionic Tetrakis(μ-pyrophosphito)diplatin(II) complexes in gas phase</i> “
04/2007 – 12/2008	Civilian service, Westpfalz-Klinikum, Kaiserslautern
08/1998 – 03/2007	Sickingen-Gymnasium, Landstuhl School degree: Abitur

TUK: Technische Universität Kaiserslautern (Germany)

Teaching Experience

SS (2017, 2018)	Training supervisor for exercises to the lecture „Thermodynamik und Kinetik, PC I für LA, LM und WI-Chem“
WS (2017/18, 2018/19)	Training supervisor for exercises to the lecture „Atom- und Molekülbau, Spektroskopie und Elektrochemie, PCII für LA, LM und WI-Chem“
2016-2019	Technical support and scientific advice for 4 research internships

Technical support and scientific advice for diploma and bachelor theses:

- WS 2016/17 „Massenspektrometrische Untersuchung von kationischen Ag/Au-Phosphinkomplexen und deren Halogenidaddukten“
Bachelor thesis of Michael Borchers
- 01-09/2017 „Charakterisierung von homo- und heterometallischen (Cu, Ag, Au) Phosphinkomplexen mittels Stoßinduzierter Dissoziation (CID) und Infrarot-Multiphotonen Dissoziation (IRMPD)“
Diploma thesis of Björn Kwasigroch
- WS 2017/18, SS 2018 „UV-Photodissoziationsspektroskopie und massenspektrometrische Untersuchungen an Tris(3-(pyridin-2-yl)pyrazol) ruthenium(II) Münzmetall(M)-Komplexen und ihren (M/H)-Kongeneren“
Bachelor thesis of Marcel J. P. Schmitt
- SS 2019 „In situ-Synthese und massenspektrometrische Untersuchung multinuklearer Münzmetallkomplexe“
Bachelor thesis of Isabel Manes

SS: summer semester, WS: winter semester

Academic working experiences

- 04/2017 – 12/2020 Scientific staff member at physical chemistry dept. TUK (67% position, 26 h/w, funded by 3MET, project C4).
- 12/2014 – 03/2017 Graduate research assistant in the group of Priv.-Doz. Dr. Christoph Riehn, (10 h/w), TUK
- 07/2012 – 02/2013 Undergraduate research assistant in the group of Prof. Dr. Markus Gerhards, TUK

„3MET“: DFG funded Transregional Collaborative Research Center (SFB/TRR 88), „Cooperative Effects in Homo- and Heterometallic Complexes“

Research Visits

05/2019 Beam time at the Free Electron Laser for Infrared eXperiments (FELIX) facility, Nijmegen, Netherlands (FELIX-2 beam-line, may 2019).

Languages

German: fluent (mother tongue)

English: fluent

Supplementary qualifications

Attended course (certificate): MATLAB Fundamentals (MathWorks training services), TUK, Kaiserslautern, 11/2014.

Attended course (certificate): Vakuumtechnology (OPTIMAS course program), TUK - IFOS, Kaiserslautern 02-03/2015.

Awards and Grants

Poster Prize: 2nd International Conference in Bimetallic Complexes 2013 (3MET), Karlsruhe, 23-25.09.2013, KIT, Karlsruhe, Germany

Travel Grant: Mobility funding from the TU Nachwuchsring for “XX International Conference on Ultrafast Phenomena (UP 2016), 2016, Santa Fe, USA”

Travel Grant: Mobility funding from the TU Nachwuchsring for “XXI International Conference on Ultrafast Phenomena (UP 2018), 2018, Hamburg, Germany”

KIT: Karlsruhe Institute of Technology

Oral Presentations

2016

S. V. Kruppa, „Ultrafast vibrational and electronic dynamics of metal-metal interactions studied by transient photofragmentation in gas phase“

1. *Promovierendenseminar des Fachbereichs Chemie (TUK)*,
22.09.2016, Kaiserslautern Germany

Poster Presentations

2013

S. Kruppa, Y. Nosenko, C. Riehn, “Photodynamics of [HAgPt₂(POP)₄]²⁻ investigated by femtosecond pump – probe photofragmentation in gas phase”

2nd International Conference in Bimetallic Complexes 2013 (3MET), 23-25.09.2013, Karlsruhe, Germany.

2014

S. Kruppa, Y. Nosenko, C. Riehn, B. Burgard, F. Rupp, R. Diller, „Photodynamics of [HAgPtPOP]²⁻ and [Ag₂PtPOP]²⁻“

Bunsentagung 2014 (113th General Assembly of the German Bunsen Society for Physical Chemistry), 29-31.05.2014, Hamburg, Germany.

2015

S. Kruppa, B. Burgard, D. Maué, Y. Nosenko, F. Rupp, F. Liedy, R. Diller, C. Riehn, „Ultrafast photodynamics of multimetallic Ag(I) and Pt(II) complexes: gas phase and solution“

Femto 12, The Hamburg Conference on Femtochemistry (Frontiers of ultrafast phenomena in physics, chemistry and biology), 12-17.07.2015, Hamburg, Germany.

2016

S. V. Kruppa, F. Böppler, Y. Nosenko, S. P. Walg, R. Diller, C. Riehn, „Ultrafast Vibrational and Electronic Dynamics of Metal-Metal Interactions Studied by Transient Photo-Induced Dissociation (Gas Phase) and Transient Absorption (Solution)“

XX International Conference on Ultrafast Phenomena (UP 2016), 17-22.07.2016, Santa Fe, USA.

S. V. Kruppa, F. Böppler, S. P. Walg, Y. Nosenko, R. Diller, C. Riehn, „Ultrafast Vibrational and Electronic Dynamics of Meta-Metal Interaction Studied by Transient Photo-Induced Dissociation (Gas Phase) and Transient Absorption (Solution)“

3rd International Conference on Bimetallic Complexes 2016 (3MET), 05-07.10.2016, Kaiserslautern, Germany.

2017

S. V. Kruppa, F. Böppler, Y. Nosenko, S. P. Walg, R. Diller, W. Klopper, C. Riehn, „Ultrafast Vibrational and Electronic Dynamics of Coinage Metal-Phosphine Complexes in an Ion Trap and in Solution“

Bunsentagung 2017 (116th General Assembly of the German Bunsen Society for Physical Chemistry), 25-27.05.2017, Kaiserslautern, Germany.

S. V. Kruppa, F. Böppler, Y. Nosenko, S. P. Walg, R. Diller, W. Klopper, C. Riehn, „Ultrafast electronic dynamics of bridged, binuclear Ag/Au-phosphine complexes in an ion trap and in solution“

28th International Conference on Photochemistry (ICP 2017), 16-21.07.2017 Strasbourg, France.

2018

S. V. Kruppa, F. Böppler, C. Holzer, R. Diller, W. Klopper, C. Riehn,
„Excited State Vibrational Coherence in a Binuclear Metal Adduct:
Wave Packet Phase Dependent Molecular Fragmentation Under
Variation of Ligand Size“

XXI International Conference on Ultrafast Phenomena (UP 2018), 15-
20.07.2018, Hamburg, Germany.

Eidesstattliche Erklärung

Hiermit bestätige ich, Dipl.-Chem. Sebastian Volker Kruppa, dass die vorliegende Arbeit gemäß der Promotionsordnung des Fachbereichs Chemie der Technischen Universität Kaiserslautern selbstständig und unter der Verwendung der angegebenen Quellen und Hilfsmitteln angefertigt wurde.

Kaiserslautern, den

Sebastian Kruppa

